Oil & Natural Gas Technology

DOE Award No.: DE-FC26-03NT15408

Final Technical Report

Fundamentals of reservoir surface energy as related to surface properties, wettability, capillary action, and oil recovery from fractured reservoirs by spontaneous imbibition

Submitted by:
University of Wyoming
Laramie, WY 82071

Prepared for:
United States Department of Energy
National Energy Technology Laboratory

October 29, 2008

Office of Fossil Energy

Fundamentals of reservoir surface energy as related to surface properties, wettability, capillary action, and oil recovery from fractured reservoirs by spontaneous imbibition

DE-FC26-03NT15408

FINAL REPORT
07/01/2003 – 6/30/2008

Norman R. Morrow, Principal Investigator
Herbert Fischer
Yu Li
Geoffrey Mason
Douglas Ruth
Siddhartha Seth
Zhengxin Tong
Evren Unsal
Siluni Wickramathilaka
Shaochang Wo
Peigui Yin

September 2008

Submitted by:
Chemical & Petroleum Engineering
University of Wyoming
Dept. 3295, 1000 E. University Ave
Laramie, WY 82071

DISCLAIMER

ABSTRACT

The objective of this project is to increase oil recovery from fractured reservoirs through improved fundamental understanding of the process of spontaneous imbibition by which oil is displaced from the rock matrix into the fractures. Spontaneous imbibition is fundamentally dependent on the reservoir surface free energy but this has never been investigated for rocks. In this project, the surface free energy of rocks will be determined by using liquids that can be solidified within the rock pore space at selected saturations. Thin sections of the rock then provide a two-dimensional view of the rock minerals and the occupant phases. Saturations and oil/rock, water/rock, and oil/water surface areas will be determined by advanced petrographic analysis and the surface free energy which drives spontaneous imbibition will be determined as a function of increase in wetting phase saturation. The inherent loss in surface free energy resulting from capillary instabilities at the microscopic (pore level) scale will be distinguished from the decrease in surface free energy that drives spontaneous imbibition.

A mathematical network/numerical model will be developed and tested against experimental results of recovery versus time over broad variation of key factors such as rock properties, fluid phase viscosities, sample size, shape and boundary conditions. Two fundamentally important, but not previously considered, parameters of spontaneous imbibition, the capillary pressure acting to oppose production of oil at the outflow face and the pressure in the non-wetting phase at the no-flow boundary versus time, will also be measured and modeled. Simulation and network models will also be tested against special case solutions provided by analytic models.

In the second stage of the project, application of the fundamental concepts developed in the first stage of the project will be demonstrated. The fundamental ideas, measurements, and analytic/numerical modeling will be applied to mixed-wet rocks. Imbibition measurements will include novel sensitive pressure measurements designed to elucidate the basic mechanisms that determine induction time and drive the very slow rate of spontaneous imbibition commonly observed for mixed-wet rocks. In further demonstration of concepts, three approaches to improved oil recovery from fractured reservoirs will be tested; use of surfactants to promote imbibition in oil wet rocks by wettability alteration: manipulation of injection brine composition: reduction of the capillary back pressure which opposes production of oil at the fracture face.

TABLE OF CONTENTS

LIST OF FIGURES

INTRODUCTION

Objectives

The long-range objective of this project is to improve oil recovery from fractured reservoirs through improved fundamental understanding of the process of spontaneous imbibition by which oil is displaced from the rock matrix into the fractures. Spontaneous imbibition is fundamentally dependent on the surface energy. An initial objective is to determine the surface energy and relate the dissipation of surface energy to the mechanism of spontaneous imbibition. A parallel objective is to model the mechanism of spontaneous imbibition by a combination of network analysis and numerical modeling. Also fundamentally important, but not previously considered, parameters of spontaneous imbibition, the capillary pressure acting to oppose production of oil at the outflow face and the pressure in the non-wetting phase at the no-flow boundary (in effect within oil in the non-invaded zone of the rock matrix) versus time, will also be measured and compared with values predicted by the mathematical model. The next objective is to measure surface energy and related spontaneous imbibition phenomena for mixed-wettability rocks prepared by adsorption from crude oil. The dissipation of surface free energy must then be related to oil production at mixed-wet conditions. The final objective is to apply the results of the project to improved oil recovery from fractured reservoirs in three ways: reduction of the capillary force that opposes oil production at the fracture face; change in wettability towards increased water wetness; identification of conditions where choice of invading brine composition can give improved recovery.

Tasks

Budget period 1, July 1, 2003 through June 30, 2005 – Ideas and Concept development: Fundamentals of Spontaneous Imbibition

Task 1. *Work of displacement and surface free energy.* Obtain complementary sets of capillary pressure drainage and imbibition data and data on changes in rock/brine, rock/oil, and oil/brine interfacial areas with change in saturation for drainage and imbibition for at least two rock types (sandstone and carbonate). Determine free-energy/work-of-displacement efficiency parameters for drainage and imbibition for at least two rock types so that changes in rock/wetting phase/non-wetting phase surface areas can be closely estimated from capillary pressure measurements.

Task 2. *Imbibition in simple laboratory and mathematical network models.* Study imbibition in at least three simple tube networks that can be modeled analytically to establish and/or confirm fundamental aspects of the pore scale mechanism of dynamic spontaneous imbibition with special emphasis on determining how spontaneous imbibition is initiated and the key factors in how the saturation profile develops with time. Incorporate rules developed from laboratory measurements on relatively simple networks into the design of a computational network model. Use the network model to obtain an account of the mechanism by which imbibition is initiated, the saturation profile is developed, and the rate of spontaneous imbibition in terms of the dissipation of surface free energy that accompanies change in saturation.

Task 3. *Novel observations on fluid pressures during imbibition and the mechanism of non-wetting phase production at the imbibition face.* Make novel observations on the imbibition mechanism including details of the mechanism of oil production at the outflow rock face and the

change in the non-wetting phase pressure at the no-flow boundary of the core during the course of spontaneous imbibition for at least 16 distinct combinations of rock/ fluid properties.

Task 4. *Network/numerical model and new imbibition data.* Develop a numerical simulator specifically designed for spontaneous imbibition. Incorporate the network model to obtain a network/numerical model that includes matching the measured pressure in the non-wetting phase at the no-flow boundary, and the pressure that opposes production of oil at the open rock face. Imbibition data will be obtained for at least 10 rocks with over six-fold variation in permeability, and at least 6 orders of magnitude variation in viscosity ratio, and at least 10 variations in sample size, shape, and boundary conditions.

Task 5. *Comparison with similarity solutions.* Compare results given by simulation with special case analytic results given by similarity solutions for spontaneous imbibition for at least five distinct cases of rock and fluid properties.

Budget Period 2, July 1, 2005 through June 30, 2008 - Demonstration of concept: Application to mixed wettability rocks and improved oil recovery from fractures reservoirs.

Task 6. *Rock preparation and Work of displacement and surface areas*
Obtain a range of rock types and identify and obtain crude oils that induce stable mixed wettability. Prepare at least 25 rocks with mixed wettability through crude oil/brine/rock interactions. Determine work of displacement for drainage and imbibition and measure the variation in rock/brine, rock/oil, and oil/brine interfacial areas during the course of drainage and imbibition for at least two examples of mixed wettability.

Task 7. *Novel imbibition measurements on mixed-wet rock and network models.* Obtain, for at least six mixed-wet rocks, spontaneous imbibition data that includes measurements of the non-wetting phase pressure at the no-flow boundary, observations on the capillary pressure that resists production at the open rock face.

Task 8. *Application of network/numerical model to mixed wet rocks.* Use network models to relate dissipation of surface energy to rate of spontaneous imbibition and to account for the frequently observed induction time prior to the onset of spontaneous imbibition into mixed wettability rocks.

Task 9. *Increased oil recovery by spontaneous imbibition.* The mechanism of increased recovery from mixed wet rocks by use of surfactants that promote spontaneous imbibition by favorable wettability alteration will be investigated for at least four distinct examples of crude oil/brine/rock/surfactant combinations. The mechanism of increased recovery by manipulation of brine composition will be investigated for at least four crude oil/brine/rock combinations. Addition of very low concentration surfactants to the imbibing aqueous phase will be explored as a means of increasing the rate of oil recovery by reducing the capillary forces which resist production of oil at the fracture face. At least twelve combinations of rock and fluid properties including both very strongly wetted and mixed wet rocks will be tested.

EXECUTIVE SUMMARY

This report presents the results of a five year investigation of the fundamentals of reservoir surface energy as related to surface properties, wettability, capillary action, and oil recovery from fractured reservoirs by spontaneous imbibition. The subject is of special importance in fractured reservoirs because production often depends on recovery of oil by spontaneous imbibition of injected brine into the rock matrix so that oil is driven into the fractures and then swept by the flow through the fractures to the production wells. The project consisted of 9 interrelated tasks.

Task 1 concerned the surface energy of the reservoir that is available to drive the imbibition process. The maximum possible surface energy created by drainage was determined from capillary pressure data. However, the surface energy which drives imbibition is less than the work of drainage because of the capillary instabilities that accompany displacement. The conversion of work of drainage to surface energy was determined for sandstones and carbonates by direct measurements of increase in surface areas. The measurements are the first of their kind. They show that the conversion of work to surface energy is very inefficient, being only about 36% for sandstone and 16% for an oolitic limestone. The low efficiencies are ascribed to the high ratio of pore throat to pore body size, known as the aspect ratio.

The dynamics of the imbibition process was examined under Task 2. The behavior of interfaces was investigated in a hub and spoke network model of cylindrical tubes for a wide range of tube sizes and four orders of magnitude variation in viscosity ratio and three boundary conditions. This work was extended to modeling the spontaneous imbibition process in strongly water wet cores and extensive testing of the model was carried out under Task 3. Under Task 3 new methods of simultaneous determination of pressures acting during counter current spontaneous imbibition, the fluid produced and the location of the imbibition front are presented. Results include production by imbibition of incompressible (oil) and compressible (air) non-wetting phases. Measurements of the effective capillary pressure at the imbibition front are also reported. The effective capillary pressure at the front is essentially constant with respect to rate of advance of the front.

Under Task 4 a numerical simulator was developed that was specifically designed to model spontaneous imbibition. Scaling of imbibition data was tested extensively through new imbibition data obtained for a wide range of viscosity ratios and boundary conditions. Imbibition data was obtained for 6 orders of magnitude variation in viscosity ratio and a wide range of sample size, shape, and boundary conditions. Data was fitted with a new mathematical model of imbibition.

Task 5 concerned analytic modeling of the imbibition process. All of the results point to the validity of similarity solutions and that rate of interface advance depends basically on the square root of time. Models of spontaneous imbibition range from similarity solutions to piston-like displacement models, both of which can be adequate for the period before the imbibition front reaches the core boundary. An approximate analytic solution to the imbibition process is reported that provides solutions to the saturation profile, the time dependence, and the pressure distributions.

Mixed wettability is now the most widely accepted model of reservoir wettability. Imbibition rates for mixed wet rocks are often orders of magnitude slower than for strongly wetted rocks. Studies

of changes in interfacial area and the driving force for imbibition have been extended to mixed wettability rocks under Task 6. Implications of results obtained under Task 1 on interfacial areas are extended to the complex reservoir wettability conditions that can arise within oil reservoirs. It is shown that the fraction of rock surface that is likely to undergo wettability alteration by adsorption from crude oil is only a very small fraction of the total rock surface. Because of the complex interactions between pore geometry and contact angle, contact angle measurements alone do not provide reliable prediction of spontaneous imbibition behavior. Using modification of the techniques developed under Task 3, the imbibition driving pressures for mixed wet rocks have been measured for the first time. As expected, these pressures are much lower than for strongly wetted rocks.

Under Task 7 development of pressure measurement techniques was extended to estimating the capillary pressure acting at the imbibition front under dynamic conditions. Results were obtained for both oil/water and air/oil imbibition tests and results were found to be mutually consistent. Modeling work was extended to a detailed examination of the effect of sample shape on production curves for spontaneous imbibition. The results show the conditions under which commonly-used semi-empirical scaling factors for geometry and boundary conditions are satisfactory.

Task 8 presents advances in modeling the effect of viscosity ratio on spontaneous imbibition and studies of imbibition in a series of well-defined pore geometries. The geometries could be analyzed in detail to provide direct comparison between theory and experiment for both co and counter-current spontaneous imbibition. The geometric features that were analyzed included independent tubes of non axi-symmetric geometry, tubes with lateral connection that allows cross flow, and bubble snap-off and capillary back pressure. Also reported under Task 8 is an analytical model for prediction of the shape of the production curve. Solutions include the most commonly tested case of imbibition into cylindrical cores immersed in brine with all faces open to imbibition.

Methods of improved oil recovery by spontaneous imbibition are addressed under Task 9.
A wide range of anionic, cationic, nonionic, and amphoteric surfactants were screened for phase behavior and for ability to provide enhanced oil recovery by spontaneous imbibition. One purpose of using surfactant was to reduce the back pressure associated with production of bubbles of oil from the rock face by locally lowering the interfacial tension. The most effective surfactant was used in extensive testing of the mechanism of surfactant imbibition, including measurement of the pressures acting at the imbibition front. As the imbibition front advances, surfactant adsorbs, the interfacial tension increases, and the rate of oil recovery is significantly increased. A preliminary mathematical analysis of the results is presented. Other aspects of imbibition that were tested for carbonates were the effect of sulfate ions in the brine and the effect of dilution of the imbibing brine. Neither of these approaches provided enhanced imbibition for the tested limestone.

In the final stage of Task 9, improved oil recovery after completion of spontaneous imbibition was tested by immersion of cores in surfactant solutions. Significant improvements in recovery were observed for some surfactants. Results were consistent for two types of limestone. Large increases in recovery for the second stage of imbibition were obtained for the oolitic limestone.

PROJECT FINAL REPORT BY TASK

Task 1. *Work of displacement and surface free energy.*

Introduction

Capillary pressure curves, when observed in microscopic details, consist of a series of steps that can be classified as reversible (ison) and irreversible (rheons). During an ison the conversion of work to surface energy is 100%, whereas during a rheon the work done is 0 and, for the case of drainage, there is loss of surface energy. Hence the total work done obtained from integrating under the capillary pressure, in the case of drainage, will be more than the change in surface energy of the system and vice versa would be true for imbibtion. During imbibition/drainage only a fraction of the total surface area, as measured by BET, is contacted by the invading non-wetting phase. Multi phase flow and mass transfer are intricately related to the surface area between the three phases. The method proposed in this work utilizes thin section analysis from samples obtained from outcrops to determine fluid saturation and interfacial surface areas between the solid–non wetting, solid–wetting and wetting – non-wetting after solidification of epoxy resin that contain two different colors, one representing water the other oil. Theory of stereology was used to estimate three-dimensional information such as interfacial areas between the two fluid phases from the two dimensional image of the phases obtained from the thin section.

Experimental

All porous media exhibit some residual wetting phase saturation when drained. In the case of case of a pack of uniform sized sphere, similar to on used by Morrow (1970), the capillary pressure curve is universal with a well-defined residual saturation. Corresponding to the residual there is a surface area associated with the wetting phase that is a measure of the inefficiency of conversion of work of displacement to the surface energy created during the drainage process and hence the work of drainage will always exceeds surface free energy. In the case of a glass bead pack the efficiency of displacement was reported to be 79%. For a more complex geometry, like that in a porous media the residual saturation is not a unique value it rather depends on the pore structure of the rock. In general the amount of microporosity tends to dictate the efficiency of conversion. The International Union of Pure Applied Chemistry defined the different types of pores as follows:

Micropores: r < 2 nm
Mesopores: r = 2 – 50 nm
Macropores: r > 50 nm

The micropores retain the wetting at very high capillary pressure and during drainage the fluid in these pores is not accessed by the invading non-wetting phase. The work of displacement was calculated using the area under the capillary pressure curve that can be obtained form mercury injection, centrifuge, porous plate or any other technique.

$$\text{Work of displacement} = V_b * \phi \int_{100}^{Swi} P_c * dS_w \qquad 1.1$$

Where, P_c is the capillary pressure

S_w is the saturation of the wetting phase

V_b is the volume of the bulk phase
φ is the porosity of the sample

Work done under the capillary pressure was used to calculate the area corresponding to it:

$$A_{mercury} = \int_{100}^{Swi} P_c * dS_w \; / (\sigma_{w\text{-}nw} * \rho_{Rock}) \qquad 1.2$$

Where, ρ_{Rock} is the density of the rock matrix (2.65 g/cc)
$\sigma_{w\text{-}nw}$ is the interfacial tension between the wetting and the non-wetting phase

The change in surface free energy of the system is a function of the interfacial area created by the invading non-wetting phase. For this paper this value has been calculated using thin section analysis using the equation:

$$\Delta F = \sigma_{w\text{-}nw}(\Delta A_{w\text{-}nw} + \Delta A_{s\text{-}nw} \cos\theta) \qquad 1.3$$

Where, ΔF is change in the surface free energy
$\Delta A_{w\text{-}nw}$ is the interfacial area between the wetting and non-wetting phase
$\Delta A_{s\text{-}nw}$ is the interfacial area between the solid and the non-wetting phase
$\cos\theta$ is the contact angle

Capillary pressure measurements were by mercury injection

Petrophysical Properties of The Rock
Permeability and porosity
The air permeability and the porosity of the sandstone sample (PH2) was 740 md and 22% respectively.

Surface Area And Pore Size Distribution Analysis
Mercury injection
Mercury injection has been widely used to estimate capillary pressure and pore size distribution for porous media. Mercury porosimetry is based on the Washburn (1921) equation. This method has the advantage of producing fast results over a large range of pore radii (10 nm - 200 μm). Fig 1.1 shows the raw capillary pressure curve that was obtained by mercury injection. The kink observed in the data at S_w ~20 % was due to switching from the low pressure to the high pressure cell during the experiment. At the beginning of the experiment the mercury fills up areas of contact between the core and the core holder. This raw data was corrected for the entry region using the following procedure (shown diagrammatically in Fig 1.2)

1. Two tangents to the curve were made one for the flat portion and other for the entry region (T1 and T2)
2. A line was drawn from second data point at S_w ~95% (T3)
3. The mid point of T1 andT3 was normalized to S_w = 100 %

4. The pink in the data at S_w ~20% was smoothed.

The final smoothed capillary pressure curve that was used for obtaining the work done and the depth of investigation is shown in Fig 1.3. The area obtained corresponding to the work done calculated using Eq 1.2 is shown in Fig 1.4. Fig 1.4 conclusively shows that the amount of surface created by the invading non wetting phase (mercury) was a small fraction of the surface area obtained by the BET surface area analysis. At a residual wetting phase saturation of S_w ~5 % the total area created is 0.11 m^2/g which was about ~ 17 % of the BET surface area (0.626 m^2/g). The reason for this difference is that most of the BET surface area in the case of the PH2 sample is due to microporous region that is not invaded by non wetting phase, even though the pore space is 95% filled.

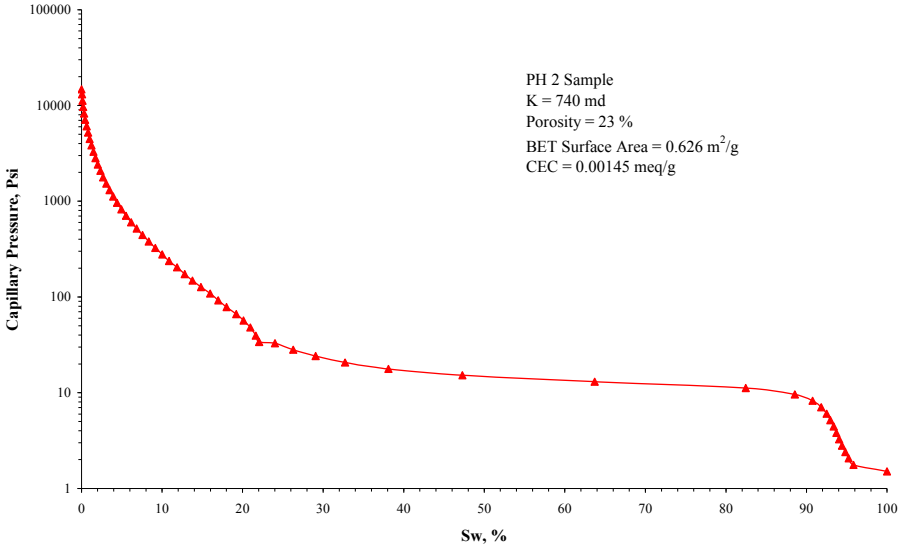

Fig. 1.1 Raw capillary pressure data for PH2 sample.

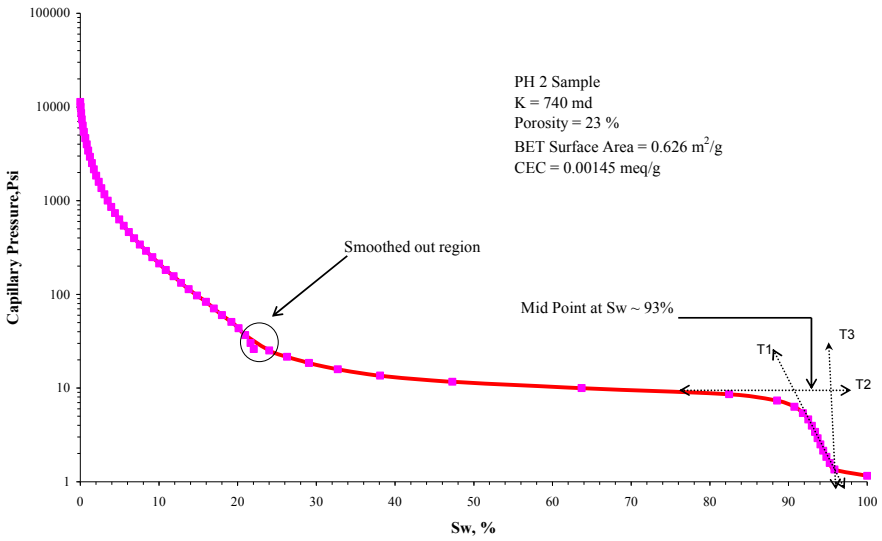

Fig. 1.2. Steps to smooth out the raw mercury injection data.

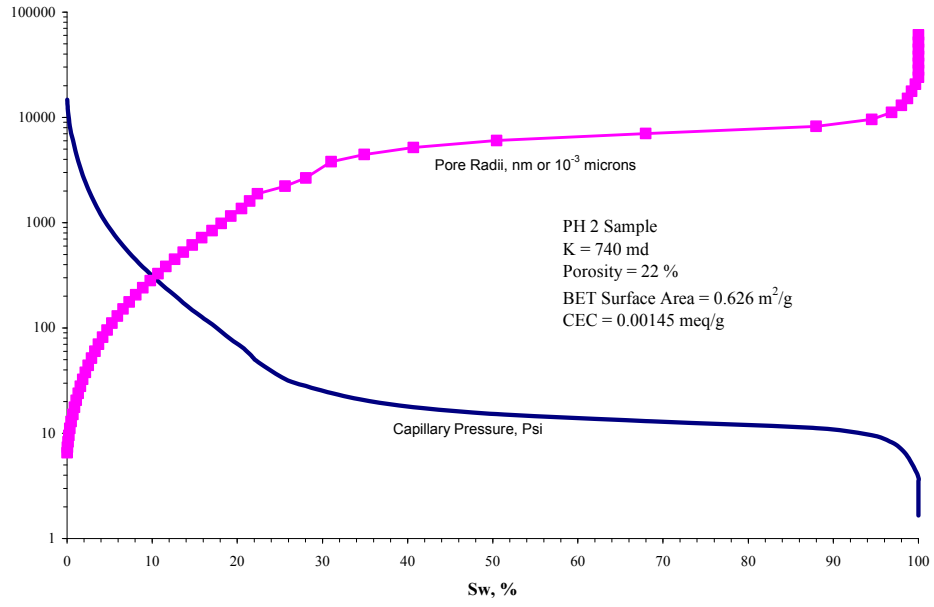

Fig. 1.3. Corrected capillary pressure curve and the radii of investigation for Sandstone (PH2).

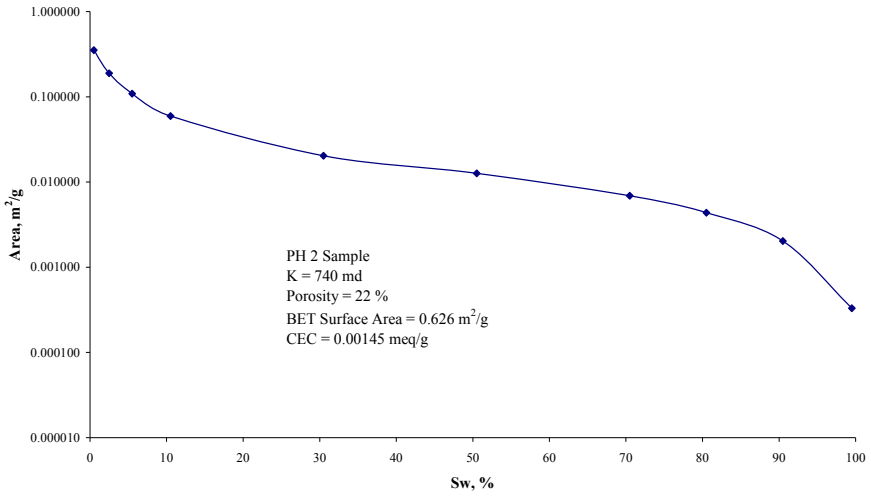

Fig. 1.4. Area obtained by integrating under the capillary pressure curve for the PH2 sample.

Results and Discussion

Theory of Stereology

Stereology is a science that provides us with a tool for calculating three dimensional information such as surface to volume ratio from a given two dimensional figure of the three dimension object. The various sampling probes that are commonly used are points, lines and planes. The fundamental relationships of stereology make no geometric assumption (Russ and Dehoff, 2000). The intersection of the probe with the image account for the geometric shape regardless of the way the body is embedded in the structure. However the values of these counts calculated from these interactions are then used to relate various geometric property of the body, such as surface to volume ratio, that are a defined as fundamental relationships. A detailed analysis of the fundamental theorems, including proof and application is discussed by Underwood (1970) and Russ and Dehoff (2000).

Some fundamental theorems were applied to the data presented in this paper: For a particular phase, *a*, embedded in a second phase, *b*,

$$\langle P_a \rangle = A_a = V_a \qquad 1.4$$

Where, <> denotes that the equation is applicable to the average value of the population of the probe in 3 D space. P_a is the ratio of number of points lying in the phase *a* to the total number of points. A_a is the ratio of area occupied by phase *a* to the total area of the image. V_a is the ratio of volume occupied by the phase, *a*, to the total volume of the sample.

$$\langle L_a \rangle = 4 * V_a / S_a \qquad 1.5$$

Where, L_a is the mean intercept length of the phase *a*. V_a/ S_a is the volume to surface ratio for the phase *a* in the image.

Using the above two relationships we obtain

$$S_v = (4/<L_a>) * (P_a) \qquad 1.6$$

Where, S_v is the surface area of the phase *a* per unit volume of the sample.
For the present analysis there are three phases, wetting phase (blue), non-wetting phase (red) and solid (white). Since the above mentioned analysis is valid for two phases, we used a three step procedure to get the interfacial areas between the three phases. The procedure involved doing the line counts to get mean intercept length, which is then converted to interfacial surface areas using Eq. 1.3, of a particular phase while considering the other two phases as one phase. This generated three numbers that correspond to the mean intercept length of

- Red phase (non-wetting) and white (solid), S_R
- Blue phase (wetting) and white (solid), S_B
- White (solid) and liquid (red +blue), S_L

It is important to note that because there may be non-wetting and wetting phase (red-blue interface), the values of interfacial areas are calculated as:

Interfacial area between red (non-wetting) and blue (wetting) phase, $S_{RB} = S_R + S_B - S_L$
Interfacial area between red (non-wetting) and white (solid) phase, $S_{RS} = S_R - S_{RB}$
Interfacial area between blue (wetting) and white (solid) phase, $S_{BS} = S_B - S_{RB}$

This method of analysis can be extended for the case in which there are *n* phases. In that case there will be *n* sets of equations and *n* variables that can be solved easily. Two additional quantities that are calculated are the total surface area and the created surface area.

Total surface area, $TSA = S_{RS} + S_{BS}$
Created surface area, $CSA = S_{RB} + S_{RS}$

Software - Theory

RGB approach

For every image that is created or stored on a computer the information, corresponding to the colors that are seen, is stored in the pixel format. Each pixel has three values corresponding to red, green and blue (RGB) and each of the three can have a value ranging from 0 to 255. All the colors seen in an image are a combination of RGB values between this range. The basic idea, while using this approach, was to read out the RGB value of each pixel one by one and identify whether it is red, blue or something else. The red color corresponds to the non-wetting phase, the blue is the wetting-phase and rest of the image is solid.
For the cases of a simple network model, drawn using any available commercial software similar to Adobe Photoshop, the size of the pixel and the values for RGB can be defined, for e.g. for red the RGB values are 255,0,0 and for blue 0,0,255. The software would then need to pick out, in a

set of three, the value of RGB from the file containing the information about each pixel in the image. The format of this file is generally binary or ASCII.

HSV approach
Color can also be represented in the Hue/Saturation/Value (HSV) color model instead of the more standard Red/Green/Blue (RGB) model. The HSV color space is more intuitive to use and is much easier to divide into regions which correspond to perceptually recognized colors such as blue, green, pink etc. It is based on such intuitive color characteristics as tint, shade and tone (or family, purety and intensity). The coordinate system is cylindrical, and the colors are defined inside a hexcone. The hue value, H, ranges from 0 to 360 degrees. The saturation, S, is the degree of strength or purity and this ranges from 0 to 1. Purity is how much white is added to the color, so S=1 makes the purest color (no white). Brightness, V, ranges from 0 to 1, where 0 is black.

In order to use an image obtained from the microscope an intermediate processing step was needed because when an image of an actual sample was taken, it was found that the color of the epoxy (red or blue) varied from light to darker shades of their respective colors. In order to process this added complexity, the HSV approach is used to convert the raw image data in RGB format to HSV format to identify the variation in red and blue and also to pick out a range for other colors such as yellow, brown, purple etc.. Since the variation in red and blue in the raw picture varied between light pink to red for the non-wetting phase and purple to light blue to dark blue for wetting phase, these ranges of colors from the HSV format were used to generate the processed image that had only the type of pixels pure red (255,0,0), pure blue (0,0,255) and white (255,255,255). This processed file was then used for further analysis such as point counts and line counts.

Fig. 1.5 and 1.6 show the conversion of an original thin section image for Berea sandstone to the modified file containing only three colors i.e. red, blue, white. Further analysis of the picture including the accuracy of the computer generated image is being investigated. The next step will involve point and line counting to get saturations and interfacial surface areas using the fundamental equations of stereology.

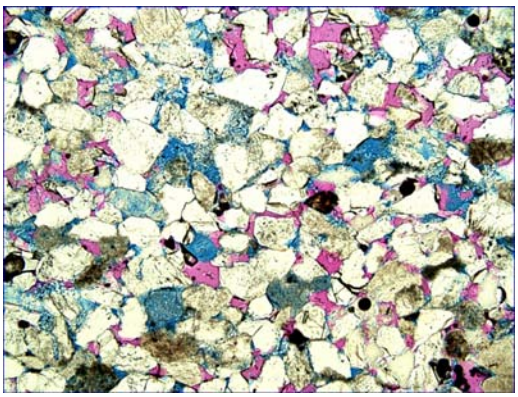

Fig. 1.5 Thin Section

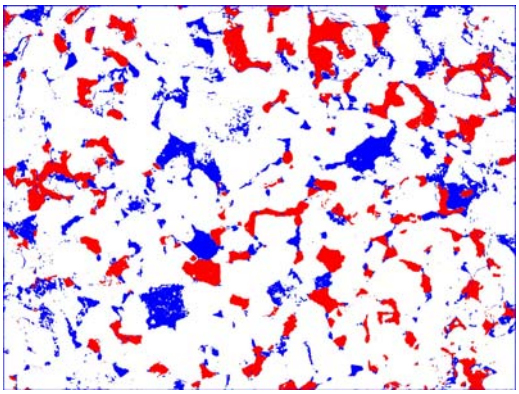

Fig. 1.6 Converted image

Surface area analysis

The results for the surface area analysis for the sandstone sample are presented here. From the capillary pressure curve the range for which the thin section analysis using the 10X magnification was valid was found to be between (S_w = 22 – 100 %). The size of the pixel using this magnification was 2 microns and hence (as shown in Fig.1.7) the wetting phase (blue) present in the pores smaller than 2 micron was not visible under the microscope.

The interfacial area between the wetting and the non-wetting phase (red – blue) interface is of much interest and many researchers (Jain et al., 2003; Kim et al., 1997; Gladkikh et al., 2003; Bradford and Leij, 1997) have used indirect methods to estimate this area in a variety of porous media. As can be seen from Fig. 1.8 this area increased from 0 (at S_w = 100%) to about 0.053 % of the BET surface area (0.626 m^2/g) at S_w = 75 % and then decreased to 0 at S_w = 0%. This is because the red-blue interface can form only in the pores, which constitute only a small fraction of the total surface area (TSA) available to the invading non-wetting phase. Alpak et al. (1999) had also suggested that the interfacial area between the liquid – liquid interfaces should pass through at least one maximum for some intermediate saturation. Morrow (1970) reported similar results on a pack of glass beads.

Created surface area, CSA, is the area created by the invading non-wetting phase as it displaces the wetting phase. This area increases with the decrease in the wetting phase saturation and at very low wetting phase saturation is approaches the total surface area (TSA). CSA was calculated as the sum of interfacial area between solid – red and the red – blue phase (Fig. 1.9). Most of the area related to fluid displacement is associated with the solid surface.

The TSA is only a small fraction of the BET surface area because much of the surface area is associated with microporosity. Wetting phase is not displaced from these regions. In the case of the PH2 sample the TSA exposed was 0.009m^2/g (average), which, corresponded to only about 1.4 % of the BET surface area. TSA was calculated by adding the interfacial area between the solid – red and the solid – blue phase (Fig 1.10).

Magnification of 10 X the total length of each picture analyzed was used to obtain the surface energy of 0.27 cm (diameter of the core was 4 cm). Hence the scatter in the data may well be related to heterogeneity at the scale at which the analysis was made. The reason for choosing this magnification was that, at lower resolution, the saturations in the regions of kaolinite and dissolved feldspar would not be distinguishable from the rest of the matrix. Higher magnification would require a very large number of pictures and extremely large storage and processing capabilities.

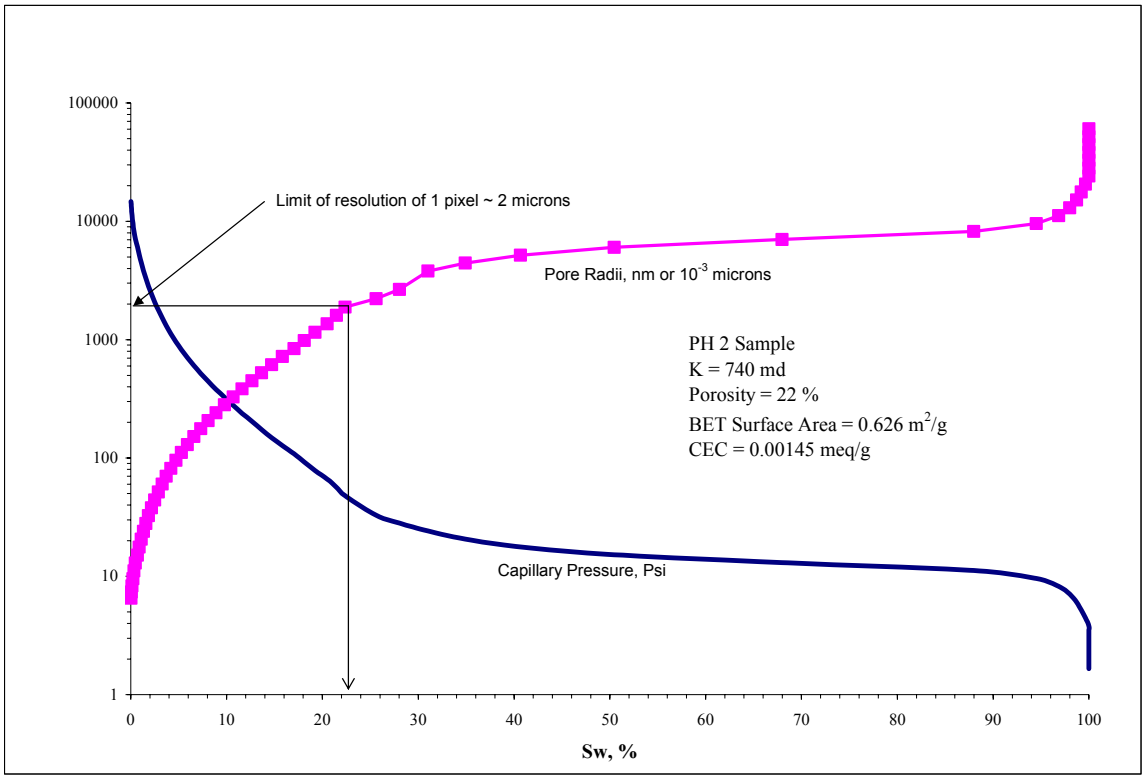

Fig. 1.7 Corrected capillary pressure curve and the radii of investigation for Sandstone (PH2).

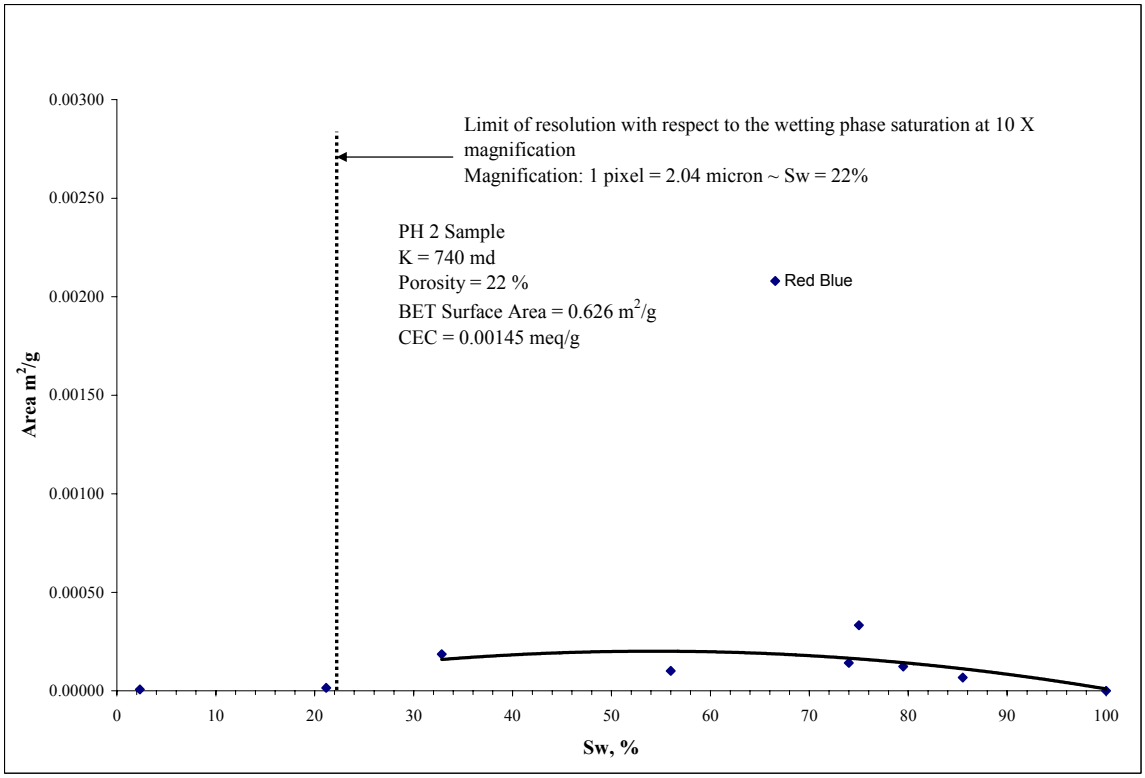

Fig 1.8 Variation in area between the wetting and non wetting phase as a function of the wetting phase saturation.

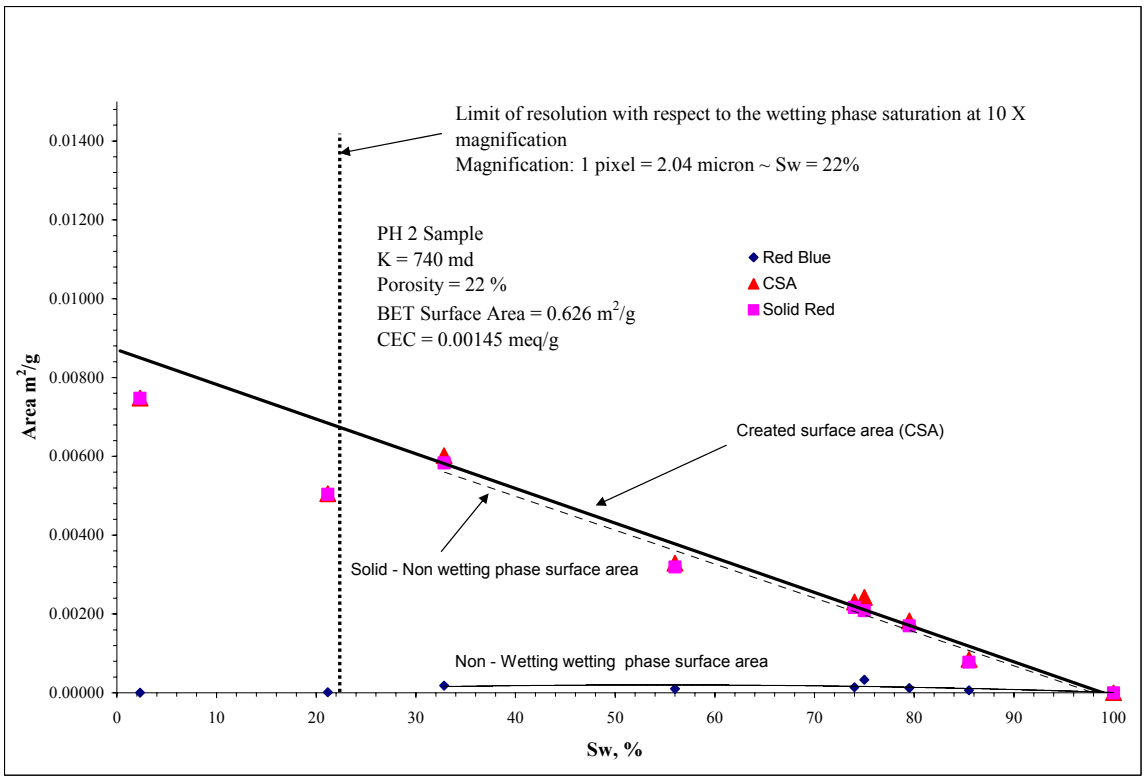

Fig. 1.9 Variation in Created Surface Area (CSA) as a function of the wetting phase saturation.

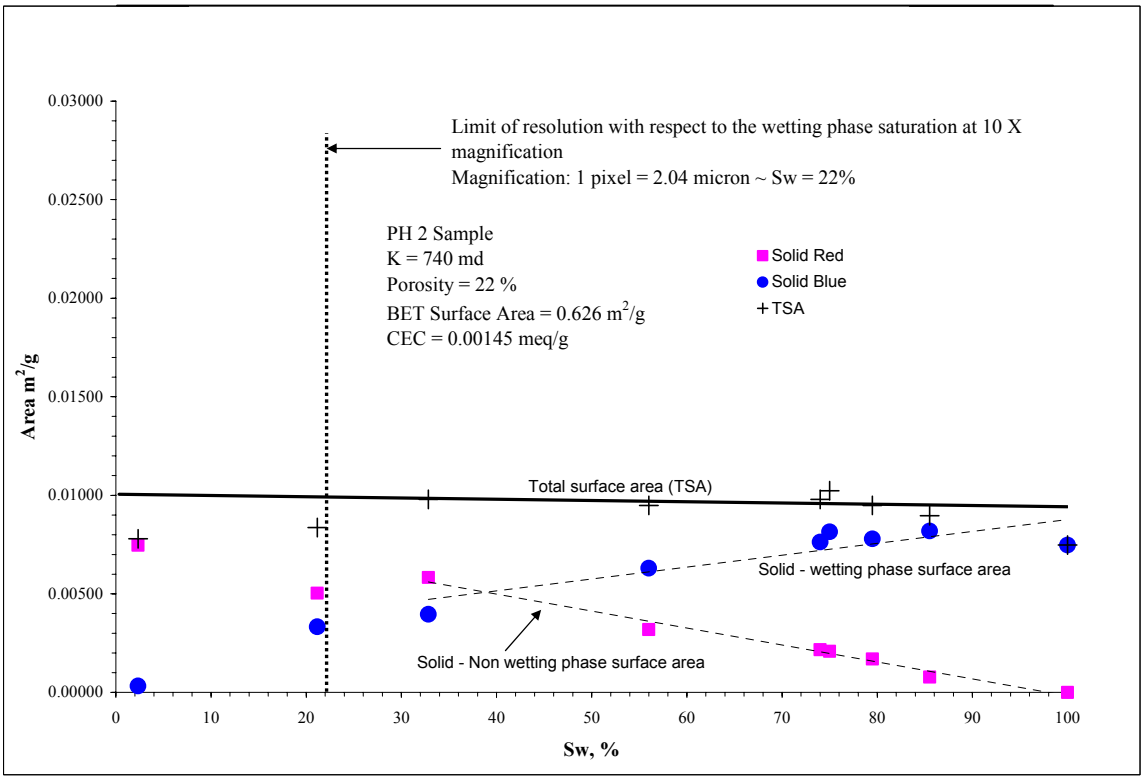

Fig. 1.10. Total Surface Area (TSA) as a function of the wetting phase saturation.

Task 2. *Imbibition in simple laboratory and mathematical network models.*

Introduction

In spontaneous imbibition, capillary pressure is the dominant force. Poiseuille flow covers practically the whole of the flow regime. Based on the Poiseuille's law, analytical or numerical solutions of spontaneous imbibition in cylindrical capillary tubes and Hub-and-Spoke Units have been derived. Results presented in the previous quarterly reports, reveal the dependency of the advancing position of the wetting phase on the viscosity ratio as well as the ratio of the pore radii occupied by the wetting and non-wetting phases. Those results have led to new understanding of how to model the spontaneous imbibition processes in strongly water-wet cores, in which a relatively constant saturation is often observed in the imbibing water phase at the displacement front. Consequently, simple analytical models have been derived to model imbibition processes under different core boundary conditions. Namely, linear (one end or two ends open), radial (two end closed), and whole core (all faces open) flow patterns. The models have been tested against experimental data. The model provides a satisfactory fit to almost all of the experimental data.

Experimental

Modeling the spontaneous imbibition process in strongly water-wet cores

When cores are strongly water wet, a piston-like frontal movement of the imbibing water is commonly observed for all boundary conditions namely one-end-open (OEO), two-ends-open (TEO), two-ends-closed (TEC), and all-faces-open (AFO). This visual observation indicates that the pore volume ratio between the smaller pores occupied by the invading water and the larger pores occupied by the replaced oil is relatively constant behind the front. This is also consistent with the simulation results in the Hub-and-Spoke Units, where the outgoing or trapped oil is always being pushed into the larger spokes. As illustrated in Figure 2.1, the assumption is that the replaced oil is either being trapped or being pushed count-currently via the networks that are connected by the largest pores. Under this assumption, a relationship between the frontal position and the imbibition time can be derived based on the Poiseuille's law.

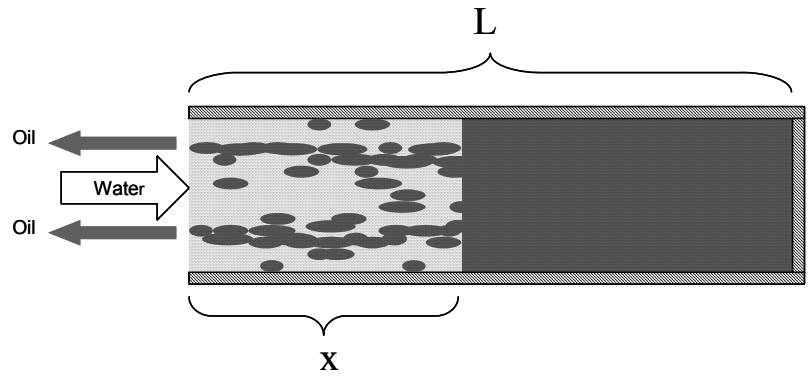

Figure 2.1. The conceptual frontal displacement of the counter-current spontaneous imbibition in strongly water-wet cores.

Similar to the spontaneous imbibition in cylindrical tubes, we model the frontal displacement as the imbibition in a set of U-shaped tubes with the water-oil contact at the bottom of the U tubes. Moreover, the radii of the two legs of the U tubes can be different. Under this configuration, the advance of the front is described as the cumulative effect of the imbibing water in individual tubes, in which the tube legs are in effect lengthened with time but the contact position remains at

the bottom of the U tubes. By applying the Poiseuille's law, we obtain a mass balance equation of water flow, Eq. 2.1, at the water-oil contact front, where P_c is the capillary pressure at the contact. r_w and r_o represent the average pore radii occupied by the water and oil phases, respectively. R, ϕ, A, μ_w, μ_o are the oil recovery, core porosity, cross-section area, water and oil viscosities, respectively.

$$q_w dt = R\phi A dx, \qquad \text{where } q_w = \frac{\pi P_c r_w^4}{8x} \frac{1}{\mu_w + \mu_o (r_w^4 / r_o^4)} \tag{2.1}$$

Integration of Eq. 2.1, gives an analytical relationship between the normalized position of the front and the imbibition time, as shown by Eq. 2.2.

$$\left(\frac{x}{L}\right)^2 = \frac{\pi P_c r_w^4}{4R\phi A L^2} \frac{t}{\mu_w + \mu_o (r_w^4 / r_o^4)} \tag{2.2}$$

In the following, we propose a dimensionless model that has the same parameter setting as in Eq. 2.2. Leverett has derived a relationship between permeability, porosity, tortuosity and the radius of a parallel bundle of equal size cylindrical tubes. Intuitively, a dimensionless form of Eq. 2.2 can be rewritten as

$$x_D^2 = E(\eta) t_D \tag{2.3}$$

Here, t_D is a dimensionless time normalized by the same scaling group proposed by Ma *et al* (1997).

$$t_D = \sqrt{\frac{k}{\phi}} \frac{\sigma t}{\sqrt{\mu_o \mu_w} L_C^2} \tag{2.4}$$

The characteristic length, L_C, depends on the respective boundary conditions. Specifically, in linear flow, $L_C = L$ for OEO and $L_C = L/2$ for TEO. In radial flow, $L_C = \frac{d}{2\sqrt{2}}$ for TEC. In spherical flow, $L_C = \frac{d}{2\sqrt{3}}$. In Eq. 2.2, x_D denotes the normalized position of the front, η is the square root of the viscosity ratio, and $E(\eta)$ is a dimensionless function defined by

$$x_D = \frac{x}{L}, \qquad \eta = \sqrt{\frac{\mu_o}{\mu_w}}, \qquad E(\eta) = \frac{a}{\frac{1}{b\eta} + b\eta} \tag{2.5}$$

In addition to the viscosity ratio, $E(\eta)$ is a function of two dimensionless parameters, *a* and *b*. As indicated in Eq. 2.2, they are determined by the factors related to the imbibing flow path of the wetting phase as well as the outflow path of the non-wetting phase. When cores are water wet, the average radius of pores occupied by the wetting phase is smaller than the average radius of pores occupied by the non-wetting phase. Because parameter *b* indicates the squared ratio of average pore radii occupied by the wetting and non-wetting phases, *b* should be between 0 and 1.

By assuming a piston-like frontal displacement, we can estimate the normalized recovery, R_D, as a function of t_D from Eq. 2.3. For linear, radial or spherical flows, the conversion between x_D and R_D is given by Eq. 2.6, 2.7, or 2.8, respectively.

Linear flow: $x_D = R_D$ 2.6

Radial flow: $x_D = 1 - \sqrt{1 - R_D}$ 2.7

Spherical flow: $x_D = 1 - (1 - R_D)^{\frac{1}{3}}$ 2.8

Because of the non-symmetrical flow pattern, it is difficult to derive a simple analytical model for the imbibition process of AFO. However, an AFO imbibition process can be approximated by a combination of radial flow and spherical flow. Equivalent in total volume, the shape of a regular core with a diameter of *d* and a length of *L* is close to a cylinder with hemispherical ends. The rod has a length of *L - 4d/3*. Both the rod and the two half spheres have the same diameter, *d*. Finally, the recovery of AFO can be estimated from the combined recoveries from the rod and from the two half spheres.

$$R_{D\_AFO} = (1 - \frac{2d}{3L}) R_{D\_radial} + \frac{2d}{3L} R_{D\_spherical} \quad 2.9$$

When the same value of *E* is assumed for both radial and spherical flows, the normalized recovery for AFO can further be derived as a function of the dimensionless time of the radial flow, Eq. 2.10.

$$R_{D\_AFO} = (1 - \frac{2d}{3L})(1 - (1 - \sqrt{Et_{D\_radial}})^2) + \frac{2d}{3L}(1 - (1 - \sqrt{\frac{3}{2} Et_{D\_radial}})^3) \quad 2.10$$

The proposed models of Eq. 2.3 and 2.10 were tested against experimental data. A linear correlation between the advancing front and the imbibition time is evident on the log-log plot for almost all cases but the slope of 0.5 was not always obtained, especially for linear flow. By freeing the power index, we propose an extended imbibition model of Eq. 2.11.

$$x_D^n = E(\eta) t_D \quad 2.11$$

The extended model of Eq. 2.11 has three dimensionless parameters, *n*, *a*, and *b*. For matched-viscosity cases, i.e. *η=1*, Eq. 2.11 reduces to a 2-parameter model in *n* and *E(1)*.

Results and Discussion

The extended imbibition model, Eq. 2-11, has also been tested in comparison against experimental data. The tested data set includes the OEO, TEC, and AFO cases under matched viscosities as well as AFO cases under non-matched viscosities. Apart from data recorded at the initial or final stages of the experiments, a clear linear correlation between the advancing front and the imbibition time emerges on the log-log plot for almost all of tested cases. It supports the assumption applied in the model derivation. When *n=2*, it indicates a linear correlation between x_D and $\sqrt{t_D}$. For tested TEC and AFO cases, we found that the best fit consistently result in *n* values around 2. However, a larger range of *n*, between 1.6 and 2, was observed in modeling the OEO cases. As examples, comparisons between the experimental data and modeled curves are presented in Figure 2.2 and 2.3. The core and fluid properties for these three examples are given in Table 2.1. The table also shows the *n* and *E(1)* values that are used to plot the modeled curves. Note that, the AFO example in Figure 2.3, both the modeled and experimental plots are scaled by the t_D of radial flow.

In summary, the 3-parameter imbibition model, Eq. 2-11, provides a satisfactory fit to most of the experimental data. The model is reduced to a 2-parameter model, i.e. *n* and *E(1)*, for matched-viscosity imbibition. As observed for much of the experimental data, a linear correlation between the advancing front and the square root of the time, i.e. *n=2*, implies that the spontaneous imbibition process is largely dominated by "local phenomena", in which the capillary pressure at the water-oil contact generates many local inlet-outlet flow paths. Further testing of the model will be conducted when new experimental data become available.

Table 2.1. Core and fluid properties of the three imbibition experiments used in the comparison. The matched-viscosity experiments were modeled by two parameters, *n* and *E(1)*.

	OEO	TEC	AFO
L [cm]	6.603	6.428	6.435
d [cm]	3.741	3.736	3.761
L_C	6.603	1.321	1.229
kg [cm^2]	7.723E-10	6.99E-10	5.952E-10
σ [dynes/cm]	33.86	33.86	32.36
μo [cp]	21.87	21.870	59.130
μw [cp]	22.52	22.520	59.300
Φ	0.169	0.173	0.178
n	2	2	2
E(1)	0.014	0.0025	0.0038

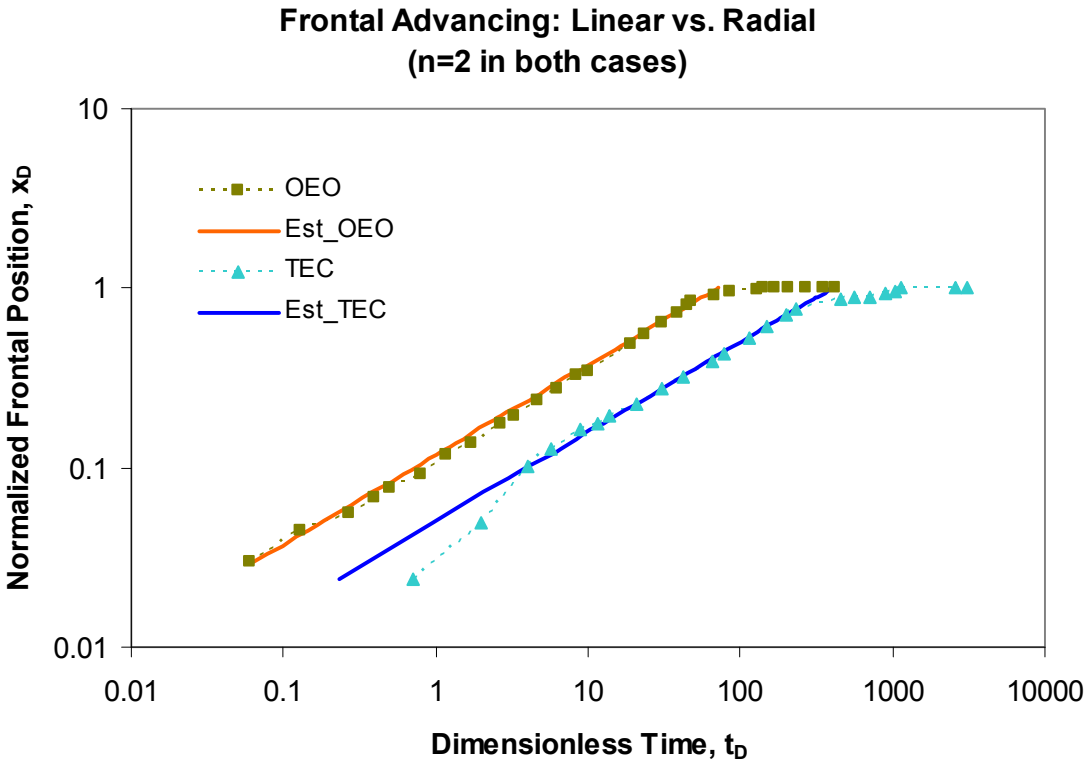

Figure 2.2. Examples of the linear correlation between x_D and $\sqrt{t_D}$, i.e. n=2, where a matched viscosity of 22 cp was used for both OEO and TEC cases.

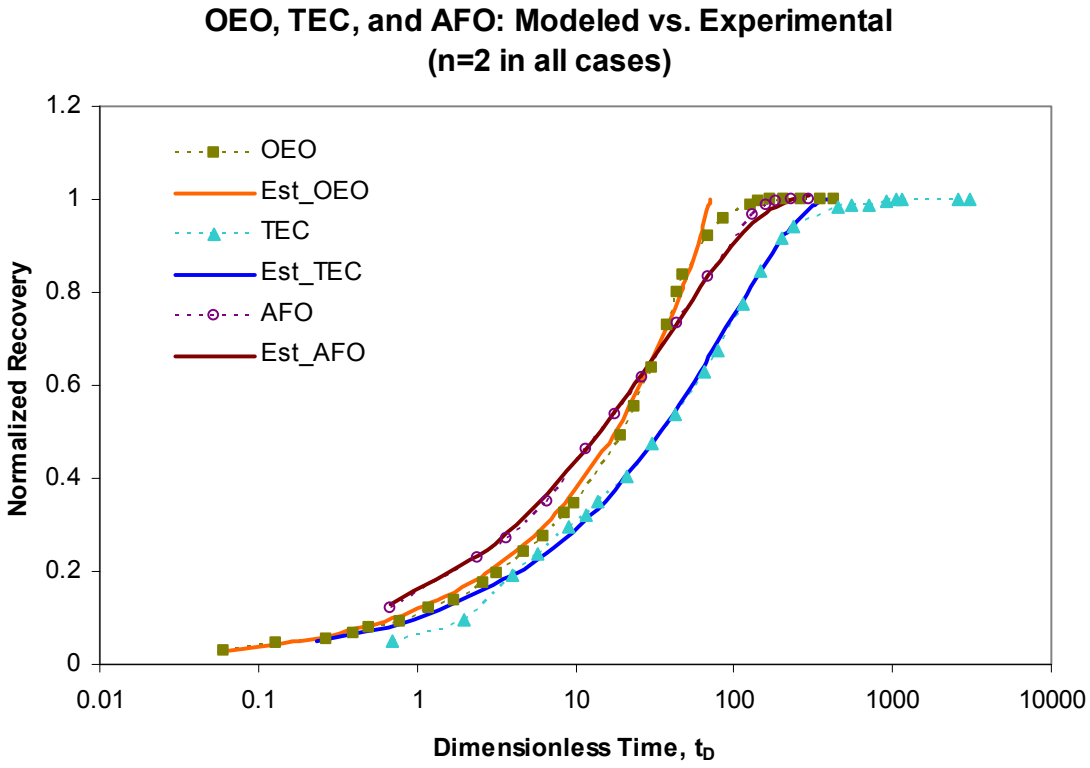

Figure 2.3. Comparison between the modeled recoveries (solid curves) and the experimental data (dashed lines with dots).

Task 3. *Novel observations on fluid pressures during imbibition and the mechanism of non-wetting phase production at the imbibition face.*

Pressures Acting in Counter-Current Spontaneous Imbibition

Y. Li, D. W. Ruth, G. Mason, and N.R. Morrow
Journal of Petroleum Science and Engineering, vol. 52, 1-4, 87-99.

Abstract
Four water/oil and four oil/air linear counter-current spontaneous imbibition experiments were performed on Berea sandstone cores with permeabilities ranging from 0.065 to 1.094 $\square m^2$. The cores were initially 100% saturated with non-wetting phase and all faces except one end were sealed. The experiments showed a clear frontal displacement mechanism. Capillary pressure was the driving force of the imbibition process. As well as viscous drag in both phases between the imbibition front and the open face, there is a significant opposing capillary back pressure associated with production of non-wetting phase at the open face. The location of the imbibition front, the overall changes in core saturation, and the pressure in the nonwetting phase in the dead end space ahead of the imbibition front, were monitored during the course of imbibition. The dead end pressure was essentially constant after a short start-up period. The distance advanced by the imbibition front was proportional to the square root of time. Based on the assumption that the properties of Berea sandstone of different permeabilities can be scaled, the experimental data were matched by numerical simulation to predict the saturation and pressure profiles, the saturation and capillary pressure at the imbibition front, and the capillary back pressure at the open face. The ratio of the capillary back pressure to the estimated capillary pressure at the imbibition front ranged from approximately 1/3 to 2/5, for oil displacing air, to approximately 1/9 to 1/4, for water displacing oil.

Introduction
The process of displacement of a nonwetting phase (NWP) from a porous medium by spontaneous imbibition of a wetting phase (WP) is often counter current (Morrow and Mason, 2001). In core analysis studies, spontaneous imbibition measurements are usually made on cylindrical cores with all faces open to imbibition. However, the use of cylindrical cores with only one end face open simplifies the analysis of the process because it forces the displacement to be linear with equal and opposite volumetric flows of WP and NWP at all distances from the open face. A similarity solution for one-dimensional COUCSI with a semi-infinite boundary has been reported (Li *et al.*, 2003)

During counter current spontaneous imbibition (COUCSI) at very strongly wetted (VSW) conditions, displaced NWP is produced as bubbles at the open face (Li *et al.* 2003). The pressure associated with these bubbles, which we will term the capillary back pressure, P_{cb}, opposes production of NWP and can be significant. P_{cb} is proportional to the interfacial tension (the term interfacial tension is applied to both oil/water and air/oil) and depends inversely on the size of the large pore throats at the surface and the size of pores connected with them in the open face region, through which the NWP exits the core.

One way to reduce the outlet NWP pressure is to allow NWP to vent from the otherwise sealed end of the core thus making the process co-current. Wang (1999) showed that this increased the

rate of recovery of air by imbibition of oil by about an order of magnitude. However, when the flow is co-current, the mechanism of imbibition is distinctly different from COUCSI.

In the present study of COUCSI, results were obtained for displacement of mineral oil by water, and of air by the same mineral oil, for three distinct types of Berea sandstone. These fluid pairs give very strongly wetted conditions with about 800 fold difference in viscosity ratios of the nonwetting to wetting phases. The pressure at the dead end, P_{end}, the location of the imbibition front, and production versus time were recorded. The information obtained by experiment was matched by numerical simulation in order to estimate the saturation and pressure profiles, the capillary pressure, P_{cf}, at the front, and the capillary back pressure at the open core face, P_{cb}.

Experiments

Eight Berea sandstone core samples, 3.8 *cm* in diameter and about 7 *cm* in length, were selected from three distinct types of Berea sandstone. Permeability ranged from 0.065 μm^2 to 1.094 μm^2 and porosity from 17% to 22%. The cylindrical surface and one end-face of each core were sealed with transparent epoxy resin. One end of a Nylon tube (inner diameter of 1.5 *mm* and outer diameter of 3 *mm*) was embedded a short distance into the core at the otherwise sealed end. The other end of the tube was connected to a pressure transducer. The tube and the connected transducer space were filled with oil.

Table 3.1 Core and fluid properties and measured characteristics of imbibition tests.

COUCSI	OIL / WATER				AIR / OIL			
μ_{nw}/μ_w	0.0038 *Pa.s*/0.00102 *Pa.s*				0.000018 *Pa.s*/0.0038 *Pa.s*			
σ	48.85*mN/m*				25.87*mN/m*			
CORE	H8O	H2O	M3O	L8O	H8A	H4A	M3A	L5A
d (cm)	3.796	3.794	3.792	3.797	3.789	3.789	3.793	3.8
L (cm)	6.864	6.18	7.493	6	7.12	7.523	7.365	6.806
K (μm^2)	1.094	1.048	0.681	0.065	1.054	0.973	0.503	0.07
Φ	0.221	0.22	0.208	0.171	0.219	0.217	0.202	0.172
t_{FAB} (hr)	2.5	2.1	4.7	14.9	7.1	7.9	13.9	66.7
t_{ep} (hr)	8.3	6.3	15	41.7	19.4	20.8	36.1	152
S_{w0}	0.5	0.5	0.52	0.43	0.5	0.5	0.52	0.53
$P_{end}(kPa)$	3.140	3.120	4.830	9.080	1.950	2.240	2.700	4.600

Four water/oil and four oil/air imbibition tests were performed (Table 3.1). For each fluid pair, duplicate tests were run on the highest permeability sandstone and single tests on the intermediate and low permeability rock. All experiments were conducted at ambient conditions, 21^oC and atmospheric pressure (79 *kPa,* 2300 *m* elevation). Soltrol 220®, of 0.0038 *Pa.s* viscosity, was used as the oil phase. Polar impurities were removed from the refined oil by flow through silica gel and alumina. In the water/oil experiments the aqueous phase was 10,000 *ppm* NaCl brine of 0.00102 *Pa.s* viscosity. Interfacial tensions were 48.9*mN/m* for the water/oil phase and 25.9*mN/m* for oil/air. The viscosity of air was 0.000018 *Pa.s*. In each imbibition experiment, volumetric production, imbibition front position, and NWP dead end pressure were measured simultaneously by techniques described below.

Water/oil imbibition
In the water/oil experiments, the core was positioned with the open face up. The recovery was determined from the volume of produced oil collected in an inverted closed funnel above the core (Fig. 3.1). A series of electrodes were embedded in the core. The distance of frontal advance was detected from the onset of electrical conductivity when the brine front contacted a particular electrode.

Oil/air imbibition
In the oil/air experiments, the core was immersed in oil contained in a beaker with the open face down (Fig. 3.2). The beaker was set on a balance with the pressure sensing tube fixed to a stand. The recovery was determined from the incremental loss in weight resulting from imbibition of oil into the core. The ratio of the outside radius of the nylon tube connected to the transducer to the inside radius of the beaker and decrease in the oil level in the beaker were both so small that the influence of buoyancy on recovery could be neglected. However, for measurements that lasted for more than about one day, a small correction was made for loss of oil by evaporation. In these tests, the distance advanced by the oil was obtained by direct observation of the invading front through the transparent resin coating.

Capillary pressure at the displacement front
In order to estimate the capillary pressure at the imbibition front, preliminary studies were run on the highest permeability sandstone butted to a section of low permeability sandstone which served as a semi permeable membrane set at the end face. Further details are given with the results.

Results and Discussion
Effect of gravity
The effect of gravitational forces acting over the core length is generally very small compared to capillary forces. Imbibition tests performed with the open end of the core facing either upward or downward showed very little difference in recovery behavior.

Mode of nonwetting phase production.
It was observed that the mode of NWP production was very different for the two fluid pairs. For imbibition of water, oil is produced almost instantaneously after immersion in brine. The oil appears as numerous small bubbles which tend to coalesce at the open face. For oil/air imbibition, there is no immediate production of air. When air bubbles do appear, they come from only one or two points on the open face.

Water/oil imbibition
Results presented for Core H80 in Fig 3.3 are typical of the four data sets obtained for water/oil imbibition. During the frontal flow period, the volume of water imbibed, Q_w, the distance advanced by the imbibition front, x_f, and the end pressure, P_{end} , were recorded. P_{end} , rose quickly for the first 60 seconds. It then remained constant at about 3.140 *kPa* until the front reached the end of the core (after 2.5 *hours*). The ratio of $Q_w/V_{\square}$ to x_f/L_c (the average saturation behind the front) was 0.42 until the imbibition front reached the end of the core. This behavior is consistent with the existence of a self-similar displacement. Both the fractional pore space filled ($Q_w/V_{\square}$) and the fractional distance imbibed (x_f/L_c) were proportional to the square root of time (Fig. 3.3).

After the front reached the end of the core, the rate of oil recovery decayed away from the square root of time relationship. The pressure measured at the closed end (P_{end}) decreased and eventually dropped to zero about 9 *hours* after the start of imbibition, possibly because of gradual loss of connectivity between the nonwetting phase in the core and that in the transducer. The final recovery was 50%.

Qualitatively comparable results were obtained for all four Berea sandstones with permeability ranging from 0.065 to 1.048 μm^2 (see Table 3.1). All end pressures eventually dropped to zero after the front reached the end of the core.

Oil/air imbibition

Example results for oil/air imbibition are presented in Fig. 3.4 (Core H8A). After the start of imbibition, P_{end} rose to a peak value of 2.118 *kPa* at 150 seconds and then dropped to 1.980 *kPa*. The initial build up in pressure corresponded to compression of the air initially contained in the core. No air was produced until about 3% pore volume had been invaded for the high permeability cores. After the drop in pressure that followed the very short initial compression stage, P_{end} remained constant whilst the imbibition front traversed the core. In contrast to water/oil, the pressure decreased only slightly after the front reached the closed end. This may be because the air in the tube connected to the transducer is connected to pockets of trapped air. Pressure is maintained because, unlike an essentially incompressible liquid phase, the trapped air can undergo changes in volume with only small change in pressure. Apart from the early time behavior, the overall increase in oil saturation and the distance of invasion were, as for water/oil imbibition, proportional to the square root of time during the frontal flow period. When the front reached the closed end of the core 7 *hours* after the start of imbibition, the NWP recovery, given by Q_w/V_ϕ , was 42%.

After the frontal flow period, the rate of recovery decayed and had almost ceased after 22 *hours* by which time the recovery had risen to 50%. After the front had reached the end of the core, the end pressure dropped by about 1% (about 0.020 *kPa*) even though no air was being produced.

Qualitatively comparable oil/air results were obtained for all four Berea sandstones with permeability ranging from 0.070 to 0.973 μm^2 (see Table 3.1). During the post contact period, the decrease in P_{end} tended to be slightly more for the less permeable cores. However, even for the least permeable core, L5A (0.070 μm^2), P_{end} had decreased only by 2% after 86 *hours*.

Estimation of capillary pressure at the imbibition front, Pcf

For the highest permeability Berea, an estimate of the frontal capillary pressures, P_{cf}, during COUCSI was made. The principle of the method is that if the frontal capillary pressure, P_{cf}, is lower than the capillary back pressure, P_{cb}, COUCSI will stop and the transducer will indicate a pressure which is assumed to be equal to the frontal capillary pressure. This was achieved by butting a slice of low permeability sandstone at the open face of a high permeability core. COUCSI initially occurred in the low permeability slice. Movement of the imbibition front eventually stopped in the high permeability core because the capillary pressure at the front was less than P_{cb} for the low permeability sandstone end piece. Estimates of P_{cf} in cores with permeability of about 1.05 μm^2 for both water/oil and oil/air cases were obtained from the increase

in end pressure. Details of core properties and results are given in Table 3.2. The estimated frontal interfacial curvatures (P_c/σ) were the same (0.254 μm^{-1}) for the two cases. The agreement of the curvatures, is consistent with the assumption that very strongly wetted conditions pertained for both water/oil and oil/air imbibition.

Table 3.2. Capillary pressures at the imbibition front.

COUCSI	**OIL/WATER**	**AIR/OIL**
μ_{nw}/μ_w	**0.0038 *Pa.s*/0.00102 *Pa.s*3.7255**	**0.000018 *Pa.s*/0.0038 *Pa.s***
σ	**48.85*mN/m***	**25.87*mN/m***
CORE	**H6O**	**H5A**
***d*(cm)**	**3.795**	**3.79**
***L*(cm)**	**6.967**	**8.04**
***K*(□m²)**	**1.067**	**1.042**
□	**0.222**	**0.221**
P_{cf}**(*kPa*)**	**12.359**	**6.600**
P_{cf}/□ μm^{-1}	**0.253**	**0.255**

Simulation

Differential equations for the imbibition behavior in terms of permeability, relative permeability, and capillary pressure were solved numerically. Details of the simulation are provided in Appendix A. A set of k_{rw}, k_{rnw} and P_c curves were found that were consistent with that of water/oil and oil/air COUCSI performance in the Berea sandstone with a permeability of 1.050 μm^2. It was assumed that the relative permeabilities and the interfacial curvature (P_c/σ) versus saturation relationships were correlated. Solutions were repeated to find the equation parameters that best simulated the experimental results (see Appendix B). The simulation variables of the curves for the 8 cores are shown in Table 3.3.

Table 3.3 Parameters of relative permeability and capillary pressure functions

COUCSI	OIL/WATER				AIR/OIL			
CORE	H8O	H2O	M3O	L8O	H8A	H4A	M3A	L5A
S_{wi}	0	0	0	0	0	0	0	0
S_{w0}	0.525	0.54	0.56	0.44	0.505	0.49	0.515	0.53
S_{wf}	0.29	0.25	0.3	0.32	0.29	0.285	0.26	0.345
k_{rw} at S_{w0}	0.6	0.6	0.6	0.6	0.75	0.75	0.75	0.75
k_{rnw} at S_{w0}	10^{-10}	10^{-10}	10^{-10}	10^{-10}	10^{-10}	10^{-10}	10^{-10}	10^{-10}
N_{nw}	2.6	2.6	2.6	2.6	2.6	2.6	2.6	2.6
k_{rnw} at S_{wf}	10^{-10}	10^{-10}	10^{-10}	10^{-10}	10^{-10}	10^{-10}	10^{-10}	10^{-10}
k_{rw} at S_{wf}	0.04	0.04	0.04	0.04	0.0582	0.0582	0.0582	0.0582
N_w	3	3	3	3	3	3	3	3
P_c at S_{wf} (kPa)	12.359	12.000	14.000	23.200	6.500	6.650	7.590	10.260
P_c at S_{w0} (kPa)	1.300	1.100	2.800	5.730	1.940	2.200	2.660	4.400
N_{pc}	1.75	1.75	1.75	1.75	1.75	1.75	1.75	1.75

Experimental and simulated results are presented in Fig. 3.5 for water/oil (Core H8O) and in Fig. 3.6 for oil/air (Core H8A). The initial period during which the air was compressed is not simulated because, in the present analysis, the fluids are assumed to be incompressible.

Saturation profiles

The simulation showed the conditions under which the frontal wetting phase saturations are finite. The measured WP saturations of both water/oil and oil/air imbibition when the front arrives at the dead end boundary were between 0.38 and 0.46 for the 8 samples. The final wetting phase saturations for both water/oil and oil/air imbibition were between 0.43 and 0.53 for all tested samples. The development of the simulated saturation profiles as the front travels through the core is illustrated in Fig. 3.7. The simulated profiles for water/oil are more curved at both the imbibition front and at the open face than for oil/air. This reflects the lower mean transmissibility at the front and at the exit end of the profile when oil is the nonwetting phase. The frontal WP saturations for both oil/air and water/oil imbibition were between 0.25 and 0.345 for the simulations for all tested samples. Because of the similarity solution, the profiles in the frontal flow period can be collapsed into a single curve by normalization with respect to distance advanced. The saturations in the post contact period rise globally and eventually reach the saturation at the outlet, S_{w0}.

It is noted that, even though the viscosity of air is lower than water and the oil is 3.8 *cp* in both water/oil and oil/air imbibition, the frontal period flow rate in the water/oil case is about three times faster than in the oil/air case for the same recovery. For example, from Figs. 3.5 and 3.6 and Table 3.1, t_{FAB} for water/oil is 2.5 *hours* versus 7 *hours*. for oil/air. An important contributing factor to this difference is that the interfacial tension of water/oil is almost twice that for oil/air. Also the viscosity of the WP in the oil/air case is 3.8 times the viscosity of the WP in the water/oil case. Because relative permeability for the WP in Berea sandstone is much lower than relative permeability for the NWP over a large part of the saturation range, WP viscosity also contributes to lower flow rate of WP (oil) in the oil/air case. From the two phase flow analysis presented in Appendix A, it is shown that the rate depends on the integral of the mobility

Pressure profiles

As imbibition progresses, the pressure profiles stretch over an increasing distance from the core inlet as shown in Fig. 3.8 for water/oil and in Fig. 3.9 for oil/air. The value of capillary back pressure, P_{cb}, was determined from the difference between $P_{end,}$ measured during the frontal flow period, and the pressure drop in the NWP that drives the viscous flow. For imbibition of brine against 0.0038 *Pa.s* oil, the value of P_{cb} was 1.3 *kPa* in the 1.094 μm^2 Berea sandstone core. The measured P_{end} during the frontal flow period was 3.140 *kPa*. For the oil/air results, from the enlarged simulated distribution of the NWP pressure shown in Fig. 9, it can be seen that the behavior of P_{nw} in the oil/air case is comparable to that in the water/oil case; however, P_{end} is only 0.038 *kPa* higher than P_{cb}. This difference can be neglected for most practical purposes.

The overall character of the pressure behavior is consistent with expectations based on the similarity solution. The solution infers that for the advance of any particular saturation, S_w, along the core, the difference between its associated capillary pressure and the back capillary pressure ($P_c(S_w) - P_{cb}$) is constant until the front contacts the closed end of the core.

COUCSI displacement curvatures

Through simulation it was found that the experimental COUCSI behavior in both water/oil and oil/air cases could be matched closely by typical relative permeability and capillary pressure curves (Appendix B). Simulations performed for water/oil COUCSI in core H8O and for oil/air COUCSI in H8A (Figs. 3.5 and 3.6) are of special interest because this was the high permeability sandstone (K=1.05 μm^2) for which P_{cf} had been estimated by experiment (see Table 3.2). If the relative permeabilities, scaled for differences in end points, are assumed to be identical for all permeabilities and the capillary pressures scale by the Leverett (1939) function, then the pair of P_{cf} and P_{cb} for any core can be found by running the simulations until the three experimental curves prior to FAB are matched. This stage of the simulation provides the average saturation from the open face to the imbibition front. Simulation of the changes in saturation profile along the core requires that the post contact production also be matched.

The simulated values of P_{cf} and P_{cb} in water/oil and oil/air cases determined for the different permeability Berea sandstones are listed in Table 2. The P_{cb} in the oil/air cases is almost equal to P_{end} in the frontal flow period because resistance to flow of the very low viscosity NWP (air) is very small. For water/oil imbibition, P_{cb} is significantly lower than P_{end} in the frontal flow period because of the viscous resistance to flow of the NWP liquid.

Comparison of water/oil and oil/air capillary displacement mechanisms can be made in terms of effective radii given respectively by capillary pressure and permeability. Porous media can be characterized by the radius of an equivalent parallel bundle of equal tubes model (the Leverett microscopic pore radius), $r_L = \sqrt{8K/\phi}$. Pore radii corresponding to capillary pressure at the core face or the front (P_{cb} or P_{cf}) are given by $2\sigma/P_c$. Plots of the interface radius of curvature versus the Leverett radius are presented in Fig. 3.10. Both radii increase together as expected. Interfacial curvatures at the displacement front, P_{cf}/σ, for a given core are the same for both water/oil and oil/air imbibition (see Fig. 10).

The radii at the open face, r_b, (associated with the capillary back pressure, P_{bp}), are much lower for production of oil (water/oil imbibition) than for production of air (oil/air imbibition). This is probably due to the differences in conditions at the onset of production. For imbibition of water against oil, oil is produced almost instantaneously after immersion in brine. For imbibition of oil against air, because of the compression period, production of air bubbles is delayed. As oil invades the core, oil/air interfaces drive into the core building up the air pressure until the compressed air counterflows through a series of pore throats and vents at the open face. The selectivity of gaining the path by which gas is produced explains why gas bubbles are produced from only one or two locations on the open face. Furthermore the exit pores are not likely to be the largest pores at the core face. In contrast, oil bubbles appear almost instantaneously at many points on the open face. The oil bubbles come from throats and pores of larger than average size in the vicinity of the open face.

The scaled interfacial curvature, P_{cb}/σ, associated with back pressure at the open face in the oil/air case range from about 2/5 down to 1/3 of the interface curvature at the front, C_f. For water/oil COUCSI the ratio of C_b ranges from about 1/4 down to 1/9 of C_f. Thus the contribution

to the relative reduction in rate of flow of the NWP because of the capillary back pressure at the open face for oil/air imbibition is about 2.4 to 3 times that for water/oil imbibition.

Conclusions

1. A period of frontal flow has been identified for linear COUCSI during which the distance advanced by the front is proportional to the square root of time. This result is consistent with a similarity solution for the frontal advance period.

2. The pressure of the nonwetting phase in the dead end space ahead of the imbibition front is constant from a short time after the onset of imbibition until the front arrives at the core boundary.

3. The capillary back pressure associated with production of NWP at the open face of the sample, is essentially constant during the frontal flow period. The production mechanism at the open face is basically a drainage process.

4. If the capillary pressure in the core is higher than the capillary back pressure, imbibition will occur. The rate of counter-current imbibition is proportional to the interfacial tension and depends on the integral of the mobility along the invaded portion of the core.

5. The capillary pressure and wetting phase effective permeability at residual nonwetting phase saturation can be determined from measurements of the location of the imbibition front versus time, recovery versus time, the dead-end non-wetting-phase pressure, and the absolute permeabilities to brine and oil. Typical relative permeabilities and imbibition capillary pressure curves can be tuned to match the capillary pressure at the front and the back pressure associated with production of the nonwetting phase.

6. From simulations that assume fixed relative permeabilities and scaled imbibition capillary pressure, the capillary back pressure in the oil/air case is about 2/5 down to 1/3 and in the water/oil case about 1/4 down to 1/9 of the capillary pressure at the imbibition front in Berea sandstone with permeabilities ranging from 0.065 to 1.1 μm^2.

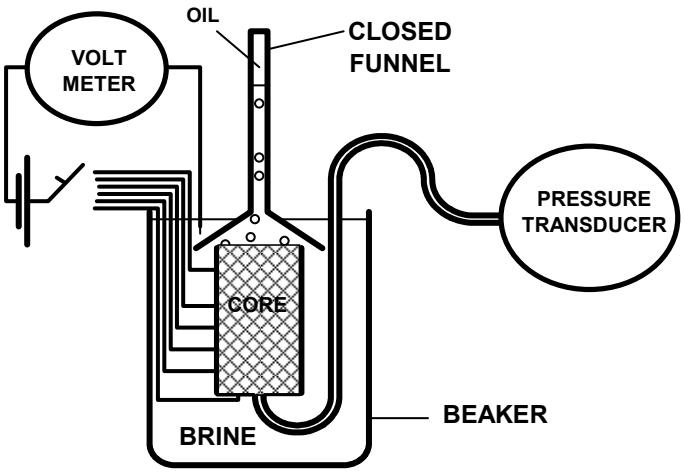

Fig. 3.1 Apparatus for simultaneous measurements of production, location of the front, and dead end pressure during water/oil spontaneous imbibition.

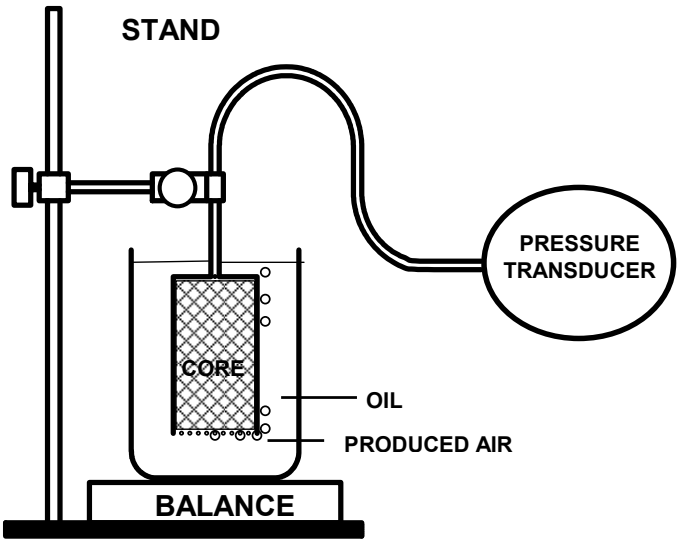

Fig. 3.2 Apparatus for simultaneous measurements of production, location of the front, and dead end pressure during oil/air spontaneous imbibition.

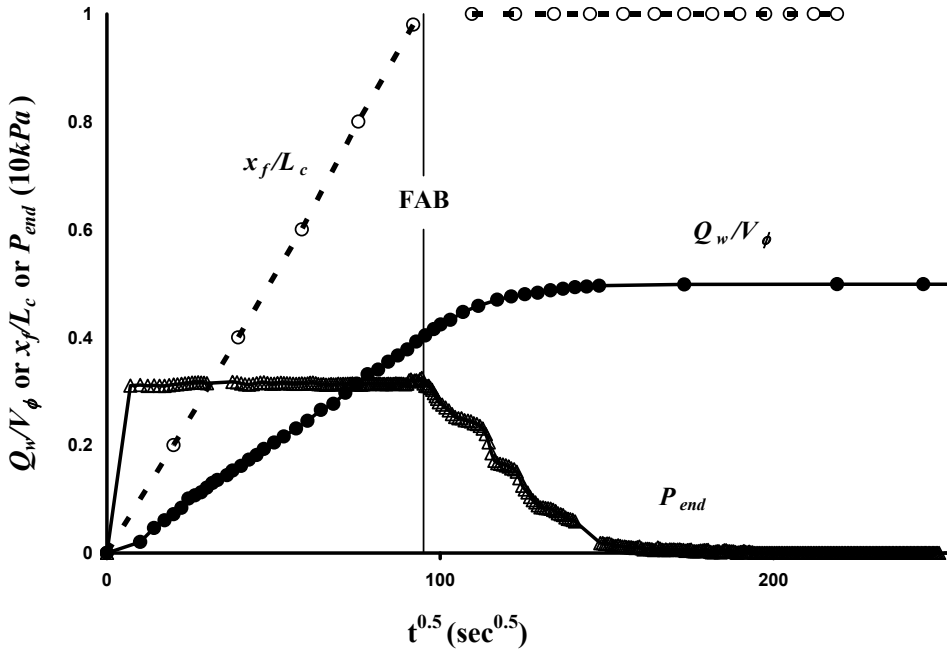

Fig. 3.3 Typical experimental results for water displacing oil versus square root of time (Core H8O). Qw/Vφ is the fractional saturation of total pore space filled by the invading wetting phase. xf/Lc is the fraction of the bulk volume of the core (proportional to fraction of pore volume and also the fractional distance through which the front has advanced as determined by electrical contact. Pend is the pressure measured at the dead end. FAB (front at boundary) indicates the time when the front arrives at the dead-end. Apart from very early time, the distance advanced by the front and the production prior to FAB are proportional to the square root of time.

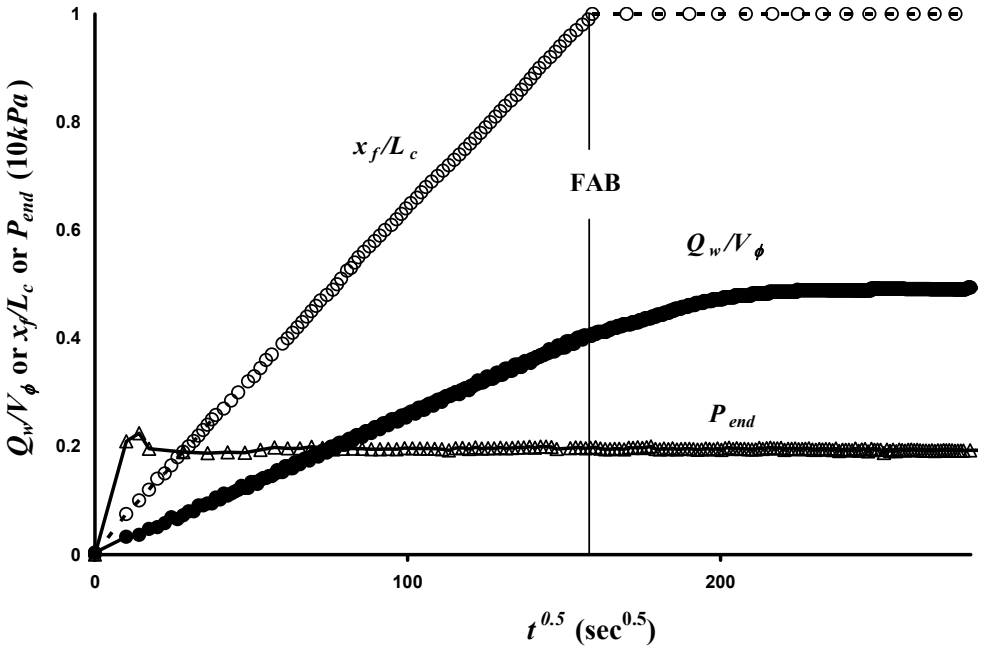

Fig. 3.4 Typical experimental results for imbibition of oil against air versus square root of time (Core H8A). Apart from very early time, the distance advanced (determined visually) and the production prior to FAB are proportional to the square root of time.

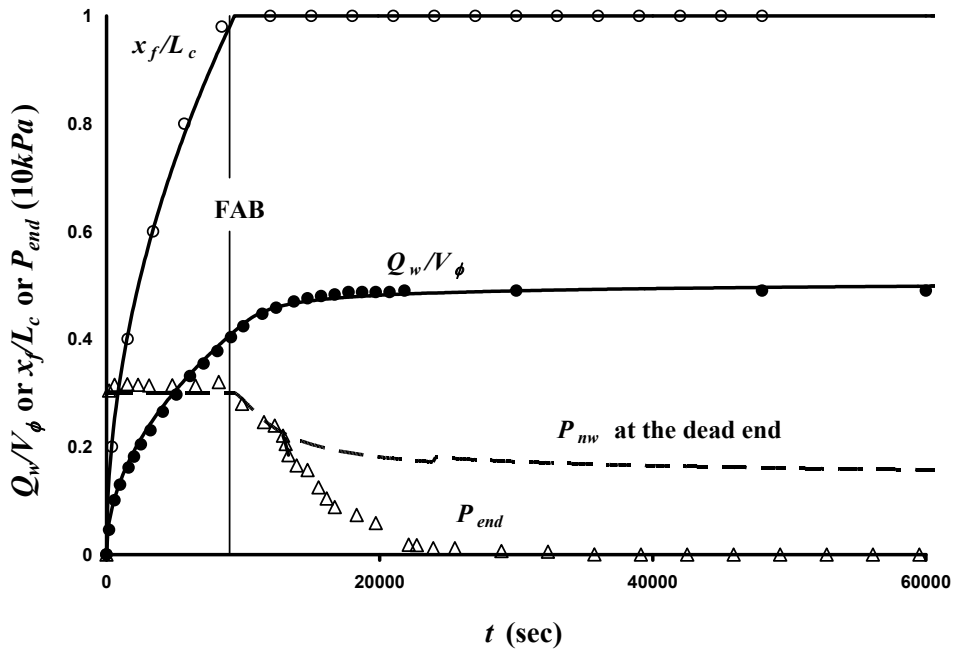

Fig.3.5 Comparison of experimental and simulated results for imbibition of brine against oil (Core H8O). The points (reduced in number from the results presented in Fig. 3.3) are the experimental data; the lines are from simulations.

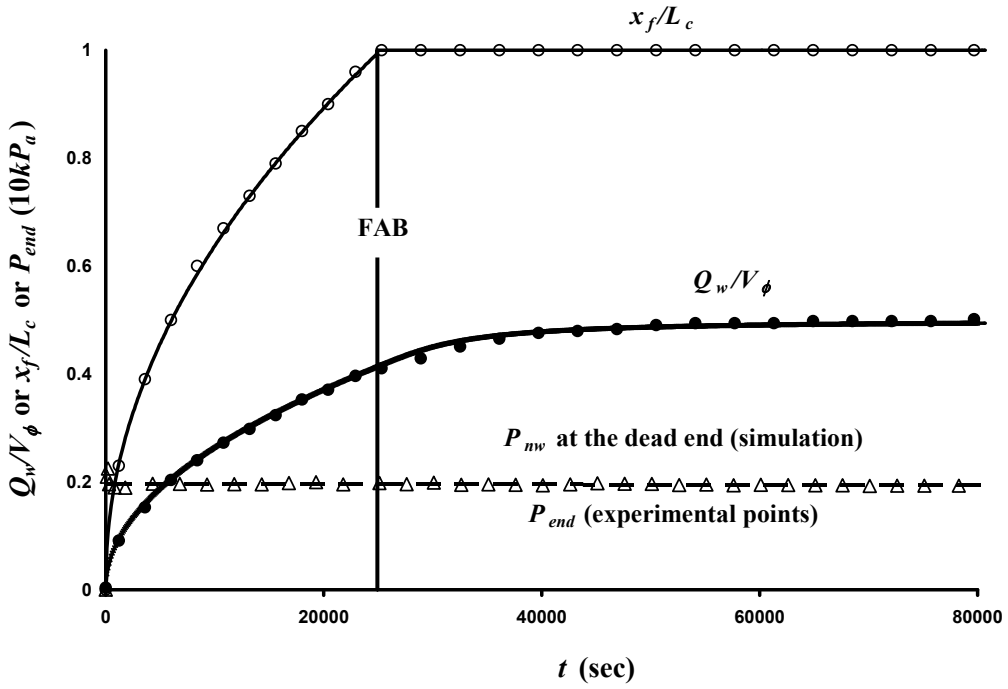

Fig. 3.6 Comparison of experimental and simulated results for imbibition of oil against air (Core H8A). The points (reduced in number from the results presented in Fig. 3.4) are the experimental data; the lines are from simulation.

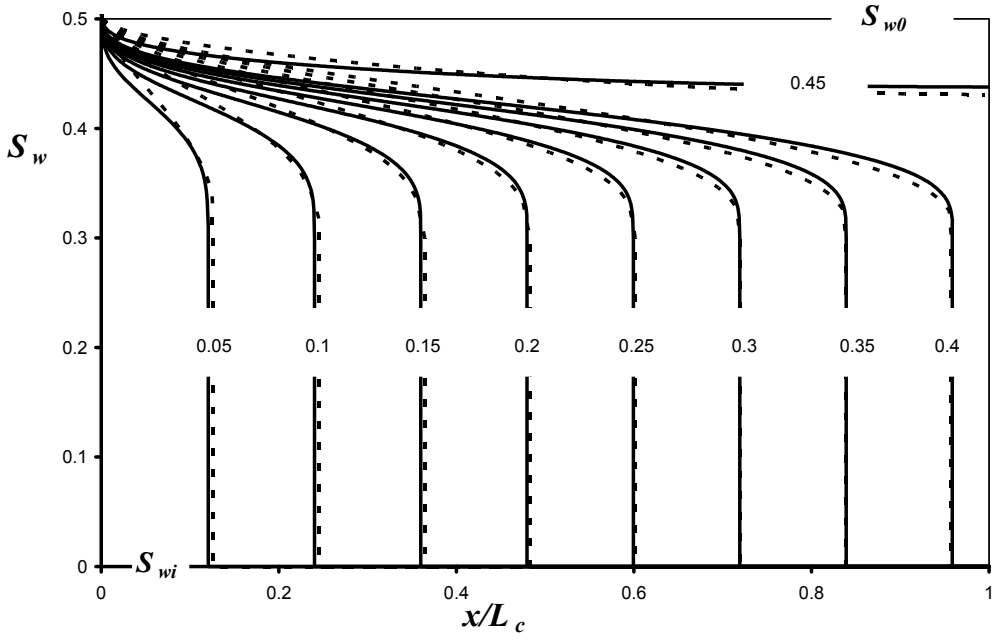

Fig. 3.7 Simulated saturation profiles during water/oil COUCSI for Core H8O (solid lines) and oil/air COUCSI for core H8A (dashed lines). The intervals of the recovery, Qw/Vϕ are 0.05.

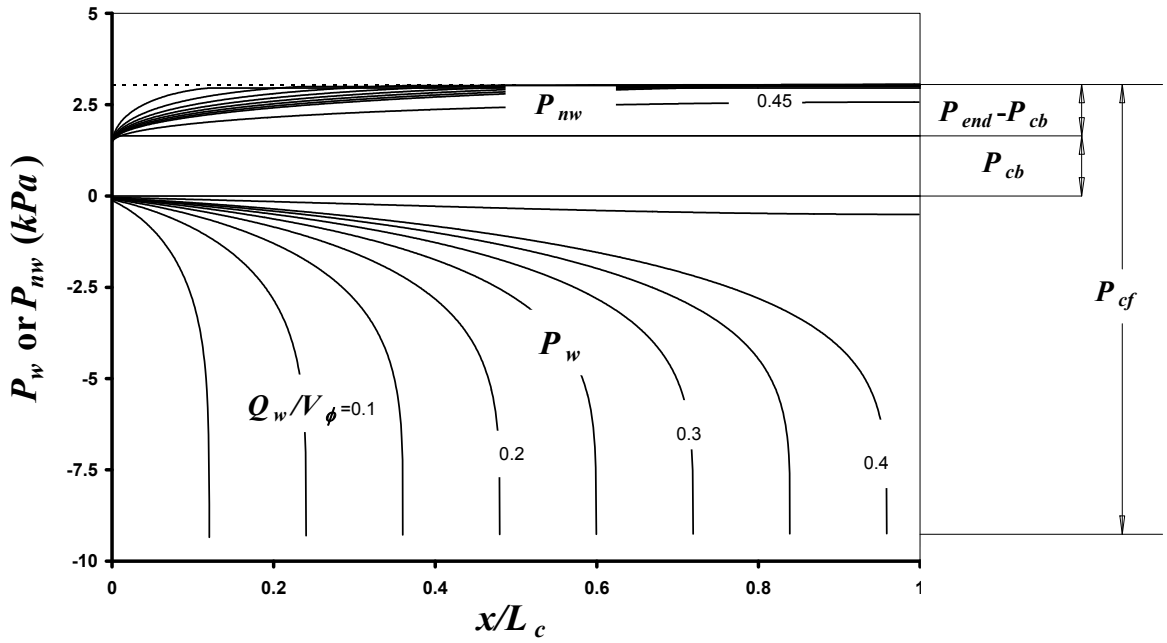

Fig. 3.8 Pressures profiles of WP and NWP during water/oil COUCSI in Core H8O determined by simulation. The maximum difference between Pnw and Pw is equal to the capillary pressure, Pcf, at the front (the value is 12.359 kPa).

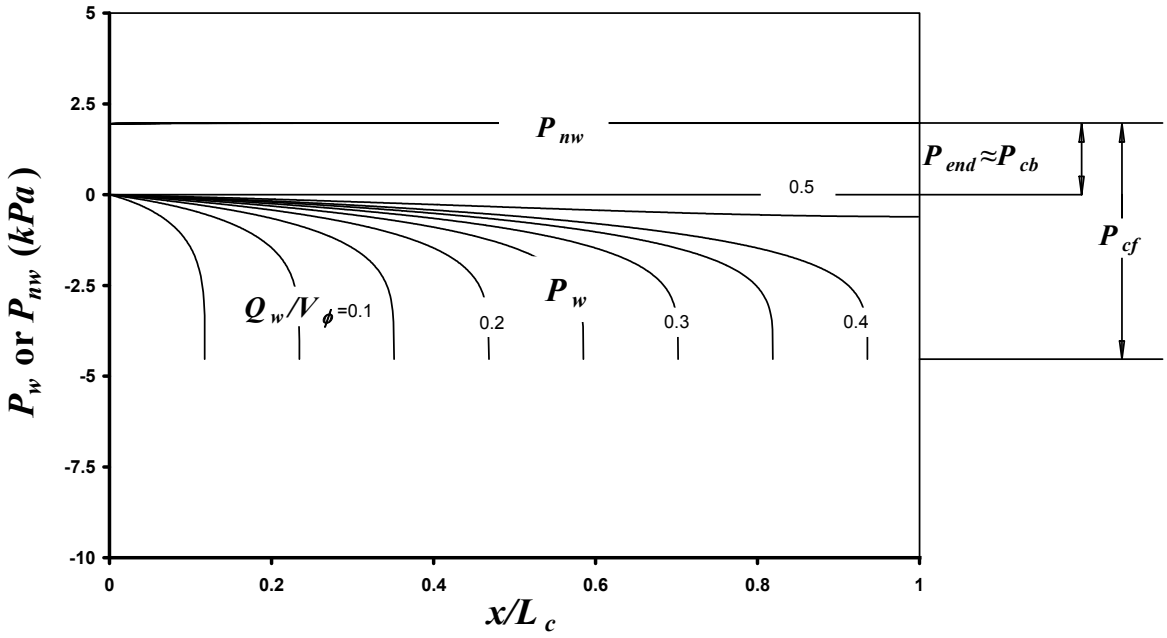

Fig. 3.9 Pressures profiles in WP and NWP during oil/air COUCSI in Core H8A determined by simulation. The maximum difference between P_{nw} and P_w is equal to the capillary pressure at the front, P_{cf}, (the value is 6.500 kPa). For oil/air, the difference between the end pressure, P_{end}, and back capillary pressure, P_{cb}, is hard to distinguish at the scale of the diagram.

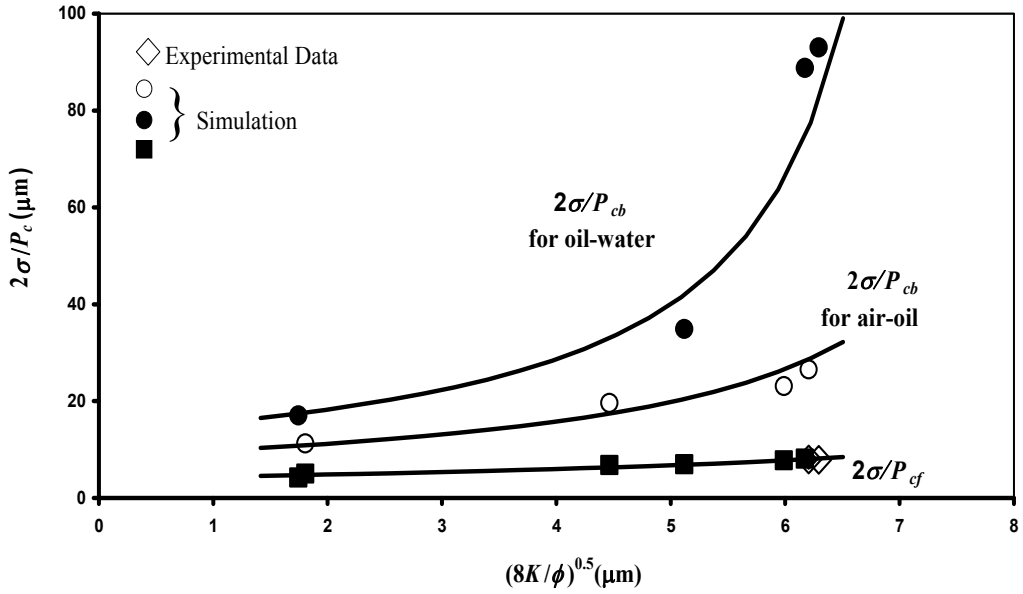

Fig. 3.10 Relationships between meniscus radii at the front and at the open face compared with the Leverett radius. Solid circles represent the water/oil data (σo-w = 48.85 mN/m) and open circles the oil/air data (σa-o = 25.87 mN/m).

Appendix 3A

Mathematical model

The basic equations used for deducing the similarity solutions have been given in the simulation method described in Ruth et al., 2000.

$$\frac{\partial}{\partial x}\left[\bar{\lambda}\frac{\partial P_c}{\partial x}\right]=\phi\frac{\partial S_w}{\partial t} \qquad 3A.1$$

where S_w is saturation of wetting phase, P_c is capillary pressure and average mobility, $\bar{\lambda}$, is a function of saturation only and is defined as

$$\bar{\lambda}=\frac{Kk_{rw}k_{rmw}}{\mu_w k_{rmw}+\mu_{nw}k_{rw}} \qquad 3A.2$$

where K is absolute permeability to air, k_{rw} is relative permeability of wetting phase, k_{rnw} is relative permeability of non-wetting phase and μ_{nw} and μ_w are viscosities of the non-wetting phase and wetting phase respectively.

Note that this equation is not a pair of simultaneous parabolic partial differential equations in unknown pressure in the WP and NW as is usually obtained. Instead it is only one parabolic partial differential equation in known capillary pressure, P_c. A finite difference equation can be derived immediately (Eq. 3A.1).

$$\Delta S_{w(i)}=\frac{1}{V_\phi}[Tr_{(i-1+1/2)}(P_{c(i)}-P_{c(i-1)})-Tr_{(i+1/2)}(P_{c(i+1)}-P_{c(i)})]\Delta t \qquad 3A.3$$

where i is the ordinal number of the grids, and $Tr_{(i+1/2)}=\frac{A}{2\Delta x}(\bar{\lambda}_{(i)}+\bar{\lambda}_{(i+1)})$ is the mean transmissibility from midpoint weighting. This approximation is of second-order, which helps to produce fast convergence of results (Fig. 3A.1). The more common upsteam weighting is a first-order approximation. Using this weighting, no convergence could be obtained for the water/oil case. Even using a fast personal computer, a single simulation was not found even after many days. The midpoint weighting is used in both water/oil and oil/air simulations, even through the correct simulation results for oil/air cases can be obtained by using upstream weighting. Why upsteam weighting can not produce results in some COUCSI simulations in a timely manner needs to be further explored.

The starting condition for COUCSI is

$$S_w=S_{wi} \qquad 3A.4$$

for the partial differential equation (Eq. 3A.1), where S_{wi} is the original WP saturation.
in the finite difference equation (Eq. 3A.3)

$$S_{w(i)}=S_{wi(i)} \qquad 3A.5$$

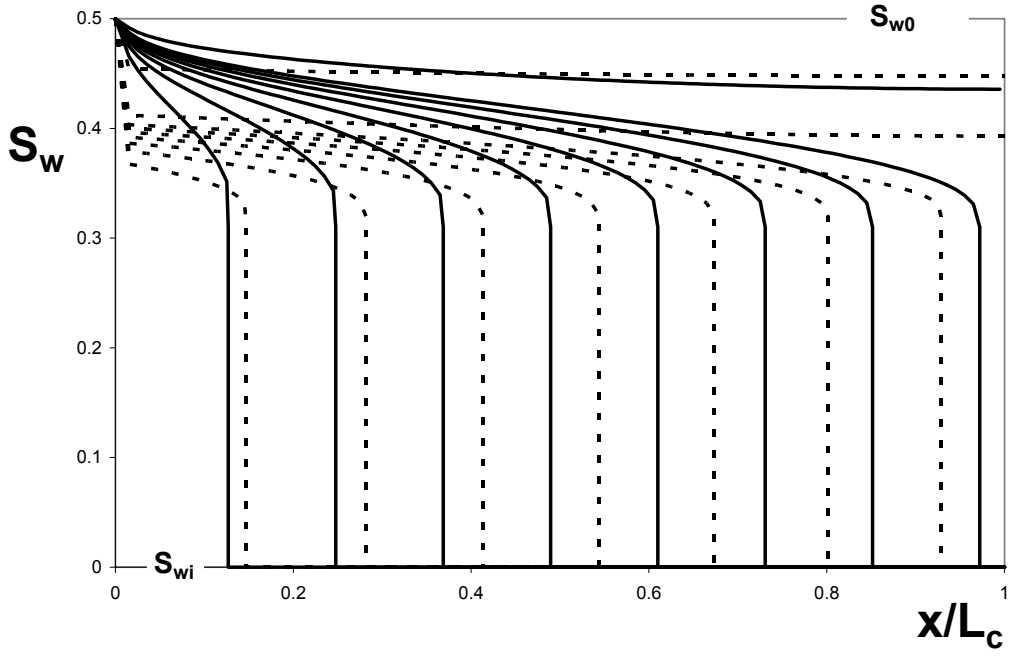

Fig. 3A.1 Comparison of the profiles calculated from the programs based on midpoint weighting (solid lines) and upsteam weighting (broken lines) The results were generated for Δx=100, Δt=0.05. The intervals of recovery, Qw/Vϕ, are 0.05.

With the boundary condition for the general COUCSI partial differential equation (Eq. 3A.1) as:

$$P_w = 0 \quad at \quad x = 0 \tag{3A.6}$$

Also

$$q_w = q_{nw} = 0 \quad at \quad x = L_C \tag{3A.7}$$

where P_w is the pressure in wetting phase, x is the distance from the open face, L_c is the core length, q_w is the flow rate of wetting phase and q_{nw} is the flow rate of non-wetting phase.

If the number of grid blocks for the core is *N-2* and if Grid *1* is for the *WP* reservoir and Grid *N* is for the grid with a mirror image of the last core grid, Grid *N-1*, the corresponding boundary condition for the above general finite difference equation can be written as

$$S_{w(1)} = S_{w0} \qquad at \quad i = 1 \tag{3A.8}$$

and

$$S_{w(n)} = S_{w\ (n-1)} \qquad at \quad i = N \tag{3A.9}$$

where S_{mw0} is the final recovery for COUCSI in the simulation.

Since every parameter or variable is known, the finite difference equation (Eq. 3A.3) is an explicit function, by which the saturation increment for each grid can be calculated for each time step. The numerical simulation will produce a saturation profile varying with time. q_w, q_{nw}, P_w and P_{nw} need not be calculated directly in the simulation. They can be readily obtained from the saturation profiles in the output file.

To obtain the saturation profile without distortion ('in conditional stability' as described in Aziz, 1979) the time step, Δt, must be less than a limit for a certain division x/L_c. From this study, if x/L_c is fixed and Δt is under the time step limit, the resultant profile will be the same no matter what Δt is used. As is already known (Richtmyer and Morton, 1967), there exists a constant $(x/L_c)\Delta t$, the upper limit for which is the so called 'condition of stability' in the simulation of a given Buckley-Leverett flow. However for our program, it was found that there existed a constant $(x/L_c)^2\Delta t$ for the upper limit (Fig. 3A.2) in COUCSI. Therefore, to obtain a COUCSI result with a high degree of convergence, much more calculation time is
required.

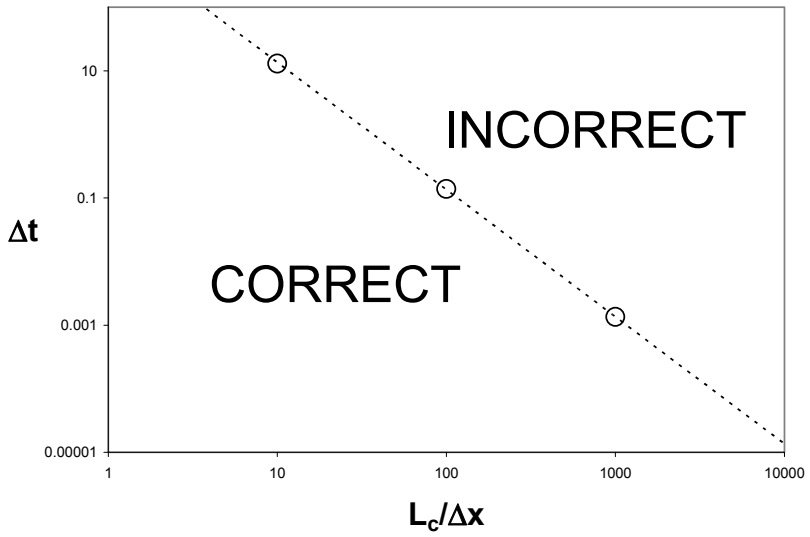

Fig. 3A.2 Condition for the results without distortion in H8O simulation. Points represent the tested critical points. The broken line represents the division between 'correct' and 'incorrect' results for any chosen grid. Correct results do not depend on the size of the time step. 'Incorrect' results vary with the size of the time step.

Appendix 3B

Construction of P_c/σ and krw/Kwe and k_{rnw}/K_{nwe} functions

For the measured relative permeability curves of Berea sandstone [Fulcher, 1985], the relative permeabilities were modeled by,

$$k_{rnw}/K_{nwe} = (k_{rnw0} - k_{rnwf})\left(\frac{S_{wo} - S_w}{S_{wo} - S_{wf}}\right)^{N_{nw}} + k_{rnwf} \qquad 3B.1$$

and

$$k_{rw}/K_{we} = (k_{rwf} - k_{rw0})\left(\frac{S_{wf} - S_w}{S_{w0} - S_{wf}}\right)^{N_w} + k_{rw0} \qquad 3B.2$$

where K_{we} and K_{nwe} are the effective permeabilities for the WP and the NWP respectively, S_{wf} is the S_w at the front, k_{rwf} is the relative permeability at the front, and k_{rw0} is the relative permeability at the open face.

K_w (brine) is 0.55 times K_g (gas) (Chatzis and Morrow, 1984). The permeability to oil, K_o was 0.8 times K for air (K_{air}) (Fig. 3B.1). The relative permeability for brine, K_w at the residual oil saturation (S_{or}), $K_w(S_{or})$ is 0.0458. In simulation we adopted 0.04 as the value of the brine relative permeability at the open face and 0.0727 for oil.

The imbibition capillary pressure curve for Berea sandstone was assumed to be parabolic in form.

$$P_c = (P_{cf} - P_{c0})\left(\frac{S_{wo} - S_w}{S_{wo} - S_{wf}}\right)^{N_{pc}} + P_{c0} \qquad 3B.3$$

The variables of the curves used for each core are listed in Table 3.2. Results for Core H8A are plotted in Fig. 3B.2.

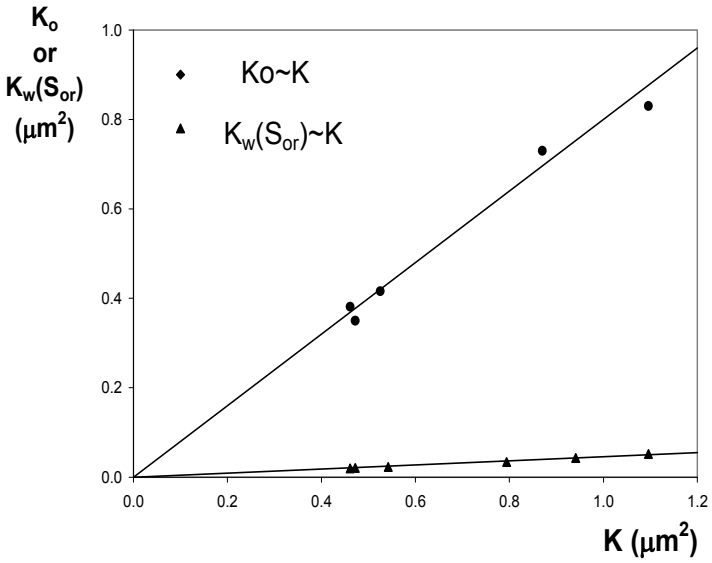

Fig. 3B.1 K_o versus K (gas permeability) and $K_w(S_{or})$ versus K

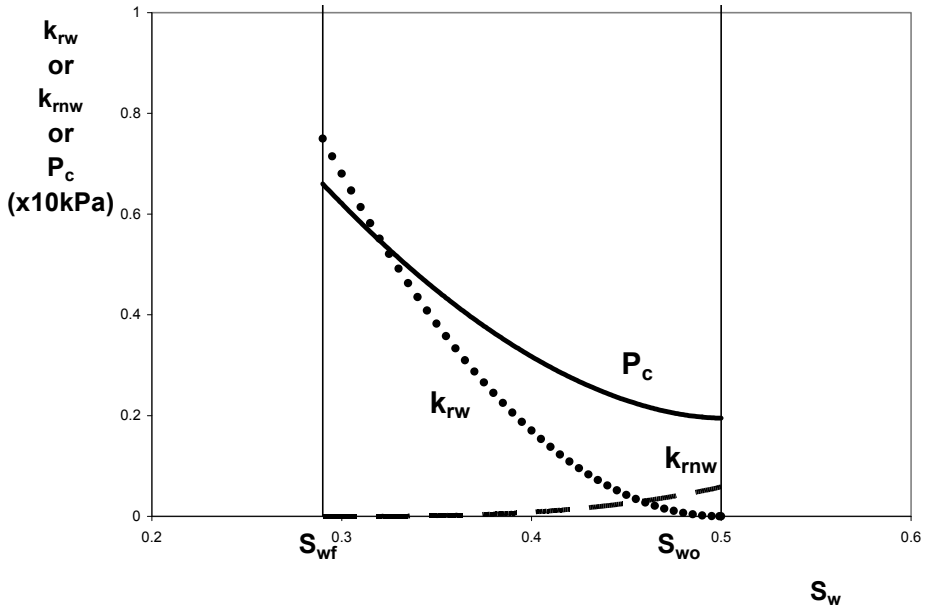

Fig. 3B.2 Relative permeabilities and capillary pressure for Core H8A

Even with constraint on the possible sets of k_{rw}, k_{rnw} and P_c curve shapes, simulations could be performed which provided a close match with the three measured parameters of a COUCSI experiment. Furthermore, a single set of k_{rw}, k_{rnw} and P_c curves can be obtained for both water/oil and oil/air COUCSI experiments with duplicate core samples. A quick search for the appropriate set of k_{rw}, k_{rnw} and P_c curves was performed using the following steps.

a. Fix S_{w0} at the experiment value, fix k_{rw} at S_{w0} as 10^{-10} (using 10^{-10} instead of zero to avoid occurrence of a zero-divide), fix k_{rnw}/K_e at S_{wf} at an arbitrary value, say 0.8 and k_{rw}/K_e at S_{w0} as $0.04/K_e$. Fix N_{nw} at an arbitrary value, say 2 (In the oil/air case the resistance to flow of the NWP is very small). Find appropriate N_{pc} and N_w and S_{wf} values to match the oil/air experiments. (The simulated final saturation can be lower).
b. Increase the simulation S_{w0} to match the final recovery (This procedure will adjust k_{rnw} at the experimental S_{w0} to be finite.).
c. Change N_w and P_{cb} so that the simulation curves match the water/oil performances (P_{nw} at the dead end during the post contact period can be different from P_{end} after WP has arrived at the dead end.)
d. With N_{nw}, N_w and N_{pck} fixed, change P_{cf} and P_{cb} (neither is directly measured) to match the results of the six other experiments of this study.
e. If the P_{cf} points scatter on the $P_{cf} \sim K$ plot, change k_{rnw} at the S_{wf} (k_{rnw} has been roughly estimated before) to obtain a smoother distribution.

If the post contact performance still has the same positive or negative errors within the comparable stages, use of a multiple-term formula instead of parabolic expressions should be considered. (However, such errors were not found in the present study).

Task 4. *Network/numerical model and new imbibition data.*

Scaling of Oil Recovery by Spontaneous Imbibition for Wide Variation in Aqueous Phase Viscosity with Glycerol as the Viscosifying Agent

H. Fisher and N.R. Morrow
Journal of Petroleum Science and Engineering, 2006, vol. 52, 1-4, 35-53

Abstract
Oil production by spontaneous imbibition can be the key mechanism for oil recovery from naturally fractured reservoirs. Laboratory results of oil recovery through spontaneous imbibition are commonly scaled-up to forecast oil recovery at the reservoir scale. Numerous questions arise with respect to the theory of spontaneous imbibition and valid scaling of laboratory imbibition data.

Use of glycerol as a viscosifying agent for aqueous solutions has many advantages and applications. A systematic study has been made of the physical and interfacial properties of glycerol/water and glycerol/brine (synthetic sea water) solutions. The solutions were used to investigate oil recovery by spontaneous imbibition at very strongly water-wet conditions for aqueous phase viscosities ranging from 1-1650 cP.

Results for aqueous/oleic liquid pairs with matched viscosities were correlated satisfactorily by the Mattax and Kyte scaling group. Data were also obtained for a wide range of unmatched viscosities. Three data sets for unmatched viscosity were obtained with oil viscosity fixed at 4, 22, or 43 cP and aqueous phase viscosity varied from 1 to 1650 cP. Use of the geometric mean viscosity (Ma et al., 1997) in the definition of dimensionless time gave satisfactory correlation of data for brine/oil viscosity ratios of up to about 4. A slight trend of increase in dimensionless time with viscosity ratio within the correlated data became accentuated with increase in viscosity ratio above about four. Residual oil saturation attained by spontaneous imbibition showed an overall small decrease with increase in viscosity of the aqueous phase.

Introduction
Oil production from naturally fractured reservoirs often depends on spontaneous imbibition of brine into oil bearing matrix blocks. The rate and extent of recovery depends on both rock and fluid properties and rock/fluid interactions (Zhou et al., 2000; Xie et al., 2000). Oil recovery is often estimated by scaling laboratory imbibition measurements on core plugs to oil production on a reservoir scale. Mattax and Kyte (1962) introduced a scaling group based on the theoretical analysis of Rapoport and Leas (1953) and Rapoport (1954). Six necessary conditions were identified for the scaling group to be applicable, one being that viscosity ratios are identical. Experimental investigation of imbibition for unmatched viscosities with over two orders of magnitude variation in oil phase viscosity showed that results were closely correlated by the geometric mean viscosity of the oleic and aqueous phases (Ma et al., 1997). In the present work, aqueous phase viscosity was varied over three orders of magnitude through use of glycerol as a viscosifying agent. Extensive spontaneous imbibition data sets are reported for both matched and unmatched viscosities.

Experimental

Materials

Liquids

Aqueous Phase. In this study, glycerol ($CH_2OHCHOHCH_2OH$), supplied at 99.5% purity by EMD Chemicals, Inc., was utilized to viscosify the wetting phase. In previous studies, glycerol was used to viscosify the aqueous phase for the purpose of adjusting the oil/aqueous phase viscosity ratio (Leverett et al., 1941; Rapoport and Leas, 1953; Kyte and Rapoport, 1958). None of the reports give detailed information on the physical properties of aqueous glycerol solutions.

Glycerol is a trihydric aliphatic alcohol of great industrial importance (Monick, 1968). It is an odor- and colorless liquid with a molecular weight of 92.09. The density of the supplied glycerol is 1.261 g/cm^3 at 20ºC. One of the pronounced physical properties of glycerol is its viscosity. For glycerol as supplied, the viscosity is 1650 cP at 20ºC and is highly sensitive to temperature. Whereas the viscosity decreases with temperature and the addition of water, electrolytes cause an increase of the viscosity of anhydrous glycerol as well as its aqueous solutions. The refractive index of glycerol at 20ºC is 1.4740. Glycerol boils at 290°C at atmospheric pressure but boiling is accompanied by decomposition. The freezing point of glycerol is about 18°C. In the anhydrous state, glycerol is a highly hygroscopic material. Glycerol is soluble in water in all proportions and insoluble in hydrocarbons. The surface tension is 63.4 dyn/cm at 20ºC, less than the surface tension of water, but higher than the surface tension of most organic liquids. Considerable attention has been given to molecular modeling of the nature of hydrogen bonding in glycerol (Root et al.1997).

In the present work synthetic seawater (Table 4.1) rather than distilled water was used in preparation of glycerol/brine solutions in order to avoid possible problematic aqueous phase/rock interactions associated with ionic strength. Mixtures of seawater and glycerol were prepared based on constituent weight percent. Ionic strength was not adjusted for the addition of glycerol and so decreased with decrease in water content. Before use in imbibition experiments, the aqueous phase was evacuated for 3 hours to minimize the possibility of the evolution of gas during the imbibition process. Specific aqueous phase properties were measured directly before a spontaneous imbibition test.

Oleic Phase. The oil phase was composed of Soltrol 220® (hereafter described as low viscosity oil, LVO) of 3.9 cP viscosity and 173 cP white mineral oil (hereafter described as high viscosity oil, HVO) (Table 2). Polar contaminants were removed from the mineral oils by contacting the oil with alumina and silica gel either in packed columns (LVO) or by suspension followed by filtration (HVO). Mixtures of the two oils were used to prepare oils of intermediate viscosity. Each mixture was evacuated for about 3 hours to remove any dissolved gas prior to measurement of the physical properties of a specific mixture.

Sandstone

Cylindrical Berea sandstone cores with a nominal diameter, d, of 3.81 cm and a nominal length, l, of 6.35 cm were cut from three different Berea sandstone blocks. The cores were washed, dried at ambient temperature for one day and then oven dried at 105°C for two days. Subsequently, nitrogen gas permeability, k_g, was measured in a Hassler-type core holder at a confining pressure of 300 psi. The permeability to nitrogen ranged from 59 to 85 md. Core porosity was calculated

from the increase in mass that resulted from saturation of a core sample with oil. The rock porosity varied from about 16 to 18%. Core properties are provided with the individual data sets. The characteristic length, L_c, for each core for all faces open to imbibition is given by (Zhang et al., 1996)

$$L_c = \frac{ld}{2\sqrt{d^2 + 2l^2}} \qquad 4.1$$

All cores were cut to nominally the same size and so had essentially the same characteristic length of about 1.24 cm.

Procedure

Liquid Properties

The density of the liquid mixtures was measured by Paar Density Meter DMA 48 at 20°C. The liquid viscosities were measured with Cannon viscometers. The surface tension of the aqueous phase was measured by the dynamic Wilhelmy plate method (Krüss Processor Tensiometer K12) using a platinum plate. The same equipment was used to determine contact angles on quartz plates. Interfacial tension was obtained with a Krüss Drop Volume Tensiometer DVT-10. Viscosity, surface and interfacial tension, and contact angle were measured at ambient temperature (very close to 20ºC).

Spontaneous Imbibition

In all experiments, the initial water saturation was 0, a condition which has been adopted as a convenient reference starting condition in previous studies (Mattax and Kyte, 1962; Zhang et al., 1996; Ma et al., 1999). The boundary condition for each core was all faces open.

Oil recovery versus time was measured in standard glass imbibition cells at ambient temperature. Results are reported as four experimental data sets. The first set was for matched fluid viscosities ranging from 4 to 172 cP. Three data sets were obtained for unmatched viscosity with each set distinguished by the choice of oil phase viscosity, the values being 4, 22, and 43 cP. Imbibition results for matched viscosity were correlated by the scaling group proposed by Mattax and Kyte,

$$t_{D,MK} = t\sqrt{\frac{k}{\phi}}\frac{\sigma}{\mu_w}\frac{1}{L^2} \qquad 4.2$$

Results for the unmatched viscosity were correlated by the modified Ma et al. scaling group

$$t_D = t\sqrt{\frac{k}{\phi}}\frac{\sigma}{\mu_g}\frac{1}{L_c^2} \qquad 4.3$$

where $\mu_g = \sqrt{\mu_w \mu_o}$ is the geometric mean viscosity.

Results and Discussion

Properties of Brine/Glycerol Solutions

Density. Measured densities of glycerol/synthetic seawater along with reported densities (CRC Handbook, 1976-7) for distilled water/glycerol mixtures are shown in Fig. 4.1. For both distilled water and brine there is no significant volume change of mixing with glycerol. The aqueous phase density increases linearly with increase in glycerol concentration from 1.0238 g/cm^3 for seawater to 1.2616 g/cm^3 for glycerol.

For aqueous phase prepared with seawater, the density can be fitted by

$$\rho_{ap} = 0.0024 C_{gl} + 1.024 \qquad 4.4$$

For distilled water the aqueous phase density is closely approximated by

$$\rho_{ap} = 0.0027 C_{gl} + 0.995 \qquad 4.5$$

Viscosity. The viscosities of glycerol/brine mixtures and literature values for glycerol/distilled water are shown in Fig. 2 as a semilog plot. The viscosity of glycerol (described as > 99.5% purity) at ambient temperature is 1647 cP. However, addition of a small volume of water causes enormous reduction in aqueous phase viscosity. For example addition of 3 wt % water halves the viscosity of glycerol. At 18 wt % water, the mixture viscosity is about 100 cP.

The measured viscosity data for glycerol/brine lay on a smooth curve that was matched almost precisely by a modified expression for the viscosity of dispersions of spherical particles (van de Ven, 1989). The glycerol concentration in the mixture, C_{gl}, is expressed as a weight fraction.

$$\mu_{ap} = \mu_w \left[\frac{1 - C_{gl}/1.9}{1 - 1.451(C_{gl}/1.9)} \right]^{10.53} \qquad 4.6$$

Detailed discussion of the choice of parameters and their physical significance is beyond the scope of this paper. Literature results for distilled glycerol/water are also closely fitted by equation (7)

$$\mu_{ap} = \mu_w \left[\frac{1 - C_{gl}/1.9}{1 - 1.537(C_{gl}/1.9)} \right]^{8.85} \qquad 4.7$$

The viscosity for pure glycerol is specified as 1759.6 cP (CRC Handbook, 1976-7). In this study a viscosity of 1646.6 cP was measured for the as-supplied glycerol. Because of the extreme sensitivity of viscosity to very low water content, these differences have little effect on the overall match provided by equations 4.6 and 4.7.

Surface Tension. Decrease in surface tension of the aqueous phase with increase in glycerol concentration is very close to linear (Fig. 4.3). This indicates that there is no preferential adsorption of either water or glycerol at the interface. The results were closely fitted by

$$\sigma_{ap/air} = 72.81 - 0.09C_{gl} \qquad 4.8$$

Interfacial tension (IFT). The values for brine/HVO and brine/LVO interfacial tension are shown in Fig. 4. IFT decreases close-to-linearly with increase of the glycerol concentration for both oils. The IFTs for pure seawater and HVO were 51.3 dynes/cm and 29.4 dynes/cm for glycerol and HVO. All data were closely fitted by

$$\sigma_{ap/HVO} = 51.29 - 0.218C_{gl} \qquad 4.9$$

For pure seawater/LVO the IFT was 50.4 dynes/cm and 27.6 dynes/cm for LVO against glycerol. The IFT data show very little scatter. Values for mixtures were closely fitted by

$$\sigma_{ap/LVO} = 49.48 - 0.218C_{gl} \qquad 4.10$$

Contact angle. Contact angles, from force-distance measurements on quartz plates, were zero (see Figs. 4.3, 4.4) for glycerol/sea water mixtures against n-decane or air. Perfect wetting was confirmed by the mirror-like appearance of the plates in reflected light (Menella et al., 1995). A working assumption was therefore made that Berea sandstone was also very strongly water wet for all imbibition tests.

Spontaneous Imbibition

Matched Viscosities

The scaling equation of Mattax and Kyte was proposed for the special case of matched viscosities. In the present work the equation was tested for a constant viscosity ratio very close to unity for a wide range of matched viscosities. The viscosity ratio, Ψ, is defined by

$$\Psi = \mu_{ap} / \mu_o \qquad 4.11$$

Table 4.3 lists the core and liquid properties used in imbibition tests performed with closely matched oleic and aqueous phase viscosities.

Relationships between oil recovery and imbibition time are presented in Fig. 4.5. The rate of oil recovery decreases systematically as viscosity increases (Fig. 4.5a). The Mattax and Kyte scaling group gave close correlation of results over the entire viscosity range (Fig. 4.5b). Correlated oil recovery curves all had the same shape and there was no distinct trend with respect to absolute values of viscosity. In general, final oil recovery showed slight overall increase with viscosity ratio. However, all data points except one fell within 52% ± 1 (Fig. 4.5c).

The dependency of the imbibition time for specific fractions of normalized final recovery for the nine matched viscosity experiments is depicted in Fig. 4.6a. The curves become increasingly close to parallel alignment with increase in recovery. The dimensionless times for a specific recovery fall close to horizontal straight lines that correspond to perfect correlation (Fig. 4.6b).

Non-matched (NM) Viscosities

Spontaneous imbibition is a complex process. As yet, there is no published theory for correlation of data sets for which the viscosity ratio is a variable; results obtained by simulation have been reported (Ruth et al., 2000). Experimental results for imbibition of water for oil viscosities ranging from about 1 to 160 cP were closely correlated by the geometric mean of the oil and water viscosity (Zhang et al., 1996). In the present work, this empirical correlation has been tested for a wide range of variation in the aqueous phase viscosity for oil viscosities of 4, 22, and 43 cP.

Set NM(4): μ_o= 4 cP. Core and fluid properties are listed in Table 4.4. The aqueous phase viscosity for these spontaneous imbibition experiments covers the entire range from 1.1 cP for seawater to 1646.6 cP for glycerol.

The imbibition curves for recovery of 4 cP oil for different aqueous phase viscosities are shown in Fig. 4.7a. The rates of recovery decreased systematically by over 2½ orders of magnitude with increase in aqueous phase viscosity. The data were closely correlated by plots of oil recovery versus dimensionless time, t_D, (see Fig. 4.7b). However the slopes of the scaled curves decreased slightly with increase in aqueous phase viscosity and also show a small but systematic increase in t_D with increase in aqueous phase viscosity. Final oil recoveries tended to increase with viscosity ratio, apart from a plateau in the viscosity ratio range of 4 to 60 (see Fig.4.7c).

The trends shown in Fig. 4.7 may be related to subtle changes in the displacement mechanism. The increase in displacement efficiency with viscosity ratio (Fig. 4.7c) may be related to the improved mobility ratio or perhaps to the effect of the aqueous phase on the microscopic mechanism of displacement whereby snap-off is retarded by the viscosity of the aqueous phase. In comparable studies of recovery of refined oil by imbibition of brine, final oil recovery was independent of oil viscosity for values ranging from 1 to 160 cP (Zhang et al., 1994).

Log-log plots of imbibition time versus viscosity ratio for specific normalized oil recoveries show close to parallel alignment (Fig. 4.8a). This kind of plot relates the time needed to recover a certain percentage of the total recoverable oil for a given viscosity ratio. Times for 100% (i.e. final) recovery are not identified because the recovery curves at late time are essentially asymptotic. The variation in t_D versus viscosity ratio, for different levels of recovery, illustrates the closeness to perfect scaling given by the geometric mean viscosity (Fig. 4.8b). Overall there is a tendency for t_D to increase with viscosity ratio.

Set NM(22): μ_o= 22 cP. The properties of the cores and liquids utilized to obtain the data set for 22 cP mineral oil are presented in Table 4.5. Cores cut from the same block of sandstone had permeability and porosity that was consistently of about 67 md and 17% respectively. One core, C5-19, cut from a different Berea sandstone block, had somewhat higher than average permeability and porosity.

Imbibition results are displayed in Fig. 4.9. For viscosity ratios up to 4, results were closely correlated, with slight, but systematic, increase in dimensionless time with increase in aqueous phase viscosity. For higher viscosities, there was a distinct increase in dimensionless time for imbibition with increase in μ_{ap} and stretching of the curves at later recovery times.

As for the NM(4) set, oil recovery increased from about 50 to 53% with increase in viscosity ratio for viscosity ratios of up to about 4; above 4, the final recoveries were 53% ± ½ (Fig. 4.9c).

Log-log plots of t versus viscosity ratio for different normalized oil recovery factors give close to parallel relationships (Fig. 4.10a). The graphs of t_D versus viscosity ratio in Fig. 4.10b are all close to horizontal up to a viscosity ratio of around 4. For viscosity ratios higher than 4, the dimensionless times for a specific recovery show distinct increase with increase in Ψ.

Set NM(43): μ_o= 43 cP. Table 4.6 lists the core and fluid properties for the data set obtained for recovery of 43 cP oil. Of the 9 cores, C5-21 and C5-17 were cut from the aforementioned higher permeability Berea sandstone block.

Results for Set NM(43), except for core C5-17 being somewhat out of sequence, showed comparable characteristics to those of data set NM(22) (Fig. 4.11a). Imbibition curves were closely correlated for the lower μ_{ap} tests (up to 99.9 cP) but as for Set NM(4) and Set NM(22), there was still a slight systematic increase in t_D with μ_{ap} (see Fig. 4.11b). At higher μ_{ap} the dimensionless times increased as μ_{ap} increased, and as for data set NM(22) became stretched with increase in recovery. As for Sets NM(4) and NM(22), the final oil recovery factor increased slightly with increase in viscosity ratio up to a viscosity ratio of about 4. At higher viscosity ratio, the residual oil was close to constant at 52.5% ± ½ (Fig. 4.11c).

Plots of time versus viscosity ratio with normalized recovery as parameter are shown in Fig. 4.12a. Relationships between dimensionless time and viscosity ratio (Fig. 4.12b) are closely comparable to those given by Set NM(22). Again, the recovery curves show only slight increase in t_D with increase in Ψ up to 4 and marked systematic increase at higher values of viscosity ratio.

Comparison of all final oil recoveries and imbibition plots

Final oil recovery versus viscosity ratio (Fig. 4.13a) for all matched and unmatched viscosity data exhibit an overall trend of increase in recovery at lower viscosity ratios. Beyond a viscosity ratio of 4, the final oil recoveries reach a plateau at about 52.5% final oil recovery. Final recoveries for matched viscosities fit an overall trend when all final recovery data are plotted against aqueous phase viscosity (Fig. 4.13b).

Inspection of data sets NM(4), NM(22) and NM(43) show that close correlation of imbibition data is obtained if the aqueous phase viscosity is no more than about 4 times greater than the oil viscosity. Plots of recovery versus t_D are shown in Fig. 4.14 for all three NM sets together with a best fit to the correlated data for matched viscosity.

Averaged imbibition curves for both the matched and unmatched viscosity data up to a viscosity ratio of 4 are presented in Fig. 4.15. The averaged recovery curves, presented in Fig. 4.15, show very close agreement for NM(22), NM(43), and the matched viscosity data. The lower viscosity

oil exhibits slightly longer dimensionless times for recovery. Overall the recovery curves are close to a correlation established for very strongly water wet Berea 500 (permeability to nitrogen 500 md) at early time and to VSWW Berea 90 (permeability to nitrogen 90 md) at late time. Previous studies have shown variation in the location of the scaled imbibition curves for Berea sandstone of about 90 md permeability (Tong et al., 2001).

Results for the non-matched data sets NM(4), NM(22) and NM(43) obtained for viscosity ratios in the range of 0.25 to 74 are plotted in Fig. 4.16 as t_D versus viscosity ratio for recoveries of 20%, 50%, 80% and 98% of original oil in place. Overall there is slight increase in t_D for Ψ up to 4. Above 4 there is a more marked overall increase in t_D which is well illustrated by the results for Set NM(22) and Set NM(43) (see Fig. 4.10b and Fig. 4.12b respectively).

Modification of the scaling equation

The systematic increase in dimensionless time with viscosity ratio for the non-matched viscosity data sets NM(4), NM(22) and NM(43) shows that empirical correlation of these data sets can be improved. The common range of viscosity ratios for all three data sets lies between 0.3 and 38. The curves for fractional recoveries of 50% and higher in Fig. 4.16 are characterized by near parallel slopes on a log-log scale. Average curves were determined for recoveries of 40, 50, 60, 70, 80, and 90%. The average curves were then normalized with respect to the dimensionless time at a viscosity ratio of 1 for each specific level of oil recovery. (No systematic trends were observed for the matched viscosity data (Fig. 4.6b)). From the six resulting normalized curves, an average curve was evaluated which represents the overall dependence of the average normalized dimensionless time on the viscosity ratio expressed as the viscosity ratio factor, $f(\Psi)$. The dimensionless time (Ma et al., 1997) is then divided by $f(\Psi)$ to obtain a modified dimensionless time, t_{DM}. The dependence of the viscosity ratio factor on the viscosity ratio over the range of 0.3 to 40 was fitted by two functions, one for the viscosity ratio range of 0.3 to 14 and the other for a viscosity ratio range of 14 to 40:

For $\Psi \leq 14$,

$$f_1(\Psi) = 1.122 \ln \Psi - 0.794 \quad \text{and} \quad 4.12$$

$$t_{DM} = t_D / f_1(\Psi) \quad 4.13$$

For $14 < \Psi < 40$,

$$f_2(\Psi) = -0.007\Psi^2 + 0.203\Psi + 0.759 \quad \text{and} \quad 4.14$$

$$t_{DM} = t_D / f_2(\Psi) \quad 4.15$$

The viscosity ratio factors, $f(\Psi)$, given by these two functions, are shown graphically in Fig. 4.17.

The adjusted results are shown in Fig. 18 as normalized oil recovery versus modified dimensionless time, t_{DM}, for NM(4) (Fig. 18a) for viscosity ratios for up to 25, and NM(22) (Fig. 4.18b), and NM(43) (Fig. 4.18c). (For Set NM(22), $f_2(\Psi)$ derived from the experimental data was extrapolated to the viscosity ratio of 74 in order to include all of the Set NM(22) data.) Significant improvement of the correlation was achieved.

Fig. 4.19 shows the average imbibition curves obtained from the correlation given by the modified scaling equation for both the matched and unmatched viscosity data. The improvement of the correlation is demonstrated by the even closer agreement of all four curves when compared with Fig. 4.15, for which only viscosity ratios of up to 4 were taken into account.

Conclusions

- Glycerol serves as a near-ideal aqueous phase viscosifying agent. Density, surface tension and interfacial tension were linearly dependent on concentration. All glycerol/water mixtures exhibited zero contact angle (spreading) against both air and n-decane on quartz surfaces. Increase in viscosity with glycerol concentration was highly non linear. Small consistent shifts in physical properties were observed between glycerol/distilled water and glycerol/sea water mixtures.

- Imbibition data obtained for matched viscosities (the special case of constant viscosity ratio of unity) were correlated satisfactorily by the Mattax and Kyte scaling group. Final oil saturations increased only slightly with increase in matched viscosity.

- Rate of spontaneous imbibition decreased and oil recovery increased slightly with increase in aqueous phase viscosity.

- Imbibition results for viscosity ratios of less than 4 were closely correlated by the Ma et al. scaling group with only very small but systematic dependence of dimensionless time on viscosity ratio. However, final oil recovery for unmatched liquid viscosities increased slightly with increase in aqueous phase/oil viscosity ratio up to about 4. Increase in dimensionless time for imbibition with viscosity ratio was observed for viscosity ratios greater than 4 but final oil recoveries were close to constant.

- Improved correlation of imbibition data was obtained by compensating the geometric mean of the viscosities for an overall systematic increase in dimensionless time for recovery.

Table 4.1
Synthetic Seawater
Composition and Properties

ρ_w= 1.0238 (g/cm^3), μ_w= 1.1 (cP)		
NaCl	28.0000	(g/L)
KCl	0.9350	(g/L)
$MgCl_2$	5.3625	(g/L)
$CaCl_2$	1.1900	(g/L)
NaN_3	0.1000	(g/L)
TDS	35.5875	(g/L)

Table 4.2
Mineral Oil Properties

	LVO	HVO
Density ρ, (g/cm^3)	0.782	0.872
Viscosity μ, (cP)	3.9	173.0

Table 4.3
Rock and Fluid Properties, Matched Viscosities

Core #	L_c (cm)	k_g (md)	Φ (%)	σ_{ow} (dyn/cm)	ρ_{ap} (g/cm^3)	ρ_o (g/cm^3)	μ_{ap} (cP)	μ_o (cP)	μ_g (cP)
C1-20	1.239	71.2	17.4	40.2	1.119	0.782	4.3	4.0	4.1
C1-24	1.240	59.7	17.4	36.8	1.170	0.817	13.6	13.6	13.6
C1-21	1.238	72.2	17.5	34.4	1.185	0.828	20.9	20.9	20.9
C1-19	1.237	69.9	17.5	33.3	1.204	0.843	43.9	44.1	44.0
C1-23	1.244	66.5	17.7	32.0	1.213	0.851	59.3	59.3	59.2
C1-22	1.236	69.7	17.9	31.8	1.220	0.858	80.2	80.1	80.1
C3-30	1.238	63.1	17.1	30.5	1.226	0.863	99.7	99.1	99.4
C5-4	1.230	69.6	17.4	30.1	1.231	0.869	140.0	141.7	140.8
C3-34	1.242	75.8	17.7	30.3	1.235	0.873	171.2	173.0	172.1

Table 4.4
Rock and Aqueous Phase Properties
NM(4): μ_o= 4 (cP), ρ_o= 0.782 (g/cm^3)

Core #	L_C (cm)	k_g (md)	Φ (%)	σ_{ow} (dyn/cm)	ρ_{ap} (g/cm^3)	μ_{ap} (cP)
C3-1	1.247	63.5	16.9	48.9	1.026	1.1
C1-1	1.242	62.3	16.9	39.8	1.121	4.4
C3-9	1.242	70.5	16.9	37.6	1.152	8.7
C1-2	1.230	64.5	16.9	35.3	1.172	15.2
C3-6	1.241	66.7	17.0	34.4	1.186	21.8
C3-8	1.241	62.7	17.0	32.9	1.200	39.5
C3-7	1.237	64.5	16.9	32.1	1.211	59.4
C1-3	1.242	62.7	16.8	31.2	1.222	99.8
C1-16	1.237	69.9	17.3	30.6	1.243	185.0
C1-20	1.239	71.2	16.8	28.3	1.255	826.9
C1-25	1.238	71.5	17.4	27.7	1.262	1646.6

Table 4.5
Rock and Aqueous Phase Properties
NM(22): μ_o= 22 (cP), ρ_o= 0.828 (g/cm^3)

Core #	L_c (cm)	k_g (md)	Φ (%)	σ_{ow} (dyn/cm)	ρ_{ap} (g/cm^3)	μ_{ap} (cP)
C1-7	1.238	65.1	17.0	52.4	1.024	1.1
C1-9	1.242	65.4	17.0	41.2	1.121	4.4
C1-10	1.240	68.8	16.8	37.3	1.152	8.7
C1-8	1.239	69.7	17.1	35.9	1.172	15.2
C1-6	1.241	65.5	17.0	34.5	1.185	22.0
C1-4	1.238	66.1	16.9	33.1	1.201	39.6
C1-5	1.239	68.0	16.9	32.5	1.222	96.6
C1-22	1.236	69.7	16.0	30.8	1.237	228.4
C5-19	1.227	85.7	17.9	29.5	1.249	522.7
C1-26	1.219	67.8	17.4	28.6	1.261	1646.6

Table 4.6
Rock and Aqueous Phase Properties
NM(43): μ_o= 43 (cP), ρ_o= 0.843 (g/cm^3)

Core #	L_c (cm)	k_g (md)	Φ (%)	σ_{ow} (dyn/cm)	ρ_{ap} (g/cm^3)	μ_{ap} (cP)
C1-11	1.237	68.7	17.1	53.1	1.024	1.1
C1-12	1.242	62.5	17.2	41.7	1.121	4.4
C1-13	1.238	55.6	16.7	36.4	1.172	15.2
C1-15	1.241	70.4	17.2	34.6	1.197	35.4
C1-14	1.240	70.0	17.2	32.4	1.220	96.6
C5-21	1.234	82.0	18.2	31.9	1.222	99.9
C1-19	1.237	69.9	16.8	31.1	1.237	228.4
C5-17	1.236	77.2	18.0	29.6	1.249	522.7
C1-18	1.236	67.4	16.2	28.5	1.262	1646.6

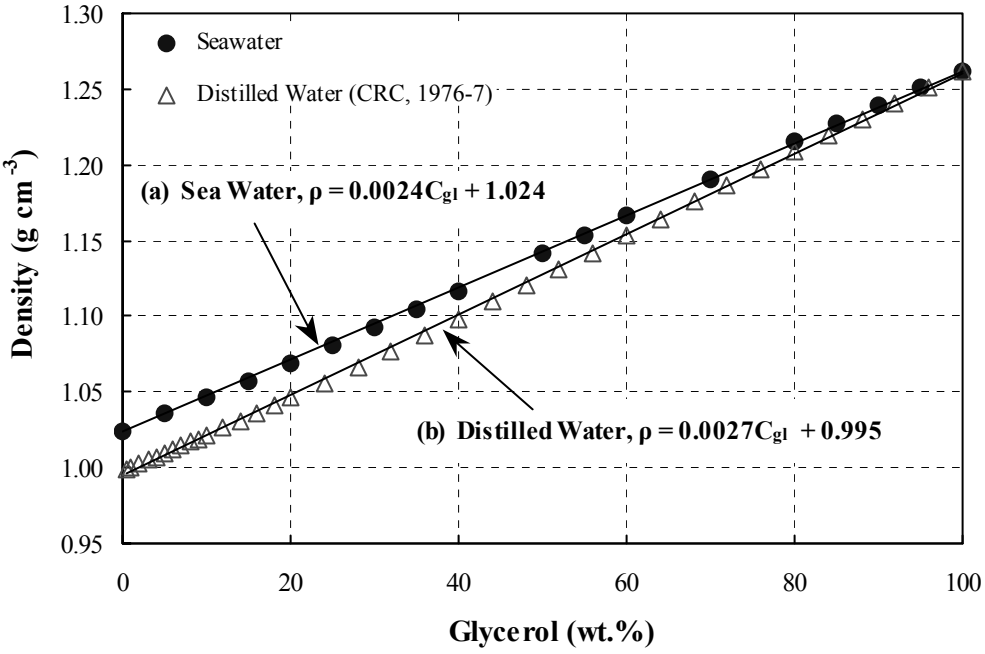

Fig. 4.1 Aqueous phase density of (a) glycerol/sea water and (b) glycerol/distilled water.

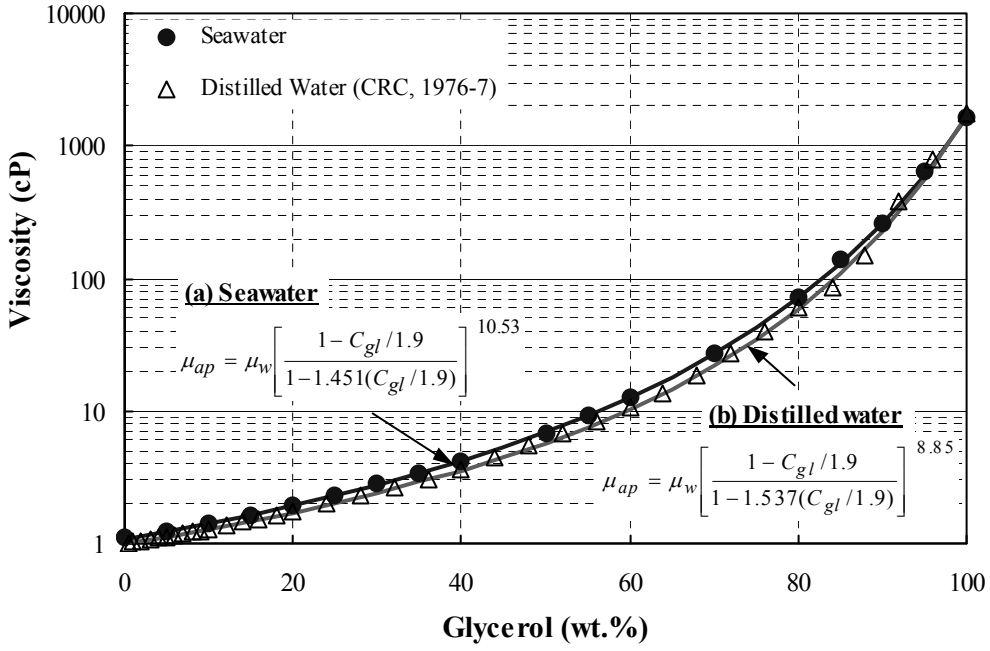

Fig. 4.2 Aqueous phase viscosity of (a) glycerol/brine and (b) glycerol/distilled water.

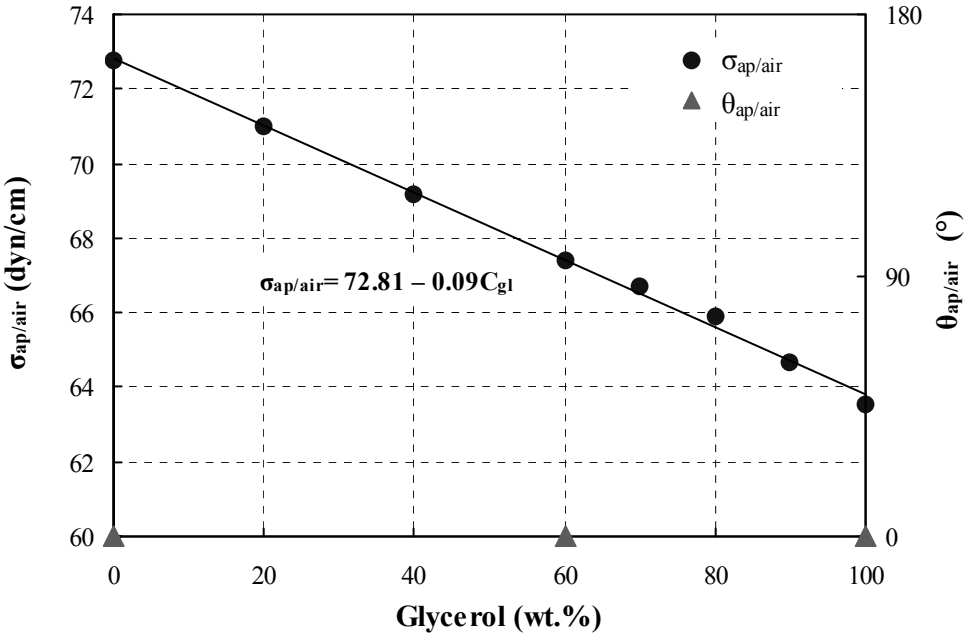

Fig. 4.3 Aqueous phase surface tensions and contact angles of glycerol/brine against air.

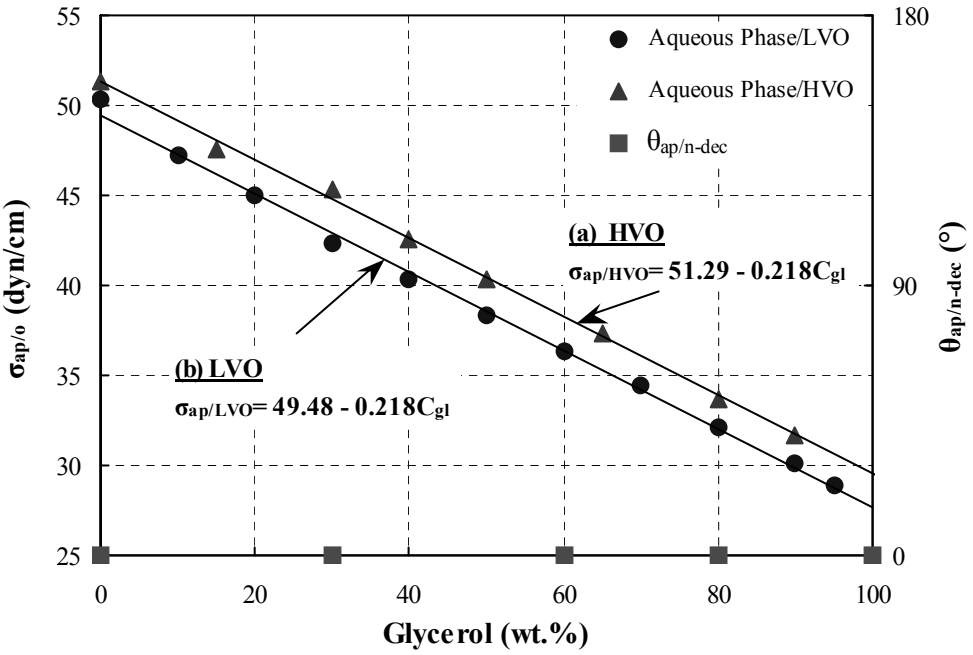

Fig. 4.4 Contact angle against quartz (aqueous phase/decane) and interfacial tensions of aqueous phase against: (a) high viscosity oil, μ (HVO) = 173 cP and (b) low viscosity oil, μ (LVO) = 4 cP.

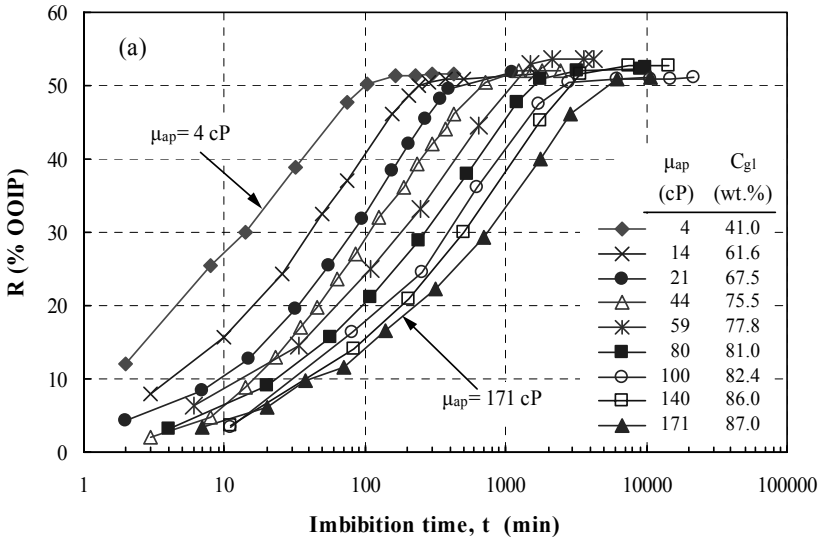

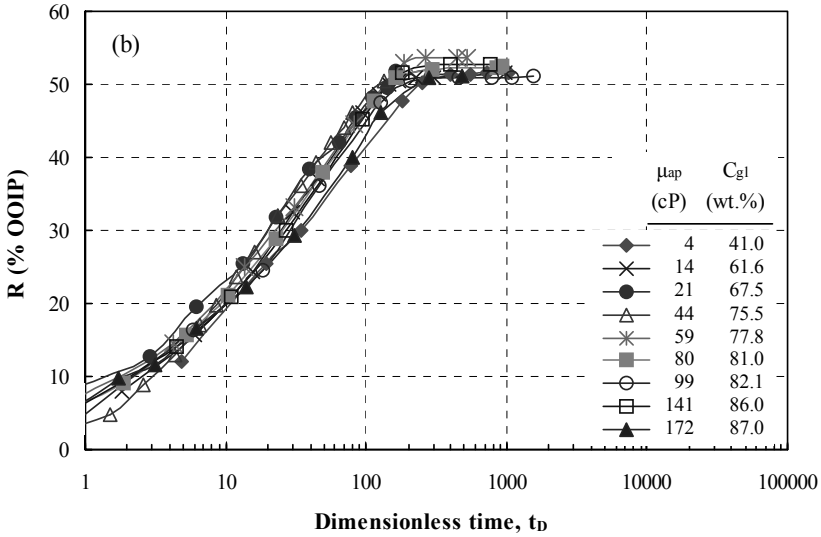

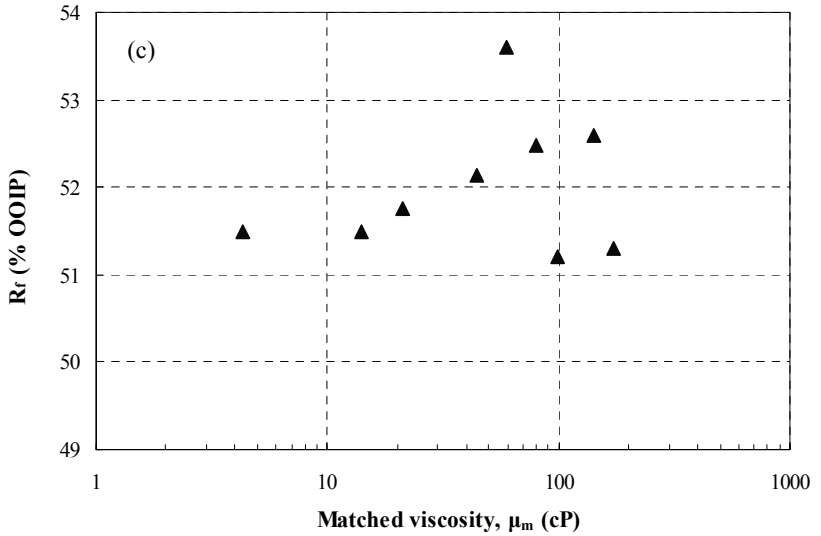

Fig. 4.5 Recovery of oil by spontaneous imbibition for matched phase viscosity versus (a) time and (b) dimensionless time; (c) final oil recovery, R_f, versus viscosity

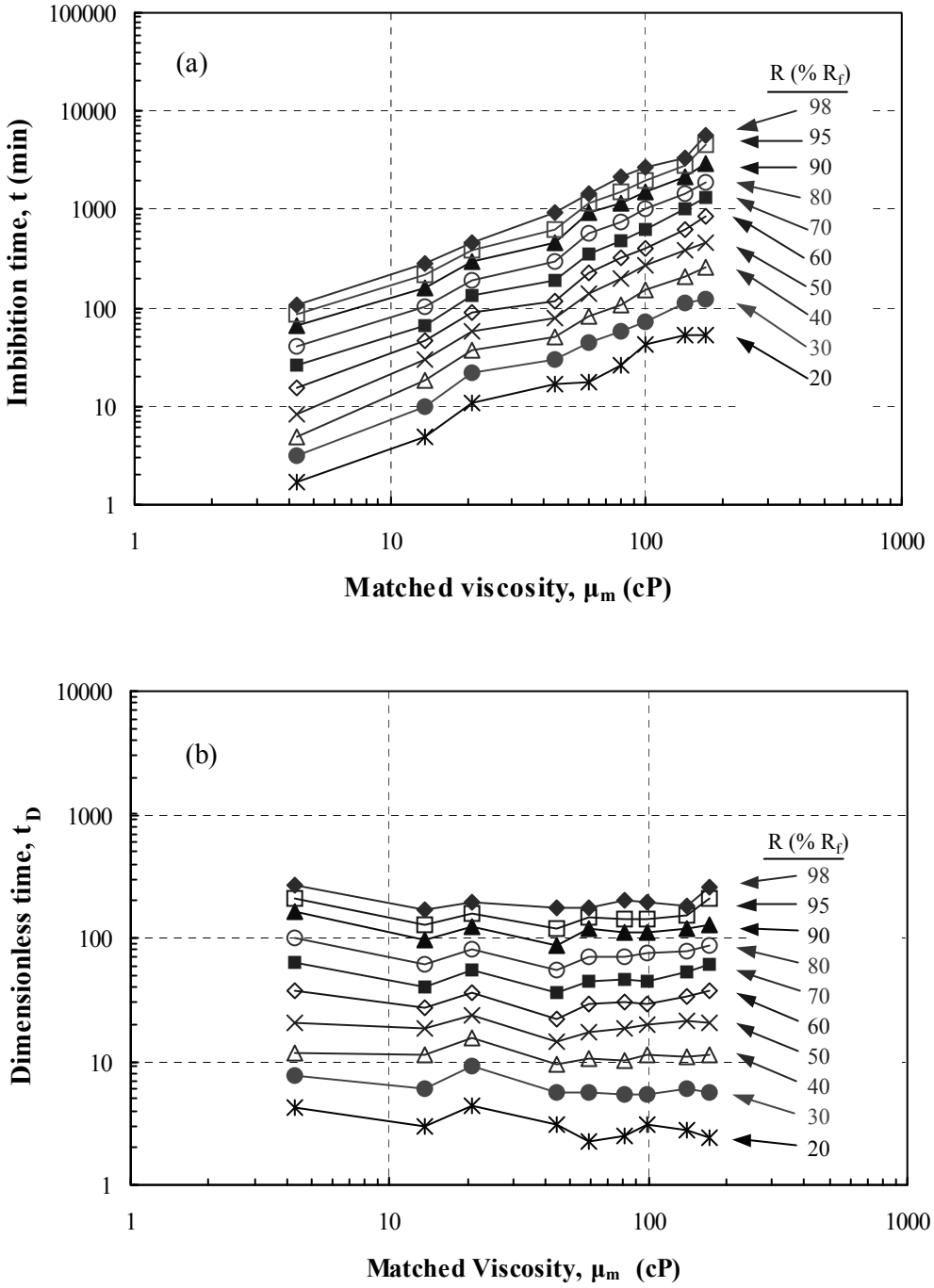

Fig. 4.6 Imbibition time (a) and scaled time (b) versus matched viscosity for fractional recoveries, R, ranging from 20% to 98% (interpolated values for individual cores).

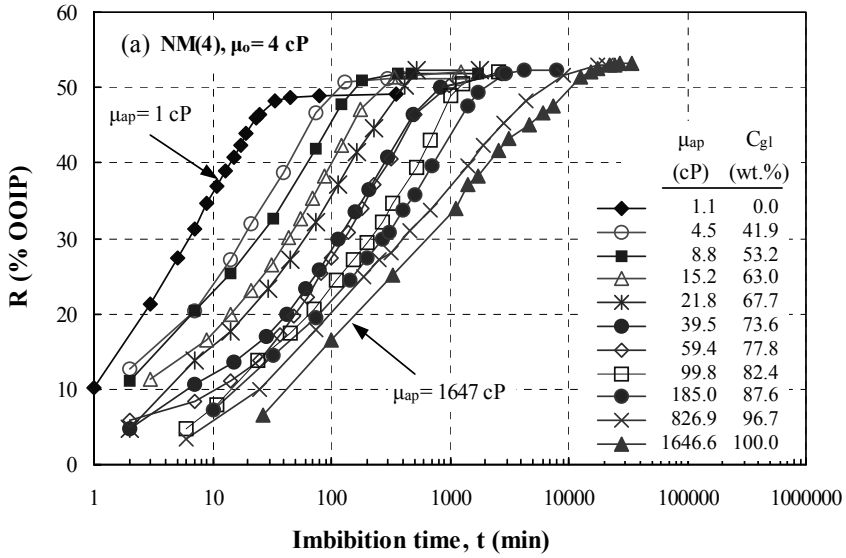

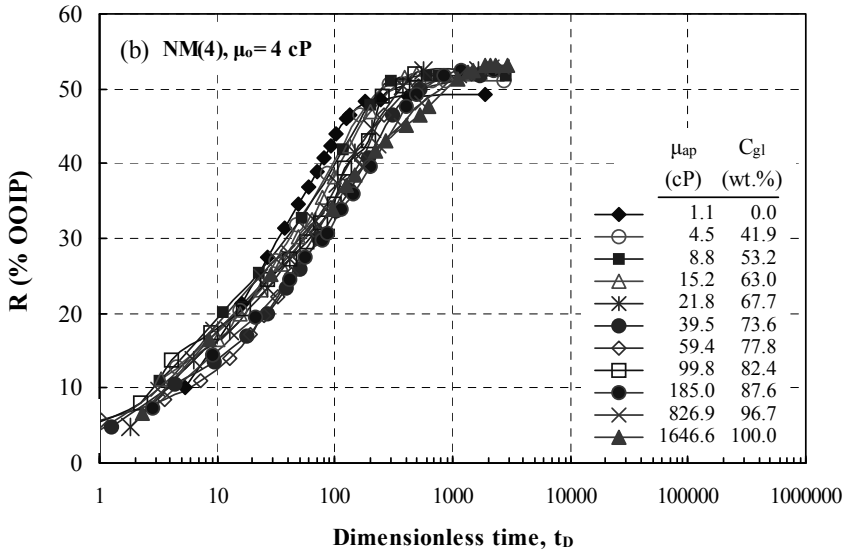

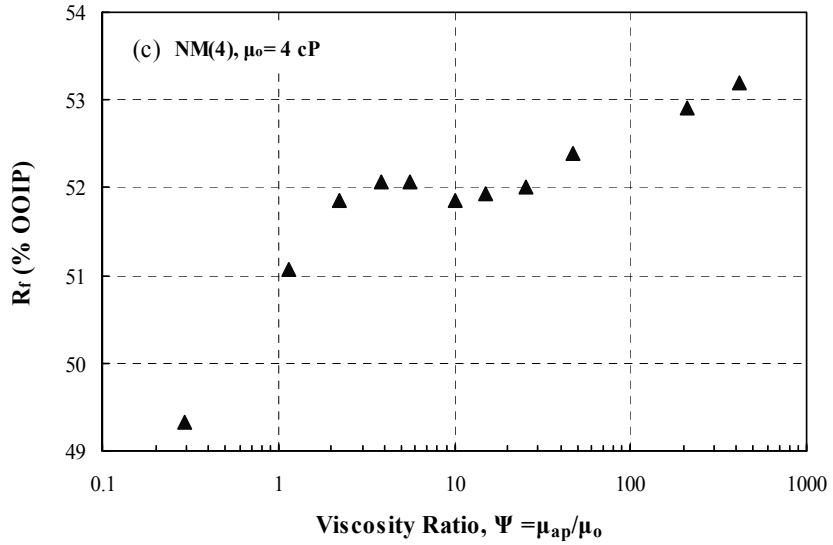

Fig. 4.7 Recovery of 4 cP oil by spontaneous imbibition for variation in aqueous phase viscosity versus (a) time and (b) dimensionless time; (c) final oil recovery, Rf, versus viscosity ratio.

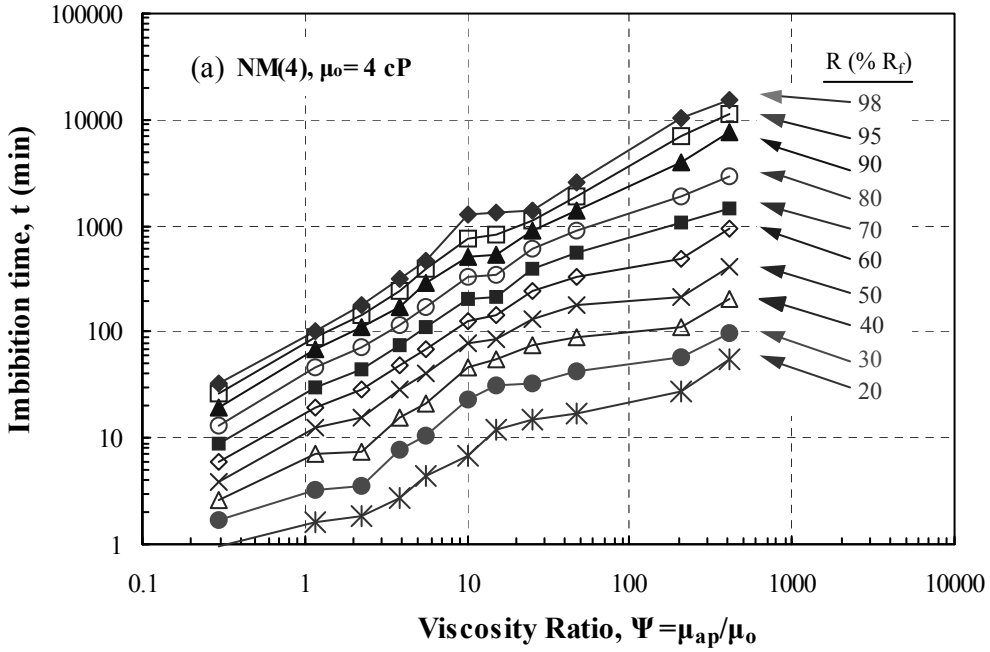

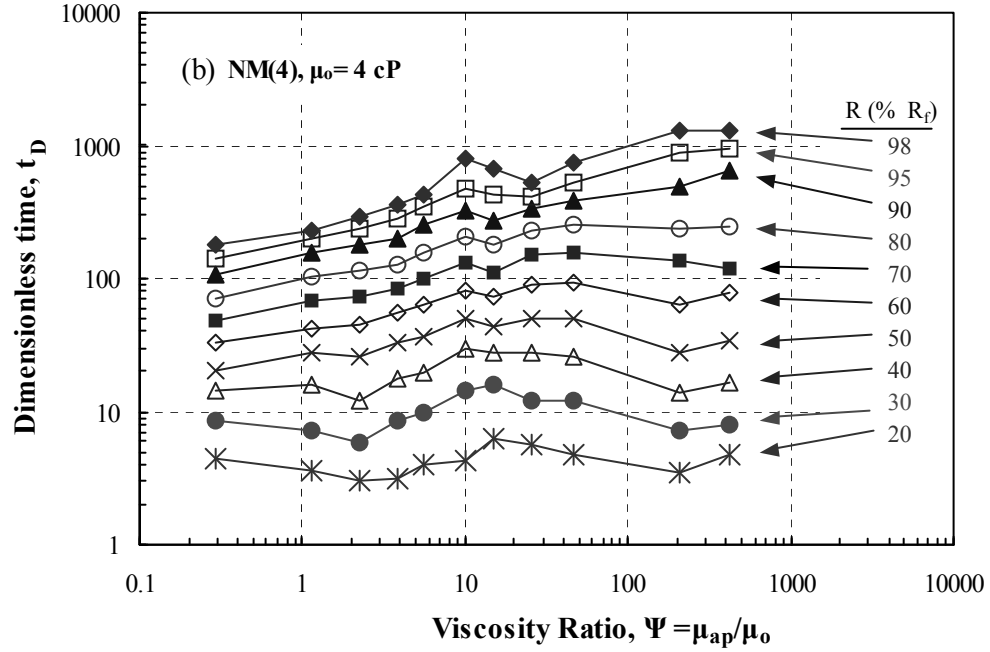

Fig. 4.8 Imbibition time (a) and dimensionless time (b) versus viscosity ratio (μ_o = 4 cP) for fractional recoveries, R, ranging from 20% to 98% (interpolated values for individual cores).

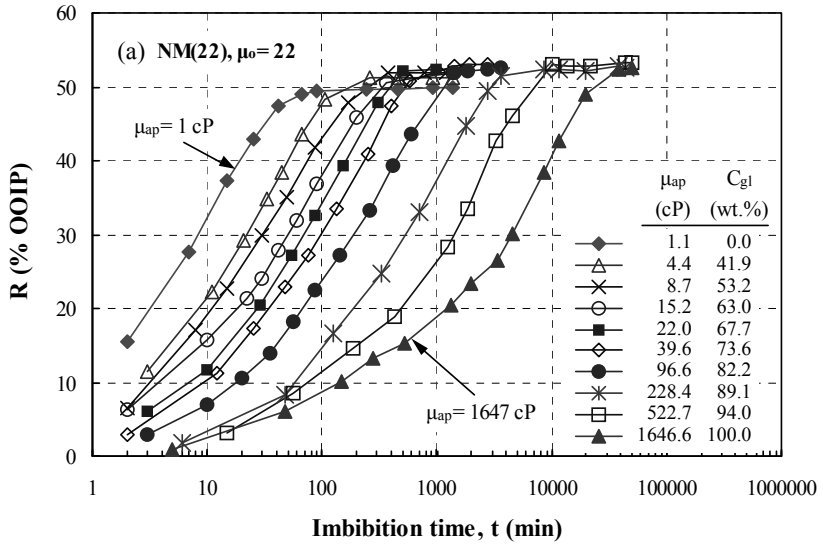

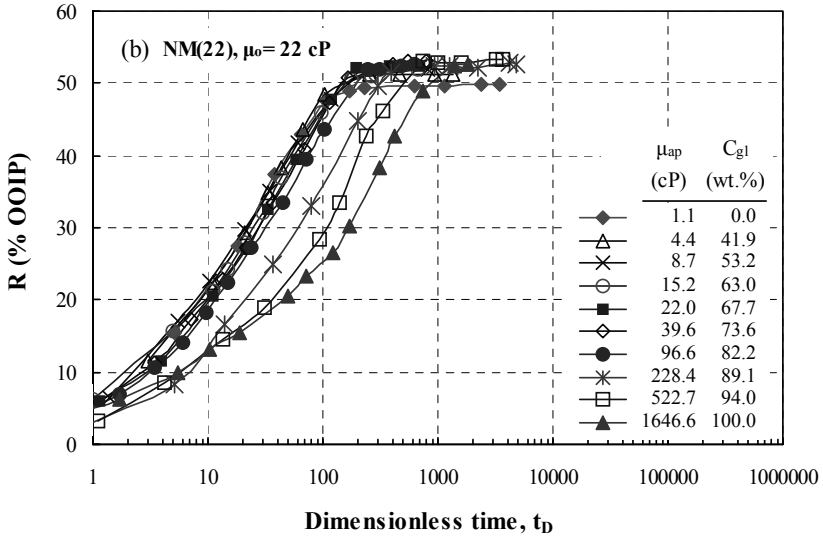

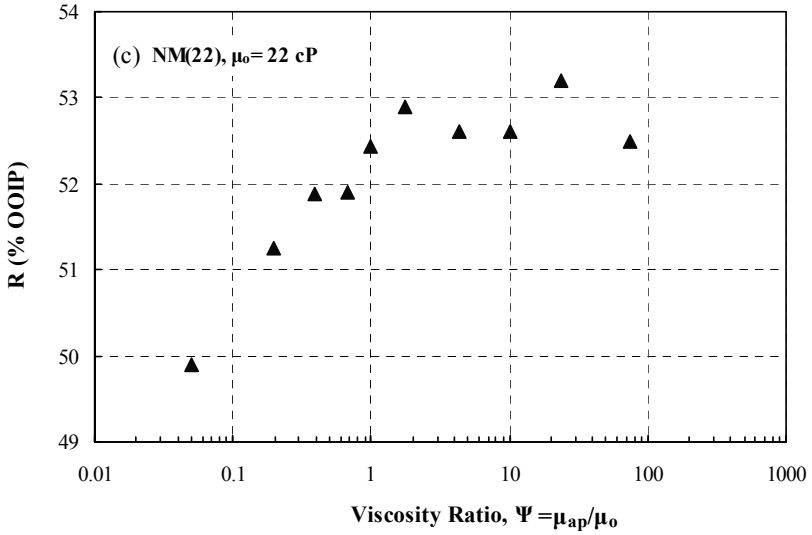

Fig. 4.9 Recovery of 22 cP oil by spontaneous imbibition for variation in aqueous phase viscosity versus (a) time (b) dimensionless time; (c) final oil recovery, Rf, versus viscosity ratio.

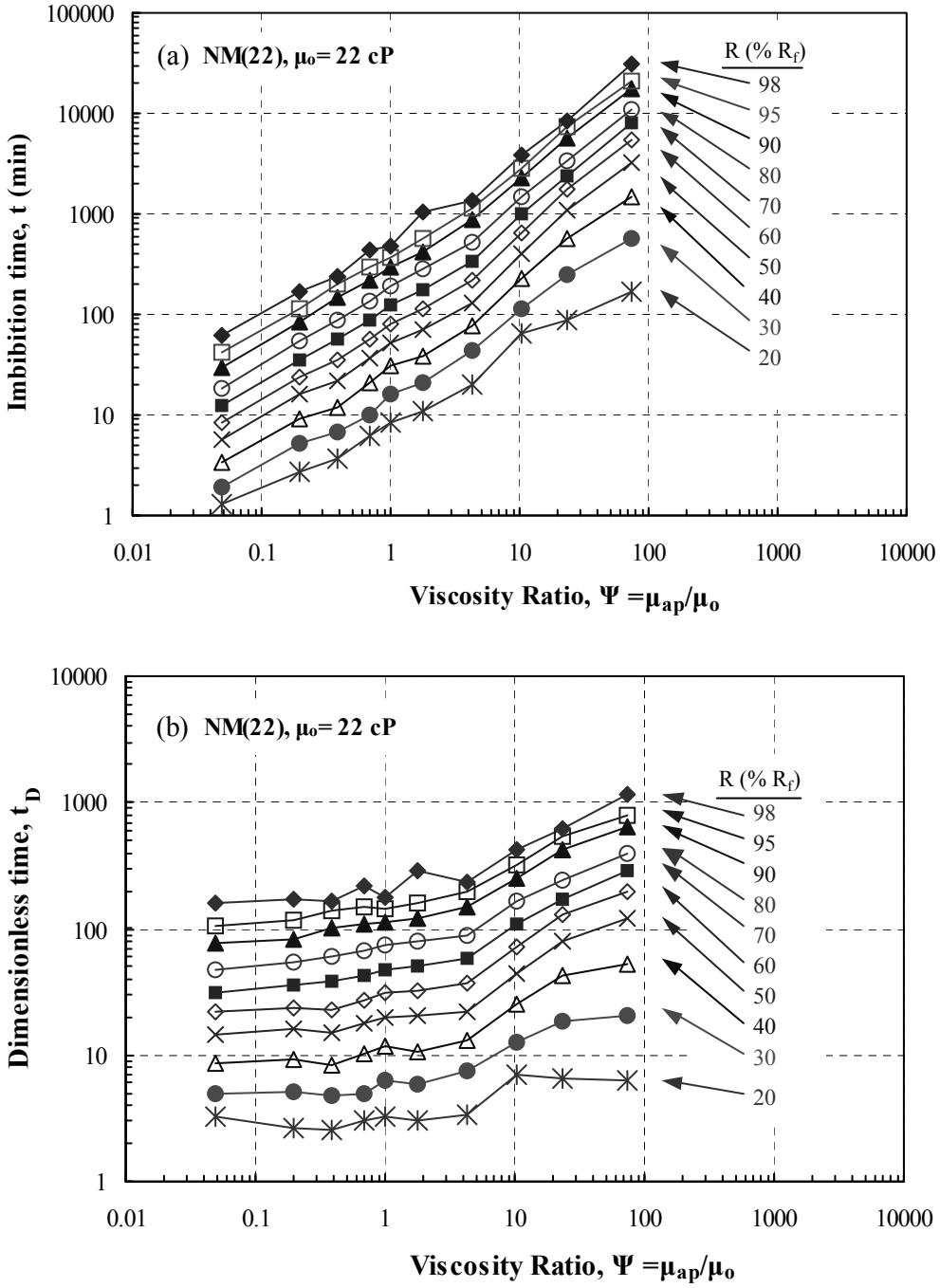

Fig. 4.10 Imbibition time (a) and dimensionless time (b) versus viscosity ratio (μ_o = 22 cP) for fractional recoveries, R, ranging from 20% to 98% (interpolated values for individual cores).

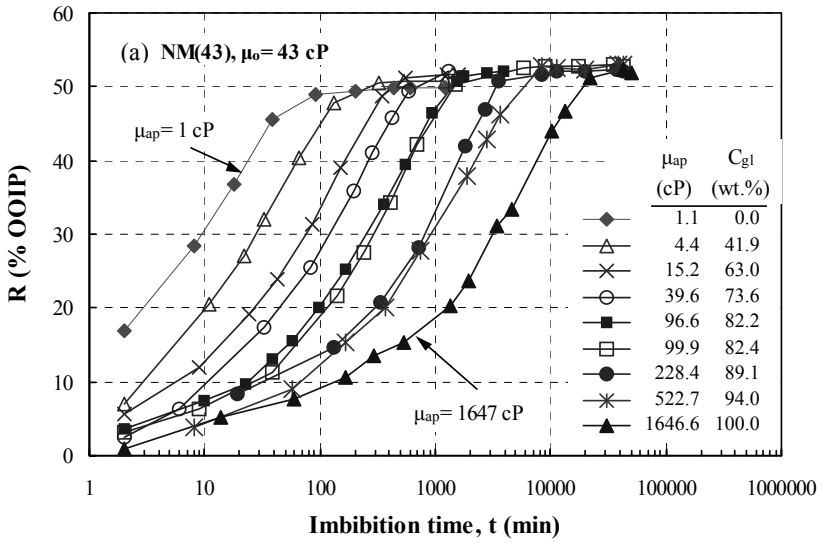

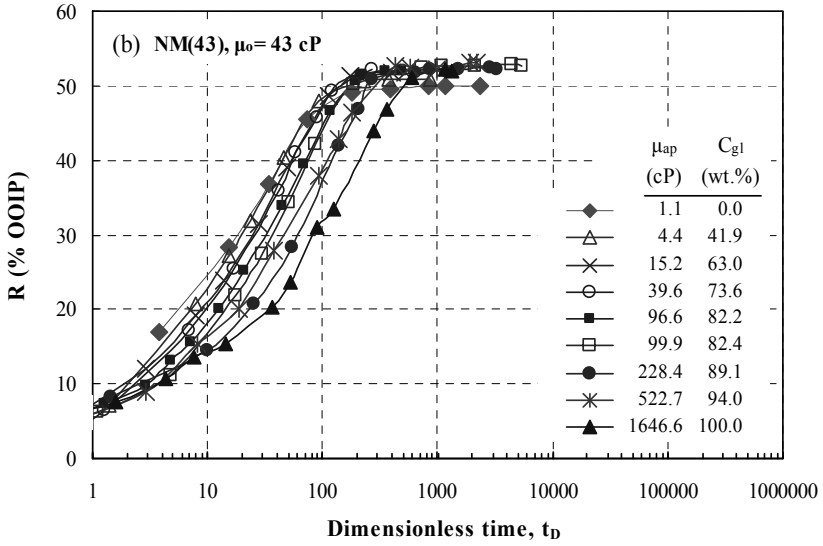

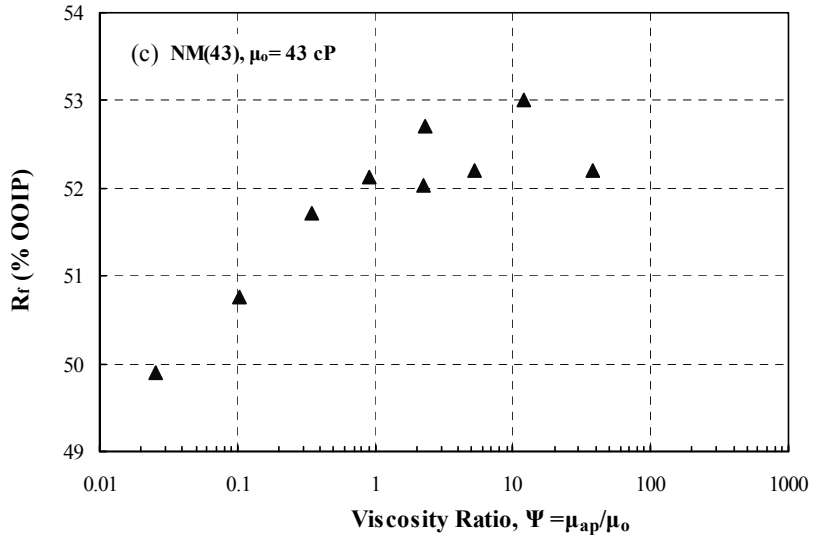

Fig. 4.11 Recovery of 43 cP oil by spontaneous imbibition for variation in aqueous phase viscosity versus (a) time and (b) dimensionless time; (c) final oil recovery, Rf, versus viscosity ratio.

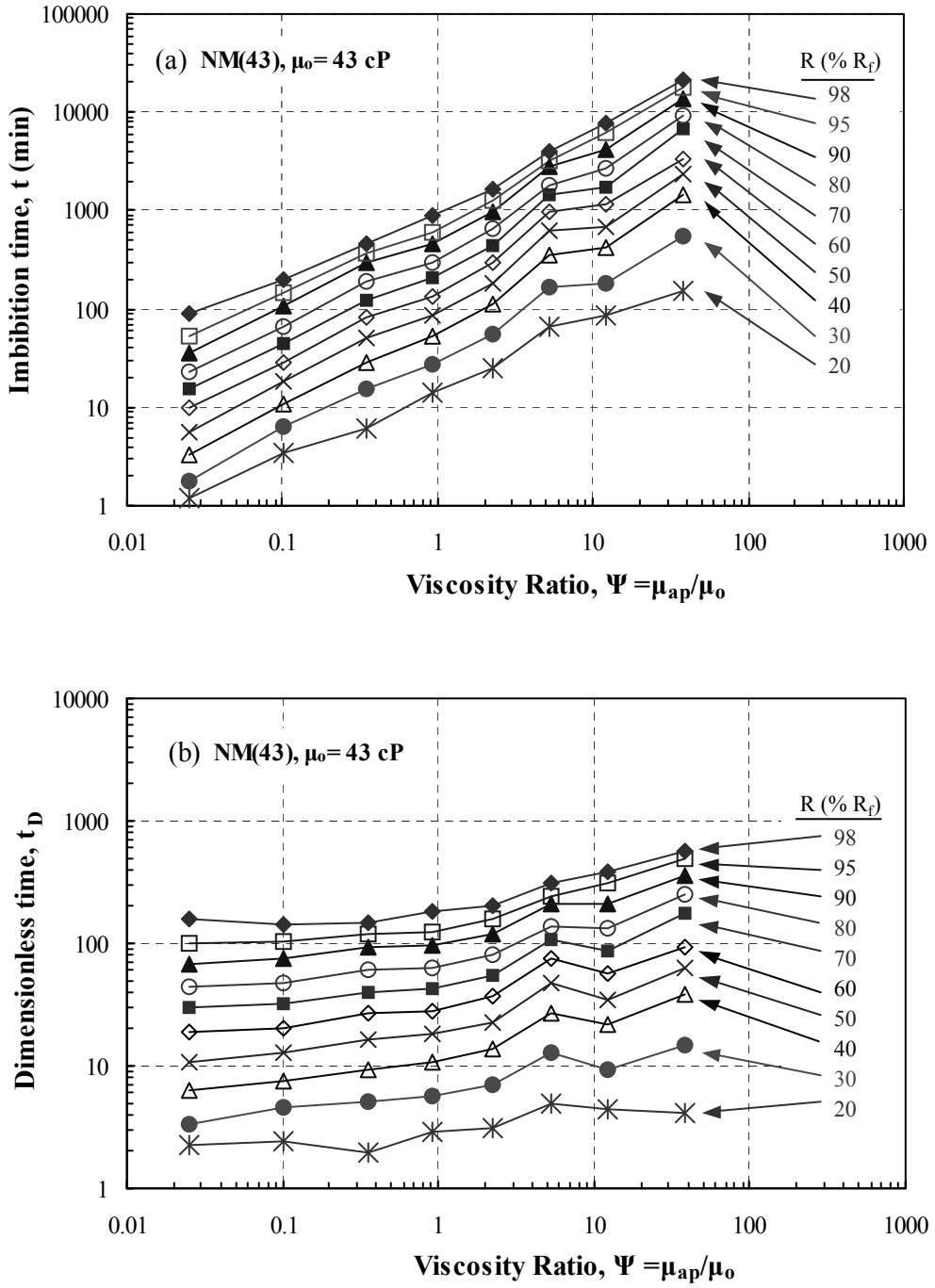

Fig. 4.12 Imbibition time (a) and dimensionless time (b) versus viscosity ratio (μ_o= 43 cP) for fractional recoveries, R, ranging from 20% to 98% (interpolated values for individual cores).

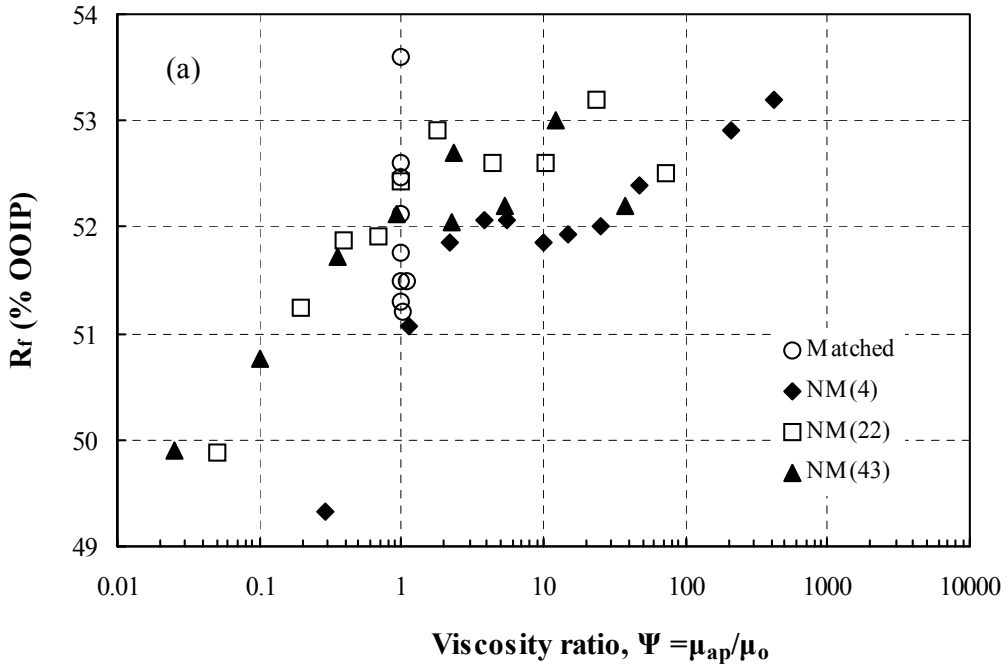

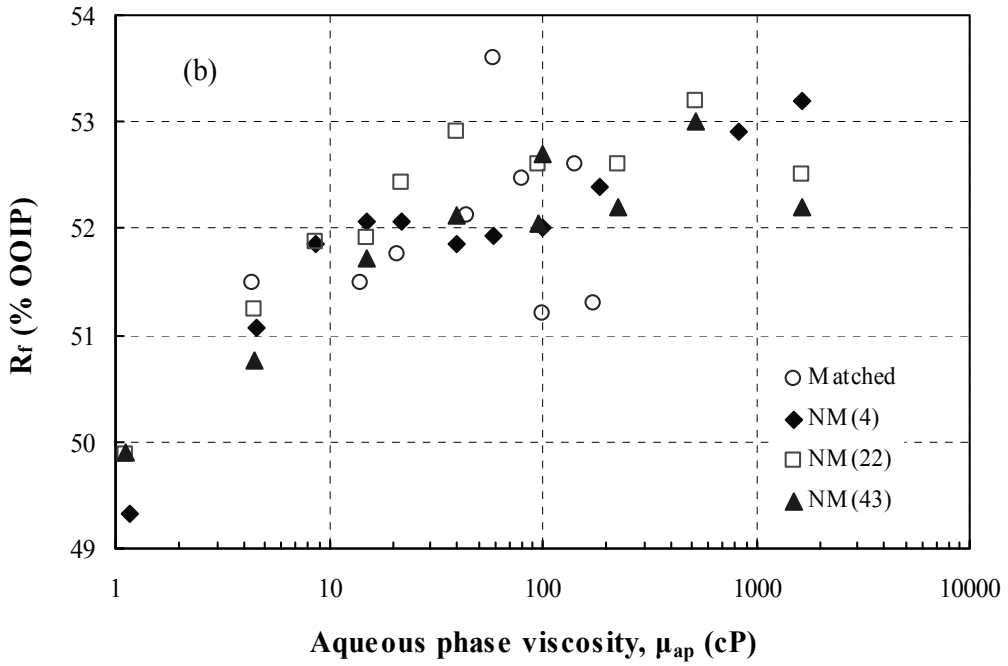

Fig. 4.13 Final oil recovery for all data sets versus (a) viscosity ratio and (b) aqueous phase viscosity.

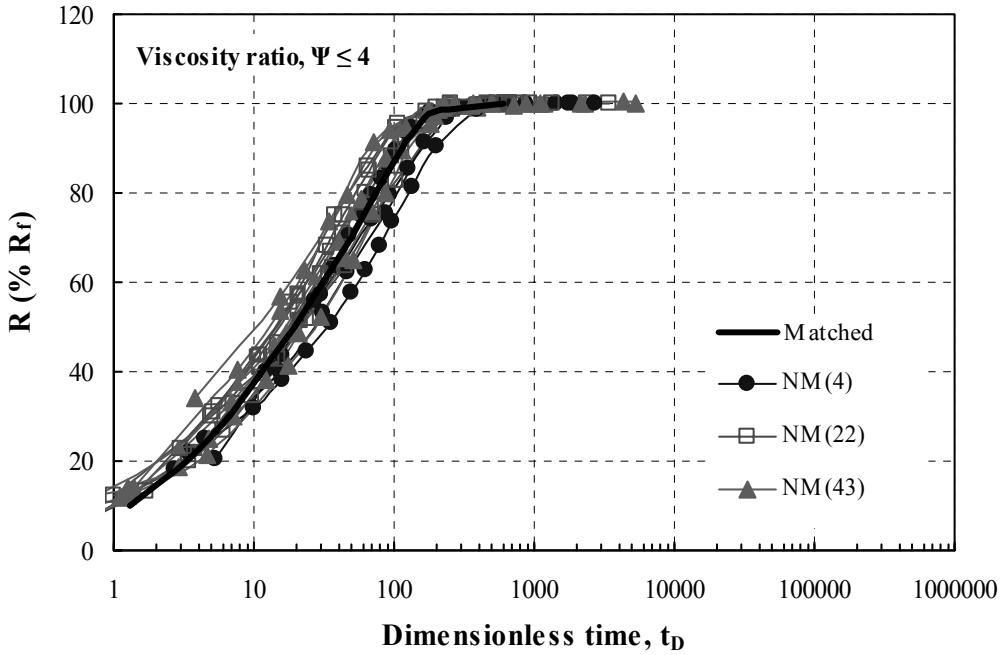

Fig. 4.14 Normalized recovery of matched viscosity oil, 4 cP, 22 cP and 43 cP oil by spontaneous imbibition for viscosity ratios ≤ 4 versus dimensionless time.

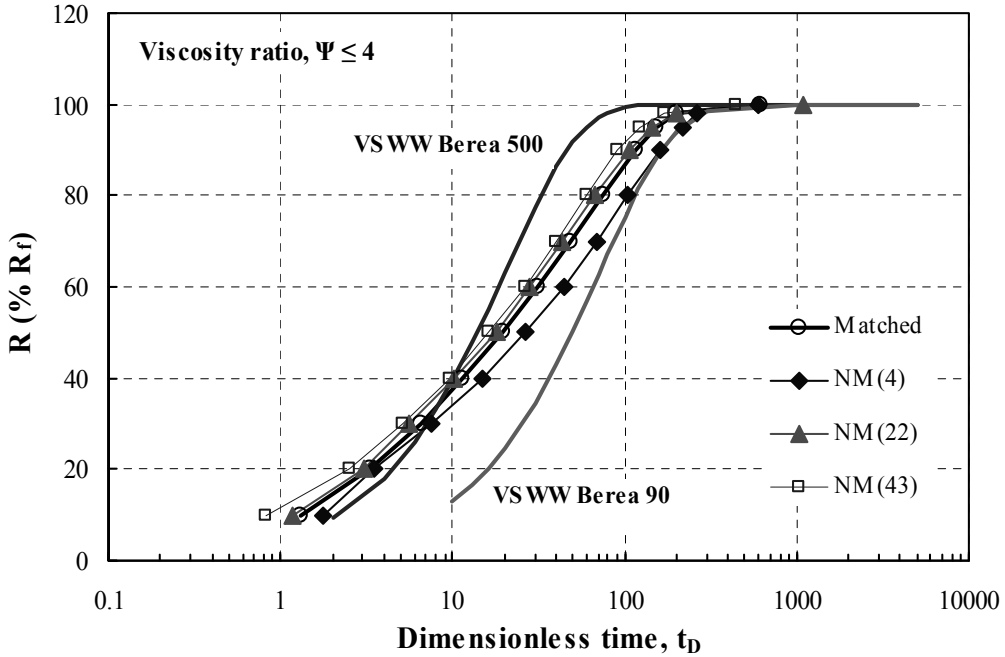

Fig. 4.15 Normalized recovery of averaged imbibition curves with viscosity ratios ≤ 4 versus dimensionless time.

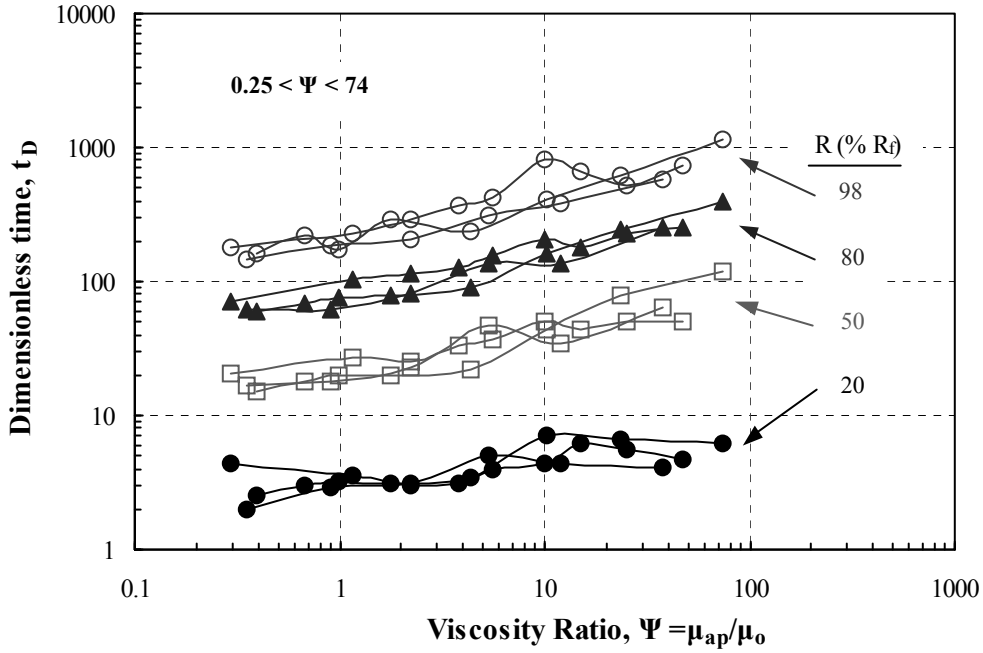

Fig. 4.16 Relationship between dimensionless time and viscosity ratio for 20%, 50%, 80% and 98% of recoverable oil for viscosity ratios from 0.25 to 74 from data sets NM(4), NM(22) and NM(43).

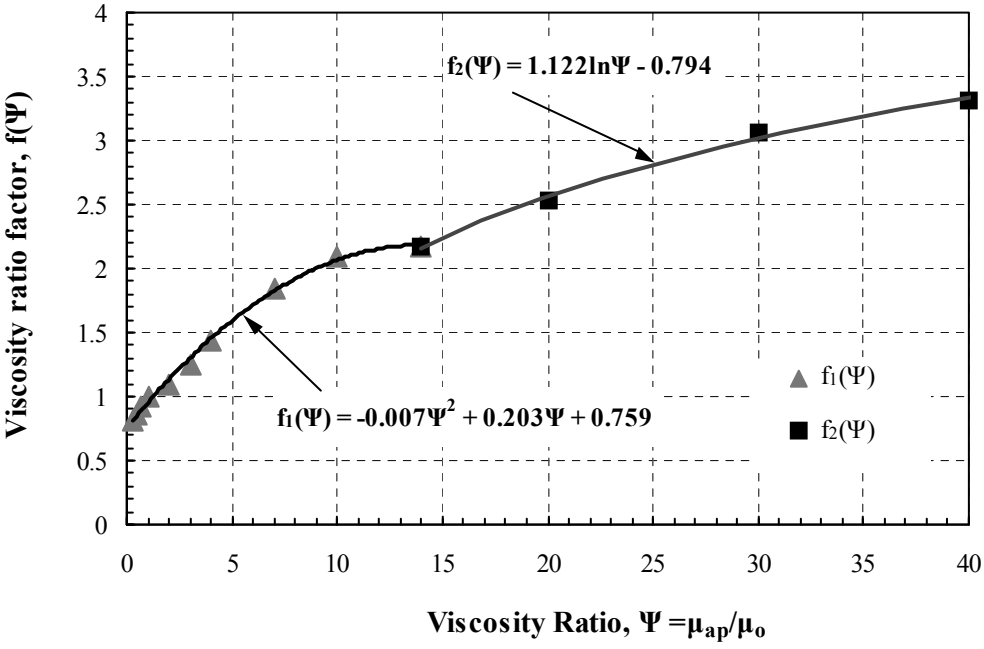

Fig. 4.17 Viscosity ratio factor, f(Ψ), as a function of viscosity ratio.

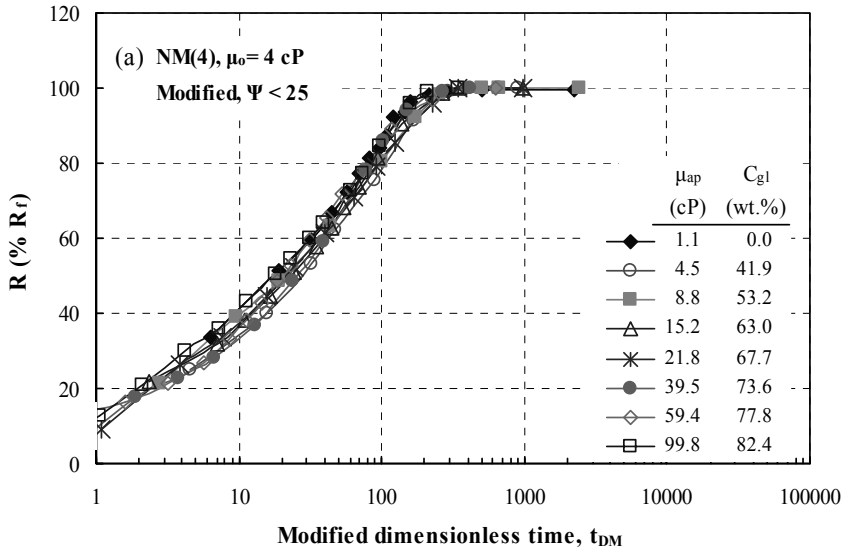

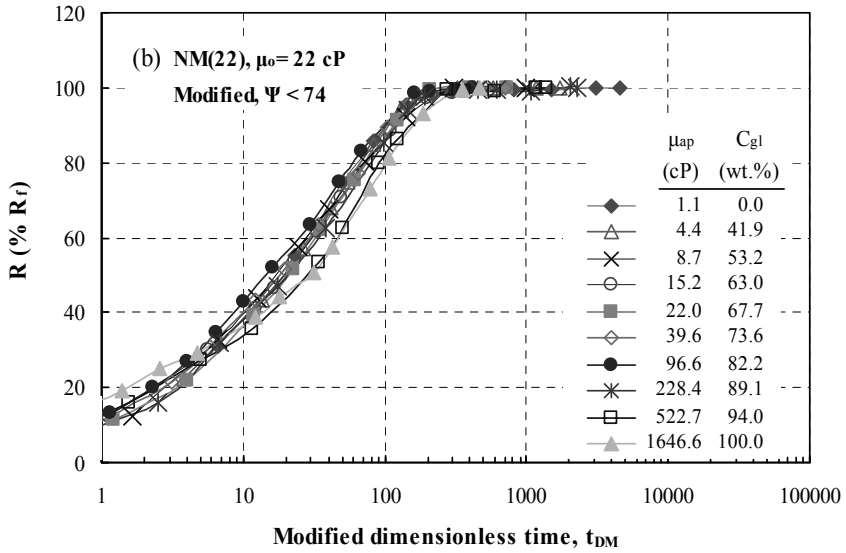

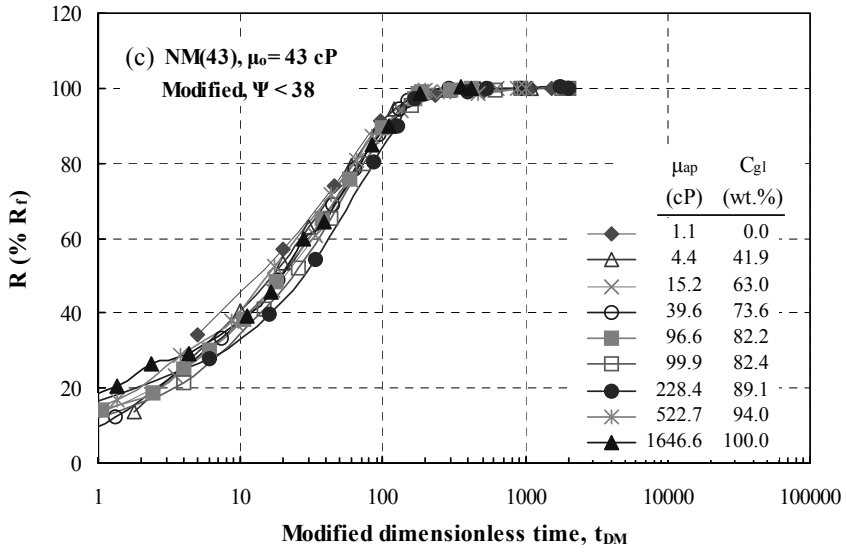

Fig. 4.18 Normalized recovery for (a) 4 cP oil, (b) 22 cP oil and (c) 43 cP oil versus modified dimensionless time, t_{DM}, for variation in aqueous phase viscosity.

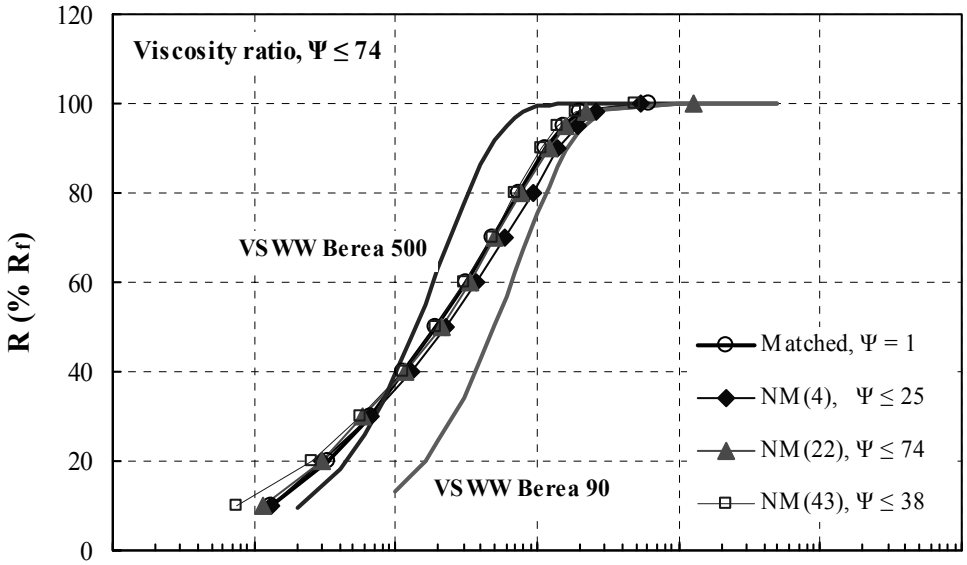

Fig. 4.19 Normalized recovery versus modified dimensionless time, t_{DM}.

Task 5. *Comparison with similarity solutions*.

An Analytical Solution for Counter-Current Spontaneous Imbibition

D.W. Ruth, Y. Li, G. Mason and N.R. Morrow
Transport in Porous Media, 2007, 66, 373-390

Abstract
An approximate analytical solution is provided for one-dimensional, counter-current, spontaneous imbibition of a wetting phase (water) into a semi-infinite porous media. The solution is based on the assumptions that a similarity solution exists for the displacement process. This assumption, in turn, rests on the assumption that the set of relative permeability and capillary pressures curves are unique functions of saturation and do not depend on the nature of the displacement. It further rests on the assumption that the saturation at the imbibition face does not vary with time. It is demonstrated that the solution is in agreement with results obtained from experiments and also numerical analyses of these experiments. The experiments utilize cylindrical samples with the radial surface and one end-face sealed and with imbibition proceeding from the open end-face. The stage of experiment that is modeled by the present solution is the period before the imbibition front contacts the sealed end-face. An important finding of the present analysis is that the pressure upstream of the advancing invasion front is a constant. A second, improved solution is also presented, this solution is an iterative, series solution of a integral-differential equation. It converges to a stable solution in very few terms.

Introduction
The displacement process in porous media is a notoriously non-linear and complex problem; therefore, it is no surprise that only a few cases have been found to have exact analytical solutions. The Buckley-Leverett (1942) solution predicts the forced displacement of one fluid by another provided that capillary pressure is zero. This is a restrictive condition for most real displacement problems. Another solution was developed by Yortsos and Fokas (1983). Although this solution allows for the existence of capillary pressure, the shapes for the capillary pressure and relative permeability functions are constrained. This solution is very useful as a test case for other analytical methods because it is the only analytical solution available that includes all of the important mechanisms. However, it is not applicable for general displacement problems with arbitrary relative permeability and capillary pressure curves.

There are a number of approximate analytical solutions in the literature for two-phase flow; we consider below those solutions that can be applied to countercurrent, spontaneous imbibition. Chen (1988) obtained analytical solutions for countercurrent spontaneous imbibition that were asymptotic in nature. His paper contains a review of previous work by Chinese and Russian authors. Being asymptotic, these solutions do not cover the entire mobile saturation range. McWhorter and Sunada (1990) presented an integral solution for counter-current spontaneous imbibition that is similar to the solution in the present paper. In the present paper, a method is proposed to obtain approximate analytical solutions to the integrals. The recent work of Kashchiev and Firoozabadi (2003) provides analytical solutions for countercurrent imbibition but these solutions depend on capturing the dependence of the capillary pressure and relative permeabilities on saturation by means of a specific functional form; as a result, the equations are approximations to the equations that apply to the original problem.

There is a large literature, dating back until at least Rapoport (1955) and Handy (1960) that show that under certain conditions the process of counter-current spontaneous imbibition results in saturation profiles that are self-similar(see Morrow and Mason (2001) for a recent review). Self-similarity implies that the process of counter-current spontaneous imbibition scales with the square-root of time. The conditions of self-similarity and square-root of time scaling have been assumed in the work of Chen (1988) and McWhorter and Sunada (1990) and most previous analytical work. Li *et al* (2003) explored this behaviour both experimentally and mathematically; results from their work are used to validate the solution presented in the present paper.

There is an alternate approach to the analysis of counter-current, spontaneous imbibition that does not admit a similarity solution and the resulting square-root of time scaling. This approach is founded on the assumption that relative permeability curves are not unique functions of saturation but depend on the nature of the process. Essentially, the assumption that steady-state and non-steady-state processes can be predicted by a single set of relative permeability curves is claimed to be invalid, that is, non-equilibrium processes have different curves than equilibrium processes. This work has largely been pursued by Barenblatt and his co-workers. Early work only available in Russian is reviewed in Barenblatt et al., (1990); the model is further pursued in the work by Barenblatt and Gil'man (1987) and Silin and Patzek (2004). The process they propose is to use the same curves but to transform the actual saturation into an effective saturation using particular mapping processes. This work has been successful in modeling some experimental results, particularly at early times during the process. This suggests that there may be conditions under which similarity exists and others where it does not. The present work is valid where experimental results demonstrate that square-root of time scaling exists.

The solution developed in the present paper is general in nature, allowing for any shape of capillary pressure and relative permeability functions. The solution is valid even if the saturation of the wetting phase at the front differs from the initial wetting phase saturation. Although the solution is not closed-form, it requires only straightforward, numerical integrations of well defined functions to achieve numerical results. The solution is verified by comparing production and pressure histories directly with experimental results, and by comparing saturation profiles with a numerical analysis of a set of experimental data. The simulator used is essentially the same as that described previously by Ruth *et al* (2003). Subsequent to the submission of the original version of the present paper, a preliminary version of the theory presented below was used to explore the influence of viscosity on spontaneous counter-current imbibition (Ruth *et al.* 2004).

Experimental

The counter-current, spontaneous imbibition of a wetting phase against a non-wetting phase in a homogeneous porous medium is considered for the case in which the fluids are incompressible and immiscible, and the process is modeled by relative permeability and capillary pressure curves that are unique function of the local saturation. The motion is originated by preferential wettability and sustained by the capillary pressure gradient that results from the saturation gradient. Gravity effects are neglected. A mathematical model for this process is developed for the case of linear flow along the axis of a columnar sample of infinite length with the columnar surface sealed. Hence, for a finite length sample, the solution is valid until the wetting phase front reaches the

downstream end of the sample. A final assumption is that the saturation at the imbibition face remains constant.

The Solution for the Saturation Profile

The basic equations governing counter-current, spontaneous imbibition flow are the generalized Darcy law

$$q_w = -\frac{K k_{rw} A}{\mu_w} \frac{\partial P_w}{\partial x} \qquad 5.1$$

and

$$q_{nw} = -\frac{K k_{rnw} A}{\mu_{nw}} \frac{\partial P_{nw}}{\partial x} \qquad 5.1$$

the capillary pressure definition

$$P_c = P_{nw} - P_w \qquad 5.3$$

the continuity of flow

$$q_w = -q_{nw} \qquad 5.4$$

and the conservation of mass equations

$$\phi A \frac{\partial S_w}{\partial t} + \frac{\partial q_w}{\partial x} = 0 \qquad 5.5$$

and

$$\phi A \frac{\partial S_{nw}}{\partial t} + \frac{\partial q_{nw}}{\partial x} = 0 \qquad 5.6$$

Combining equations 5.1 through 5.4 results in

$$q_w = \frac{K k_{rw} k_{rnw} A}{\mu_w k_{rnw} + \mu_{nw} k_{rw}} \frac{\partial P_c}{\partial x} \qquad 5.7$$

or in terms of saturation

$$q_w = \frac{K k_{rw} k_{rnw} A}{\mu_w k_{rnw} + \mu_{nw} k_{rw}} \frac{\partial P_c}{\partial S_w} \frac{\partial S_w}{\partial x} \qquad 5.8$$

Defining the variable (here termed the "mobility variable")

$$M_w = \frac{K k_{rw} k_{rnw}}{\mu_w k_{rnw} + \mu_{nw} k_{rw}} \frac{\partial P_c}{\partial S_w} \qquad 5.9$$

then

$$q_w = M_w A \frac{\partial S_w}{\partial x} \qquad 5.10$$

This equation may be recast as

$$\partial x = \frac{M_w A}{q_w} \partial S_w \qquad 5.11$$

which may be integrated to yield

$$x_{S_w} = \int_{S_{wo}}^{S_w} \frac{M_w A}{q_w} \partial S_w \qquad 5.12$$

This equation is equivalent to the expression derived by McWhorter and Sunada (1990).

Here x_{S_w} is the location of a saturation point as a function of time. The integral can be evaluated if we can determine a function for the flow rate in terms of saturation and time.

Eq. 5.5 can be rewritten in terms of the classic "frontal advance theory." At a fixed time, the derivative of the flow rate with position is given by

$$\left(\frac{\partial q_w}{\partial x}\right)_t = \left(\frac{\partial q_w}{\partial S_w}\right)_t \left(\frac{\partial S_w}{\partial x}\right)_t \qquad 5.13$$

S_w is a function of both x and t. It follows that

$$dS_w = \left(\frac{\partial S_w}{\partial x}\right)_t dx + \left(\frac{\partial S_w}{\partial t}\right)_x dt \qquad 5.14$$

Consider the case where we wish to follow the movement of the location of a point with a given saturation. The locus of such a point is defined by setting the total differential of saturation equal to zero in Eq.5.14. After rearranging we obtain

$$\left(\frac{\partial S_w}{\partial t}\right)_x = -\left(\frac{\partial S_w}{\partial x}\right)_t \left(\frac{\partial x}{\partial t}\right)_{S_w} \tag{5.15}$$

Substituting Eqs. 5.13 and 5.15 into Eq. 5.5 and factoring out the common term

$$\left(\frac{\partial x}{\partial t}\right)_{S_w} = \frac{1}{\phi\, A}\left(\frac{\partial q_w}{\partial S_w}\right)_t \tag{5.16}$$

If the solution is self-similar, then the saturation profile must simply stretch along the *x*-direction with time. For such a stretching, the necessary condition is that

$$\left(\frac{\partial x}{\partial t}\right)_{S_w} = a(t) F\left(S_{wo} - S_w\right) \tag{5.17}$$

where $a(t)$ is a function of time, $F\left(S_{wo} - S_w\right)$ is a function only of saturation, and S_{wo} is the saturation at the open face. In the present paper, S_{wo} will be assumed as constant throughout the displacement. If this saturation is not constant, then the similarity condition does not hold. As a first approximation, the function of saturation will be approximated by the expression:

$$F\left(S_{wo} - S_w\right) = \left(S_{wo} - S_w\right) \tag{5.18}$$

Combining Eqs. 5.16 through 5.18, and integrating

$$q_w = -a(t)\,\phi\, A\,\frac{\left(S_{wo} - S_w\right)^2}{2} + C \tag{5.19}$$

where *C* is a constant of integration.

Imbibition experiments can be run with any initial water saturation, S_{wi}, of almost any value between 0 and 1. Because flow is sustained by saturation gradients, the initial, constant saturation in the sample cannot result in any flow, despite the fact that the two phases may be mobile. It follows that the constant in Eq. 5.19 can be recovered by setting the flow rate at S_{wi} to zero. Therefore

$$C = a(t)\,\phi\, A\,\frac{\left(S_{wo} - S_{wi}\right)^2}{2} \tag{5.20}$$

and

$$q_w = -a(t)\,\phi\, A\left(\frac{(S_{wo}-S_w)^2-(S_{wo}-S_{wi})^2}{2}\right) \qquad 5.21$$

Equation 5.5 may be written as

$$\phi A\frac{\partial S_w}{\partial t}+\frac{\partial q_w}{\partial S_w}\frac{\partial S_w}{\partial x}=0 \qquad 5.22$$

or by means of Eq. 5.21

$$\frac{\partial S_w}{\partial t}+a(t)(S_{wo}-S_w)\frac{\partial S_w}{\partial x}=0 \qquad 5.23$$

The self similar variable for this equation is of the form

$$\eta=\frac{x}{\sqrt{t}} \qquad 5.24$$

It follows that

$$\frac{\partial}{\partial x}=\frac{\partial \eta}{\partial x}\frac{\partial}{\partial \eta}=\frac{1}{\sqrt{t}}\frac{\partial}{\partial \eta} \qquad 5.25$$

and

$$\frac{\partial}{\partial t}=\frac{\partial \eta}{\partial t}\frac{\partial}{\partial \eta}=-\frac{1}{2}\frac{\eta}{t}\frac{\partial}{\partial \eta} \qquad 5.26$$

Equation 5.23 then becomes

$$-\frac{1}{2}\frac{\eta}{t}\frac{dS_w}{d\eta}+a(t)\;\left[(S_{wo}-S_w)\right]\frac{1}{\sqrt{t}}\frac{\partial S_w}{\partial \eta}=0 \qquad 5.27$$

This equation suggests that for similarity to hold,

$$a(t)=\frac{a_c}{\sqrt{t}} \qquad 5.28$$

and

$$a_c\left(S_{wo}-S_w\right)=\frac{\eta}{2} \tag{5.29}$$

which is a relatively simple relationship between saturation and the similarity variable.

The solution in Eq. 5.29 bears much similarity with the well known approximate method proposed by Goodman (1964) and used extensively in the analysis of transient heat transfer problems. In these problems, an approximate temperature profile is assumed and parameters in this equation are found in such a way that they satisfy global (that is, integral) conditions. By analogy, we could have started with Eq. 5.29 and proceeded in reverse. The present solution also has similarities to that developed in Barenblatt *et al* (1990). In their case, they approximated a slightly different form of the equation but arrived at a form that has many similarities to Eq. 5.21. Their approximation was to assume that (in the present notation)

$$\int_0^{S_w} M_w\, dS_w = C_1 + C_2\left(S_{wo}-S_w\right)^n \tag{5.30}$$

where C_1 and C_2 are constants. As such, their solution bears similarity to the approach taken by Kashchiev and Firoozabadi (2003). Another difference is that they assumed that the saturation at the inlet face was the value that leads to the condition $P_c=0$.

The present method provides more flexibility in deriving a saturation profile. By assuming a simple relation for the stretching parameter, and not the saturation profile, it is possible to derive an alternate function for the profile of the saturation. Combining Eqs. 5.10, 5.21, 5.25, and 5.28

$$-\phi\ \ a_c\left(\frac{\left(S_{wo}-S_w\right)^2-\left(S_{wo}-S_{wi}\right)^2}{2}\right)=M_w\frac{\partial S_w}{\partial \eta} \tag{5.31}$$

Integrating this equation gives a second equation relating saturation and the similarity variable

$$\frac{1}{\phi}\int_{S_{wo}}^{S_w}\frac{2M_w}{a_c\left(\left(S_{wo}-S_w\right)^2-\left(S_{wo}-S_{wi}\right)^2\right)}dS_w=-\eta_{S_w} \tag{5.32}$$

where the condition

$$\eta_{S_{wo}}=0 \tag{5.33}$$

has been applied. In opposition to Equation 5.29, Equation 5.32 accounts for the complexities introduced by the mobility variable M_w. The present solution therefore shares a basic principle with the Goodman solution, but applies it to a different variable.

The mean saturation is given by

$$\bar{S}_w = \frac{1}{\eta_f}\int_0^{\eta_f} S_w d\eta \qquad 5.34$$

Using Equation 5.31 to change the integration variable and Equation 5.32 to calculate the value of the similarity variable at the front

$$\bar{S}_w = \frac{\int_{S_{wo}}^{S_{wf}} \frac{M_w S_w}{\left(\left(S_{wo}-S_w\right)^2-\left(S_{wo}-S_{wi}\right)^2\right)} dS_w}{\int_{S_{wo}}^{S_{wf}} \frac{M_w}{\left(\left(S_{wo}-S_w\right)^2-\left(S_{wo}-S_{wi}\right)^2\right)} dS_w} \qquad 5.35$$

This equation do not constitute a complete solution because the values of S_{wo} and S_{wf} must be provided independently. However, if the values of these parameters are known, then this equation has great utility in predicting the performance of the imbibition process.

The Solution for the Time Dependence

Because the profile is only stretched along the *x*-axis with time, the average saturation between the open face and x_f must remain constant and the amount of wetting phase that penetrates the sample is given by

$$Q_w = \phi\, A\, x_f(t)\left(\bar{S}_w - S_{wi}\right) \qquad 5.36$$

where S_{wi} is the initial wetting phase saturation and $x_f(t)$ is the location of the front. The total wetting phase imbibed is also given by the equation

$$Q_w = \int_0^t \left(q_w\right)_o \, dt \qquad 5.37$$

where $(q_w)_o$ is the flow at the open face. From Eq. 5.21, this flow rate is given by

$$\left(q_w\right)_o = a(t)\,\phi\, A\, \frac{\left(S_{wo}-S_{wi}\right)^2}{2} \qquad 5.38$$

It follows that

$$a_c \frac{\left(S_{wo}-S_{wi}\right)^2}{2}\int_0^t \frac{dt}{\sqrt{t}} = x_f(t)\left(\bar{S}_w - S_{wi}\right) \qquad 5.39$$

or

$$x_f(t) = \frac{a_c \sqrt{t}\left(S_{wo} - S_{wi}\right)^2}{\left(\overline{S}_w - S_{wi}\right)} \qquad 5.40$$

Combining Equations 5.24 and 5.32 evaluated at the front

$$x_f(t) = -\frac{\sqrt{t}}{\phi} \int_{S_{wo}}^{S_{wf}} \frac{2M_w}{a_c\left(\left(S_{wo} - S_w\right)^2 - \left(S_{wo} - S_{wi}\right)^2\right)} dS_w \qquad 5.41$$

Equating the last two equations and rearranging

$$a_c = \sqrt{-\frac{2}{\phi}\frac{\left(\overline{S}_w - S_{wi}\right)}{\left(S_{wo} - S_{wi}\right)^2} \int_{S_{wo}}^{S_{wf}} \frac{M_w}{\left(\left(S_{wo} - S_w\right)^2 - \left(S_{wo} - S_{wi}\right)^2\right)} dS_w} \qquad 5.42$$

The Pressure Distributions

Rewriting Eqs. 5.1 as

$$\frac{\partial P_w}{\partial x} = -q_w \frac{\mu_w}{K k_{rw} A} \qquad 5.43$$

and using Eq. 5.10

$$\frac{\partial P_w}{\partial x} = -\frac{\mu_w M_w}{K k_{rw}} \quad \frac{\partial S_w}{\partial x} \qquad 5.44$$

This equation may be integrated from the open face of the sample to any S_w section to obtain the pressure in the wetting phase at that S_w section

$$P_w - P_{wo} = -\frac{\mu_w}{K} \int_{S_{wo}}^{S_w} \frac{M_w}{k_{rw}} dS_w \qquad 5.45$$

where P_{wo} is the pressure in the wetting phase at the open face. This pressure will always be zero. The pressure in the non-wetting phase at this S_w section is

$$P_{nwf} = P_{wf} + P_c \qquad 5.46$$

Eq. 5.45 provides a very interesting result. Because the integral is constant with time, depending only on the saturation profile shape, the pressure at the front is also constant! It must be noted that

this is an exact result and does not depend on the approximation represented by Eq. 5.18. It does however rely on the assumptions that enable similarity to exist.

An Improved Solution

An improved solution for the saturation profile may be obtained as follows. Combining equations 5.22, and 5.24 through 5.26 results in

$$-\phi A\frac{1}{2}\frac{\eta}{t}\frac{dS_w}{d\eta}+\frac{\partial q_w}{\partial S_w}\frac{1}{\sqrt{t}}\frac{\partial S_w}{\partial \eta}=0 \qquad 5.47$$

The flow rate scales as

$$q_w=\frac{q_s}{\sqrt{t}} \qquad 5.48$$

Therefore

$$-\phi A\frac{\eta}{2}\frac{dS_w}{d\eta}+\frac{\partial q_s}{\partial S_w}\frac{\partial S_w}{\partial \eta}=0 \qquad 5.49$$

or

$$-\phi A\frac{\eta}{2}\frac{dS_w}{d\eta}+\frac{\partial q_s}{\partial \eta}=0 \qquad 5.50$$

Combining Eqs. 5.10, 5.25 and 5.48

$$q_s=M_w A\frac{\partial S_w}{\partial \eta} \qquad 5.51$$

Eq. 5.50 may therefore be written as

$$-\phi\frac{\eta}{2}\frac{dS_w}{d\eta}+\frac{\partial}{\partial \eta}\left(M_w\frac{\partial S_w}{\partial \eta}\right)=0 \qquad 5.52$$

Let

$$\Lambda=\frac{\eta}{\eta_f} \qquad 5.53$$

Then

$$-\phi\frac{\eta_f^2}{2}\Lambda\frac{dS_w}{d\Lambda}+\frac{\partial}{\partial\Lambda}\left(M_w\frac{\partial S_w}{\partial\Lambda}\right)=0 \qquad 5.54$$

By the product rule

$$-\phi\frac{\eta_f^2}{2}\left(\frac{d\Lambda S_w}{d\Lambda}-S_w\right)+\frac{\partial}{\partial\Lambda}\left(M_w\frac{\partial S_w}{\partial\Lambda}\right)=0 \qquad 5.55$$

Integrating between $\Lambda=0$ and any arbitrary value

$$\phi\frac{\eta_f^2}{2}\left(\int_0^\Lambda S_w d\Lambda-\Lambda S_w\right)+M_w\frac{\partial S_w}{\partial\Lambda}-\left(M_w\frac{\partial S_w}{\partial\Lambda}\right)_{\Lambda=0}=0 \qquad 5.56$$

The saturation may now be expanded in a series (this stage represents a generalization of Goodman's solution method)

$$S_w=\sum_{i=0}a_i\,\Lambda^i \qquad 5.57$$

to obtain

$$\phi\frac{\eta_f^2}{2}\left(\sum_{i=0}\frac{a_i}{i+1}\Lambda^{i+1}-\sum_{i=0}a_i\,\Lambda^{i+1}\right)+M_w\sum_{i=1}ia_i\,\Lambda^{i-1}-M_{w0}\,a_1=0 \qquad 5.58$$

or

$$\sum_{i=1}a_i\left(M_w i\,\Lambda^{i-1}-M_{w0}\,\delta_{1i}-\phi\frac{\eta_f^2}{2}\frac{i}{i+1}\Lambda^{i+1}\right)=0 \qquad 5.59$$

This equation may be solved by the least squares method to obtain the coefficients of the series. The value of the mobility variable can be evaluated using the saturation solutions given by Eq. 5.32 as a first approximation to obtain values of saturation that correspond to values of Λ. The value of η_f can be found from the limiting value of the integral in Eq. 5.32. The boundary conditions for the series can be found from the two equations

$$S_{wo}=a_0 \qquad 5.60$$

and

$$S_{wf} = \sum_i a_i \tag{5.61}$$

The solution can then be refined by successive approximations using the previous series to obtain new values for the series constants. However, new values of η_f must be obtained for each refinement. These new values can be obtained as follows.

The mean saturation may be calculated by inserting the series solution into the integral

$$\overline{S}_w = \int_0^1 S_w d\Lambda \tag{5.62}$$

to obtain

$$\overline{S}_w = \sum_i \frac{a_i}{i+1} \tag{5.63}$$

Using this equation and Eq. 5.24, Eq. 5.36 may be written as

$$Q_w = \phi\ A\ \eta_f \sqrt{t} \left(\sum_i \frac{a_i}{i+1} - S_{wi} \right) \tag{5.64}$$

Using Eq. 5.10, 5.53 and 5.25, Eq. 5.37 may be written as

$$Q_w = \frac{M_{w0} A}{\eta_f} \left(\frac{\partial S_w}{\partial \Lambda} \right)_0 \int_0^t \frac{1}{\sqrt{t}}\, dt \tag{5.65}$$

and

$$Q_w = \frac{2 a_1 M_{w0} A}{\eta_f} \sqrt{t} \tag{5.66}$$

Equating 5.64 and 5.66, and solving for η_f

$$\eta_f = \sqrt{\frac{2 a_1 M_{w0}}{\phi \left(\sum_i \frac{a_i}{i+1} - S_{wi} \right)}} \tag{5.67}$$

This equation has an unforeseen consequence. Because it depends directly on M_{w0}, it is obvious that M_{w0} cannot be equal to zero or the similarity variable at the front would be identically zero and imbibition would not proceed. Therefore, the saturation of the non-wetting phase at the entrance cannot be at the residual value.

Results and Discussion

The approximate analytical solutions were studied by comparison with experimental results and a numerical analysis of those results. The numerical work used an explicit, two-phase simulator. The simulator was used to history match the experiments, thereby obtaining a set of relative permeability and capillary pressure curves that allowed prediction of the experimental data. These curves were then used in the similarity solution. The simulator was also used to predict saturation profiles that could be directly compared with those predicted by the similarity solution.

The curves used are of the form

$$k_{rnw} = k_{roe}\left(\frac{1 - S_w - S_{rnw}}{1 - S_{rnw} - S_{rw}}\right)^{n_{nw}} \qquad 5.68$$

$$k_{rw} = k_{rwe}\left(\frac{S_w - S_{rw}}{1 - S_{rnw} - S_{rw}}\right)^{n_w} \qquad 5.69$$

and

$$P_c = P_{cp}\left[1 - \frac{P_{cp} - P_{ct}}{P_{cp}}\left(\frac{S_w - S_{rw}}{1 - S_{rnw} - S_{rw}}\right)^{n_P}\right] \qquad 5.70$$

Here S_w is the wetting phase saturation. S_{wr} is the residual saturation of wetting phase and S_{rnw} is the residual saturation of the non-wetting phase. The endpoint relative permeabilities are denoted by k_{rnwe} and k_{rwe} while n_{nw} and n_w are exponents that control the shapes of the curves. The final counter-current, spontaneous imbibition saturation, which corresponds to the saturation at the open face, S_{wo}, is always lower than the final co-current spontaneous imbibition saturation or the final forced imbibition saturation, (1-S_{or}) [see Li *et al*, 2003]. S_{nwr} is the residual non-wetting phase saturation, the saturation when the remaining oil is discontinuous in the porous media, and should never correspond to 1-S_{wo} because mobility of the non-wetting phase at the face is required for this phase to be produced. For the capillary pressure (P_c) curve during counter-current, spontaneous imbibition, P_{ct} is the capillary pressure when S_w is at its maximum value 1-S_{rnw} and P_{cp} is the capillary pressure when S_w is at its minimum value S_{rw}.

The data used to test the analytical model is based on one of the cases published by Li, *et al* (2004) (Sample H8O). The experimental data included both production and pressure data. In order to model this data, a history matching process, based on a numerical simulation, was used. This

resulted in the values given in Table 5.1. The numerical model was then used to calculate saturation profiles that could be directly compared with the similarity solutions.

Table 5.1: The test parameters considered in the present study.

Variable	Value	Units	Variable	Value	Units
ϕ	0.221	-	K	1.094	mD
L	6.864	cm	D	3.796	cm
μ_{nw}	3.8	cp	μ_w	1.19	cp
k_{rnwe}	0.6	-	k_{rwe}	0.04	-
n_{nw}	2.6	-	n_w	3.0	-
S_{wo}	0.525	-	P_{cp}	6.5	kpa
P_{ct}	2.55	kpa	n_P	1.75	-

Figure 5.1 shows the curves for both the relative permeability and capillary pressure. These curves are typical for Berea sandstone.

Figure 5.2 shows results for the saturation profiles calculated from the numerical model and those calculated using the model derived in the Pressure Distributions Section, referred to here as the base case. The dots represent the numerical solution while the line is the results from the base case. The solution, although approximately, shows very good agreement except very near the front. Figure 5.3 shows a similar comparison using the improved solution from the Improved Solution Section, utilizing 3, 6 and 12 terms. (A solution using 9 terms was essentially the same as the 12-term case.) The 12-term case gives very good agreement.

Figure 5.4 shows a comparison for production versus time, of the experimental results and those for the base case and the 12-term case. Again the base case shows good agreement but the 12-term case shows better agreement.

Figure 5.5 demonstrates that the pressure ahead of the front is indeed constant. Except for the last point, theory and experiment are in essentially exact agreement. The last point is influenced by the fact that the front is approaching the end of the sample.

Conclusions

The present study has presented an analytical solution for one-dimensional, linear, counter-current, spontaneous imbibition into a porous sample for the period before the invading phase contacts the end of the sample. The analytical method is valid for arbitrary relative permeability, capillary pressure, and other sample parameters. In order for the solution to be used, the saturation at the open face and the saturation at the front must be specified.

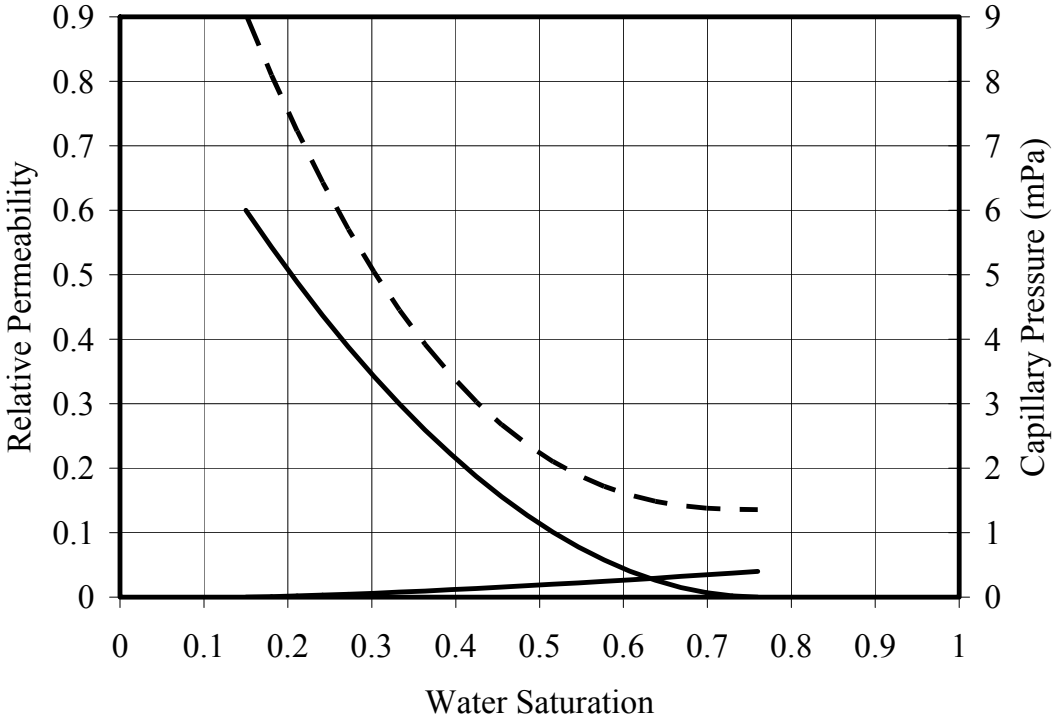

Figure 5.1 The relative permeability and relative permeability curves. The solid lines are the relative permeability curves and the capillary pressure is shown by the broken line.

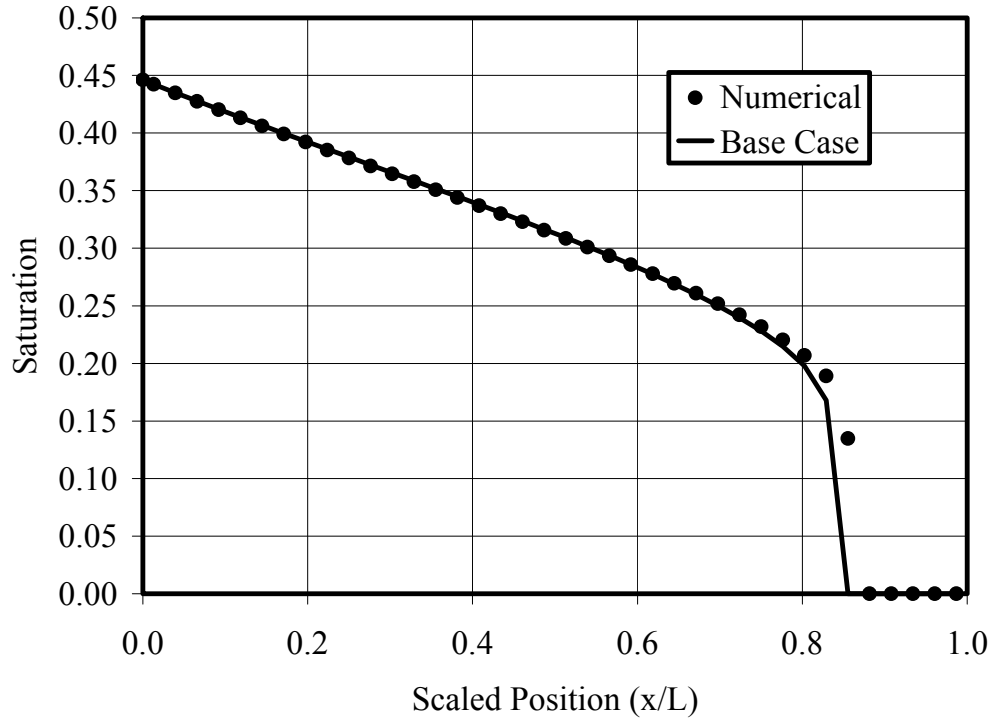

Figure 5.2 The saturation profile as calculated by the numerical simulation and the base model represented by Eq. 5.32.

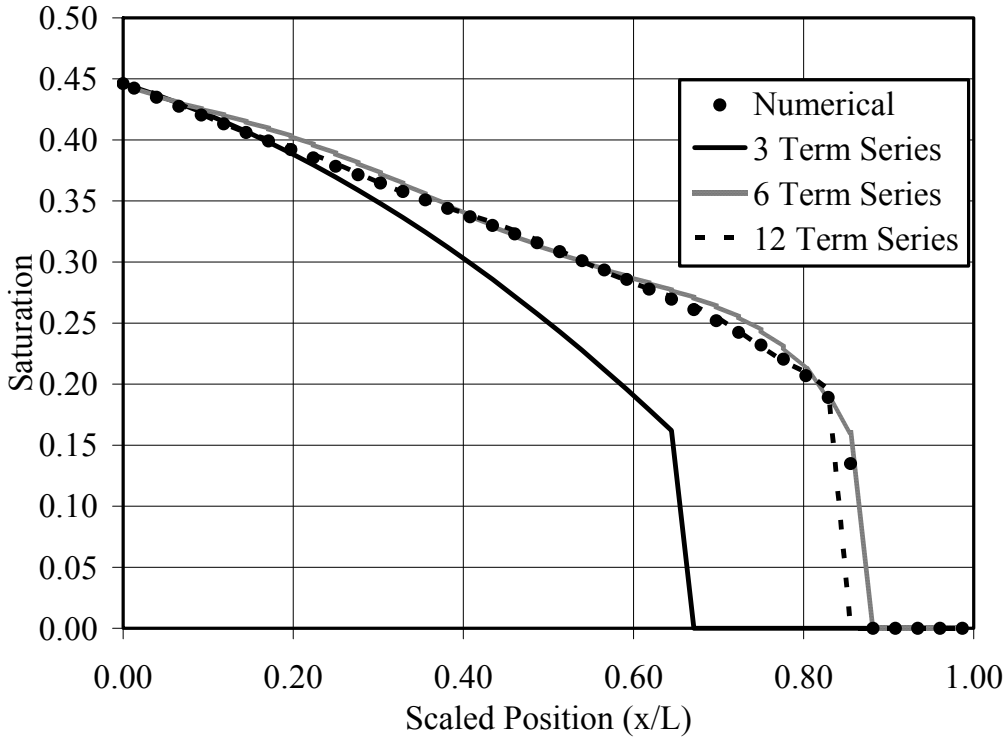

Figure 5.3 The saturation profile as calculated by the numerical simulator and three series with 3, 6, and 12 terms respectively.

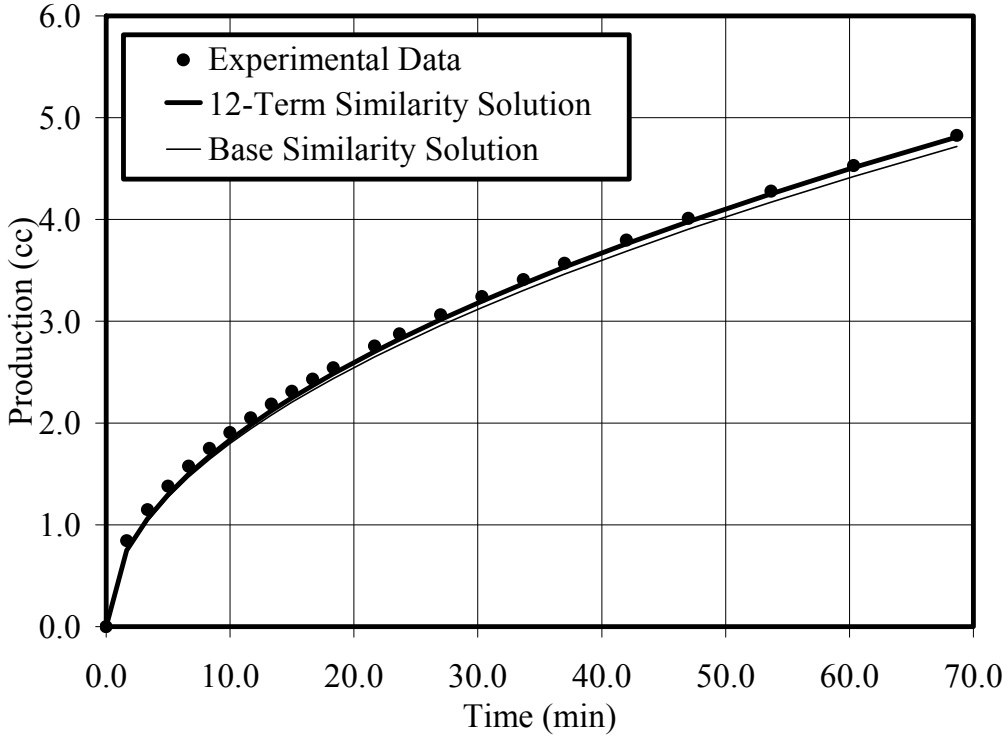

Figure 5.4 The production versus time as measured experimentally and predicted by the base model and the 12 term series model.

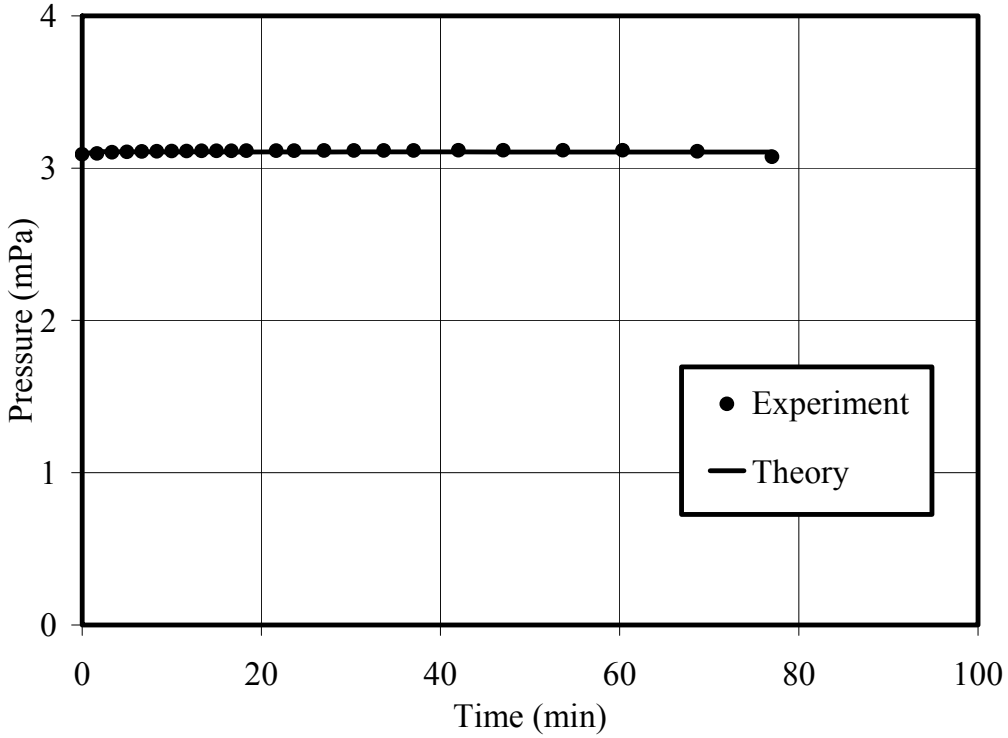

Figure 5.5 The pressure upstream of the front as measured in the experiment and predicted by the theory.

Task 6. *Rock preparation and Work of displacement and surface areas*

6.1 Efficiency of the Conversion of Work of Drainage to Surface Energy for Sandstone and Carbonate

SPE 102490, Published in SPE Reservoir Evaluation & Engineering, August 2007
Siddhartha Seth, and Norman R. Morrow

Summary
The increase in surface energy resulting from drainage of a wetting phase from a porous medium is often equated to the work of displacement determined from the area under its capillary pressure curve. However, capillary pressure vs. saturation relationships are not reversible and do not represent quasistatic displacement. The increase in surface energy is less than the work done because of inherent capillary instabilities that are the basic cause of capillary pressure hysteresis. Nevertheless, relating the area under a capillary pressure curve to the thermodynamic work of displacement can be justified by interpreting the curve as a series of alternating isons (reversible displacements) and rheons (spontaneous redistribution at constant saturation). The efficiency of conversion of work to surface energy, E_d, depends on the increase in surface area that accompanies drainage. Surface areas of nonwetting phase/solid and nonwetting phase/wetting phase have been determined through displacement of a colored low-viscosity liquid resin that can be solidified so that thin sections reveal the distribution of phases and surfaces within the pore space of the rock. Two-dimensional images obtained from thin sections were analyzed using stereology to obtain estimates of saturations and interfacial areas in three dimensions. For drainage of Berea sandstone to 20% wetting-phase saturation, E_d was 36%, which was less than one-half of the efficiency of 85% for the same range of change in saturation determined previously for random packings of equal spheres. Values of E_d for the tested carbonate were approximately one-half of those for sandstone. The wide variation is explained in terms of a simple pore model that relates E_d to aspect ratio.

Introduction
Changes in fluid saturations during multiphase displacements in porous media are accompanied by changes in interfacial surface area between the phases. Interfacial areas are directly related to surface energy and are fundamental to spontaneous-imbibition phenomena, to multiphase transport properties such as relative permeability, and to processes that involve mass transfer between phases (Haines 1930; Leverett 1941; Rapoport and Leas 1951; Payne 1953; Rootare and Prenzlow 1967; Hassanizadeh and Gray 1993; Reeves and Celia 1996; Kim et al. 1997; Alpak et al. 1999; Schaefer et al. 2000a, 2000b; Beliaev and Hassanizadeh 2001; Wan and Tokunaga 2002; Jain et al. 2003; Cheng et al. 2004). The relationship between work of displacement from capillary pressure data to changes in surface energy from direct measurements of surface areas has been reported in detail for drainage, imbibition, and secondary drainage for random packings of equal spheres (Morrow 1970a). The first measurements of relationships between work and increase in surface energy for porous rocks are reported here for primary drainage of a sandstone and a limestone.

Theory
Capillary pressure data for porous media exhibit hysteresis between drainage and imbibition, basically because of capillary instabilities that accompany saturation change. The concepts of

quasistatic displacement that often have been applied to obtain direct relationships between work of displacement, derived from the area under a capillary pressure curve, and change in surface free energy are therefore inapplicable. Justification for interpreting the area under capillary pressure curves as work of displacement has been presented (Morrow 1970a). In fine detail, the curves were interpreted as a series of reversible displacements (termed isons) linked by spontaneous redistributions at constant saturation (termed rheons). Demonstration of this mechanistic interpretation has been provided for bead packs (Morrow 1970a) and for porous rocks by low-rate constant-flow mercury porosimetry, referred to as the Apparatus for Pore Examination (APEX) (Yuan 1991).

The external work, W, needed to reduce the saturation of the wetting phase, α, of a porous solid with bulk volume of V_b and porosity, ϕ, from 100% to a saturation S_α is given by

$$W_{100,S_\alpha} = V_b \phi \int_{100}^{S_\alpha} P_c \mathrm{d}S_\alpha \qquad 6.1\text{-}1$$

where P_c is the capillary pressure.

The change in surface free energy, ΔF, is a function of the interfacial area created by the invading nonwetting phase:

$$\Delta F = \sigma_{\alpha\beta} (\Delta A_{\alpha\beta} + \Delta A_{\beta\gamma} \cos\theta) \qquad 6.1\text{-}2$$

where $\sigma_{\alpha\beta}$ is the interfacial tension, mN/m; θ is the contact angle; β is the nonwetting phase; $\Delta A_{\alpha\beta}$ is the interfacial area between the wetting and nonwetting phases; and $\Delta A_{\beta\gamma}$ is the interfacial area between the nonwetting phase, β, and solid phase, γ.

If θ is zero, the increase in surface free energy that accompanies drainage is given by

$$\Delta F = \sigma_{\alpha\beta} (\Delta A_{\alpha\beta} + \Delta A_{\beta\gamma}) \qquad 6.1\text{-}3$$

Because of inherent instabilities in the drainage process, the increase in surface free energy is less than the work done. The net efficiency (%), E_d, of conversion of work to surface energy for primary drainage to saturation, S_α, is given by

$$E_d = \frac{\sigma_{\alpha\beta} (\Delta A_{\alpha\beta} + \Delta A_{\beta\gamma})}{V_b \phi \int_{100}^{S_\alpha} P_c \mathrm{d}S_\alpha} 100 \qquad 6.1\text{-}4$$

The value of E_d has been reported for random packings of equal spheres (Morrow 1970a). Determination of E_d for rocks and other types of natural porous media presents far greater challenges with respect to obtaining consistent capillary pressure data and determination of changes in interfacial areas.

Rock Characterization

Berea sandstone (referred to as Berea PH 2) from Cleveland Quarries, Ohio, and an Edwards limestone (referred to as Edwards GC) from near Garden City, Texas, were obtained in the form of 6×12×12-in. blocks. Values of porosity, permeability, BET surface area (Brunauer et al. 1938) (surface area of the solid obtained from nitrogen adsorption), cation exchange capacity (CEC), and clay analysis by X-ray diffraction (sandstone only) are included in Table 1.

Examples of thin sections for the sandstone PH 2 are shown in Figs. 6.1-1a and b**,** and scanning electron micrographs (SEMs) are shown in Figs. 6.1-1c and d. The matrix consists mainly of quartz grains and includes lesser fractions of rock fragments and partially dissolved feldspars. The SEMs show kaolinite and partially dissolved feldspar grains in detail.

The Edwards (GC) sample was composed of calcite minerals (Figs. 6.1-2a and b) with pore space consisting mainly of moldic pores (clearly derived from dissolution of fossils) and interparticle porosity. The original interparticle porosity had been reduced significantly by recrystallization of calcite both within and outside these pores. The SEMs (Figs. 6.1-2c and d) clearly show that moldic pores have been partially refilled through recrystallization of calcite.

Mercury-injection capillary pressure data for Berea PH 2 sandstone and Edwards GC Block 2 limestone are shown in Figs. 3a and 3b**,** respectively. Respective pore-size distributions, shown in Figs. 6.1-3c and d, were derived from a combination of mercury-injection and desorption isotherm [BJH analysis (Barrett et al. 1951)] measurements [see Fig. 6.1-3c for the sandstone PH 2 and Fig. 6.1-3d for the limestone (Edwards GC Block 2)]. The portion of the pore-size distribution shown as a dashed curve in Fig. 6.1-3d was estimated because the mercury-injection test involved changing the pressure cell during the course of the test.

Experimental Procedures: Capillary Pressure and Interfacial Areas

Capillary Pressure Measurements for Primary Drainage.

Primary drainage capillary pressure measurements were made with a Beckman J 6B centrifuge. Cores of 3.81 cm [1.5 in.] diameter and up to 6 cm [2.36 in.] in length were first saturated with brine. Each core was then set in a sleeve that fitted into an Exxon core holder. A confining pressure of 15 bar [220 psi] was applied. For the sandstone, only displacement of brine by air was measured. For the carbonate sample (Edwards GC Block 2), displacement of brine by air and brine by decane (interfacial tension against brine as supplied was 35 mN/m) were measured.

The capillary pressure depends on the angular speed of rotation, ω, and the density difference, $\Delta\rho$, between the two fluids and is given by

$$P_c = \frac{\omega^2 \Delta\rho (r_o^2 - r^2)}{2} \qquad 6.1\text{-}5$$

where r_o is the distance from the center of rotation to the outermost face of the core, and r is the distance from the center of rotation to any point in the core. The average saturation, $S_\alpha\,(r,\omega)$, of the core is given by

$$S_\alpha\,(r,\omega) = \frac{1}{L\pi R_c^2} \int S_{r,\omega} \mathrm{d}V_c \qquad 6.1\text{-}6$$

where L is the length of the core, and R_c and V_c are the radius and volume, respectively.

Various methods of obtaining solutions to Eq. 6.1-6 have been proposed that involve converting the volume of fluid produced at any speed to saturation at the inlet face of the core. In a survey conducted by the Society of Core Analysts, Forbes (1997) compared 19 different solutions to Eq. 6.1-6 and concluded that the final capillary pressure curve varied quantifiably from one method to another. In the present work, the cubic spline and the Ruth-Wong 1st method (Ruth and Wong 1988, 1991) were used for the sandstone, and the Bentsen Version 2 was used for the carbonates

(Bentsen and Anli 1977). These methods were selected on the basis of experience with respect to the fit to the raw data and the form of the derived capillary pressure data.

Interfacial Areas. The following procedure was used to visualize the fluid distribution and interfacial areas that develop in a core under primary drainage. First, the core was saturated with a low-viscosity resin containing a blue dye using both vacuum and high pressure in consecutive steps. Second, the fully saturated sample was centrifuged (air displacing the blue-dyed epoxy) to a particular net saturation at a selected speed for 72 hours. The temperature in the centrifuge was then raised so that the epoxy resin became solidified in situ with the core still spinning. The core was then placed in a pressure vessel, and the air was evacuated, followed by forcing the red-dyed resin into the sample at a final pressure of 1,500 psi. The second resin was then solidified by raising the temperature. Thin sections prepared from the core showed the areas of occupancy by the blue and the red (nominally) epoxy resins, which corresponded to the location of the wetting phase and the nonwetting phase, respectively (Figs. 6.1-14a and b). Further details of the procedure are available (Seth 2006).

Image Analysis

Optical images obtained with a petrographic microscope under reflected light provided satisfactory approximation to 2D images. The images were processed to obtain a description with only three types of pixels (blue, red, and white) that represented the wetting phase, α, the nonwetting phase, β, and the solid phase, γ, respectively. A grid was overlain on the processed image, and point counts and line intercepts were measured with in-house software. The point counts and line intercepts in conjunction with theorems of stereology (Underwood 1970) provided the saturations and surface-to-volume ratios of the three phases (Seth 2006).

For the sandstone, a total of 85 micrographs were taken from 14 different thin sections made from five different cores. The results for an individual micrograph were averaged. Seven thin sections were evaluated at 10X resolution, whereas the rest were analyzed at 20X as a check that values were not biased by the scale of measurement. The pixel sizes at 20X and 10X magnification were 0.74 and 2.04 microns, respectively (the pixel size did not vary linearly with magnification because different microscope/camera combinations were used for each of the magnifications). The size of each picture so obtained was 0.08 cm^2 at 10X magnification, which was only about 1/140 of the cross-sectional area of each thin section. Scatter in the data is to be expected because of the small area sampled for each image. A 1×1 pixel grid (the finest grid possible) was used for analysis.

The fundamental assumption of stereology is that the 2D image is representative of the 3D sample. Agreement in global properties, such as porosity (3D property) obtained from thin sections and that obtained volumetrically, provided an indication that the micrographs provided satisfactory resolution. If, for a particular thin section, the variation in global properties was large from one micrograph to another and also from that obtained volumetrically, then a lower magnification was used. For example, the use of 40X magnification leads to a large variation in porosity between images because of the small area scanned at this magnification. For the data presented, magnifications of 10X and 20X gave close values of average porosity (17.1 and 16.9%). These values were consistent with respect to the volumetrically determined values of 21% because fine pore structure cannot be resolved by petrographic analysis.

For the limestone, one core was cut from Edwards GC limestone Block 1 and the other from Block 2. Nine thin sections (five from Block 1 and four from Block 2) were prepared. A total of 57 micrographs were analyzed (22 from Block 1 and 35 from Block 2) at 20X magnification. The average porosity of 20.5% from the thin sections was consistent with the volumetrically measured value of 23%.

Three interfacial areas expressed in m^2/g: Wetting phase/solid, $A^*_{\alpha\gamma}$, nonwetting phase/solid, $A^*_{\beta\gamma}$, and wetting/nonwetting phase, $A^*_{\alpha\beta}$, were derived from the micrographs. Two additional areas, the total solid surface area and the created surface area, also expressed as m^2/g of dry rock, were defined by these areas. Total solid surface area, $\sum A^*_\gamma$, was operationally defined by the imaging procedure. For the images that contained resins of two colors, $\sum A^*_\gamma$ was obtained from the sum of the interfacial areas between the solid-red, A^*_γ, and solid-blue, $A^*_{\alpha\gamma}$, interfaces. The values of $\sum A^*_{\beta\gamma}$ provided indication that the solid surface areas derived from petrographic analysis of the either the blue or red/blue resin impregnated thin sections were consistent. Ideally, $\sum A^*_\gamma$ should be constant. The created surface area, $\sum A^*_\beta$, associated with invasion of the nonwetting phase, was given by the sum of the solid-red, $A^*_{\beta\gamma}$, and the red-blue, $A^*_{\alpha\beta}$, surface areas.

Results and Discussion

Work of Primary Drainage from Capillary Pressure Curves.

Raw centrifuge data and derived drainage capillary pressure curves by three methods for displacement of brine by air are shown in Fig. 6.1-5a for Berea sandstone PH 2. The work of displacement per gram of dry solid, *W**, obtained by integrating under the capillary pressure curve, is shown in Fig. 6.1-5b. Results for two Edwards GC limestone cores cut from Block 2, one for displacement of brine by air and the other for brine by decane, are presented in Figs. 6.1-6a and b, respectively.

After scaling the capillary pressure for difference in interfacial tension, the curvature, $P_c/\sigma_{\alpha\beta}$, for air/brine was higher than that of oil/brine. Also, displacement curvatures for mercury injection (given by scaling the capillary pressure data shown in Figs. 6.1-3a and b with respect to interfacial tension and the cosine of contact angle (for either 0° or 40°) did not scale consistently with either air/brine or oil/brine centrifuge data. Relationships between work of displacement and increase in surface free energy are summarized in Table 6.1-2. Many examples of inconsistency between capillary pressure data sets have been reported previously (Sallier and Hamon 2005; Purcell 1949; Sabatier 1994; Morrow et al. 1990; Melrose et al. 1994; Wells and Amaefule 1985; Hamon and Pellerin 1997). The most complete capillary pressure data sets obtained for rocks used in the present work were for displacement of brine by air; analysis is based mainly on these data.

Total Solid $\sum A^*_\gamma$ and Created $\sum A^*_\beta$ Surface Areas.

Sandstone. The average value of $\sum A^*_\gamma$ (see Fig. 6.1-7a), approximately 0.01 m^2/g, was operationally defined by the imaging procedure. $\sum A^*_\gamma$ was almost two orders of magnitude less

than the area of 0.626 m^2/g, operationally defined by gas adsorption, because the optical imaging does not resolve details of the surfaces of clays and other forms of microporosity that are the major contributors to the BET surface area.

The interfacial area between the wetting and nonwetting phase, $A^*_{\alpha\beta}$, was never more than 2% of $\sum A^*_\gamma$. $\sum A^*_\beta$ (the sum of $A^*_{\beta\gamma}$ and $A^*_{\alpha\beta}$) increased close to linearly with the decrease in the wetting-phase saturation (see Fig. 6.1-7b).

Carbonate. For Edwards GC limestone Blocks 1 and 2, solid surface areas determined from imaging, $\sum A^*_\gamma$, were, respectively, 0.0146 m2/g (7.3% of BET surface area) and 0.0133 m2/g (3.3% of BET surface area) (see Fig. 6.1-8a). As for sandstone, created surface area, $\sum A^*_\beta$, increased linearly with decrease in wetting-phase saturation for both samples (Fig. 6.1-8b). The interfacial area between the wetting and nonwetting phase, $A^*_{\alpha\beta}$, exhibited maxima that were only 5% and 2% of $\sum A^*_\gamma$ for Blocks 1 and 2, respectively (Fig. 6.1-8b).

Efficiency of Conversion of Work to Surface Energy.
Sandstone*, Ed.* The work of displacement per gram of dry solid, W*, obtained from air/brine centrifuge data (expressed as an equivalent area W*/σαβ) and the changes in created surface area, $\sum A^*_\beta$, obtained from thin sections for Berea sandstone PH 2, are shown in Fig. 6.1-9a. The efficiency of conversion of work to surface energy decreases with decrease in wetting-phase saturation (see Fig. 6.1-9b). For the sandstone PH 2, the efficiency, Ed, of primary drainage to 20% wetting-phase saturation was 36%.

Carbonate, Ed. W* for Edwards GC Block 2 obtained from air/brine centrifuge data, expressed as an equivalent area, is shown in Fig. 6.1-10a. Changes in created surface area, $\sum A^*_\beta$, obtained from thin sections for the Edwards GC Blocks 1 and 2 are also shown. The efficiency of conversion of work of primary drainage (down to Sα = 20%) to surface energy for Block 2 was only 14% (see Fig. 6.1-10b). Air/brine capillary pressure data for Block 1 were not available. Based on the air/brine capillary pressure data for Block 2, Ed for Block 1 was 18% (see Fig 6.1-10b). For limestone, an average air/brine-based value of Ed equal to 16% is used in further discussion.

Random Packings of Equal Spheres.
Random packings of equal spheres provide a readily prepared class of porous media with statistically similar geometry and porosity that is usually close to 37%. The permeability of the bead pack is proportional to the square of the sphere radius, R. Provided the ratio of gravity to capillary forces is not unusually high, and that spreading prevails (θ = 0), capillary pressure measurements for drainage, imbibition, and secondary drainage should give universal plots of dimensionless pressure ($P_cR/\sigma_{\alpha\beta}$) vs. saturation (Haines 1930).

A characteristic feature of drainage of sphere packs, which results from smooth surfaces, is that part of the wetting phase is retained as hydraulically disconnected capillary structures, the most

well-known example being pendular rings at point contacts between spheres. The capillary pressure and, hence, the surface curvature of each individual capillary structure (or the pressure acting at a semipermeable membrane) is set at the time of isolation from the continuous part of the wetting phase (Morrow 1970b). The isolated structures of the wetting phase are not in capillary equilibrium with each other or the externally measured pressure (this might be the hydrostatic head for a packed column or the capillary pressure at a semipermeable membrane). However, the times required to attain thermodynamic equilibrium by diffusion or transport in surface films are many orders of magnitude greater than the times required to reach mechanical equilibrium. The fraction of the wetting phase that is retained as an irreducible saturation with respect to mechanical equilibrium is very close to 7% for any size of sphere.

The fraction of drained sphere surface at the irreducible saturation was determined by drainage of dilute acid from packings of ball bearings followed by point counting of etched and nonetched areas. For any sphere size, the fraction of drained sphere surface was constant and equal to 71% of the total sphere surface. The wetting/nonwetting surface area at the irreducible saturation was equal to approximately 7.5% of the total sphere surface area. From these values, and the work given by the universal curve for drainage to the 7% irreducible wetting phase saturation, E_d was 79% .

E_d for sphere packs, as found for the sandstone and carbonate, also decreased with increase in nonwetting-phase saturation (see Fig. 6.1-11). For drainage of random packings of equal spheres to 20% saturation, E_d was 85%. The values of E_d for air/brine drainage of Berea PH 2 sandstone and Edwards limestone down to 20% wetting-phase saturation, are 36% and 16% respectively. The capillary pressure data and surface areas obtained for rocks involve much greater uncertainties than for sphere packs. However, even for the range of values given by the different conditions of measurement of capillary pressure data, values of E_d for the sandstone and limestone (see Table 6.1-2) are always much lower than for spheres.

Effect of Aspect Ratio on Ed.

If the work of displacement in moving an interface is reversible, as in displacement in a cylindrical tube, the efficiency of conversion of work to surface free energy is 100%. Loss of surface free energy during drainage of porous media is caused by capillary instabilities. For example, consider a pore consisting of a spherical cavity of radius R_{sp} with throat radius r_t (see Fig. 6.1-12a).

The length, L_t, of a cylindrical tube of radius r_t having the same volume as the sphere of radius (R_{sp}) is given by

$$\pi r_t^2 L_t = \frac{4}{3}\pi R_{sp}^3 \qquad 6.1\text{-}7$$

and

$$L_t = \frac{4R_{sp}^3}{3r_t^2} \qquad 6.1\text{-}8$$

The capillary pressure needed to drain the spherical cavity is set by the pore-throat size. At this pressure, the interface becomes unstable and passes through the cavity. The ratio of the area created in draining the spherical cavity (we assume that upon drainage, the cavity becomes filled by the nonwetting phase, and, as a first approximation, we neglect the area of the sphere

associated with its throats) to that for reversible drainage of the equivalent cylindrical pore gives the efficiency, E_d, of conversion of work to surface free energy.

$$E_d = \frac{4\pi R_{sp}^2}{2\pi r_t L_t} \qquad 6.1\text{-}9$$

Substituting for L_t, the efficiency, E_d, is given by

$$E_d = \frac{1.5 r_t}{R_{sp}} \qquad 6.1\text{-}10$$

If the ratio of pore body to throat radius, commonly referred to as the aspect ratio, is denoted as ξ,

$$E_d = \frac{1.5}{\xi} \qquad 6.1\text{-}11$$

Results obtained for displacement efficiencies as a function of the aspect ratio given by Eq. 6.1-11 ($\theta = 0^0$) are shown in Fig. 6.1-12b. The efficiency of drainage is highly sensitive to the ratio of pore throat to pore body size. In addition to aspect ratio, the accessibility of individual pores will contribute to the inefficiency of drainage. The magnitude of the sudden pressure changes measured by Yuan (1991) indicate that drainage of pores often occurs in large clusters. Then, the pressure of drainage may not be set by the penetration pressure of the pore throat of an individual pore but by some other pore throat that controls access and only empties at higher capillary pressure. In effect, this increases the work of displacement for such pores.

Aspect ratios also have been related to snapoff and the tendency for the nonwetting phase to become trapped during imbibition processes at very strongly water-wet conditions (Wardlaw and Casson 1979). For cubic and hexagonal packings of spheres, the aspect ratios are 1.45 and 2.67, respectively, based simply on inspheres for the pore throats and bodies.

The reported residual oil for random sphere packs is only 15.5% (Morrow et al. 1988). For Berea sandstone, the aspect ratio from the data presented by Wardlaw et al. (1987) was 7.7, and from Chatzis et al. (1983), the aspect ratio ranged from 4 to 6.7. The residual saturation to the nonwetting phase for very strongly water-wet Berea sandstone is typically about 50% of the initial oil saturation. For the Edwards GC carbonates, the range of aspect ratio is very high, as given by the ratio of the moldic pore sizes, indicated by SEM and micrographs of thin sections (Figs. 6.1-2c and d), to the throat sizes, indicated by the mercury-injection capillary pressures for drainage (Fig. 6.1-3b). Trapping of the nonwetting phase for the Edwards GC limestone used in the present work was approximately 65% (Tie and Morrow 2005).

Aspect Ratio and Wettability.

If the contact angle for the pore model of Fig. 6.1-12a is θ, the surface energy of the drained cavity is given by

$$4\pi R_{sp}^2 \cos\theta \qquad 6.1\text{-}12$$

If the drainage pressure is proportional to the cosine of the contact angle, as for a cylindrical tube, then E_d is independent of wettability. However, if the drainage pressure of the cavity is insensitive to contact angle because of factors, such as edges, surface roughness, and converging-diverging pore shapes, that result in low effective receding contact angles (Morrow and McCaffery 1978; Morrow 1975), the efficiency is given by

$$E_d = \frac{1.5\cos\theta}{\xi} \qquad 6.1\text{-}13$$

Drainage efficiencies can then be very low. On the other hand, if a significant fraction of the bulk wetting phase is retained by surface roughness, microporosity, and macrosized pore throats, at otherwise drained pore surfaces, values of E_d will be correspondingly higher.

Conclusions

1. A technique involving centrifuging and solidification of liquid resins enabled the distribution of wetting and nonwetting phases and interfacial areas to be determined from thin sections for sandstone and carbonate.
2. The total area created by invasion of the nonwetting phase increased linearly with decrease in wetting-phase saturation for both sandstone and carbonate. The interfacial area between the wetting and nonwetting phase was always only a small fraction of the nonwetting phase/solid area.
3. Comparison of created surface area with rock surface area measured by gas adsorption showed that, after primary drainage to 20% wetting-phase saturation, most of the rock surface area is still overlain by bulk wetting phase.
4. The efficiency of conversion of work of displacement (based on air/brine capillary pressure measurements) to surface free energy for displacement to 20% wetting-phase saturation was only 36% for sandstones and 16% for limestone. These values are very low compared to the value of 85% measured for sphere packs.
5. Drainage of a spherical cavity provides an explanation of how aspect ratio (pore body to pore throat size) can have a dominant effect on the efficiency of conversion of work of displacement to surface free energy.

Nomenclature

A	interfacial area, m^2
A^*	interfacial area, m^2/g of dry rock
A_w^*	surface area equivalent to scaled work of displacement, W^*/σ, m^2/g
$\sum A_\beta^*$	created surface area, m^2/g of dry rock
$\sum A_\gamma^*$	total solid surface area, m^2/g of dry rock
E_d	efficiency (%) of conversion of work of drainage to surface free energy
k	permeability of the core sample, md
L	length of tube or core, cm
P_c	capillary pressure, KPa
r, R	radius, cm
V	bulk volume, cm^3
W	work of drainage, KJ
W^*	work per gram of dry rock, KJ/g
θ	contact angle, degrees
ξ	aspect ratio
ρ	density of the fluid, g/cm^3
σ	interfacial tension, mN/m

ϕ porosity
ω angular speed of rotation, rad/sec

Subscripts
b bulk
c core
sp spherical
t throat
α wetting phase
β nonwetting phase
γ solid phase

Acknowledgments
Funding for this research was provided by the US Department of Energy, National Energy Technology Laboratory contract #DE-FC26-03NT15408, and the University of Wyoming Enhanced Oil Recovery Institute (UW EORI). Special thanks are due to Peigui Yin, UW EORI, for assistance with rock characterization; Shaochang Wo, UW EORI, for help in developing image-analysis software; Geoffrey Mason, University of Loughborough, for discussion and suggestions; Arne Graue, University of Bergen, for use of centrifuge equipment; Douglas Ruth, University of Manitoba, for detailed assistance on interpretation and processing of centrifuge data; and James Howard, ConocoPhillips, for providing the mercury-injection data.

SI Metric Conversion Factors

bar	×	1.0*	E + 05 = Pa
Btu	×	1.055 056	E + 00 = kJ
dyne	×	1.0*	E – 02 = mN
ft	×	3.048*	E – 01 = m
ft^2	×	9.290 304*	E – 02 = m^2
in.	×	2.54*	E + 00= cm
$in.^2$	×	6.451 6*	E + 00= cm^2
$in.^3$	×	1.638 706	E + 01= cm^3
psi	×	6.894 757	E + 00= kPa

*Conversion factor is exact.

Table 6.1-1 Rock properties

Rock	Solid Density, g/cc	Porosity,%	Permeability, md	CEC, meq/100g	BET Surface Area,m^2/g
Berea Sandstone PH 2*	2.65	21	650	0.145	0.626
Edwards GC (Block 1) Limestone	2.69	24	15-Oct	-	0.2
Edwards GC (Block 2) Limestone	2.69	24	20 - 30	0.026	0.4

* XRD clay ratios: chlorite; illite; kaolinite -16; 27; 57

Table 6.1-2 Comparison of efficiency of drainage E_d, obtained based on primary drainage capillary pressure curves obtained by different methods for sandstone and limestone

Capillary pressure method	P_c equivalent area A_w^*, m^2/g	Area from thin section ΣA_β^*, m^2/g	E_d %
Berea sandstone PH 2			
Centrifuge (air/brine)	0.0226	0.0081	35.8
Mercury injection (Hg/air)	0.03987	0.0081	20.3
Edwards GC limestone			
Centrifuge (air/brine) Block 1	0.06	0.011	18.3
Centrifuge (air/brine) Block 2	0.06	0.0086	14.3
Centrifuge (oil/brine) Block 2	0.042	0.0086	20.5
Mercury injection (Hg/air) Block 2	0.0475	0.0086	18.1

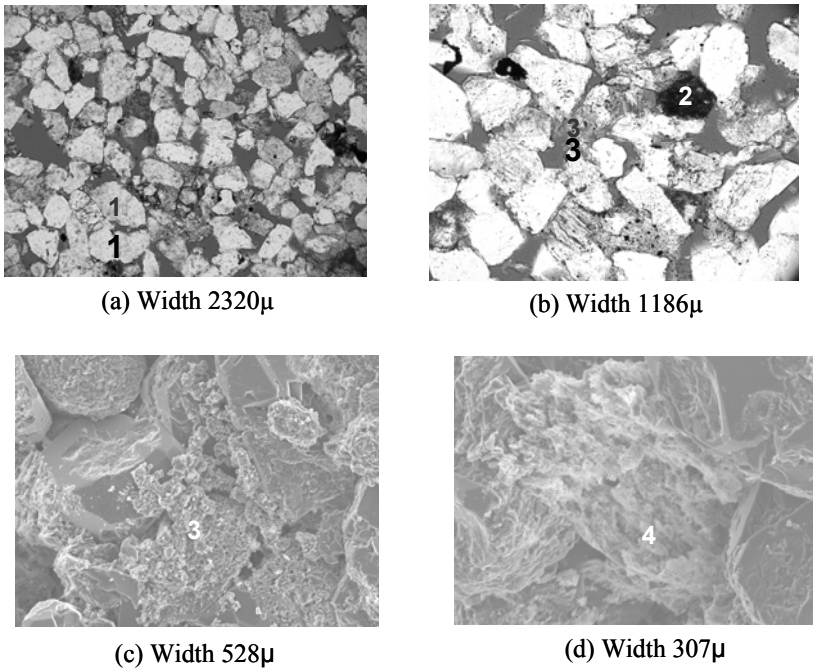

Fig. 6.1-1 Features of Berea sandstone PH 2 from thin section, (a) and (b) and SEM, (c) and (d): quartz grain (1), rock fragments (2), kaolinite (3), partially dissolved feldspar (4).

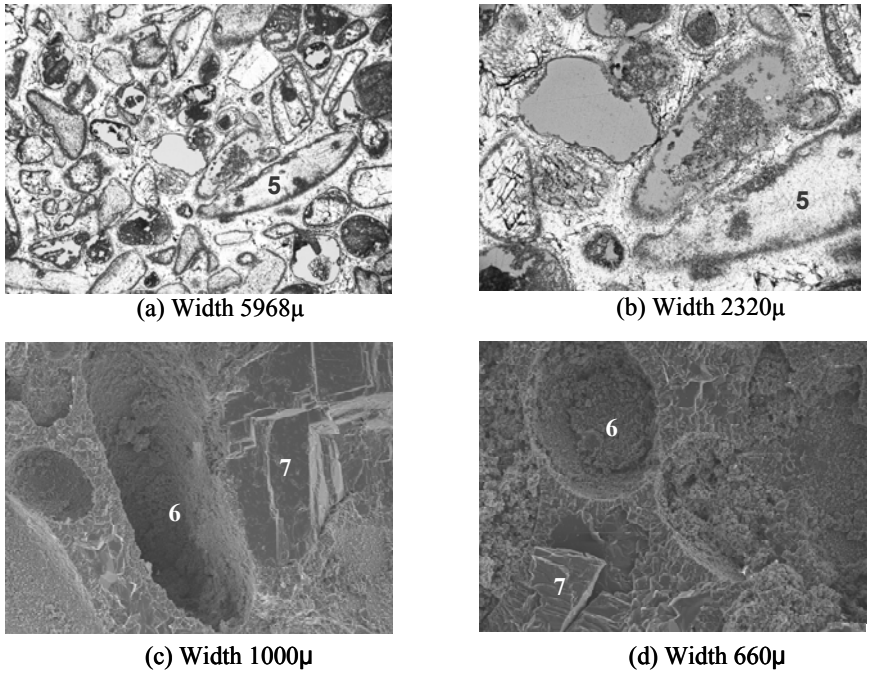

Fig. 6.1-2 Features of Edwards GC Block 1 from thin section, (a) and (b), and SEM, (c) and (d): calcite grains (5); poorly connected moldic pores, (6) calcite cement (7).

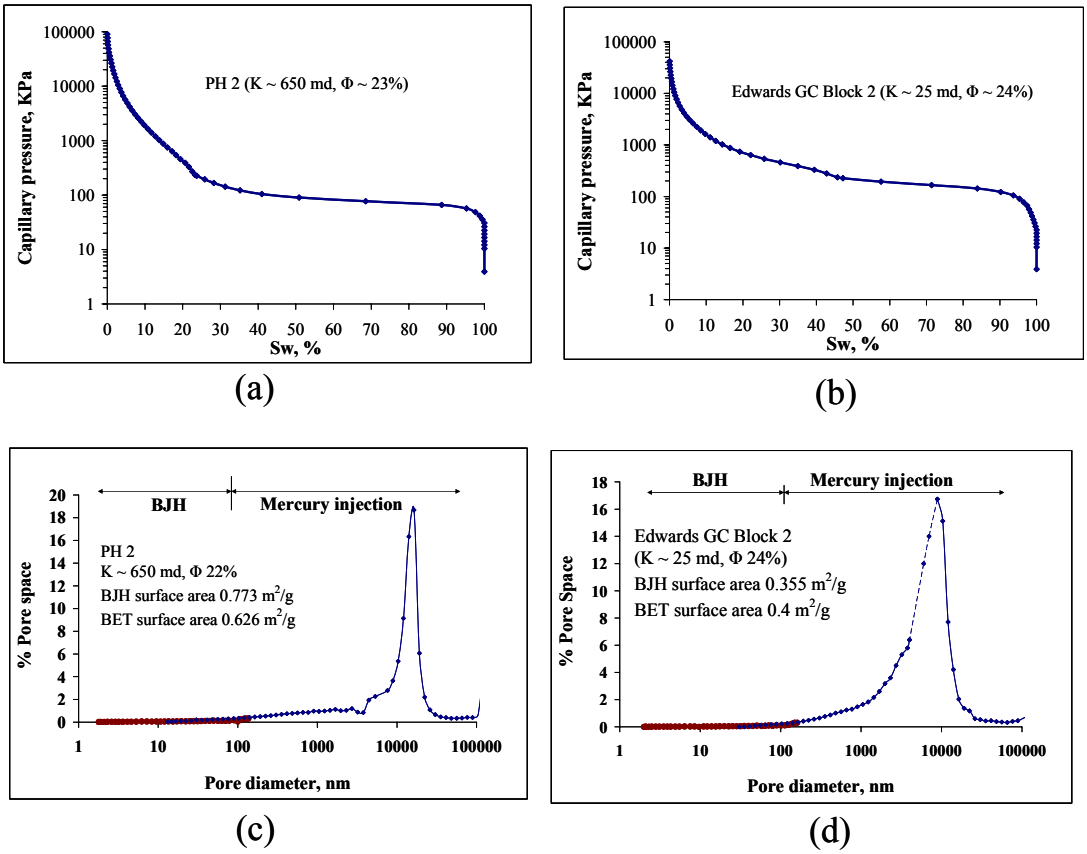

Fig. 6.1-3 Mercury injection capillary pressure curves for (a) Berea sandstone PH 2 (b) Edwards GC Block 2 limestone. Pore size distribution as a function of the pore volume for (c) sandstone (d) limestone.

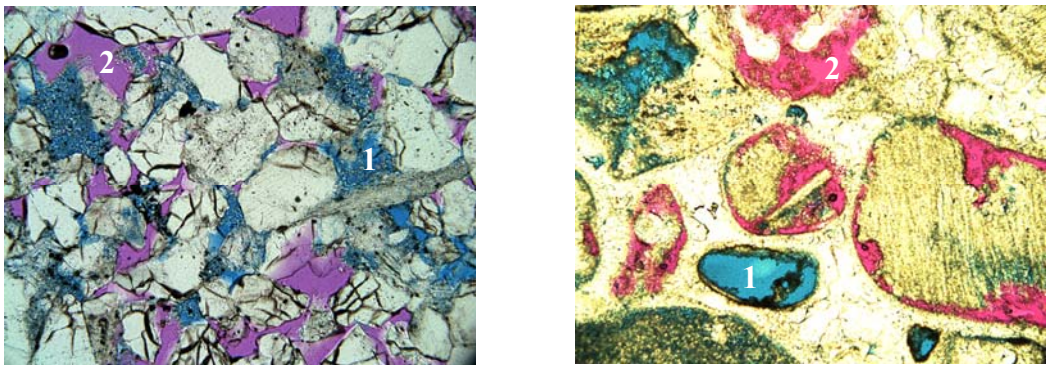

Fig. 6.1-4 Blue (wetting phase) (1), and red/purple (non-wetting phase) (2), in: (a) Berea sandstone PH 2 at wetting phase saturation S_α = 55%; (b) Edwards GC limestone Block 2, wetting phase saturation, S_α= 12%.

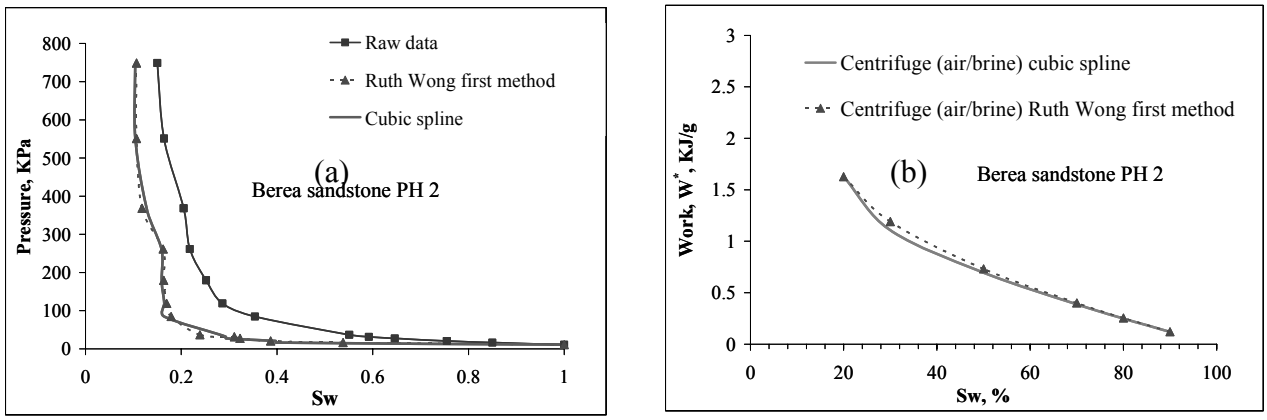

(a) (b)

Fig. 6.1-5 (a) Capillary pressure curves derived by two examples of methods of converting raw centrifuge data to saturation at the inlet core face for sandstone (air-brine displacement). (b) Work of primary drainage per gram of dry solid, W^*, for sandstone obtained by integrating under the derived capillary pressure curves.

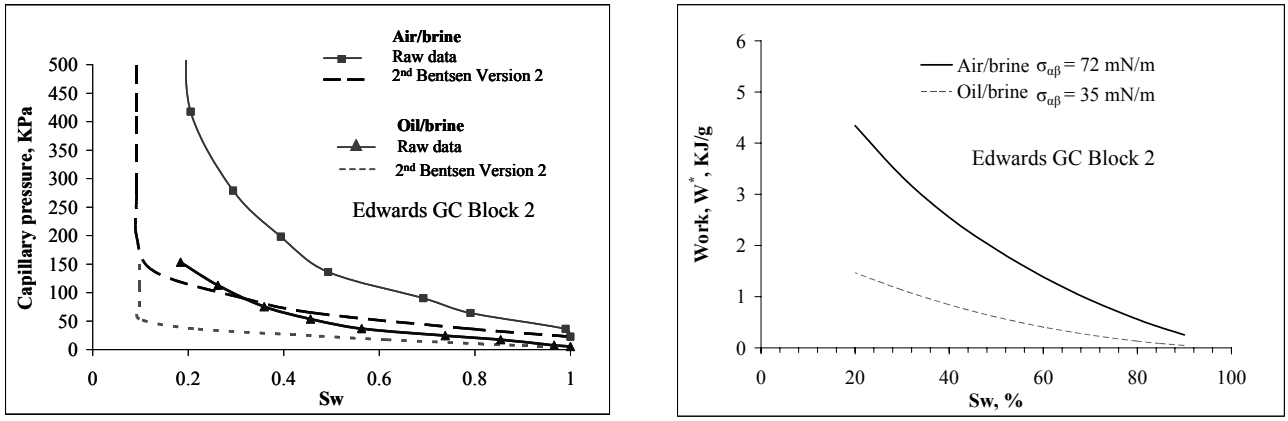

(a) (b)

Fig. 6.1-6 (a) Capillary pressure curves derived by converting raw centrifuge data to saturation at the inlet core face for limestone. (b) Work of primary drainage per gram of dry solid, W*, for limestone obtained by integrating under the derived capillary pressure curves.

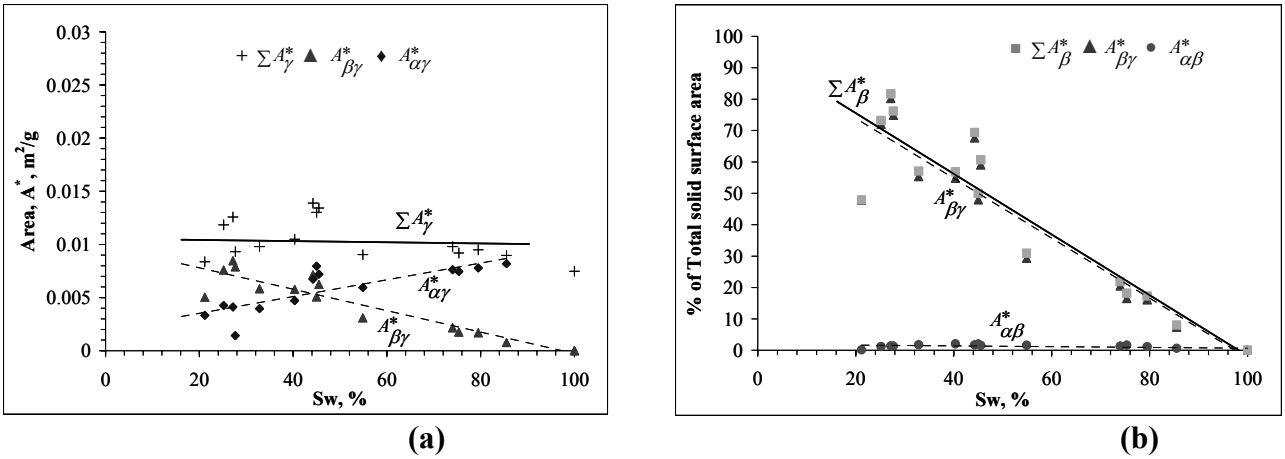

Fig. 6.1-7 Results from thin section analysis for Berea sandstone PH 2: (a) total solid surface area, $\sum A^*_\gamma$; (b) created surface area, $\sum A^*_\beta$.

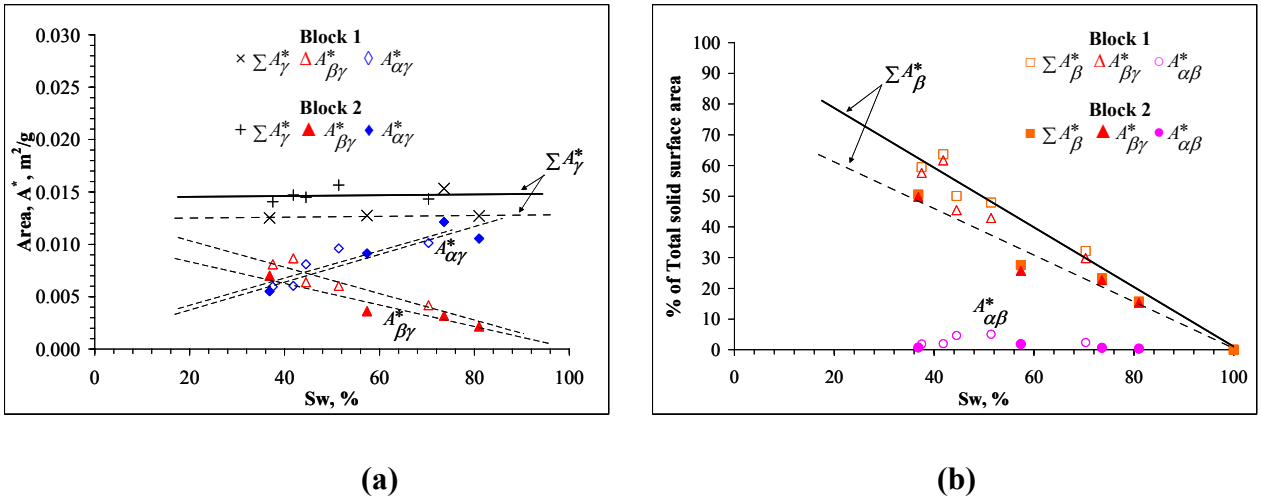

Fig. 6.1-8 Results from thin section analysis for Edwards GC limestone Blocks 1 and 2: (a) total solid surface area, $\sum A^*_\gamma$; (b) created surface area, $\sum A^*_\beta$.

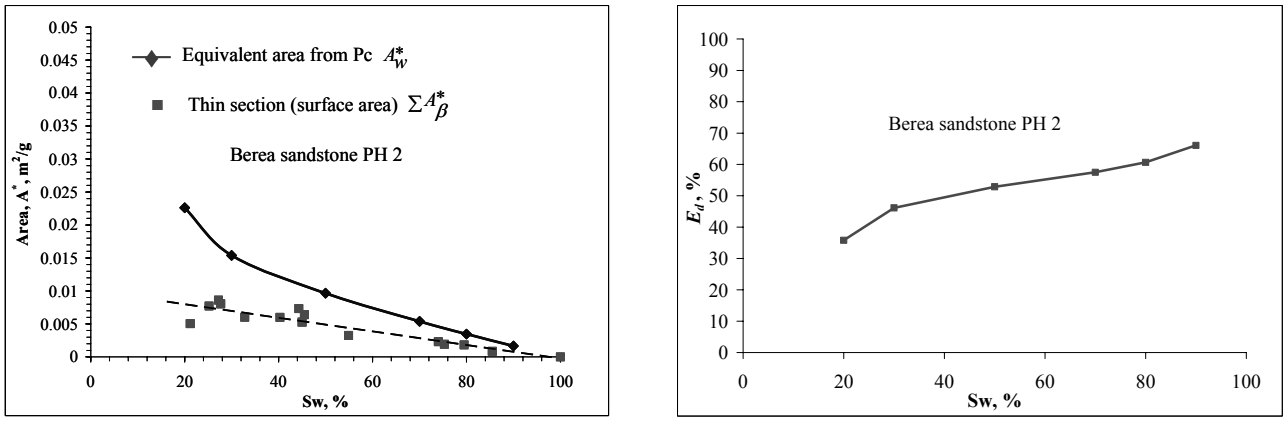

(a) **(b)**

Fig. 6.1-9 (a) Equivalent area, A_w^*, equal to scaled work, W*/σαβ, obtained by integrating under the capillary pressure curve (air/brine centrifuge) and the corresponding change in surface area, $\sum A_\beta^*$, obtained from thin section analysis. (b) Efficiency as a function of the wetting phase saturation for the sandstone.

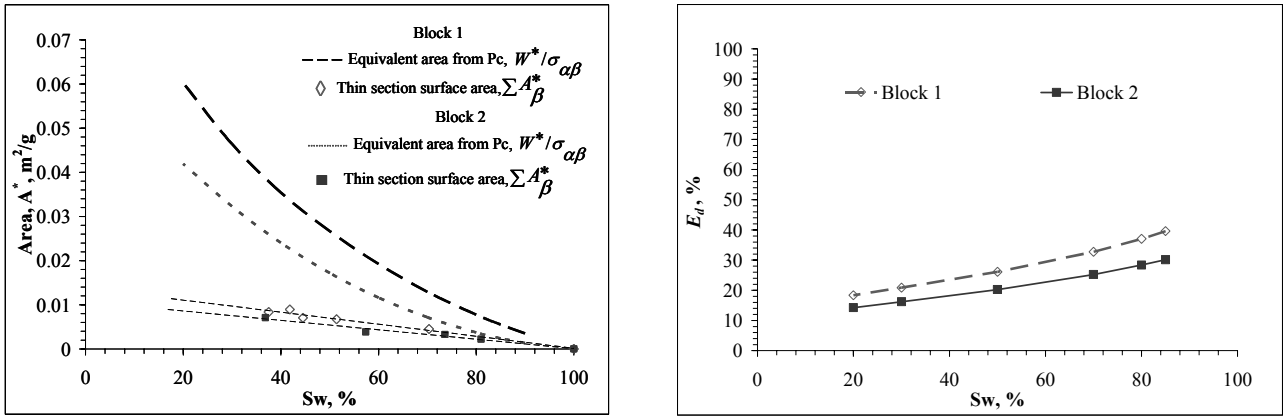

(a) **(b)**

Fig. 6.1-10 (a) Comparison of equivalent area, A_w^*, equal to scaled work done (W*/σαβ) obtained by integrating under the capillary pressure curve (air/brine and oil/brine centrifuge) and the corresponding change in surface area, $\sum A_\beta^*$, obtained from thin section analysis for Edwards GC limestone Blocks 1 and 2. (b) Efficiency as a function of the wetting phase saturation for the limestone based on air-brine centrifuge results for Block 2.

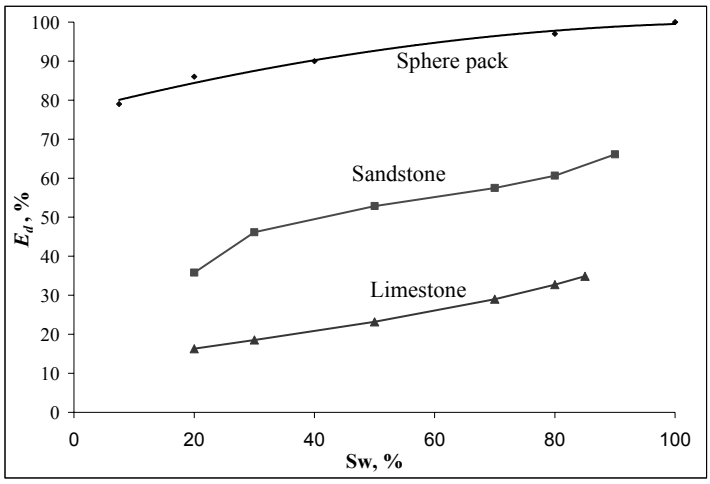

Fig. 6.1-11 Comparison of efficiency, E_d, of primary drainage for packings of equal spheres with values obtained for sandstone and limestone (average for Edwards GC, Blocks 1 and 2) based on air/brine capillary pressure data.

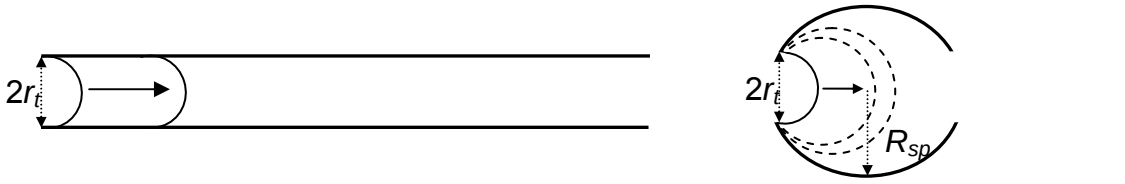

(i) reversible displacement in a cylindrical pore (ξ = 1)

(ii) unstable displacement in a spherical cavity (ξ = 2.4)

(a)

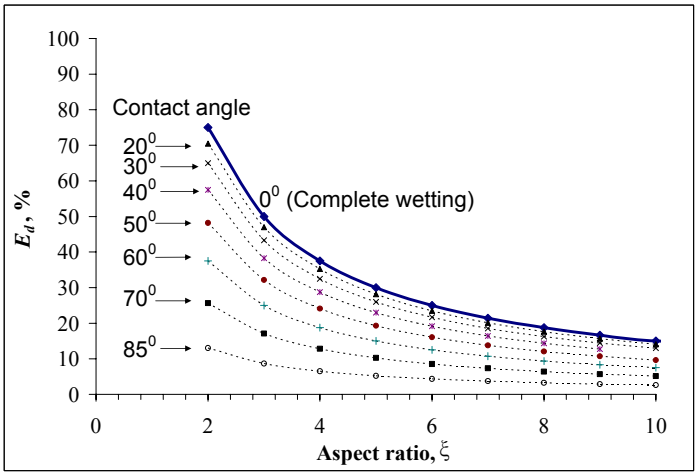

Fig. 6.1-12 Effect of aspect ratio on the efficiency of displacement, E_d, for a spherical pore. (a) Cylindrical and spherical pores of equal volume. (b) Effect of aspect ratio on the efficiency of displacement for the spherical pore model Ed vs ξ (entry pressure of cavity assumed to be independent of contact angle).

6.2 Rocks Without and With Initial Water Saturation

A novel approach to measurement of pressures acting during imbibition has been applied to strongly water wet rocks and to rocks with wettability altered by aging with crude oil. The study included mixed wet rocks obtained by aging with crude oil in the presence of an initial water saturation. Results for strongly water-wet rocks with and without initial saturation provide a reference for wettability alteration induced by aging with crude oil. Imbibition rates for mixed-wet rocks were generally much slower than for strongly wetted conditions. Surface free energy at the start of imbibition and capillary pressures acting during imbibition must be correspondingly low. The measured pressures are considered for most practical purposes to be the maximum pressures that can be generated by spontaneous imbibition.

Experimental

Rocks

All tested cores were selected from high permeability Berea sandstone (D=3.2~3.8 cm, L=6.2 cm~6.6cm, ϕ=22 %~22.7%, K=0.86 μm^2 to1.07 μm^2). All low permeability core segments were cut from Texas Leuders limestone (D=3.88 cm, L=1. 6 cm, ϕ=16 %, K=0.002 μm^2). The low permeability core was selected so that it would be partially drained by influx of oil from the main core but still remain below the percolation threshold for oil production.

Oils and brine.

Refined oil was used in the very strongly water wet tests. The oil was cleaned by flow through a mixture of silica gel and alumina. Cottonwood crude oil was selected for wettability control because it gives moderate wettability alteration. The density of Cottonwood crude oil is 0.8874 (20^oC) and the viscosity is 24.1 *Pa.s*. The brine (10,000 *ppm* NaCl) had a viscosity of 0.00102 *Pa.s* and density of 0.998 (20^oC). Initial water saturations were established with tap water to give the contrast in conductivity needed to detect the location or distance of advance of the brine along the core. The interfacial tension between Cottonwood crude oil and the brine is 29.7 mN/m.

Initial water saturation

Initial water saturation, S_{wi} was established by flow of Viscous Mineral oil (VMO) (commercial name is "Extra Heavy Oil", viscosity of 173.0 cP). Tests were run for Soltrol 220 refined oil (viscosity of 0.0038 *Pa.s*) with S_{wi} of 17.9% and 25.2%. If mineral oil was chosen as the nonwetting phase, the VMO used to establish the initial water saturation was displaced by Soltrol 220 (total injection volume was 5 PV). For tests with crude oil, the viscous oil was displaced by 5 PV decalin followed by injection of 5 PV of crude oil through each end of the core. For the two MXW tests with Cottonwood crude oil (viscosity of 0.0241 *Pa.s*) S_{wi} was 16.8 % and 25.3 %. Cores were aged with Cottonwood crude oil at 75°C for 10 days. The initial saturation was established with low ionic strength brine so that the advance of the imbibition front of the invading brine along the core could be tracked from the change in electrical conductivity between electrodes spaced along the core. Any permeability damage due to salinity contrast will be minimal because the main segment has high permeability and the amount of brine that enters the core is very restricted. In some cases the distance of advance was detected by slicing the core along its length and using electrodes to locating a sharp rise in electrical resistivity.

Composite cores

Composite cores were prepared by butting the main core segment containing oil (either with or without an initial water saturation) against a low permeability segment that was fully saturated with brine. Core properties are given in Table 6-1. A slurry formed from oil and powder (crushed core) was placed between the butted faces to ensure hydraulic contact. The cores are sealed except for the low permeability end face. The closed end of the high permeability segment is connected to a sensitive pressure transducer. The open face of the core is then exposed to brine as shown in Fig. 6.2-1. The approach is to measure the end pressure, $P_{end,}$ for one-face-open cores during restricted COUCSI. (Observed fluctuations (usually minor) in the pressure data are ascribed to diurnal variation in temperature and atmosphere pressure.) Further details are given with the results.

Cores initially saturated with mineral oil VSWW,S_{wi} =0

H6O(VSWW, S_{wi} =0)

The low permeability segment was a 2.351 *cm* long core of Berea sandstone with permeability of 0.065 μm^2.

Movement of the water front was detected by the onset of electrical conductivity when invading brine contacted a particular electrode. Results for test H6O are shown in Fig. 6.2-1. The end pressure rose quickly to 11 *kPa* but took a further 2.08 *days* to reach its highest value of 12.36 *kPa.* At that time, the front had penetrated 3.25 cm into the high *K* core segment (x_f/L_c =0.47) for the main core. The pressure was monitored for a further 1.8 days to confirm that a stable end pressure had been attained. No oil production was observed from the open face throughout the whole process. Thus the increase in saturation of the main segment was through exchange of water by oil in the contacting powder and the larger pores of the low permeability segment that connected to the region of contact between the two cores. At the end of the test, the main core was sawed open along its length for measurement of electrical conductivity from the butted face to the front. The maximum advance of the interface was identified from sharp increase in electrical conductivity from the butted face to the electrode test point.

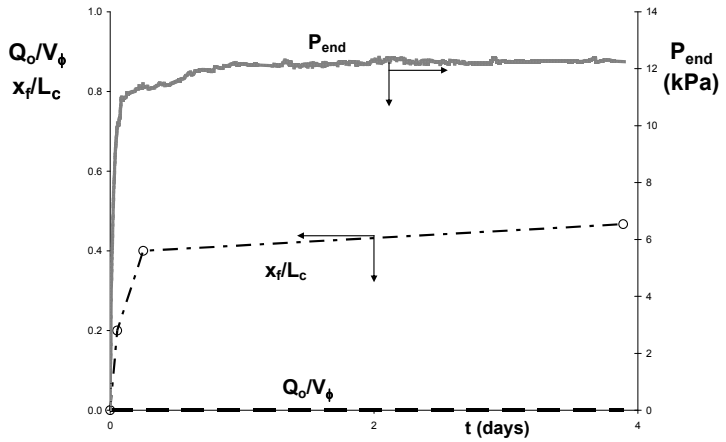

Fig. 6.2-1 Values of the end pressure, distance of invasion and oil production versus time for 1.067 µm^2 Berea sandstone core initially saturated with mineral oil. (Core H6O,VSWW,S_{wi} =0)

.

OW2(VSWW, S_{wi} =0)

The low *K* segment in Test OW2 was prepared as in Test OW2. The main segment was shorter (3.17 *cm*) than in Test OW2(6.97 *cm*). For restricted COUCSI, the end pressure rose to 13.7 *kPa* within 1 day and reached its highest value of 14.4 *kPa* after 2 *days* (Fig. 6.2-2). From resistivity measurements for electrode set along the core and also from pressure decline, the brine had penetrated the whole length of the main segment 3.3 *days* after the start of imbibition. The pressure then decreased to 12.550 *kPa* after a further half day.

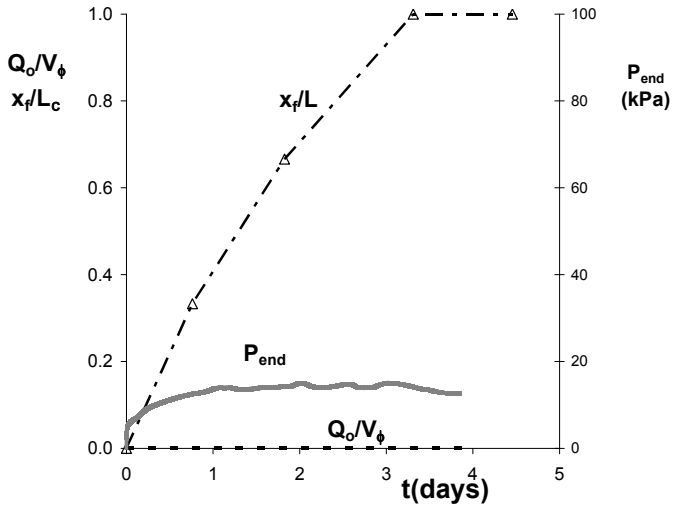

Fig. 6.2-2 Values of the end pressure, distance of invasion and oil production versus time for 0.964 μm^2 Berea sandstone initially saturated with mineral oil (S_{wi}=0). Core OW2,(VSWW, S_{wi} =0)

Cores initially saturated with crude oil CO,S_{wi} =0

HC4, CO,S_{wi} =0

Results for test H4C are shown in Fig. 6.2-3. The end pressure rose to 1.8 *kPa* within 15 minutes then slowly fell to 1.6 *kPa* after 2.9 hours. The drop may have been related to the presence of the thin layer of powdered core placed between the butted ends to ensure capillary contact. As confirmation of this explanation, the end tube was opened and the end pressure fell to zero. After closing the end, the end pressure rose to 1.6 *kPa* and recovered its initial value after 7.1 hours. At that time the onset of electrical conductivity when the brine front contacted a particular electrode showed that the front had penetrated 0.202 of the main core length (1.32 *cm*). The pressure was monitored for a further 22 *hours* to confirm that a stable end pressure had been attained. No oil production was observed from the open face throughout the test.

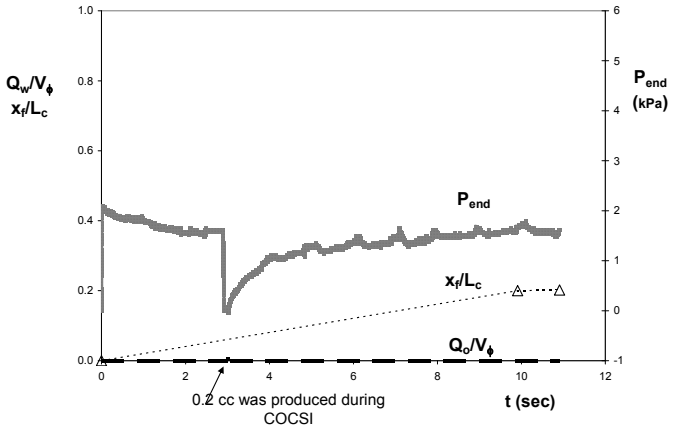

Fig. 6.2-3 The end pressure, distance of invasion and oil production for an aged core H4C initially saturated with Cottonwood crude oil (S_{wi}=0). No oil was produced. (HC4, CO,S_{wi} =0)

HE2, CO,S_{wi} =0%

The end pressure rose to a maximum value of about1.64 *kPa* after 16days. At this time the brine had already contacted the second electrode located at 0.2 (1.27 cm) of the main core length. No oil production was observed from the open face throughout the test.

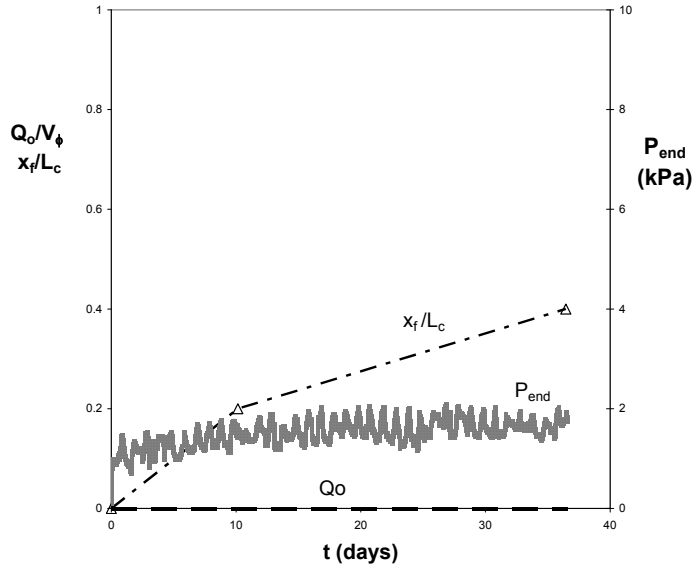

Fig. 6.2-4 The end pressure and distance of invasion for an aged core HE4 initially saturated with Cottonwood crude oil (Swi=0). No oil production was observed from the open face of the low permeability core. (HE2, CO,Swi =0)

Cores containing mineral oil and an initial water saturation. VSWW,S_{wi}

HB1, VSWW, S_{wi} = 17.9%

The end pressure rose to 1.7 *kPa* 0.8 days after the composite core was immersed in brine. Results for test HB1 are shown in Fig. 6.2-5. Then the end pressure gradually rose to about 4.7 *kPa*. The invading brine reached the dead end (5 days after the composite core had been immersed). The end pressure then slowly fell to about 2 *kPa* 30 days later.

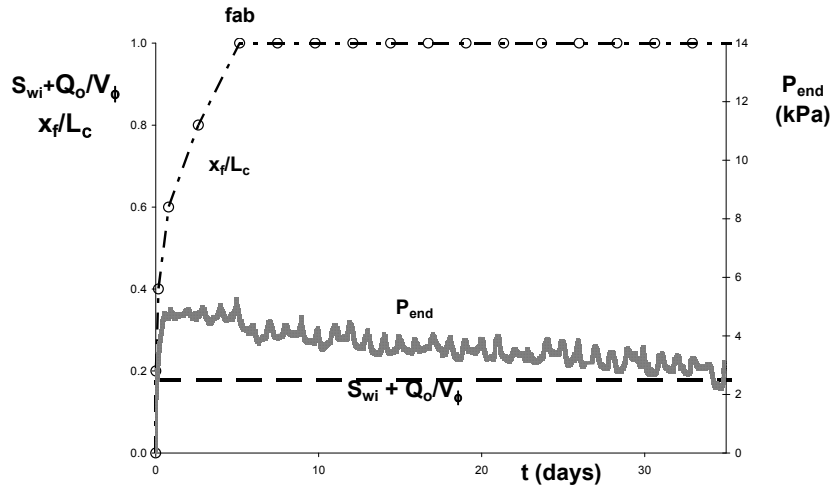

Fig. 6.2-5 The end pressure, distance of invasion and oil production for core HB1 (initially saturated with mineral oil, S_{wi}=17.9%).

HB3, VSWW,S_{wi} = 25 %

The semi-permeable segment was a 1.27 *cm* long segment of Texas Leuders limestone with permeability of 0.002 μm^2. The low K segment had been fully saturated by brine before being butted against the main segment, which contained 75% mineral oil and 25% tap water. Results for HB3 are shown in Fig. 6.2-6.

The end pressure rose to 3.25 *kPa* 0.9 days after the composite core was immersed in brine and then remained at 3.3 *kPa* until the front reached the dead end (4.5 days after the composite core had been immersed). The end pressure then slowly fell to about 0.15 *kPa* after 19 days.

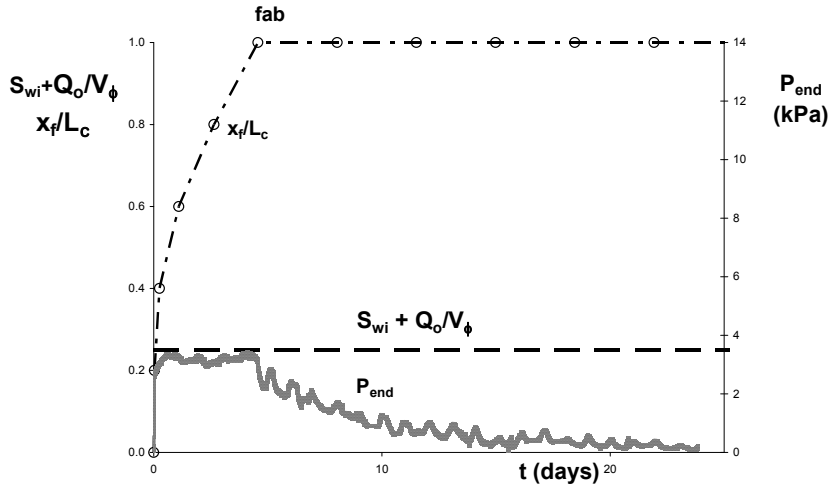

Fig. 6.2-6 The end pressure, distance of invasion and oil production for core HB3 (initially saturated with mineral oil, S_{wi}=25%). (HB3, VSWW,S_{wi} = 25 %)

Cores aged with crude oil with an initial water saturation. MXW

HD2, MXW,S_{wi} =16.8 %

The main core segment was saturated with 83.2% Cottonwood crude oil and 16.8% initial water saturation, and then aged at 75°C for 10 days.

The end pressure rose to 2.7 *kPa* within 1.3 days after the composite core was immersed in brine and remained at about 2.8 *kPa* until the invading brine reached the dead end (4.5 days after the composite core had been immersed). Results for core HD2 are shown in Fig. 6.2-7. The end pressure gradually fell over 29 days to 0.3 *kPa* and then remained close to this value for 16 days.

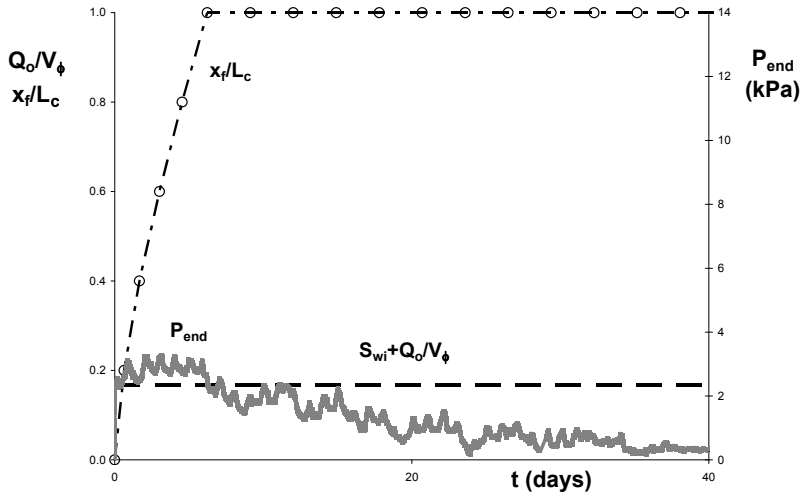

Fig. 6.2-7 Measurement of P_{end} (MXW) for core HD2 initially saturated with crude oil at S_{wi}=16.8% and then aged. HD2, MXW,S_{wi} =16.8 %

HO3, MXW,S_{wi} =25.3 %

The main core segment was aged at 75°C for 10 days with Cottonwood crude oil at 25.3% initial water saturation.

The end pressure rose to 5.2 *kPa* within 0.3 hours of the composite core being immersed in brine and remained at 5.6 *kPa* until the front reached the dead end (14 days after the composite core had been immersed). Results for core HO3 are shown in Fig. 6.2-8. The end pressure then fell. The end pressure dropped to 3.5 *kPa* 0.4 days after the front reached the dead end.

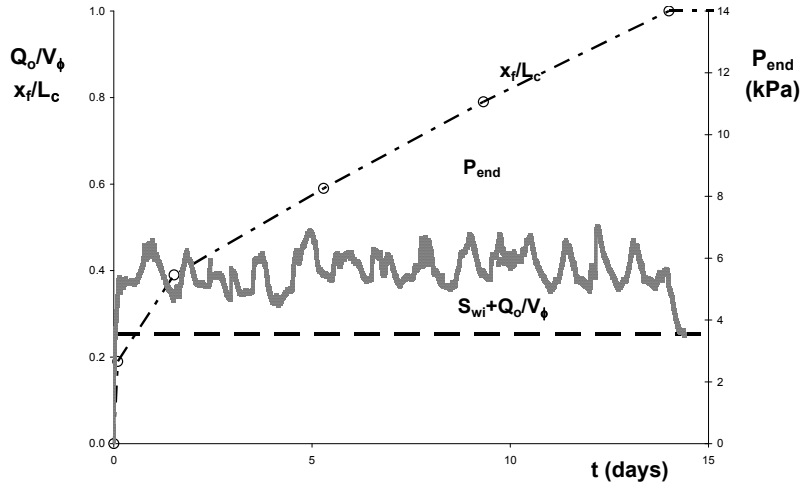

Fig. 6.2-8 Measurement of P_{end} (MXW) for core HO3 initially aged with crude oil at 25.3% initial water saturation.

Table 6.2-1

HIGH K CORE	D (cm)	L_c (cm)	K (μm^2)	ϕ (%)	Swi %	ρ_o	μ_o (Pa.s)	P_{cf} (kPa)	σ mN/m	Pcf/σ (μm^{-1})	TYPE	PROBE OIL
H6O	3.795	6.967	1.067	22.2	0	0.783	0.0038	12.40	48.85	0.254	VSWW	Mineral
HF4	3.37	3.171	0.964	22.3	0	0.783	0.0038	14.4	48.85	0.295	VSWW	Mineral
HC4	3.406	6.555	0.991	22	0	0.8874	0.2041	1.6	29.7	0.054	WWW	Crude
HE2	3.599	6.332	0.991	22	0	0.8874	0.2041	1.64	29.7	0.055	WWW	Crude
HB1	3.343	6.567	0.86	21.5	17.9	0.783	0.0038	4.70	48.85	0.096	VSWW	Mineral
HB3	3.248	6.555	1.022	22.2	25	0.783	0.0038	3.30	48.85	0.068	VSWW	Mineral
HD2	3.151	6.215	1.055	22.7	16.8	0.8874	0.0241	2.66	29.7	0.090	MXW	Crude
HO3	3.703	6.45	1.026	22	25.3	0.8874	0.0241	5.50	29.7	0.185	MXW	Crude

6.3 Mixed Wet Rocks with Initial Water Saturation

Introduction

The approach used in investigation of MXW cores is to obtain the end pressure, P_{end} for one-face-open cores during COUCSI and obtain the values of P_{cf} and P_{cb} separately from the measured P_{end} for cores with and without a low permeability core segment at the open end of the core. In section 6.2 results for restricted imbibition were presented for very strongly water wet (VSWW), weakly water wet (WWW) given by aging a core 100% saturated with Cottonwood crude oil, and mixed wet, (MXW) given by aging with Cottonwood crude after establishing an initial water saturation. Results have been obtained under comparable conditions for unrestricted COUCSI.

Experimental

Data sets have been obtained for Berea sandstone. The cores were high permeability Berea sandstone (D=3.2 to3. 8 cm, L= 3.9 cm to 6.9cm, ϕ=21.6 % to22.6%, K=0.86 μm^2 to1.094 μm^2).

Cottonwood crude oil was selected as a wettability alteration agent because it has been found to give moderate wettability alteration, so that cores still exhibited spontaneous imbibition. The density of Cottonwood crude oil is 0.8874 (20^oC) and the viscosity is 24.1 *Pa.s*. The brine was 10,000 *ppm* NaCl (viscosity of 0.00102 *Pa.s* and density of 0.998 at 20^oC). The interfacial tension between Cottonwood crude oil and the brine was 29.7 mN/m.

Initial water saturation

In tests that included an initial water saturation, S_{wi}, it was established by flow of Viscous Mineral Oil (VMO) (commercially described as "Extra Heavy Oil") which was then displaced by 3.8 cP mineral oil for the VSWW tests. For tests with crude oil, the viscous oil was displaced by 5 PV decalin to avoid destabilization of the crude oil followed by injection of 5 PV of crude oil through each end of the core. For tests that started with the core at an initial water saturation, it was established with low salinity brine so that the advance of the imbibition front of the invading brine along the core could be tracked from the change in electrical conductivity between electrodes spaced along the core.

Aging

Cores were aged with Cottonwood crude oil at 75^{o}C for 10 days either with or without an initial water saturation.

Results for Countercurrent Spontaneous Imbibition into One-End-Open Cores

Zero initial water saturation

Core H8O, VSWW, S_{wi} = 0%, 3.8 cP mineral oil

The 1,094 md core with one end open was immersed in brine to begin COUCSI. P_{end} rose quickly for the first 60 *seconds*. It then remained constant at about 3.14 *kPa* until the front reached the end of the core (after 2.5 *hours*). The ratio of Q_w/V_ϕ to x_f/L_c (the average saturation behind the front) was 0.42 until the imbibition front reached the end of the core (Fig. 6.3-1). The rate of oil recovery then decayed and the end pressure (P_{end}) decreased and eventually dropped to zero about 9 *hours* after the start of imbibition.

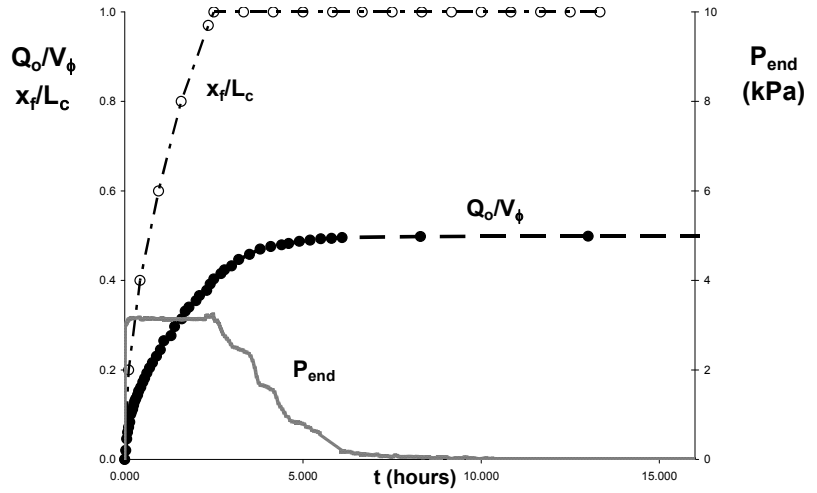

Fig. 6.3-1 Distance of advance, volume of produced oil and end pressure versus time for Core H8O (1,094 md) initially saturated with mineral oil (S_{wi}=0).

Core HC4a, WWW, Cottonwood crude oil, S_{wi} =0

In the measurement of P_{cf} on Core HC4 (991 md) included in the previous semi-annual report, brine only penetrated about 1 cm into the core under restricted COUCSI conditions. The invaded end of HC4 was cut off, and the remaining part (5.2 cm long) of the core, which was still saturated with Cottonwood crude oil was designated HC4a. From rate of imbibition behavior this core was described as weakly water wet (WWW). After the core was immersed in brine, P_{end} rose to 0.3 *kPa* within 100 *seconds*. It then slowly reached about 0.4 *kPa* after 3 days. After 6.4 days, the front reached the end of the core and the end pressure was 0.43 *kPa.*. Thus, the end pressure was less than one seventh of that for the VSWW core H80, and the time taken for the front to traverse the core was over 60 times longer. Even so, the ratio of Q_w/V_ϕ to x_f/L_c was again constant at 0.415 throughout the frontal advance. This was very close to the value of 0.42 determined for the VSWW core. After the front reached the end of the core, the rate of oil recovery decayed. P_{end} decreased and eventually dropped to zero about 14 *days* after the start of imbibition**.**

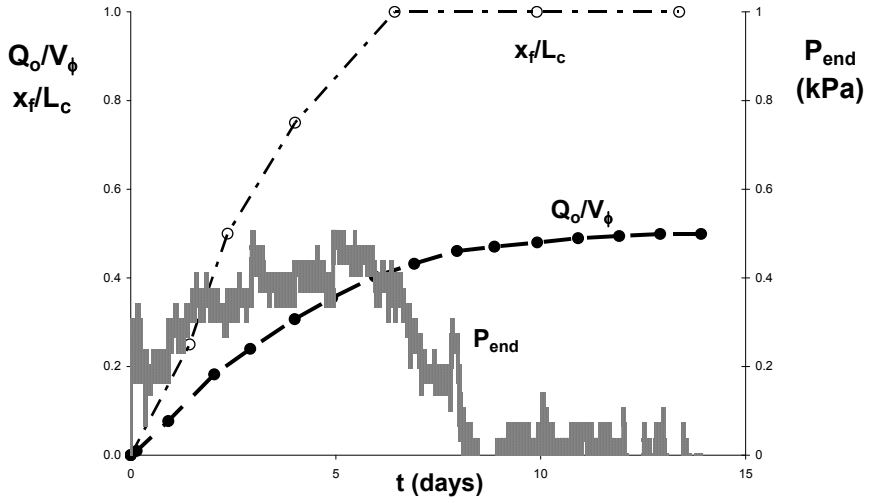

Fig. 6.3-2 Distance of advance, volume of produced oil and end pressure versus time for Core HC4a (991 md) initially saturated and aged with Cottonwood crude oil(S_{wi}=0).

Core HC2a, WWW, Cottonwood crude oil, S_{wi} =0

A 3.9 cm long core was cut from a longer core that had been completely saturated with Cottonwood crude oil and aged. After immersing the core in brine, P_{end} rose quickly to over 0.2 *kPa* and reached 0.38 *kPa* within 22 *hours*. It then slowly rose to 0.41 *kPa* after 3 days and remained close to constant until the front reached the end of the core (5 *days* after the start of imbibition). The ratio of Q_w/V_ϕ to x_f/L_c was 0.43 when the imbibition front reached the end of the core (Fig. 6-3). Then the rate of oil recovery decayed and the end pressure (P_{end}) decreased and eventually dropped to zero about 13 *days* after the start of imbibition. The results are closely comparable to those obtained for Core HC4a.

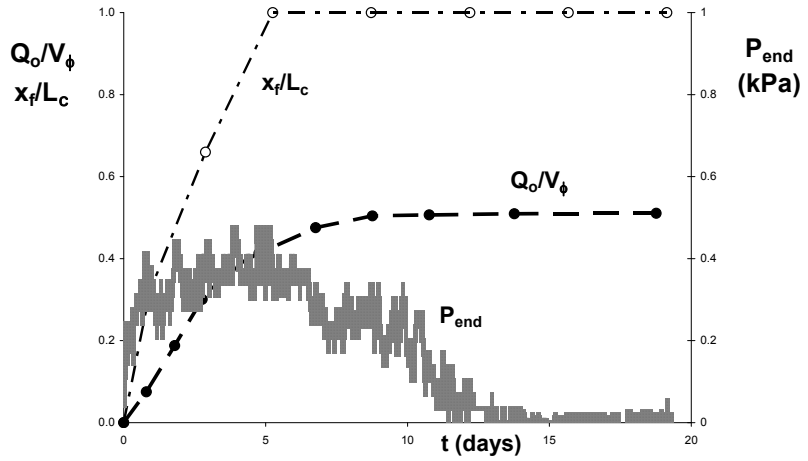

Fig. 6.3-3 Distance of advance, volume of produced oil and end pressure, versus time for Core HC4a (991 md) initially saturated and aged with Cottonwood (S_{wi}=0).

Cores containing an initial water saturation

Core HA1, VSWW, 3.8 cP mineral oil, S_{wi} = 18.7%

Core HA1 contained 3.8 cP mineral oil and had an initial water saturation of 18.7%. After the core was immersed in brine, P_{end} rose quickly for 700 *seconds*. It then remained constant at about 1.8 *kPa* until the front reached the end of the core (2.8 *hours* after the start of imbibition). The ratio of Q_w/V_ϕ to x_f/L_c was 0.296 when the imbibition front reached the end of the core (Fig.6.3-4). The rate of oil recovery decayed and the end pressure (P_{end}) decreased and eventually became zero about 38 *hours* after the start of imbibition.

Core HA3 (894 md), VSWW, 3.8 cP mineral oil, Swi = 25.2%

The initial water saturation was 25.2%. After the core was immersed in brine, P_{end} rose quickly to 1.5 *kPa* within 1000 *seconds* (Fig.6.3-5) and remained constant at about 1.57 *kPa* until the front reached the end of the core (3 *hours* after the start of imbibition). The ratio of Q_w/V_ϕ to x_f/L_c was 0.27 when the imbibition front reached the end of the core. Then the rate of oil recovery decayed and the end pressure (P_{end}) decreased and eventually dropped to zero about 12 *hours* after the start of imbibition. The results closely match the form of those shown in Fig. 6.3-4 for 18.7% S_{wi}. Core HA3 with the higher initial water saturation had, as expected, the lower end pressure.

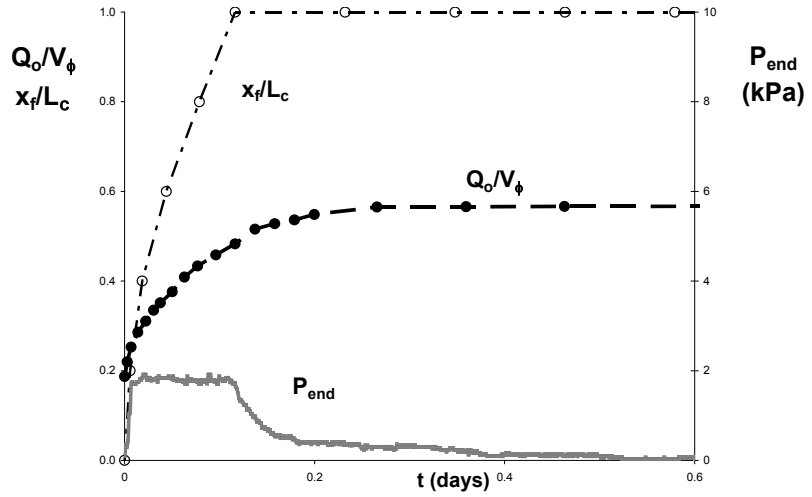

Fig. 6.3-4 Distance of advance, volume of produced oil and end pressure, versus time for Core HA1 (894 md). The core initially contained 0.38 cP mineral oil at 18.7% Swi.

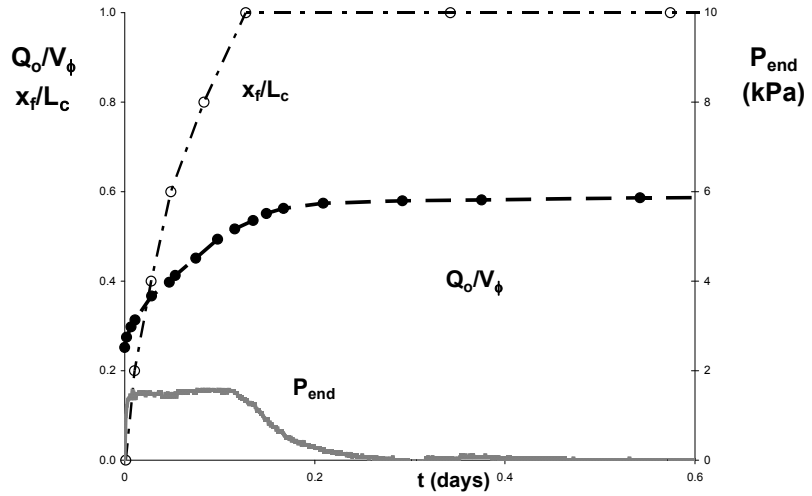

Fig. 6.3-5 Distance of advance, volume of produced oil and end pressure, versus time for Core HA3 (894 md). The core initially contained 0.38 cP mineral oil at 18.7% S_{wi}

Core HD3 (1,039 md), MXW, Cottonwood crude oil, S_{wi} = 22.4%

The core was aged in Cottonwood crude oil, at an initial water saturation of 22.4% to obtain a mixed wettability state. After the core was immersed in brine, P_{end} rose quickly within a few *seconds* and remained constant at about 0.24 *kPa* until the front reached the end of the core (2.5 *days* after the start of imbibition). The ratio of Q_w/V_ϕ to x_f/L_c was 0.16 when the imbibition front

reached the end of the core (Fig.6.3-6). Then the rate of oil recovery decayed and the end pressure (P_{end}) decreased and eventually dropped to zero about 16 *days* after the start of imbibition.

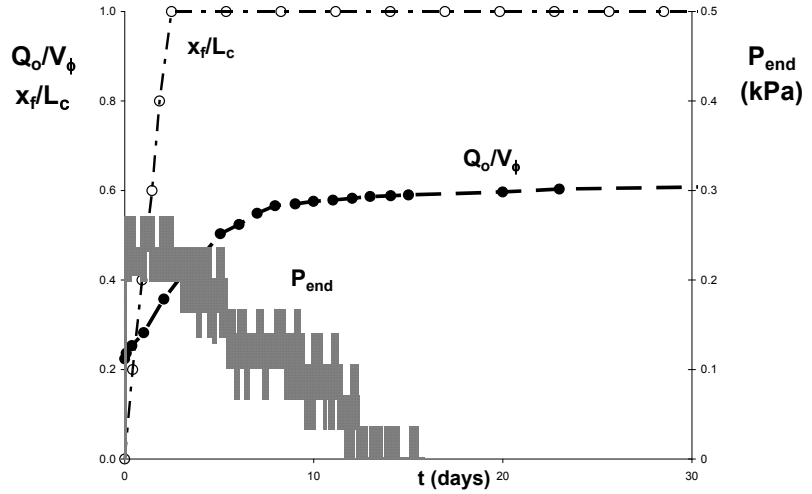

Fig. 6.3-6 Distance of advance, volume of produced oil and end pressure, versus time for Core HA3 (894 md). The core initially contained Cottonwood crude oil at 22.4% S_{wi}.

Core H01 (1,046 md), MXW, Cottonwood crude oil, S_{wi} = 25.2%

The core was aged with Cottonwood crude oil at an initial water saturation of 25.2% to obtain an MWX state. When the core was immersed in brine, P_{end} rose almost immediately to about 0.24 *kPa* and remained constant until the front reached the end of the core (2.4 *days* after the start of imbibition). The ratio of Q_w/V_ϕ to x_f/L_c was 0.13 when the imbibition front reached the end of the core (Fig. 6.3-7). The rate of oil recovery decayed and the end pressure (P_{end}) decreased and eventually dropped to zero about 20 *days* after the start of imbibition. Results are closely comparable to those for Core HD3.

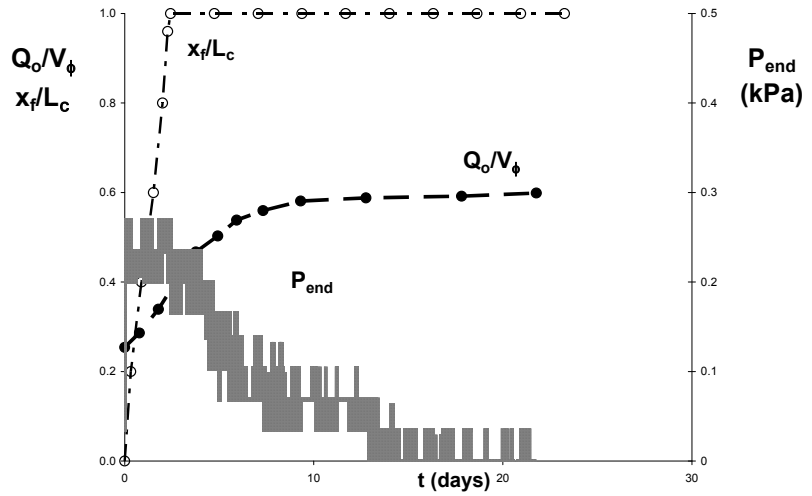

Fig. 6.3-7 Distance of advance, volume of produced oil and end pressure, versus time for Core HA3 (894 md). The core initially contained Cottonwood crude oil at 25.2% S_{wi}

Summary

Results are summarized in Table 6.3-1.

Table 6.3-1 Results of P_{end} during COUCSI

HIGH K CORE	D (cm)	L_c (cm)	K (μm^2)	ϕ (%)	S_{wi} %	1-Sro %	ρ_o	μ_o (Pa.s)	P_{end} (kPa)	σ mN/m	P_{end}/σ (μm^{-1})	TYPE	PROBE OIL
H8O	3.796	6.864	1.094	22.1	0	0.5	0.783	0.0038	3.14	48.85	64	VSWW	Mineral
H2O	3.794	6.18	1.084	22.0	0	0.5	0.783	0.0038	3.12	48.85	64	VSWW	Mineral
HC4a	3.406	5.2	0.991	22.0	0	0.5	0.8874	0.0241	0.43	29.7	14	WWW	Crude
HC2a	3.43	3.895	1.054	22.2	0	0.5	0.8874	0.0241	0.41	29.7	13	WWW	Crude
HA1	3.3	6.594	0.894	21.6	18.7	0.58	0.783	0.0038	1.80	48.85	37	VSWW	Mineral
HA3	3.248	6.594	0.894	21.6	25.2	0.59	0.783	0.0038	1.57	48.85	32	VSWW	Mineral
HD3	3.23	6.476	1.039	22.6	22.4	0.61	0.8874	0.0241	0.24	29.7	8	MXW	Crude
HO1	3.67	6.438	1.046	22.2	25.2	0.60	0.8874	0.0241	0.24	29.7	8	MXW	Crude

6.4 Areas of crude oil/rock contact that govern the development and surface energy of mixed wet rocks.

Background

Mixed wettability, a widely accepted model of reservoir wettability, arises when parts of the pore walls of a rock are altered by adsorption of polar components from crude oil. A basic premise of the mixed wettability model is that the initial displacement of water during accumulation of oil occurs under strongly water wet conditions. Areas of pore surfaces, $A_{R/W,}$ that are overlain by bulk water remain strongly water wet. Gas adsorption measurements of rock surface area, $A_{R,}$ are typically in the range of 0.5 to 3 m^2/g. It will be shown that the area of the rock surface that undergoes wettability alteration by contact with crude oil is critical to imbibition behavior, even though this area is only a small fraction of the total surface area of the rock.

Introduction

The concept of mixed wettability was developed during investigation of the long term recovery behavior of the East Texas Field that resulted in low residual oil saturations (Salathiel, 1973). Salathiel observed that adsorption from a crude-oil/heptane mixture overlying brine in a test tube resulted in wettability alteration of the area contacted by the oil but not that overlain by brine. For a rock with surface area, A_R, Salathiel postulated that adsorption from crude oil occurs onto areas of rock surface in contact with crude oil, $A_{R/CO}$, but not onto the areas of rock surface overlain by connate water, $A_{R/W}$. The area, $A_{R/W}$, overlain by bulk capillary-retained connate water complements the patterns of altered wettability resulting from contact between reservoir rock surfaces and crude oil, $A_{R/CO}$.

The wettability condition given by the distributed areas of water wet and oil wet areas was described by Salathiel as mixed wettability. Mechanisms for the steps involved in wettability change by adsorption from crude oil have been discussed by Buckley and Liu (1998). Removal of a water film between the oil and the solid substrate is recognized as a necessary first step in wettability alteration.

The most commonly used method of performing laboratory core floods at reservoir conditions is to first remove hydrocarbons and salts from a core by cleaning. An initial water saturation that is representative of the reservoir is established, and then the core is aged with live crude oil at reservoir temperature and pressure for about three to six weeks. This restoration procedure is expected to produce a distribution of adsorbed crude oil components according to the mixed wettability model.

Continued oil production, even for injection of up to 5,000 PV of water, was ascribed by Salathiel to the presence of adsorbed oil-wet films on the rock surface that provided continuous flow paths for oil. In many instances, although core preparation conditions result in distinctly altered wetting, extended production of crude oil is not observed. In the present work, the term mixed wettability implies the presence of wetting patterns on rock surfaces as determined by the relative distribution of $A_{R/CO}$ and $A_{R/W}$. The wettability, in terms of the contact angles acting over the area $A_{R/CO}$, depends on complex crude oil/brine/rock interactions that involve the mineralogy and detailed morphology of pore surfaces. Observations on wettability changes at mineral surfaces after adsorption from crude oil show that the changes depend on the conditions of treatment. Contact angles at nominally smooth mineral surfaces exhibit a wide range of values. Wettability alteration by crude oil usually gives advancing contact angles that fall in the range of 40 to 140 degrees. Large hysteresis between advancing and receding values is typical, for advancing contact angles in the range of 90 to 140 degrees. Even higher advancing values of about 160 degrees are observed if crude oil is displaced by an alkane (Buckley and Liu 1998).

It is also possible that water soluble components and surface migration of components adsorbed from crude oil play a role in wettability change, but at present there is no direct evidence for such mechanisms. In general, experimental results tend to support the working assumption that the distribution of connate water is established by drainage under water wet conditions prior to development of mixed wettability. For example, the mixed wettability concept is supported by the effect of initial water saturation at the time of aging in crude oil on spontaneous imbibition (Xie and Morrow, 2001) and on drainage capillary pressure behavior (Masalmeh, 2002). The basic distribution of brine, established by drainage under strongly water wet conditions, is assumed to be unaltered by subsequent wettability change over geologic time to a mixed wet condition. A further working assumption, of special importance to the interpretation of electric logs and other forms of *in situ* measurement, is that the initial drainage of the reservoir during accumulation of oil occurs under strongly water wet conditions. The initial connate water distribution is assumed to represent the water distribution in the reservoir even though there is subsequent change in wettability from mixed wet to water wet (Swanson, 1980).

However, once the mixed wettability is established at some initial water saturation, the wettability of the rock is not necessarily robust with respect to subsequent change in water saturation. After increase in water saturation by waterflooding followed by aging of a mixed wet core, the wettability changed towards more water wet, indicating that wettability changes induced by crude oil can be at least partially reversed (Tang and Morrow, 1997). Comparable change in wettability was reported for reservoir cores taken before and after waterflooding (Zhang et al., 1995). Although numerous possible complexities of wetting behavior are recognized, the basic concepts of mixed wettability are gaining increasing acceptance. Although contact angles provide the basic

universal measure of wetting, they are of limited value in prediction of the wettability and displacement behavior of crude oil/brine/rock combinations. Besides the difficulty of determining the values of contact angles acting at rock surfaces, a key factor, the amount and distribution of connate water must be taken into account. In this paper the question of the fraction of rock surface that is altered by adsorption from crude oil is addressed.

Pore scale modeling of mixed wet rocks.

Mixed wettability is illustrated in Fig. 6.4-1a for a pore modeled as a tube with the cross section of an equilateral triangle (Morrow, 1990, Ma et al., 1996). Such tubes with corners provide a model of mixed wettability, with the area of drained surface being the area of altered wettability by adsorption. The amount of water retained in the corners of the tube in Fig 6.4-1a corresponds to the special case of the interfacial curvature given by the MS-P solution for drainage of a completely wetted tube (Mason and Morrow, 1991). After drainage, the areas overlain by bulk water and oil are each proportional to the sum of the perimeter lengths, L_{os} and L_{ws}, for oil and water respectively. Mixed wettability is generated by adsorption from crude oil onto the pore surface in the tube. If the capillary pressure (the curvature times the interfacial tension) in the pore is increased, the amount of water retained in the corners is decreased and the area of adsorption is increased (see Fig. 6.4-1B). Clearly the wettability of the single pore, as, for example, indicated by spontaneous imbibition behavior, depends on the relative surface areas and is not simply a function of the water advancing contact angle alone (Ma et al., 1996).

The distribution of areas of wettability change and other aspects of change in interfacial areas provide guidance as to the features of displacement mechanisms that should be included in pore scale modeling of reservoir rocks. Individual pores in rocks and other porous materials are commonly modeled as either tubes of constant cross section, such as cylinders or tubes with corners, or as geometries of non-uniform cross section, such as given by sphere packs. Mayer and Stowe (1965) developed solutions to displacement curvatures for a range of pore shapes formed by spheres. Princen (1969 Part ii) independently presented identical values of displacement curvature for pores formed by rods. The solutions are exact for interfaces of constant curvature in pores of uniform cross section and were also shown to hold for wide variation in contact angle (Mason et al. 1983). Princen pointed out that they would be approximate for capillary rise because of the effect of gravity on interface shape. However, in the first extensive experimental test of the theory, Mason and Morrow (1984) showed that the theory, referred to as the MS-P method, accurately predicted capillary rise for capillaries of small cross section. Even for tubes formed by a plate and two rods of almost 1 cm diameter, capillary rise of iso-octane against air was accurately predicted after making a Rayleigh correction of about 10% for the effect of gravity on the meniscus shape. Mason and Morrow (1991) also presented MS-P solutions for all possible shapes of completely wetted triangular pores and showed that uniform tubes could exhibit hysteresis in drainage and imbibition and feature trapping of the non-wetting phase. The analysis was later extended to finite contact angles in triangles and in pores of distributed size formed by rods (Morrow 1990, Ma et al. 1996, Princen, 1992).

Precise values of displacement curvatures for pores formed by spheres such as in cubic or triangular array is a classic problem in capillarity. Experimentally determined displacement curvatures for pores formed by rods versus pores formed by spheres shows close agreement for perfect wetting (Mason and Morrow, 1986). However, the MS-P solutions for finite contact angles

must be treated with caution when applied to pores of non-uniform cross-section as originally proposed for spheres by Mayer and Stowe (1965). The large effect of the interaction of pore geometry and contact angle on displacement curvatures for finite contact angles is illustrated by the classic analysis of doughnut shaped pore throats given by Purcell (1950). At the maximum curvature needed for penetration, the pressure becomes highly dependent on the location of the interface. Approximate solutions for the effect of the interaction of pore geometry and contact angle on drainage and imbibition for pores formed by spheres have been presented by Melrose (1965) and later by Mason and Morrow(1994), and Gladkikh and Bryant (2006 and 2007).

Examples of change in drainage curves for zero contact angles are presented in Figs. 6.4-1a and b. An interesting feature of imbibition behavior is that even though the advancing contact angle may be high and there is no change in location of the three phase line of contact, spontaneous imbibition can still occur to a limited extent simply through decrease in curvature. (see Fig. 6.4-1c). The wetting properties of a pore can be strongly dependent on details of surface topology. For example, if the surface of the triangle is grooved along its surface, as illustrated in Fig. 6.4-1d, the MS-P solutions for curvature can still be obtained from the oil/water plus oil/solid contact profile. For a fixed contact angle, the oil/solid area (degree of truncation) determines the effective contact angle. (The shape and surface area of the parts of the pore that remain overlain by water have no effect on the MS-P displacement curvature.) Thus the MS-P analysis illustrates the strong dependence of wetting on the contacted surface and associated cross section and, also the lack of direct dependence on the pore geometry that remains overlain by bulk water.

MS-P solutions can also be applied to double displacement whereby water is retained in corners and oil is displaced by invading water to leave a retained oil saturation that overlies the corner water. This model is used to explain production of oil down to very low saturations (Kovsec, et al., 1993). Direct observation of overlaying films and flow of liquid in corners has been reported by Buckley (Buckley, 2008).

MS-P solutions for different pore shapes (mainly triangular) and wetting conditions have been applied extensively to network modeling of multiphase flow (Oren et al., 1998; Patzek, 2001; Blunt, 1997). The distribution of areas of wettability alteration as a result of adsorption from crude oil is basic to realistic modeling of mixed wet displacements. When complex wetting and related interfacial and colloidal phenomena are introduced, questions of the effects of finite pore lengths, pore scale morphology including converging-diverging pores, and initial saturation conditions, present a range of critical issues with respect to network modeling of mixed wet rocks.

Interfacial areas of adsorption in rocks

From the forgoing working assumptions, and the wetting properties of model pores, it is clear that the area of contact with crude oil is a key parameter of the wettability of rocks. Consideration will now be given to estimation of the rock surface area, $A_{R/CO,}$ over which wettability is changed by adsorption.

Work of drainage

For reversible displacements of interfaces, such as in uniform tubes with no contact angle hysteresis, direct relationships can be obtained between work of displacement and change in surface free energy. Relationships between capillary pressure and saturation for rocks are not

reversible, as evidenced by hysteresis even for completely wetted rock surfaces. However, the work of drainage from 100% initial water saturation is given by the area under a capillary pressure drainage curve (Morrow, 1971). The work of drainage sets a maximum upper limit to the surface free energy of the solid/NW W/NW phase surface areas created as a result of drainage.
Fig 6.4-2 shows a relationship between the log of capillary pressure and pore space saturation. It is based on a combination of data from Shaw et al. for saturations down to about 20% and from Melrose for lower saturations. The Melrose data consists of a combination of centrifuge, porous plate and desorption isotherm data. Consistency in the data obtained by the three distinct techniques indicates that equilibrium interfacial curvatures were established within the rock and that they correspond to the recorded pressures. Under these conditions, curvature increases with increase in pressure; the data do not exhibit an irreducible saturation.

Integration of the area under the drainage curve gives the work of drainage as a function of wetting phase saturation Fig 6.4-3. At 20% saturation the maximum theoretically possible surface area is about 0.012 m^2g. This is only 1% the typical surface area of 1.2 m^2/g Berea sandstone measured by the BET method (nitrogen adsorption). The work of drainage increases sharply as the saturation decreases and trends towards the BET surface area. Details of surface area on a linear scale versus water saturation are shown in Fig. 6.4-4.

Efficiency of displacement
The increase in interfacial areas, $A_{R/CO}$ plus Aw/o, depends on the efficiency of conversion of work of drainage to surface energy (Seth and Morrow 2007). Determination of the efficiency requires direct measurements of change in interfacial areas with saturation. Measurement of interfacial areas is more problematic than measurement of capillary pressure drainage curves. Data was presented in Section 6.1 for increase in solid/nonwetting phase (S/NWP) and wetting/nonwetting phase (W/NWP) interfacial areas with drainage for Berea sandstone and for an oolitic limestone. The rocks were first saturated with a low viscosity resin. The liquid resin was then partially displaced by air by centrifuging the sample at elevated temperature. The resin was set up while the centrifuge was spinning. A range of saturations is obtained because the WP saturation decreases with distance from the axis of rotation. The procedure was repeated using duplicate core plugs and different centrifuge speeds for each plug in order to widen the range of established WP saturations. A second dyed resin was injected to mark the space invaded by air during centrifuging and to give the cores sufficient integrity for preparation of thin sections.

The thin sections were taken at different distances along the core length. Point counting and line cuts were used to evaluate WP and NWP saturations and interfacial areas respectively. Saturations were determined by point counting. Interfacial areas, $A_{R/CO}$ and $A_{W/O}$, were determined from line segments. Results are shown in Fig. 6.4-5. The area of the O/W interface is small compared to the S/NWP area. The displacement efficiency is given by the ratio of total created surface area at a specific saturation to the work of drainage for the same saturation. At 20 % saturation the efficiency of conversion of work to free surface energy for the sandstone is 36 %. For an oolitic carbonate the efficiency is only 16%. For bead packs, the efficiency of drainage to 20% WPS was 85%. The range of values was ascribed to the large differences in pore throat to pore diameter, the aspect ratio, for the three distinctly different types of porous media.

Fraction of rock surface exposed to crude oil

The work of displacement estimated from the Shaw/Melrose data for Berea sandstone after primary drainage to 20% is equivalent to 0.013 m^2/g. If this value is multiplied by 0.36, the efficiency of displacement determined for sandstone, the total S/NW plus WP/NWP surface area exposed to the nonwetting phase wetting phase saturation is only 0.0047 m^2/g. The total rock surface area of the Berea sandstone, AR, as determined by the BET method, is typically about 1.2 m^2/g . Therefore the S/NW plus WP/NWP surface area created by drainage is only 0.39% of the rock surface area. The WP/NWP interfacial area is approximately 10% of the total surface area created by drainage. Thus the area of contact over which crude oil adsorbs according to the mixed wettability model is only about 0.35% of the rock surface.

Surface roughness and microporosity

If the identified NWP/S areas of contact measured by the resin drainage technique could be examined in fine detail, it is likely that they would include areas of surface roughness and micro-porosity that would feature microscopically distributed areas of retained bulk water. These features would increase the WP/NPW area and reduce S/NWP area of contact with crude oil. Areas of the pore surface of the rock overlain by WP/NWP, are in effect equivalent to strongly water wet. They will reduce the area of contact between crude oil and the rock surface. The overall effect will be to make mixed-wet rocks with rough surfaces more water wet than rocks with smooth crystalline surfaces under otherwise equivalent conditions.

Contact angles and wettability

Contact angles provide the most widely used measure of wettability. There are obvious limitations to characterization of the wettability of crude oil/brine/rock combinations from contact angle measurements. The measurements are usually made at smooth surfaces based on a the main mineral constituent such as quartz for sandstone and calcite for limestone (Treiber et al., 1972). Careful petrographic examination is needed to check that other types of mineral, such as pore-lining clays may be more representative of the mineral surfaces involved in determination of wetting properties. Even if representative minerals are identified, the interplay of contact angle and surface morphology under static and dynamic conditions can have a wide range of effects multiphase displacement behavior. From the forgoing discussion of wettability alteration by adsorption from crude oil, it is clear that high advancing contact angles measured at smooth surfaces do not necessarily imply that a rock will exhibit oil-wet behavior.

Change in waterflood efficiency and rate and extent of recovery by spontaneous imbibition.

Although the areas of adsorption are small, the effect on two phase displacement behavior is still large, mainly because the adsorption occurs at the parts of the pore surfaces that have a dominant effect on recovery behavior. For example, increase in the area exposed to adsorption that results from reduction in initial water saturation from 30% to 10% can decrease rates of recovery of crude oil by spontaneous imbibition by several orders of magnitude (Xie and Morrow, 2001). The mechanistic reasons for these order of magnitude change in imbibition rates is not yet understood.

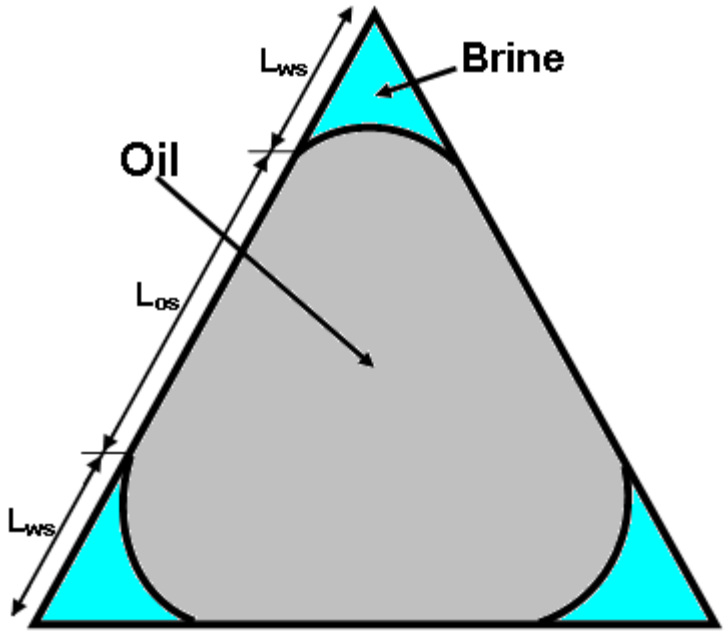

(6.4-1a) Distribution of oil and brine at the MS-P curvature for drainage of a pore with the equilateral triangular cross-section

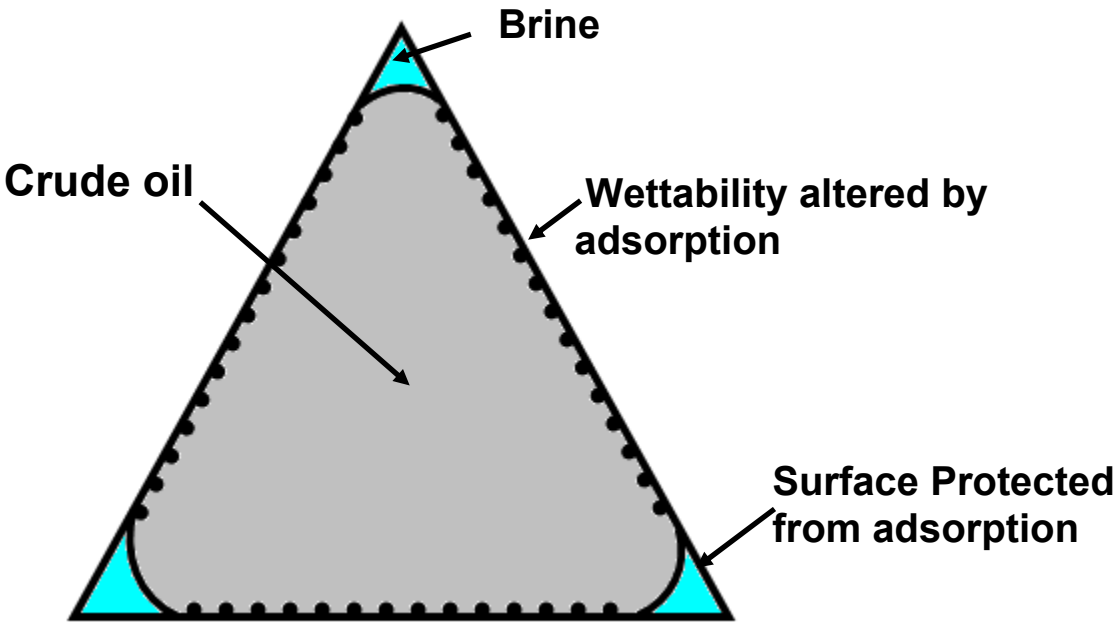

(6.4-1b) A mixed wet pore with areas of adsorption from crude oil at a drainage curvature (capillary pressure) higher than the MS-P value.

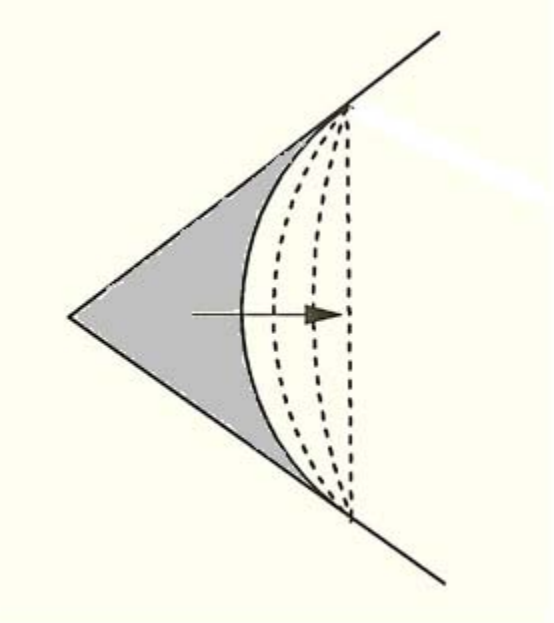

(6.4-1c)Imbibition with a fixed three pase line of contact- in a mixed-wet equilateral triangular pore with an advancing contact angel greater than 60º. There is a small increase in the corner liquid saturation as the capillary pressure falls to zero.

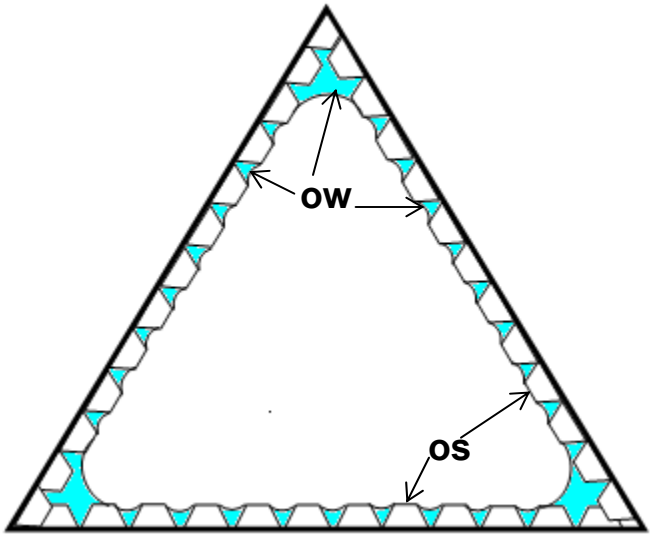

(6.4-1d) Model of mixed-wet pore with surface roughness based on truncated triangles. Areas in the corners and grooves are protected from adsorption. The MS-P length over which wettability is changed is given by the length of the exposed truncated tops of the triangles. For zero lengths (no truncation) the surface remains completely wetted. Without the surface roughness, the wettability of all of the exposed surface is changed as shown in 1 (b).

Fig 6.4-1. Drainage Areas

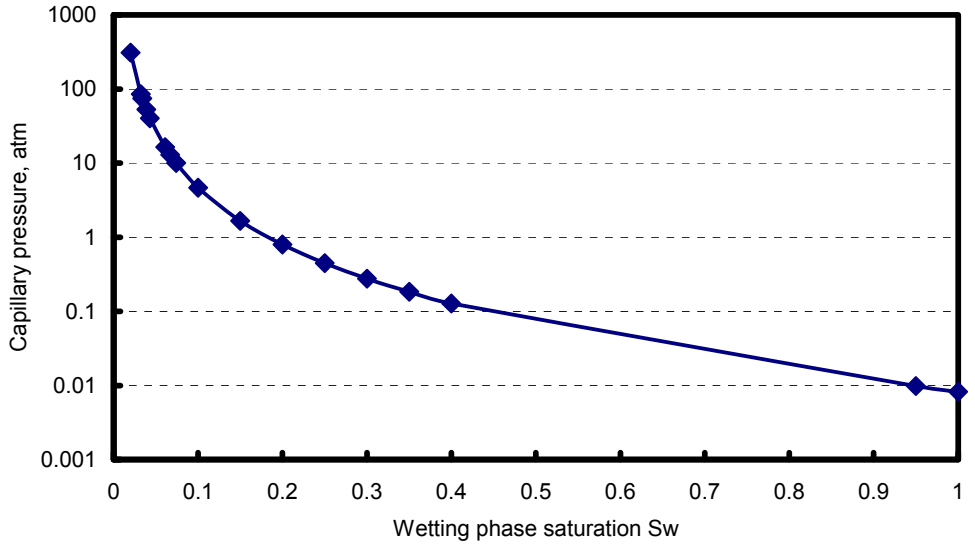

Fig. 6.4-2 Composite capillary pressure drainage curve based on the combined data of Melrose and Shaw

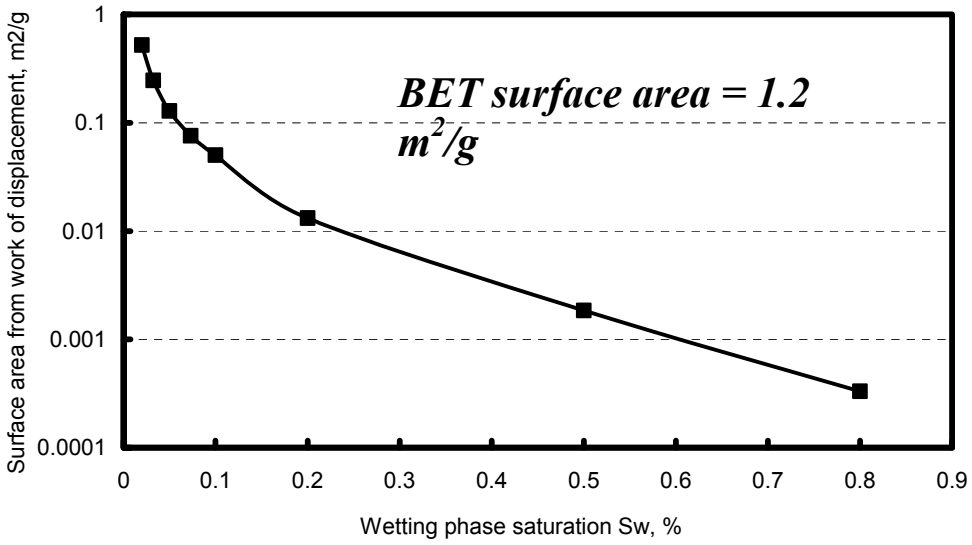

Fig. 6.4-3 Work of drainage versus wetting phase saturation from the data shown in Fig. 6.4-1.

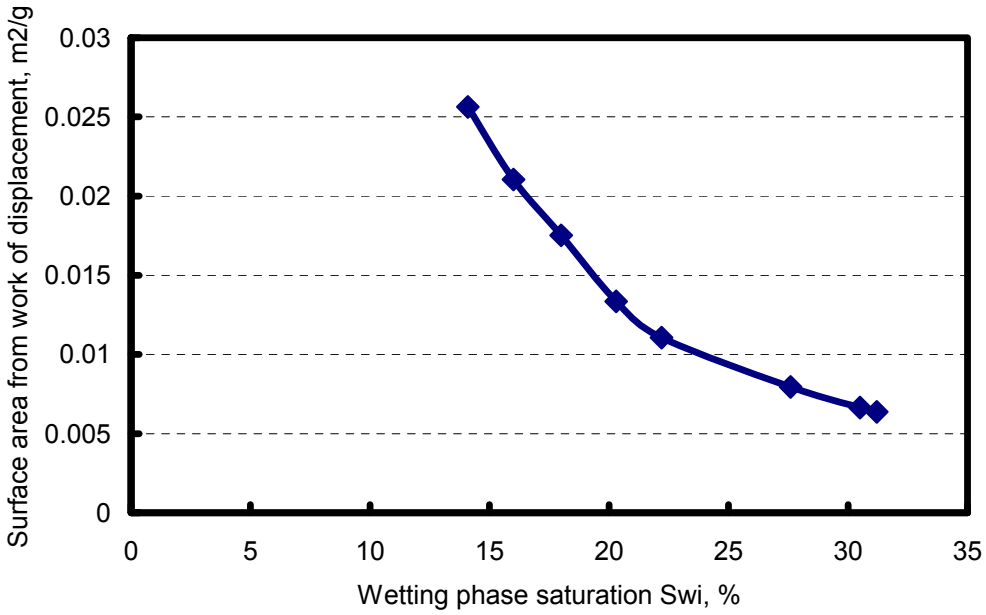

Fig. 6.4-4 Work of drainage on a linear scale versus wetting phase saturation.

Task 7. *Novel imbibition measurements on mixed-wet rock and network models.*

7.1 CAPILLARY PRESSURE AT THE IMBIBITION FRONT DURING WATER-OIL COUNTER-CURRENT SPONTANEOUS IMBIBITION

Li, Y., Mason, G., Morrow, N.R., and Ruth, D.W.
in press: *Transport in Porous Media*

Abstract

Counter-current spontaneous imbibition (COUCSI) in porous media is driven by capillary forces. Capillary action results in a high capillary imbibition pressure at the imbibition front and a low capillary drainage pressure at the outlet face. It is the difference between these two pressures that draws in the wetting phase and pushes out the non-wetting phase. A technique for measuring the capillary pressure at an imbibition front under restricted flow conditions has been developed and applied to Berea sandstone with a range of permeabilities. In the experiments, brine was the wetting phase and refined oil was the nonwetting phase. One end face of a sandstone core was butted to a short section of a finer-pored rock. The composite core surface was then sealed, apart from the end face of the low permeability segment. A connection to a pressure transducer was set in the opposite end face of the core. Initially, the main core segment was filled with oil. In most cases, the finer-pored segment was filled with brine. Imbibition was started by immersing the core in brine. The purpose of the finer-pored segment was to prevent the escape of non-wetting phase from the open face. For some tests there was an initial period of co-current spontaneous imbibition (COCSI) created by allowing production of non-wetting phase through an outlet tapping in the sealed end face. The outlet was then connected to the transducer and the imbibition changed to COUCSI. There followed an increase in the monitored end pressure to a maximum as fluid redistributed within the core. For the tests in which the fine-pored segments were pre-saturated with brine, even without an initial period of co-current imbibition, limited invasion of the main core segment by brine resulted in an asymptotic rise of the end pressure to a maximum as the imbibition front dispersed. To confirm that the dispersing front did not reach the dead end of the core, the distance of advance of the wetting liquid was detected by a series of electrodes. The maximum value of the end pressure provides an estimate of the capillary pressure at an imbibition front for COUCSI. The maximum capillary pressure generated by the invading fluids ranged from 6.6 *kPa* to 42 *kPa* for sandstone with permeabilities between 1.050 $(\mu m)^2$ and 0.06 $(\mu m)^2$.

Introduction

Imbibition arises in many everyday situations, and can be a dominant mode of production of oil from the rock matrix of fractured reservoirs (Morrow & Mason, 2001). Understanding the mechanism requires knowledge of multiphase flow and transport in porous media (Blunt, 2001). One special and instructive case is Counter-Current Spontaneous Imbibition (COUCSI) in which a wetting phase (WP) front spontaneously invades a porous medium and forces the non-wetting phase (NWP) to flow counter to the invading WP. The essence of the process is that a pressure difference, P_c, between the two phases is developed by capillary action and it is at a maximum, $P_{c,f}$ at the displacement front. When gravity can be ignored, the imbibition capillary pressure is the sole driving force that pulls wetting phase into the porous medium, drives the non-wetting phase out, and also overcomes the opposing drainage capillary pressure at the outlet face.

This raises an interesting question: does the value of $P_{c,f}$ change with the velocity of the advancing front? There is strong indication that it is constant. For example, in one-dimensional COUCSI, the velocity of frontal advance slows down because the flow path (the distance behind the front) is increasing. However, the volume imbibed usually varies linearly as the square root of time over a very wide range of front velocities (Li et al., 2006). This can only be so if the capillary pressure at the front is independent of front velocity and if the hydraulic resistances behind the front are self similar, making the saturation profile self similar (Ruth et al, 2007). There is a large literature, dating back until at least Rapoport (1955) and Handy (1960), on conditions under which imbibition results in saturation profiles that are self-similar.

The capillary pressure at the saturation front ultimately drives the whole process and is the cut-off point for any equation describing the capillary pressure curve (Li et at., 2006), but measurement of this special key pressure is difficult. In this paper we develop a method for measuring the capillary pressure at the imbibition front, or at least a closely related pressure, and apply it to a range of cores. The technique centers on measuring the pressure P_{end} in the non-wetting phase at the dead end of a core undergoing counter-current imbibition but where the production of non-wetting phase from the open face of the core is inhibited.

During unrestricted spontaneous imbibition, the WP moves in the direction of the positive capillary pressure gradient. The driving capillary pressure is at its highest at the WP front regardless of the shape of the saturation profile behind it. The lowest capillary pressure is at the open core face; this pressure, where NWP bubbles from the core, is referred to as the capillary back pressure, $P_{c,b}$. There will be local fluctuations in the non-wetting phase pressure because of the nature of the bubbling process, but it is not zero as is often assumed.

There are several special cases of COUCSI. If the ratio of the viscosity of the non-wetting phase to the viscosity of the wetting phase is very low, then the pressure drop for flow of non-wetting phase through the core will also be very low and the pressure in the non-wetting phase just ahead of the front, P_{end}, will be close to the capillary back pressure, $P_{c,b}$. If the viscosity ratio is very high, then very little pressure is required to draw in the wetting phase and P_{end} will be close to the capillary pressure at the front, $P_{c,f}$. Here we adopt an approach in which a short core segment with a high $P_{c,b}$ is butted to a main core segment with a lower $P_{c,f}$ so that the non-wetting phase cannot leave the open face of the main core. As a consequence, the imbibition flows slowly decline without change in the net saturation. When there is essentially no flow, the pressure in each phase becomes constant and P_{end} equals $P_{c,f}$. Also, in the experiments that follow, the measured pressure stays remarkable steady whilst the front disperses and eventually stops moving. This constancy of pressure under restricted flow conditions provides further indication that the ultimate driving force for spontaneous imbibition is not rate dependent. The technique also demonstrates the existence of $P_{c,b}$ and shows that by careful manipulation, it can be made large enough to actually block the production of nonwetting phase by counter-current imbibition.

Method

A diagram of the pressure distribution between the open face and the front during unrestricted COUCSI is shown in Figure 7.1-1.

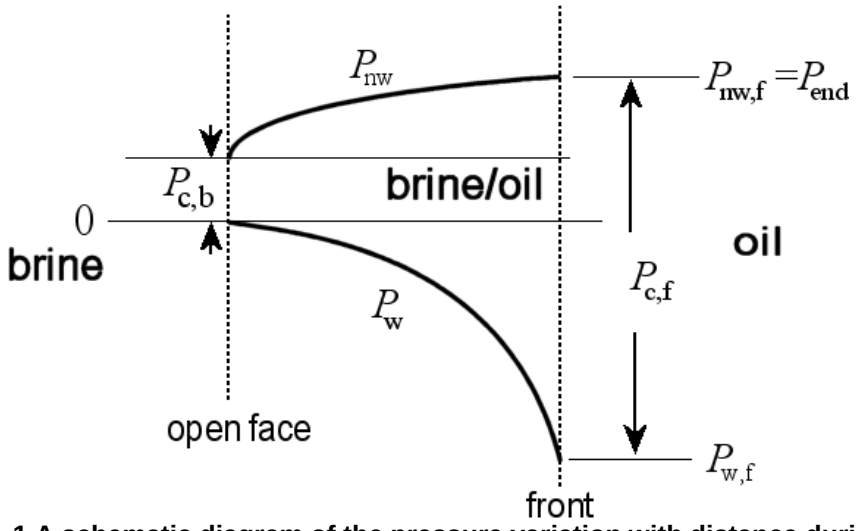

Fig. 7.1-1 A schematic diagram of the pressure variation with distance during unrestricted counter-current imbibition when the initial water saturation is zero. The pressure drops with distance within the wetting phase. There is a sharp rise in pressure, $P_{c,f}$, when moving from wetting phase to non-wetting phase at the imbibition front. The pressure in the wetting phase declines with distance going back towards the open face. There is a finite pressure, the capillary back pressure, $P_{c,b}$, that is required to produce the droplets of non-wetting phase at the open face.

The capillary pressure at the saturation front ($P_{c,f}$) is the driving force of imbibition. The technique designed to evaluate $P_{c,f}$ is unusual and is shown schematically in Figure 7.1-2. Basically a fine-pored rock is butted to the rock under investigation with a means of maintaining hydraulic contact between the segments. The entire surface is sealed, except for one face of the finer-pored segment and a pressure tapping at the opposite end. Imbibition can be started in co-current mode by immersing the core, pre-saturated with oil, in brine and disconnecting the tubes to the pressure transducer. COUCSI is started by reconnecting the tubes to the transducer. The end pressure in the oil phase is monitored. The imbibing brine redistributes in the composite core and the pressure rises to a value which remains steady even though the fluids are still redistributing (i.e. advancing and receding simultaneously within the core at constant saturation). This steady value is the effective capillary pressure at the imbibition front. The dead end pressure and the position of the front in the high permeability segment are both monitored during fluid redistribution. Because the pressures are small (10 to 45 kPa) a sensitive pressure transducer is needed. It also has to be capable of working when the pressured side of the membrane is full of liquid. Although simple in principle, there are several experimental challenges. The two core segments have to be matched such that the imbibition pressure in the high permeability segment may force oil no more than part way back through the low-permeability segment. i.e. the $P_{c,b}$ for the finer-pored segment has to be greater then the $P_{c,f}$ of the main coarser-pored segment. However, if the permeability of the butted

segment is too low, then the velocity of the front during any initial period of COSCI will be very slow.

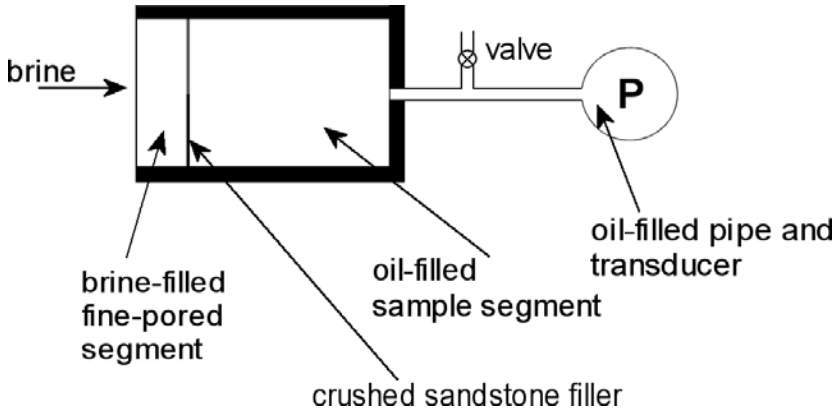

Fig. 7.1-2 Illustration of the measurement technique. A core sample is enclosed by epoxy resin with a butted fine-pored segment of rock at one face. Brine imbibing through the finer-pored segment induces a pressure in the oil which initially fills the main segment. A pressure transducer measures the pressure of the oil in the core.

Consider linear invasion of a wetting phase into a core with only one end face open. By definition, the effective capillary pressure at the WP front, $P_{c,f}$, is the difference in pressure between the non-wetting phase and the wetting phase at the front

$$P_{c,f} = P_{nw,f} - P_{w,f} \qquad 7.1\text{-}1$$

$P_{nw,f}$ is the pressure in the NWP and $P_{w,f}$ is the pressure in the WP, both at the front.

For a core initially saturated with NWP, there is only NWP between the front and the sealed end. Because there is no flow in the dead end pore space, the value of P_{end} is equal to the value of $P_{nw,f}$.

$$P_{end} = P_{nw,f} \qquad 7.1\text{-}2$$

Combining Eq. 7.1-1 and Eq. 7.1-2 yields

$$P_{end} = P_{c,f} + P_{w,f} \qquad 7.1\text{-}3$$

When the front is in movement, $P_{w,f}$ must be less than 0 (the pressure value in the WP reservoir) and so

$$P_{end} < P_{c,f} \qquad 7.1\text{-}4$$

If the dispersed front becomes essentially stationary, as is observed with a suitable choice of conditions, the pressure in the WP becomes zero (equal to the pressure value in the WP reservoir). Also the pressure in all of the contiguous NWP will be constant and equal to the dead end

pressure, P_{end}. Consequently, under the no-flow constraint, the value of the end pressure becomes equal to the value of $P_{c,f}$.

$$P_{end} = P_{c,f} \qquad 7.1\text{-}5$$

Ideally, the experiments therefore seek to measure P_{end} when there is no-flow of either WP or NWP in the core. Under the no-flow constraint, equilibrium requires that the whole contiguous interface between the WP and NWP has to have constant curvature.

Experiments

Composite cores

A schematic diagram of the arrangement of the butted core is shown in Figure 7.1-2. A short segment of low permeability core was chosen which had significantly smaller pores than the main core. It was either a limestone of 0.003 $(\mu m)^2$ permeability with an oil/water breakthrough pressure of 109 *kPa* or a low permeability sandstone of 0.065 $(\mu m)^2$ permeability with a breakthrough pressure of 19 *kPa.* The short segment was butted at the joint with each tested sandstone core, with a 0.1 *cm* thick layer of powder, derived from crushed Berea sandstone, to ensure hydraulic contact. All surfaces of the composite core were sealed with epoxy resin, except for the outer face of the low permeability segment. Except for one case (OW1), the short segment was initially pre-saturated with WP. This segment served as a semi-permeable membrane that allows WP to enter the core and, ideally, prevents NWP from leaving at the open face. A nylon tube with an inner diameter of 1.5 mm and an outer diameter of 3 mm, embedded in the otherwise sealed end of the main core, served as a pressure tapping. Details of each composite core are given in Table 7.1-1. The location of the front was detected by a series of electrodes that were embedded in the surface of the core and fixed in place with epoxy resin.

Measurements on composite cores

After assembly, the composite core was immersed in the wetting phase using the arrangement shown in Figure 7.1-3. The change in pressure in the NWP at the end of the core was monitored with a sensitive differential pressure transducer (Validyne DP15-32 to 40). Saturation changes were determined gravimetrically. The distance of advance of brine into the open core was detected from the onset of electrical conductivity between electrodes embedded in the core and an electrode in the brine. This was a much more sensitive way of establishing that the leading edge of the saturation front had not reached the end of the core than either X-ray or NMR tomography. All experiments were conducted at room temperature (about 21^oC) and atmospheric pressure (79 *kPa*). Some tests were begun with a short period of invasion of wetting phase into the main core segment with the connection fitting on the pressure tap left open to allow flow of oil. After closing this vent, the rise in P_{end} that accompanied transition from COCSI to restricted COUCSI was monitored while the fluids redistributed within the main core segment. The development of the saturation profile for restricted COUCSI was essentially complete, as indicated by a maximum in P_{end}, before the WP reached the far end of the main core.

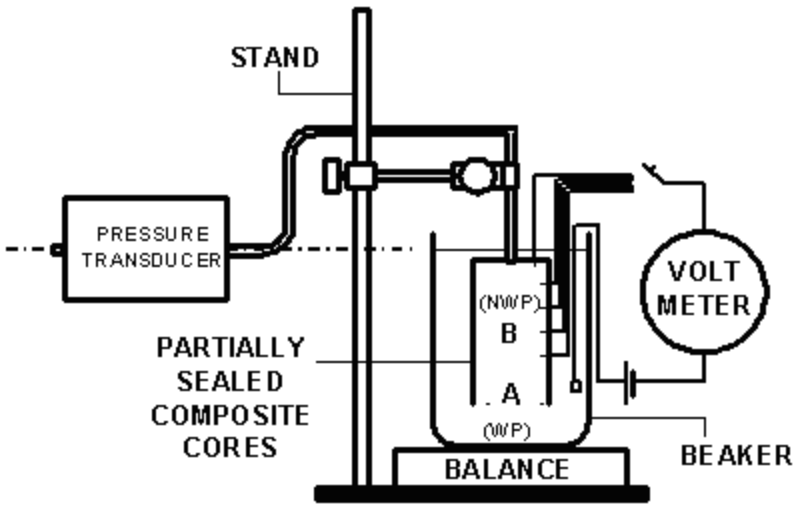

Fig. 7.1-3 Apparatus for measurement of the frontal capillary pressure in COUCSI. A is the low permeability core segment. B is the high permeability core segment. The fitting on the transducer could be loosened to allow oil to escape, thus permitting COCSI. Imbibition of brine into the core was measured by the change in weight indicated by the balance.

Rock and fluid properties

Five Berea sandstone cores, of 3.8 *cm* diameter and about 3 *cm* to 7 *cm* in length, with permeabilities ranging from 0.06 $(\mu m)^2$ to 1.067 $(\mu m)^2$ (see Table 7.1-1) were tested. It was the range of permeabilities that was the key variable, rather than any other parameter. All gas permeabilities in Table 1 were measured with air under a mean flowing pressure of 15 *kPa*. In one case (OW3) permeability to oil was measured before and after spontaneous imbibition using standard techniques. Refined oil (Soltrol 220, viscosity 0.0038 *Pa.s*) served as the oil phase. Brine with a salinity of 10,000 ppm NaCl and a viscosity of 0.00115 *Pa.s* was the wetting phase. The interfacial tension between brine and oil was 48.8 *mN/m*. All properties were measured at ambient conditions.

Table 7.1-1 Measurement of $P_{c,f}$ in COUCSI

TEST NO.	LOW K CORE ID	D (cm)	L_c (cm)	K $((\mu m)^2)$	ϕ (%)	MAIN CORE ID	D (cm)	L_c (cm)	K $((\mu m)^2)$	ϕ (%)	P_{cf} (kPa)	P_{cf}/σ (μm^{-1})
OW1	LS2	3.8	2.07	0.065	17.1	H70	3.8	6.90	1.052	22.1	>12.17	>0.249
OW2	LS3	3.8	2.35	0.065	17.1	H6O	3.8	6.97	1.067	22.2	12.4	0.254
OW3	TL9	3.8	1.84	0.002	16.0	HF4	3.4	3.17	0.964	22.3	14.4	0.295
OW4	TL8B	3.8	1.71	0.003	16.8	M10	3.8	6.00	0.492	20.2	30.0	0.614
OW5	TL3	3.8	1.49	0.003	16.8	L60	3.8	6.18	0.060	19.6	42.0	0.860

Results

Test OW1

In this preliminary test, the two core segments were sealed together and both segments of the composite core were completely filled with oil. After immersion in brine, a period of COCSI was allowed by loosening the fitting on the tube to the transducer so that oil was released. Response of an electrode at the joint indicated that the COCSI front had crossed the joint between the segments after 0.45 *hour*. After 2.6 *hours* the front had penetrated 2.75 *cm* into the high *K* core segment. The fitting on the tube of the transducer was then sealed so that COSCI ceased and imbibition changed to COUCSI. At the start of COUCSI, the end pressure rose quickly and reached its highest value of 12.17 *kPa* after 0.37 *days* (see Figure 7.1-4). Eventually, oil was seen to appear as droplets at the open face of the low permeability segment and the measured end pressure started to fall. The brine imbibition into the low permeability segment had not sealed the open face to oil. However, the whole purpose of the low permeability segment was to prevent oil from escaping from the open face of the core, otherwise the maximum front pressure is not reached. In subsequent tests the technique was modified by filling the low permeability segment with brine and this successfully prevented the escape of oil from the open face. Without this production of oil at the open face, the measured pressure in Test OW1 would have reached a higher value.

Subsequently the fitting on the tube of the transducer was reopened making the end pressure fall to zero. This transition from COUCSI to COCSI resulted in oil recovery increase from 28% to 48 % within 1.2 days (see Figure 7.1-4**).**

Test OW2

This time, the cylindrical sides of each segment were separately coated with epoxy. The low-permeability segment was then saturated with brine (instead of oil, as previously) and the high-permeability segment was saturated with oil. The two segments were then epoxied together with a layer of water-saturated crushed sandstone serving to give hydraulic contact between the segments. The main segment in Test OW2 was a duplicate of that used in Test OW1. The composite core was then immersed in brine to initiate the restricted COUCSI imbibition. The end pressure rose to 11 *kPa* within 2 *hrs* and reached its highest value of 12.4 *kPa* after 2.08 *days* (see Fig. 7.1-5). By that time, the front had penetrated 3.25 cm into the high permeability core segment. The pressure was monitored for a further 1.8 days to confirm that the end pressure was stable. There was no production of oil from the open face (unlike Test OW1 in which the low permeability oil segment was initially oil saturated). Nevertheless, the stable end pressure of 12.9 *kPa* was only 0.26 *kPa* higher than the maximum value of P_{end} for Test OW1. Movement of the invading brine along the core was detected by the onset of electrical conductivity when the front contacted a particular electrode.

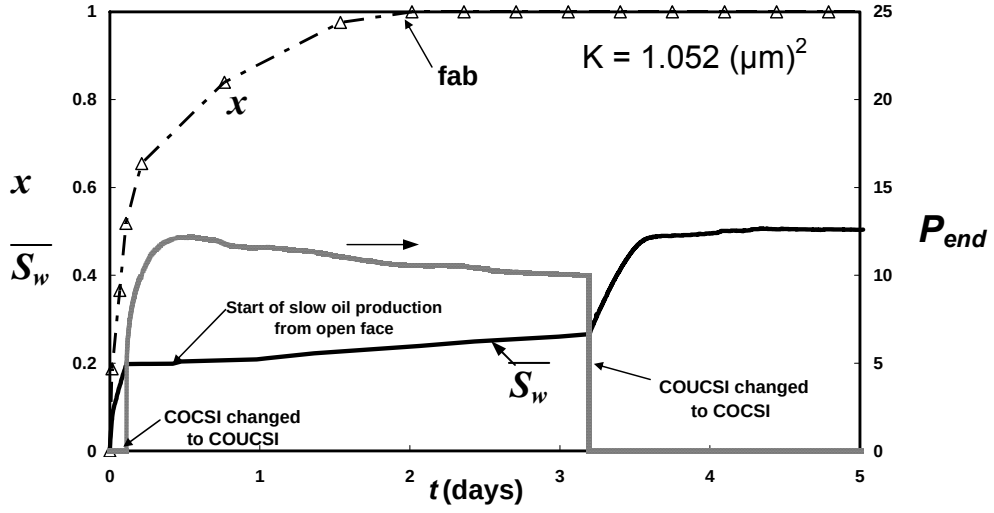

Fig. 7.1-4 Fractional distance of advance of brine, x, average brine saturation, $\overline{S_w}$, and end pressure, Pend, versus time for Test OW1. The arrival of the front at the end of the core was detected by an electrode and is indicated as "fab" – front at boundary. Imbibition was changed from COUCSI to COCSI after 3.2 days by opening the end tube to atmosphere.

After 3.9 *days*, the core was removed from the apparatus and sawn in half along its axis. An electrode was advanced along the exposed axis of the sliced core. A sudden increase in conductivity showed that the brine had penetrated 3.13 *cm* into the core. It could also be seen that oil had penetrated part way into the low-permeability segment.

Test OW3

The low permeability segment in Test OW3 was set up as in Test OW2 using limestone as the low permeability segment (see Table 7.1-1). The main segment was 3.17 *cm* (less than half the main core length used in Test OW2).

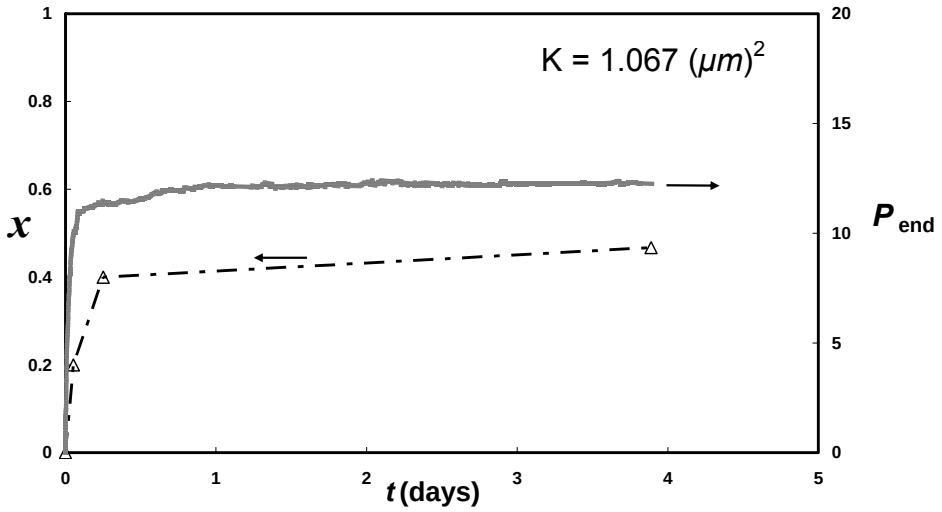

Fig. 7.1-5 Fractional distance of frontal advance along the core, x, and end pressure versus time for Test OW2.

Restricted COUCSI imbibition was conducted on the composite core. The end pressure rose to 13.7 *kPa* within 1 *day* and reached its highest value of 14.4 *kPa* after 2 *days* (Figure 7.1-6). The front reached the end of the main segment 3.3 *days* after the start of imbibition. The pressure then decreased to 12.55 *kPa* over a further half day.

In Test OW 3, the permeability of the main segment to oil was 0.674 $(\mu m)^2$ when fully saturated with oil. For Berea sandstone and many other rock types, liquid permeabilities are typically lower than the gas permeability even after correction for slippage. After imbibition was complete, the core was removed and the low permeability segment and 0.92 *cm* of the neighboring part of the main core was cut off. The relative permeability to oil of the remaining brine invaded portion of the main core was 0.573 $(\mu m)^2$. Thus, the relative permeability to oil behind the front after imbibition is high, being about 85% of the permeability when fully saturated with oil. This implies that the frontal saturation and effective capillary pressure depend on the largest of the invaded pores at the front and their values must be finite during COUCSI. The same conclusion was reached for two-phase flow simulations in 3-D pore-networks (Li et al, 1986).

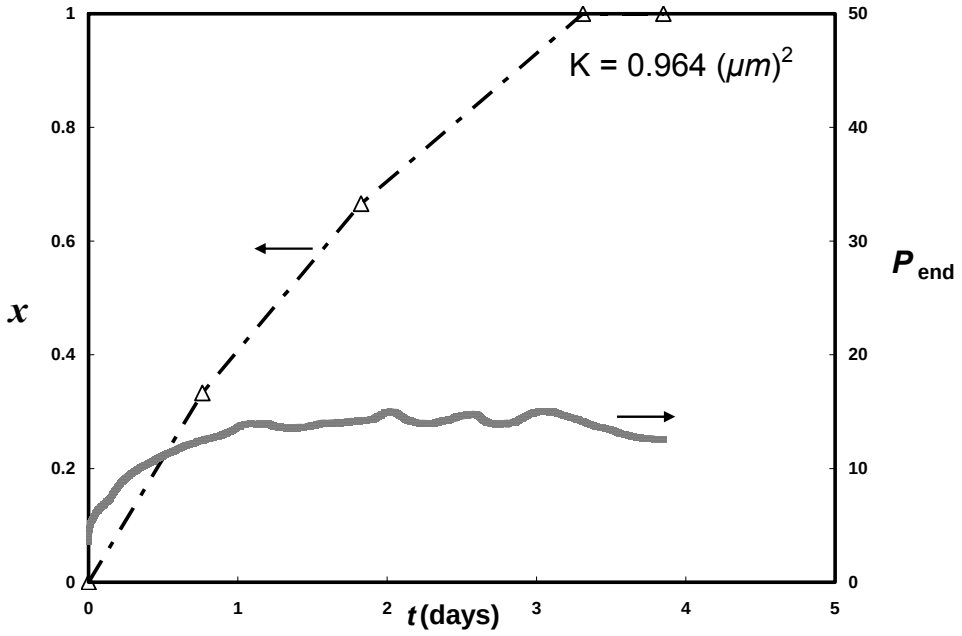

Figure 7.1-6 Fractional distance of frontal advance along the core, x, and end pressure versus time for Test OW3.

Test OW4

The tested sandstone segment was 6 *cm* long with permeability of 0.492 $(\mu m)^2$. A low permeability limestone segment of 1.714 *cm* length and permeability of 0.003 $(\mu m)^2$ was used as the semi-permeable membrane. The low permeability segment was initially saturated with brine as in OW2 and OW3.

The end pressure rose to 29.3 *kPa* after 1.5 *days* and remained high (see Figure 7.1-7). After 8 *days*, the electrical conductivity measurement indicated that the brine had penetrated at least 3.6 *cm* into the main segment (x= 0.6). The average fractional brine saturation $\overline{S_w}$ of the main segment as determined from the weight change of the brine reservoir rose to 0.064. The initial sharp rise probably represents the volume of oil required to displace the transducer diaphragm. The slower subsequent rise is likely caused by dissolution of traces of air trapped in the fine media paste and in the plastic tubing. Either way it does not significantly affect the measured pressure. After 12 *days*, the fitting near to the transducer was opened and imbibition changed from COUCSI to COCSI; oil recovery increased from 6.4% to 52.4% within 1 *day*.

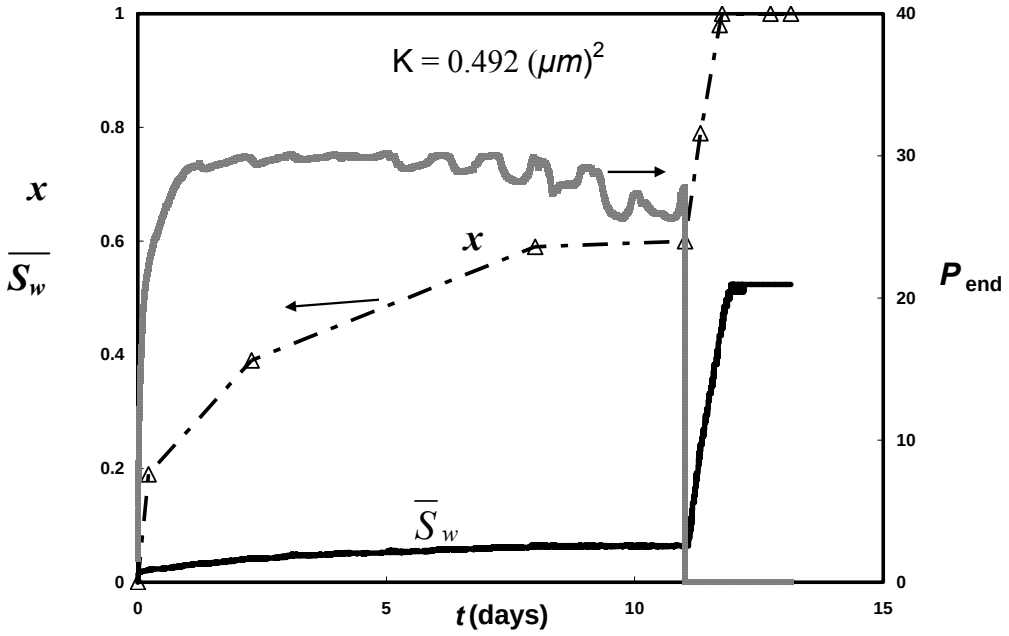

Fig. 7.1-7 Fractional distance of advance of front, x, average imbibed brine saturation, $\overline{S_w}$, and end pressure versus time for Test OW4.

Test OW5

The main sandstone segment was 6.175 *cm* long with permeability of 0.06 $(\mu m)^2$. This was the same sandstone that had served as the low permeability segment in Tests OW1 and OW2. A low permeability limestone segment was 1.489 *cm* long and was initially saturated with brine. The end pressure rose very quickly to over 40 *kPa*, within 1.2 *days* and increased only slightly over the next 7 *days* to 42 *kPa* (Figure 7.1-8). Electrical conductivity indicated that the front had penetrated at least 2.6 *cm* into the main segment ($x = 0.42$). No oil production was observed at the open face throughout the 8 *day* test. Invasion of brine was allowed mainly by compression of some residual gas in the tube to the transducer.

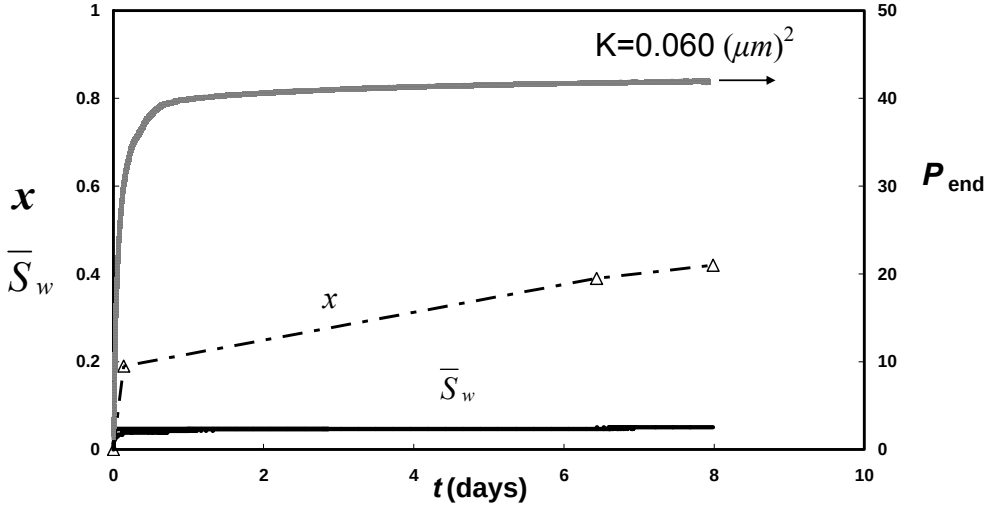

Fig. 7.1-8 Fractional distance of advance of front, x, average imbibed brine saturation, $\overline{S_w}$, and end pressure versus time for Test OW5.

Discussion

Dispersion during restricted COUCSI

The transition from COCSI to restricted COUCSI at essentially constant overall saturation is accompanied by dispersion at the front because of capillary action. As the WP advances at the front, the disperse region grows and the NWP pressure increases. WP is drawn into smaller pores previously occupied by NWP and NWP is driven back into the larger pores previously occupied by WP, thus maintaining the mass balance. A remarkable feature of the experimental results is that the end pressure remains essentially constant as the wetting phase redistributes within the core.

Effective capillary pressure at the imbibition front.

The maximum stable value of P_{end} before the front reaches the end of the core provides an estimate of the effective capillary pressure acting at the imbibition front. The maximum values of P_{end} for Berea sandstones with permeabilities from 1.067 to 0.06 μm^2 ranged from 6.6 to 21.3 *kPa* for water/oil. For strongly wetted systems such as this one, the effective pore radius at the front is given by $2\sigma/P_{\text{c,f}}$. An overall, but different, pore radius for the core can be obtained from the permeability using the Leverett radius, $2\sqrt{2K/\varphi}$ (Leverett, 1941). If the pore geometry of the sandstones maintains similarity with change in grain size, a plot of $2\sigma/P_{\text{c,f}}$ versus $2\sqrt{2K/\varphi}$ should be a straight line passing through the origin. However, for the four tests OW2 through OW5 for which $P_{c,f}$ was measured, this plot is not linear (Figure 7.1-9). The inference is that the diagenetic changes that determine the ultimate porosity and permeability produce pore sizes and distributions that do not scale linearly with the square root of permeability. This is not surprising because, even though there is little difference in grain size between the tested sandstones, their permeabilities varied by more than an order of magnitude. Furthermore, the capillary pressure at the front will depend on the largest sections of the smaller effective pores of the rock, whereas the

permeability will depend on the network of the larger pores. It is likely that a change in the spread of the pore size distributions of the various sandstones is the main reason for the deviation from linearity shown in Figure 7.1-9.

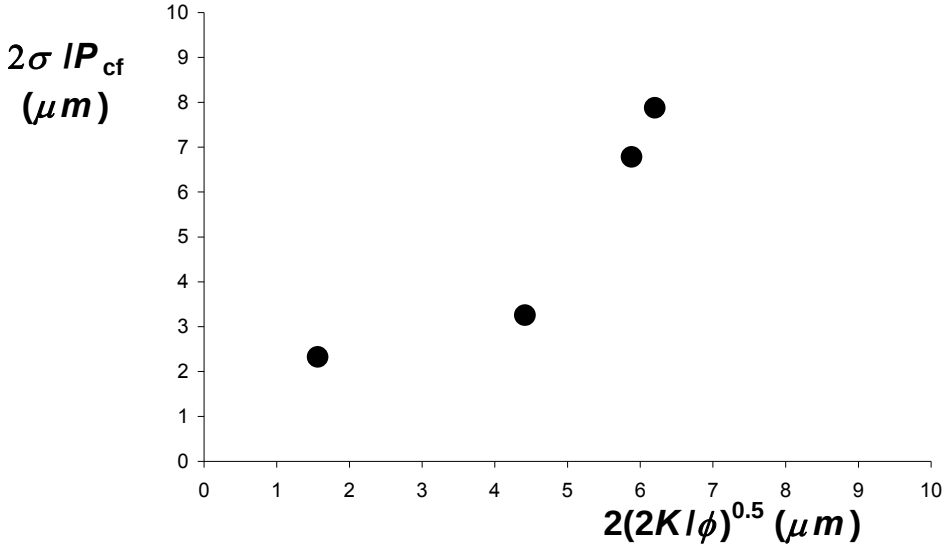

Fig. 7.1-9 The pore radius calculated from the capillary pressure at the front plotted against the pore radius derived from the rock permeability. If the pore geometries of the rocks scaled exactly, this plot would be a straight line. A gradient of unity would not be expected. The scatter probably arises from the effect of diagenetic differences on pore geometry.

Conclusions

1. If the uptake of wetting phase for linear imbibition is proportional to the square root of time, the capillary pressure acting at the imbibition front has to be independent of imbibition rate. For such a system, monitoring the end pressure for one-end-open linear imbibition under conditions of restricted COUCSI where the production of non-wetting phase is prevented provides an estimate of the capillary pressure acting at a slow-moving to essentially static imbibition front.
2. During restricted COUSCI, after limited invasion of WP, the end pressure in the NWP rises to a maximum value and shows only small decline as the WP redistributes by simultaneous imbibition and drainage without change in the overall brine content.
3. The capillary pressures at the oil/water displacement front ranged from 6.6 to 21.3 *kPa* for Berea sandstones with permeabilities between 1.067 and 0.06 $(\mu m)^2$. Frontal_capillary pressures for different Berea sandstones did not give a direct correlation with permeability as would be given by porous media with different pore length scales but with similar pore geometry.

Nomenclature

D	core diameter (m)
K	permeability to air (m^2)
L_c	core length (m)
P_c	capillary pressure (Pa)
$P_{c,b}$	capillary back pressure (Pa)
$P_{c,f}$	capillary pressure at the imbibition front (Pa)
P_{end}	pressure measured at the dead end (Pa)
P_{nw}	pressure in the nonwetting phase (Pa)
$P_{nw,f}$	pressure in the non-wetting phase at the front (Pa)
P_w	pressure in the wetting phase (Pa)
$P_{w,f}$	pressure in the wetting phase at the front (Pa)
$\overline{S_w}$	average WP saturation
x	fractional distance reached by the front along the main core segment
σ	interfacial tension (N/m)
ϕ	porosity

Acronyms/abbreviations

fab	front at boundary
WP	wetting phase
NWP	nonwetting phase
COCSI	co-current spontaneous imbibition
COUCSI	counter-current spontaneous imbibition

Acknowledgements

The authors acknowledge support from ARAMCO, British Petroleum, ChevronTexaco, Total, ConocoPhillips, StatoilHydro, Shell, the Enhanced Oil Recovery Institute at the University of Wyoming, the National Petroleum Technology Office of the US Department of Energy, the UK Engineering and Physical Sciences Research Council, and the Natural Science and Engineering Research Council of Canada.

7.2 EFFECT OF SAMPLE SHAPE ON COUNTER-CURRENT SPONTANEOUS IMBIBITION PRODUCTION VERSUS TIME CURVES

G. Mason, H. Fischer, N.R. Morrow, D.W. Ruth & S. Wo
Submitted to *Journal of Petroleum Science and Engineering*

ABSTRACT

Counter-current spontaneous imbibition experiments on porous media are usually carried out using cylindrical core samples. Sometimes the cores are sealed on some of the faces, and experiments then give production curves of significantly different duration and slightly different shape. Results can be correlated for rock properties (porosity and permeability) and fluid properties (viscosity and interfacial tension). A single overall scale factor is usually used to correlate for different core sizes and shapes. Although the real imbibition process is actually quite complicated, by making the approximations that there is (a) frontal displacement and (b) constant saturation behind the front, a simple analytical solution is possible. The analysis gives the production *vs* time function and a new core shape scale factor. These assumptions also allow the scale factors of Ma *et al*. (Ma, S., Morrow, N.R. & Zhang, X., 1997, *J. Pet. Sci. Eng.*, **18**, 165-178) and Ruth *et al.* (Ruth, D., Mason, G. & Morrow, N.R., 2003, *Proc. Soc. Core Analysts Symp., Pau*, SCA2003-16, 1-12) to be used to predict the shape of the production *vs* time curves. In order to challenge the predictions of the production *vs* time curves and the Ma, Ruth and new scale factors, counter-current spontaneous imbibition experiments were carried out with matched oil-saturated cores of different shape using brine to spontaneously displace the mineral oil. Amongst others, cylindrical cores with an axial hole were used with either the inner or outer cylindrical face open. These have radial geometry with imbibition into a contracting or expanding volume. Analysis of the experimental results with the new theory confirmed that the Ma and Ruth scale factors are good to excellent for most situations but that the new one is marginally better for extreme shape variations. The theory also predicts that all of the results should be linked by a universal properties factor (G). The variability of the G factor can be explained by some of the cores not having enough exposed surface and not enough rock depth. These factors seem to be of greater importance than the differences between the scale factors. For reproducible results it appears that a core should have an imbibition face area of at least 40 cm^2 and a thickness (open face to no-flow boundary) of at least 1 cm.

Introduction

Counter-current spontaneous imbibition occurs when a wetting fluid displaces a less-wetting fluid from the pore space of a porous medium. The wetting fluid imbibes into the pore space and the non-wetting fluid is expelled. Under these circumstances, the mass balance requirement means that the volumetric flows of the two fluids are locally everywhere equal but in opposite directions. Also, in some circumstances, particularly when the porous medium is initially filled with non-wetting phase, a saturation front is observed to advance through the system. A positive pressure has to build up at the dead end of the system and it is this pressure that pushes the non-wetting phase back through the invading wetting phase. Counter-current imbibition is believed to be a mechanism by which oil can be displaced from the rock in fractured reservoirs (Morrow & Mason, 2001).

Countercurrent imbibition in reservoir rocks is usually studied at the core level using cylindrical cores about 70mm long and with a diameter of about 35 to 50mm. A typical experiment consists

of saturating a core with oil and then immersing it in brine. The expelled oil is collected and its volume is measured. Results are recorded as the total amount of oil produced at various time intervals. Attempts have been made to correlate results for very strongly water wet (VSWW) imbibition so that the effect of changing interfacial tension, rock porosity and permeability can be predicted (Mattax & Kyte, 1962). There are two additional factors - the viscosities of the two phases and the shape of the sample. This paper primarily addresses the latter factor. Frequently, cores used in experiments have all faces of the cylinder open to the invading phase. The experiments give rapid and reproducible results but the flow patterns are complex and, therefore, difficult to model. If the ends of the core cylinder are sealed then the flows become radial. The simplest case, however, reducing imbibition to a one-dimensional, linear situation, is to seal the outer surface plus one end, thus leaving one end open for the imbibition and production to take place. Because the shape of the sample makes a difference to both the time and the shape of the production *vs* time results, it would be convenient to be able to transform experimental results obtained from one core geometry into those from another (Behbahani *et al*., 2006). A function involving the core sample shape which has been found to correlate available data reasonably well is (Ma *et al*. 1997):

$$t_{\mathrm{D}} = \frac{1}{L_{\mathrm{c}}^2}\sqrt{\frac{K}{\varphi}}\frac{\sigma}{\sqrt{\mu_{\mathrm{w}}\mu_{\mathrm{nw}}}}t \qquad 7.2\text{-}1$$

where L_{c} is a characteristic length, K the rock permeability, φ its porosity, σ is the interfacial tension between the phases, and μ_{w} and μ_{nw} are the viscosities of the wetting and non-wetting phases. Ma's semi-empirical correlation for the general characteristic length L_{c} is

$$L_{\mathrm{c}} = \sqrt{V \Big/ \sum_{i=1}^{n} A_i / x_{A,i}} \qquad 7.2\text{-}2$$

where V is the bulk volume of the matrix, A_i is the area open to imbibition in the ith direction, $x_{A,i}$ is the distance from A_i to the no-flow boundary and n is the number of faces open to imbibition. For linear imbibition L_{c} is simply the length of the core. For a cylindrical core with all faces open it becomes

$$L_{\mathrm{c}} = \frac{L_{\max} d}{2\sqrt{d^2 + 2L_{\max}^2}} \qquad 7.2\text{-}3$$

where $L_{\max}$ is the core length and d is the core diameter. Yildiz *et al,* (2006) have recently calculated characteristic lengths for many situations including square and triangular prisms. L_c is only a function of the core size and shape. Figure 7.2-1 shows a correlation (Fischer, 2006) using the t_{D} factor for matched viscosities and linear one end open imbibition. The correlation only involves the time axis; the other axis is usually presented as the fraction of the pore volume filled with wetting phase (i.e. the recovery) as in Figure 7.2-1, although sometimes this is normalised with respect to the oil recovered at infinite time. Note that although the correlation is good, there are still sufficient differences between the results to prevent perfect correlation.

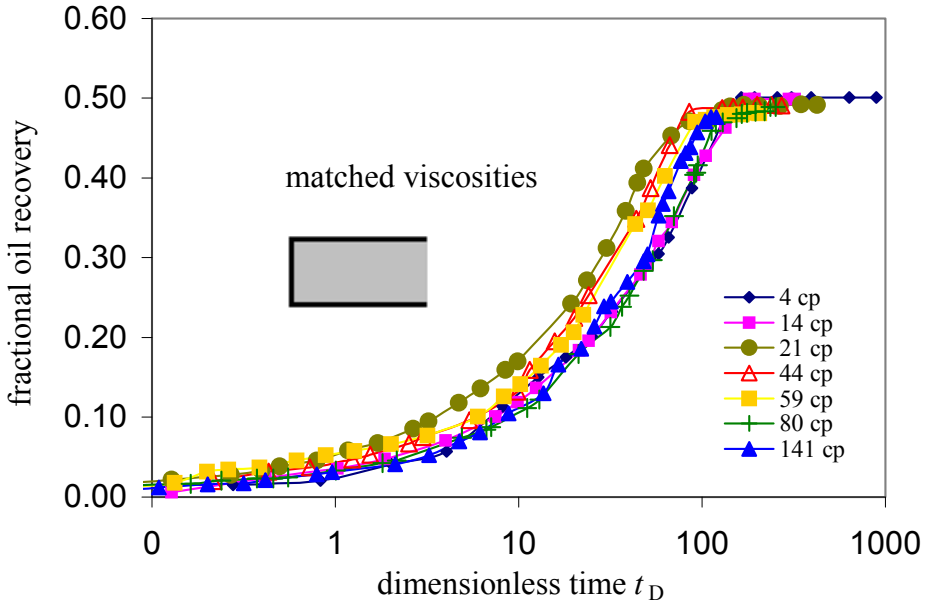

Fig. 7.2-1. Typical experimental data correlated by Eq. 7.2-1. The data is for linear counter-current spontaneous imbibition into one-end-open cores with similar properties using liquids with matched viscosities. Note that although the correlation is good, it is still not perfect.

The t_D factor is a normalised dimensionless time and it is obtained by multiplying the actual time (t) by a function of rock and fluid properties. Note that the correlation just brings the data together and on, a $\log_{10}$ scale; any change in the characteristic length L_c only moves the production curves left and right; it does not change the shape of the production curve and so it cannot explain any differences in shapes of production *vs* t_D curves.

The core shape factor which determines the characteristic length L_c has been investigated in some detail by Ma *et al*. (1997) and was later modified by Ruth *et al*. (2003). However, their work was mainly concerned with the general correlation of the imbibition curve's *location* on a $\log_{10} t$ scale rather than the changes in the shape of the production *vs* time function brought about by differences in sample shape. Ruth *et al*. (2003) calculated the scale factors for some extraordinary core shapes and it was their predictions that gave rise to the current experiments. Recent experiments (Fischer & Morrow, 2005, 2006) have demonstrated that there are small but systematic differences in the shape of imbibition production curves, particularly between the one-dimensional and all-faces-open configurations that are normally used in experiments. For co-current imbibition Zimmerman *et al*. (1990) predicted such differences in shape using both numerical simulation and an approximation method. It is the purpose of this paper to indicate an *a priori* shape for the counter-current imbibition production function and to quantify the small differences in function shape caused by different sample geometry.

In some cases one-dimensional counter-current imbibition is primarily a frontal process because, during experiments, a liquid front can actually be seen to advance along the core (Li *et al.,* 2003, 2006). This observation confirms that of Baldwin & Spinler (1999) and Kashchiev & Firoozabadi (2002). The step change in saturation at the front can be found from the volume imbibed and the

distance that the front has advanced multiplied by the core porosity. The final amount imbibed, relative to the total volume of the pore space, gives an indication of the final saturation. From these values, one can conclude that about 80% of the imbibition recovery reported by Li *et al*. (2003) occurs as frontal displacement. This does not mean that *all* counter-current spontaneous imbibition is a frontal process, just that in some circumstances it is, particularly when the core is initially saturated with non-wetting phase (Rangel-German & Kovscek, 2002).

Frontal Imbibition. General

In simulation of one-dimensional counter-current imbibition, it has been shown (Li *et al.,* 2003) that the front and its small amount of dispersed imbibition could be represented by a self-similar front. By self-similar we mean that the saturation profile with distance is always the same provided that the distance to the front is properly scaled. The self-similar front is a consequence of the mathematical formulation of counter-current imbibition (Ruth *et al*., 2007). There are three functions, all of saturation; there is the capillary pressure, and two relative permeabilities, one for the wetting phase and the other for the non-wetting phase. The consequence is that, for a thin slice of core, if the counter-current relative permeability for one phase is fixed then there is only a single value for the relative permeability for the other phase. Added to this is the fact that, for pure counter-current spontaneous imbibition, the flow of one phase through the slice is exactly equalled by the reverse flow of the other phase, and both these are over the same area. The prediction of a self-similar front in 1-D imbibition goes back a long way, at least as far as Rapoport (1955) and Handy (1960). The concept of a single function representing capillary pressure was challenged by Barenblatt *et al*. (2002) and more recently by Le Guen & Kovscek (2006) who suggested that so-called non-equilibrium effects should be taken into account. There is then no self-similar front, and another variable is added to the mathematical model.

As a limiting case, following Cil & Reis (1996), we could imagine that *all* of the saturation change takes place at the saturation front where the saturation makes a step change from S_{wi} (the initial wetting phase saturation) to S_{wf} (the wetting phase saturation at the front). This assumption means that the saturation behind the front is constant at S_{wf}. Behind the front therefore, the relative permeabilities of each of the two phases are also constant. Also, because there is no change in saturation behind the front, the flow of wetting phase (q_{w}) at one instant in time is invariant with distance from the open face. Up to the front, the flow of non-wetting phase (q_{nw}) is also invariant. It must be stressed that this is an approximation, but it provides a tractable model that may be approximately realistic for some cases of imbibition. Darcy's law gives the two flows:

$$q_{\mathrm{w}} = -\frac{Kk_{\mathrm{rw}}A}{\mu_{\mathrm{w}}}\frac{\partial P_{\mathrm{w}}}{\partial x} \qquad 7.2\text{-}4$$

$$q_{\mathrm{nw}} = -\frac{Kk_{\mathrm{rnw}}A}{\mu_{\mathrm{nw}}}\frac{\partial P_{\mathrm{nw}}}{\partial x} \qquad 7.2\text{-}5$$

where K is the permeability, k_{rw} and k_{rnw} are the relative permeabilities, μ_w and μ_{nw} are the viscosities, A is the area and x is a distance. The capillary pressure P_c is the difference between the pressure in the non-wetting phase (P_{nw}) and the pressure in the wetting phase (P_w).

$$P_c = P_{nw} - P_w \qquad 7.2\text{-}6$$

and flow continuity gives:

$$q_w = -q_{nw} \qquad 7.2\text{-}7$$

Combining equations 7.2-4 to 7.2-7 gives:

$$q_w = \frac{K k_{rw} k_{rnw} A}{\mu_w k_{rnw} + \mu_{nw} k_{rw}} \frac{\partial P_c}{\partial x} \qquad 7.2\text{-}8$$

Because the saturation has been assumed to be constant behind the front, a large part of this equation will be constant. Let M be a mobility factor and let

$$M = \frac{k_{rw} k_{rnw}}{\mu_w k_{rnw} + \mu_{nw} k_{rw}} \qquad 7.2\text{-}9$$

For constant saturation, the relative permeabilities have to be constant, consequently the factor M will be constant and so, behind the front

$$q_w = KMA \frac{\partial P_c}{\partial x} \qquad 7.2\text{-}10$$

It should be noted that for the assumption that the saturation behind the front is constant to be approximately true, P_c has to be able to vary a lot (so as to be able to drive the flows) for negligible changes in S_w (i.e. the gradient of the capillary pressure curve with saturation is steep).

Because the mobility factor M is constant for the flows behind the wetting front, Eq. 7.2-10 can be integrated between the open face of the core and the front. For one-dimensional imbibition, the area A will be a constant. However, for radial flows into a cylinder with capped ends, the area A will vary with distance and so the function for the amount of imbibition *vs* time will be different. It is the effect of the change in areas with distance on the overall resistance to flow and the changes it makes to the rate of frontal advance that are the main factors in the following analysis.

The flow of wetting phase arriving at the front advances the position of the front. A mass (volume) balance gives

$$\frac{\mathrm{d}x_\mathrm{f}}{\mathrm{d}t} = \frac{q_\mathrm{w}}{\varphi A\left(S_\mathrm{wf} - S_\mathrm{wi}\right)} \qquad 7.2\text{-}11$$

where x_f is the distance of the front from the open face. S_wi is the initial saturation and S_wf is the saturation behind the front.

One dimensional linear counter-current imbibition

The experimental situation is of a core initially mostly filled with non-wetting phase and sealed on all faces except one end. Starting with Washburn (1921), for co-current imbibition this case has been investigated many times. It has also been investigated many times for counter-current imbibition, almost always with the prediction that the production (or volume imbibed) varies as $\sqrt{time}$ (Akin *et al*., 2000; Cil & Reis, 1996; Reis & Cil, 1993). It gives the base case with which other core shapes can be compared.

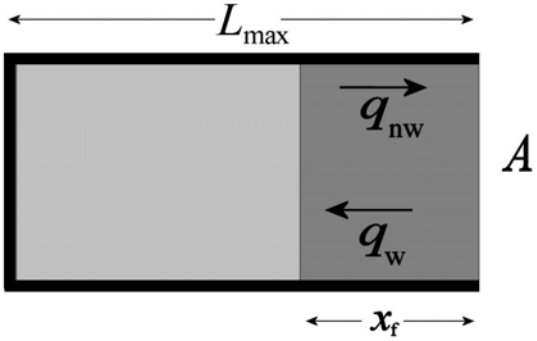

Fig. 7.2-2. Diagram showing linear counter-current imbibition.

In Eq. 7.2-10 q_w, *M* and *A* do not vary with *x* and so the equation can be integrated between the open face and the front to give:

$$q_\mathrm{w}\left(x_\mathrm{f} - 0\right) = KMA\left(P_\mathrm{cf} - P_\mathrm{co}\right) \qquad 7.2\text{-}12$$

P_cf is the capillary pressure difference at the front. P_co is the capillary pressure difference at the open face. At the open face the pressure in the wetting phase is zero but the pressure in the non-wetting phase is not zero. It is not zero as is commonly assumed because non-wetting phase has to bubble from the rock into the wetting phase (Li *et al*., 2006). Substituting for q_w using Eq. 7.2-12 in Eq. 7.2-11 and integrating between the open face and the distance to the front, x_f, gives:

$$x_\mathrm{f}^2 = \frac{2KM\left(P_\mathrm{cf} - P_\mathrm{co}\right)}{\varphi\left(S_\mathrm{wf} - S_\mathrm{wi}\right)}t \qquad 7.2\text{-}13$$

The time *t* is zero when the front is at the open face. If *f* is the fractional amount of non-wetting phase produced at time *t*, then, for core length L_max, $f = x_\mathrm{f}/L_\mathrm{max}$ and

$$f^2 = \frac{2}{L_{\max}^2}\frac{KM\left(P_{\mathrm{cf}} - P_{\mathrm{co}}\right)}{\varphi\left(S_{\mathrm{wf}} - S_{\mathrm{wi}}\right)}t \qquad 7.2\text{-}14$$

For cylindrical tubes the capillary pressure is related to tube radius r_{mean} by

$$P_{\mathrm{c}} = \frac{2\sigma}{r_{\mathrm{mean}}} \qquad 7.2\text{-}15$$

and r_{mean} is related to the permeability and porosity by (Leverett, 1941, Pirson, 1958)

$$r_{\mathrm{mean}} = \sqrt{\frac{8K}{\varphi}} \qquad 7.2\text{-}16$$

Eq. 7.2-12 contains a difference in capillary pressures $\left(P_{\mathrm{cf}} - P_{\mathrm{co}}\right)$. The capillary pressure at the front $\left(P_{\mathrm{cf}}\right)$ is mainly produced by the smaller pores and the capillary pressure at the open face $\left(P_{\mathrm{co}}\right)$ is mainly produced by the larger pores. The difference between them is thus related to the spread of the pore size distribution. For a spread of pore sizes, $\left(P_{\mathrm{cf}} - P_{\mathrm{co}}\right)$ can be related to the mean capillary pressure, P_{c}, by a factor C_{spread} which is in some way determined by the breadth and shape of the pore size distribution. For narrow pore size distributions, C_{spread} will be small and for wide pore size distributions C_{spread} will tend to unity or larger. We thus obtain

$$P_{\mathrm{cf}} - P_{\mathrm{co}} = C_{\mathrm{spread}}P_{\mathrm{c}} = C_{\mathrm{spread}}\frac{2\sigma}{r_{\mathrm{mean}}} = C_{\mathrm{spread}}2\sigma\sqrt{\frac{\varphi}{8K}} \qquad 7.2\text{-}17$$

Eliminating $\left(P_{\mathrm{cf}} - P_{\mathrm{co}}\right)$ from Eq. 7.2-14 gives

$$f^2 = \frac{1}{L_{\max}^2}\sqrt{\frac{2K}{\varphi}}\frac{MC_{\mathrm{spread}}\sigma}{\left(S_{\mathrm{wf}} - S_{\mathrm{wi}}\right)}t \qquad 7.2\text{-}18$$

Eq. 7.2-18 can be rearranged so as to be explicit for *t*:

$$t_{f,\mathrm{Linear}} = \sqrt{\frac{\varphi}{2K}}\frac{\left(S_{\mathrm{wf}} - S_{\mathrm{wi}}\right)}{MC_{\mathrm{spread}}\sigma}L_{\max}^2 f^2 \qquad 7.2\text{-}19$$

This equation now predicts the time for fractional production *f* from a core of length $L_{\max}$ for linear imbibition. When experiments are carried out, both the time and fractional production are determined. Thus the shape of the experimental production curve can be compared to the theoretical prediction. The time for the front to reach the end of the core, t_{end}, when imbibition ceases will be

$$t_{\text{end}} = L_{\text{max}}^2 \sqrt{\frac{\varphi}{2K}} \frac{(S_{\text{wf}} - S_{\text{wi}})}{MC_{\text{spread}}\sigma} \qquad 7.2\text{-}20$$

Note that Eq. 7.2-19 gives the production *vs* time function and that Eq. 7.2-20 gives the scale factor. Comparison of Eq. 7.2-20 with the correlation of Eq. 7.2-1 shows close similarity. Both give the characteristic length as the length of the core. Eq. 7.2-20 also agrees with most other models of imbibition in making the fractional production, *f,* proportional to $\sqrt{time}$. The spread in pore size distributions may well make C_{spread} constant for related rock types (Berea sandstone, for example). It is, however, likely to be a function of S_{wi}. The major difference between the two equations is the way in which the viscosities of the two phases enter the functions. In Eq. 7.2-1 it is as the geometric mean and in Eq. 7.2-20 it is in the mobility factor *M* as a combination of relative permeabilities and viscosities plus the effect of C_{spread}. The above analysis is for 1-D linear imbibition. If the core is a cylinder sealed at each end, then the imbibition is radial and the area at the front now varies with position, complicating the analysis. Radial imbibition has been studied very recently by Standnes (2006) using a slightly different analysis of the problem. He compared his results with the predictions of Aronofsky *et al.* (1958).

Radial Countercurrent Imbibition

Radial inwards

For radial inwards imbibition the core sample is a cylinder with or without a central cylindrical hole, radius R_{closed}, and with both the ends of the core and the surface of the inner hole sealed. Imbibition is radial inwards towards the core axis from the outside of the cylinder. At time, *t,* the front has reached a position R_{f} (measured from the core axis) from its starting position at R_{open} (see Fig. 7.2-3). Again, by assuming that the core has a constant saturation behind the front, S_{wf}, the total radial flow inwards does not vary with distance behind the front.

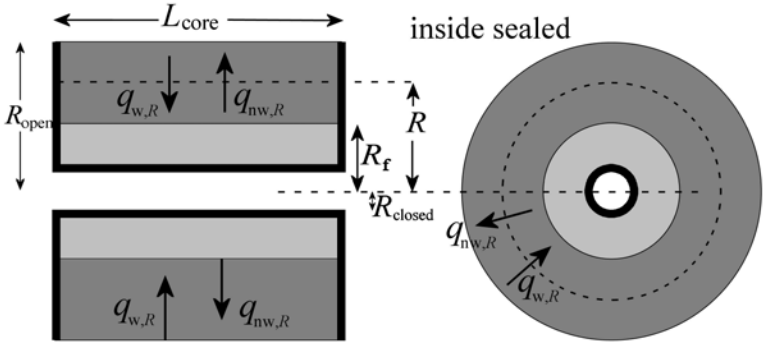

Fig. 7.2-3 Diagram of dimensions in radial imbibition. There is a sealed hole in the center of the core so that imbibition takes place from the outside moving in. The total radial flow is constant everywhere behind the front. Compared to linear imbibition, proportionally more of the core is near the open face.

For some general intermediate position, *R*, between the front and the outside of the core, Eq. 7.2-10 applies

$$q_{w,R} = KMA_R \frac{\partial P_c}{\partial x} \qquad 7.2\text{-}21$$

Unlike the linear case the area, A_R, is now a function of *R*. If the core length is L_{core} then the area A_R becomes $2\pi RL_{core}$ and ∂x becomes $-\partial R$. Hence

$$q_{w,R} = -KM\,2\pi RL_{core} \frac{\partial P_c}{\partial R} \qquad 7.2\text{-}22$$

As before $q_{w,R}$ is invariant (with *R*) and so Eq. 7.2-22 can be integrated to give

$$\ln \frac{R_f}{R_{open}} = -\frac{KM\,2\pi L_{core}\left(P_{cf} - P_{co}\right)}{q_{w,R}} \qquad 7.2\text{-}23$$

Again, the mass balance Eq. 7.2-11 gives the distance advanced by the front (-dR_f) in time d*t* in terms of $q_{w,R}$

$$\frac{dR_f}{dt} = -\frac{q_{w,R}}{2\pi R_f L_{core}\varphi\left(S_{wf} - S_{wi}\right)} \qquad 7.2\text{-}24$$

except that, unlike the linear case, the area A_R is not constant but is a function of R_f. Eliminating $q_{w,R}$ between Eq. 7.2-23 and Eq. 7.2-24 gives

$$\frac{R_f}{R_{open}} \ln \frac{R_f}{R_{open}} d\left(\frac{R_f}{R_{open}}\right) = \frac{1}{R_{open}^2} \frac{KM\left(P_{cf} - P_{co}\right)}{\varphi\left(S_{wf} - S_{wi}\right)} dt \qquad 7.2\text{-}25$$

Integration of Eq. 7.2-25 from $t = 0$, $R_f = R_{open}$ to (t, R_f) gives

$$1 + 2\left(\frac{R_f}{R_{open}}\right)^2 \ln \frac{R_f}{R_{open}} - \left(\frac{R_f}{R_{open}}\right)^2 = \frac{4}{R_{open}^2} \frac{KM\left(P_{cf} - P_{co}\right)}{\varphi\left(S_{wf} - S_{wi}\right)} t \qquad 7.2\text{-}26$$

Replacing the P_c's with *K*, φ, and C_{spread} as before using Eq. 7.2-17 gives,

$$1 + 2\left(\frac{R_f}{R_{open}}\right)^2 \ln \frac{R_f}{R_{open}} - \left(\frac{R_f}{R_{open}}\right)^2 = \frac{2}{R_{open}^2} \sqrt{\frac{2K}{\varphi}} \frac{C_{spread} M\sigma}{\left(S_{wf} - S_{wi}\right)} t \qquad 7.2\text{-}27$$

From basic geometry, the fraction of the total imbibition when the front is at R_f is

$$f = \frac{R_{\text{open}}^2 - R_{\text{f}}^2}{R_{\text{open}}^2 - R_{\text{closed}}^2} \qquad 7.2\text{-}28$$

giving

$$\left(\frac{R_{\text{f}}}{R_{\text{open}}}\right)^2 = 1 - f\left(1 - \left(\frac{R_{\text{closed}}}{R_{\text{open}}}\right)^2\right) \qquad 7.2\text{-}29$$

Thus, in terms of t and f

$$f - f\left(\frac{R_{\text{closed}}}{R_{\text{open}}}\right)^2 + \left(1 - f + f\left(\frac{R_{\text{closed}}}{R_{\text{open}}}\right)^2\right)\ln\left(1 - f + f\left(\frac{R_{\text{closed}}}{R_{\text{open}}}\right)^2\right) = \frac{2}{R_{\text{open}}^2}\sqrt{\frac{2K}{\varphi}}\frac{MC_{\text{spread}}\sigma}{\left(S_{\text{wf}} - S_{\text{wi}}\right)}t \qquad 7.2\text{-}30$$

The time taken for the front to reach the centre of the core $\left(R_{\text{f}} = R_{\text{closed}}\right)$ when imbibition stops, t_{end}, is

$$t_{\text{end}} = \frac{1}{2}\left(R_{\text{open}}^2 + 2R_{\text{closed}}^2 \ln\frac{R_{\text{closed}}}{R_{\text{open}}} - R_{\text{closed}}^2\right)\sqrt{\frac{\varphi}{2K}}\frac{\left(S_{\text{wf}} - S_{\text{wi}}\right)}{MC_{\text{spread}}\sigma} \qquad 7.2\text{-}31$$

The term to the left of the square root sign in Eq. 7.2-31 is the scale factor for radial inwards imbibition. The characteristic length given by Ma's equation for a solid cylinder of infinite length is $L_{\text{c}} = R_{\text{max}}/\sqrt{2}$ and agrees exactly with Eq. 7.2-31 when $R_{\text{closed}} = 0$. However, when the core has an inner circular hole, Ma's method for calculating the characteristic length gives

$$L_{\text{c,Ma}}^2 = \frac{\left(R_{\text{open}} - R_{\text{closed}}\right)^2}{2}\left(1 + \frac{R_{\text{closed}}}{R_{\text{open}}}\right) \qquad 7.2\text{-}32$$

Ruth *et al.* (2003*)* improved on this factor by compensating for situations where incremental volumes of the sample do not have the same sizes at different distances from the open face. If the Ruth factor is scaled relative to the Ruth linear function and is factorised, one obtains

$$L_{\text{c,Ruth}}^2 = \frac{\left(R_{\text{open}} - R_{\text{closed}}\right)^2}{3}\left(1 + 2\frac{R_{\text{closed}}}{R_{\text{open}}}\right) \qquad 7.2\text{-}33$$

The new factor in Eq. 7.2-31 (now called $L_{\text{c,Mason}}$ for short) not only compensates for incremental volumes being different at different distances (like Ruth's) but also compensates for the variation in resistance with distance between the incremental volume and the open face to give:

$$L_{\text{c,Mason}}^2 = \frac{1}{2}\left(R_{\text{open}}^2 + 2R_{\text{closed}}^2 \ln\frac{R_{\text{closed}}}{R_{\text{open}}} - R_{\text{closed}}^2\right) \qquad 7.2\text{-}34$$

Note that all three scale factors agree when R_{closed} is almost equal to R_{open} so that L_{c} equals $R_{\text{open}} - R_{\text{closed}}$. This is not surprising because this geometry is a thin laminar sheet in which imbibition is linear and the radial geometry has no effect.

Radial outwards

The situation of radial outwards imbibition is shown in Fig. 7.2-4. The equation governing flow is the same as Eq. 7.2-23 because of the way R_{closed} and R_{open} have been defined.

$$\ln\frac{R_{\text{f}}}{R_{\text{open}}} = -\frac{KM\,2\pi L_{\text{core}}\left(P_{\text{cf}} - P_{\text{co}}\right)}{q_{\text{w},R}} \qquad 7.2\text{-}35$$

The analysis is as before with $q_{\text{w},R}$ being invariant with R. Its elimination, followed by integration from $t = 0$, $R_{\text{f}} = R_{\text{open}}$ to (t, R_{f}) and replacement of the P_{c}'s with K, φ, and C_{spread}, gives exactly the same equation as Eq. 7.2-27. Even the equation for the fraction of imbibition, f, is unchanged. It follows that the equation for the time taken for the front to reach the closed boundary, t_{end}, is also unchanged as is the scale factor, L_{c}^2. Numerically the times and scale factors between radial inwards and radial outwards imbibition will differ because R_{open} and R_{closed} are different. The basic equations, however, are the same. The aspect factor will be defined as $R_{\text{closed}} / R_{\text{open}}$.

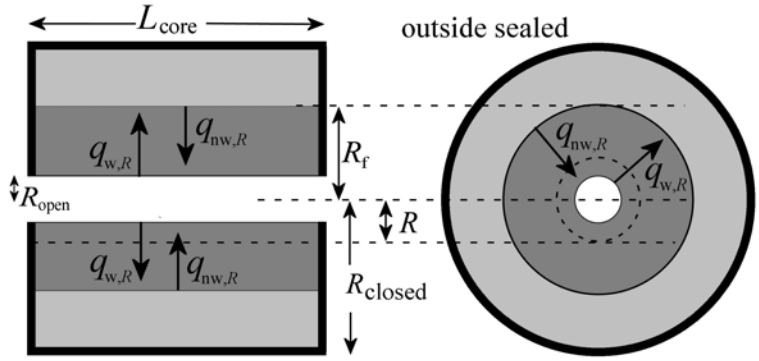

Fig. 7.2-4. Diagram showing the variables for a cylindrical core sealed on the outside with counter-current imbibition occurring from a cylindrical central hole. Compared to linear imbibition, proportionally more of the core is further from the open face.

Simultaneous inward and outward imbibition

A fairly simple geometry for which experiments can be readily performed is a cylindrical core with a central axial hole and with both flat ends sealed. Such a geometry exhibits simultaneous outward imbibition from the central hole and inwards imbibition from the outer surface. It is difficult to predict the scale factors using the Ma and Ruth methods because the required position of the no-flow boundary is not obvious. However, if there is frontal imbibition, then the no-flow boundary is where imbibition ceases at the time t_{end}. This is where the two scale factors (one inward, one outward) are equal. The end point and associated no-flow boundary are thus

connected by the scale factors. Consequently, if R_{nf} is the radius at this no-flow boundary then, at the end of imbibition, R_{nf} is the same for the radial inwards front and the radial outwards front. If R_{outer} and R_{inner} are the two core boundary radii then, for the Ma function, Eq. 7.2-32 gives

$$L_{c,Ma}^2 = \frac{\left(R_{outer} - R_{nf}\right)^2}{2}\left(1 + \frac{R_{nf}}{R_{outer}}\right) = \frac{\left(R_{inner} - R_{nf}\right)^2}{2}\left(1 + \frac{R_{nf}}{R_{inner}}\right) \qquad 7.2\text{-}36$$

A similar equation can be written for the Ruth function, Eq. 7.2-31 and for the Mason function, Eq. 7.2-34. The Ma and Ruth functions both give cubics for R_{nf} but the Mason function gives an analytic expression for the final position of the no-flow boundary

$$R_{nf}^2 = \frac{\left(R_{outer}^2 - R_{inner}^2\right)}{\ln\left(\frac{R_{outer}^2}{R_{inner}^2}\right)} \qquad 7.2\text{-}37$$

The scale factor can be calculated by substituting R_{nf} for R_{closed} in Eq. 7.2-34. Predicting the production *vs* time curve is less straightforward because the positions of the two fronts at a particular time are needed. If R_{nf} is known, then Eq. 7.2-30 can be used to find the imbibition volumes for radial inward and radial outward imbibition. No analytic solution for the positions of the two fronts is possible and so numerical solutions are required.

Properties of the radial scale factors

Equations 7.2-30, 7.2-31, and 7.2-32 give the scale factors for the Ma, Ruth and the current analysis. They are all slightly different and only agree when the hole is virtually the same diameter as the core and imbibition becomes essentially linear. For the radial inwards situation a comparison of the various functions can be made in different ways. Figure 7.2-5 shows the scale factors plotted against the aspect factor, R_{closed}/R_{open}, of the hole in the cylinder and with a cylinder diameter of unity. Considering their different functional form, the Ma and Mason functions are surprisingly close.

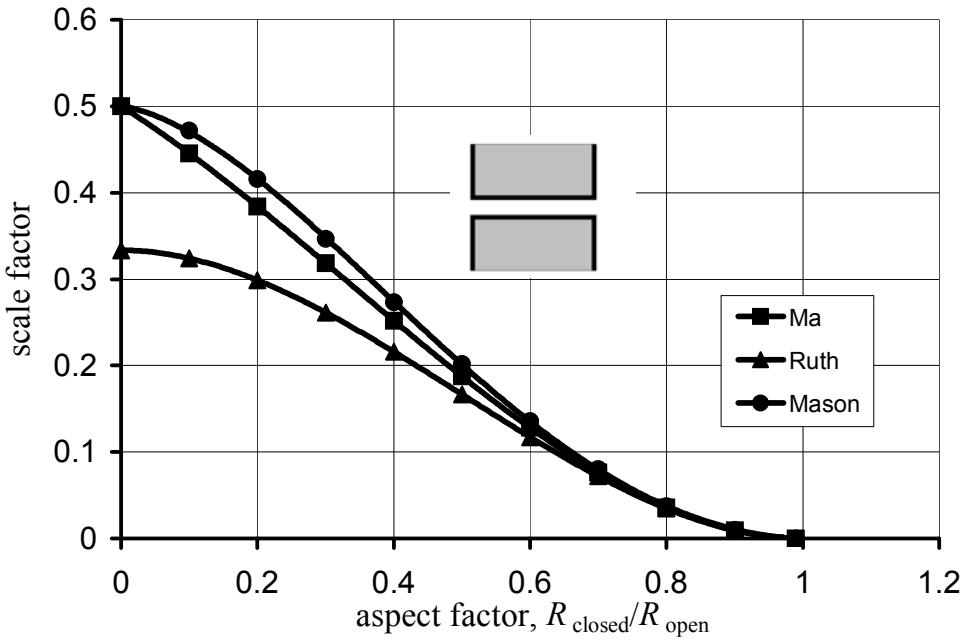

Fig. 7.2-5. Comparison of the scale factors calculated using the Ma, Ruth and present (Mason) functions for radial-inwards imbibition. Note that all three start at the same values when R_{closed} is almost equal to R_{open} which approximates to the linear situation.

Scale factors can be normalised with respect to the square of the distance from the open face to the no-flow boundary, $(R_{open} - R_{closed})^2$, see Fig. 7.2-6. Linear imbibition scaled in the same way has a normalised scale factor of unity.

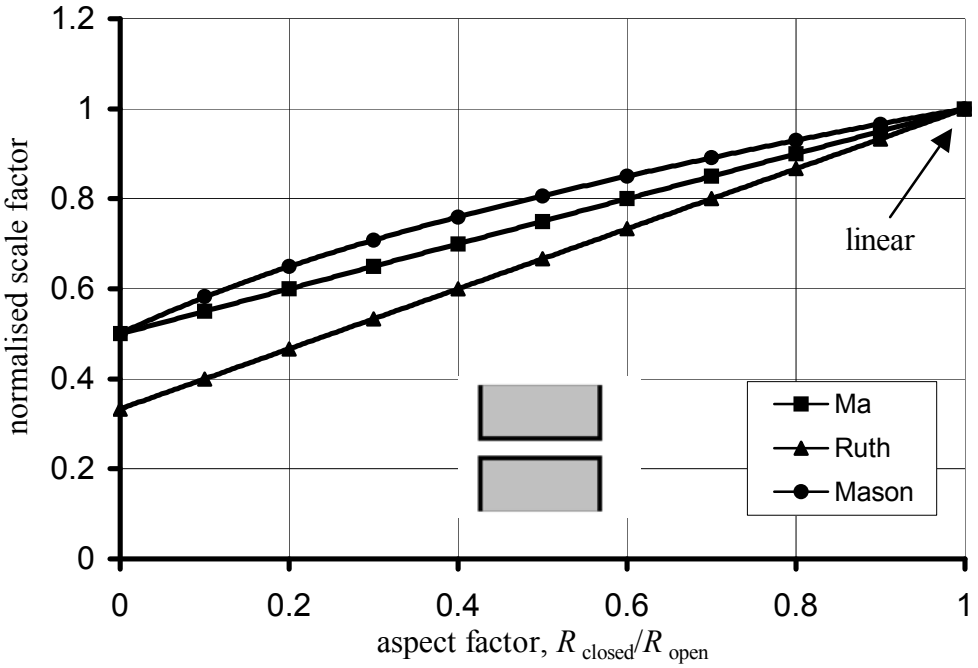

Fig. 7.2-6 The normalised scale factor is obtained by dividing the scale factor by the square of the distance from the open boundary to the closed boundary.

Compared to linear imbibition for equivalent distances (L_{max} in one case, $(R_{open} - R_{closed})$ in the other), radial inward imbibition is always faster and, for the solid cylinder is predicted by the Ma and Mason functions to take half of the time. There are two reasons. One is that there is less volume swept and the other is that proportionally more of the core is nearer the open face in the radial situation. The volume to be filled tends to zero as the axis of the core is approached by the front, whereas in linear imbibition there is no change in pore volume with position as the front approaches the end of the core.

For the radial outwards situation the scale factors become infinite as the radius of the hole in the center of the core goes to zero. Consequently we restrict ourselves to practical ratios. Normalised scale factors for radial outwards imbibition are shown in Fig. 7.2-7. It can be seen from Fig. 7.2-7 that the three scale factors begin to differ significantly once the aspect factor (R_{closed}/R_{open}) goes much above 2.

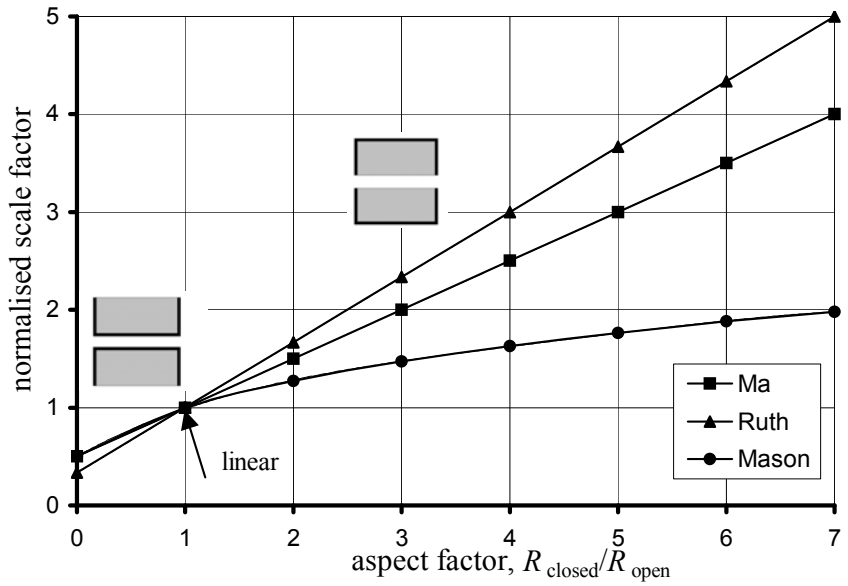

Fig. 7.2-7. Radial imbibition outwards is where the aspect factor is greater than unity.

Variation of production with time

The previous section has described the calculation of an overall core shape factor based on the assumption of piston-like displacement with the shape factor being given by the time, t_{end}, taken for the front to reach the no-flow boundary. Because the front position does not depend on the location of the no-flow boundary until it actually reaches it (i.e. before t_{end}), it follows that the first part of the production *vs* time curve is independent of the position of the no-flow boundary location. It is the shape factor that is determined by the location of the no-flow boundary. The production *vs* time curve is determined by intermediate positions of the front. For radial imbibition and a fractional production, *f*, the value of R_{f} is given by Eq. 7.2-28, or explicitly

$$R_{\text{f}}^2 = R_{\text{open}}^2 - f\left(R_{\text{open}}^2 - R_{\text{closed}}^2\right) \qquad 7.2\text{-}37$$

Substitution of R_{f} into Eq. 7.2-27, also 7.2-38 gives the time, $t_{f,\text{Mason}}$, for fractional production, *f*,

$$t_{f,\text{Mason}} = \frac{1}{2}\sqrt{\frac{\varphi}{2K}}\frac{\left(S_{\text{wf}} - S_{\text{wi}}\right)}{C_{\text{spread}} M\sigma}\left(R_{\text{open}}^2 + 2R_{\text{f}}^2 \ln\frac{R_{\text{f}}}{R_{\text{open}}} - R_{\text{f}}^2\right) \qquad 7.2\text{-}38$$

The time t_{end} is where R_{f} equals R_{closed}. Different core geometries produce different shaped production *vs* time curves. For example, Eq.7.2-19 predicts the production *vs* time function for linear imbibition and Eq. 7.2-37 and Eq. 7.2-38 apply to radial imbibition. Radial and linear imbibition are compared on Fig. 7.2-8 using the conventional $\log_{10} t$ on the *x*-axis. Although one curve is displaced relative to the other, the actual shapes look very similar when plotted in this way. The difference in shape between radial and linear imbibition production can be emphasised if, for the same *f*, each time is normalised with respect to its own t_{end}.

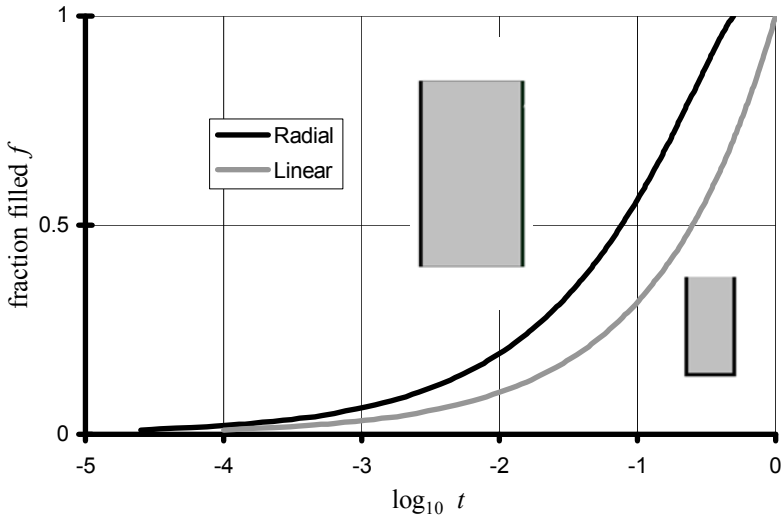

Fig. 7.2-8 Comparison of linear and radial inwards imbibition. The fraction imbibed is plotted *vs* $\log_{10} t$. The length of the core in linear imbibition and the radius of the core in radial imbibition were set to unity to make the distance traveled the same in both geometries. The factor $\sqrt{\frac{2K}{\phi}}\frac{MC_{\text{spread}}}{(S_{\text{wf}}-S_{\text{wi}})}$ has also been set at 1. No adjustment for the different characteristic lengths has been made and so the time when imbibition is completed (t_{end}) for radial imbibition is half that for linear imbibition. These curves have very similar shape, but they are not identical.

A similar analysis can be followed using the Ma and Ruth scale factors and the entire production *vs* time curve can be predicted. Different aspect ratio cores can be considered with imbibition radial inwards or radial outwards and for all three functions (Ma, Ruth, Mason). There are clearly a large number of possible comparisons. However, it is known from past experiments that the shapes of counter-current imbibition production curves are similar, especially when plotted on a $\log_{10} t$ scale (see Fig. 7.2-8). In fact, although they look very different mathematically, the three functions (Ma, Ruth, Mason) give very similar production curves for most practical situations. To show differences one needs to go to unusual core geometries, for example a core with a central cylindrical hole with a diameter of 0.2 times the core diameter. If sealed on the inside and both ends, this geometry gives radial inwards imbibition with an aspect factor ($R_{\text{closed}}/\text{R}_{\text{open}}$) of 0.2. If sealed on the outside and both ends, the geometry is radial outwards with an aspect factor of 5. For the same distance travelled by the front, radial inwards imbibition goes faster than linear imbibition and radial outwards imbibition goes slower. To allow comparison of the shapes of the different production curves, one can normalise by the respective time at which each imbibition is completed, t_{end}. Another benefit of plotting the fraction imbibed *vs* $\sqrt{t/t_{\text{end}}}$ is that it makes the linear imbibition production curve a straight line. Figure 7.2-9 shows the production curves for a core with a central hole 0.2 times the core diameter for radial inwards, radial outwards and linear imbibition. All three functions agree fairly closely with the Mason function being closest to the two outer limits of the other functions.

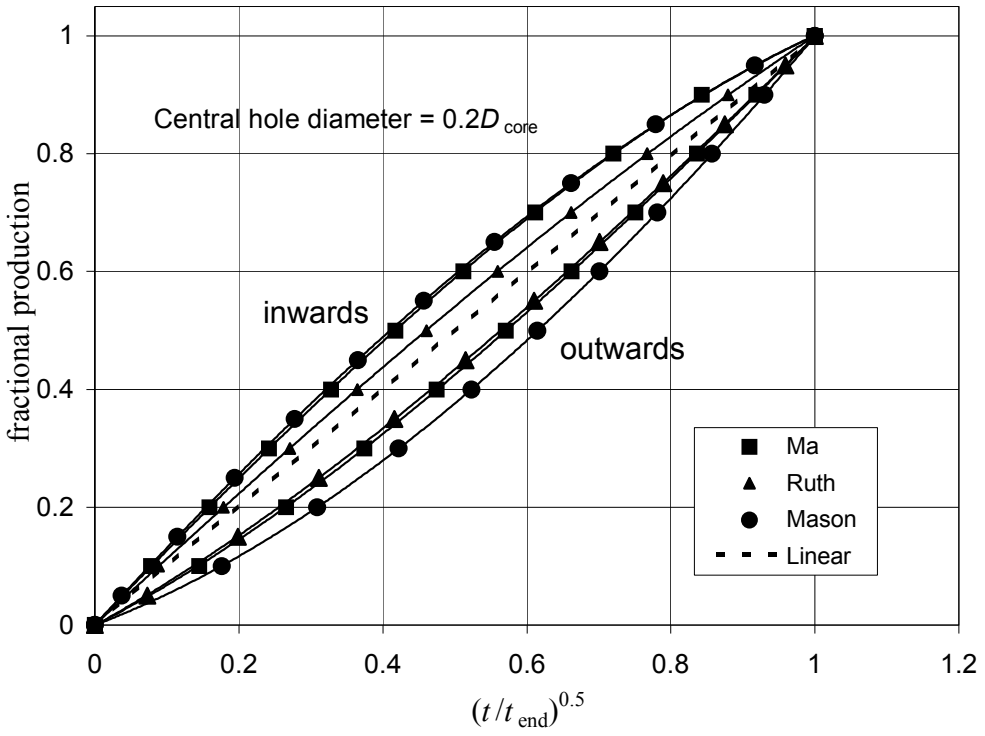

Fig. 7.2-9 Comparison of the three functions for radial inwards, aspect factor (R_{closed}/R_{open}) of 0.2 (the three left hand curves) and radial outwards, aspect factor of 5 (the three right hand curves) for a core with an axial hole diameter of 0.2 times the outer core diameter. Note that all of the curves are similar and, when plotted in this way, are almost linear. For inwards imbibition the Ma and Mason functions are almost coincident. For outwards imbibition the Ma and Ruth functions are almost coincident.

Experimental

Experiments

Countercurrent spontaneous imbibition experiments were carried out on a series of cylindrical matched Berea Cx sandstone cores which had been cut to have different diameter holes in the center and which had different faces sealed with epoxy resin so that imbibition would be linear, radial inwards or radial outwards, or both. The aims were to find out if any differences in the shapes of the production *vs* time curves could be detected and how the scale factor, L_c^2, varied with the dimensions. This rock is characterised by a very narrow air permeability range close to 70 md.

TABLE 7.2-1. CORE PROPERTIES

Linear –One End Open

Core No.	Length (cm)	Outer dia (cm)	Inner dia (cm)	Aspect ratio $\frac{R_{inner}}{R_{outer}}$	Aspect factor $\frac{L_{nf}}{L_{open}}$	Initial volume oil (mL)	Porosity
C4-9	6.50	5.13	0	0	1	21.99	0.163
C4-8	6.62	5.13	0	0	1	23.59	0.172
C4-12	6.47	5.13	1.03	0.204	1	20.20	0.157
C-1	5.90	5.07	2.23	0.440	1	15.37	0.160
C1-25	5.97	5.07	3.01	0.593	1	12.48	0.159
C1-24	5.72	5.07	4.16	0.821	1	5.55	0.148
C1-25	5.93	5.07	4.15	0.818	1	5.47	0.138

Linear –Both Ends Open

Core No.	Length (cm)	Outer dia (cm)	Inner dia (cm)	Aspect ratio $\frac{R_{inner}}{R_{outer}}$	Aspect factor $\frac{L_{nf}}{L_{open}}$	Initial volume oil (mL)	Porosity
C4-5	6.50	5.13	0	0	1	22.45	0.167
C1-25	6.32	3.48	0	0	1	9.50	0.158
C4-11A	6.58	5.13	1.03	0.201	1	21.23	0.163
C-5	5.88	5.06	2.22	0.439	1	15.67	0.164
C4-4	6.55	5.13	2.19	0.427	1	16.44	0.148
C-7	5.92	5.07	3.02	0.595	1	12.69	0.164
C4-6	6.10	5.12	3.01	0.588	1	12.90	0.157
C1-26	5.99	5.06	4.15	0.819	1	6.27	0.157
C-9	6.13	5.07	4.15	0.818	1	6.03	0.147

Radial Inwards

Core No.	Length (cm)	Outer dia (cm)	Inner dia (cm)	Aspect ratio $\frac{R_{inner}}{R_{outer}}$	Aspect factor $\frac{R_{closed}}{R_{open}}$	Initial volume oil (mL)	Porosity
C4-10	6.57	5.13	0	0	0	23.10	0.170
C4-11	6.50	5.13	1.02	0.199	0.199	21.86	0.169
C-8	5.88	5.06	2.23	0.440	0.440	16.13	0.169
C4-14	6.15	5.13	3.00	0.585	0.585	13.61	0.163
C1-28	5.88	5.07	4.14	0.816	0.816	6.52	0.164

Radial Outwards

Core No.	Length (cm)	Outer dia (cm)	Inner dia (cm)	Aspect ratio $\frac{R_{inner}}{R_{outer}}$	Aspect factor $\frac{R_{closed}}{R_{open}}$	Initial volume oil (mL)	Porosity
C4-13A	6.53	5.14	1.02	0.199	5.04	21.38	0.165
C4-1	6.41	5.13	2.25	0.440	2.28	17.53	0.163
C1-21	6.20	5.07	3.02	0.585	1.68	13.16	0.162
C1-22	5.71	5.07	4.16	0.816	1.22	6.36	0.167

Radial Inwards and Outwards

Core No.	Length (cm)	Outer dia (cm)	Inner dia (cm)	Aspect ratio $\frac{R_{inner}}{R_{outer}}$	Aspect factor $\frac{R_{nf}}{R_{open}}$ outer inner	Initial volume oil (mL)	Porosity
C4-10	6.57	5.13	0	0	0	23.10	0.170
C4-13	6.56	5.13	1.01	0.2	0.543 2.760	22.84	0.175
C-2	6.09	5.06	2.22	0.44	0.699 1.596	16.75	0.169
C-11	5.73	5.07	3.01	0.59	0.788 1.326	12.89	0.173
C1-19	6.22	5.07	4.13	0.81	0.905 1.111	7.45	0.176

After the cores were cut, they were dried, evacuated and completely filled with oil. Their porosity was calculated from the weight difference between the empty and oil-filled states. Oil recovery *vs* time was measured in standard glass imbibition cells at ambient temperature. The oil was Soltrol 220, cleaned by passage through alumina and silica gel, and had a viscosity of 3.996 cp. The invading phase was brine with a viscosity of 1.147 cp. The interfacial tension was 45.2 dynes/cm. Linear imbibition was conducted with cores filled with oil and sealed over all faces except one end. The data is shown in Figure 7.2-10. Different maximum volumes of brine are imbibed because some cores had large holes in them. Also the cores did not have identical length.

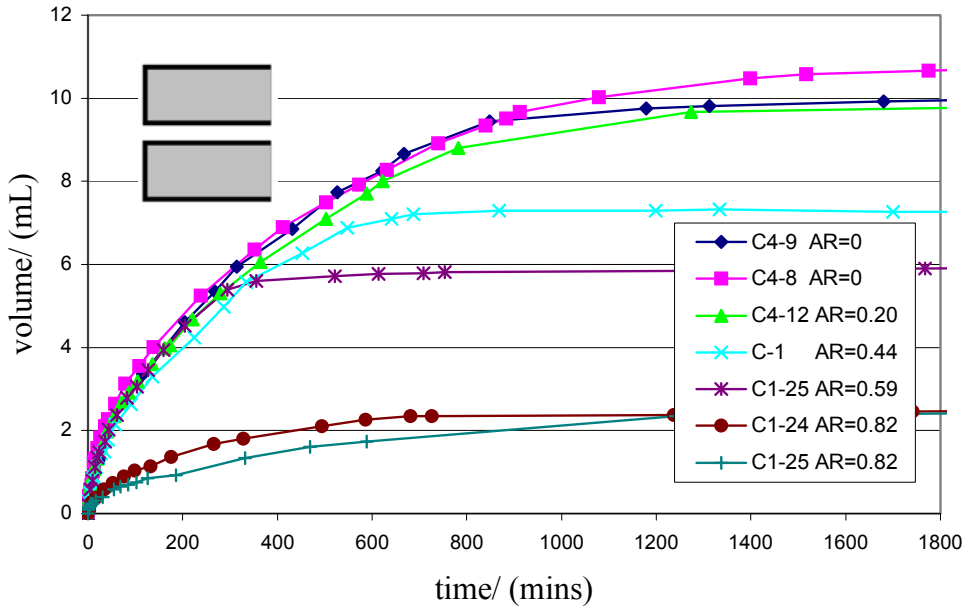

Fig. 7.2-10 Imbibition volume vs time results for linear (one-end-open) counter-current imbibition into cylindrical cores with sealed axial holes. The cores have different pore volumes because they have holes in the middle and are of slightly different lengths.

Similar experiments were performed on cores sealed on the inside and outside but with both ends open. Imbibition thus took place from both ends simultaneously. The results are shown in Fig. 7.2-11.

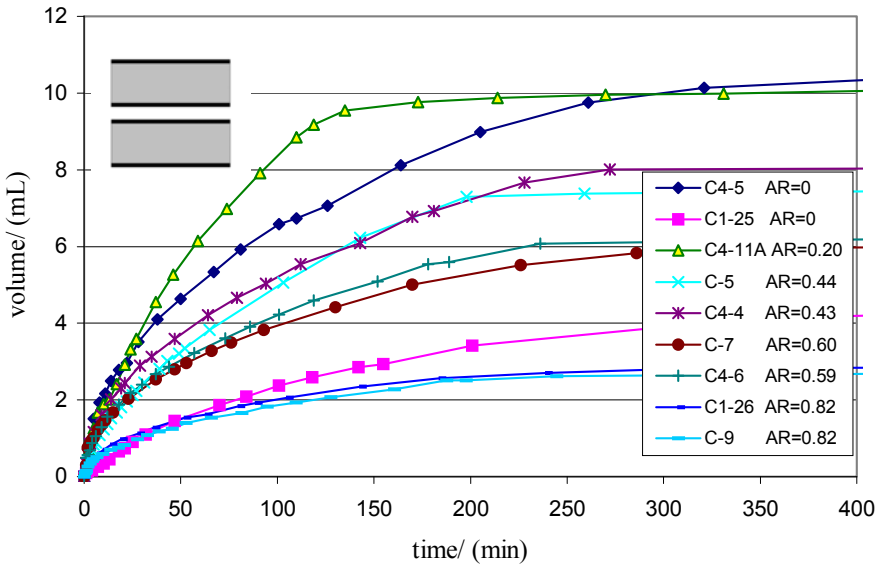

Fig. 7.2-11 Imbibition volume vs time for linear imbibition into cores with both ends open. Note that imbibition is much faster than with only one end open (compare with Fig. 7.2-10).

There were three radial boundary conditions. If the only face left open is the outer one, then imbibition is radial inwards. If the inner face is the only face open, then imbibition is radial outwards. If both faces are open there is combined inwards and outwards radial imbibition. Results for radial inwards are shown in Figure 7.2-12. If the core properties were identical, then the initial production curves for radial inwards imbibition should all fall on the same curve. This is because all of the cores have almost the same open face dimension and the position of the closed boundary cannot affect the front until the front reaches it. It can be seen that the production curves do all start together, although when the aspect ratio is 0.82 the production curve soon starts to fall off.

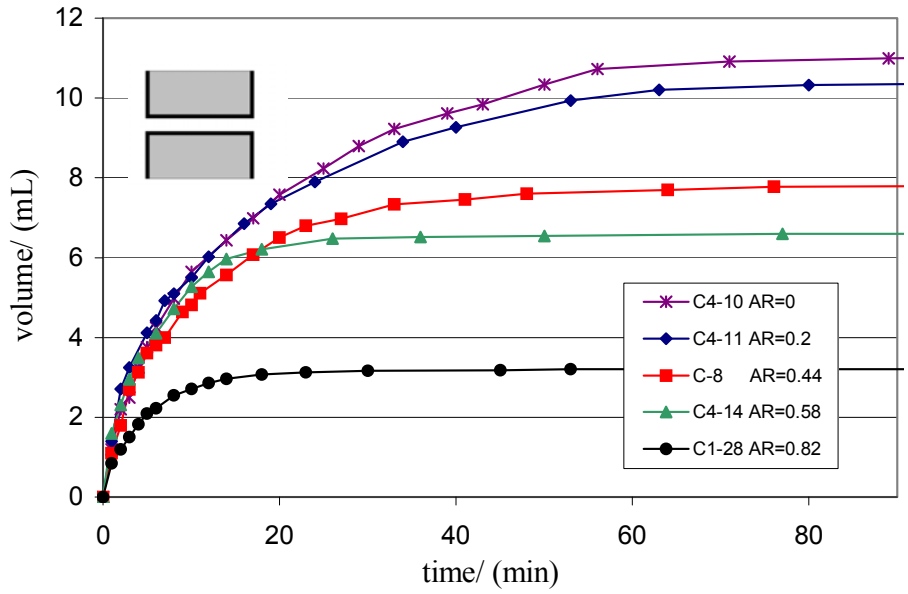

Fig. 7.2-12 Production volume vs time for radial inwards imbibition into cores with all faces except the outer surface sealed.

Results for radial outwards imbibition are shown in Figure 7.2-13. Because the cores all had the same outer diameter but had different diameter holes cut along the axis, the radius of the open face was now different from core to core. Consequently the production curves should have significantly different shapes. It can be seen that this is actually the case and imbibition from a small radius hole outwards is almost linear. The reason is that most of the viscous pressure drop occurs close to the inner open boundary and so the front position makes little difference to the production rate.

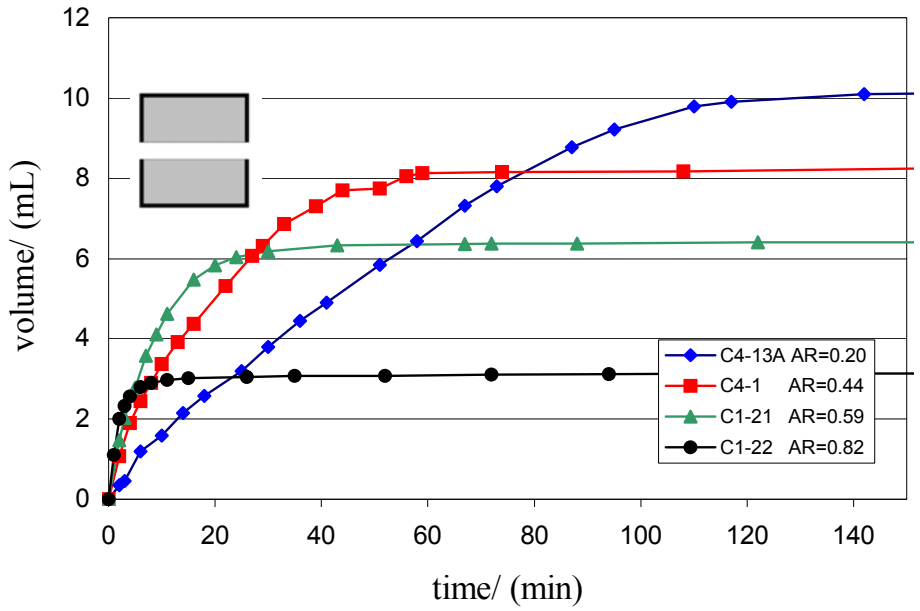

Fig. 7.2-13 Production volume vs time results for imbibition into cores with all faces except the surface of the axial hole in the core sealed. Note that for the core with the smallest axial hole, the production volume varies almost linearly with time.

Results for simultaneous radial inwards and outwards imbibition are shown in Fig. 7.2-14. Note that, as would be expected, the time taken for imbibition to be completed is much shorter.

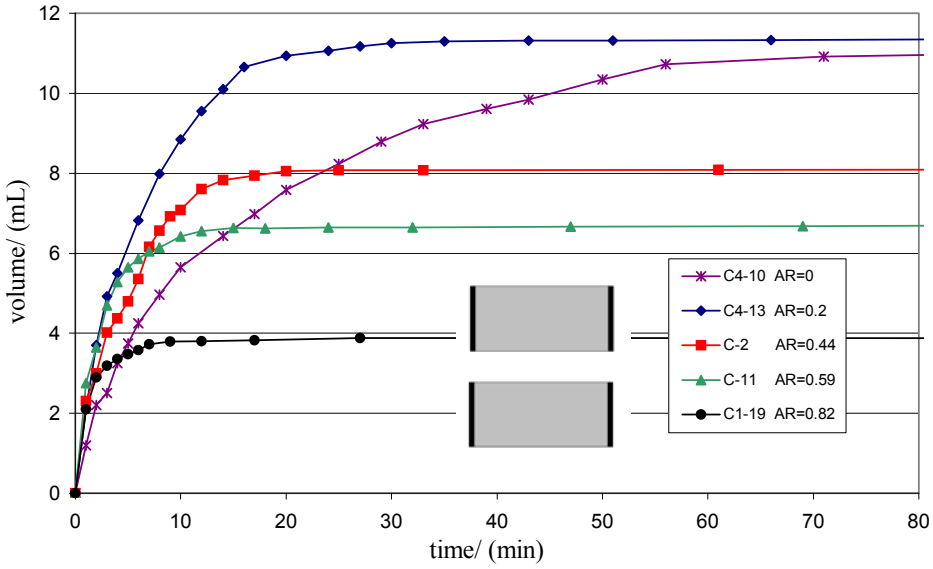

Fig. 7.2-14 Production volume vs time results for cores with both ends closed. When imbibition takes place from both the inside hole and the outside surface imbibition is much faster. The exception is C4-10 which has no central hole.

Interpretation of experimental results.
The experimental results need to be compared with the predictions of the theory. There are two main questions; the first is whether or not the theory can match the *shape* of the production *vs* time curves. The second is whether the common physical properties factor of the rock-oil-brine system calculated from the production *vs* time curves are *consistent* between the linear, radial inwards and radial outwards experiments. Testing whether or not the experiments can be matched by theory can be done in several ways. Here, the variables are linearised so that a good match of *shape* will be indicated by a straight line plot. *Consistency* of the physical properties factor will be indicated the straight lines from all of the imbibition experiments having the same gradient.

Matching the shapes of the production vs time curves
Fractional production can be determined for every experiment. This fraction can be inserted into the relevant functions relating time to fractional production (Eq. 7.2-37 and Eq. 7.2-38) and a time (multiplied by a constant factor) determined. Let this time calculated from *f* be t_f. The variable t_f is an experimental quantity calculated from the fractional production.
For linear imbibition Eq. 7.2-18 rearranges into

$$t_{f,\text{Linear, Mason}} = \sqrt{\frac{\varphi}{2K}} \frac{\left(S_{\text{wf}} - S_{\text{wi}}\right)}{MC_{\text{spread}}\sigma} L_{\max}^2 f^2 \qquad 7.2\text{-}39$$

and for the Ma-Ruth function

$$t_{f,\text{Linear,Ma}} = C_{\text{Ma}} \sqrt{\frac{\varphi}{K}} \frac{\sqrt{\mu_{\text{w}}}\mu_{\text{nw}}}{\sigma} L_{\max}^2 f^2 \qquad 7.2\text{-}40$$

where C_{Ma} is a constant. Let the physical properties factors be

$$G_{\text{Mason}} = \sqrt{\frac{\varphi}{2K}} \frac{\left(S_{\text{wf}} - S_{\text{wi}}\right)}{MC_{\text{spread}}\sigma} \qquad 7.2\text{-}41$$

and

$$G_{\text{Ma}} = C_{\text{Ma}} \sqrt{\frac{\varphi}{K}} \frac{\sqrt{\mu_{\text{w}}}\mu_{\text{nw}}}{\sigma} \qquad 7.2\text{-}42$$

As functions of *f,* Eq. 7.2-39 and Eq. 7.2-40 differ only by the constants G_{Mason} and G_{Ma}. Both Equations 7.2-39 and 7.2-40 predict that the fractional production during linear imbibition varies as the square root of time. This is not surprising because the driving pressures are constant but the resistances to flow vary as the distance that the front has advanced. In Eq. 7.2-39 and Eq. 7.2-40 the core length is a parameter and this is best incorporated with *f*. Thus a plot of $L_{\max}^2 f^2$ versus the actual time for the fractional production *f* should be a straight line. Actually, because the production varies as the square root of time, it is better to take the square root of both axis variables because this spreads out the experimental points better. We thus have

$$L_{\max} f = \frac{\sqrt{t_{f,\text{Linear, Mason}}}}{\sqrt{G_{\text{Mason}}}} \qquad 7.2\text{-}43$$

and

$$L_{\max} f = \frac{\sqrt{t_{f,\text{Linear, Ma}}}}{\sqrt{G_{\text{Ma}}}} \qquad 7.2\text{-}44$$

The *y*-axis is proportional to the oil produced. Results showing $L_{\max} f$ plotted against the square root of the experimental time are shown in Fig. 7.2-15.

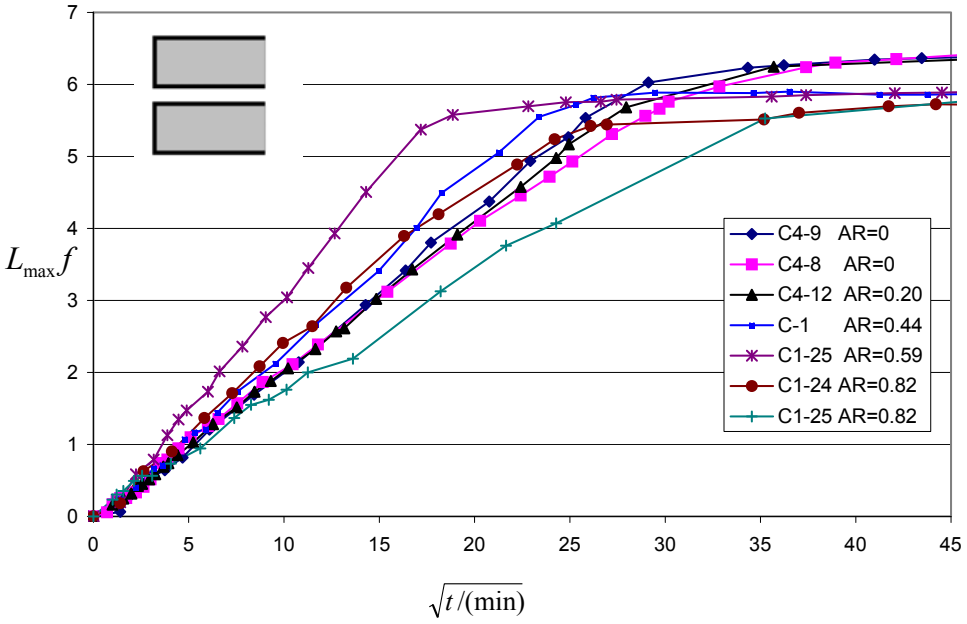

Fig. 7.2-15 Experimental results for linear imbibition plotted as $L_{\max} f$ *vs* the square root of the experimental time. The straight lines for the initial parts of the curves are predicted by the theory. If all of the cores had identical properties, all the curves should fall on the same straight line. The greatest deviations from the average slope are for cores which are near to a shell (aspect ratio 0.59 and 0.82) possibly because of the limited volume and limited area open to the invading phase.

Figure 7.2-16 shows the results for linear imbibition with both ends open plotted in the same format but with the *y*-axis plotted as $L_{\max} f/2$ to allow for the effective length of the cores being halved. Again, the plots are all straight lines. However, although the majority of the gradients are the same, the one for C4-11A is significantly different. There are two open faces for these cores and imbibition production can sometimes be predominantly from one face. The equations for flow indicate that, ahead of the front, there is a constant pressure in the non-wetting phase. This dead-end pressure drives the non-wetting phase back through the wetting phase and overcomes the capillary back (bubble) pressure at the open face. When there are two open faces it may be that the capillary back pressures at the open faces are not equal or, because of inhomogeneity in the core, the permeability may not be evenly distributed. In both of these cases the rate of frontal advance will not be symmetric between the core ends. The production should still vary linearly with the square root of time, but the gradient will be different.

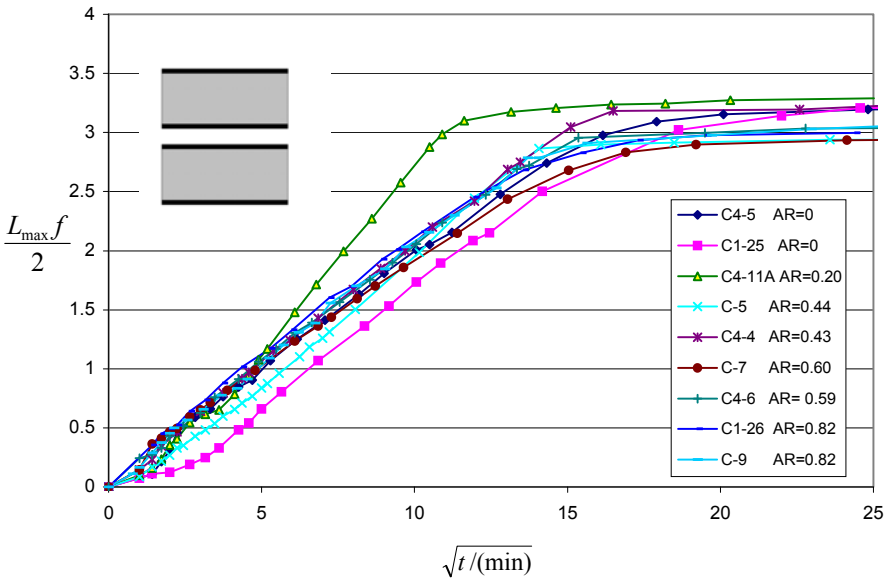

Fig. 7.2-16 Results for linear imbibition with both ends open plotted as $L_{\max} f/2$ *vs* the square root of the measured time. The scale factor allowing for the different effective length has been incorporated and so ideally the gradients of these functions should be the same as in Fig. 7.2-15. All of the analyses (Ma, Ruth and Mason) predict that these functions should be straight lines.

The same general method can be followed for radial imbibition. Now, however, the Ma, Ruth and Mason functions give different predictions. Eq. 7.2-37, gives R_f as a function of f

$$R_{\mathrm{f}}^2 = R_{\mathrm{open}}^2 - f\left(R_{\mathrm{open}}^2 - R_{\mathrm{closed}}^2\right) \quad 7.7$$

Then

$$t_{f,\mathrm{Ma}} = C_{\mathrm{Ma}} \sqrt{\frac{\phi}{K}} \frac{\sqrt{\mu_{\mathrm{w}}}\,\mu_{\mathrm{nw}}}{\sigma} \frac{\left(R_{\mathrm{open}} - R_{\mathrm{f}}\right)^2}{2} \left(1 + \frac{R_{\mathrm{f}}}{R_{\mathrm{open}}}\right) \quad 7.2\text{-}45$$

$$t_{f,\mathrm{Ruth}} = C_{\mathrm{Ma}} \sqrt{\frac{\phi}{K}} \frac{\sqrt{\mu_{\mathrm{w}}}\,\mu_{\mathrm{nw}}}{\sigma} \frac{\left(R_{\mathrm{open}} - R_{\mathrm{f}}\right)^2}{3} \left(1 + 2\frac{R_{\mathrm{f}}}{R_{\mathrm{open}}}\right) \quad 7.2\text{-}46$$

and

$$t_{f,\mathrm{Mason}} = \sqrt{\frac{\phi}{2K}} \frac{\left(S_{\mathrm{wf}} - S_{\mathrm{wi}}\right)}{C_{\mathrm{spread}} M \sigma} \frac{1}{2} \left(R_{\mathrm{open}}^2 + 2R_f^2 \ln \frac{R_{\mathrm{f}}}{R_{\mathrm{open}}} - R_{\mathrm{f}}^2 \right) \quad 7.2\text{-}47$$

If we define

$$F_{f,\mathrm{Ma}}^2 = \frac{\left(R_{\mathrm{open}} - R_{\mathrm{f}}\right)^2}{2} \left(1 + \frac{R_{\mathrm{f}}}{R_{\mathrm{open}}}\right) \quad 7.2\text{-}48$$

$$F_{f,\mathrm{Ruth}}^2 = \frac{\left(R_{\mathrm{open}} - R_{\mathrm{f}}\right)^2}{3} \left(1 + 2\frac{R_{\mathrm{f}}}{R_{\mathrm{open}}}\right) \quad 7.2\text{-}49$$

$$F_{f,\text{Mason}}^2 = \frac{1}{2}\left(R_{\text{open}}^2 + 2R_{\text{f}}^2 \ln\frac{R_{\text{f}}}{R_{\text{open}}} - R_{\text{f}}^2 \right) \qquad 7.2\text{-}50$$

then the squares of these F factors are proportional to the appropriate times ($t_{f,\text{Ma}}$, $t_{f,\text{Ruth}}$, $t_{f,\text{Mason}}$) *via* Eq.7.2-44. Thus plotting the squares of the F factors against the actual experimental times for the same fractional production, f, should give straight lines through the origin. Again, to spread out the data points approximately with the volume of oil produced, it is better to plot the square roots of both axis variables. The results should still be straight lines.

Figure 7.2-17 shows the results for radial inwards imbibition. In order to generate these plots, the experimental fractional productions, f, were used in Eq. 7.2-44 to determine a series of R_{f}'s. Then these value of R_{f} were used to calculate the three values of F_f using Eq. 7.2-48 to Eq. 7.2-50. The x-axis is the time associated with the fractional production. All of the plots until late time are close to linear. At short and even medium times there is not much to choose between the three functions. However, at longer times the differences are significant, especially for the low aspect ratio cores. Because the Mason factor is linear for the longest times for the low aspect ratio core, it is marginally the best.

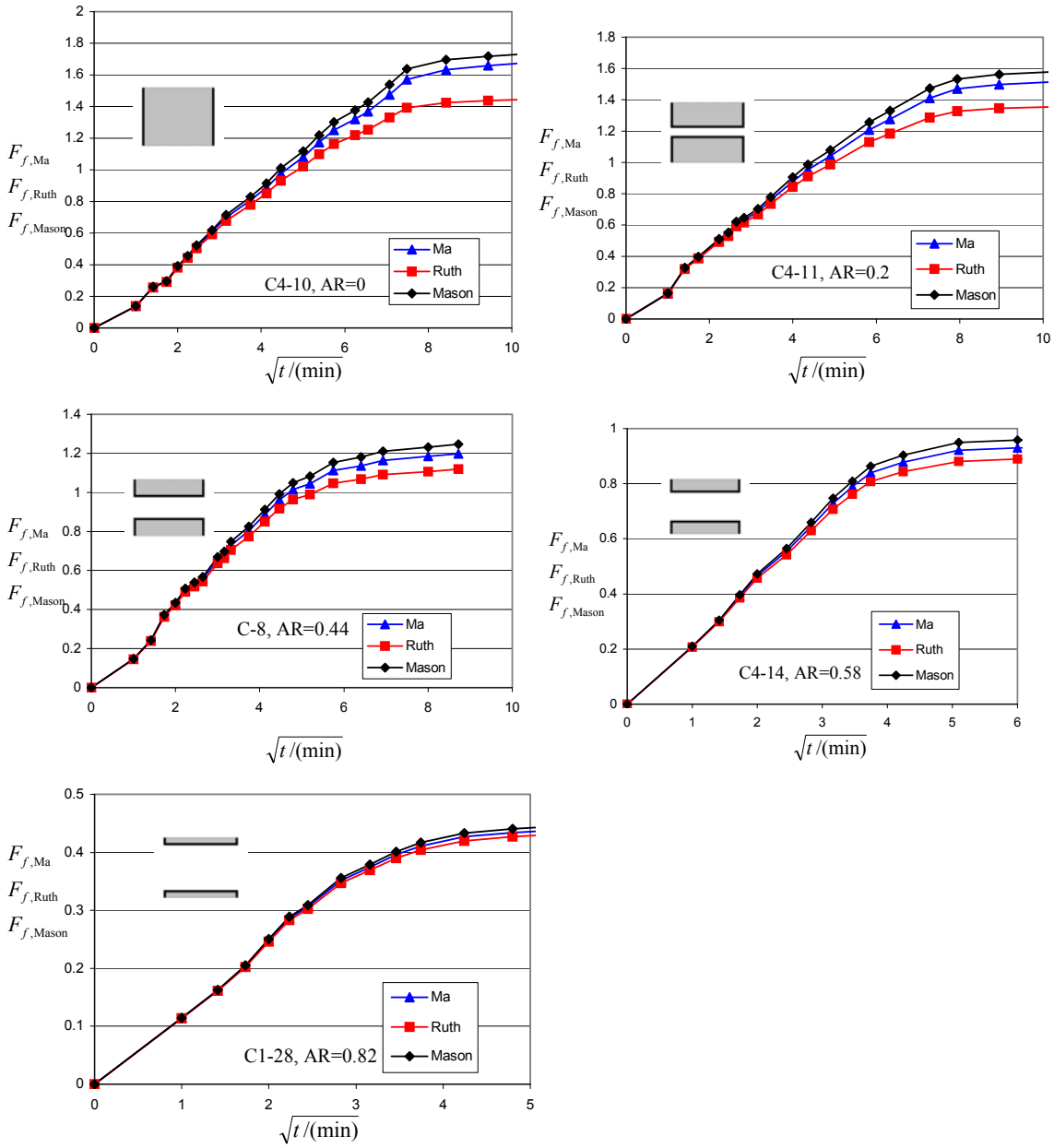

Fig. 7.2-17 Comparison of the three functions calculated from the fractional production for radial inwards imbibition for cores with five different aspect ratios. The gradients are all similar and close to the gradients for linear imbibition in Figs 7.2-15 and 16. The Mason function is closest to linearity. Only the gradient for imbibition with an aspect ratio of 0.82 differs significantly, it being too low by a factor of about 2. Because it is a thin shell (it was about 5mm thick) the leading part of the imbibition front may reach the closed boundary before the front is fully developed.

Figure 7.2-18 shows the results for radial outwards imbibition. Again, for the high aspect ratio core, the Mason factor produces the closest approximation to linearity, but otherwise there is not much difference between them, and virtually no difference at short times.

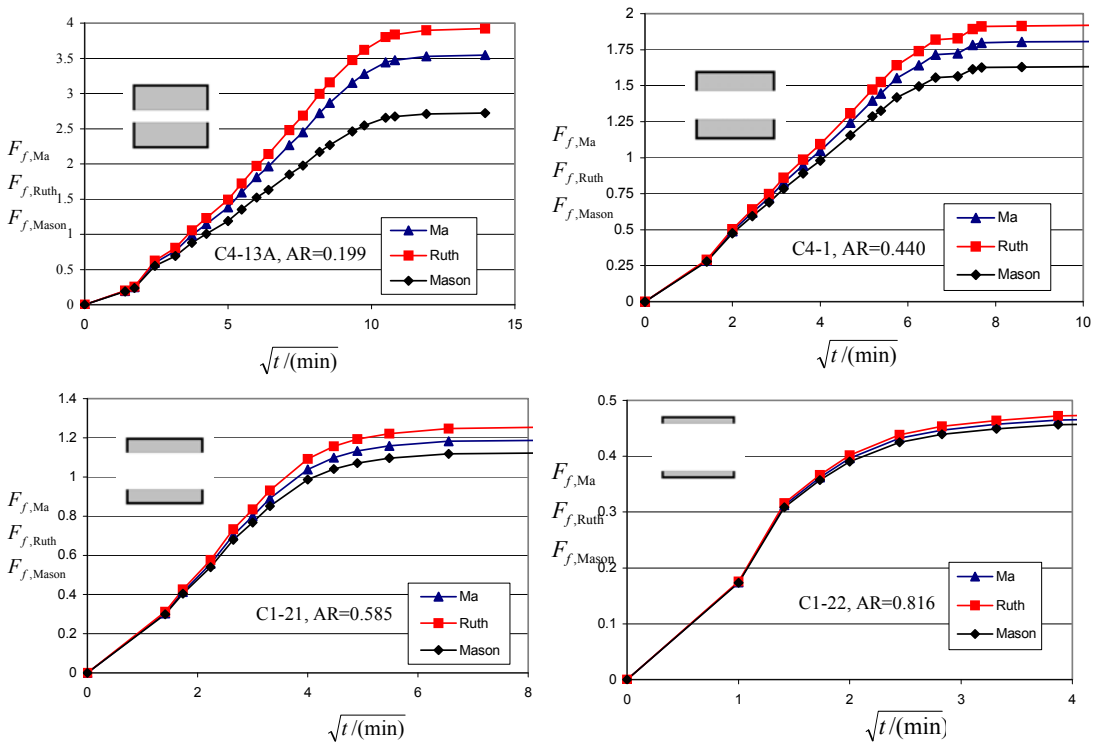

Fig. 7.2-18 Radial outwards imbibition for cores with four different aspect ratios. There are only significant differences between the three functions for the high aspect ratio core (AR= 0.199).

Results for the two ends closed cores which had simultaneous radial inwards and outwards imbibition were more difficult to analyse. Consequently they have only been interpreted using the Mason function. Essentially two versions of Eq. 7.2-38 were used, one for the outer front position and the other for the inner front position but with the times to reach these positions equal. Also, the fraction filled depends on the positions of both fronts. Consequently, for a fixed fraction filled, an iterative routine calculated the position of the two fronts and also the resulting time. Knowing the position of the front associated with an open face enabled $F_{f,\mathrm{Mason}}$ to be calculated using Eq. 7.2-50. Figure 7.2-19 shows the results. They are, again, except for the high aspect ratio core, close to being straight lines with the same gradient.

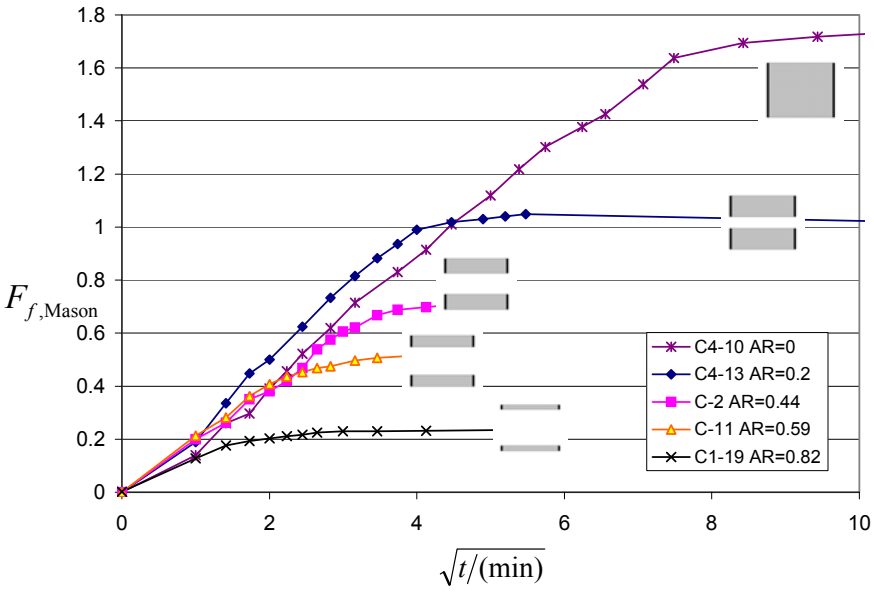

Fig. 7.2-19 Results for cores with both ends closed. The analysis is more difficult for this case because there are two fronts moving radially in opposite directions at different places and at different rates. Except for the most extreme aspect ratio (0.82), the results give close-to straight lines of almost the same gradient. Some times are very short, especially for the high aspect ratios, making the experiments relatively inaccurate.

In order to make a direct comparison of how well the Mason function fits the actual shape of the production curves, the amount of oil produced as a function of time was calculated for all of the radial outwards experiments using a fixed value of 15 for the physical properties factor. Radial outwards was selected because, for this shape, the results deviate the most from $\sqrt{time}$ behaviour. The results are shown on Fig. 7.2-20. The early time data shows a reasonable fit except for AR=0.2. The function over-predicts production at short times.

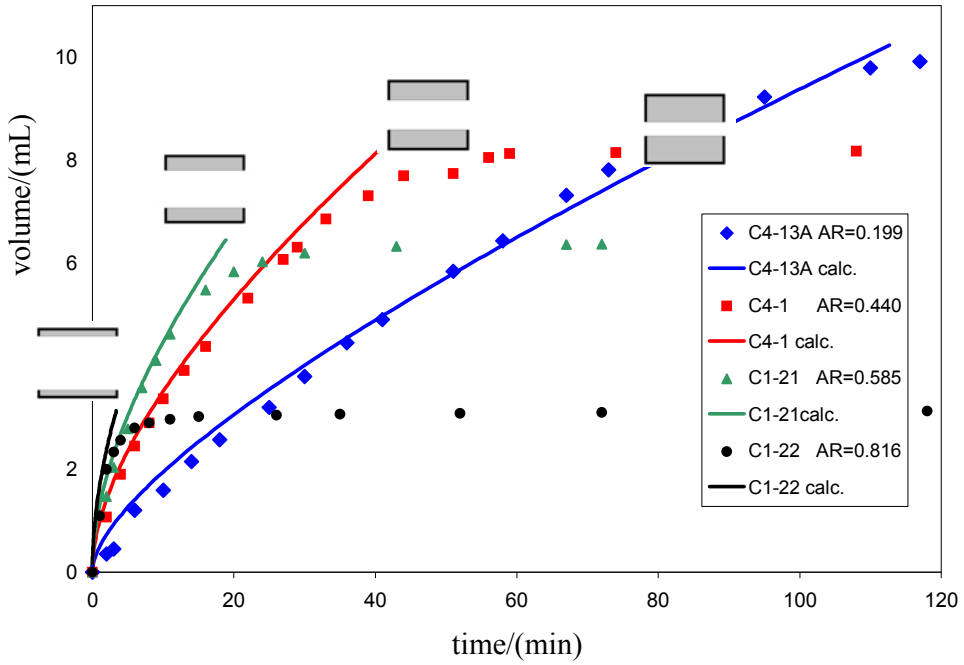

Fig. 7.2-20 Comparison between experimental measurements and calculated values for radial outwards imbibition. Except for an aspect ratio of 0.2 the fits are quite good for the first 70% of the volume imbibed.

Consistency of the system properties factor G

Because the rock and fluid properties are essentially the same in all of the experiments, ideally the physical properties factors from all of the experiments should not depend on core shape. The Mason and Ma properties factors, *G*, are defined in Eq. 7.2-41 and 42. The reciprocals of the squares of the gradients of all of the results were calculated and are typically values for about 75% of recovery. For Figs 7.2-17 to 19 one might arguably subtract about half a minute (or a quarter, when squared) from the start times. If there was perfect consistency, all of these reciprocal gradients would be the same irrespective of the aspect ratio The squares of the gradients are shown on Fig. 7.2-21 with the 'both ends closed' results omitted because they were only calculated for the Mason function and the aspect factor has two values depending on which open face is considered. There were multiple results for linear imbibition and so an average result has been taken for this shape. The aspect factor of 1 covers all of the linear imbibition results (one end or both ends open). It can be seen from Fig. 7.2-21 that the most constant physical properties factor is given by the Mason functions.

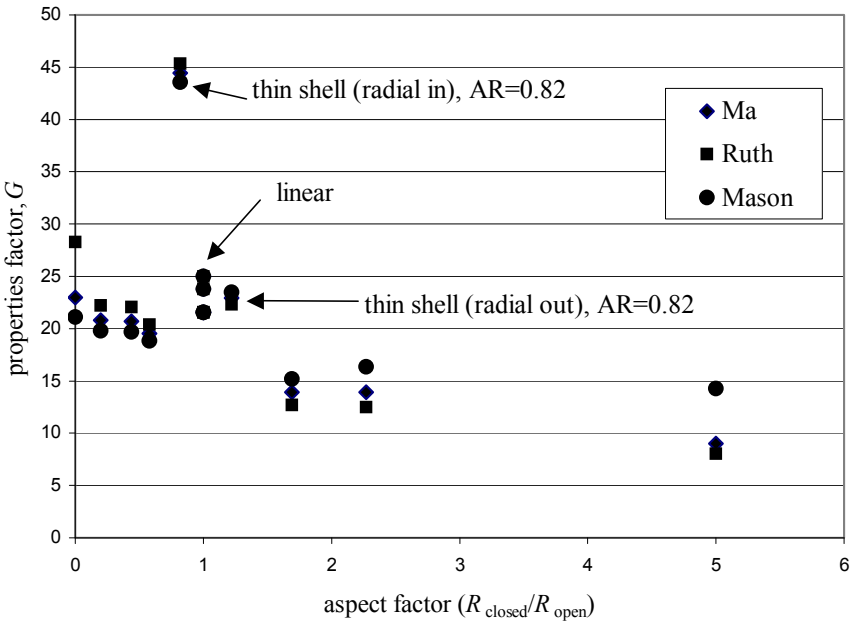

Fig. 7.2-21 Comparison between the squares of the reciprocals of the gradients of Figs 7.2-17 to 19. These gradients are the *G* factors defined by Eq. 7.2-41, and 42. Because they are properties of just the rock and fluids, they should, if the shape factor is correct, ideally all have the same value. Because it gives the most consistent *G* factor, the Mason scale factor is probably the best of the three. The value for an aspect factor of 0.82 is too high by a factor of two. This is probably because it is only a thin shell about 5mm thick making imbibition times very short.

Discussion

Optimum core size and shape

There is significant variation between the properties factors obtained from cores of different size and shape. Ideally, because the same rock type and liquids were used throughout, all of these gradients should be the same. Set against this is the vast range of times for imbibition to be virtually complete; 2 minutes for the fastest and 1000 minutes for the slowest. Figure 7.2-22 shows the properties factor *G* plotted against the Mason characteristic length, $L_{c,Mason}$. The biggest scatter is for characteristic lengths of less than 1 cm. There is still significant scatter of the other *G* values but careful analysis indicates that this might be a consequence of the limited face area open to imbibition.

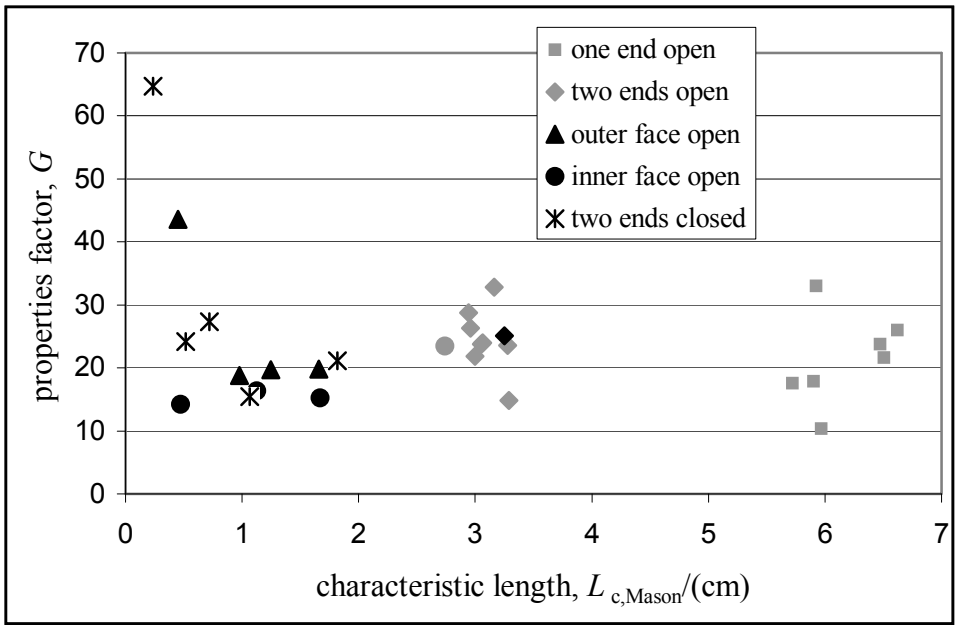

Fig. 7.2-22 The properties factor G plotted against characteristic length. Ideally, because the rock and liquids are the same, the value of *G* should be constant. It seems that the widest spread of values is for the cores with a characteristic length less than 1 cm. These are only a thin shell The solid points are for cores with an active face area greater than 40 cm^2 and these are more consistent than the cores with active areas less than 40 cm^2 (grey points).

The results shown in Fig. 7.2-22 indicate that the most consistent values of G are obtained when the characteristic length is greater than 1 cm and the surface area open for imbibition is greater than 40 cm^2. It may be that for the tested sandstone this area is the minimum required to give access of the produced non-wetting phase to the largest pores and thus the lowest and most-consistent capillary back pressure. With too little area, the capillary back pressure will likely to be too high with the result that imbibition will be slower, and thus G higher. Radial inwards imbibition appears to be the best core geometry to meet these requirements. Yildiz *et al*. (2006) concluded that all-faces-open imbibition gave the most consistent results and very recently Hatiboglu & Babadagli, 2007 showed results for linear imbibition into 50mm diameter cores to be more consistent than for smaller diameters.

However, in general the overall, the intrinsic variability between experiments seems to be greater than the errors incurred by differences in the shape factors. But, as well as having different shapes, the cores have a range of volumes and this may go some way to explaining the variability. Also the capillary back pressure required to force oil from the cores is produced by the biggest connected pores at the open face and, statistically, this will probably depend on the surface area of the cores.

Relative permeabilities during counter-current imbibition

If we take an overall average value for G of about 20 then Eq. 7.2-41 gives

$$G_{\text{Mason}} = \sqrt{\frac{\varphi}{2K}} \frac{\left(S_{\text{wf}} - S_{\text{wi}}\right)}{MC_{\text{spread}}\sigma} \qquad 7.2\text{-}41$$

The dimensions of G are TL^{-2}. Converting into internally consistent units and taking typical values for porosity and permeability gives

$$\frac{1}{M\mu_{\text{w}}} = \frac{1}{k_{\text{rw}}} + \frac{\mu_{\text{nw}}}{\mu_{\text{w}} k_{\text{rnw}}} \approx 1000 C_{\text{spread}} \qquad 7.2\text{-}51$$

The viscosity ratio was about 3.5. Using the data of Li *et al* (2006) the value of C_{spread} can be estimated to be between 0.5 and 1. Consequently k_{rw} cannot be less than 0.002 and k_{rnw} cannot be less than 0.007. If k_{rw} and k_{rnw} are about equal then they will be about 0.009. Of course if C_{spread} is less or the capillary pressure at the front is not determined by the Leverett radius (and interfacial tension) then the relative permeabilities will have to be be higher.

Conclusions

An approximate analytic solution for countercurrent imbibition was obtained by assuming a frontal displacement with constant saturations ahead of and behind the front, and taking the capillary back pressure at the open face to be a constant fraction of the capillary pressure at the front. This gives the production *vs* time functions for different core shapes. Comparison of these functions with experimental data using Berea sandstone and refined oil for both the linear and radial cases shows reasonable agreement. In practice, variability between the cores caused by not having enough surface area and not enough volume seems of greater importance than the precise core scale factor functions. For consistent data the core should have a surface area of 40 cm^2 and an imbibition depth greater than 1 cm.

Acknowledgements

The authors acknowledge support from the UK Engineering and Physical Sciences Research Council, British Petroleum, ChevronTexaco, Total/Fina/ELF, Phillips, the Enhanced Oil Recovery Institute at the University of Wyoming, the National Petroleum Technology Office of the US Department of Energy, and the Natural Science and Engineering Research Council of Canada.

Task 8. *Application of network/numerical model to mixed wet rocks.*

8.1 Modeling the Effect of Viscosity Ratio on Spontaneous Imbibition

Herbert Fischer, Shaochang Wo, and Norman R. Morrow
SPE Reservoir Evaluation & Engineering, June 2008, 577- 589.

Abstract
Spontaneous imbibition data for Berea sandstone cores, that are very strongly wetted by the aqueous phase and initially 100% saturated with mineral oil, are reported for linear, radial, and all-faces-open boundary conditions. Oil viscosities were 4, 63 and 173 cP and aqueous phase viscosities ranged from 1 to 495 cP. Oil/aqueous phase viscosity ratios were varied by over four orders of magnitude (0.01 to 173.1). Near-linear relationships, with slopes close to one half, between the frontal position and imbibition time on a log-log scale were obtained for both linear and radial counter-current flow. Behavior is consistent with near piston-like displacement by the imbibing aqueous phase. The results are analyzed by a new mathematical model that accounts for counter-current spontaneous imbibition with symmetrical flow patterns. The model assumes that saturation and permeabilities to counter-flowing phases behind the front are constant and that any effect of local change in interfacial curvature with distance is negligible. The results from the model are used to extend scaling to include the measured effect of viscosity ratio for linear and radial flow. For the all-faces-open boundary condition, commonly used in core analysis studies, oil recovery vs. imbibition time is estimated by a combination of spherical and radial flow. Consistently close agreement was obtained between experiments and behavior predicted by the model.

Introduction
Laboratory spontaneous imbibition experiments are commonly used to investigate the mechanism of oil recovery from fractured reservoirs. The rate of oil transfer from the rock matrix into the fractures determines oil production. Although capillary force is the dominant driving mechanism for spontaneous imbibition, the rate of oil recovery depends on many factors, including relative permeability, fluid viscosities, sample size, shape and surfaces open to imbibition (Ma *et al*., 1997; Mason and Morrow, 2005). A model of spontaneous imbibition is needed that, can be verified by laboratory experiments and has predictive capability.

Differential equations of mass balance and extension of Darcy's equation to two-phase flow in porous media (Blair, 1964) often serve as the basis for modeling countercurrent spontaneous imbibition. For counter-current flow, the rate of water imbibition is assumed to be equal and opposite to the rate of oil production. If boundary conditions, relative permeability, and capillary pressure functions are specified, the progress of saturation and pressure profiles can be calculated. The effect of relative permeability and capillary pressure functions may be lumped together as a single saturation function (Pooladi-Darvich and Firoozabdi, 2000; Kashchiev and Firoozabadi, 2002; Li *et al*, 2003; Wo, 2002) in order to reduce the number of function parameters. However, determination of relative permeabilities and capillary pressures that pertain to spontaneous imbibition is highly problematic. In practice, saturation functions have to be tuned to either match the measured saturation profiles or the imbibition rate calculated by integration of the saturation profiles. When cores are very strongly water-wet, it can be difficult to tune the saturation functions to match the sharp imbibition front. More significantly, because of lack of experimental data, the

traditional approach has not been fully tested against imbibition experiments under different flow patterns and a wide range of viscosity ratios.
Another approach to prediction of the rate of imbibition involves development of dimensionless scaling groups that compensate for the effects of sample size, shape, boundary condition and rock and fluid properties. A scaling group proposed by Mattax and Kyte (1962) was later modified by Ma *et al.* (1997) to give a dimensionless time t_D defined by

$$t_D = t\sqrt{\frac{k}{\phi}}\frac{\sigma}{\sqrt{\mu_o \mu_w}}\frac{1}{L_c^2} \qquad 8.1\text{-}1$$

where t is the imbibition time, k is the rock permeability, ϕ is rock porosity, σ is the water/oil interfacial tension, μ_w and μ_o are the water and oil viscosities, and L_c is the characteristic length, which depends on the sample size, shape, and boundary conditions. The scaling group (Eq. 8.1-1) correlated available oil/water imbibition data satisfactorily (Ma *et al.*, 1997; Zhang *et al.*, 1996).

Use of the geometric mean of the oil and water viscosities was based on experiment and, particularly for the complex process of spontaneous imbibition, cannot be safely assumed to hold outside the range of measurement conditions. Extension of experimental data to three orders of magnitude variation in aqueous phase viscosity showed large systematic increase in t_D for oil/water viscosity ratios smaller than 0.25 (Fischer and Morrow, 2005). These results indicate that correlation of imbibition data can be extended to a wider range of conditions simply by inclusion of a viscosity ratio term. In addition, based mainly on extensive scaled imbibition data for fluid viscosity ratios of unity, small differences in shape of the recovery curves have been identified for radial vs. linear flow and should also be taken into account (Fisher and Morrow, 2005). This paper presents correlations of new data for a wide range of viscosity ratios for linear and radial imbibition and for imbibition into cylindrical cores with all faces open.

Experimental Procedure and Materials
Experimental procedures are described by Fischer and Morrow (2005).

Liquids
Oleic phase. The oil phase was composed of refined oil; a mineral oil (Soltrol 220®) with a viscosity of 3.9 cP and a 173 cP white mineral oil. An oil with viscosity of 63.3 cP was prepared from a mixture of the two minerals oils. Prior to use, polar contaminants were removed and the oils were evacuated to remove dissolved gas.

Aqueous phase. Glycerol, supplied at 99.5% purity by EMD Chemicals Inc., was mixed with brine to obtain different aqueous phase viscosities. For the data obtained in this study, the ionic strength of the brine was adjusted for addition of glycerol to give glycerol/water mixtures of constant ionic strength (equal to synthetic sea water, Table 8.1-1). Prior to use, each aqueous mixture was evacuated to minimize the possibility of evolution of gas during imbibition tests. Density and viscosity of the aqueous phase, and interfacial tension against the selected oleic phase were measured.

Sandstone

Twenty six cylindrical Berea sandstone cores with nominal diameter, d, of 3.81 cm and nominal lengths, L, of either 6.35 or 7.62 cm were cut from a single Berea sandstone block, designated as EV6. These were rinsed, dried for one day at ambient temperature and oven-dried at 105°C for two days. Permeability to nitrogen, k_g, was measured using a Hassler-type core holder at a confining pressure of 300 psi. Gas permeabilities ranged from 106.1 md to 153.5 md. Porosities for Block EV6 cores ranged from 17.8 to 19.3 % (see Tables 8.1-2 through 8.1-4). Two additional cores, C1-1 and C1-3, were cut from a separate block designated as C1; permeabilities were 62.3 and 62.7 md and porosities were 16.9 and 16.8 %, respectively.

Boundary Conditions

Specific core surfaces were sealed with epoxy resin (Devcon® 5 Minute® Epoxy and 5 Minute® Epoxy Hardener) to establish no flow boundaries. Inspection of the sealed surfaces showed that distance of invasion of the resin was no more than a few pore diameters. The boundary conditions were chosen to investigate linear (one-end-open, OEO), radial (two-ends-closed, TEC) and the more complex all-faces-open (AFO) flow (see Table 8.1-5).

Ma *et al*. (1997) defined a characteristic length, L_C, by

$$L_c = \left(V_b / \sum_{i=1}^{n} \frac{A_i}{l_{A_i}} \right)^{0.5} \qquad 8.1\text{-}2$$

where V_b is the bulk volume, A_i is the area of the ith face open to imbibiotion, and x_i is the distance of the face to the no-flow boundary. L_c correlated the effect of boundary conditions satisfactorily for a wide range of spontaneous imbibition data (Ma *et al*., 1997; Zhang *et al*., 1996; Fischer and Morrow, 2006; Fischer and Morrow, 2005). Table 8.1-5 lists expressions for L_C. Specific values of L_C for individual cores are included in Tables 8.1-2 through 8.1-4.

Spontaneous Imbibition

Spontaneous imbibition data were obtained for three boundary conditions, three oil viscosities, and up to six aqueous phase viscosities. A total of 28 data sets were obtained. The initial water saturation was zero in all experiments. Oil production as a function of time was measured in standard imbibition cells at ambient temperature (close to 20°C).

Results

One-end-open (OEO)

Core and fluid properties for 10 linear spontaneous imbibition tests, are listed in Table 8.1-2. For each of the two oleic phase viscosities, five aqueous phase viscosities were prepared. The viscosity ratio, Ψ, where

$$\Psi = \mu_o / \mu_w \qquad 8.1\text{-}3$$

ranged from 0.01 to 63.30.

The imbibition curves for recovery of 4 cP and 63 cP oil are shown in Fig. 8.1-1a. For either oil viscosity, the rate of oil recovery decreased systematically over almost three orders of magnitude with increase in aqueous phase viscosity. Plots of recovery versus dimensionless time are shown in Fig. 8.1-1b. Close correlation was obtained for imbibition curves with viscosity ratios of 0.65 to 3.90. Slightly faster imbibition with increase in viscosity ratio was observed for viscosity ratios of

15.44 and 63.30. However, scaled imbibition time showed marked increase with decrease in viscosity ratio below 0.25.

Final oil recoveries (% OOIP) were all within 47 ± 1.7 % (Fig. 8.1-1c). Within this range, consistent trends of increase in recovery with decrease in viscosity of the aqueous phase were observed. At a fixed viscosity ratio, recovery of 4 cP oil was nearly 2 % higher than for 63 cP oil. These trends in recovery indicate subtle changes in the pore level displacement mechanism with change in viscosities. Previously it was observed that for *linear* spontaneous imbibition with *matched* liquid viscosities, final oil recoveries decreased by 2.5% with increase in viscosity from 4 to 141cP (Fischer and Morrow, 2005).

Two-ends-closed (TEC)

A total of twelve radial (TEC) imbibition tests were made with viscosity ratios ranging from 0.01 to 173.1. Table 8.1-3 lists the rock and fluid properties for the two-ends-closed experimental set. Oil recovery as a function of imbibition time for 4 cP, 63 cP, and 173.1 cP oil, each with aqueous phase viscosities of 1, 4, 28, 98 and 495 cP, are displayed in Fig. 8.1-2a. The rate of oil recovery decreased with increase in aqueous phase viscosity.

Fig. 8.1-2b shows that, as was observed for the OEO results, the dimensionless time, t_D, gave close correlation of imbibition curves for viscosity ratios of 0.65 and larger, whereas for $\Psi \leq 0.14$ the scaled times showed distinct increase with decrease in Ψ.

Final oil recovery versus viscosity ratio is displayed in Fig. 8.1-2c. In contrast to the results for OEO, with the exception of one data point ($\Psi = 2.28$), final oil recoveries for radial flow decrease with increase in viscosity ratio and overlap for the three tested oil viscosities (4, 63 and 173 cP, see Fig. 8.1-2c). For every viscosity ratio, final oil recoveries for radial imbibition (they ranged from about 51 to 53.3 %) are distinctly higher than for linear imbibition (45.3 to 48.7%).

All-faces-open (AFO)

Table 8.1-4 lists the core and fluid properties for the tests with all-faces-open. The flow can be considered as a combination of linear and radial imbibition. Porosities for the four Berea EV6 cores ranged from 18.6 to 19.2 % and were thus somewhat higher than for the two Berea C1 cores (16.8 and 16.9 %). The permeability to nitrogen for the EV6 cores was significantly higher (112.3 to 148.4 md) than for the Berea C cores (62.3 and 62.7 md). Results for cores EV6-72, EV6-73, EV6-80 and EV6-81 are presented in Fig. 8.1-3a. Results for cores C-1 and C-3, taken from Fischer and Morrow (2005) are also included. After scaling (see Fig. 8.1-3b), all imbibition curves, except one obtained for the lowest viscosity ratio ($\Psi = 0.04$) of the AFO data set, were closely correlated.

Results for the all-faces-open cores of the ratio of length to diameter used in this work are dominated by radial flow (Fisher and Morrow, 2005). Contrary to the results for OEO and as for the TEC cores (radial flow), final oil recoveries for the all-faces-open cores (Fig. 8.1-3c) show decrease with increase in viscosity ratio. However, unlike the results for the TEC cores, the final recoveries for the 4 cP oil do not overly those for the 63 cP oil, possibly because the 4cP data were obtained with Berea Block C1.

Mathematical Model

The effect of pore geometry and wetting on capillary displacement pressure has been calculated for a wide variety of pore shapes formed by rod, plate and sphere combinations (Mason *et al.*, 1983; Mason and Morrow, 1986; Mason and Morrow, 1987; Mason and Morrow, 1991; Ma *et al.*, 1996; Unsal *et al.*, 2005). Many pore network models have been analysed for quasi-static displacement (Dixit *et al.*, 1999; Blunt, 1997; Oren *et al.*, 1998). However, relatively little attention has been paid to treatment of spontaneous imbibition as an inherently dynamic process. For example, a longstanding assumption in modeling linear (OEO) spontaneous imbibition has been that capillary pressure at the open face is zero and corresponds to development of a residual non-wetting phase saturation (Blair, 1964; Pooladi-Darvish and Firoozabdi, 2000). However, the oil saturation retained behind the front must provide flow paths for the oil (Li *et al.*, 2003; *Li et al.*, 2006). Raimondi and Torcaso (1964) showed that the *onset* of trapping of residual oil by co-current viscous displacement does not occur until the saturation is within about 5% PV of attaining the trapped residual oil saturation. Thus, for displacement of oil by imbibition, the fraction of trapped oil over the range of saturation behind the imbibition front is probably low except when the viscosity ratio is so low that the pore volume occupied by the counterflowing oil is also very low.

Model Derivation

The assumptions used to develop the imbibition model of this study are mainly based on the experimental observations. In the definition of t_D (Eq. 8.1-1), the basis for inclusion of the geometric mean of the oil and water viscosities, $(\mu_w\mu_o)^{0.5}$ was empirical (Ma *et al*., 1999). In extending tests of scaling by t_D, imbibition data have been obtained for very low oil-water viscosity ratios, mainly by increasing the viscosity of the aqueous phase. The results for increase in the range of investigation of viscosity ratio of liquids to over four orders of magnitude (see Figs. 8.1-1, 2 and 3) indicate that the correlation can be improved, particularly at low viscosity ratio, by including an appropriate function of viscosity ratio. Also, expected small systematic differences in the shape of scaled curves have recently been demonstrated for linear vs. radial flow (Fischer and Morrow, 2005). Thus, the scaling could also be improved by taking boundary conditions into account.

Comparison of distance of advance of the imbibition front with the volume of imbibed wetting phase indicates near-piston-like displacement (Li *et al.*, 2003; Li *et al.*, 2006). It follows that the ratio of smaller pores that tend to be invaded by water to the larger pores that tend to remain filled with connected oil is nearly constant behind the front. (Retained oil saturations behind the saturation front are all within 56±5% of the original oil content.) A further key observation for linear imbibition is that the pressure in the nonwetting phase ahead of the displacement front (in the dead end), p_{of}, quickly rises to, and usually maintains, a stable value, even though the rate of advance of the imbibition front decreases with time (Li *et al.*, 2006). Clearly, behavior of this type should not be modeled as a quasi-static process.

The effective capillary pressure at the displacement front, p_{cf}, and the back pressure at the open face are fundamental to the imbibition process. In development of a mathematical model it is assumed that p_{cf} is a constant that depends mainly on interfacial tension and rock properties. It is further assumed that counter current flow behind the front occurs as two essentially independent processes. This assumption implies that the pressure gradient in each phase decreases with time

even though the water and oil saturations remain constant. Consequently, capillary pressure varies linearly with distance to the imbibition front, but there is no change in saturation. This condition can be closely realized physically because pore throat shape and roughness and edge effects can permit change in interface curvature without significant change in location of the three phase lines of contact. The interfacial area between oil and water is only about 3% of the interfacial area associated with the flow of oil Seth and Morrow, 2007). It is therefore reasonable to model the effects of counter-flow at these interfaces as negligible, through the assumption of independent flow of each phase. The linear pressure distribution in each region is illustrated in Fig. 8.1-4 for the one-dimensional OEO case, where p_{cb} is the capillary pressure at the open boundary. This pressure has also been described as the bubble or back pressure (Li *et al.*, 2003; Li *et al.*, 2006). Although the back pressure fluctuates locally with bubble growth and snap-off, the overall effective back pressure can be treated as constant so that

$$p_{cb} = p_{ob} - p_{wb} \qquad 8.1\text{-}4$$

where p_{ob} is the oil phase pressure at the open boundary and p_{wb} is the water phase pressure at the open boundary.

The pressure gradient in the oil and aqueous phase behind the imbibition front is determined by the fluid viscosities. Because, in a piston-like displacement, oil recovery is directly related to the position of the imbibition front, a relationship between the frontal position and imbibition time can be predicted from linear imbibition data.

Application of Darcy's law to both regions gives the oil out-flow rate, q_o, and the water in-flow rate, q_w, respectively,

$$q_o = A_o \frac{k_{Ao}}{\mu_o} \frac{p_{of} - p_{ob}}{x} \qquad 8.1\text{-}5$$

$$q_w = A_w \frac{k_{Aw}}{\mu_w} \frac{p_{wb} - p_{wf}}{x} \qquad 8.1\text{-}6$$

where x is the frontal position, A_o is the cross-sectional area of the oil-filled region and k_{Ao} is the associated permeability of that region when the viscosity of the oil phase is μ_o. A_w is the cross-sectional area of the aqueous phase region, plus any disconnected oil, and k_{Aw} is the associated permeability to the aqueous phase with viscosity equal to μ_w. p_{of} and p_{wf} are the respective oil and aqueous phase pressures at the imbibition front. The areas identified with flow of each phase adjust in opposite directions with change in viscosity ratio as a result of viscous coupling.

In the conventional description of immiscible multiphase flow, capillary pressure and relative permeabilities are assumed to be unique functions of the saturation. However, this assumption does not take into account the effects of dynamic capillary pressure and viscous coupling that arise in spontaneous imbibition. Moreover, Bourbiaux and Kalaydjian (1990) have reported that realitive permeabilities for linear cocurrent flow differ from those for linear countercurrent flow. Zhou *et al.* (2002) proposed scaling by a dimensionless time that included mobility ratios, but this requires knowledge of the effective relative pemeabilities.

Viscous coupling is expressed by the effect of viscosity ratio on saturation behind the imbibition front. To avoid the difficulty of defining the appropriate relative permeability concept for countercurrent flow under conditions where the saturation behind the front self adjusts to compensate for change in viscosity ratio, a mechanistic model of separate flow regions for the oil and water phases is adopted. If both water and oil are considered incompressible, the oil flow rate derived from Eqs. 8.1-5 and 6 with the counter-current condition, $q_o = -q_w$, is given by

$$q_o = \frac{p_{cf} - p_{cb}}{x} \frac{1}{\frac{\mu_o}{A_o k_{Ao}} + \frac{\mu_w}{A_w k_{Aw}}} \qquad 8.1\text{-}7$$

The capillary pressure at the imbibition front, p_{cf}, is defined as

$$p_{cf} = p_{of} - p_{wf} \qquad 8.1\text{-}8$$

When the imbibition front advances, the differential equation of the dynamic mass balance is described by

$$q_o dt = R\phi A dx \qquad 8.1\text{-}9$$

where t is the imbibition time, R is the oil recovery, ϕ is the rock porosity, and A is the cross-sectional area of the core. Substituting Eq. 8.1-7 into Eq. 8.1-9 and integrating, an analytic function is obtained that relates the frontal position to the imbibition time

$$x^2 = t \frac{2(p_{cf} - p_{cb})}{R\phi A(\frac{\mu_o}{A_o k_{Ao}} + \frac{\mu_w}{A_w k_{Aw}})} \qquad 8.1\text{-}10$$

Eq. 8.1-10 can be expressed in dimensionless form as,

$$x_D^2 = E(\eta) t_{D,lin} \qquad 8.1\text{-}11$$

where x_D is the normalized frontal position and $t_{D,lin}$ is the linear-case dimensionless time as defined by Eq. 8.1-1, with the characteristic length equal to the core length L,

$$t_{D,lin} = \sqrt{\frac{k}{\phi}} \frac{\sigma t}{\sqrt{\mu_o \mu_w} L^2} \qquad 8.1\text{-}12$$

In Eq. 8.1-11, $E(\eta)$ is a dimensionless function of η, the square root of the viscosity ratio,

$$\eta = \sqrt{\frac{\mu_o}{\mu_w}} \qquad 8.1\text{-}13$$

The form of the dependence of imbibition rate on viscosity ratio indicates that the function of viscosity ratio, $E(\eta)$ can be expressed in terms of two dimensionless parameters, a and b, such that

$$E(\eta) = \frac{a}{\frac{1}{b\eta} + b\eta} \qquad 8.1\text{-}14$$

where, from Eq. 8.1-10, a and b are given by

$$a = \frac{2(p_{cf} - p_{cb})}{\sigma R}\sqrt{\frac{A_o A_w k_{Ao} k_{Aw}}{\phi k A^2}} \qquad 8.1\text{-}15$$

$$b = \sqrt{\frac{A_w k_{Aw}}{A_o k_{Ao}}} \qquad 8.1\text{-}16$$

The linear model of Eq. 8.1-11 was tested against the OEO experimental data. A linear correlation between $\log(x_D)$ and $\log(t_{D,lin})$ was evident for almost all cases. The slopes of the linear correlations were, as expected, always close to 0.5. A linear correlation was also obtained between $\log(x_D)$ and $\log(t_D)$ for the radial flow cases where the characteristic length, $L_c = \frac{r}{\sqrt{3}}$ for radial flow, is used to define $t_{D,rad.}$. Eq. 8.1-11 should also be applicable to spherical flow with the characteristic length being $\frac{r}{\sqrt{3}}$.

On the basis of this empirical observation, by replacing $t_{D,lin}$ with t_D (as defined by Eq. 8.1-1) and freeing the power index of x_D, Eq. 8.1-9 can be empirically extended to a more general model of the form

$$x_D^n = E(\eta) t_D \qquad 8.1\text{-}17$$

In Eq. 8.1-17 the parameter n extends the model to cases where the log-log plot is linear but the slope varies (usually only slightly) from 0.5, probably because of pore-space heterogeneity. The conversions between the normalized front position, x_D, and oil recovery, R_N, normalized with respect to final recovery for the three flow patterns are given in Eqs. 8.1-18 through 20.

For linear flow,

$$x_D = R_{N,lin} \qquad 8.1\text{-}18$$

For radial flow,

$$x_D = 1 - \sqrt{1 - R_{N,rad}} \qquad 8.1\text{-}19$$

For spherical flow,

$$x_D = 1 - \sqrt[3]{1 - R_{N,sph}} \qquad 8.1\text{-}20$$

Cylindrical Cores

For cylindrical cores (AFO), the non-symmetrical flow pattern does not permit a simple analytical model. As an approximation, the imbibition into an open core can be estimated by a combination of spherical and radial flow. One approach is to model a cylindrical core of length L and diameter d by a cylinder with a half sphere attached at each end, with the volume of the new shape equal to the volume of the core. Both the half spheres and the central cylinder have diameter d. The cylinder length is $L - 2d/3$. The estimated normalized recovery for the all-faces-open boundary

condition through combination of the recovery from the central cylinder and both half spheres is then given by

$$R_{N,cyl} = \left(1 - \frac{2d}{3L}\right) R_{N,rad} + \frac{2d}{3L} R_{N,sph} \qquad 8.1\text{-}21$$

***Regression and Prediction of* E(η)**

Procedure

The experimental data obtained for all three boundary conditions were used for the validation of the proposed model. Firstly, all experimental spontaneous imbibition data from radial flow (TEC), the largest and most consistent data set, were fitted manually with the model given by Eq. 8.1-17. The parameters *E(η)* and *n* were adjusted to fit the experimental data. *E(η)* was then plotted against the respective square root of viscosity ratio, η. Regression of the parameters *a* and *b*, resulted in a curve fit of $E(\eta)$ over the entire experimental range of η. The evaluated function of $E(\eta)$ was then applied to spontaneous imbibition data for the boundary conditions OEO (linear flow) and AFO (linear and radial flow) for values of η tested by experiment. The quality of the match was then tested by comparison with the experimental results.

Fitting of TEC Data

The experimental spontaneous imbibition results for the two-ends-closed boundary condition are plotted on a log-log scale as normalized frontal position, x_D, versus dimensionless time, t_D. The oil recovery (normalized with respect to final recovery), R_N, for radial flow (TEC) must be converted to the normalized position of the front, x_D, by means of Eq. 8.1-19. The experimental data are then fitted by Eq. 8.1-17, rearranged to

$$t_D = \frac{x_D^n}{E(\eta)} \qquad 8.1\text{-}22$$

For a given data set, parameters $E(\eta)$ and *n* were adjusted to predict a dimensionless time, t_D, for a specific normalized frontal position, x_D, to obtain the best fit with the experimental data. Fig. 8.1-5 is a compilation of the results obtained for each tested value of η. Apart from a few data points at early time and the expected departure from linearity at the final stages of imbibition, the experimental spontaneous imbibition data exhibit a distinct linear correlation on a log-log plot of normalized front position, x_D, vs. dimensionless time, t_D. The base model as defined in Eq. 8.1-17 corresponds to a linear correlation between x_D and $\sqrt{t_D}$, with a slope of 0.5 ($n = 2$) on a log-log scale. For the twelve experimental TEC data sets in Fig. 8.1-5, the best fit of *n* for the respective η was close to 2 except for $\eta = 1.97$ for which the power index was 1.73 (see Table 8.1-6). However, the viscosity ratio $\eta = 1.97$, was tested for the lowest values of oil and aqueous phase viscosity (4 cP and 1 cP respectively). Experimental errors in the readings of oil recovery can be expected because imbibition was very fast.

Table 8.1-6 also includes the values of $E(\eta)$ obtained from the data fit. Fig. 8.1-6 is a plot of $E(\eta)$ as a function of η. At low values of η the values for $E(\eta)$ sharply increased up to a maximum at $\eta \approx 4$ and then show relatively gradual decrease with further increase in η. Evaluation of the parameters *a* and *b* by regression to give a match with the data is given in the Appendix. The values of $E(\eta)$, given by the regression curve for radial flow, were then tested for predictive capability against the data for linear (OEO) and cylindical (AFO) flow.

Matching of OEO (Linear Flow) Data

The proposed imbibition model (Eq. 8.1-17) was tested against experimental data for linear flow (one-end-open) (see Fig. 8.1-1 and Table 8.1-2). Ten predictions were made for viscosity ratios identical to the radial flow experimental set. The dimensionless time, t_D, for a specific normalized front position, $x_{D,}$ was matched using Eq. 8.1-22. For linear flow, the normalized front position corresponds to the normalized oil recovery (Eq. 8.1-18). $E(\eta)$ for a specific η was determined from the regression curve obtained from fitting the radial flow experimental data (Fig. 8.1-6). The power index n was adjusted to obtain the best possible fit with the experimental data. Results for the match of linear imbibition for each fluid viscosity pair as well as direct comparison with the respective experimental results are displayed in Fig. 8.1-7. The match is very close except that for $\eta \leq 0.36$ the dimensionless times for recovery predicted by E(η) are slightly longer than the measured values. Table 8.1-7 lists the calculated parameter $E(\eta)$ and the adjusted power index n for each η. For the two data sets with the lowest η (0.09 and 0.20), the mathematical model predicts longer t_D than the experimental values. Overall, the proposed mathematical model produces satisfactory linear flow predictions (see Fig. 8.1-7) and n was consistently close to 2. The close-to-linear correlation between the advancing front and the square root of time (n ≈ 2) implies that local phenomena at the imbibition front dominate the spontaneous imbibition process.

Matching AFO Flow

Finally, the analytical model was tested for six all-faces-open data sets (Table 8.1-4). The normalized recovery, $R_{N,cyl}$, is predicted for specific dimensionless times, t_D, according to Eq. 8.1-21. The terms $R_{N,rad}$ and $R_{N,sph}$ in Eq. 8.1-21 need to be evaluated separately (values of L_c for radial and spherical flow are given in Table 8.1-5).

For $R_{N,rad}$ (from Eq. 8.1-19):

$$R_{N,rad} = 1 - (1 - x_D)^2 \qquad \text{8.1-23}$$

Substituting for x_D as defined in Eq. 8.1-17 yields

$$R_{N,rad} = 1 - \left(1 - [E(\eta) t_D]^{\frac{1}{n}}\right)^2 \qquad \text{8.1-24}$$

For $R_{N,sph}$ (from Eq. 8.1-20):

$$R_{N,sph} = 1 - (1 - x_D)^3 \qquad \text{8.1-25}$$

Substituting x_D as defined in Eq. 8.1-17 yields:

$$R_{N,sph} = 1 - \left(1 - [E(\eta) t_D]^{\frac{1}{n}}\right)^3 \qquad \text{8.1-26}$$

For each of the six matches, the normalized recovery for all-faces-open, $R_{N,cyl}$, was calculated for exactly those imbibition times, t, for which an actual data point (the oil recovery) was measured. Comparison of the imbibition model results with the experimental results is shown in Fig. 8.1-8. Both the recovery and the shape of the imbibition curves were closely matched. The distinct deviation of the matched curve from the experimental data for η = 0.20 at later dimensionless

times may have been caused by core heterogeneity. Also, slight differences between the predicted and the experimental data are evident at very early dimensionless times, especially for η = 7.96. However, the all-faces-open boundary condition gives the fastest imbibition rate and there is inherent error in the accurate determination of oil recovery at very early times if the geometric mean of the viscosities is low.

Overall, the matches given by the analytic approximation for the combination of linear and radial flow are satisfactory. One feature of the modeling results, however, needs further investigation; from Table 8.1-8 it is seen that the power index n shows larger variation around the value of 2 (from 1.67 to 2.28) than for linear (OEO) and radial (TEC) flow.

Inclusion of Vscosity Ratio in Scaling of Imbibition Data

Fig. 8.1-9 is a plot of the scaled imbibition data scaled by t_D for all boundary conditions (Eq. 8.1-1). The scaled data for a wide range of viscosity ratio still span 1¼ log-cycles. A significantly improved correlation is given by plotting dimensionless front position, x_D, vs. the n-th root of the product of t_D and $E(\eta)$ (Fig. 8.1-10a). The values of n were as given in Tables 8.1-6 through 8. The data spread was narrowed down from 1 ¼ log-cycles to approximately one fifth of a log-cycle. On a log-log scale, a linear correlation is obtained between x_D and the n-th root of t_D^* (see Fig. 8.1-10b) for linear, radial and the combination of linear and radial flow. Furthermore, the close match with the data plotted in Figs. 8.1-10a and b by the curves given by n = 2 indicates that the correlation has promising predictive capability.

The new form of correlation defined by

$$t_D^* = t_D\, E(\eta) \qquad 8.1\text{-}27$$

gives

$$t_D^* = t\sqrt{\frac{k}{\phi}\frac{\sigma}{L_c^2}\frac{ab}{\mu_w + \mu_o b^2}} \qquad 8.1\text{-}28$$

The core samples used in this study belong to a group of commercially available low permeability Berea sandstones that do not match a correlation found for a wide body of very strongly water-wet rocks scaled by root k/φ (Ma *et al.*, 1997; Zhang *et al.*, 1996; Tie *et al.*, 2003; Viksund *et al.*, 1998). Further experimentation is needed to test the dependency of $E(\eta)$ on η for other rock types to check that results can be described in terms of dimensionless parameters a and b that are independent of viscosity ratio, and to determine how much they may vary for individual rock types. In any application of the frontal displacement model, careful testing is needed to check the validity of the basic assumption of the model of piston-like displacement. For example, high initial water saturation or change to reduced water wetness have both been observed to result in a much greater tendency for global rather than frontal displacement (Baldwin and Spinler, 1999).

Conclusions

- Spontaneous imbibition for a wide range of oil to water viscosity ratios and three boundary conditions showed systematic dependence on viscosity ratio with strong dependence for values less than 0.25.

- A mathematical model based on displacement as a piston-like front with counter-flow of oil related imbibition time to the position of the advancing front.
- The model correlates results for different boundary conditions through the conversion of the oil recovery to frontal position.
- The model takes into account the experimentally observed effects of viscosity ratio by the definition of a dimensionless function of viscosity ratio, $E(\eta)$. Dimensionless parameters of $E(\eta)$ that were independent of η were obtained by fitting experimental data to the model.
- The model relates the dimensionless position of the front to the n-th root of dimensionless time t_D* given by the product of dimensionless time, t_D, (Ma *et al*.) and a dimensionless function of viscosity ratio $E(\eta)$.
- The model gives a linear correlation between the normalized frontal position, x_D, and t_D* with a slope (power index) of 0.5 (n= 2) on a log-log scale.
- Comparison with experimental data showed that the values of $E(\eta)$ determined from radial imbibition data provided close match with linear imbibition (one-end-open, OEO) and with imbibition into cylindrical cores, modeled as a combination of spherical and radial flow (all-faces-open, AFO).
- A very close correlation of all data was obtained when imbibition data were plotted as normalized frontal position versus the n-th root of t_D*. Predictive capability is indicated by the close match with the correlation given by n = 2.
- Additional experimental work is required to evaluate the dependency of the dimensionless function $E(\eta)$ on the square root of the viscosity ratio, η, for other rock types.

Appendix

Regression of* a *and* b *from experimental radial flow (TEC) data

Eq. 8.1-14 can be rewritten as

$$\frac{1}{E(\eta)} = \alpha \frac{1}{\eta} + \beta\eta \qquad \text{8.1-A1}$$

where

$$\alpha = \frac{1}{ab} \qquad \text{8.1-A2}$$

and

$$\beta = \frac{b}{a} \qquad \text{8.1-A3}$$

Let $(\eta_i, E(\eta)_i), i = 1 \sim N$, be the parameter set, in which E_i is obtained from fitting the experimental corresponding to η_i. Then α and β are evaluated so that

$$F(\alpha,\beta) = \sum_i [\frac{1}{E(\eta)_i} - (\alpha \frac{1}{\eta_i} + \beta\eta_i)]^2 \qquad \text{8.1-A4}$$

is minimized.

Two necessary conditions for minimizing $F(\alpha,\beta)$ are

$$\frac{\partial F}{\partial \alpha} = 0 \qquad \text{8.1-A5}$$

and

$$\frac{\partial F}{\partial \beta} = 0 \qquad \text{8.1-A6}$$

From Eq. 8.1-A5 and A6

$$\alpha\sum_i \frac{1}{\eta_i^2} + N\beta - \sum_i \frac{1}{\eta_i E(\eta)_i} = 0 \qquad \text{8.1-A7}$$

$$N\alpha + \beta\sum_i \eta_i^2 - \sum_i \frac{\eta_i}{E(\eta)_i} = 0 \qquad \text{8.1-A8}$$

Therefore, α and β can be solved from Eq. 8.1-A3 and A4:

$$\alpha = [\sum_i \frac{\eta_i}{E(\eta)_i} - \frac{1}{N}\sum_i \eta_i^2 \sum_i \frac{1}{\eta_i E(\eta)_i}]/[N - \frac{1}{N}\sum_i \eta_i^2 \sum_i \frac{1}{\eta_i^2}] \qquad \text{8.1-A9}$$

$$\beta = \frac{1}{N}[\sum_i \frac{1}{\eta_i E(\eta)_i} - \alpha\sum_i \frac{1}{\eta_i^2}] \qquad \text{8.1-A10}$$

The parameters *a* and *b* can be calculated from

$$a = \sqrt{\frac{1}{\alpha\beta}} \qquad \text{8.1-A11}$$

and

$$b = a\beta \qquad \text{8.1-A12}$$

Regression of the parameters *a* and *b* from the radial imbibition data of Fig. 8.1-5 gave a = 0.01609 and b= 0.23300.

Acknowledgements

Funding for this research was provided by the US Department of Energy, National Energy Technology Laboratory contract #DE-FC26-03NT15408, and the University of Wyoming Enhanced Oil Recovery Institute. Special thanks are expressed to Dr. Geoffrey Mason, Loughborough University, for stimulating discussions.

Nomenclature

a	dimensionless parameter in $E(\eta)$
A	cross-sectional area, cm^2
A_i	area open to imbibition, cm^2
A_o	cross-sectional area of the region of oil flow, cm^2
A_w	cross-sectional area of the region of the aqueous phase, cm^2
b	dimensionless parameter in $E(\eta)$
d	core diameter, *cm*
$E(\eta)$	dimensionless function of η
k_g	gas permeability, *darcy*
k_{Ao}	permeability to oil associated with A_o, *darcy*
k_{Aw}	permeability to water associated with A_o, *darcy*
l_{Ai}	distance traveled by imbibition front from the open surface
L	core length, *cm*
L_c	characteristic length, *cm*
n	power index
p_{cb}	capillary pressure at the open boundary, *atm*
p_{cf}	capillary pressure at the displacement front, *atm*
p_{ob}	oil phase pressure at the open boundary, *atm*
p_{of}	oil phase pressure at the displacement front, *atm*

p_{wb}	water (aqueous phase) pressure at the open boundary, *atm*
p_{wf}	water (aqueous phase) pressure at the displacement front, *atm*
q_o	rate of oil production, *cc/sec*
q_w	rate of water (aqueous phase) production, *cc/sec*
R	oil recovery, *% OOIP*
R_f	final recovery, *%*
R_N	normalized oil recovery, fraction or %
$R_{N,rad}$	normalized oil recovery from radial flow, fraction or %
$R_{N,sph}$	normalized oil recovery from spherical flow, fraction or %
$R_{N,cyl}$	normalized oil recovery for the all-faces-open boundary condition, fraction or %
t	imbibition time, *min*
t_D	dimensionless imbibition time
$t_{D,lin}$	linear case dimensionless imbibition time
t_D^*	dimensionless imbibition time
V_b	core bulk volume, cm^3
x	frontal position, *cm*
x_D	normalized frontal position, fraction
α	dimensionless function of *a* and *b*
β	dimensionless function of *a* and *b*
ϕ	porosity, *%*
η	square root of viscosity ratio
μ_{gm}	geometric mean viscosity, *cP*
μ_o	oil viscosity or viscosity of the dispersion medium, *cP*
μ_w	water viscosity, *cP*
σ	surface or interfacial tension, *dynes/cm*
Ψ	oil/water viscosity ratio

Acronyms

AFO	all-faces-open
OEO	one-end-open
TEC	two-ends-closed

Table 8.1-1. Synthetic seawater Ionic strength

NaCl	28.0000	g/l
KCl	0.9350	g/l
$MgCl_2$	5.3625	g/l
$CaCl_2$	1.1900	g/l
Na_2SO_4	4.0000	g/l
NaN_3	0.1000	g/l
TDS	39.5875	g/l

Table 8.1-2 Rock and fluid properties
Boundary condition: One End Open (OEO), linear flow

Core	L_c cm	k_g md	ϕ %	σ dyn/cm	μ_{ap} cP	μ_o cP	μ_{gm} cP	ψ
EV6-13	7.75	113.2	18.4	50.5	1.0	3.9	2.0	3.90
EV6-14	7.66	127.2	17.8	41.2	4.1	3.9	4.0	0.95
EV6-21	7.70	107.3	18.7	34.3	27.8	3.9	10.4	0.14
EV6-23	7.36	132.1	17.9	31.3	97.7	3.9	19.5	0.04
EV6-22	7.18	109.2	18.0	28.9	494.6	3.9	43.9	0.01
EV6-18	7.62	140.0	18.1	51.3	1.0	63.3	8.0	63.30
EV6-20	7.52	132.9	18.1	41.7	4.1	63.3	16.1	15.44
EV6-16	7.78	136.8	18.1	34.8	27.8	63.3	41.9	2.28
EV6-17	7.54	128.1	19.0	32.1	97.7	63.3	78.6	0.65
EV6-15	7.73	107.0	18.3	29.8	494.6	63.3	176.9	0.13

Table 8.1-3 Rock and fluid properties
Boundary condition: Two Ends Closed (TEC), radial flow

Core	L_c cm	k_g md	ϕ %	σ dyn/cm	μ_{ap} cP	μ_o cP	μ_{gm} cP	ψ
EV6-69	1.34	146.6	19.3	50.5	1.0	3.9	2.0	3.90
EV6-71	1.34	149.1	19.3	41.2	4.1	3.9	4.0	0.951
EV6-67	1.34	110.0	18.6	34.3	27.8	3.9	10.4	0.14
EV6-66	1.34	145.0	19.1	31.3	97.7	3.9	19.5	0.04
EV6-76	1.34	146.8	19.0	28.9	494.6	3.9	43.9	0.01
EV6-74	1.34	106.1	18.6	51.3	1.0	63.3	8.0	63.30
EV6-75	1.34	146.3	18.7	41.7	4.1	63.3	16.1	15.44
EV6-79	1.34	137.9	19.1	34.8	27.8	63.3	41.9	2.277
EV6-77	1.34	128.0	18.8	32.1	97.7	63.3	78.6	0.65
EV6-70	1.34	153.5	19.2	29.8	494.6	63.3	176.9	0.13
EV6-8	1.34	151.4	19.8	52.8	1.0	173.1	13.2	173.10
EV6-8A	1.34	138.7	19.4	43.1	4.9	173.1	29.1	35.33

Table 8.1-4 Rock and fluid properties
Boundary condition: All Faces Open (AFO)

Core	L_C cm	k_g md	ϕ %	σ dyn/cm	μ_{ap} cP	μ_o cP	μ_{gm} cP	ψ
C1-1 *	1.24	62.3	16.9	39.8	4.4	3.9	4.1	0.89
C1-3 *	1.24	62.7	16.8	31.2	99.8	3.9	19.7	0.04
EV6-72	1.23	112.3	18.6	51.3	1.0	63.3	8.0	63.30
EV6-80	1.23	148.4	19.2	41.7	4.1	63.3	16.1	15.44
EV6-81	1.23	136.7	19.1	34.8	27.8	63.3	41.9	2.28
EV6-73	1.24	143.9	19.1	32.1	97.7	63.3	78.6	0.65

* Fischer and Morrow, 2004

Table 8.1-5 Flow regimes and the respective characteristic lengths

Boundary condition	1) Flow regimes	*Characteristic length,* L_c
One End Open (OEO)	Linear	$L_c = l$
Two Ends Closed (TEC)	Radial (2D)	$L_c = \frac{d}{2\sqrt{2}}$
Cylindrical (AFO)	Complex	$L_c = \frac{ld}{2\sqrt{d^2 + 2l^2}}$
Sphere	Radial (3D)	$L_c = \frac{d}{2\sqrt{3}}$

Table 8.1-6 Values of *E*(*η*) and *n* for TEC (radial flow)

η	$E(\eta)$	n
0.09	0.00057	2.12
0.20	0.00111	2.09
0.36	0.00171	2.10
0.38	0.00163	2.11
0.81	0.00320	2.04
0.98	0.00374	1.97
1.51	0.00497	1.97
1.97	0.00540	1.73
3.93	0.00782	1.94
5.94	0.00753	1.95
7.96	0.00657	2.04
13.15	0.00486	2.00
a = 0.01609		
b = 0.23300		

Table 8.1-7 BC: OEO (linear flow) Predicted *E*(*η*) (*a* and *b* values from TEC data the fit to TEC data) TEC data

η	E(η)	n
0.09	0.00034	2.20
0.20	0.00076	2.13
0.36	0.00134	2.12
0.38	0.00158	2.13
0.81	0.00294	2.13
0.98	0.00358	2.00
1.51	0.00504	1.97
1.97	0.00613	1.87
3.93	0.00781	1.87
7.96	0.00638	2.10

Table 8.1-8 BC: AFO (cylindical flow). Predicted *E*(*η*) (*a* and *b* from the fit to

η	$E(\eta)$	n
0.20	0.00076	2.28
0.81	0.00294	1.99
0.98	0.00354	1.74
1.51	0.00537	1.80
3.98	0.00802	1.67
7.96	0.00638	1.96

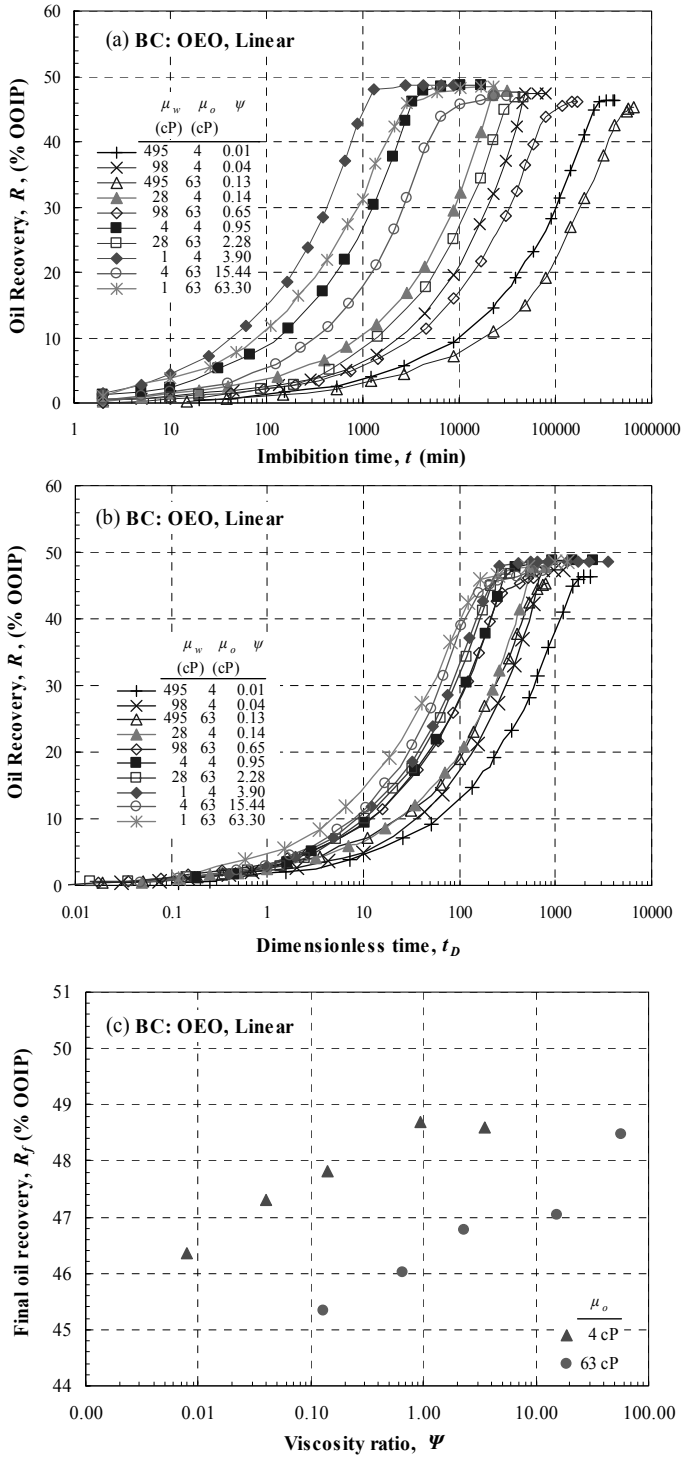

Fig. 8.1-1 Recovery of oil by spontaneous imbibition for one-end-open cores and non-matched viscosity versus (a) time, *t*, and (b) dimensionless time; t_D, (c) final oil recovery, R_f, versus viscosity ratio, Ψ.

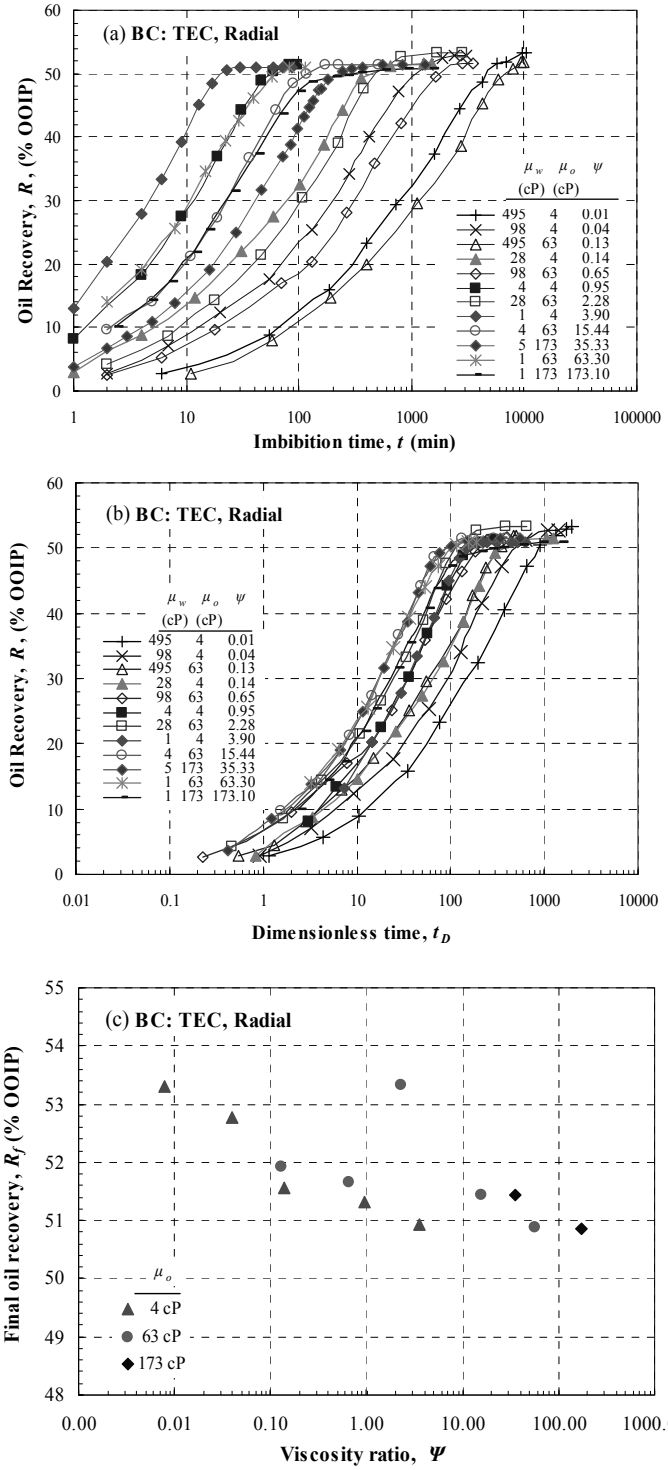

Fig. 8.1-2 Recovery of oil by spontaneous imbibition for two-ends-closed cores and non-matched viscosity versus (a) time, t, and (b) dimensionless time; t_D, (c) final oil recovery, R_f, versus viscosity ratio, Ψ.

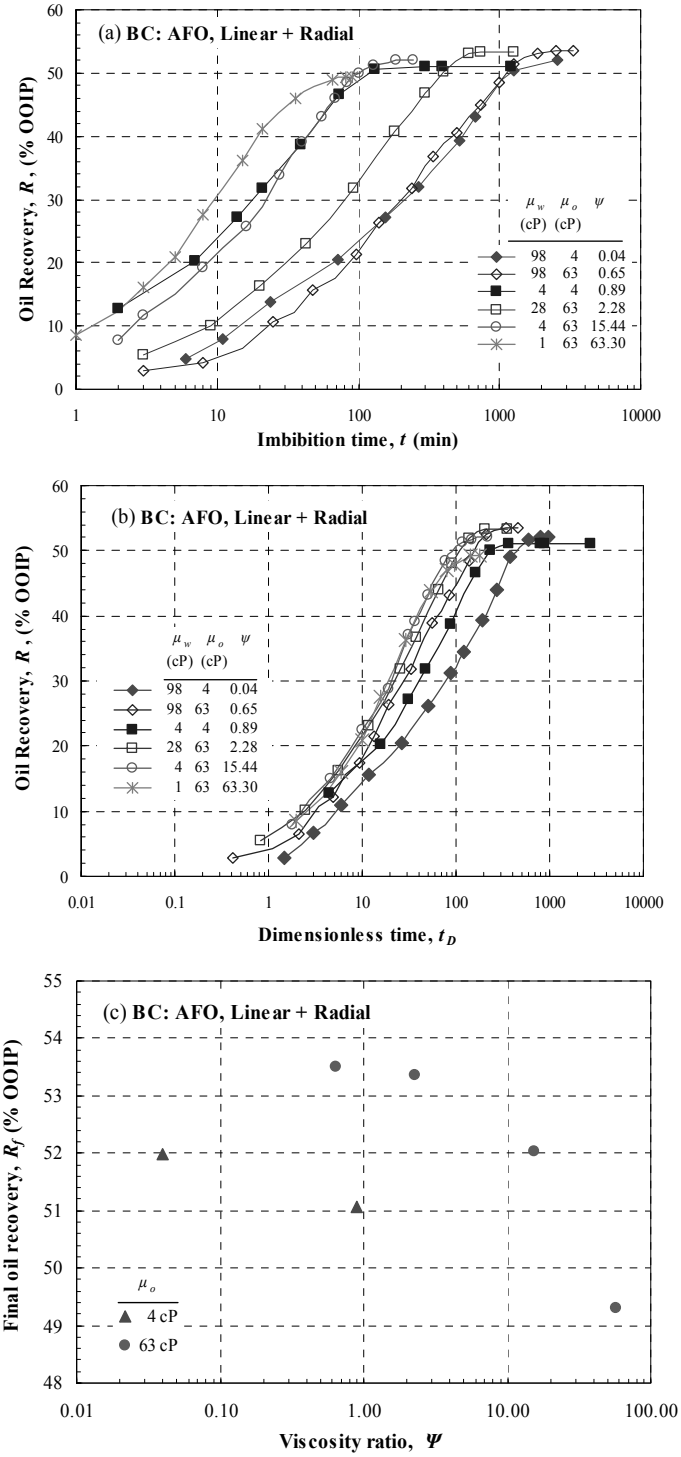

Fig. 8.1-3 Recovery of oil by spontaneous imbibition for all-faces-open cores and non-matched viscosity versus (a) time, *t*, and (b) dimensionless time; t_D, (c) final oil recovery, R_f, versus viscosity ratio, Ψ.

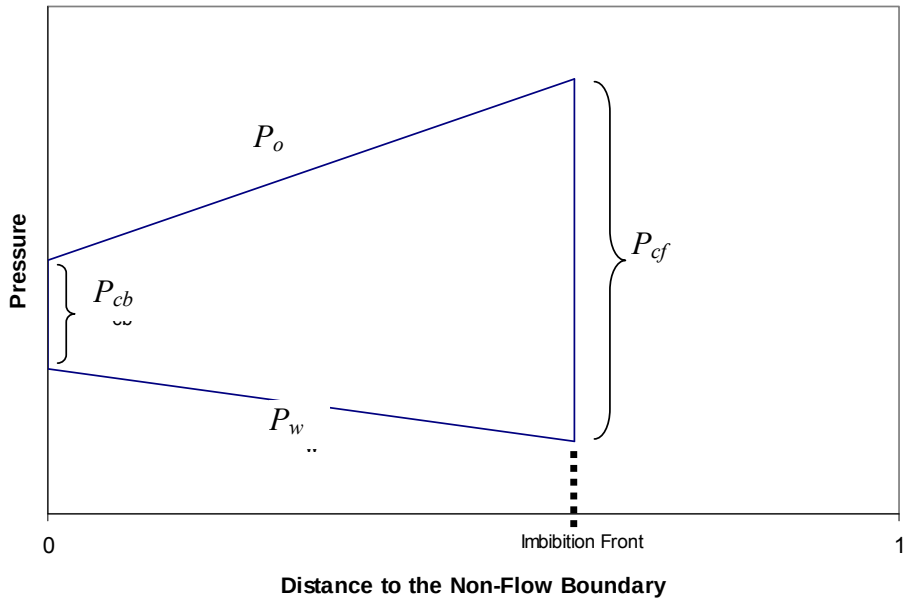

Fig. 8.1-4 Conceptual pressure distributions for the frontal displacement model of counter-current spontaneous imbibition in strongly water wet cores.

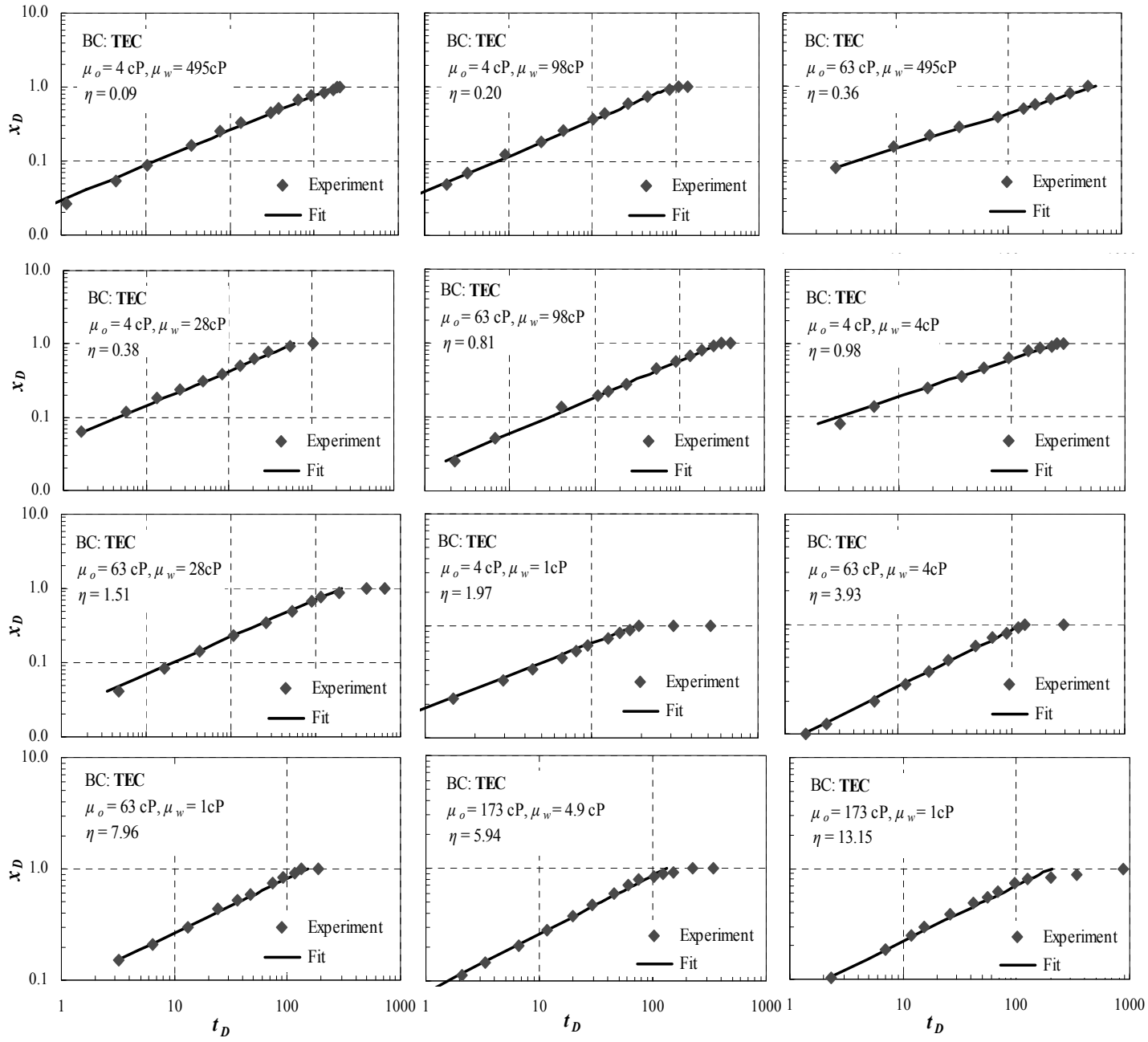

Fig. 8.1-5 TEC (radial flow) experimental data and the respective best fit by adjustment of the parameters $E(\eta)$ and n.

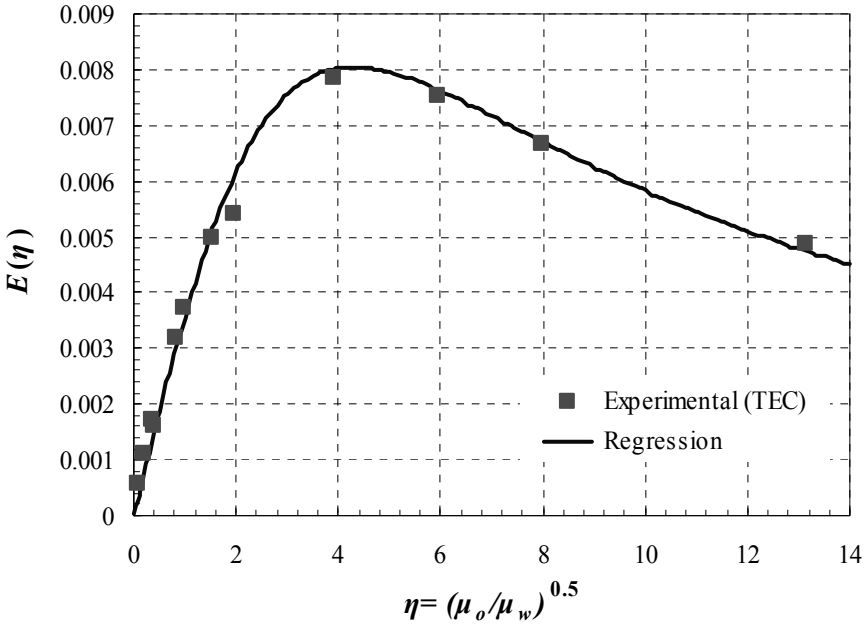

Fig. 8.1-6 Fit to experimental data for radial flow (TEC) of $E(\eta)$ versus η.

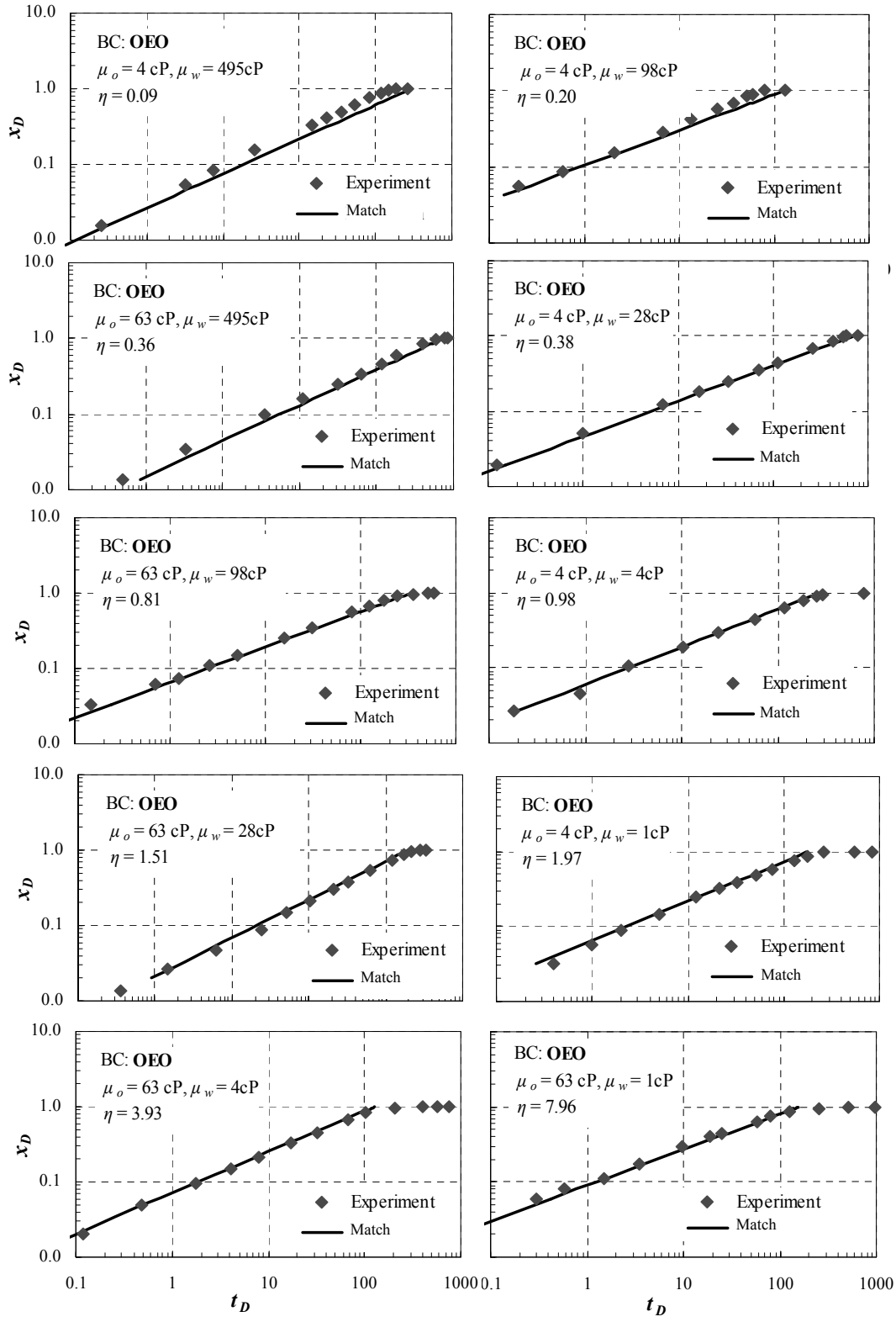

Fig. 8.1-7 OEO (linear flow) experimental data and the respective match by the mathematical model.

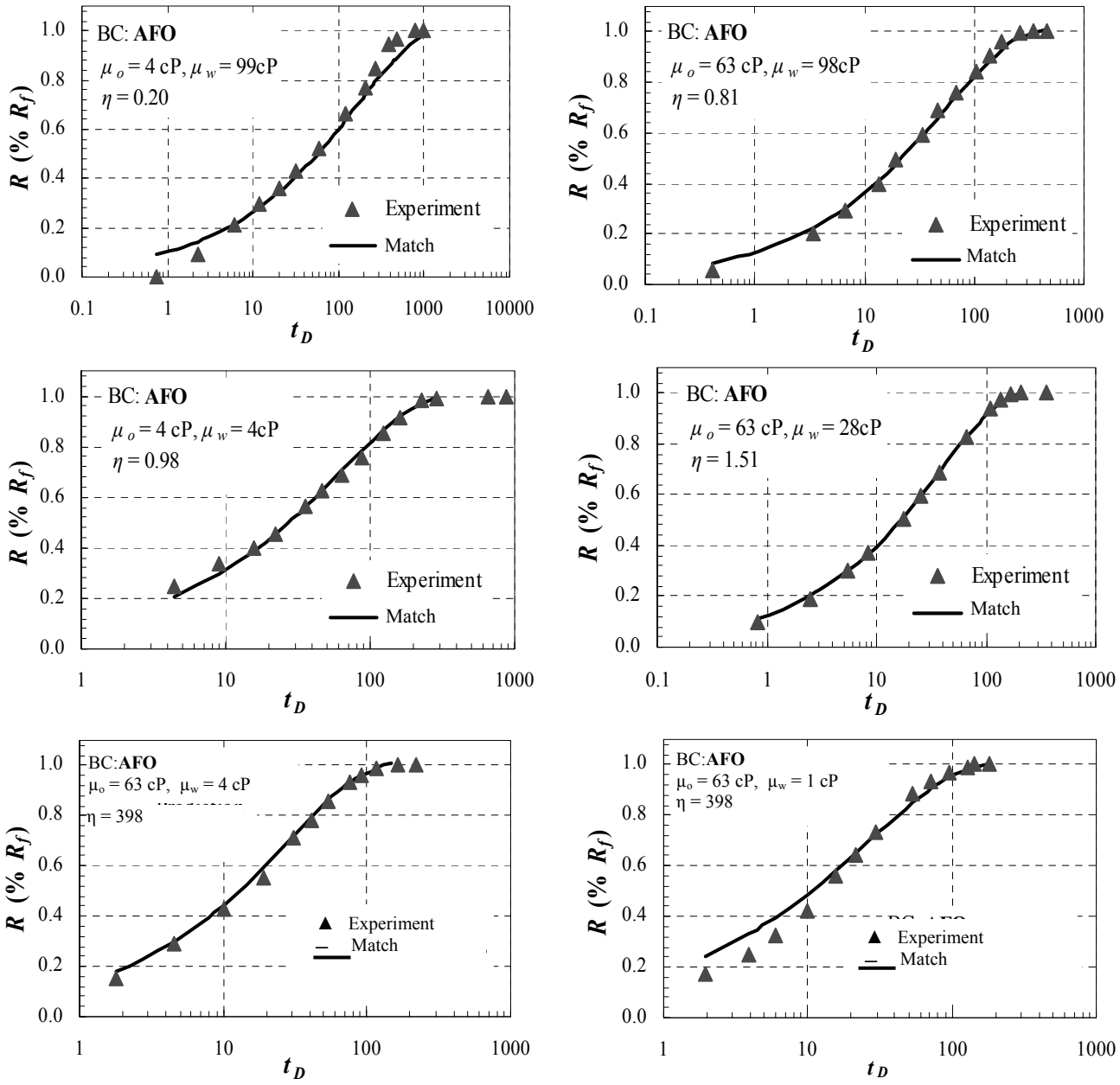

Fig. 8.1-8 Experimental data for cylindrical cores (AFO) and respective match from the mathematical model.

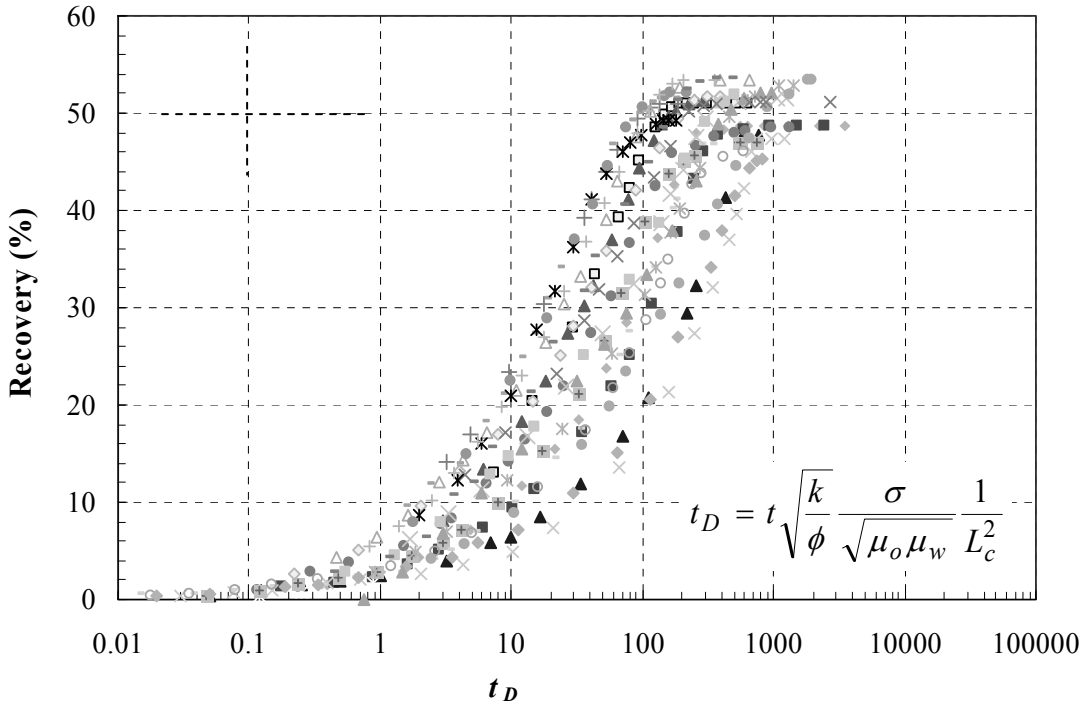

Fig. 8.1-9 Recovery of oil by spontaneous imbibition versus t_D for 10 One End Open, 12 Two Ends Closed and 6 AFO data sets.

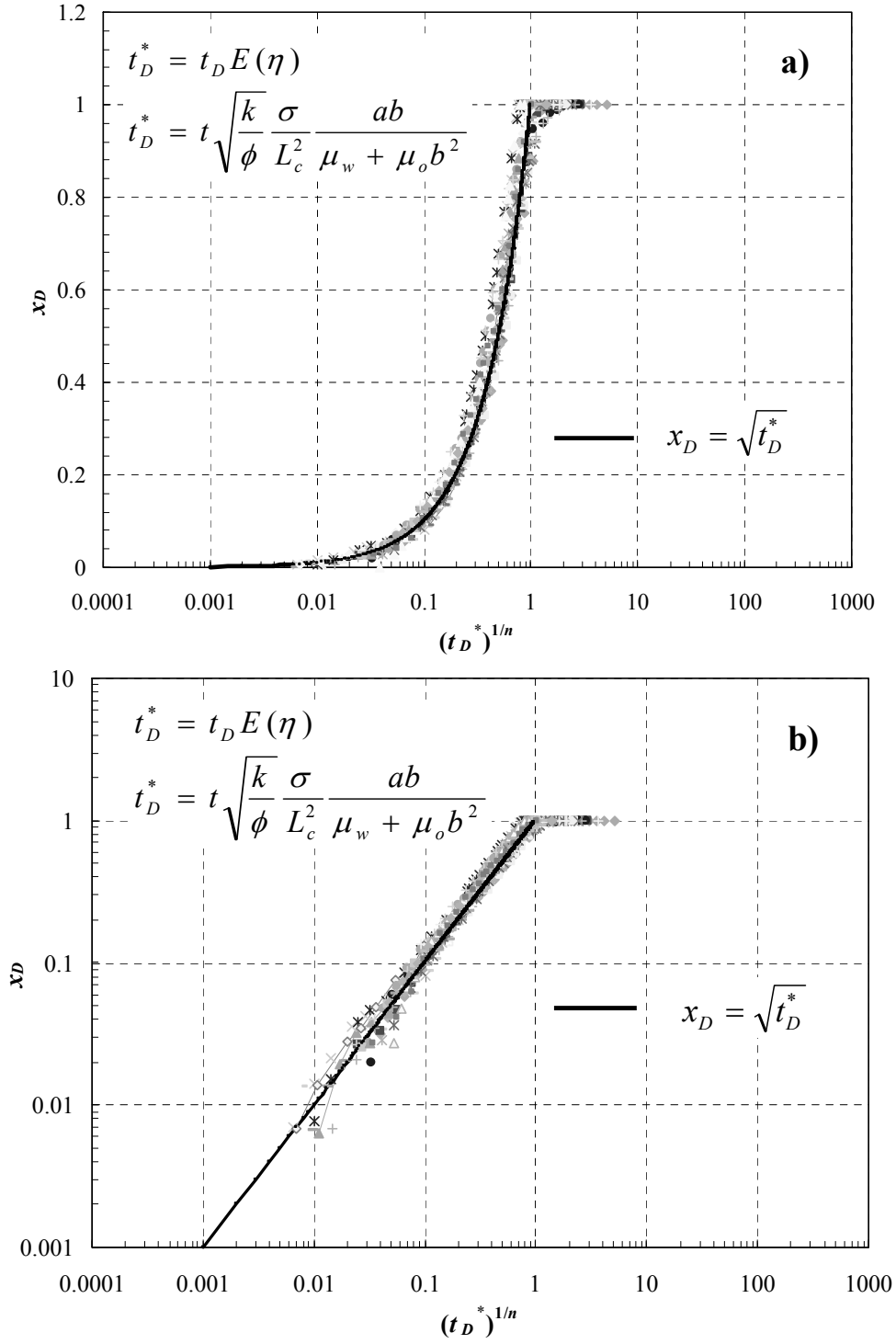

Fig. 8.1-10 Normalized front position versus the *n*-th root of $t_D E(\eta)$ for 10 One End Open, 12 Two Ends Closed and 6 AFO imbibition data sets on a (a) semilog plot and (b) log-log plot. A close match with the correlation is given by *n* = 2

8.2 Co-current and counter-current imbibition in independent tubes of non-axisymmetric geometry

E. Unsal, G. Mason, N.R. Morrow, and D. Ruth
Journal of Colloid and Interface Science, 2007, 306, 105 – 117.

Abstract
Experiments that illustrate and quantify the basics of co- and countercurrent spontaneous imbibition have been conducted in a series of simple model pore systems. The fundamental pore geometry is a rod in an angled round-bottomed slot with the rod touching a capping glass plate. The capillaries thus formed by the surfaces of the slot, rod and plate do not have circular cross-sections but more complicated geometric structures with angular corners. The tubes formed at each side of the rod connect at both ends. A viscous, refined oil was applied from one end. For co-current experiments, the opposite end was left open to the atmosphere and oil imbibed into both tubes. For countercurrent experiments the opposite end was sealed and connected to a sensitive pressure transducer. Oil imbibed into the smaller capillary and expelled air as a series of bubbles from the end of the larger capillary. Bubble snap-off was observed to be rate-dependent and occurred at a lower curvature than that of the cylindrical meniscus that just fits inside the tube. Only the corners of the larger capillary filled with oil during countercurrent imbibition. Meniscus curvatures were calculated using the Mayer and Stowe-Princen method and were compared with actual values by measuring the capillary rise in the tubes; agreement was close. A simple model for co-current and countercurrent imbibition has also been developed and the predictions compared with the experimental results. The model results were in agreement with the experiments. The experiments demonstrate that the capillary back pressure generated by the interfaces and bubbles in countercurrent imbibition can slow the process significantly.

Introduction
A key process in the production of oil from fractured reservoirs is spontaneous imbibition. Such spontaneous imbibition may be either co-current or countercurrent, the second being more common. The main difference between the two mechanisms for imbibition is the direction of flow. In a co-current displacement the wetting and the non-wetting fluids move in the same direction with the non-wetting phase being pushed out ahead of the wetting phase. In countercurrent imbibition the phases move in opposite directions. The flows of both phases require a pressure gradient to drive them and, because the flows of each phase are in opposite directions, the pressure gradients have to be in opposite directions as well (Reis and Cil, 1993; Cil and Reis, 1996; Li et al., 2003). In general, the rate of co-current imbibition is about four times faster than that of countercurrent imbibition.

The physics of immiscible displacement in porous media has been simulated extensively by many researchers using a bundle of independent capillary tubes as the model (Nicholson, 1971; Nicholson, 1973; Lenormand et al., 1988; Dullien, 2000). In some of these models, the capillaries are uniform and identical, while in others they are uniform but have different diameters. The most important feature of these models is that there is no interaction between the tubes. Therefore the flow within each tube is independent of the others. The effect is that the menisci in the larger tubes advance faster than the ones in the smaller tubes. Dong and Dullien (1997) developed a capillary model for studying countercurrent flow, the model consisted of two capillary tubes connected by two short capillaries at the ends of the tubes. Only the two capillaries were involved. They

analysed the saturation profiles during countercurrent imbibition inside the tubes. Dong et al (1998) published a theoretical paper that introduced the concept of two parallel tubes for which the water in each tube at a single position along the tubes had the same pressure and the oil in each tube at the same position along the tubes had the same pressure. However, if one tube contained water and the other tube contained oil at the same position, the pressures of the two fluids could be different. They showed that, under these conditions, the invading fluid in the small tube always leads the invading fluid in the large tube. Ruth and Bartley (2003) extended this model by allowing for cross-flow without pressure-drop, what they termed "perfect cross-flow", between many tubes. They simulated co-current flow through sixty cross-connected capillaries of different sizes. In this situation, the menisci in the smaller tubes always lead the menisci in the larger tubes, the reverse of the independent tube model. The flow of a single phase in any tube is governed by the Hagen-Poiseuille equation. The Ruth and Bartley cross-flow model yielded results consistent with the Darcy model for two phase flow. Dong et al (2005; 2006) published further work that analyzed immiscible displacement through interacting capillaries; their results were consistent with those of Ruth and Bartley and with laboratory experiments using simple pore geometries.

As yet, the fundamentals of spontaneous countercurrent imbibition are still not completely understood. Our objective was to carry out experiments on some simple precise model systems and compare the results with theoretical predictions. Once the correct assumptions are known, they can be incorporated into continuum and pore network models so that they can better simulate imbibition. One key effect that we wished to observe was the actual process by which the non-wetting phase is ejected from the model pores; we also wished to measure the pressure that the process generates.

Design and capillary properties

Because the pores in oil reservoir rocks are normally angular, our model pores were designed to have angular corners. Based on past experience (Mason, 1983; Mason and Morrow, 1985; Mason et al., 2000), we decided to use a rod in a round-bottomed slot capped by a glass plate. The glass plate enabled the behavior of the menisci to be observed. The slot was not vertical but angled slightly so that the tubes formed on each side of the rod were of different shape and size. In co-current imbibition, both tubes filled together. In countercurrent imbibition, the small tube and the corners of the large tube filled and the displaced fluid (air) was driven out of the larger tube as a series of bubbles. Interconnection between the tubes can be made by making the slot deeper so that there is a gap between the rod and the plate. Experiments with this system will be reported separately.

The relationship between pore size and capillary pressure is straightforward for capillaries with circular cross-sections but is more complicated when the cross-section is irregular. For example, the meniscus in a tube with triangular cross-section is of complex shape because liquid is held in the corners of the tube (Mason et al., 2000). In order to model imbibition mathematically, the capillary properties of each of the two tubes have to be understood. The important properties are the meniscus curvatures at which the non-cylindrical pores fill or drain. The pore geometries of the experimental models used in this study are given by a rod in an angled slot with the rod touching (|AB|) or slightly spaced from a glass plate (Figure 8.2-1). Because the slot is angled, the tubes at the side of the rod have different sizes and shapes (Figure 8.2-1c). The situation gets more complicated if there is a gap, *d*, present between the rod and the plate, because, in effect, a third

capillary structure can form in the gap and cross-flow between the two tubes can occur (Figure 8.2-1d). With a very large gap, the tube acts as a single capillary.

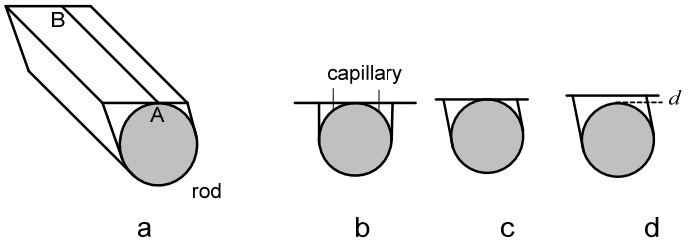

Figure 8.2-1. a) The pore geometry; a rod in an angled slot. b) Diagram of the cross-section of a rod in a square slot. c) Cross-section with the tube down one side larger than the other. d) Cross-section when the rod is spaced away from the capping glass plate. Three potential menisci are possible depending on the gap width: one large tube, one small tube and the meniscus in the gap.

The displacement curvatures of interfaces in uniform tubes of triangular, square or much more complex cross-section can be calculated using the Mayer and Stowe-Princen (MS-P) theory (Mayer and Stowe, 1965; Princen, 1969a; Princen, 1969b; Princen, 1970; Ma et al., 1996). The interface curvatures for menisci in complex cross-sections (three rods and a plate) such as those shown in Figure 8.2-1 have been calculated previously using the theory (Mason et al., 2000; Mason and Morrow, 1984). The behavior is quite complicated with, in some cases, as many as 3 coexisting menisci.

The curvatures of menisci in a rod-slot geometry with a general angle have been calculated using MS-P theory. The theory covers all cell angles but only cells with slot angles (β) of 65º, 75º and 85º were built for the experimental investigations. Typical relationships between meniscus curvatures and the width of the rod-plate gap are shown in Figure 8.2-2 for the various possible meniscus configurations.

As seen in Figure 8.2-2, for small gaps ($d/R < 0.13$) there are three menisci; a potentially very highly curved one in the gap between the rod and the plate, a less highly curved one in the small tube, and a meniscus in the large tube with about half of the curvature of the small tube meniscus. The lowest curvature indicated on Figure 8.2-2 is that of a cylindrical meniscus in the large tube; it corresponds to the curvature at which a bubble would snap off in this tube (Ma et al., 1996). For larger gaps ($0.13<d/R<0.42$), the distinct two-sided meniscus between the rod and the plate which separates the menisci in the large and small tube no longer exists. There is instead a capillary structure between the rod and the plate which is shared by the meniscus in the large tube and the meniscus in the small tube. For large spacings between the rod and the plate ($d/R>0.42$), this structure disappears and, apart from the arc menisci in the corners, the tube is spanned by a single meniscus.

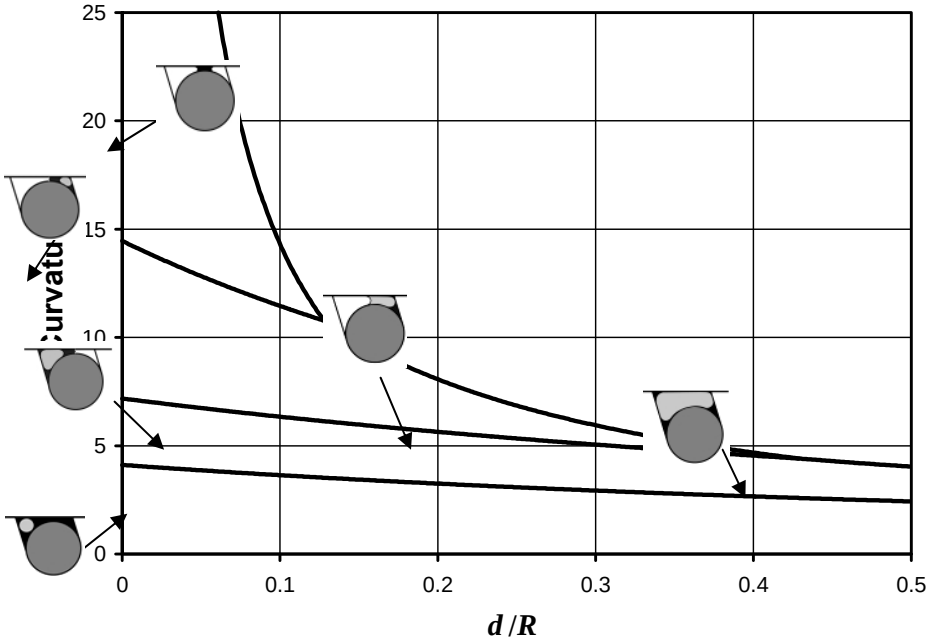

Figure 8.2-2. Meniscus curvatures normalised with respect to rod radius as a function of gap size, d, for a rod in an angled slot such as that shown in Figure 8.2-1(d). Slot angle β is 75º, d is the normalized gap size between the rod and the plate. R is the rod radius. The white areas show the tube space, black shows the wetting phase, and the grey shows the nonwetting phase, for each arc meniscus configuration.

Theoretical analysis

The experimental cell used to demonstrate the capillary properties of the rod-slot arrangement consists of two capillary tubes, one small (1) and one large (2), of the same length but of different cross-sections, plus the separate additional capillary. Initially all are completely filled with air (non-wetting phase) and at time t=0 the capillaries 1 and 2 are exposed to oil (wetting fluid) and oil partly fills the additional capillary. The interface in the additional capillary develops a pressure; this effect needs to be included in the analysis. General positions of the oil/air menisci during the process of oil displacing air are shown in Figure 8.2-3. During experiments the meniscus positions were video-taped so that the change in position of the interfaces with time could be determined.

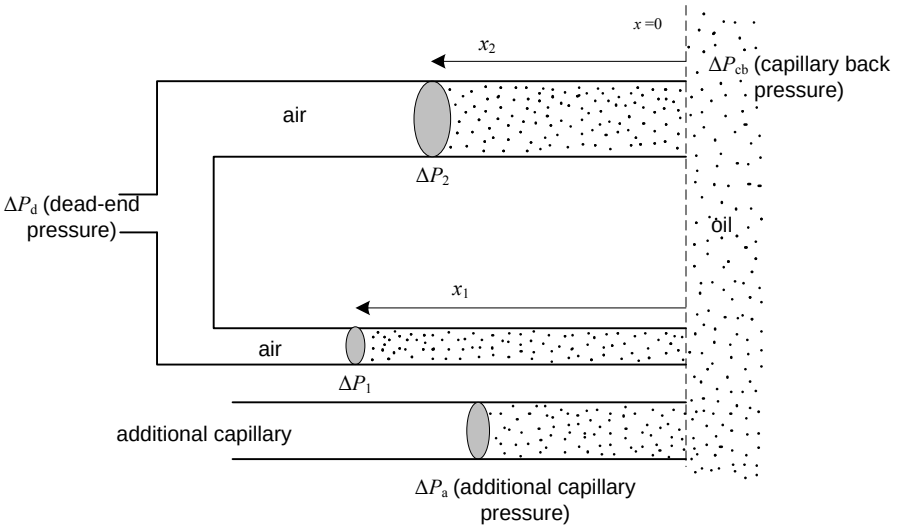

Figure 8.2-3. The positions of the oil/air menisci in the capillaries at time (t) in the process of oil displacing air.

The cell is operated horizontally to minimize the gravity effects. If both ends of the capillaries are open and the invading fluid is contacted with one end, then there will be co-current imbibition. The meniscus in the large tube will always be ahead of the meniscus in the small tube. Two menisci (one in each tube) will advance with the distance traveled varying as $(\text{time})^{1/2}$ (Washburn, 1921). There are also arc menisci in the corners of the tubes. If the air-filled end is closed, then countercurrent imbibition occurs. The flows of each phase are now in opposite directions with oil flowing into the small tube and air out of the large tube. The curvature of the meniscus spanning each tube will equal to the local curvature of the arc menisci in the tube corners (the basis of the MS-P theory). Eventually, air will reach the oil end of the large tube and an air bubble will form from the center. The arc menisci in the corners are initially highly curved and their curvature decreases as they expand away from the corners. In the air-filled large tube, the curvature of the arc menisci near the oil end almost equals the curvature of the bubble leaving the tube center. When these arc menisci overlap the bubble will snap off. When the small tube is filled to the end with oil, imbibition will cease with the center of the large tube still filled with air. The rate at which imbibition occurs will depend on the sizes of the two tubes.

Theory of co-current imbibition

The theory for co-current imbibition is less complicated than for countercurrent imbibition. The relation between the distance that the meniscus advances, x, in terms of volumetric flow rate Q and time t is,

$$\bar{u} = \frac{dx}{dt} = \frac{Q}{A} \qquad 8.2\text{-}1$$

where $\bar{u}$ is the average velocity and A is the cross-sectional area of the capillary. The cross-sectional area and the perimeters of the side capillaries for two tubes with a cell angle β are shown in Figure 8.2-4.

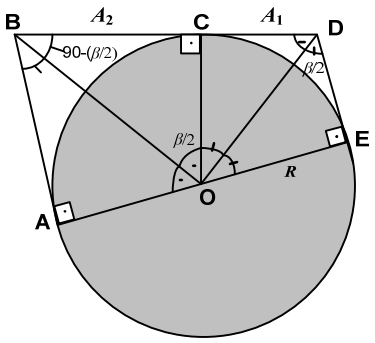

Figure 8.2-4. Cross-sections of capillaries.

$$A_1 = R^2 \tan(90 - \beta/2) - [\pi R^2 (180 - \beta)/360] \quad 8.2\text{-}2$$

$$A_2 = [R^2 \tan(\beta/2)] - [\pi R^2 \beta/360] \quad 8.2\text{-}3$$

$$S_1 = 2R \tan(90 - \beta/2) + 2\pi R((180 - \beta)/360) \quad 8.2\text{-}4$$

$$S_2 = 2R \tan(\beta/2) + 2\pi R(\beta/360) \quad 8.2\text{-}5$$

where A_1 is the cross-sectional area of the small capillary, A_2 is the cross-sectional area of the large capillary, S_1 is the perimeter of the small capillary, S_2 is the perimeter of the large capillary and R is the rod radius. For laminar flow, $\overline{u}$, is given by,

$$\overline{u} = \frac{dx}{dt} = \frac{k}{\mu}\delta^2 \frac{P}{x} \quad 8.2\text{-}6$$

where δ is a dimension associated with the tube, μ is the fluid viscosity, x is the length, P is the pressure difference driving the flow and k is a shape factor. For co-current flow, the cell is open to the atmosphere so P is the difference between the pressure across the interface (ΔP) and the pressure developed by the additional capillary (ΔP_a) (see Equation 8.2-7).

$$\overline{u} = \frac{dx}{dt} = \frac{k}{\mu}\delta^2 \frac{(\Delta P - \Delta P_a)}{x} \quad 8.2\text{-}7$$

Note that air is being displaced and, because the viscosity of air is so small, this takes virtually no pressure drop. The fluid imbibing into the tubes is drawn from the additional capillary, which, because of its large cross-section, also takes virtually no pressure drop. For a particular tube let $k\delta^2 = K$, a constant. Thus the variables can be separated giving,

$$\int_{x_0}^{x_t} x dx = \frac{K(\Delta P - \Delta P_a)}{\mu} \int_{t_0}^{t} dt \quad 8.2\text{-}8$$

and

$$K_1 = \frac{(x_{1,t}^2 - x_{1,0}^2)\mu}{2(\Delta P_1 - \Delta P_a)(t - t_0)} \quad \text{and} \quad K_2 = \frac{(x_{2,t}^2 - x_{2,0}^2)\mu}{2(\Delta P_2 - \Delta P_a)(t - t_0)} \quad 8.2\text{-}9$$

In Equation 8.2-9, the variables μ, $(\Delta P_1 - \Delta P_a)$, $(\Delta P_2 - \Delta P_a)$, K_1 and K_2 are all constants, so a plot of $(x_{1,t}^2 - x_{1,0}^2)$ and $(x_{2,t}^2 - x_{2,0}^2)$ vs $(t\text{-}t_0)$ should be a straight line, with a gradient of $m_1 = \frac{2(\Delta P_1 - \Delta P_a)K_1}{\mu}$ for the small capillary and $m_2 = \frac{2(\Delta P_2 - \Delta P_a)K_2}{\mu}$ for the large capillary. In addition, eliminating $(t - t_0)$ from Equation 8.2-9 gives

$$x_{1,t}^2 - x_{1,0}^2 = \frac{(\Delta P_1 - \Delta P_a)}{(\Delta P_2 - \Delta P_a)} \frac{K_1}{K_2} (x_{2,t}^2 - x_{2,0}^2) \qquad 8.2\text{-}10$$

In Equation 8.2-10, a plot of $x_{1,t}^2$ vs $x_{2,t}^2$ should be a straight line, with a gradient of $m = \frac{(\Delta P_1 - \Delta P_a)}{(\Delta P_2 - \Delta P_a)} \frac{K_1}{K_2}$ and intercept of $(x_{1,0}^2 - m x_{2,0}^2)$ since the variables $x_{1,0}^2$, $x_{2,0}^2$, K_1, K_2, $(\Delta P_1 - \Delta P_a)$ and $(\Delta P_2 - \Delta P_a)$ are constants.

In an experiment, the x values can be determined from time-spaced video images. The capillary pressure ($\Delta P_1, \Delta P_2, \Delta P_a$) can be measured in separate experiments and so the values of K_1 and K_2 can be determined. Because these factors depend only on the geometry of the capillaries, they will be the same for both co- and countercurrent imbibition. Therefore the co-current experiments can be used to obtain values for parameters in the countercurrent experiments which cannot otherwise be measured.

Theory of countercurrent imbibition

For countercurrent imbibition, the flow equation is the same as Equation 8.2-6 but the driving pressures are different. There is an additional pressure at the end of the cell which drives the countercurrent flow in the large tube but also slows the flow in the small tube. If ΔP_d is the pressure difference between atmospheric and that in the dead end then the pressure during flow in the small (tube 1) is

$$[\Delta P_1 - \Delta P_a - \Delta P_d] \qquad 8.2\text{-}11$$

In the larger capillary, the pressure during the countercurrent flow is

$$[\Delta P_d + \Delta P_a - \Delta P_{cb}] \qquad 8.2\text{-}12$$

where ΔP_{cb} is the capillary back pressure in tube 2. If the tube contains a meniscus then ΔP_{cb} will be ΔP_2. However, when the meniscus is not in the tube, it blows a bubble at the tube exit and the pressure ΔP_{cb} is less than ΔP_2 but it is still not zero. Eventually, the bubble snaps off and the meniscus retreats up the large tube. ΔP_{cb} then becomes equal to ΔP_2 again. The flow rates in the two tubes during countercurrent imbibition are

$$Q_1 = \overline{u}_1 A_1 = \frac{K_1}{\mu} A_1 \frac{[\Delta P_1 - \Delta P_a - \Delta P_d]}{x_1} \qquad 8.2\text{-}13$$

and

$$Q_2 = \bar{u}_2 A_2 = \frac{K_2}{\mu} A_2 \frac{[\Delta P_d + \Delta P_a - \Delta P_{cb}]}{x_2} \quad 8.2\text{-}14$$

where x_1 and x_2 are the positions of the interfaces, $K_1 = k_1\delta_1^2$ and $K_2 = k_2\delta_2^2$. When $x_2>0$ then $\Delta P_{cb}=\Delta P_2$.

As the interface in the small capillary imbibes, the interface in the larger capillary tube moves in the reverse direction. The volumetric flow rates are equal.

$$Q_1 = Q_2 \quad 8.2\text{-}15$$

giving (from Equations 8.2-13 – 8.2-15)

$$\frac{K_1}{K_2}\frac{A_1}{A_2}\frac{x_2}{x_1}[\Delta P_1 - \Delta P_a - \Delta P_d] = [\Delta P_d + \Delta P_a - \Delta P_{cb}] \quad 8.2\text{-}16$$

and if $B = \frac{K_1}{K_2}\frac{A_1}{A_2}$ 8.2-17

$$B\frac{x_2}{x_1}(\Delta P_1 - \Delta P_a - \Delta P_d) = \Delta P_d + \Delta P_a - P_{cb} \quad 8.2\text{-}18$$

and, rearranging

$$\Delta P_d = \frac{B\frac{x_2}{x_1}\Delta P_1 + \Delta P_{cb}}{1 + B\frac{x_2}{x_1}} - \Delta P_a \quad 8.2\text{-}19$$

If ΔP_{cb} equals ΔP_2, then ΔP_d can be eliminated from Equation 8.2-14 giving

$$\frac{dx_2}{dt} = \frac{K_2 A_2}{\mu x_2}\left[\left[\frac{B\frac{x_2}{x_1}\Delta P_1 + \Delta P_2}{1 + B\frac{x_2}{x_1}} - \Delta P_a\right] + \Delta P_a - \Delta P_2\right] \quad 8.2\text{-}20$$

which rearranges into

$$x_1 dx_2 + B x_2 dx_2 = \left[\frac{K_1 A_1}{\mu}(\Delta P_1 - \Delta P_2)\right]dt \quad 8.2\text{-}21$$

where $\left[\frac{K_1 A_1}{\mu}(\Delta P_1 - \Delta P_2)\right]$ is constant (= D). Volumetric flows are equal in both capillaries, so

$$A_1 dx_1 = -A_2 dx_2 \quad 8.2\text{-}22$$

Integrating Equation 8.2-21 gives

$$\frac{1}{2}B x_2^2 - \frac{1}{2}\frac{A_1}{A_2}x_1^2 = D\,t \quad 8.2\text{-}23$$

Equation 8.2-23 shows that the relationship between (x_1^2, x_2^2) and t should be linear.

Experimental
Experiments were conducted for three model pore systems using a perfectly wetting oil. With the model pore system vertical, the capillary rise in each tube was measured and the curvature of the menisci in each of the three tubes obtained. Next, with the pore system horizontal both co-current and countercurrent imbibition experiments were carried out.

Model Systems
The model is an aluminum block cell with a size 4cm x 11cm x 2cm. It has a round-bottomed angled slot precisely machined into the top surface by means of a ball ended milling cutter to exactly accommodate a steel rod (a drill blank) (Figure 8.2-5). To minimize gravity effects the cell is operated horizontally with a rod of 3.12 mm diameter. There is no hydraulic pathway beneath the rod. The slot is angled (β = 65˚, 75˚, 85˚) and the two capillaries of different sizes are completed by a glass plate above the rod.

The cell has two interconnected reservoirs, the outer (Reservoir I) and the inner (Reservoir II). Reservoir I is cylindrical, with a diameter and a depth of 1 cm. Reservoir II has an elliptical cross-section and is the same depth as Reservoir I. Reservoir II is connected to the end of the rod/slot arrangement. The glass plate covers the full length of the capillaries as well as all of Reservoir II and is secured with retainers and screws.

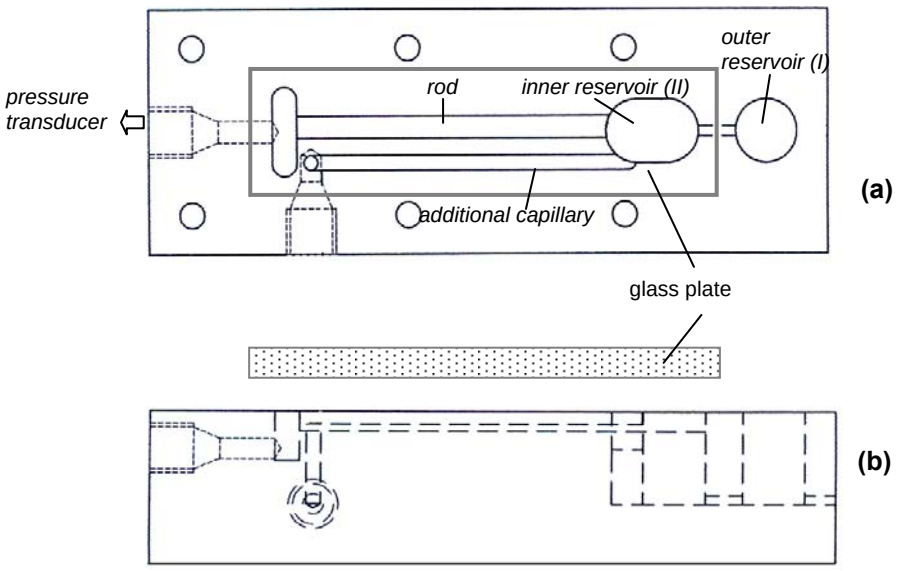

Figure 8.2-5. Sketch of the cell, (a) view from the top (b) the view from the side.

There is an additional capillary running parallel to the rod from reservoir II and which eventually leads out to the atmosphere through the side of the cell. Its purpose is to maintain a constant pressure in Reservoir II. In our initial design, Reservoir II was open to the atmosphere and oil slowly leaked along the edge between the glass plate and the cell. This leakage lowered the level in Reservoir II and produced a drift in the measured pressures. The problem was solved by capping Reservoir II and adding the additional capillary. The interface in the additional capillary also gives a volume leeway in that the meniscus can move forward and backwards at constant capillary pressure.

At the opposite end of the capillaries to Reservoir II there is a small chamber with a pressure tap for connection to one side of a sensitive differential pressure transducer (Furness Model FCO 44). The signal from the transducer is monitored by a data logger. A T-connection is placed where the additional capillary opens to the atmosphere. One end of this T-connection connects to one side of the differential pressure transducer and the other is connected to atmosphere via a long length of tubing. This design reduced the effects of short-term pressure changes in the room (i.e. doors opening).

There is a slight depression ground into the glass plate just above the ends of the capillaries in Reservoir II which allows the bubbles formed during countercurrent imbibition to drift away after they have snapped off. Without this depression a successive bubble can fuse with its predecessor and trigger premature snap-off.

Fluids

For the imbibition experiments, both co-current and countercurrent, medicinal liquid paraffin was used to displace air. For the capillary rise experiments *iso*-octane was used . The densities of the liquids were measured using a pycnometer and the surface tensions using a surface tension balance (Model DB 2kS, White Electronics, WR, UK). The viscosity of paraffin was determined using a viscotester (ThermoHaake VT550, Haake, Germany). The properties of both liquids are given in Table 8.2-1.

Table 8.2-1. Properties of liquid paraffin and iso-octane.

solution	Density	Viscosity	surface tension
Liquid paraffin	0.83 g/cm^3	180 mPa.s	33.83 dyne/cm
Iso-octane	0.71 g/cm^3	-----	19.42 dyne/cm

Meniscus curvatures

When the rod touches the plate the system is basically a rod-in-an-angled-corner configuration for which the MS-P curvatures are known (Walsh, 1989). The capillary pressures for all of the

menisci in the cells were measured by the capillary rise of *iso*-octane following the experimental procedure described by Mason and Morrow (1985). The actual capillary pressures for *iso*-octane and liquid paraffin are given in Table 8.2-2.

Table 8.2-2. Capillary pressures (in Pa) determined by capillary rise experiments for *iso*-octane (Iso.) and liquid paraffin (L.P.) in the rod-plate-contact cells.

Cell	ΔP_1		ΔP_2		ΔP_a	
	Iso.	L.P.	Iso.	L.P.	Iso.	L.P.
Slot angle β 85º	133.60	232.53	105.62	183.78	31.52	54.85
Slot angle β 75º	165.18	287.41	80.22	139.61	27.62	48.32
Slot angle β 65º	212.26	368.92	64.71	112.59	27.48	47.80

Normalized curvatures are compared with the MS-P theory in Figure 8.2-6.

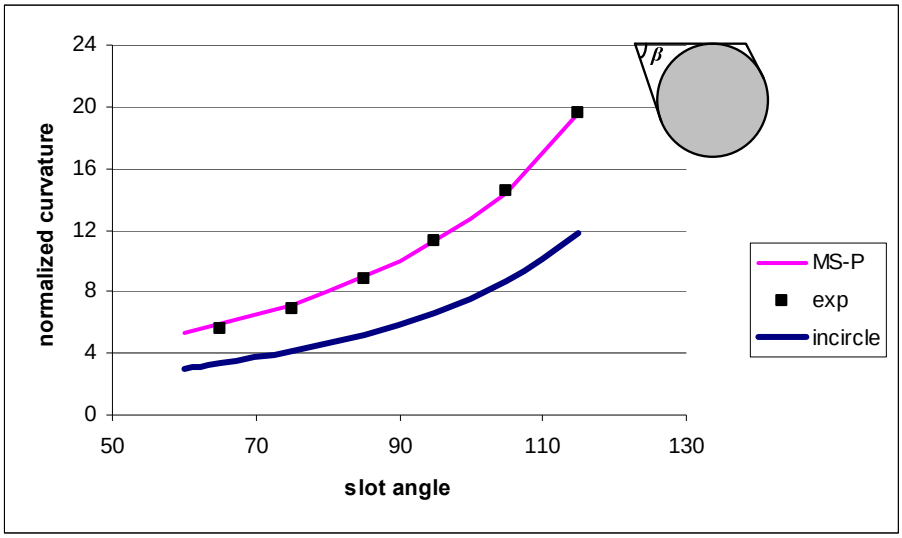

Figure 8.2-6. Comparison of measured curvatures with values calculated by MS-P method for the rod-in-angled corner geometry. Also shown is the incircle curvature (note that the insphere curvature would be double the incircle curvature).

Operation

Before the experiment began, the correct volume of liquid paraffin (determined by trial) was placed in Reservoir I. The liquid was then pushed from Reservoir I by means of a close-fitting piston into Reservoir II. As the liquid is pushed out of Reservoir I, the oil level rises in Reservoir II and finally reaches the capillaries. Excess oil flows into the additional capillary forming a

meniscus until it stops. In addition, a meniscus forms in each capillary on each side of the rod and these start to advance. For co-current imbibition, the pressure transducer is not connected to the cell. Hence, one end of the capillaries is open to the atmosphere. During countercurrent imbibition the transducer is connected and it measures the pressure build-up of the air in the dead end (ΔP_d).

For the interfaces in the two tubes there are arc menisci that advance along the corners forming liquid wedges. Although their curvature is high, their hydraulic resistance is also high (Dong and Chatzis, 1995). Consequently, as the main terminal menisci (Mason and Morrow, 1987) move along the capillaries the arc menisci do not advance far, nor carry much liquid, ahead of the main menisci.

Results

Co-current imbibition

Single frames from an experiment involving co-current flow are shown in Figure 8.2-7. The menisci have been drawn over for clarity.

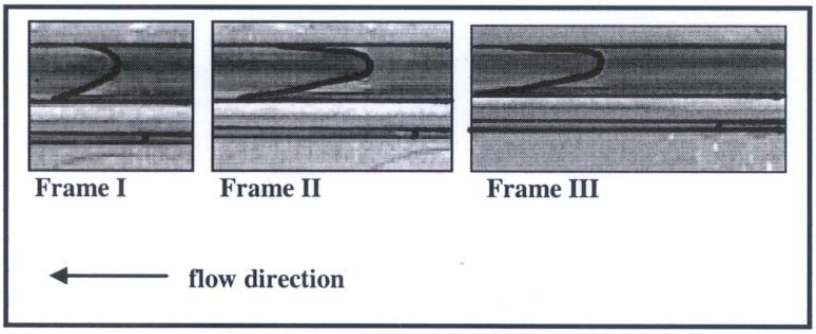

Figure 8.2-7. Single frames from an experiment involving co-current imbibition. Slot angle β is 75º. Note that small meniscus is always ahead of the larger meniscus.

Equation 8.2-9 predicts that a plot of $(x_{1,t}^2 - x_{1,0}^2)$ vs $(t - t_0)$ should be a straight line with the gradient depending on the hydraulic resistance shape factor *K*. The same is true for the other capillary tube. Figure 8.2-8 shows the result for all three cells.

The additional significance of the lines in Figure 8.2-8 being straight means that the capillary pressures generated by the menisci are constant, even though in each tube the velocity of advance varies considerably with time. The explanation is probably that the arc menisci in the corners always lead the main terminal meniscus. The significance is that in network models the interfaces are assumed to be quasi-static and generate a constant pressure. Figure 8.2-8 shows that this is probably a good approximation to the moving situation.

In addition, Equation 8.2-10 predicts that a plot of x_1^2 vs x_2^2 is a straight line. This plot is shown in Figure 8.2-9. It is interesting that the results for the 65º and 75º cells are almost coincident. This is because changes in the hydraulic resistance are almost compensated by changes in the capillary pressure.

Because the capillaries have noncircular cross-sections with corners, their true hydraulic resistances are difficult to estimate (Dong and Chatzis, 1995; Ransohoff and Radke, 1998). This is

why the shape factor, k, in Equation 8.2-7 is needed. For flow through circular tubes the average velocity, $\bar{u}$, is given by Corey (1994)

$$\bar{u} = \frac{dx}{dt} = \frac{r^2}{8\mu}\frac{P}{x} \qquad 8.2\text{-}24$$

The shape factor k is 1/8 for this case. The hydraulic radius of irregular capillaries (r_{hyd}) can be estimated from the ratio of the area to the perimeter (Corey, 1994; Sisavath et al., 2001; Patzek and Silin, 2001; Patzek and Kreistensen, 2001).

$$r_{hyd} = \frac{A}{S} \qquad 8.2\text{-}25$$

where A is the cross-sectional area perpendicular to flow, and S is the wetted perimeter. The A_1, A_2, S_1 and S_2 values are given in Equations 8.2-2 – 8.2-5.

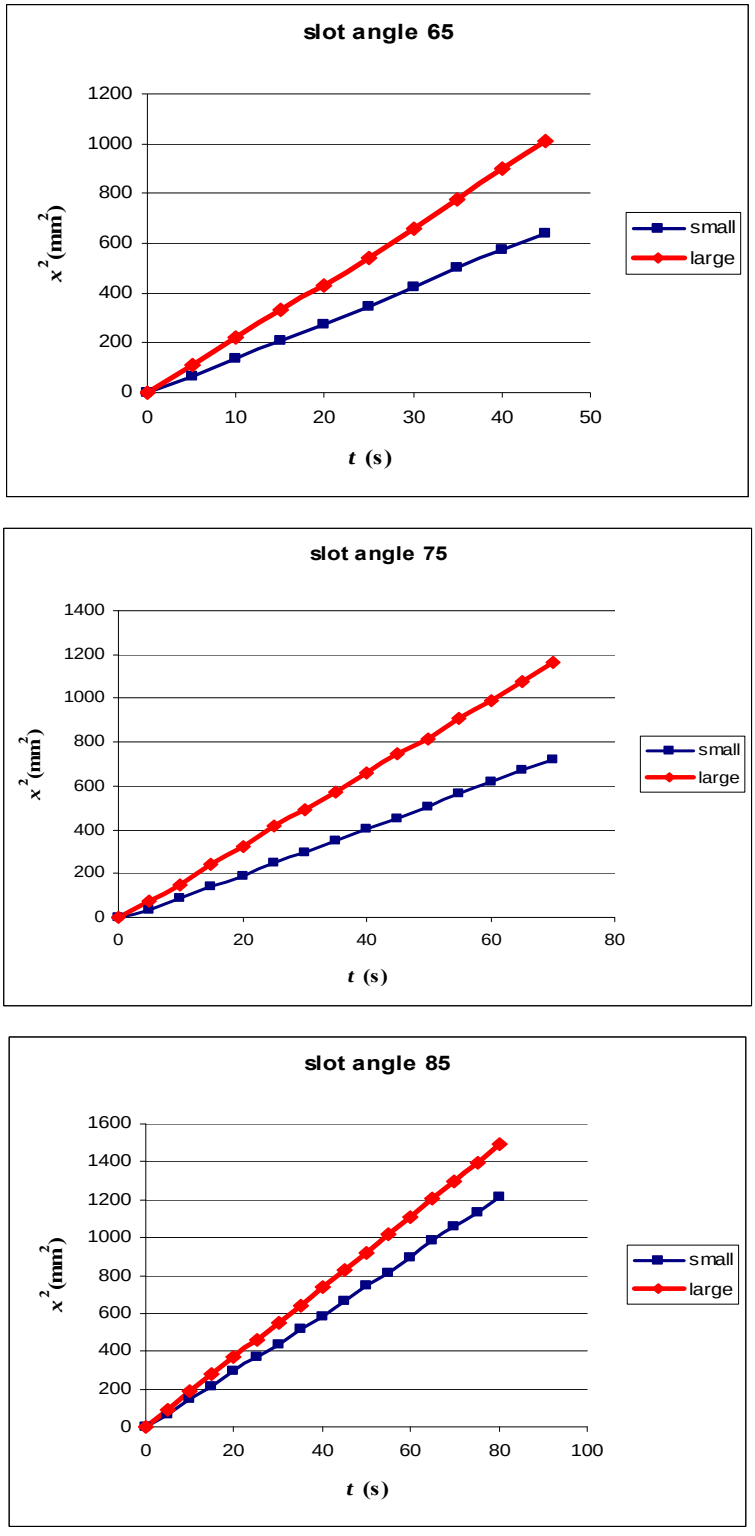

Figure 8.2-8. Plot of ($x_t^2 - x_0^2$) vs ($t - t_0$) for both capillaries in each cell. Theory predicts that the slope (*m*) should be equal to $m = \frac{2(\Delta P - \Delta P_a)K}{\mu}$ values and the lines should be straight.

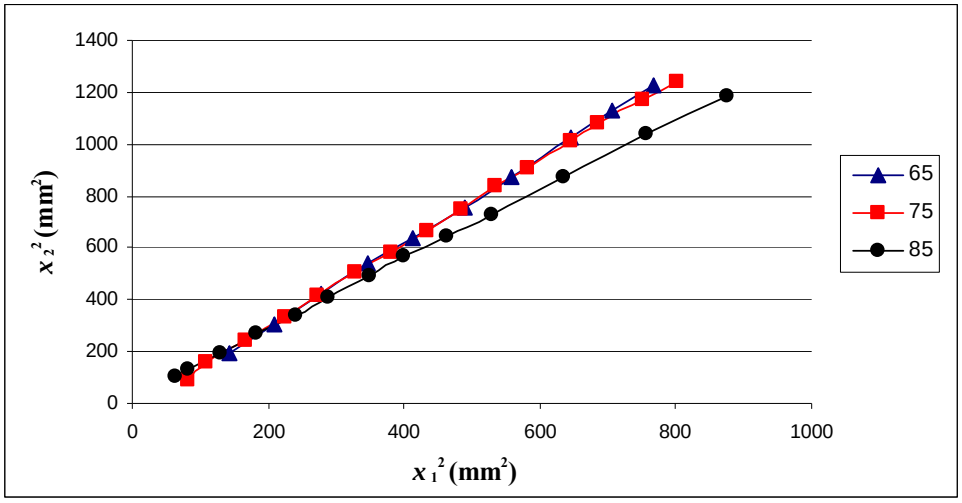

Figure 8.2-9. Plot of $x_{1,t}^2$ vs. $x_{2,t}^2$ for the cell with slot angles of 65º, 75º and 85º. Theory predicts that the relationship should be straight lines.

Using distance-time measurements for each cell (and Equation 8.2-24) the hydraulic radius value for each capillary was found. The measured and theoretical values (from Equation 8.2-25) are compared in Figure 8.2-10. Good agreement was found between the experimental and the theoretical hydraulic radii values.

Figure 8.2-10. Theoretical and experimental hydraulic radii value ratios at different slot angles (º). 'r_{hyd1}' is the hydraulic radius of the small capillary, 'r_{hyd2}' is the hydraulic of the large capillary.

Countercurrent flow

In counter- current imbibition, initially both interfaces advance, with the larger one leading. As the air is compressed, the large interface is pushed back by increasing air pressure until bubbles are blown from the large capillary tube. After each bubble snaps off, an interface advances a short way into the large capillary. Single frames from an experiment involving bubble snap-off during a countercurrent flow are shown in Figure 8.2-11. The menisci have been drawn over for clarity.

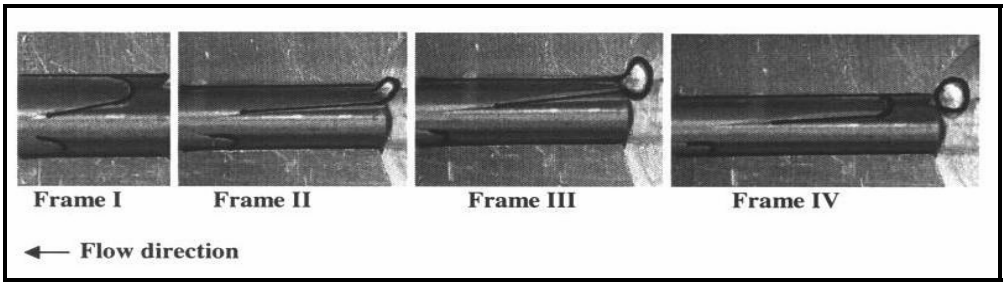

Figure 8.2-11. Countercurrent imbibition. A bubble is emerging from the large tube. After snap-off the meniscus invades the tube for some distance. Slot angle β is 75º.

At the beginning, before the oil is introduced into the capillaries, the differential pressure transducer shows a constant value of around 0 P_a. As the oil imbibes into the capillaries the pressure rises to the first positive peak. When the length of the large tube filled with oil decreases, the pressure drops slightly and then drops more rapidly as the bubble forms. Eventually the bubble snaps off and the air pressure rises back to almost the initial value and stays essentially constant until the next bubble starts to form. After the snap-off, the meniscus in the large tube appears to invade the tube for some distance but close observation shows that most of the liquid comes from drainage of the arc menisci until their curvature corresponds to that of the main meniscus. As the imbibition rate slows down, the time taken for bubble formation increases. This drop in rate is probably the cause of the slight increase in snap-off pressure of the later bubbles. With slower bubble growth the snap-off pressure moves closer to the curvature of a theoretical cylindrical meniscus within the tube.

When the meniscus forms in the additional capillary, it creates an additional capillary pressure between the atmosphere and the fluid which, in effect, shifts the zero indicated pressure of the transducer. This pressure is equal to ΔP_a and if this value is subtracted from the zero initial pressure, we obtain the 'absolute base pressure'. The pressure produced by the additional capillary was obtained from the capillary rise experiments (see Table 8.2-2). The data plot for the transducer readings (ΔP_d) of the cell with a slot angle of 85º is given in Figure 8.2-12.

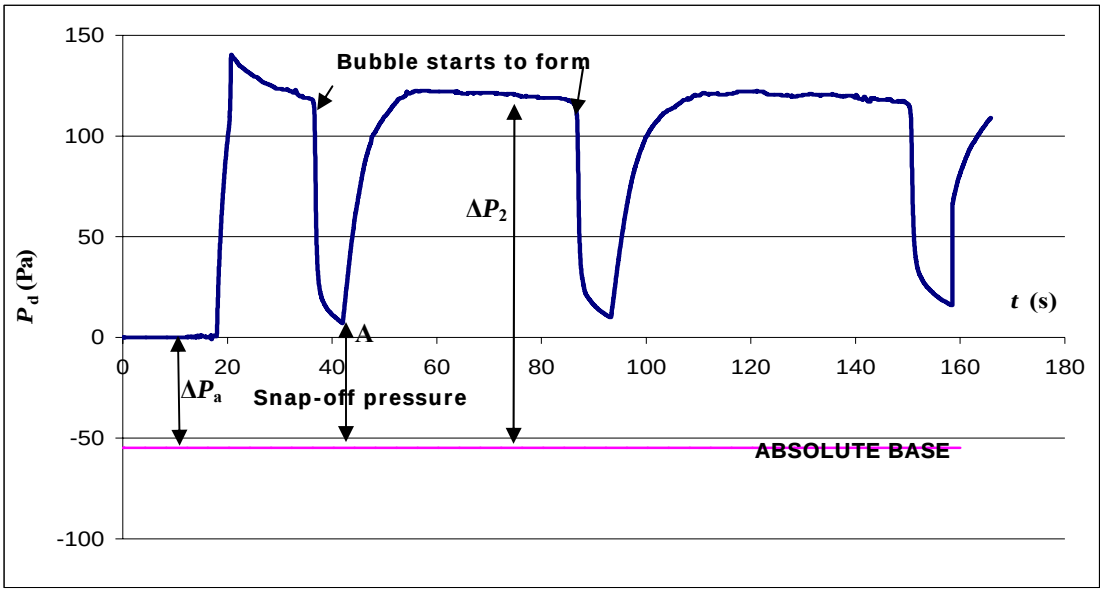

Figure 8.2-12. Transducer pressure (ΔP_d) recordings at the dead end in the cell during countercurrent flow. The slot angle β is 85º. Negative peaks indicate bubble formation. Once the snap-off is completed, the air pressure regains the initial value and stays almost constant until the next bubble starts to form.

In Figure 8.2-12, the negative peaks correspond to the onset of bubble formation. The bubble snaps off at the point 'A'. Immediately after snap-off the pressure rises again as the arc menisci shrink back to the curvature of the main meniscus that now advances in the larger tube. This takes a surprisingly long time, mainly because of the considerable resistance to flow in the arc menisci. Little additional imbibition takes place during these local events which are mainly just a rearrangement of fluid. The time between sequential bubbles increases because advance of the meniscus in the smaller capillary slows with time. There are several measurements that can be made from the data pressure plot. The snap-off pressure is equal to the pressure between the absolute base pressure and the snap-off point '*A*'. The pressure difference created by the meniscus in the large tube (ΔP_2) is almost equal to the pressure difference between the absolute base pressure and the pressure that is measured between the formation of bubbles.

When there is a constant capillary back pressure, the imbibition distance varies as $t^{1/2}$, as predicted by the Washburn equation (Washburn, 1921) for cylindrical capillaries. However, when the bubble is forming the imbibition rate increases significantly. The imbibition distance $(x - x_0)$ *vs* $t^{1/2}$ for the small capillary during countercurrent flow is shown in Figure 8.2-13. Note that when a bubble starts to form, the imbibition rate increases and that after snap-off the $t^{1/2}$ relationship is regained. The bumps on Figure 8.2-13 indicate bubble formation, the slope of the lines between bubble formation are almost the same. Comparison of Figure 8.2-12 with Figure 8.2-13 shows how the pressure change during bubble formation is matched by the increase in imbibition rate. The same data plots during countercurrent flow for the 75° and 65° cells are shown in Figures 8.2-14 through 17.

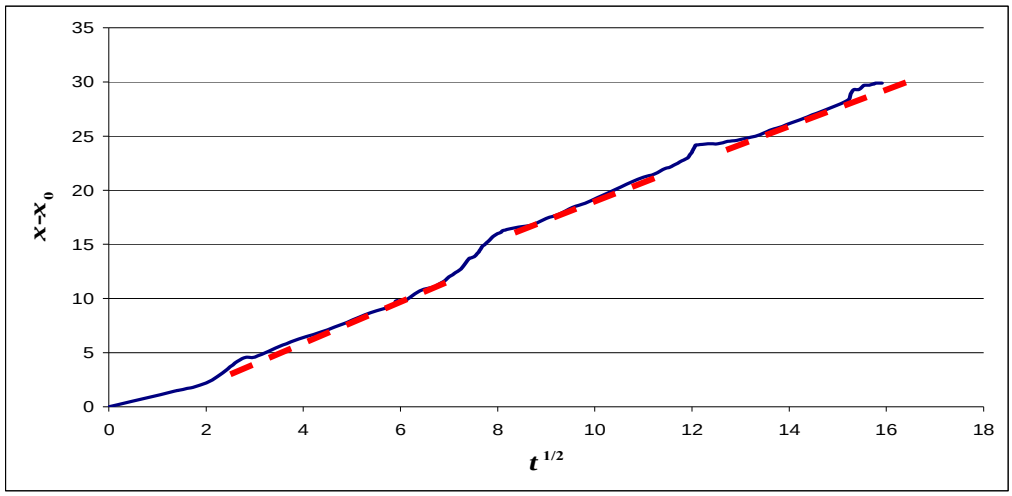

Figure 8.2-13. The rate of imbibition in the small capillary during countercurrent flow; slot angle β is 85º. The small steps accompany the formation of the bubbles. The dashed lines show that the imbibition rate is almost the same between the bubble formation.

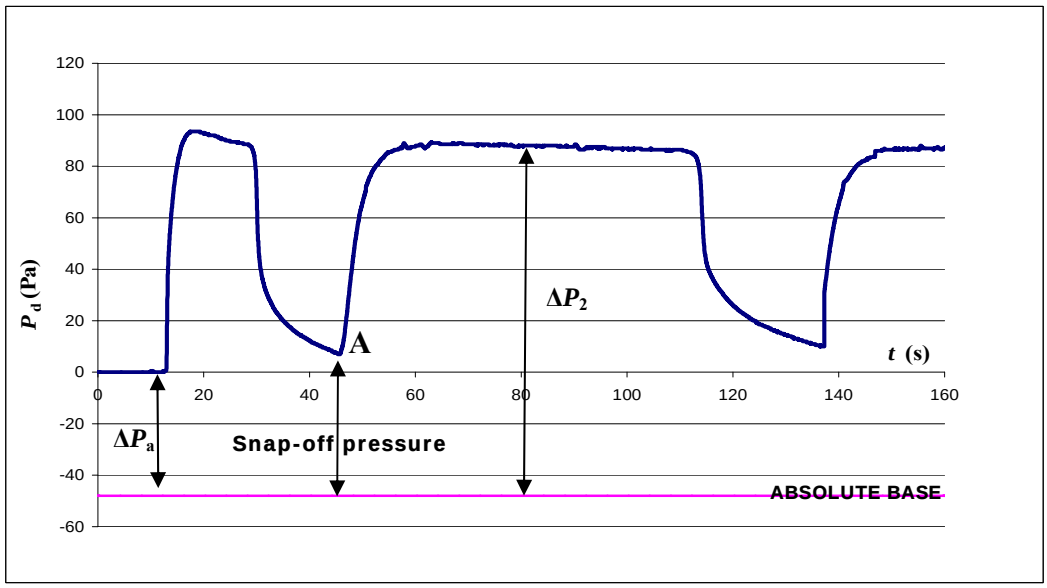

Figure 8.2-14. Pressure (ΔP_d) recordings in the cell with a slot angle of 75º during countercurrent flow.

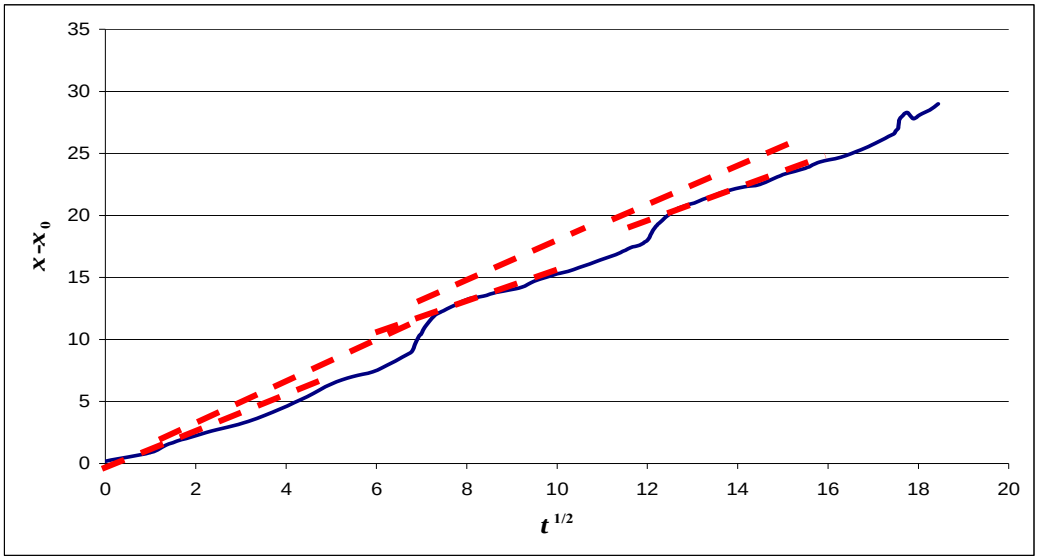

Figure 8.2-15. The rate of imbibition in the small capillary during countercurrent flow, slot angle is 75º.

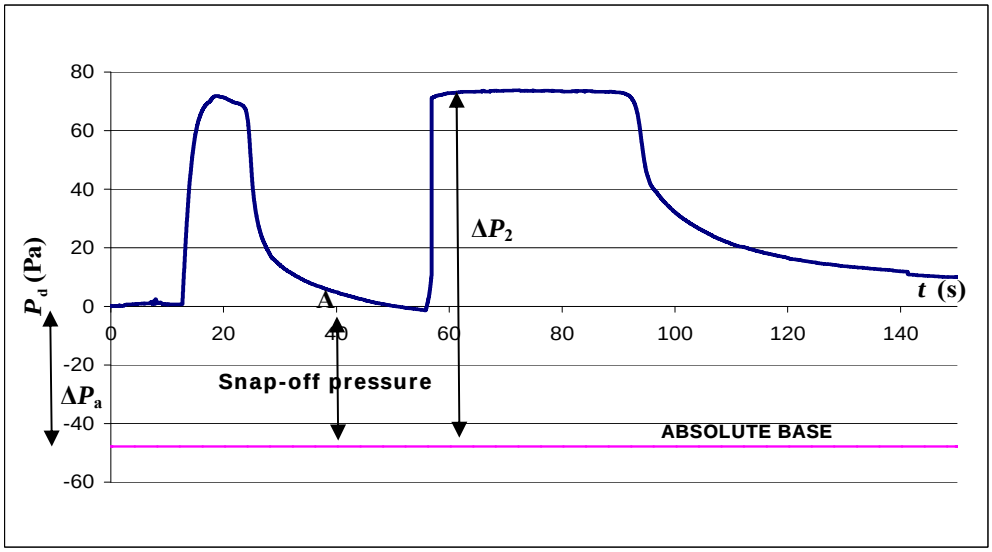

Figure 8.2-16. Pressure (ΔP_d) recordings in the cell with a slot angle of 65º during countercurrent flow.

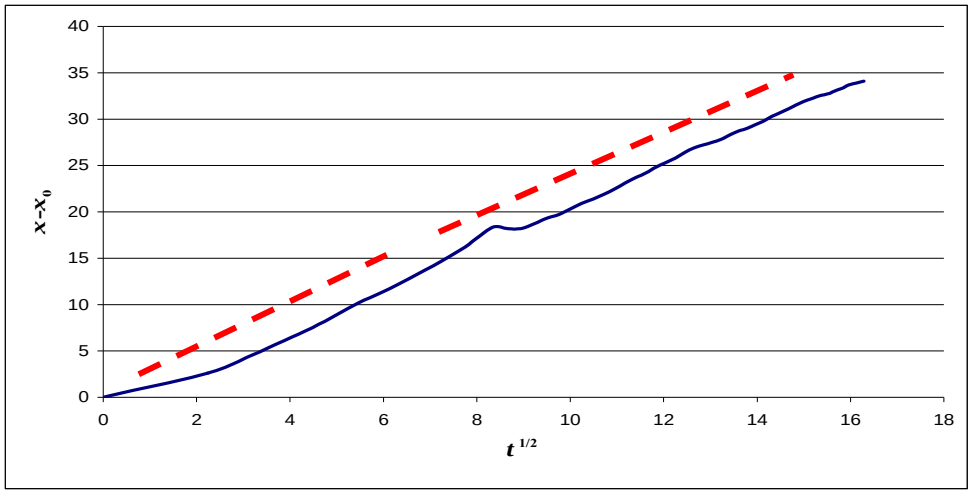

Figure 8.2-17. The imbibition rate in the small capillary during countercurrent flow; slot angle is 65º. Only one bubble was formed because of the small tube contained so little volume.

The snap-off pressure can be estimated from the incircle that just fits inside the tube (see Figure 8.2-2). For the 85º cell, the incircle normalized curvature under the condition 'd/R=0' is 5.16. Capillary pressure is related to curvature by

$$\Delta P = \sigma C/R \qquad 8.2\text{-}26$$

where ΔP is the capillary pressure, σ is the surface tension, C is the normalized curvature and R is the rod radius. From the incircle, the capillary pressure is calculated as 109 Pa. However, from the graph, the actual pressure for the first bubble is 70 Pa (Figure 8.2-12). The difference is probably because flow needs to occur for snap-off and a pressure is needed to drive this flow. The pressure at which snap- off occurs therefore depends upon the rate at which the bubble is growing, and this, in turn, depends on the position of the meniscus in the small tube. The effect can be seen in Figure 8.2-12 where the later bubbles snap off at higher pressures. The snap-off pressure therefore exhibits rate-dependency under dynamic conditions. In addition, the interface is not a perfect uniform cylinder. The measured curvatures are compared with the curvatures obtained from the incircle curvatures in Figure 8.2-18.

The pressure produced by the meniscus in the large tube (ΔP_2) can be measured from the pressure record during flow. The values for all three cells can be compared with the capillary pressures obtained using capillary rise values (Table 8.2-2) and using Equation 8.2-26, where the normalized curvatures are from the MS-P theory (Figure 8.2-2). It can be seen that they are in excellent agreement (Figure 8.2-19) indicating that flow does not greatly affect the meniscus curvature predicted by the MS-P theory. To our best knowledge this has not been reported previously in other papers.

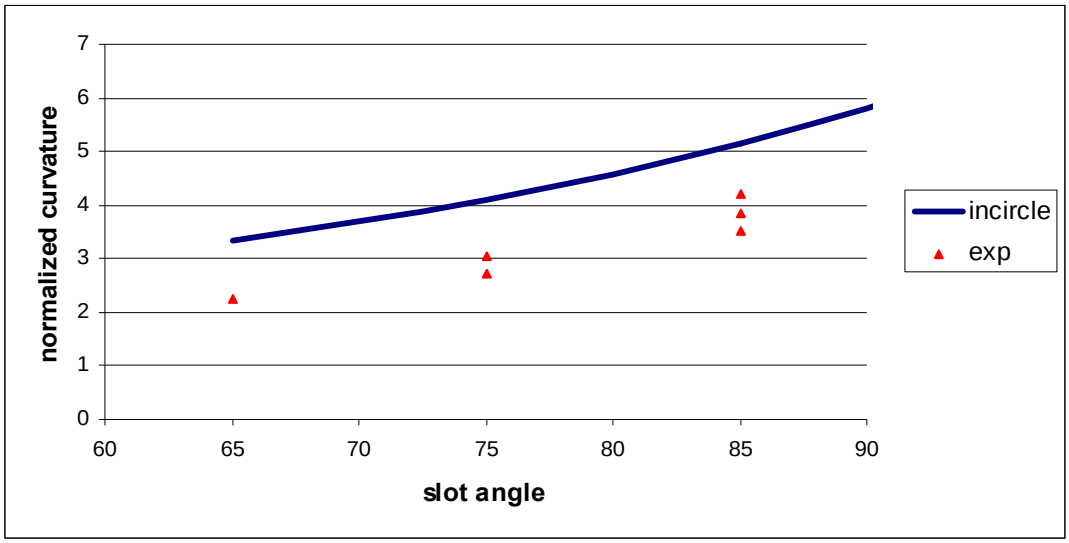

Figure 8.2-18. Comparison of incircle curvature with snap-off curvature. The snap-off pressures were read from Figures 8.2-12, 14 and 16 for the slot angles of 85º (3 bubbles), 75º (2 bubbles) and 65º (1 bubble), respectively.

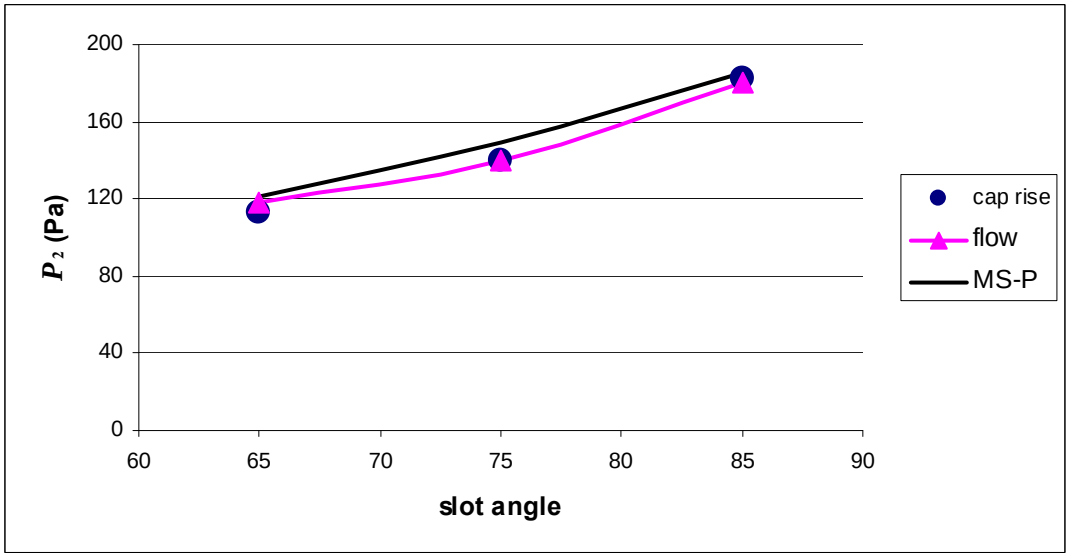

Figure 8.2-19. Theoretical MS-P and experimental (capillary rise and flow) ΔP_2 values at different slot angles (º).

Equation 8.2-19 gives the pressure difference between atmosphere and the dead end (ΔP_d) for the constant pressure periods between the release and formation of bubbles. The ΔP_d values were measured as 72 Pa, 90 Pa and 120 Pa for the cells with slot angles 65º, 75º, and 85º respectively (see Figures 8.2-12, 8.2-14 and 8.2-16). Corresponding pressure values from Equation 8.2-19 are 75 Pa, 103 Pa and 130 Pa. The countercurrent theory presented here only considers the regions between consecutive bubbles, and does not analyze behavior during bubble formation.

Equation 8.2-20 predicts interface positions during countercurrent imbibition without a bubble being formed. In one series of experiments, imbibition was initially co-current and then the end was sealed and the imbibition became countercurrent. The B coefficient values were calculated from co-current measurements for all three cells 65º, 75º and 85º as 0.015, 0.078 and 0.35 respectively, while x_1 and x_2 values were determined from the countercurrent video images. Values for A_1 and A_2 were calculated using Equations 8.2-2 and 8.2-3, respectively. Following Equation 8-23, $f\left(x_1^2, x_2^2\right)$ vs time were plotted. As expected an almost linear relationship for each cell was obtained (Figure 8.2-20).

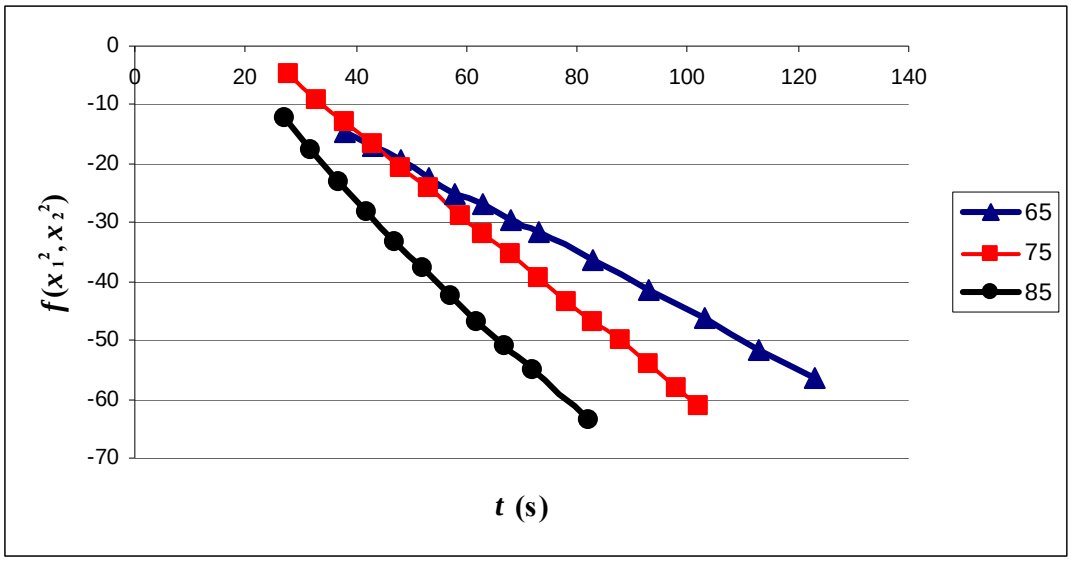

Figure 8.2-20. Relationship between function of $f\left(x_1^2, x_2^2\right)$ versus time during countercurrent flow for cell with slot angles of 65º, 75º and 85º.

Conclusions

A simple analysis of co- and counter-current imbibition for tubes of non-circular cross-section has been carried out. Shape factors were needed to describe the tube areas, hydraulic resistances and capillary pressures. Experiments using model pore systems and measurements of capillary rise were used to confirm the capillary pressures. Co-current imbibition experiments were used to measure the hydraulic resistances. Both these values were then used to quantify counter-current imbibition. When theory was compared to experiment, the agreement was generally good except that the bubble snap-off pressure was not well described by the tube incircle curvature. This was probably because the prediction of snap-off at the incircle curvature is quasi-static, whereas in the real system there was rapid bubble growth.

In general, co-current imbibition was observed to occur at about four times the rate of counter-current imbibition even though more fluid was being imbibed. Furthermore, it takes a significant positive pressure, the capillary back pressure, for air to be driven out in counter-current imbibition and this can make a significant difference to the imbibition rate. At the liquid inlet face there was growth of bubbles and subsequent snap-off giving significant fluctuations of the capillary back

pressure. Co-current theory was in good agreement with the experiments; it follows the Washburn equation.

The Mayor and Stowe–Princen theory appears to predict meniscus curvatures well, even when they are moving. This is probably because the arc menisci keep far enough ahead of the main terminal meniscus for the MS-P approximations to hold.

Acknowledgments

The authors acknowledge support from the UK Engineering and Physical Sciences Research Council, British Petroleum, ChevronTexaco, Total/Fina/ELF, Phillips, the Enhanced Oil Recovery Institute at the University of Wyoming, the Natural Petroleum Technology Office of the US Department of Energy, and the National Science and Engineering Research Council of Canada.

8.3 Co- and Counter-Current Spontaneous Imbibition into Groups of Capillary Tubes with Lateral Connections Permitting Cross-Flow

E. Unsal, G. Mason, D.W. Ruth, and N.R. Morrow

Journal of Colloid and Interface Science, 2007 315, 200 – 209.

Abstract

A model for co- and counter-current imbibition through *independent* capillaries has already been developed and experiments conducted to verify the theory [E. Unsal, G. Mason, N.R. Morrow, D.W. Ruth, J. Colloid Interface Sci. 306 (2007) 105]. In this paper, the work is extended to capillaries which are connected laterally and in which cross-flow can take place. The fundamental pore geometry is a rod in an angled roundbottomed slot with a gap between the rod and a capping glass plate. The surfaces of the slot, rod and plate form capillaries and interconnecting passages which have non-axisymmetric cross-sections. Depending on the gap size either (i) a large single meniscus, (ii) two menisci one on each side of the rod, or (iii) three menisci, one between the rod and the glass additional to the ones on each side can be formed. A viscous refined oil was applied to one end of the capillaries and co-current and counter-current spontaneous imbibition experiments were performed. The opposite end was left open to the atmosphere for co-current experiments. When the gap between the rod and the plate was large, the imbibing oil advanced into the tubes with the meniscus in the largest capillary always lagging behind the two menisci in the other two smaller capillaries. For counter-current imbibition experiments the open end was sealed and connected to a sensitive pressure transducer. In some experiments, the oil imbibed into the smaller capillaries and expelled air as a series of bubbles from the end of the largest capillary. In other experiments, the oil was allowed to imbibe part way into the tubes before counter-current imbibition was started. The meniscus curvatures of the capillaries have been calculated using the Mayer and Stowe–Princen method for different cell slot angles and gap sizes using a value of zero for the contact angle. These values have been compared with actual values by measuring the capillary rise in the tubes; agreement was very close. A model for co-current and counter-current imbibition has also been developed. The significance of this model is that some hydraulic/capillary properties are common for both co-current and counter-current imbibition. The experiments give an illustration of behavior expected in a real porous material and verify the importance of the ‘perfect cross-flow’ modification to the ‘bundle of parallel tubes’ model.

Introduction

Spontaneous imbibition is currently of interest in oil recovery because it has the potential to allow recovery from fractured reservoirs (Morrow and Mason, 2001). It is the process in which the wetting phase is drawn into a porous medium by means of capillary forces and pressures generated by the curved interfaces between the wetting and non-wetting phases. The difference in pressure, called capillary pressure, is designated by P_c and is defined by (Corey, 1994)

$$P_c \equiv P_{nw} - P_w \qquad 8.3\text{-}1$$

where P_{nw} and P_w are the capillary pressures of the non-wetting and the wetting phases, respectively.

There are two extremes to spontaneous imbibition: co-current and counter-current. In co-current imbibition both wetting and non-wetting phases move in the same direction while during counter-current imbibition the two phases move in opposite directions. Consequently, since the flows of both phases require a pressure gradient to drive them and, because the flows of the phases are in opposite directions, the pressure gradients in the flow phases have to be in opposite directions (Reis and Cil, 1993; Cil and Reis, 1996; Li et. al, 2003). The rates of the two processes are also different. In our previous investigation, which used independent tubes, it was observed that the linear rate of co-current imbibition was about four times faster than counter-current imbibition (Unsal et. al, 2007).

Co-current imbibition has been analysed many times dating back to Washburn (1921). The first models concentrated on imbibition through independent capillaries and no interaction between the capillaries was considered. Later, Dong and Dullien developed a model which considered imbibition through two interacting capillaries of different diameter (Dong et. al, 1998). Following this model, Ruth and Bartley (2002) improved the theory by allowing the cross-flow without pressure-drop (termed "perfect cross-flow") to occur between many tubes. They simulated co-current flow through sixty cross-connected capillaries of different sizes. Dong *et al*., (2005, 2006) published further work where they extended their previous model to immiscible displacement through interacting capillary bundles. The model is attractive because its behavior is closer to that of a real porous material than any model with independent tubes.

There are fewer theoretical models available for counter-current imbibition. One of the earliest studies of counter-current imbibition was done by Graham and Richardson (1959). They conducted experiments by water-flooding a scaled model of a fractured-matrix reservoir in order to evaluate the relative roles of imbibition and direct displacement. Dong and Dullien (1997) designed a capillary model for studying the saturation profiles during counter-current flow. The model consisted of two capillary tubes connected by two short capillaries at the ends of the tubes. Li *et al*. (2003) gave an analytical solution for linear counter-current spontaneous imbibition based on a similarity solution for a displacement front. Their investigation considered the case of linear counter-current imbibition through homogeneous cylindrical geometry. The same group came up with another model in which the pressures producing the flows during counter-current spontaneous imbibition were considered Li, et al., 2006). Capillary pressure was the sole driving force. There was viscous drag in both phases between the imbibition front and the open face and, importantly, there was also a significant opposing capillary back pressure associated with

production of the non-wetting phase. The saturation profile with distance produced a self-similar front.

Here, we compare, experimentally and theoretically, co- and counter-current imbibition through laterally connected capillaries. These experiments allow us to visualize the effects of "perfect cross-flow" along the capillaries. The experiments are compared with theoretical predictions. A self-similar behavior is predicted and observed.

Tubes with corners and MS-P Theory

The relationship between pore size and capillary pressure is straightforward for capillaries with circular cross-sections. However, it is more complicated when the cross-section is angular because liquid is held in the corners of the tube (Mason et al., 2000). Imbibition into such pores, i.e. those with triangular and other cross-sections, can differ significantly from the basic case of the cylinder.

The pore geometry of the experimental models used in this study is a rod in an angled slot. To achieve this geometry, a rod was placed in an angled round-bottomed slot and capped with a glass plate (Figure 8.3-1). In a previous paper (Unsal et. al, 2007), the glass was in contact with the rod, hence, two independent capillaries of different size were formed at the sides of the rod (Figure 8.3-1a). Here, a more complicated arrangement of the rod and plate is considered. The slot was machined slightly deeper than the rod diameter, thus leaving a gap between the rod and the glass (Figure 8.3-1b). At certain spacings an interface can form between the rod and the glass plate giving, in effect, a third capillary. This configuration is also more complex because there is cross-flow between the two side capillaries through the gap between the rod and the plate. This particular tube arrangement has not been studied before although its capillary behavior is somewhat similar to three rods and a plate (Mason et. al, 2000). Here we have flow in addition. For small gaps there are three distinct menisci. The one with the highest curvature is between the rod and the plate. The next most highly curved is in the small tube, and the least curved is in the large tube. Important features are that none of these capillaries has circular cross-section and there are arc menisci in the corners. At intermediate gaps, only two tube menisci form. With very large gaps, a single meniscus spans the tube but there are still arc menisci in the tube corners.

The curvature of menisci in uniform tubes of non-circular cross-sections can be calculated using the Mayer Stowe and Princen theory (Mayer and Stowe, 1965; Princen, 1969a; Princen, 1969b). A typical relationship between the curvature of all the menisci and the rod-plate gap is shown in Figure 8.3-2. The analysis is applicable to all cell angles but experimentally we have here only used cells with slot angles (β) of 65º, 75º and 85º.

Figure 8.3-2 shows that for small gaps ($d/R < 0.15$) there are three menisci; a potentially very highly curved one in the gap between the rod and the plate, a less highly curved one in the small tube and a meniscus in the large tube with about half of the curvature of the small tube meniscus. The lowest curvature indicated on Figure 8.3-2 is that of a cylindrical meniscus in the large tube and it approximates to the curvature at which a bubble would be expected to snap off in this tube (Ma et.al, 1996). For larger gaps ($0.15<d/R<0.26$), the distinct two-sided meniscus between the rod and the plate which separates the menisci in the large and small tube no longer exists. There is instead a single interface meniscus between the rod and the plate and the menisci in the large and

small tubes share it. For large spacings between the rod and the plate (d/R>0.26), this interface disappears and, apart from the arc menisci in the corners, there is only a single meniscus in the tube.

In past investigations (Mason and Morrow, 1985; Mason et. al, 2000; Unsal et. al, 2007), excellent agreement has been found between the prediction of the MS-P theory and experimental results. In this report, the analysis has been applied to the rod in an angled slot configuration with a gap between the glass and the rod.

Theoretical

Overview

Experiments involving both co-current and counter-current imbibition have been conducted. The interfaces formed in the rod-slot model will be addressed by their interface curvature. Meniscus 'a' is in the larger capillary, 'b' is in the small capillary and 'c' is between the rod and the plate. During co-current flow, when there is perfect cross-flow, meniscus 'c' leads with meniscus 'b' behind it. Meniscus 'a' in the large capillary is the last. During counter-current imbibition, meniscus 'b' and 'c' imbibe again with 'c' leading 'b', and bubbles are expelled from the tube 'a'. However, in some experiments, imbibition was started co-current and then changed to counter-current. Under these circumstances liquid imbibed in the 'b' and 'c' but flowed in the opposite direction in tube 'a'. In order to conduct the experiment, an additional, relatively large capillary was needed. Its function was to act as a small constant pressure reservoir and it was typically only partly filled with oil. All of the experiments were video-taped so that the positions of all of the interfaces at any point of time could be determined. This experimental arrangement can be modeled as three capillary tubes with perfect lateral cross-flow between them (Figure 8.3-3).

If there is perfect cross-flow then, at any distance x, the pressure is equal in the oil phase and in the air phase. If the air is assumed to be non-viscous then the pressure in the air is everywhere equal. For a range of distances, oil is present in some capillaries whilst there is air present in the others. This is the transition region (Dong et. al, 2005).

Perfect Cross-Flow Between Capillaries

Consider the three capillary tubes in Figure 8.3-4; there is perfect cross-flow between them. At any distance x, if the same phase is present in all tubes then the pressure is also the same at all tubes. Gravity is ignored. The pressure in the unfilled tubes is constant because the fluid there (air) has such a small viscosity.

The zone closest to the imbibition face will be denoted by the subscript 1 (Figure 8.3-5). This zone occupies the area between the inlet and the interface in the largest tube. In this zone, the flow of the oil (q_{o1}) can be calculated by means of the equation

$$q_{o1} = -\lambda_{o1} \frac{(P_{oa} - P_{add} + P_{dead})}{x_a} \qquad 8.3\text{-}2$$

where λ_{o1} is the resistance to flow per unit length, P_{oa} is the pressure in oil. P_{add} is the pressure in the additional capillary (which will be negative) and P_{dead} is the dead-end pressure in the air which

is zero for co-current imbibition and positive for counter-current imbibition. The resistance to flow is given by

$$\lambda_{o1} = \frac{f_a \delta_a^4}{\mu} + \frac{f_b \delta_b^4}{\mu} + \frac{f_c \delta_c^4}{\mu} \qquad 8.3\text{-}3$$

where a denotes the largest tube, b denotes the mid-size tube, and c denotes the smallest tube, f_a, f_b and f_c are factors depending on the tube shape, and δ is a tube dimension. The flow of gas in region 1 is

$$q_{g1} = 0 \qquad 8.3\text{-}4$$

In the second zone (Figure 8.3-5), which occupies the region between the interface in the largest tube and the interface in the mid-size tube, the flow rates are given by

$$q_{o2} = -\lambda_{o2} \frac{P_{ob} - P_{oa}}{x_b - x_a} \qquad 8.3\text{-}5$$

for oil and

$$q_{g2} = q_{o1} - q_{o2} \qquad 8.3\text{-}6$$

for gas where

$$\lambda_{o2} = \frac{f_b \delta_b^4}{\mu} + \frac{f_c \delta_c^4}{\mu} \qquad 8.3\text{-}7$$

In the third zone (Figure 8.3-5), which occupies the region between the interface in the mid-size tube and the interface in the smallest tube, the flow rates may be calculated from the equations

$$q_{o3} = -\lambda_{o3} \frac{P_{oc} - P_{ob}}{x_c - x_b} \qquad 8.3\text{-}8$$

and

$$q_{g3} = q_{o1} - q_{o3} \qquad 8.3\text{-}9$$

where

$$\lambda_{o3} = \frac{f_c \delta_c^4}{\mu} \qquad 8.3\text{-}10$$

The pressure values are well defined. If the air is at P_{dead} and the inlet pressure is P_{add}, then the pressures are simply given by the capillary pressures in the tubes

$$P_{oa} = -P_{ca} \qquad 8.3\text{-}11$$

$$P_{ob} = -P_{cb} \qquad 8.3\text{-}12$$

and

$$P_{oc} = -P_{cc} \qquad 8.3\text{-}13$$

The advances of the interfaces are governed by the equations

$$\frac{x_{a,n+1} - x_{a,n}}{t_{n+1} - t_n} = \frac{q_{o1} - q_{o2}}{A_a} \qquad 8.3\text{-}14$$

$$\frac{x_{b,n+1} - x_{b,n}}{t_{n+1} - t_n} = \frac{q_{o2} - q_{o3}}{A_b} \qquad 8.3\text{-}15$$

and

$$\frac{x_{c,n+1} - x_{c,n}}{t_{n+1} - t_n} = \frac{q_{o3}}{A_c} \qquad 8.3\text{-}16$$

where

$$A_a = g_a \delta_a^2 \qquad 8.3\text{-}17$$

$$A_b = g_b \delta_b^2 \qquad 8.3\text{-}18$$

and

$$A_c = g_c \delta_c^2 \qquad 8.3\text{-}19$$

Here g_a, g_b and g_c are shape factor constants depending on the tube shapes and n and $n+1$ indicate short adjacent resistances and times. Combining the equations

$$\frac{x_{a,n+1} - x_{a,n}}{t_{n+1} - t_n} = \lambda_{o1} \frac{(P_{ca} + P_{add} - P_{dead})}{A_a x_a} - \lambda_{o2} \frac{P_{cb} - P_{ca}}{A_a (x_b - x_a)} \qquad 8.3\text{-}20$$

$$\frac{x_{b,n+1} - x_{b,n}}{t_{n+1} - t_n} = \lambda_{o2} \frac{P_{cb} - P_{ca}}{A_b (x_b - x_a)} - \lambda_{o3} \frac{P_{cc} - P_{cb}}{A_b (x_c - x_b)} \qquad 8.3\text{-}21$$

and

$$\frac{x_{c,n+1} - x_{c,n}}{t_{n+1} - t_n} = \lambda_{o3} \frac{P_{cc} - P_{cb}}{A_c (x_c - x_b)} \qquad 8.3\text{-}22$$

In the limit when the time step is very small Eqs. 8.3-20 – 8.3-22 become differential equations. Multiplying each equation by the denominator on the right hand side gives:

$$A_a x_a \frac{dx_a}{dt} = \lambda_{o1} P_a - \lambda_{o2} (P_{cb} - P_{ca}) \frac{x_a}{(x_b - x_a)} \qquad 8.3\text{-}23$$

$$A_b (x_b - x_a) \frac{dx_b}{dt} = \lambda_{o2} (P_{cb} - P_{ca}) - \lambda_{o3} (P_{cc} - P_{cb}) \frac{(x_b - x_a)}{(x_c - x_b)} \qquad 8.3\text{-}24$$

$$A_c (x_a - x_b) \frac{dx_c}{dt} = \lambda_{o3} (P_{cc} - P_{cb}) \qquad 8.3\text{-}25$$

By analogy with imbibition in a porous material we expect a self-similar front to form (Li et. al, 2003). If there is a self-similar front then let

$$\frac{x_a}{x_b} = k_{ab} \qquad 8.3\text{-}26$$

and $\frac{x_{\mathrm{b}}}{x_{\mathrm{c}}} = k_{\mathrm{bc}}$ 8.3-27

where, for a self-similar front, k_{ab} and k_{bc} will both be constant. Now, the $x_a/(x_b - x_a)$ and $(x_b - x_a)/(x_c - x_b)$ terms on the right hand side of Eq. 8.3-23 and 8.3-24 remain constant; consequently the variables can be separated and Eqs. 8.3-23 – 8.3-25 integrated. When the initial conditions are $x_{\mathrm{a}} = x_{\mathrm{b}} = x_{\mathrm{c}} = 0$ at $t = 0$ then

$$\frac{1}{2} A_{\mathrm{a}} x_{\mathrm{a}}^2 = \left[\lambda_{\mathrm{o1}} (P_{\mathrm{ca}} + P_{\mathrm{add}} - P_{\mathrm{dead}}) - \lambda_{\mathrm{o2}} (P_{\mathrm{cb}} - P_{\mathrm{ca}}) \frac{k_{\mathrm{ab}}}{(1 - k_{\mathrm{ab}})} \right] t \qquad 8.3\text{-}28$$

$$\frac{1}{2} A_{\mathrm{b}} (1 - k_{\mathrm{ab}}) x_{\mathrm{b}}^2 = \left[\lambda_{\mathrm{o2}} (P_{\mathrm{cb}} - P_{\mathrm{ca}}) - \lambda_{\mathrm{o3}} (P_{\mathrm{cc}} - P_{\mathrm{cb}}) \frac{k_{\mathrm{bc}} (1 - k_{\mathrm{ab}})}{(1 - k_{\mathrm{bc}})} \right] t \qquad 8.3\text{-}29$$

$$\frac{1}{2} A_{\mathrm{c}} (1 - k_{\mathrm{bc}}) x_{\mathrm{c}}^2 = \left[\lambda_{\mathrm{o3}} (P_{\mathrm{cc}} - P_{\mathrm{cb}}) \right] t \qquad 8.3\text{-}30$$

Division of Eq. 8.3-28 by Eq. 8.3-29 shows that x_a/x_b is indeed a constant. Similarly division of Eq. 8.3-29 by Eq. 8.3-30 shows that x_b/x_c is also a constant. Therefore, one solution of Eqs. 8.3-23 – 8.3-25 is a self-similar front.

In experiments we can measure x_{a}, x_{b} and x_{c} as functions of t. Thus the gradients, G, of Eqs. 8.3-28 – 8.3-30 can be determined from the experiments. Also, because we know x_{a}, x_{b} and x_{c} the constants k_{ab} and k_{bc} can be determined. We thus have

$$G_{\mathrm{a}} = \frac{2}{A_{\mathrm{a}}} \left[\lambda_{\mathrm{o1}} (P_{\mathrm{ca}} + P_{\mathrm{add}} - P_{\mathrm{dead}}) - \lambda_{\mathrm{o2}} (P_{\mathrm{cb}} - P_{\mathrm{ca}}) \frac{k_{\mathrm{ab}}}{(1 - k_{\mathrm{ab}})} \right] \qquad 8.3\text{-}31$$

$$G_{\mathrm{b}} = \frac{2}{A_{\mathrm{b}}} \left[\frac{\lambda_{\mathrm{o2}} (P_{\mathrm{cb}} - P_{\mathrm{ca}})}{(1 - k_{\mathrm{ab}})} - \lambda_{\mathrm{o3}} (P_{\mathrm{cc}} - P_{\mathrm{cb}}) \frac{k_{\mathrm{bc}}}{(1 - k_{\mathrm{bc}})} \right] \qquad 8.3\text{-}32$$

$$G_{\mathrm{c}} = \frac{2}{A_{\mathrm{c}}} \lambda_{\mathrm{o3}} \frac{(P_{\mathrm{cc}} - P_{\mathrm{cb}})}{(1 - k_{\mathrm{bc}})} \qquad 8.3\text{-}33$$

Note that in Eq. 8.3-33, $G_{\mathrm{c}}(1\text{-}k_{\mathrm{bc}})$ should have the same value for co- and counter-current imbibition because all of the remaining variables are independent of the direction of imbibition.

Interpretation of experiments using the theory

From recordings of both co- and counter-current imbibition we have measurements of x_{a}, x_{b} and x_{c} as functions of time t. It is not possible to fill the experimental cell instantaneously and so x_{a}, x_{b} and x_{c} are not exactly zero at t=0. However, if there is a self-similar front then plots of x_{a}^2, x_{b}^2 and x_{c}^2 vs time relative to an arbitrary start should be straight lines which all pass through a common point $x_{\mathrm{a}} = x_{\mathrm{b}} = x_{\mathrm{c}} = 0$ which will give the actual zero of time. The lines will have gradients G_{a}, G_{b} and G_{c}. For counter-current imbibition, the air is produced as bubbles, which means that the capillary pressure is not constant. However, if we let imbibition start co-current and run until the

interfaces are about halfway along the tubes and then switch to counter-current imbibition by sealing the end of the tube, then the capillary pressure in the large tube will remain constant. Eqs. 8.3-28 – 8.3-30 should again give straight lines for these circumstances. The gradients G_a, G_b and G_c can be determined for the same cell during co-and counter-current imbibition, and, if the relevant k_{ab} and k_{bc}'s are known then they will be related by Eqs. 8.3-31 – 8.3-33.

Application to counter-current imbibition

For counter-current imbibition, the basic flow equations are the same for co-current imbibition but one driving pressure is different. There is an additional pressure at the end of the cell which drives the counter-current flow in the large tube and which acts equally on all of the other menisci. This additional pressure is the dead-end pressure and is P_{dead} above atmospheric pressure. It has to be high enough to force the air flow back down the large capillary.

Again Eqs. 8.3-28 to 8.3-30 apply but the behavior of 'tube a' is more complicated. The pressure governing the behavior in this tube is generated by the interaction of P_{ca} with the dead-end pressure P_{dead} and the pressure produced by the interface in the additional capillary. Because there is no net flow in the tube assembly, the volumetric flow of fluid going forward must equal the volumetric flow of air going in the opposite direction. This means that the dead-end pressure rises until it can reverse the flow in 'tube a' (the one that produces the lowest capillary pressure). As the interface in 'tube a' moves in reverse, it still generates a capillary pressure of P_{ca}. Eventually the interface in 'tube a' reaches the end of the tube and a bubble starts to form. The pressure across the bubble interface varies with the bubble size and makes the behavior complicated. However, plots of x_a^2, x_b^2 and x_c^2 versus (t-t_0) should be straight lines in the period before bubbles form. Also, from Eq. 8.3-30, $G_c(1-k_{cb})$ should have the same value for both co-and counter-current imbibition.

Experimental

A detailed description of the apparatus used to observe co- and counter-current imbibition has been given previously (Unsal et. al, 2007). The cells are composed of an aluminum block, a rod and a glass plate. The rod is placed in an angled slot which was precisely machined into the top surface of the block and capped by the glass plate. Previously the rod was in contact with the glass forming two independent capillaries, one on each side of the rod. In the present work, a gap was left between the rod and the plate so that there was cross-flow between the capillaries, and this markedly changed the behavior.

Experiments were conducted for eight model pore systems using a perfectly-wetting oil as the wetting phase and air as the non-wetting phase. With the model pore system vertical, the capillary rise in each tube was measured and, knowing the interfacial tension, the curvature of the menisci in each of the three tubes was obtained. Next, with the pore system horizontal, both co-current and counter-current imbibition experiments were carried out on all eight cells.

Fluids

In the capillary rise experiments *iso*-octane was used because it had a low viscosity and thus reached equilibrium quickly. For both co-current and counter-current experiments, a viscous liquid paraffin was used to displace air. The properties of both liquids are given in Table 8.3-1.

Meniscus curvatures

When the rod touches the plate the system is basically a rod-in-an-angled-corner and two menisci form, one on each side of the rod. However, when there is a gap, the number of individual interfaces varies with the gap size (Figure 8.3-2). There is a potential for up to three distinct interface structures, one in each side 'tube' and a third one between the rod and the plate. The displacement curvatures for all of the menisci in the cells were measured by the capillary rise method. Measured curvatures in these static experiments are shown in Table 8.3-2. The capillary pressures are also calculated using the measured curvatures and listed in Table 8.3-3. The rod radius was 1.58 mm.

Normalized curvatures were also calculated using MS-P theory and compared with the capillary rise results (Figures 8.3-6 – 8.3-8). In all cases, agreement is excellent.

Results

Co-current and counter-current imbibition when no bubbles form

Incorporating the gap between the rod and the plate makes a significant difference to the co-current imbibition behavior. When the capillaries are independent of each other, the meniscus in the larger capillary is always ahead of the one in the smaller capillary (Unsal, et al., 2007). When there is a gap between the rod and a plate, the capillaries are interconnected so that cross-flow between them can occur. Now the meniscus in the smaller capillary leads the imbibition process. Single frames from an experiment involving co-current flow are shown in Figures 8.3-9 – 8.3-10. The menisci have been drawn over for clarity.

For the counter-current imbibition experiments, the oil was allowed to imbibe co-currently until the interfaces were about a third of the way along the cell. Then the end was sealed. Subsequently, the air pressure in the dead end built up and counter-current imbibition commenced. The purpose of conducting the experiment in this way was to prevent bubbles being formed at the entrance to the large tube. In these circumstances, Eqs. 8.3-28 – 8.3-30 apply to both co-current and counter-current imbibition. In order to show the negative distance moved by the interface in the largest tube, it is better to plot the distance versus the square root of time. Eqs. 8.3-28 – 8.3-30 indicate that co-current and counter-current imbibition should both give straight line plots for x_a, x_b and x_c against $\sqrt{t-t_0}$. Because of the way the experiments are performed, it is not possible to know the exact time at which x_a, x_b and x_c are all zero. Consequently this time has to be found by extrapolating the distance versus time results backwards to find the time when x_a, x_b and x_c are all zero in co-current imbibition. An extrapolation process has also been applied to the counter-current imbibition. However, this time extrapolation lines did not go through the origin, giving not only the time but also the position when x_a, x_b and x_c all have the same value. Figure 8.3-11 – 8.3-16 show the plots for co-current and counter-current imbibition from cells in which 3 distinct menisci were observed.

The fact that all of the experimental results fall so close to straight lines confirms that self-similar fronts are formed as predicted by Eqs. 8.3-28 – 8.3-30. The slight changes in gradient are probably caused by the arc menisci in the corners reaching the end of the tubes. If the gradients in Figures 8.3-11 - 8.3-18 are g_a, g_b and g_c then

$$G_a = g_a^2,\ G_b = g_b^2 \text{ and } G_c = g_c^2 \qquad 8.3\text{-}34$$

Eq. 8.3-33 indicates that $G_c(1\text{-}k_{bc})$ [$=F_c$]) should have the same value for both co-and counter-current imbibition for each cell because λ_{o3}, A_c and (P_{cc}-P_{cb}) are the same for both co-and counter-current imbibition. Similarly from Eq. 8.3-32.

$$\left[G_b + \frac{2}{A_b}\lambda_{o3}(P_{cc} - P_{cb})\frac{k_{bc}}{(1-k_{bc})}\right](1-k_{ab}) = F_b \qquad 8.3\text{-}35$$

should also have the same value for co-and counter-current imbibition. Table 8.3-4 shows these factors for all of the cells. They are in reasonable agreement, confirming Eqs. 8.3-28 – 8.3-30. The $G_c(1\text{-}k_{bc})$ values are also listed in Table 8.3-4 for both co- and counter-current imbibition.

Counter-current flow when bubbles are formed

If the end of the cell is sealed when the oil is introduced, then in the counter- current imbibition, initially but for a very short time, all the interfaces advance but with the largest tube leading. However, as the air at the end of the cell is compressed, the large interface is pushed back by this increasing pressure. Eventually a bubble is blown from the large capillary tube. Immediately after the complete bubble snaps off, an interface forms sealing the tube. This interface then advances a short way into the large capillary. During all this bubble-blowing period, the smaller tube and the interface between the rod and the plate continue to imbibe oil. Single frames from an experiment involving bubble snap-off during a counter-current flow are shown in Figure 8.3-17.

At the beginning, before the oil is introduced into the capillaries, the differential pressure transducer shows a constant value of around 0 Pa. After the oil is introduced, the meniscus in the additional capillary creates an additional capillary pressure (the capillary pressure introduced by the reservoir that was added to the system) between the atmosphere and the fluid which, in effect, shifts the zero indicated pressure of the transducer. This pressure is equal to the P_{add} and if this value is subtracted from the zero initial pressure, we obtain the 'absolute base pressure'. The pressure produced by the additional capillary can be obtained from the capillary rise experiments (see Table 8.3-3). As the oil is applied to the capillaries and starts to imbibe, the pressure rises to the first positive peak. As the length of large tube filled with oil decreases, the pressure drops slightly. It then drops more rapidly as the bubble forms. Eventually the bubble snaps off. Once the snap-off is completed, the air pressure increases almost back up to the initial value and stays almost constant until the next bubble starts to form. After the snap-off the meniscus in the large tube appears to invade the tube for some distance but close observation shows that most of the liquid comes from the arc menisci. As the imbibition rate slows down, the time taken for bubble formation gets longer. A slight decrease in the snap-off pressure was observed with later bubbles, probably because of the fall in rate of formation.

The data plot for the transducer readings (P_{dead}) of the cell with a slot angle of 75º is given in Figure 8.3-18. The negative peaks correspond to a bubble forming. The bubble snaps off at the point 'A'. Immediately after the snap-off, the pressure rises again as the arc menisci retreat into the corners and the main meniscus advances in the larger tube. Little additional imbibition takes place at this point; it is just a rearrangement of fluid. There is a slowing as sequential bubbles are formed. This is because the meniscus advance in the smaller capillary slows with time.

The behavior of the cells when bubbles are formed during counter-current imbibition is quite complex. Consequently the analysis and full report of the experiments will be left for a subsequent paper.

Summary and Conclusions

An interacting capillary model, which is based on pressure equilibration among the capillaries with non-circular crosssections has been used to analyze a series of experiments. The model predicts a behavior that differs from the behavior of the classic 'bundle of independent cylindrical tubes' model. The model also predicts that imbibition will give a self-similar front thus making it akin to the classic analysis of Buckley and Leverett [21]. The equations do not have analytical solutions. The model is part way between network models, which are complex and which only give simulation solutions, and the independent tube model which gives analytic solutions. Analyses for both co- and counter-current imbibition have been made for non-circular tubes when one phase has zero viscosity. Shape factors are needed to describe the tube areas, hydraulic resistances and capillary pressures. Experiments in model cells having precise geometry, using co- and countercurrent imbibition when no bubbles were formed, were used to verify the theory. If air flows from the liquid inlet face, then bubbles are formed and the behavior is complex.

Acknowledgments

The authors acknowledge support from the UK Engineering and Physical Sciences Research Council, BP, ChevronTexaco, Total, the Enhanced Oil Recovery Institute at the University of Wyoming, Shell, Statoil, ARAMCO, the National Petroleum Technology Office of the US Department of Energy, and the Natural Science and Engineering Research Council of Canada. We also thank our technician Steve Bowler for making the cells.

Table 8.3-1 Properties of liquid paraffin and iso-octane

solution	density	viscosity	surface tension
Iso-octane	0.71 g/cm^3	-----	19.42 dyne/cm
Liquid paraffin	0.83 g/cm^3	180 mPa.s	33.83 dyne/cm

Table 8.3-2 The displacement curvature in cells with different d/R ratios, where *d* is the gap size and *R* is the rod radius. The a, b, and c values are the heights of each meniscus minus the height of the reference point.

Angle (°)	*d*	*d/R*	Δ a, b, c (cm)			Normalized curvature		
			Δa	Δb	Δc	a	b	c
85	0.2	0.12	1.20	1.52	2.20	7.92	8.64	12.50
	0.36	0.22	1.19	1.20	---	6.70	6.73	---
	0.45	0.28	0.98	1.11	---	6.18	6.42	---
75	0.17	0.11	1.01	1.92	2.62	5.69	10.93	14.94
	0.29	0.18	0.92	1.67	1.71	5.19	9.46	9.73
	0.42	0.26	0.81	1.10	---	4.59	6.22	---
65	0.12	0.08	0.85	2.58	3.48	4.92	14.85	19.81
	0.5	0.31	0.65	0.98	---	3.69	5.59	---

Angle	*d* (mm)	ΔP_{ca} (Pa)		ΔP_{cb} (Pa)		ΔP_{cc} (Pa)		ΔP_{add} (Pa)	
		Iso.	L.P.	Iso.	L.P.	Iso.	L.P.	Iso.	L.P.
85°	0.2	83.18	144.73	105.21	183.07	152.91	266.06	28.42	49.45
	0.36	79.15	137.72	83.18	144.73	---	---	29.23	50.86
	0.45	68.04	118.39	75.59	131.53	75.77	131.84	29.15	50.72
75°	0.17	69.69	121.26	133.76	232.74	182.77	318.02	30.122	52.41
	0.29	63.49	110.47	115.73	201.37	118.79	207.01	28.75	50.03
	0.42	56.16	97.72	76.14	132.48	---	---	29.86	51.95
65°	0.12	58.96	102.59	179.21	311.83	242.24	421.15	29.35	51.07
	0.5	45.17	75.59	68.35	118.93	---	---	29.69	51.66

Table 8.3-4 $G_c(1-k_{bc})$ values of cells during co- and counter-current imbibition. $G_{co}(1-K_{bc})$ is for co-current, $G_{cc}(1-k_{bc})$ is for counter-current imbibition

Cell (slot angle, gap size)	$G_c(1-\dot{k}_{bc})$ co-current	$G_c(1-\dot{k}_{bc})$ counter-current	F_b co-current	F_b counter-current
65°, 0.12 mm	3.47	2.73	1.26	1.24
75°, 0.17 mm	1.35	1.50	4.00	4.17
85°, 0.2 mm	1.84	1.97	3.14	3.48

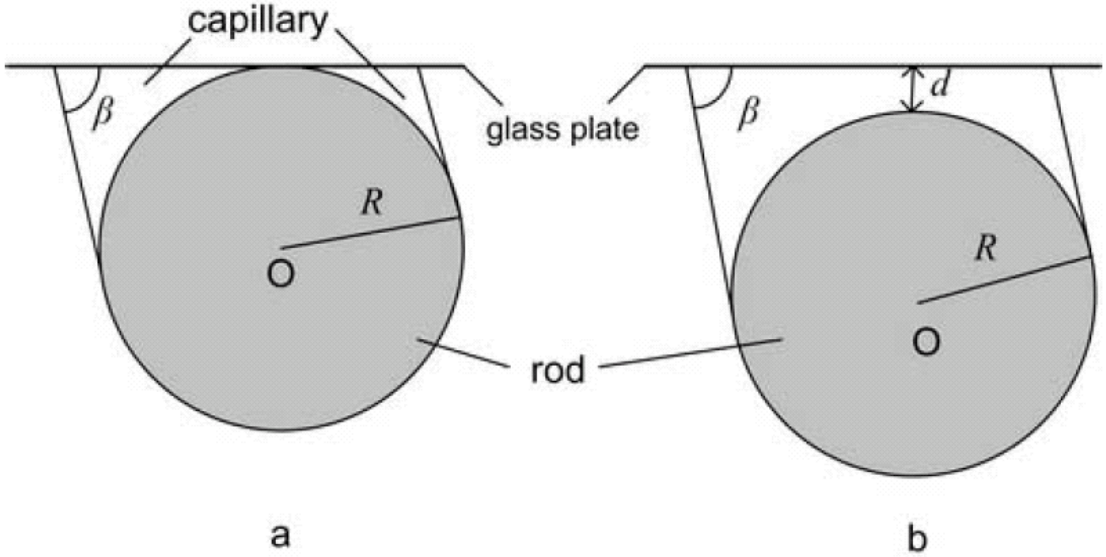

Figure 8.3-1. Structure of the capillaries. The pore geometry is a rod in an angled slot. *β* is the slot angle, *R* is the rod radius. (a) the rod is in contact with a capping glass, two independent capillaries form, (b) There is a gap, *d*, between the rod and the glass, the capillaries are interconnected.

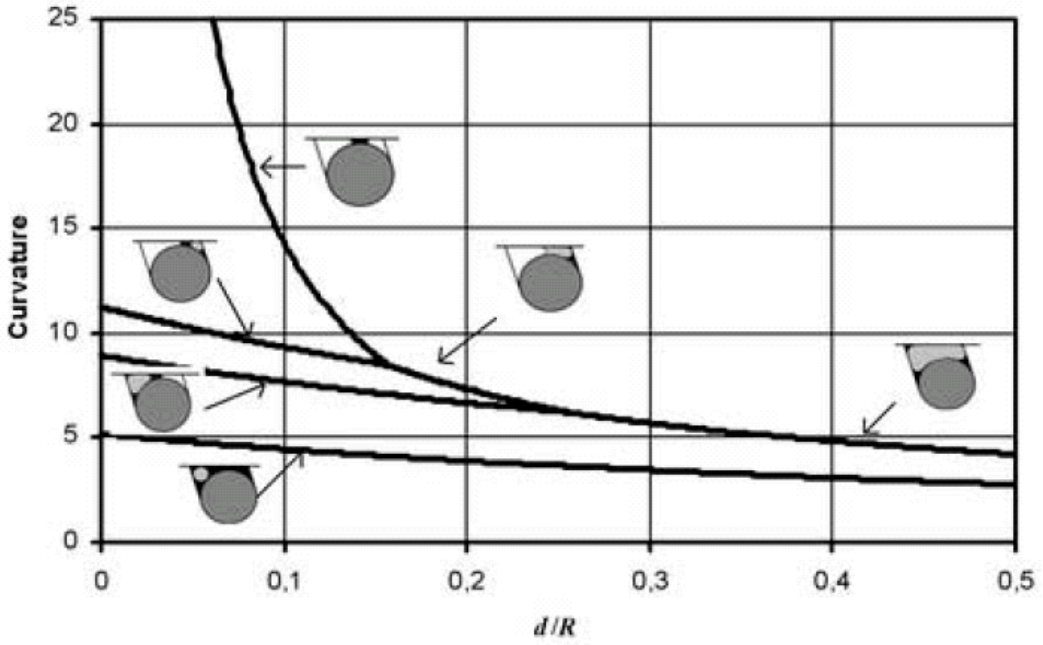

Figure 8.3-2. Meniscus curatures normalized with respect to rod radius as a function of gap size for a rod in an angled slot such as that shown in Figure 8-1b. Slot angle *β* is 85°, *d* is the size of the gap between the rod and the plat, *R*, is the rod radius. The white areas show the tube space, black shows the wetting pahse, and the gray shows the nonwetting phase, for each arc meniscus configuration.

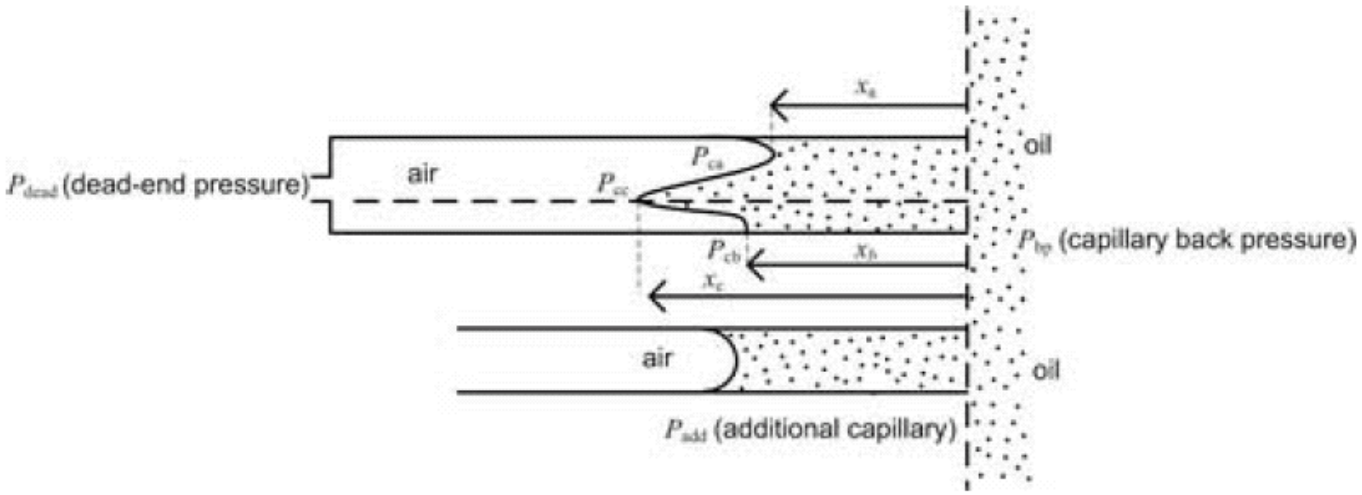

Figure 8.3-3. The positions of the oil/air meniscus in the capillaries at a point of time in the process of oil displacing air.

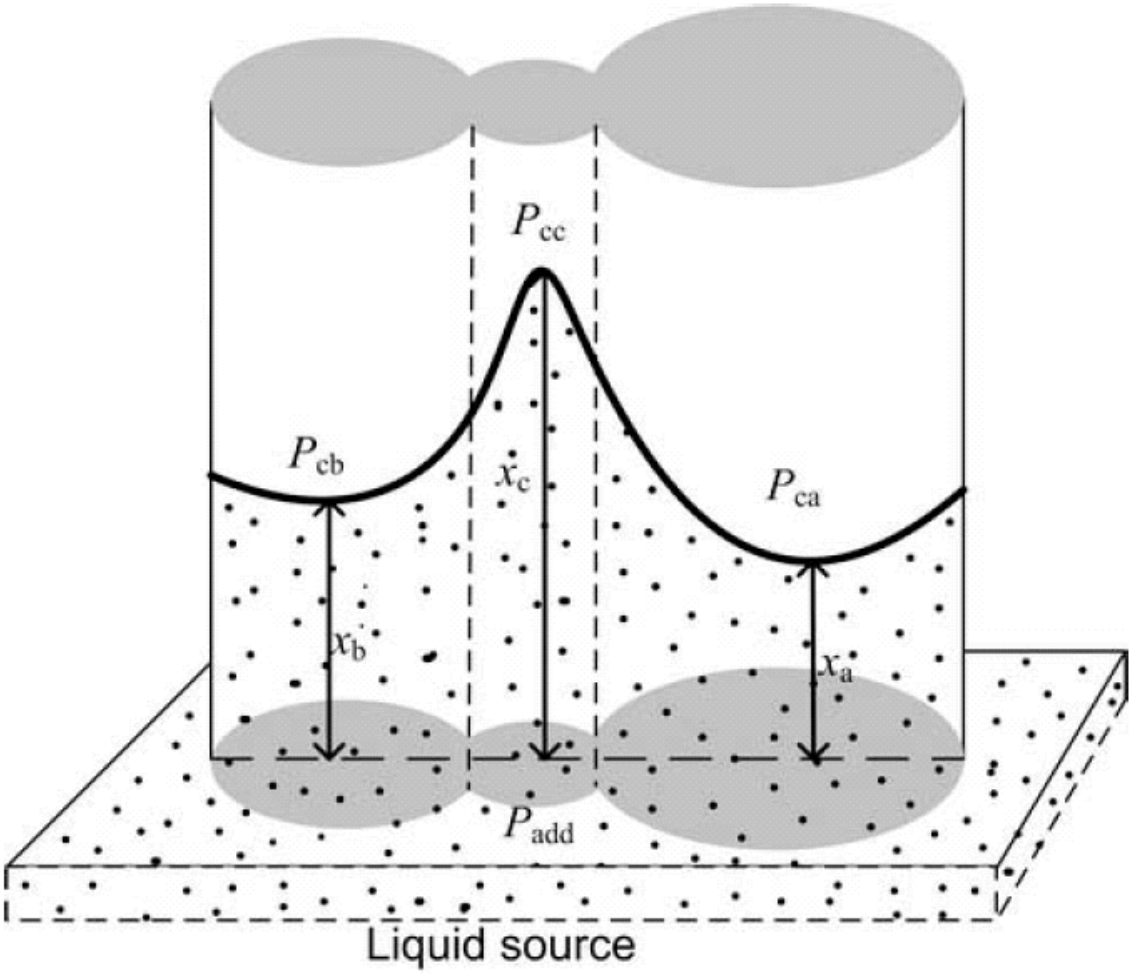

Figure 8.3-4. Perfect cross-flow model

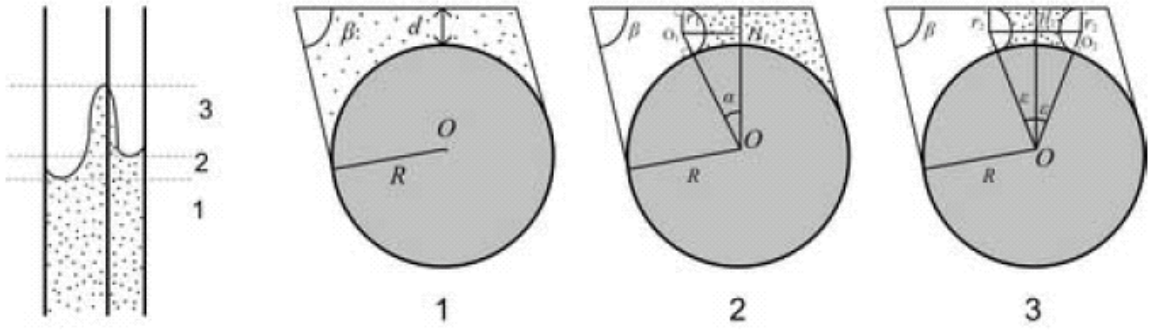

Figure 8.3-5. Cross-sectional areas of capillaries

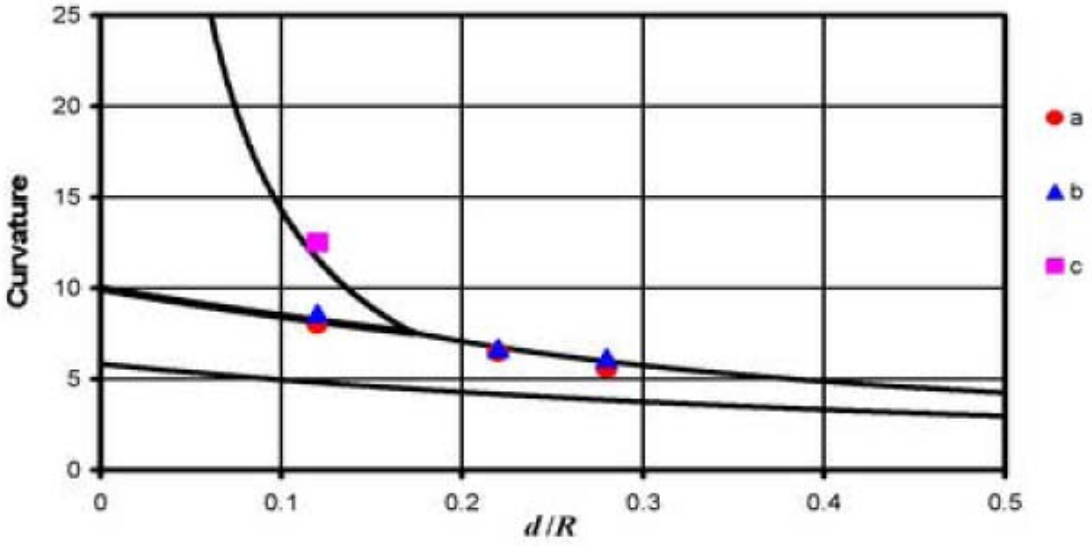

Figure 8.3-6. Comparison of measured and MS-P curvatures at different *d/R* ratios. Slot angle is 85°

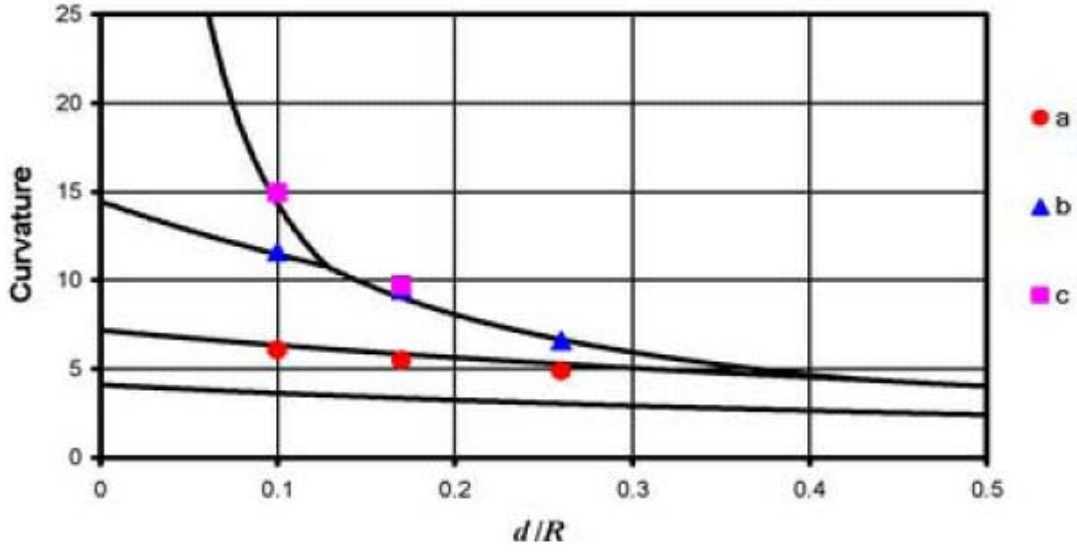

Figure 8.3-7. Comparison of measured and MS-P curvatures at different *d/R* ratios. Slot angle is 75°

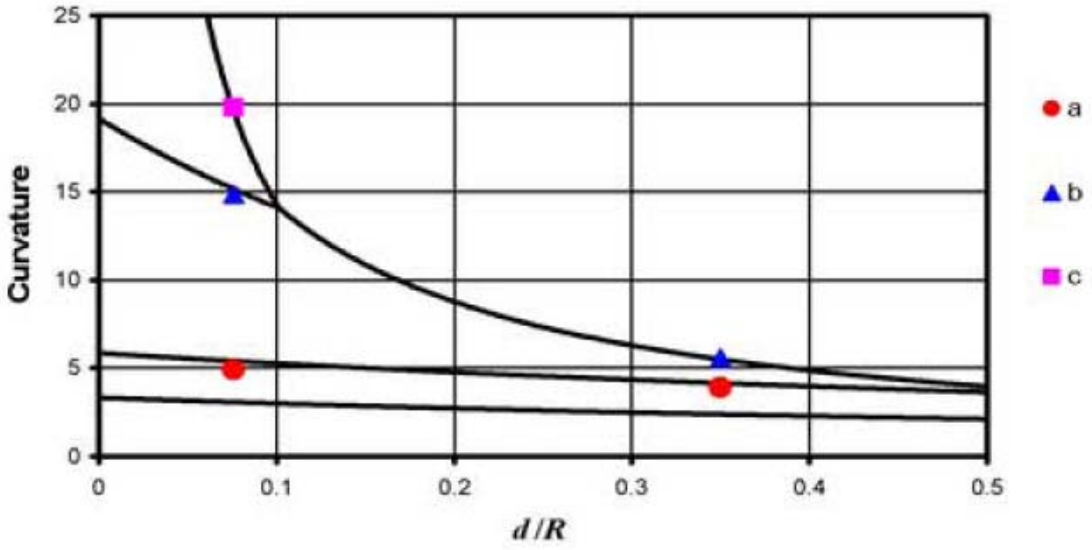

Figure 8.3-8. Comparison of measured and MS-P curvatures at different *d/R* ratios. Slot angle is 65°

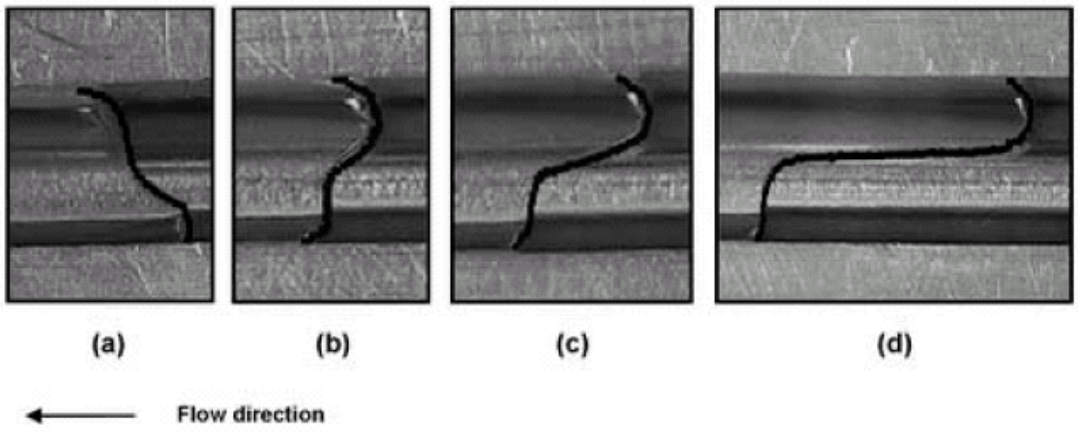

Figure 8.3-9. Single frames taken at different times during an experiment involving co-current imbibition, slot angle is 75°, gap size is 0.42 mm. In frames (a) which was taken very shortly after imbibition commenced, the interface in the large tube leads that in the small tube. This is because the cross-flow is not yet sufficient to be 'perfect'. As the flows reduce and the area for cross-flow increases, the system behaves much more like perfect cross-flow.

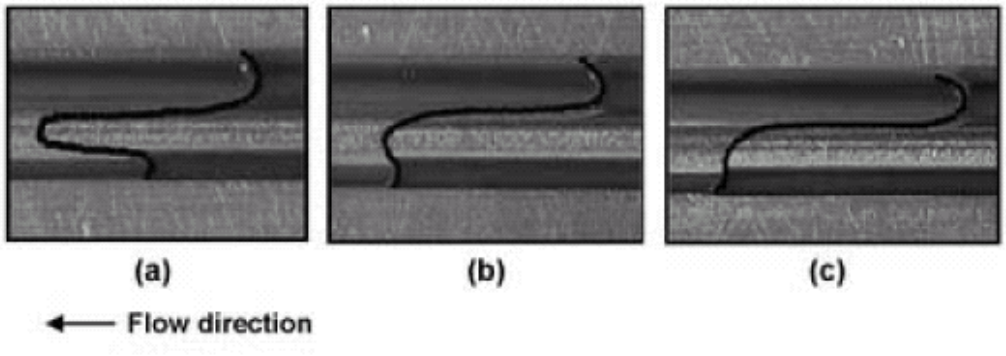

Figure 8.3-10. Menisci structures in different cells showing the effect of increasing gap size (a) Slot angle is 75°, gap is 0.17 mm, (b) Slot angle is 75°, gap is 0.29 mm, (c) Slot angle is 75°, gap is 0.42 mm.

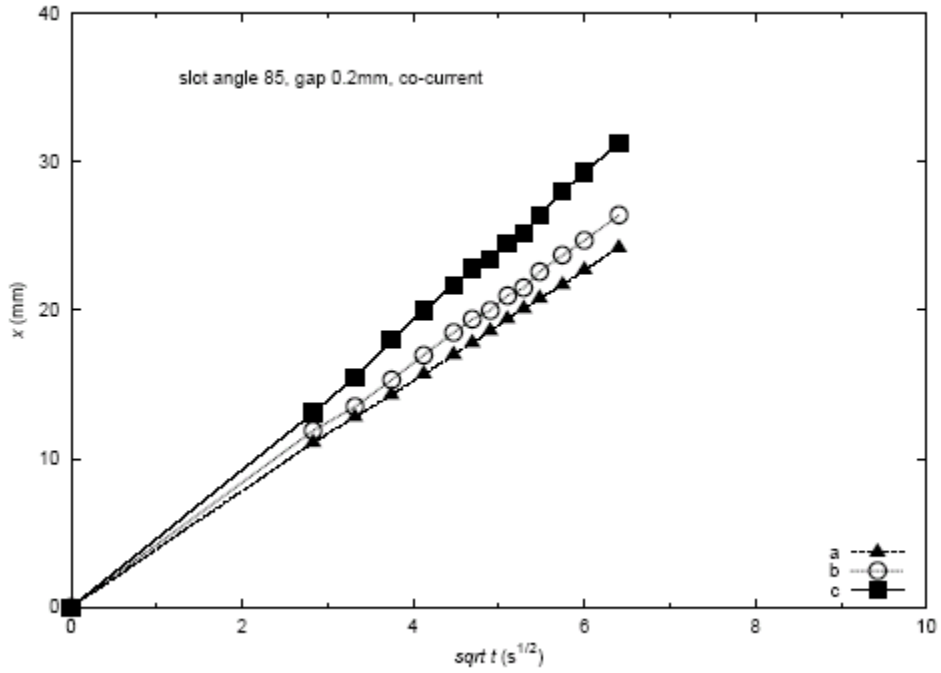

Figure 8.3-11. Relation between x_a, x_b and x_c versus $\sqrt{t}$ during co-current imbibition. Cell angle is 85° and the gap is 0.2 mm.

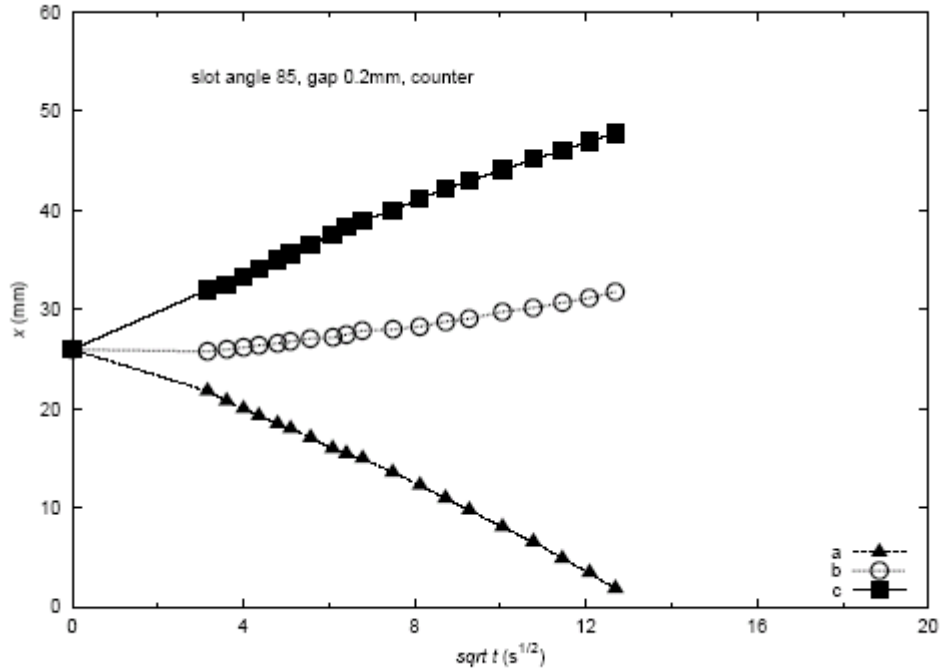

Figure 8.3-12. Relation between x_a, x_b and x_c versus $\sqrt{t}$ during counter-current imbibition. Cell angle is 85° and the gap is 0.2 mm.

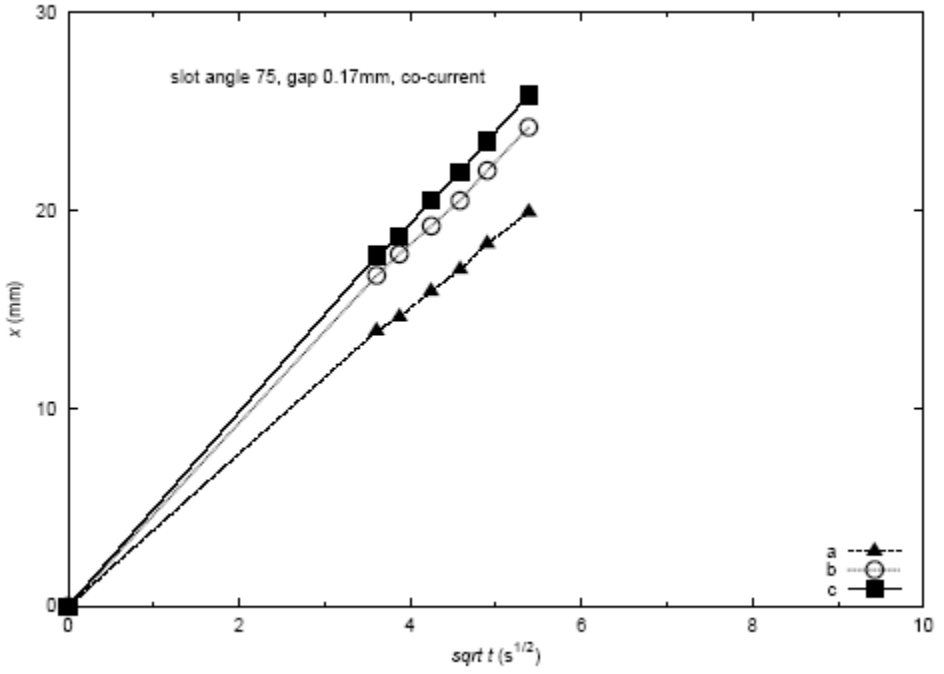

Figure 8.3-13. Relation between x_a, x_b and x_c versus $\sqrt{t}$ during co-current imbibition. Cell angle is 75° and the gap is 0.17 mm.

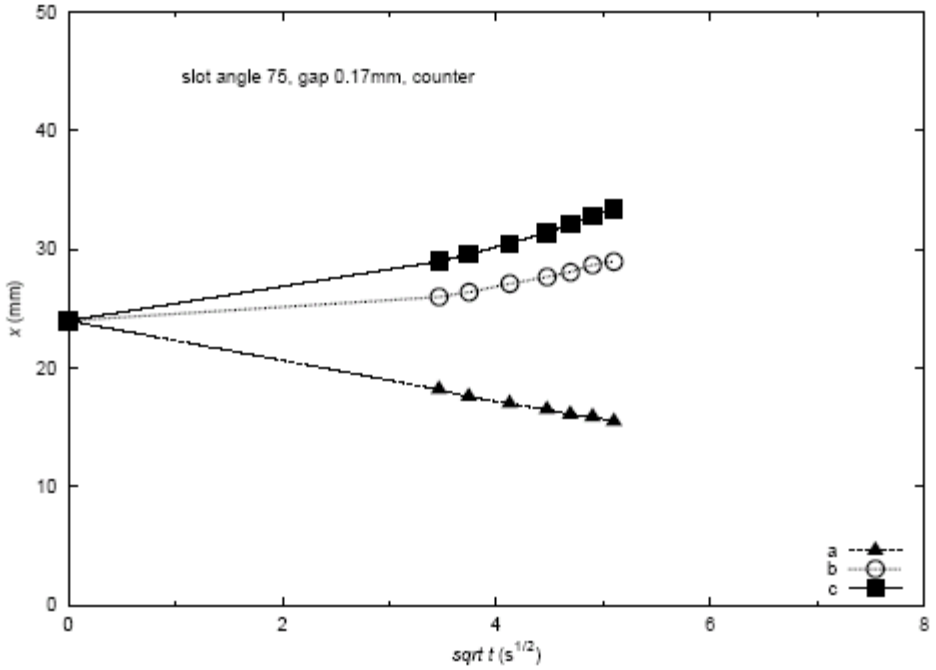

Figure 8.3-14. Relation between x_a, x_b and x_c versus $\sqrt{t}$ during counter-current imbibition. Cell angle is 75° and the gap is 0.17 mm.

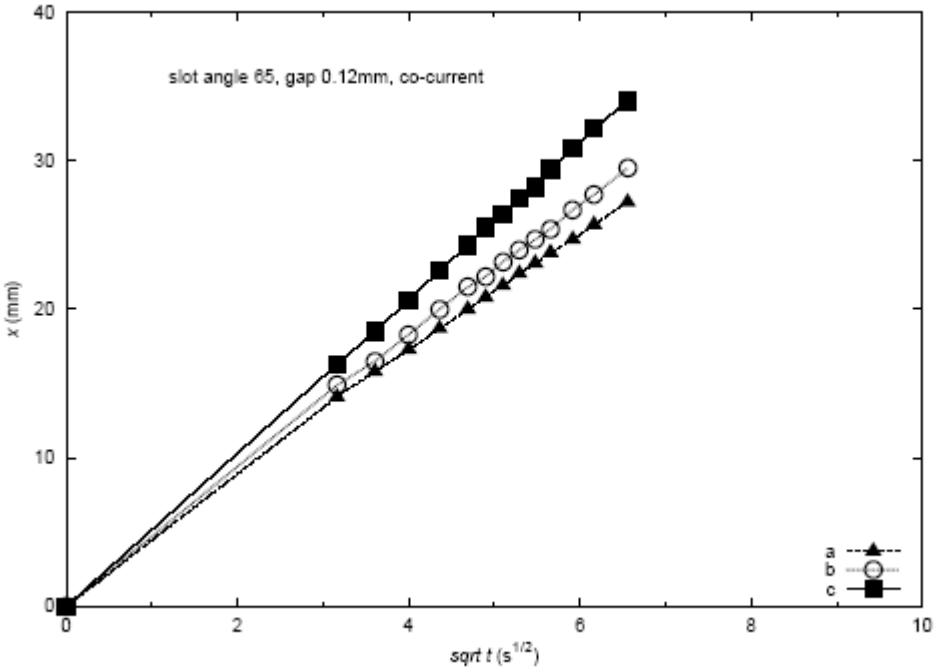

Figure 8.3-15. Relation between x_a, x_b and x_c versus $\sqrt{t}$ during co-current imbibition. Cell angle is 65° and the gap is 0.12 mm.

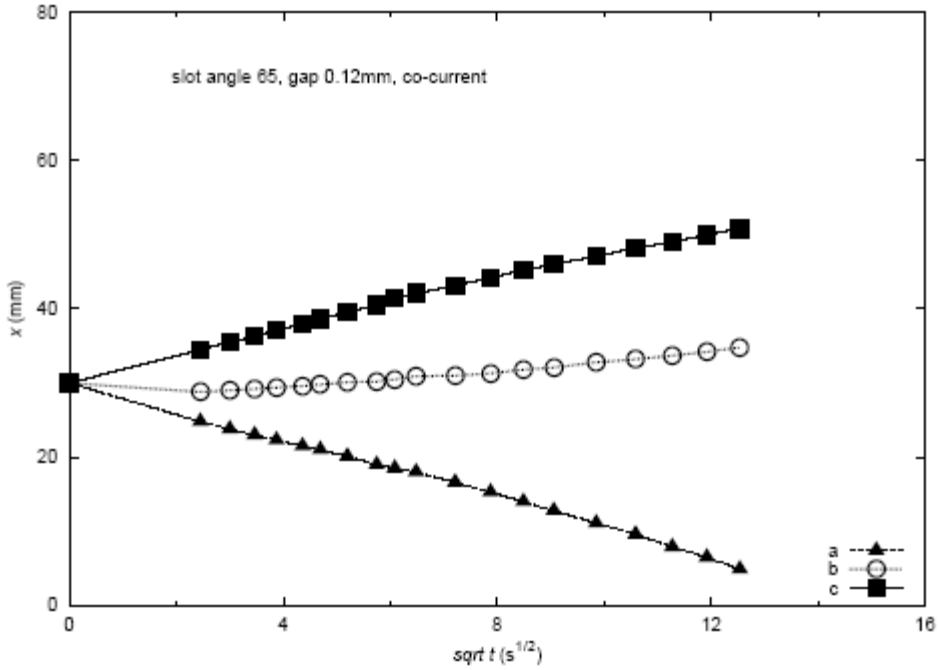

Figure 8.3-16. Relation between x_a, x_b and x_c versus $\sqrt{t}$ during counter-current imbibition. Cell angle is 65° and the gap is 0.12 mm.

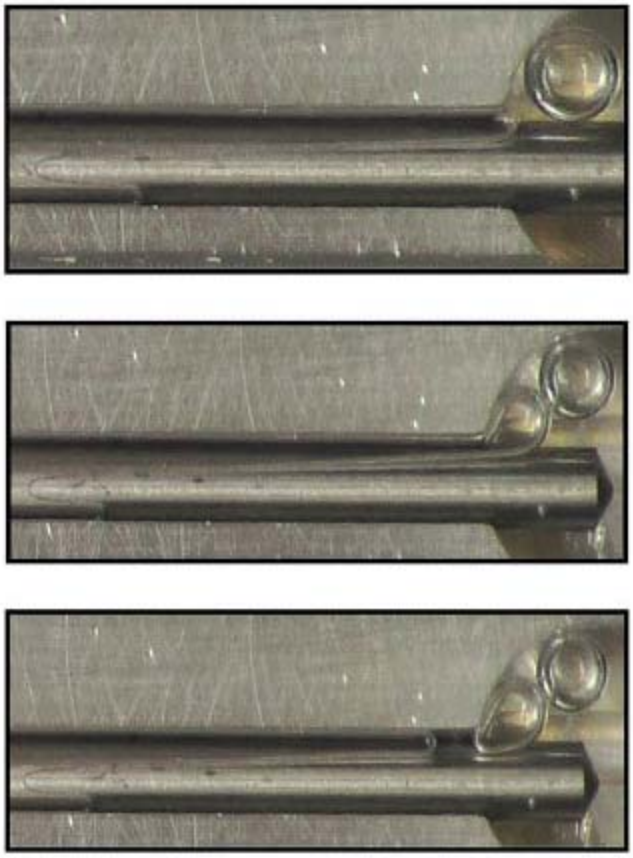

Figure 8.3-17. Counter-current imbibition. A bubble is emerging from the large tube. After snap-off, the meniscus invades the tube for some distance. However, much of this fluid comes from rearrangement of the arc menisci. Slot angle is 75° and the gap is 0.17 mm.

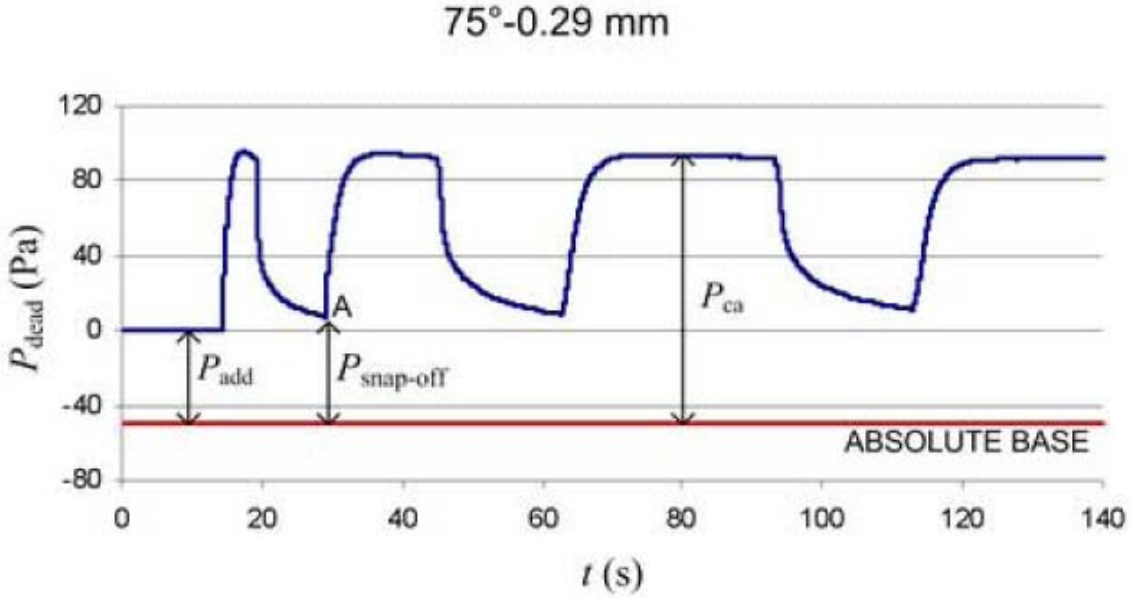

Figure 8.3-18 Pressure (P_{dead}) recordings in the cell during counter-current flow. Slot angle is 75° and the gap is 0.29 mm.

8.4 Bubble Snap-off and Capillary-Back Pressure during Counter-Current Spontaneous Imbibition into Model Pores

E. Unsal, G. Mason, N.R. Morrow and D.W. Ruth
Submitted to: *Journal of Colloid and Interface Science*

Abstract

A previous paper (Unsal, E., Mason, G., Ruth, D.W., Morrow, N.R., 2007, J. Colloid Interface Sci., **315**, 200-209) reported experiments involving counter-current spontaneous imbibition into a model pore system consisting of a rod in an angled slot covered by a glass plate. Such an arrangement gives two tubes with different cross-section (both size and shape) with an interconnection through the gap between the rod and the plate. In the previous experiments, the wetting phase advanced in the small tube and non-wetting phase retreated in the large tube. No bubbles were formed. In this paper, we study experimentally and theoretically the formation of bubbles at the open end of the large tube and their subsequent snap off. Such bubbles reduce the capillary back pressure produced by the larger tube and can thus have an effect on the local rate of imbibition. In the model pore system, the rod was either in contact with the glass, forming two independent tubes, or the rod was spaced from the glass to allow cross flow between the tubes. For small gaps, there were three distinct menisci. The one with the highest curvature was between the rod and the plate. The next most highly curved was in the smaller tube, and the least highly curved meniscus was in the large tube and this was the tube from which the bubbles developed. The pressure in the dead end of the system was recorded during imbibition. Once the bubble starts to form outside of the tube, the pressure drops rapidly and then steadies. After the bubble snaps off, the pressure rises to almost the initial value and stays essentially constant until the next bubble starts to form. After snap-off, the meniscus in the large tube appears to invade the large tube for some distance. The snap-off is the result of capillary instability because it takes place significantly inside the large tube with flow of wetting phase moving in the angular corners. As imbibition into the small tube progresses, the rate of imbibition decreases, and the time taken for each bubble to form increases, slightly increasing the pressure at which snap-off occurs. The snap off curvature is only about two thirds of the curvature of a theoretical cylindrical meniscus within the large tube and about 40% of the actual meniscus curvature in the large tube.

Introduction

The snap-off of bubbles or droplets occurs in many practical situations. Gas is often sparged into liquid through a distributor, producing bubbles and creating a large contact area. Distributors can take many forms from perforated plates (Loimer et al, 2004) to slits (Li et al., 1994). The process can be very complicated depending on the gas flow rate, the spacing of the holes and the liquid viscosity. The gas feed pressure is usually kept constant and so, once a bubble exceeds a hemisphere, it becomes unstable and grows rapidly. The actual mechanism of detachment is usually seen as the buoyancy of the bubble exceeding adhesion through surface tension (Tate, 1864), the reverse of the formation of drips (Mitrovic, 2000), although jetting and the interference of neighbouring bubbles also play a part.

Uniform drop size emulsions can be produced by forcing liquid through porous materials with small pores (Joscelyne, 2000) with the droplet size sometimes being as small as three times the diameter of the originating pores. However, they are often much larger. It seems that microporous glass membranes (Nakashima, 2000) produce the most uniform and smallest (relative to

membrane pore size) droplets. The droplets are too small to snap off through buoyancy and a high shear is usually used to get small droplets to form (Vladisavljević, 2003). However, when the droplets are very small, the shear forces alone become insufficient and another mechanism is required. Rayner (2004) postulated that drops should break off for thermodynamic reasons and calculated drop shapes. However, thermodynamic instability is not enough – a mechanism from one state to the other is also required (Everett & Haynes, 1971). The technique of etching microchannels in silicon enables drop formation from specific geometries to be studied and the snap off process visualized (Sugiura, 2001). It became clear that under certain circumstances, droplets could snap off spontaneously through capillary instability. A key requirement is that the continuous phase has to be able to flow rapidly to the unstable region so as to allow snap off without the droplet becoming oversized. This was elegantly demonstrated using CFD (Kobayashi, 2005).

The maximum bubble pressure method is used to study dynamic interfacial tensions and give information about diffusion rates of surfactants (Mysels, 1990). However, the snap off of the bubble is usually regarded as simply the creation of new surface and the apparatus is usually designed so that once the gas bubble has grown past a hemisphere, it expands very fast as the air in the system expands and it then snaps off.

In porous media containing two phases it has long been known that there can be instabilities in the way that the phases are distributed and that liquid which is initially distributed at the walls can snap off and bridge across the waists of the pores, thus blocking them (Roof, 1970). This can happen in constricted cylindrical tubes (Gauglitz & Radke, 1990) and even in uniform smooth cylindrical tubes, because a cylindrical capillary surface in which longitudinal flow is possible is unstable if it is too long (Everett & Haynes, 1971). Instability is also observed in smoothly constricted tubes with non-circular cross-section (Ransohoff et al., 1987) and in multiply-connected capillaries such as those in micromodels (Bernardiner, 1998). Snap-off is believed to be the main cause of hysteresis and entrapment in mercury porosimetry (Matthews et al., 1995) and to be one of the ways in which a foam that impedes the flow of gas can be formed in reservoir rocks (Kovscek & Radke, 2003; Rossen, 2008). Snap-off also breaks up oil into blobs during the displacement of oil from porous rocks (Li & Wardlaw, 1986a, b; Al-Gharbi & Blunt, 2005) and, in a different field, blocks elastic lung passages in some diseases (Heil & White, 2002). The basic idea is that for a fixed volume, a sphere has less surface area than a cylinder. For a perfectly wetting liquid lining the walls of a cylindrical tube the interface curvature is 1/R (where R is the tube radius) whereas if the same volume of fluid is a slug spanning the tube the curvature is 2/R and the latter has less surface energy and so is more stable.

However, there still needs to be a mechanism to get from one configuration to the other. The situation is more complicated if the tube has a triangular cross-section because the corners can hold a small amount of liquid with very high curvature. If the volume of fluid in the corners is increased, the interface curvature decreases and eventually a cylindrical interface is formed inside the tube and, depending on the length, the fluid can then redistribute and snap off to bridge the tube (Mason and Morrow, 1991; Kovscek & Radke, 1996).

Counter-current spontaneous imbibition is believed to be one of the principal mechanisms of oil recovery from fractured reservoir rocks. Basically, when brine is pumped into the porous reservoir

rock, it flows primarily through the fractures. If the brine preferentially wets the rock, then brine in the fractures is drawn into the pore space of the rock and, in order to maintain the local volume balance, oil droplets are expelled back into fluid flowing in the fracture (Rangel-German & Kovscek, 2002). This complex process depends on several variables (Behbahani et al., 2006), some of which might be controlled, and consequently understanding spontaneous imbibition has become of economic significance. The ultimate goal is to predict behaviour so as to be able to maximise production. Prediction requires quantitative knowledge of the details of the process (Hughes & Blunt, 2000). Much can be learned from direct experiments. These typically use a brine (wetting phase) to displace oil (non-wetting phase), from actual rock core samples. These are usually cylinders a few centimetres in diameter and several centimetres long. Initial conditions can be varied, starting from the simplest in which the core is completely filled with oil. After immersion in brine, the displaced oil is collected. Usually the brine slowly invades the rock, over hours, and maybe even days or weeks. The volume produced is recorded as a function of time. This experimental technique can be varied to incorporate many of the variables of real reservoir systems.

In counter-current imbibition, brine moves in one direction and the oil in the reverse direction (Li et al., 2006). Both flows require a pressure gradient to drive them and, because the flows of each phase are in opposite directions, the pressure gradients have to be in opposite directions. This is only possible by having a gradient of capillary pressure generated by the oil/brine interfaces in the core. This alters the saturation of each phase and varies their relative permeabilities. During such counter-current imbibition, it is observed that the displaced non-wetting phase is produced as drops at the surface of the open face. There has to be a pressure opposing the production of the non-wetting phase associated with the generation of these drops. It is called the capillary back pressure, P_{back}. In an earlier paper (Unsal *et al*., 2007b), counter-current imbibition was studied both theoretically and experimentally using a simple model pore system which mirrored part of actual behaviour but without bubble production. Here, we report the details of bubble production, including the pressure at which the bubbles snap off.

In almost all previous experiments, the studies have been visual. One exception is the work of Li & Wardlaw (1986a) who measured the pressure to withdraw a meniscus from a rectangular (aspect ratio 2:1) section tube and the subsequent pressure for the liquid to snap off in the tube when the fluid pressure was raised. For a perfectly wetting fluid they found that the pressure for displacement divided by the pressure for snap off was 1.49. In this work, in addition to visual observations, we also report the pressures inside the bubbles as they snap off.

In our imbibition experiments the model pore geometry is a rod in an angled slot which is capped by a glass plate (see Fig. 8.4-1). Mineral oil that wetted all of the materials of construction was used as the invading liquid, and air was the non-wetting phase. In counter-current mode, liquid imbibed into the smaller uniform cross-sectioned tubes and displaced air as a bubble from the open end of the large tube. The bubble grows to a critical size at which point the liquid in the corners of the large tube grows in and snaps off, isolating a free air bubble. The air pressure rises sharply following bubble snap-off. The new meniscus formed in the large tube by the snap-off initially retreats, but then is driven back until eventually it forms a fresh bubble. The cell is horizontal and this minimises the effect of gravity. Also, because the bubble rests against the plate, almost the entire buoyancy force is vertical and taken by the plate. The bubble does not break off

because the buoyancy force exceeds the capillary attraction but because the shape of the bubble eventually becomes unstable with respect to capillary forces. In these experiments it is not the air supply pressure that is kept constant but the rate at which air flows into the bubble. This means that the bubble is stable, even though it has grown larger than a hemisphere.

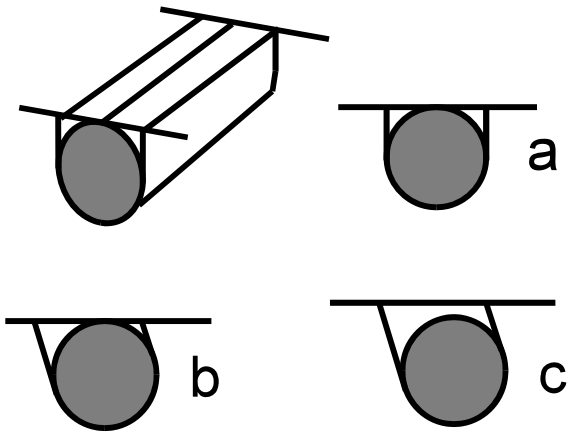

Fig. 8.4-1 a) Diagram of the cross-section of a rod in a square slot. The hole was machined with a ball ended milling cutter so that there was virtually no hydraulic pathway beneath the rod. To keep gravity effects were minimal, the cell was operated horizontally. The rod radius was 1.588 mm. b) Cross-section with the rod touching the plate and with the tube down one side larger than the other. c) Cross-section used in these experiments with the rod spaced away from the capping glass plate. There are now three potential menisci depending on the gap width: one in the large tube, one in the small tube and possibly a double-sided meniscus in the gap. Liquid imbibing into the smaller tube displaces air as bubbles via the larger tube.

THEORY

In counter-current displacement experiments, whilst air is displacing oil from the large tube and there is a meniscus spanning across the diameter of the large tube, the pressure vs time measurements show an almost constant value. Once the meniscus reaches the end of the tube an approximately hemi-spherical interface emerges from the end of the tube and then rapidly expands. As the curvature of the bubble decreases with its increasing diameter, the differential air pressure falls, rapidly at first, and then more slowly. When the differential air pressure has approximately halved, the interfaces in the tube grow inwards and snap off the bubble. The volume versus pressure relationship can be approximately modelled by considering the bubble to be a portion of a sphere anchored to a fixed circle which has the same diameter as the meniscus when it first emerges from the large tube. Such an arrangement is shown in Fig. 8.4-2.

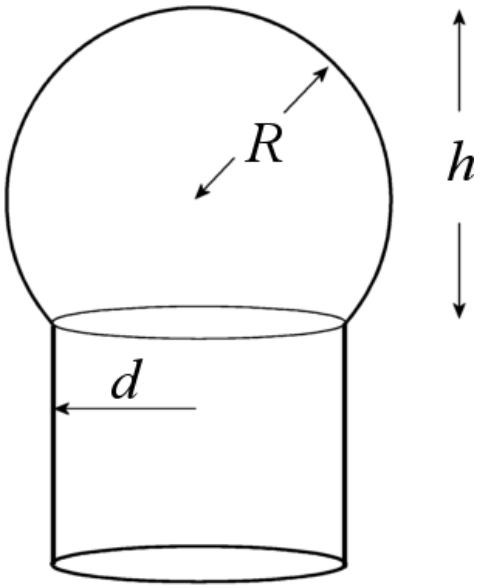

Figure 8.4-2. Diagram of a spherical bubble growing from a cylindrical tube.

The volume V of a portion of a sphere, height h, radius R, cut off by a circle, radius d, is

$$V = \frac{\pi}{3} h^2 (3R - h) \qquad 8.4\text{-}1$$

- and h is given by

$$h = R \pm \sqrt{R^2 - d^2} \qquad 8.4\text{-}2$$

But, since our bubble is always greater than a hemisphere, only the + sign is applicable. The pressure inside a spherical bubble is $2\sigma/R$ where σ is the interfacial tension. A general plot of normalized pressure ($2/R$) versus volume for a growing portion of a sphere with a fixed diameter anchored base is shown in Fig. 8.4-3 and this will approximate to the pressure response as a bubble is blown. Comparison with results shown in Unsal et al (2007a) and later in this paper confirm the approximate shape, and the conclusion that the change in pressure with volume is primarily the result of growing a spherical bubble.

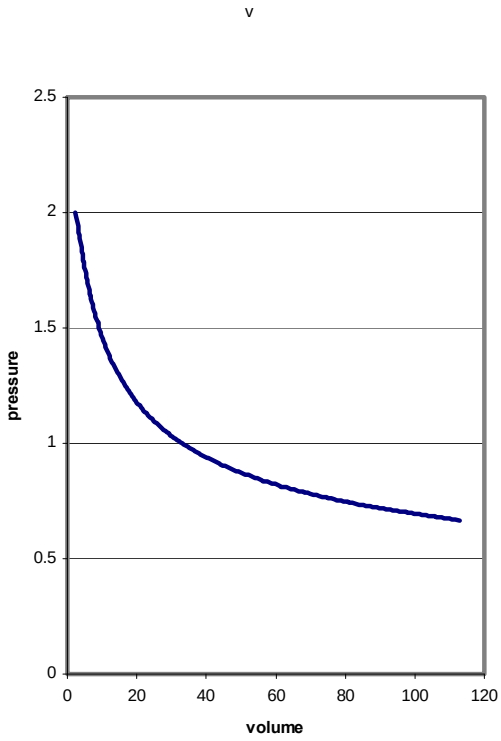

Figure 8.4-3 Graph of how the normalized pressure drops as the volume of the spherical cap increases in size. The cylindrical tube has unit radius. Snap-off is not expected until the normalized pressure has dropped to at least 1.

The volume of air in the bubble equals the volume of oil imbibed by the smaller tubes since the last bubble snapped off. The rate at which the volume of the bubble increases with time is therefore not linear. Over short periods of time the imbibition rate will be approximately constant, and this accounts for the similarity of the shape of Fig 8.4-3 to actual experiments. Over longer periods of time the rate of imbibition into the smaller tube changes significantly, varying as $\sqrt{time}$ (Washburn, 1921) and this accounts for why the pressure profiles become more extended as time progresses.

The pressure at which the bubble snaps off is determined by the mechanistic pathway that the arc (or wedge) menisci in the corners follow as they move out from the corners to span the tube. As the radius of the bubble increases, the arc menisci just inside the end of the large tubes try to match this radius and grow inwards, fed by a flow of bulk liquid. Eventually they touch and locally an almost cylindrical meniscus is formed. There is however, a second requirement and that is that the length of the cylinder has to be greater than π times its diameter (Plateau, 1873; Rayleigh, 1899; Mason, 1970). Because there has to be flow from the bulk liquid along the arc menisci (Gauglitz et al, 1987), the curvature cannot everywhere be equal and it is likely that the bubble curvature at snap off will be significantly less than the curvature of the cylinder.

Experimental

The model pore system is formed by placing a rod in a precisely-machined angled slot and capping the whole with a glass plate. Non-axi-symmetric channels with different sizes and shapes with angular corners are formed on either side of the rod. For any particular arrangement of slot and rod, the tube geometry is completely defined and fixed and so the capillary pressures can be calculated using the Mayer & Stowe-Princen (MS-P) theory (Mayer & Stowe, 1965; Princen, 1969a,b, 1970). This experimental technique differs from the use of micromodels (Kovscek et al., 2007) in that the pore geometry is much simpler, the pores are bigger, their size and shape are precisely known, and consequently the capillary pressures and resistances to flow are calculable. The experiments reported here involve counter-current imbibition into the model pore system, with a mineral oil displacing air. In general, the oil is drawn into the smaller channel and the air is forced out of the larger one, breaking off (pinching-off or snapping-off) a series of bubbles. A full description of the apparatus has been given by Unsal et al, 2007a, b. In addition to the tubes formed by the slot, there is an extra slot machined in the cell (termed the additional capillary, "add"). Its function is to act as a reservoir for excess fluid when the reservoir at the end of the slot capillaries is filled with oil at the start of an experiment. There is a sensitive differential pressure connected to the air space in the cell. The novel feature of the reported experiments is not just the unusual pore geometry but that the pressure in the air is measured at the same time, thus making possible a comparison with theoretical predictions.

The slot is angled and so the channels or tubes at the sides of the rod will have different sizes (Fig 8.4-1c). If the channels are of similar size, then imbibition into the smaller tube and production of the bubbles happens quite slowly because imbibition is driven by the difference in curvature between the interfaces in the small and large tube, and, with tubes of almost the same size, the curvature difference is small. There is an additional effect in that the hydraulic resistance of each tube depends inversely on the square of the tube size and so the rate of linear advance into the small tube depends on tube size. As a result of these two effects, the rate of imbibition depends on just how different the two tubes are in size. Counter-current imbibition with the tube size ratio too small or too large is slower than the optimum. For cylindrical tubes with hypothetical perfect cross flow and all of the viscous pressure drop in the invading fluid, the optimum ratio for maximum linear advance is when one tube has twice the diameter of the other.

During an experiment, bubbles are produced from the mouth of the larger tube, and their size is determined by the size of the larger tube. The total volume of liquid that is imbibed is determined by the size of the smaller tube. Consequently, the total number of bubbles produced depends on the sizes of both tubes. The rate at which bubbles are produced also depends on the size ratio of the two tubes and, more important during an experiment, on the distance that the interface in the small tube has already advanced (the Washburn effect, Washburn, 1921). This latter effect means that successive bubbles are grown at ever-slower rates.

When there is a gap between the rod and the plate as in Fig. 8.4-1(c), the behaviour is more complex because liquid can flow from one tube to the other through the gap. This gives an example of a system which can be fitted by the model of Ruth & Bartley (2003). When the rod contacts the plate no such cross-flow is possible.

Model cells with three angles (65°, 75° and 85°) were used. There were several slot depths for each slot angle. When the rod touches the plate, the system behaves as two separate capillary tubes linked at the end (Unsal et al., 2007a). Each tube has its own distinct meniscus (termed "a" for the larger tube and "b" for the smaller tube. For small gaps there is an extra distinct meniscus between the rod and the plate (termed "c"). Eight new cells with different slot angle and gap size were made (See Table 8.4-1). All of the meniscus curvatures for all cells were calculated using the MS-P method. Capillary rise experiments using a low viscosity fluid (iso-octane) were also performed to validate the MS-P calculations. Agreement was close (Unsal *et al*., 2007b). The pressures produced by the mineral oil (liquid paraffin BP) were calculated from the iso-octane results and are given in Table 8.4-1. Note that the pressure produced by the additional capillary is small but not insignificant. The results for $d = 0$ are taken from Unsal et al., 2007a.

Table 8.4-1. Test cell properties.

Angle	***d*** **(mm)**	*d/R*	ΔP_a (Pa) large		ΔP_b (Pa) small		ΔP_c (Pa) gap		ΔP_{add} (Pa) additional	
			Iso.	**L.P.**	**Iso.**	**L.P.**	**Iso.**	**L.P.**	**Iso.**	**L.P.**
85°	0.0	0	105.6	183.8	133.6	232.5	---	---	31.5	54.95
	0.2	0.12	83.2	144.7	105.2	183.1	152.9	266.1	28.4	49.5
	0.36	0.22	79.2	137.7	83.2	144.7	---	---	29.2	50.9
	0.45	0.28	68.0	118.4	75.6	131.5	---	---	29.2	50.7
75°	0.0	0	80.2	139.6	165.2	287.4	---	---	27.6	48.3
	0.17	0.11	69.7	121.3	133.8	232.7	182.8	318.0	30.1	52.4
	0.29	0.18	63.5	110.5	115.7	201.4	118.8	207.0	28.8	50.0
	0.42	0.26	56.2	97.7	76.1	132.5	---	---	29.9	52.0
65°	0.0	0	64.7	112.6	212.3	368.9	---	---	27.5	47.8
	0.12	0.08	59.0	102.6	179.21	311.8	242.2	421.2	29.4	51.1
	0.5	0.31	45.2	75.6	68.4	118.9	---	---	29.7	51.7

An example of bubbles emerging from the big tube and snapping off is shown in Fig 8.4-4. The highly curved interface is shown emerging from the tube. The other illustrations show the interface just prior to snap-off and a short time after. Experiments were also performed with a square ended rod not protruding from the slot but this made little difference to the pressures measured with the transducer. The new meniscus spanning the large tube retreats a significant distance back along the large tube after the bubble is detached.

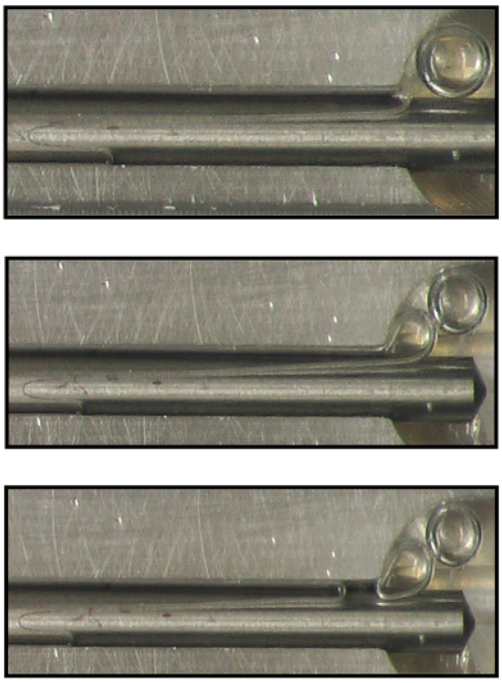

Figure 8.4-4 Bubble production during counter-current imbibition. The top picture shows a bubble is emerging from the large tube. The centre picture shows the meniscus arrangement just before snap-off. The lower picture is take just after snap-off and shows just how far the meniscus moves back along the large tube. Most of fluid for this comes from the rearrangement of the arc menisci as their radius of curvature decreases. Slot angle is 75º, gap is 0.17 mm.

RESULTS

Initially, when the cell is full of air the differential pressure transducer shows a constant value of around 0 Pa. As the oil is pushed into the chamber at the end of the cell the applied pressure pushes the oil a short distance into both capillaries. Surplus oil escapes into the additional capillary parallel to the main slot and partially fills its length. The pressure indicated by the pressure transducer rises as the oil covers the end of the capillaries and slightly compresses the air. The pressure rises to the first positive peak and remains almost steady as the meniscus in the large tube starts to be pushed backwards, driven by the air displaced as the meniscus in the small tube advances. As the length of large tube filled with oil decreases, the hydraulic resistance drops but this effect is small and the air pressure only drops slightly. Eventually the meniscus reaches the end of the large tube and a bubble starts to form. The pressure now drops rapidly as the bubble grows in size and then less-rapidly. The curvature of the interface just inside the tube drops to match that of the bubble and this eventually causes bubble snap-off. Once the snap-off is completed, the new meniscus in the large tube causes the air pressure to increase almost back to its initial value and then stay almost constant until the next bubble starts to form. As the imbibition rate in the small tube slows down, because of the increasing distance, the fluid has to travel (the Washburn effect), the time taken for bubble formation increases.

Once the meniscus forms in the additional capillary it creates an additional capillary pressure between the atmosphere and the fluid. In effect this additional interface shifts the true zero of the pressure indicated by the transducer. This pressure is equal to ΔP_{add} and if this value is subtracted

from the zero initial pressure, we obtain the 'absolute base pressure'. The pressure produced by the additional capillary was obtained from the preliminary capillary rise experiments (see Table 8.4-1) adjusted for the different interfacial tension. The data plot for the transducer readings (ΔP) of the cell with a slot angle of 85º and with a gap of 0.2mm is given in Figure 8.4-5. The rod diameter was 3.175mm.

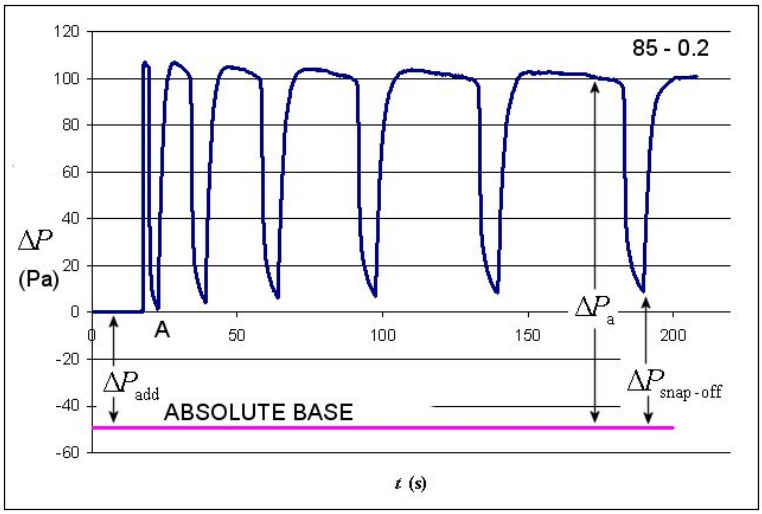

Figure 8.4-5 Pressure (ΔP) recordings in the cell during counter-current flow for a slot angle β of 85º and a gap of 0.2 mm. Negative peaks indicate bubble formation. Once the snap-off is completed, the air pressure increases back up to the initial value and stays almost constant until the next bubble starts to form. Note that the recovery of the pressure after snap-off is quite fast. This is in contrast to the situation when the rod touches the plate (Unsal et al., 2007a). Recovery is dominated by the flow areas in the arc menisci and these are much greater when the rod is spaced away from the plate.

The negative peaks shown in Fig. 8.4-5 correspond to the formation of bubbles. The bubble snaps off at the point marked 'A'. Immediately after snap-off, the pressure rises again as the arc menisci retreat into the corners and the main meniscus moves back into in the larger tube. It can be seen that there is a slowing as sequential bubbles are formed, making the time between the first and the second bubble shorter than the time between the second and the third, and so on. This is because the speed of the process is driven by the rate at which the meniscus advances in the smaller capillary and this slows with the square root of time as predicted by the Washburn equation. If all of the bubbles snap off at the same pressure then all will have equal volume and consequently the square of the bubble number should vary linearly with time. This is illustrated in Fig. 8.4-6.

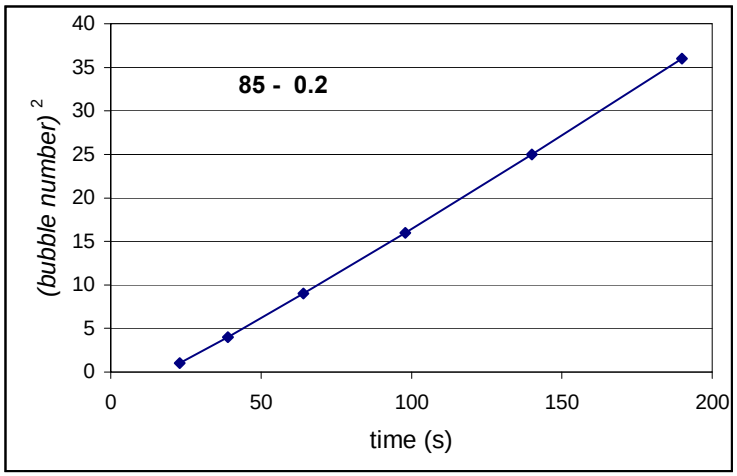

Figure 8.4-6 Plot of the square of the bubble number against time. If all of the bubbles have the same volume and the rate of imbibition depends on the distance advanced by the meniscus in the small tube, then a straight line should result.

The superimposed pressure-time responses for all of the bubbles are shown in Fig. 8.4-7. It can be seen that they are all generally of the same shape but it takes longer to generate successive bubbles. As the rate at which the bubbles are grown slows, the snap-off pressure rises slightly. The pressure recovery after snap-off is almost the same for every bubble and appears independent of the rate at which the bubble grew. The shape of the initial pressure drop response is almost the same for every bubble. This is most likely caused by the bubble being suddenly driven out of the tube because of expansion of the air in the transducer and pipes as the pressure drops. Although the pressure change is quite small, the bubble volume is also small. This explanation is supported by the comparison of the pressure-time response for bubble 3 with the pressure-volume relation for the growing spherical cap (Fig. 8.4-3). This comparison is shown in Fig. 8.4-8 with the pressure volume relation scaled to fit the start and end pressure of the bubble. If the flow of air into the bubble was constant, the spherical cap relation should be followed. In fact the initial drop in pressure with time is much faster than predicted from the spherical cap volume, indicating that the volumetric air flow is not constant and that the expansion of the slightly compressed air is detectable, but not sufficient to cause snap off.

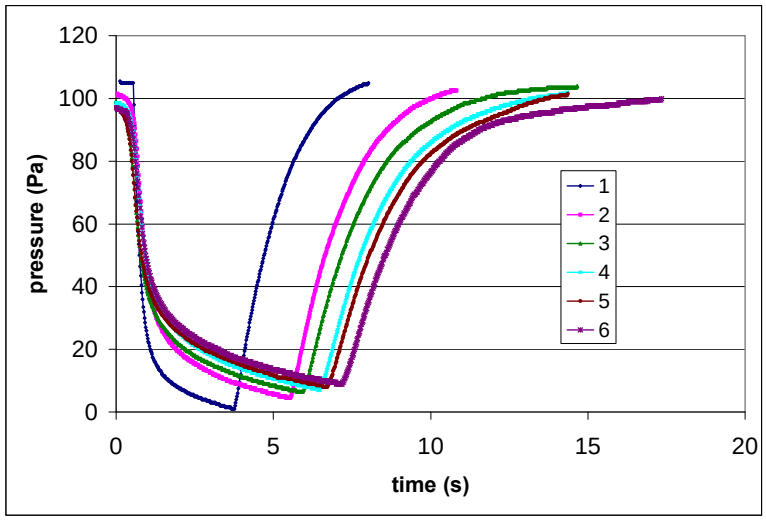

Figure 8.4-7 The negative peaks for successive bubbles for the cell with a slot angle *β* of 85º and a gap of 0.2 mm superimposed upon one another so that their shapes can be compared. The initial pressure drops are all very similar indicating a common cause. After this initial stage the bubbles grow progressively slower. The post-snap off pressure recoveries are all very similar and do not depend upon the rate at which the bubbles were grown.

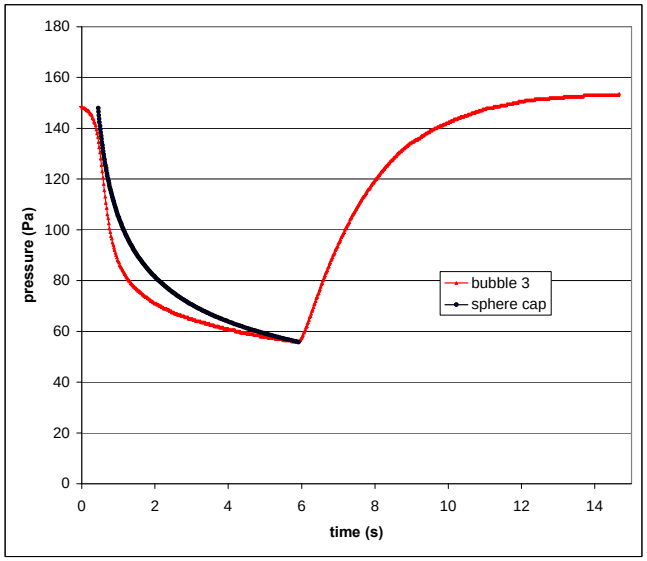

Figure 8.4-8 Comparison of the pressure profile for Bubble 3 (Fig. 8.4-5) compared to the profile expected if the bubble was a spherical cap growing at a uniform rate. The match is good but not perfect.

There are two measurements that can be made from the data pressure plot. The snap-off pressure can be determined because it is equal to the pressure difference between the absolute base pressure and the pressure at the snap-off point 'A' (see Figure 8.4-5). Also the pressure of the meniscus in the large tube (ΔP_a) can be determined because it is almost equal to the pressure difference between the absolute base pressure and the uniform pressure that is measured between the formation of bubbles. The reduction in imbibition rate with time is the most probable reason for the slight decrease in this pressure for the later bubbles. From the graph in Figure 8.4-5, the snap-off pressure for a bubble near the end, and hence growing the slowest, is around 57 Pa. Also the uniform pressure for the meniscus in the large tube is about 150 Pa for the later bubbles. If it is

assumed that snap-off occurs when the interface in the tube is a cylinder, then the pressure can be estimated from the incylinder that just fits inside the large tube (see Figure 8.4-1). This has the same radius as the incircle. For the 85º, 0.2 mm gap cell (Figure 8.4-5), the incylinder normalized curvature under the condition 'd/R=0.127' is 4.29. Capillary pressure is related to curvature by

$$\Delta P = \sigma C/R \qquad 8.4\text{-}3$$

where ΔP is the capillary pressure, σ is the surface tension, C is the normalized curvature and R is the rod radius. From the incylinder approximation, the capillary pressure is calculated as 92 Pa. The normalized curvature of the meniscus in the larger tube can be calculated from the MS-P theory and its value is 7.37 (Unsal et al, 2007a). The capillary pressure calculated using this value at the actual cell conditions is 157 Pa. This value corresponds almost exactly with the measured value of about 150 Pa. However, the measured snap-off pressure is only 57 Pa which is significantly different to that predicted by the incylinder approximation (92 Pa).

Data plots during countercurrent flow for the other cells are shown in Figures 8.4-9-15.

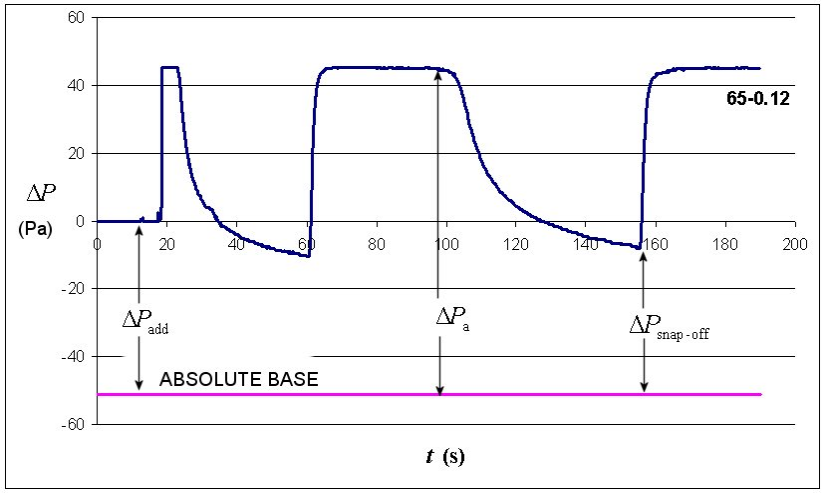

Figure 8.4-9 Pressure (Δ*P*) recordings in the cell during counter-current flow with a slot angle β of 65ºand a gap of 0.12mm. Negative peaks indicate bubble formation.

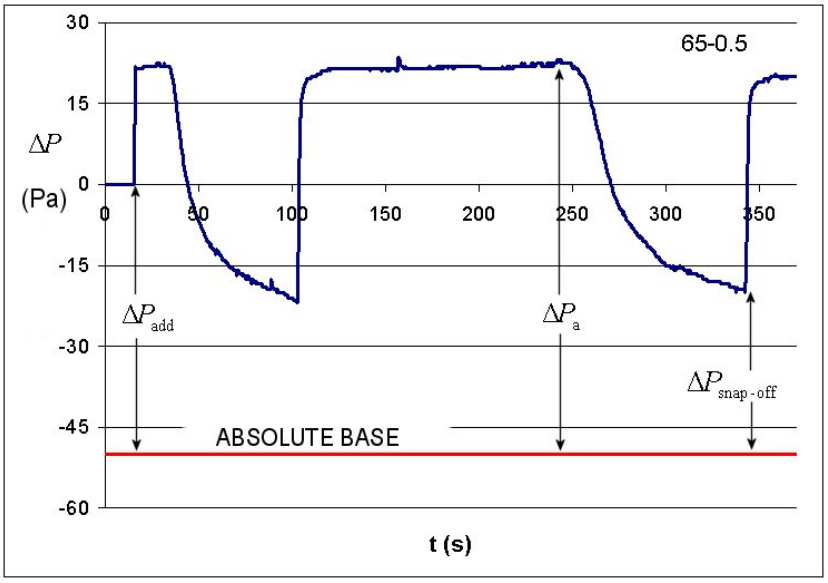

Figure 8.4-10 Pressure (Δ*P*) recordings in the cell during counter-current flow with a slot angle β of 65º and with a gap of 0.5mm. Negative peaks indicate bubble formation. Once the snap-off is completed, the air pressure increases back up to the initial value and stays almost constant until the next bubble starts to form. Note that the recovery of the pressure after snap-off is quite fast. This is in contrast to the situation when the rod touches the plate. The recovery rate is dominated by the flow areas for the arc menisci which are much greater when the rod is spaced away from the plate.

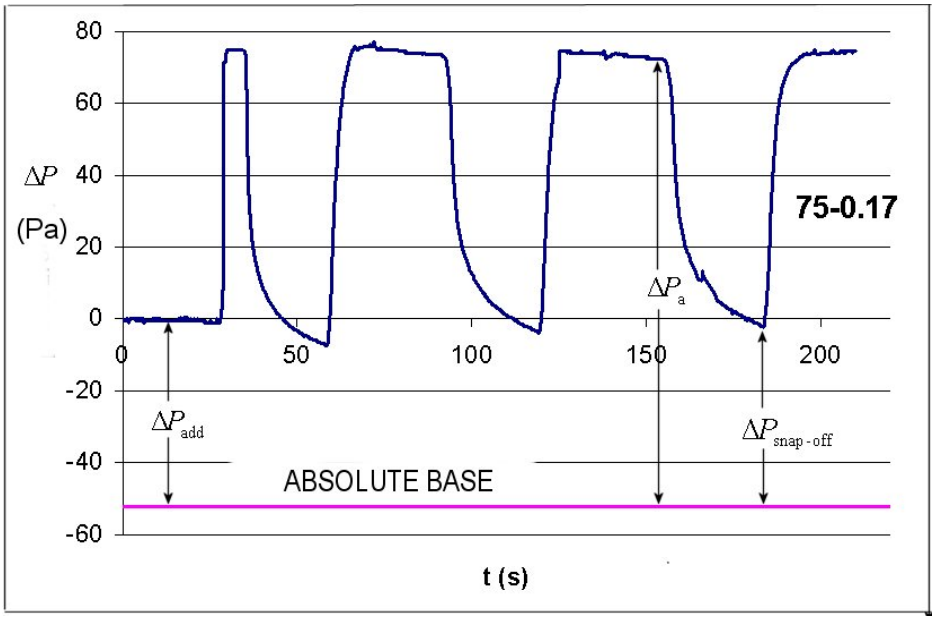

Figure 8.4-11 Pressure (Δ*P*) recordings in the cell during counter-current flow with a slot angle β of 75º, and with a gap of 0.17 mm. Negative peaks indicate bubble formation. Once the snap-off is completed, the air pressure increases back up to the initial value and stays almost constant until the next bubble starts to form.

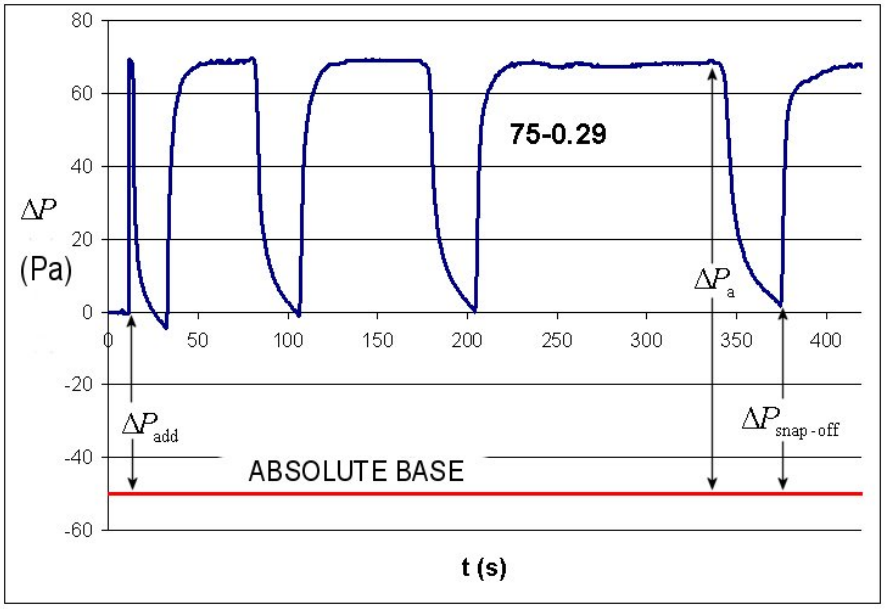

Figure 8.4-12 Pressure (Δ*P*) recordings in the cell during counter-current flow with a slot angle β of 75º and a gap of 0.29 mm.

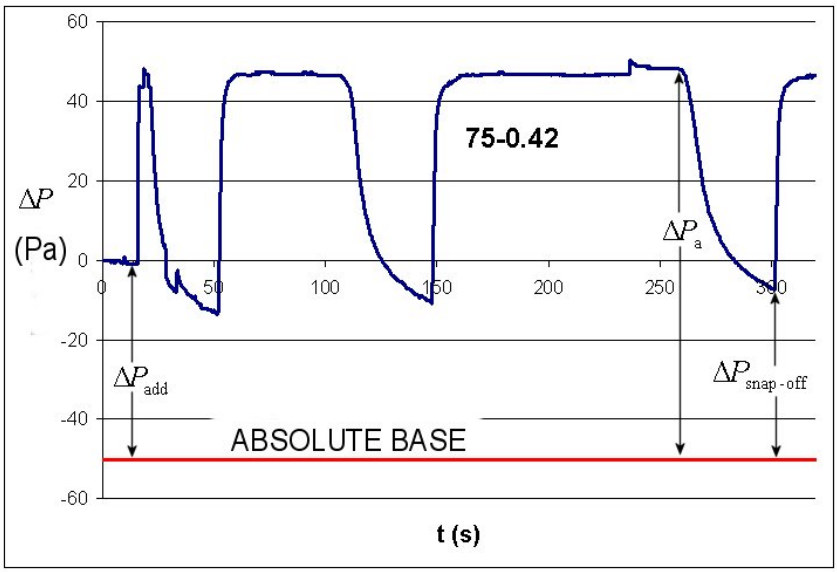

Figure 8.4-13 Pressure (Δ*P*) recordings in the cell during counter-current flow with a slot angle β of 75º and a gap of 0.42 mm. Negative peaks indicate bubble formation.

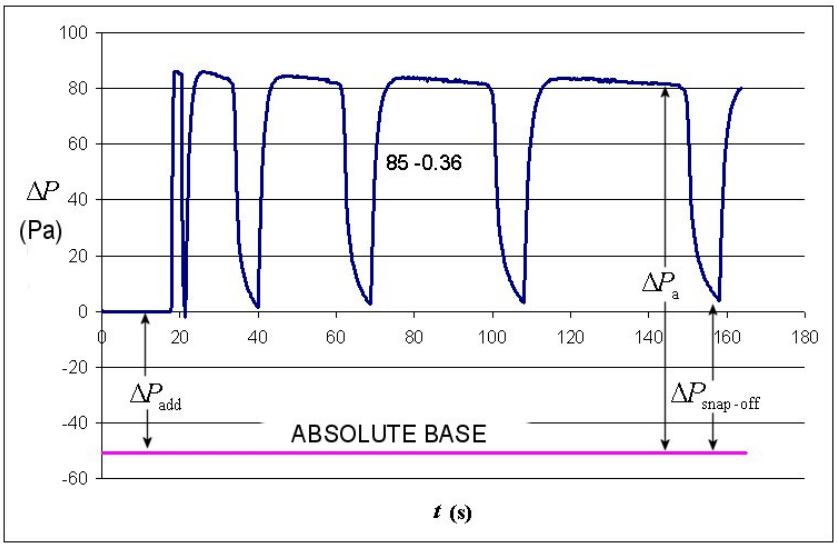

Figure 8.4-14 Pressure (Δ*P*) recordings in the cell during counter-current flow with a slot angle β of 85º and a gap of 0.36 mm. Negative peaks indicate bubble formation.

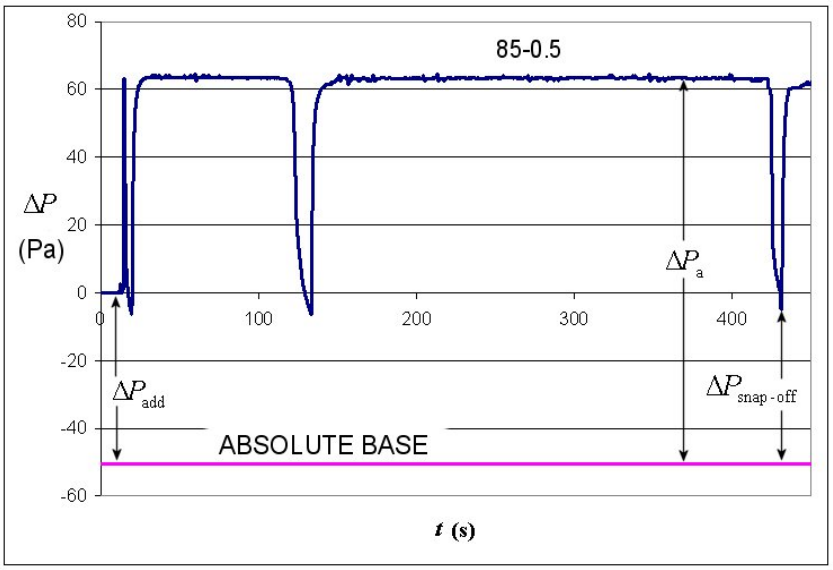

Figure 8.4-15. Pressure (Δ*P*) recordings in the cell during counter-current flow with a slot angle β of 85º and a gap of 0.5 mm. Negative peaks indicate bubble formation. The reason that imbibition is so slow is that the pressure difference between the menisci in the two tubes is small.

In some of these Figures it can be seen that later bubbles seem to snap off at slightly higher pressures. The difference is probably because later bubbles are growing more slowly and consequently can get closer to the instability limit. The snap-off pressure therefore exhibits slight rate-dependency under dynamic conditions.

Pressure recordings for the same cell angles but with the rod touching the plate are given in Unsal et al, 2007a. Results for cells with and without the rod touching the plate are included in the following discussion.

Discussion

The radius of the incylinder in a non-circular tube is the same as the radius of the incircle and the insphere. The insphere was used by Haines (1930) as an approximation to the shape of the interface spanning a non-circular tubes. Before the discovery of the MS-P method the Haines insphere was the simplest approximation for calculating capillary rise in non-circular tubes. For three touching cylinders, the Haines (1930) approximation gives a normalized curvature of 12.7 and the MS-P method gives 11.32 (Princen 1969b). The incylinder has a curvature exactly half of that of the insphere which is 6.35. The equivalent incircle and MS-P curvatures can be calculated for the tubes in the slot experiment and have been given graphically in Unsal et al 2007a. They have been recalculated specifically for the large tubes in the cells used in these experiments and the relations between the MS-P curvature and the insphere is shown in Fig 8.4-16. They are theoretical results. They all fall on a reasonably straight line through the origin with a gradient of 0.578. For the three touching rods the gradient would be 6.35/11.32 which the gradient of (0.561) is similar.

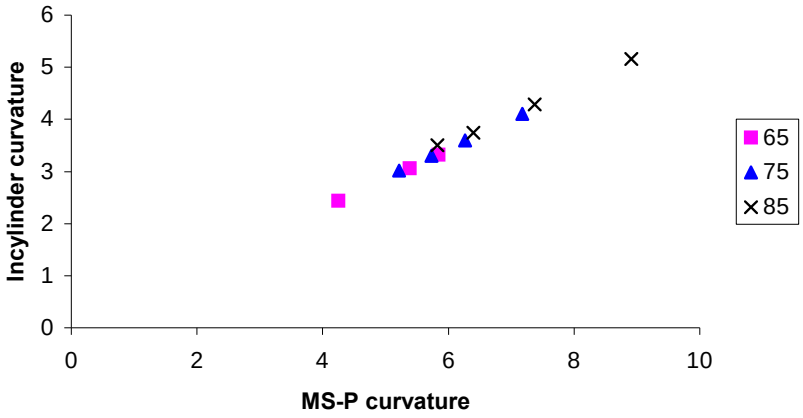

Figure 8.4-16 The curvature of the incylinder plotted against the MS-P curvature for the large tubes in the experimental cells. The points all fall on a straight line indicating an approximately linear relationship between the incylinder curvature and the MS-P curvature.

The meniscus curvature just before the bubble emerges from the large tube can be determined from the pressure-time records in Figs 8.45 and 8.4-9 to 15. Ideally these measured curvatures should be related to the interface curvature in the large tube calculated using the MS-P method. The results comparing the two values are given on Fig. 8.4-17 together with the 45 degree line. It can be seen that the relation is close but not quite perfect with most of the measured values being slightly lower than the predicted values. Although every effort was made to construct the cells accurately, there were likely small errors in manufacture which were difficult to detect. Indeed the measurement of the meniscus curvature is probably one of the best indicators of mechanical accuracy.

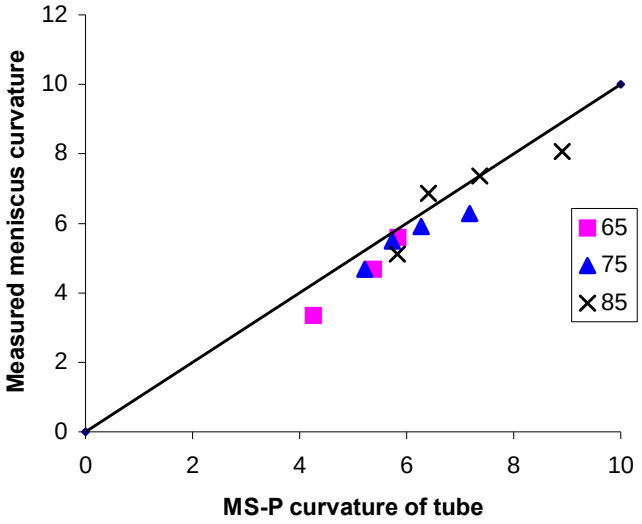

Figure 8.4-17 The measured meniscus curvature in the large tubes compared to the values predicted by the MS-P theory. The values are reasonably close. Points would be above the line if the rod was not bedded perfectly into the bottom of the slot. Points below the line might be caused by variation in the interfacial tension.

Figure 8.4-18 shows the experimental snap-off curvature plotted against the theoretical incylinder curvature. Allowing for the experimental scatter, the results fall on a straight line through the origin indicating that the snap-off curvature does depends linearly on the incylinder curvature. However, the gradient is about 0.66, meaning that snap-off occurs at a significantly lower curvature than the curvature of the incylinder.

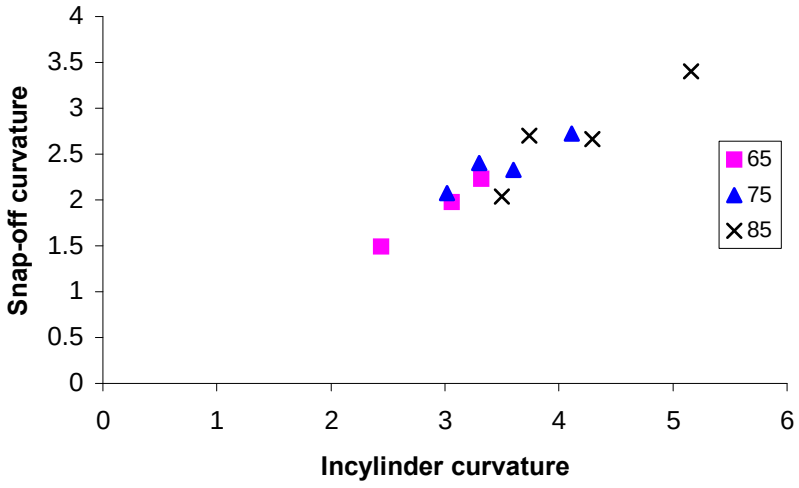

Figure 8.4-18 Snap-off curvature plotted against the incylinder curvature. It is commonly assumed in network modeling that snap off occurs at the incylinder curvature but these experiments show that snap off occurs at about 0.66 of the incylinder curvature.

Figure 8.4-14 showed that the incylinder curvature is related to the MS-P curvature for the tube, and so we would expect the snap-off curvature to be linearly related to the measured tube interface curvature. Fig 8.4-19 shows that this is so. Overall, the points are a slightly better fit to a straight line than those in Figs 8.4-17 and 18. This is probably because any mechanical errors and any small differences in surface tension are partially compensated. If, for example, the gap between the rod and the plate is different to that intended, then this will make little difference on Fig. 8.4-19 because both curvatures will move together keeping the point on the line. Similarly, if there were a variation interfacial tension, it would also affect both curvatures together and the data would still be on the same line. The gradient of the straight line through the origin which best fits the data in Fig 8.4-19 has a gradient of 0.41.

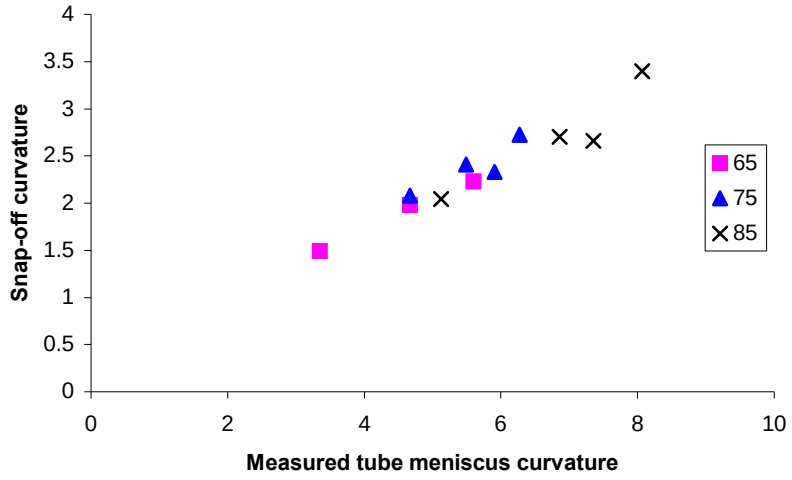

Figure 8.4-19 The measured snap off curvature plotted against the measured meniscus curvature for the larger tubes. The results are again linear showing that the snap off curvature is about 41% of the curvature of the meniscus in the tube.

The experimental results presented here indicate that snap-off in a uniform tube does not happen at a curvature corresponding to the incylinder but at a significantly lower value of about two thirds of the incylinder curvature. This makes the ratio of the bubble size to the orifice size (as measured by capillary pressure) about 2.5. The stability requirement for the bubble and its attached arc menisci in the tube depends on two factors. Firstly, the curvature has to drop to at least that of the incylinder. Secondly, the length of the cylindrical meniscus has to be at least π times its diameter. Because the bubble is stabilized by the presence of the tube it seems that interfaces with even lower curvatures are stable. The idea of snap off due to capillary instability has been applied in recent years to methods of producing uniform microemulsions from precisely etched channels (Sugiura et al., 2001). The geometry of the channel is designed so that the snap off occurs suddenly. This is usually done by forcing the drop into a slit where it forms a disc-like meniscus that grows until it escapes into the free volume at the end of the slit. The disc collapses as the droplet is formed and snaps off (Sugiura et al., 2002). However, simpler geometries such as slits and tubes have been used (Kobayashi et al., 2005a) with the basic idea of facilitating the flow of continuous phase into the region of snap off. These geometries give droplets with a diameter between 3.2 and 3.7 times the slit width. Computer simulations of droplet formation (Kobayashi et al., 2005b) shows behavior very similar to that reported here. They simulated drop formation from

an elliptical cross-section tube and the simulated pressure required to move the interface in the tube was about 2.5 times the pressure at snap off. This value is almost identical to that obtained from the reciprocal of the gradient in Fig. 8.4-19 where pressure scales as curvature. In a careful comparison of the sizes of drops produced by Shirasu porous glass (SPG), porous aluminum oxide, and microchannel devices with the pore size (as measured by capillary pressure), Vladisavljević et al (2005) found ratios of 3.5 for SPG and 2.7 for the microchannel devices. In all of these devices the key is to find a way for the snap off to be largely independent of the fluid viscosity. This means having as short a distance and as large an area between the bulk continuous phase and the snap-off region as possible. The problem is complicated because the snap off region is inside a confining geometry. Arc menisci in the corners (Gauglitz et al., 1987) of angular tubes will suffice but it may be that the unusual pore network of SPG glass is more suited to allowing flow into the snap off region from adjacent pores. The Everett-Haynes (1972) analysis of snap off in a cylindrical indicated that the snap-off curvature, normalized with respect to tube radius, was about 1.4. Tsakiroglou & Payatakes (1990) obtained a similar value for perfectly wetting liquids and the figure was confirmed by Gauglitz & Radke (1988) who reported 1.43 and gave the normalized neck radius of the unduloid at snap off as 0.4. Although the geometry is different because bubbles in these cases are trapped inside the tube rather than being free to slowly expand, the snap off curvature can be approximately related to the free-bubble situation. If we consider the tube to have an undulating profile with the shape of the unstable unduloid, then the normalized curvature of a hemispherical meniscus just passing through the waist is 2/0.4=5.0. The overall normalized curvature of the unstable unduloid is 1.43, giving a ratio of 5/1.43=3.5. This gives the upper limit of the pressure from the meniscus in the tube to the snap-off pressure. The lower limit for the uniform cylindrical tube is 2/1.43. Tsai & Miksis (1994) carried out numerical simulations of bubbles moving in constricted tubes and one of their examples shows a ratio of about 3. Many of the values that have been measured for capillary snap off fall between 1.4 and 3.5 and the general factor of 2.5 determined by these experiments is with this range.

Summary and Conclusions

The snap off pressure of bubbles emerging from a non-axisymmetic uniform tubes has been measured and compared to theoretical predictions. The snap off is caused by capillary instability of an almost-cylindrical meniscus in the tube. It was observed that snap off occurred at about 66% of the curvature of a theoretical cylindrical meniscus in the non-axisymmetric tubes. There was little dependence on the shape of the tube, or whether it was open in one part of the perimeter or not. Similarly, snap off occurred at about 41% of the curvature of a meniscus in the non-axisymmetric tube, again with little dependence on tube shape, indicating a bubble size about 2.5 times the pore size.

Acknowledgements

The authors acknowledge support from the UK Engineering and Physical Sciences Research Council and also from ARAMCO, British Petroleum, ChevronTexaco, Total, ConocoPhillips, StatoilHydro, Shell, the Enhanced Oil Recovery Institute at the University of Wyoming, the National Petroleum Technology Office of the US Department of Energy, and the Natural Science and Engineering Research Council of Canada.

8.5 An Analytical Modeal of Imbibition that includes Prediction of the Shape of the Production Curve

Counter-current imbibition occurs when brine spontaneously displaces oil from a very strongly water-wet rock. Experiments are usually carried out on cylindrical core plugs which have all of their faces open, mainly because this is easiest to do and also because it appears to give the most reproducible results. The flow patterns are complex, but a reasonable approximation can be obtained by assuming piston-like advance of fronts from the radial outer face and both flat ends. This separates the flow pattern into linear imbibition into cones and into radial imbibition into the surrounding toroid ring. Production versus time curves have been calculated for cylinders of varying aspect ratio and other core shapes. The analytical results confirm the experimental observation that sample shape does not have much effect on the shape of the production versus time curves. Bearing in mind the inherent variability of experimental results for individual core samples, the differences would be difficult to detect in experiments. The time for imbibition to be completed scales as the characteristic length. The function given by Ma et al. (1997) requires only a small correction factor for agreement with the analytical result. The present analysis makes straightforward the comparison of results from the complex flow condition of all-faces-open imbibition with results from linear and radial experiments. A comparison is made with published results.

Introduction

Imbibition occurs when the resident fluid in a porous medium (which will be referred to as the non-wetting phase) is spontaneously displaced by a more wetting fluid. When the wetting fluid imbibes into the pores, a saturation front can sometimes be seen. The driving pressure is the capillary pressure produced by interfaces in the pore space. In experiments (Li et al., 2006), a positive pressure can be detected in the non-wetting phase. This pressure pushes the non-wetting phase back through the invading wetting phase and overcomes the capillary pressure generated by interfaces at the open face. This process, referred to as counter-current imbibition, is one mechanism by which oil is displaced from the rock in fractured reservoirs (Morrow & Mason, 2001). The mass balance requirement for counter-current imbibition means that the net volumetric flows of the two fluids are equal but in opposite directions.

Counter-current imbibition in reservoir rocks is usually studied at the core level using cylindrical cores about 75mm in length and about 37mm in diameter. In fundamental studies of displacement mechanisms, the initial condition is often of complete saturation with oil. In tests of more practical interest, cores usually contain a low initial water saturation with the remaining pore space filled with oil. The core is immersed in brine and the volume of expelled oil is measured. Results are recorded as cumulative oil production versus time. In practice, experiments are easier to conduct if the core has all faces of the cylinder open to the invading phase. However, even under the ideal condition of a homogeneous porous media, this gives complex flow patterns which are awkward to model. In order to compare experimental results for the effect of changing interfacial tension (σ), fluid viscosities (μ_w and μ_{nw}), sample shape, rock porosity (φ), permeability (K) and the size, shape and boundary conditions, various scaling groups have been proposed. Ma *et al* (1997) incorporated most of these factors into a dimensionless time t_D as in Eq. 8.5-1.

$$t_{\mathrm{D}} = \frac{1}{L_{\mathrm{c}}^2}\sqrt{\frac{K}{\varphi}}\frac{\sigma}{\sqrt{\mu_{\mathrm{w}}\mu_{\mathrm{nw}}}}t \qquad 8.5\text{-}1$$

Size, shape, and boundary conditions are included as the characteristic length L_c:

$$L_{\mathrm{c}} = \sqrt{V_{\mathrm{total}} \Big/ \sum_{i-1}^{i=n} \frac{A_i}{x_i}} \qquad 8.5\text{-}2$$

where V_{total} is the total volume, A_i is the area open to imbibition in the *i*th direction, x_i is the distance travelled by the imbibition front from the open surface to the no-flow boundary and *n* is the total number of surfaces open to imbibition. The correlation appears to work quite well (Yildiz et al., 2006). For a cylinder open on all faces this equation gives (Zhang et al. 1996)

$$L_{\mathrm{c}} = \frac{L_{\mathrm{core}}d}{2\sqrt{d^2 + 2L_{\mathrm{core}}^2}} \qquad 8.5\text{-}3$$

where L_{core} is the core length and *d* is the core diameter. The correlation simply brings the production data on a $\log_{10} t$ scale together by moving the curves left and right. It does not change their shape and so does not allow cores of different geometry to have different shaped production-time curves.

The standard analysis of the flow of two phases through a porous material requires three functions: capillary pressure and the relative permeabilities, to the wetting and non-wetting phases. All are solely functions of saturation. In addition, for perfect counter-current imbibition, the flow of one phase is exactly equalled by the reverse flow of the other phase.

Direct observation indicates that one-dimensional counter-current imbibition, particularly for cores with no initial water saturation, can be primarily a frontal process (Li et al., 2006) and so, as a limiting case, we could imagine that ALL of the saturation change takes place at the saturation front where there is a step change in saturation from S_{wi} (the initial wetting phase saturation) to S_{wf} (the wetting phase saturation behind the front). The assumption makes imbibition piston-like and means that, behind the front, the relative permeabilities of each of the two phases are constant. Also, behind the front at one instant in time, the flow of wetting phase (q_w) is invariant with distance from the open face and consequently the flow of non-wetting phase (q_{nw}) is similarly invariant but in the opposite direction. Darcy's law gives the two flows:

$$q_{\mathrm{w}} = -\frac{Kk_{\mathrm{rw}}A}{\mu_{\mathrm{w}}}\frac{\partial P_{\mathrm{w}}}{\partial x} \qquad 8.5\text{-}4$$

$$q_{\mathrm{nw}} = -\frac{Kk_{\mathrm{rnw}}A}{\mu_{\mathrm{nw}}}\frac{\partial P_{\mathrm{nw}}}{\partial x} \qquad 8.5\text{-}5$$

where K is the permeability, k_{rw} and k_{mw} are the relative permeabilities to the respective phases, μ_w and μ_{nw} are the respective viscosities, A is the area and x is a distance. The capillary pressure P_c is the difference between the pressure in the non-wetting phase (P_{nw}) and the pressure in the wetting phase (P_w).

$$P_{\mathrm{c}} = P_{\mathrm{nw}} - P_{\mathrm{w}} \qquad 8.5\text{-}6$$

Perfect counter-current flow implies:

$$q_{\mathrm{w}} = -q_{\mathrm{nw}} \qquad 8.5\text{-}7$$

Combining Eq. 8.5-4 to Eq. 8.5-7 gives:

$$q_{\mathrm{w}} = \frac{Kk_{\mathrm{rw}}k_{\mathrm{rnw}}A}{\mu_{\mathrm{w}}k_{\mathrm{rnw}} + \mu_{\mathrm{nw}}k_{\mathrm{rw}}}\frac{\partial P_{\mathrm{c}}}{\partial x} \qquad 8.5\text{-}8$$

Because behind the front the saturation has been assumed to be constant, q_w will not vary between the open face and the front. Let M be a mobility factor and let

$$M = \frac{k_{\mathrm{rw}}k_{\mathrm{rnw}}}{\mu_{\mathrm{w}}k_{\mathrm{rnw}} + \mu_{\mathrm{nw}}k_{\mathrm{rw}}} \qquad 8.5\text{-}9$$

For constant saturation, the factor M will be constant and so Eq. 8.5-8 can be integrated between the open face and the front to give

$$q_{\mathrm{w}}\int_0^{x_{\mathrm{f}}}\frac{\mathrm{d}\,x}{A} = KM\left(P_{\mathrm{cf}} - P_{\mathrm{co}}\right) \qquad 8.5\text{-}10$$

Where P_{cf} is the effective capillary pressure at the imbibition front, and P_{co} is the effective capillary pressure at the open face. At the open face the pressure in the wetting phase is zero but the pressure in the non-wetting phase is not zero because the non-wetting phase forms bubbles as it exits the rock.

For cylindrical tubes, the capillary pressure is related to permeability by the Leverett (1941) relation:

$$P_c = \sigma\sqrt{\frac{\varphi}{2K}} \qquad 8.5\text{-}11$$

Eq. 8.5-10 contains a difference in capillary pressures, P_{cf} - P_{co}. The capillary pressure at the front, $P_{cf,}$ is mainly produced by the smaller pores and the capillary pressure at the open face, $P_{co,}$ is mainly produced by the larger pores. The difference between them is thus related to the spread of the pore size distribution of the rock. For a spread of pore sizes, P_{cf} - P_{co} , can be related to the mean capillary pressure, P_c, by a factor C_{spread} which is in some way determined by the breadth and shape of the pore size distribution. For narrow pore size distributions, C_{spread} will be small and for wide pore size distributions C_{spread} will be large. We thus obtain

$$P_{cf} - P_{co} = C_{spread}\sigma\sqrt{\frac{\varphi}{2K}} \qquad 8.5\text{-}12$$

Eliminating P_{cf} - P_{co} from Eq. 8.5-10 gives

$$q_w \int_0^{x_f} \frac{dx}{A} = KMC_{spread}\sigma\sqrt{\frac{\varphi}{2K}} \qquad 8.5\text{-}13$$

The flow of wetting phase arriving at the front advances the position of the front and the local mass balance gives:

$$\frac{dx_f}{dt} = \frac{q_w}{\varphi A_f (S_{wf} - S_{wi})} \qquad 8.5\text{-}14$$

Where x_f is the distance of the front from the open face and A_f is the area of the front.

Eliminating q_w between Eq. 8.5-13 and Eq. 8.5-14 gives

$$\int_0^{x_f}\left(\int_0^{x_f}\frac{dx}{A}\right)A_f\,dx_f = \sqrt{\frac{K}{2\varphi}}\frac{MC_{spread}\sigma}{(S_{wf} - S_{wi})}t \qquad 8.5\text{-}15$$

This is the fundamental equation used in the subsequent analysis.

Practical situations

Linear imbibition

For linear imbibition into a cylindrical core open at one end, the cross-sectional area is everywhere constant, making A equal A_f. Hence integration of Eq. 8.15.gives

$$x_{\mathrm{f}}^2 = \sqrt{\frac{2K}{\varphi}} \frac{MC_{\mathrm{spread}}\sigma}{\left(S_{\mathrm{wf}} - S_{\mathrm{wi}}\right)} t \qquad 8.5\text{-}16$$

showing that the distance that the front advances is proportional to $\sqrt{time}$, a well-known result for the situation in the absence of gravity before a dispersed front has reached the end of a core (Washburn, 1921; Reis & Cil, 1993; Li et al., 2003; Tavassoli et al., 2005). The time, t_{end}, taken for the front to reach the end of the core at distance L_{max} is

$$t_{\mathrm{end}} = L_{\mathrm{max}}^2 \sqrt{\frac{\varphi}{2K}} \frac{\left(S_{\mathrm{wf}} - S_{\mathrm{wi}}\right)}{MC_{\mathrm{spread}}\sigma} \qquad 8.5\text{-}17$$

Eq. 8.5-17 gives the characteristic length for linear imbibition as L_{max}, which agrees exactly with the characteristic length predicted by Eq. 8.5-2.

Radial imbibition

For radial flow into a cylinder with capped ends, the area A will vary with the distance that the front has penetrated and so the function for the amount of imbibition *vs* time will be different from linear imbibition. Let the core length be L_{core} and its radius R_{max}, and let the front penetrate to a distance x_f at time t. At distance x into the core the area is. Eq. 8.5-15 can $2\pi\left(R_{\mathrm{max}} - x\right)L_{\mathrm{core}}$ be integrated to give

$$R_{\mathrm{max}}^2 + 2R_{\mathrm{f}}^2 \ln\frac{R_{\mathrm{f}}}{R_{\mathrm{max}}} - R_{\mathrm{f}}^2 = 2\sqrt{\frac{2K}{\varphi}} \frac{MC_{\mathrm{spread}}\sigma}{\left(S_{\mathrm{wf}} - S_{\mathrm{wi}}\right)} t \qquad 8.5\text{-}18$$

From geometry, the fraction of the total imbibition when the front is at R_f is

$$f = 1 - \left(\frac{R_{\mathrm{f}}}{R_{\mathrm{max}}}\right)^2 \qquad 8.5\text{-}19$$

The time taken for the front to reach the centre of the core (the no-flow boundary) when imbibitions stops, t_{end}, is

$$t_{\mathrm{end}} = \frac{R_{\mathrm{max}}^2}{2} \sqrt{\frac{\phi}{2K}} \frac{\left(S_{\mathrm{wf}} - S_{\mathrm{wi}}\right)}{MC_{\mathrm{spread}}\sigma} \qquad 8.5\text{-}20$$

For radial imbibition the characteristic length is thus $R_{\mathrm{max}} / \sqrt{2}$ and this also agrees exactly with the characteristic length predicted by Eq. 8.5-2.

Spherical imbibition

For radial imbibition into a spherical core, radius R_{sphere}, the area at distance x into the core is $4\pi\left(R_{\mathrm{max}} - x\right)^2$ and integration of Eq. 8.5-15 gives:

$$R_{\text{sphere}}^2 - 3R_{\text{f}}^2 + 2\frac{R_{\text{f}}^3}{R_{\text{sphere}}} = 3\sqrt{\frac{2K}{\varphi}}\frac{MC_{\text{spread}}\sigma}{(S_{\text{wf}} - S_{\text{wi}})}t \qquad 8.5\text{-}21$$

when the front R_f is at (i.e. R_{max} - x) at time t. The fraction f of total imbibition when the front is at R_f is

$$f = 1 - \left(\frac{R_{\text{f}}}{R_{\text{sphere}}}\right)^3 \qquad 8.5\text{-}22$$

The time for the front to reach the centre of the sphere is

$$t_{\text{end}} = \frac{R_{\text{sphere}}^2}{3}\sqrt{\frac{\phi}{2K}}\frac{(S_{\text{wf}} - S_{\text{wi}})}{MC_{\text{spread}}\sigma} \qquad 8.5\text{-}23$$

For imbibition into a sphere the characteristic length is $R_{sphere}/\sqrt{3}$ and this agrees exactly with the characteristic length predicted by Eq. 8.5-2. It is also the same as predicted by Eq. 8.5-3 when the core has the same diameter as its length. Thus compared to a cylinder sealed on all faces but one end, a sphere fills three times faster, provided the maximum distance the front has to travel is the same.

The functional forms of the production *vs* time functions for linear, radial and spherical imbibition are quite different but, on the conventional *log_{10} time* scale, they are only slightly different (see Fig. 8.5-1). They can be compared in several ways. The first (Fig. 8.5-1) is without the adjustment for characteristic length.

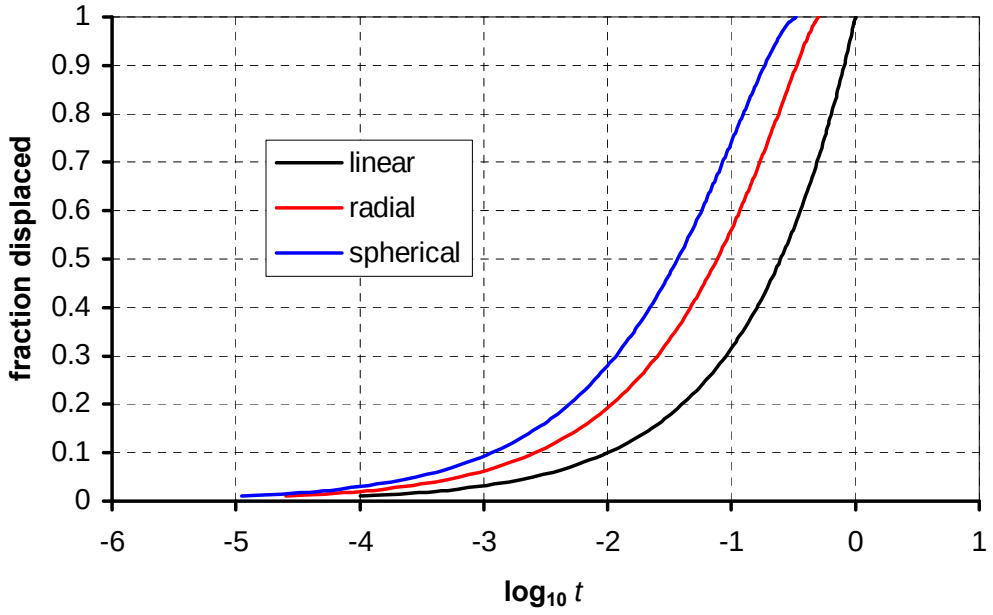

Figure 8.5-1. The fraction imbibed versus $\log_{10} t$ for linear, radial and spherical imbibition. The factor $\sqrt{\frac{2K}{\varphi}}\frac{MC_{\text{spread}}\sigma}{(S_{\text{wf}}-S_{\text{wi}})}$ has been set at 1. No adjustment for the different characteristic lengths has been made. The core length (for one end open) and radius (for radial and spherical) are also unity so that the distance the front has to travel is the same for all geometries. The sequence of shapes is similar to that given by Zimmerman et al. (1990).

If the characteristic length is incorporated, then the shape differences of the imbibition curves are more apparent (Fig. 8.5-2).

The log $_{10}$ time axis is useful because a constant factor only moves the curve left or right. It does not change its shape. However, the differences between the curves are better shown on a $\sqrt{t}$ plot on which the linear imbibition becomes a straight line (Fig. 8.5-3).

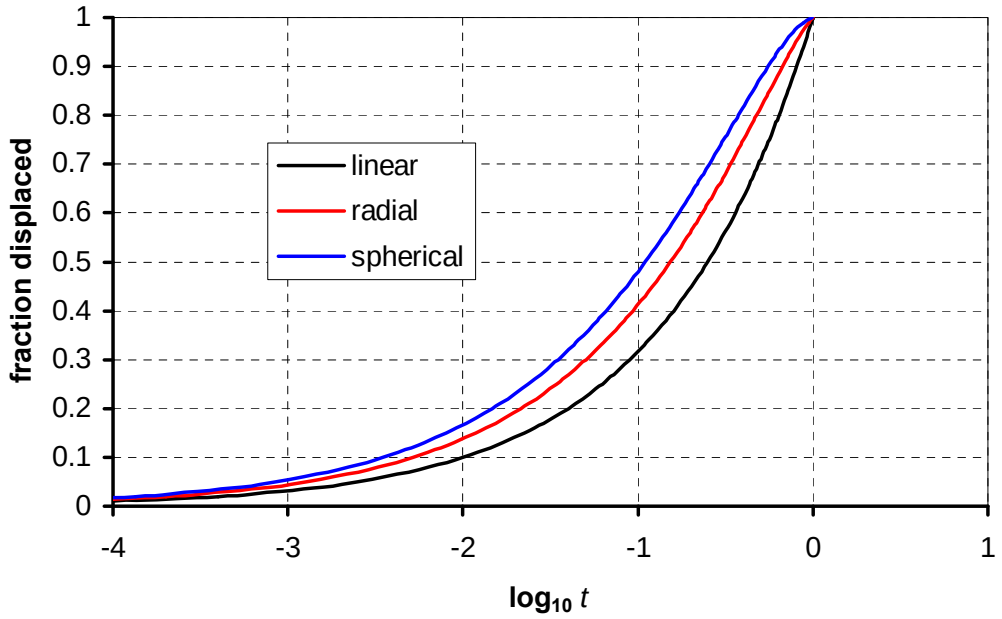

Figure 8.5-2 Imbibition curves after the characteristic length factor has been incorporated. This makes the time at which imbibition is complete the same and illustrates the similarity in shape between all of the curves. As expected the sphere imbibes fastest on average but slows most at the end.

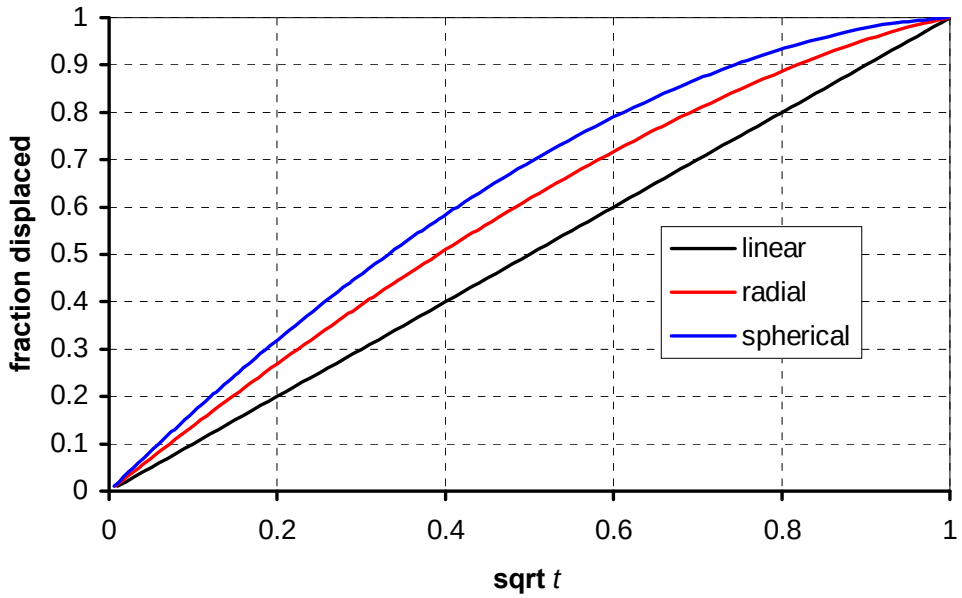

Figure 8.5-3 The imbibition curves of Fig. 8.5-2 plotted against $\sqrt{t}$. This plot enhances the differences in shape.

Conical imbibition

Frontal imbibition into a cylindrical core with all faces open can be modelled by considering the likely position of the no-flow boundary with respect to linear flow from each end and radial imbibition from the cylindrical surface. For each end, imbibition can be modelled by flow into a cone with the front advancing from the open end with the tapering conical face sealed. From the cylindrical outer face there will be radial imbibition into the remains of the cylinder (termed a toroid ring). If the core is long enough then the conical region swept by imbibition will be a full cone. However, if the half length of the core is less than the core radius then the conical imbibition region will reach the center plane of the core (and its mirror image at the other end) before the full cone is developed. This means that the imbibition from the cylindical surface will not reach the axis of the core before the core axis is enveloped by imbibition from the ends. The imbibition fronts define two cases; a long toroid ring with complete cones, and a short toroid ring that contains truncated cones (see Fig. 8.5-4).

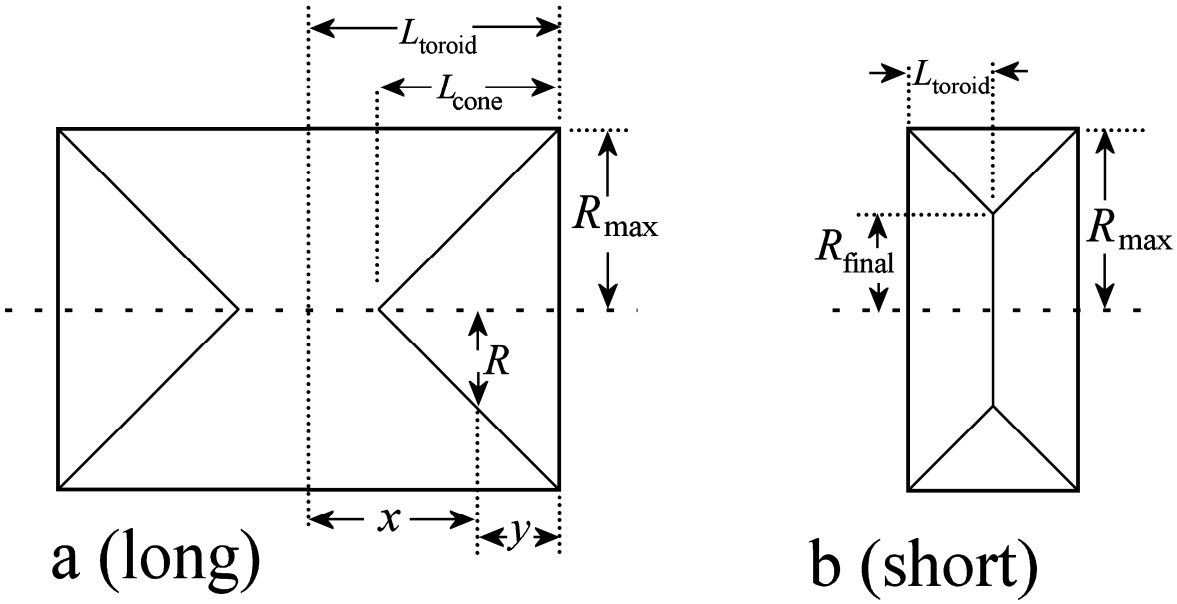

Figure 8.5-4 Diagram showing a section through a long (a) and short (b) core. The core is considered to have two imbibition regimes. The first is linear into a cone at each end, and the second is radial into the residual outer toroid. For a long core, the cones are completely filled just as the radial flow reaches the center axis. For the short core they are truncated because the fronts in each cone meet before the radial imbibition front reaches the core axis. The angle of the cone is determined by the requirement that the time taken for complete imbibition in the two regimes is the same.

The complete cone has an open base, radius, R_{max}, and the conical face is sealed. Its length is L_{cone}. At some distance y in from the base (see Fig. 8.5-4a), a section through the cone is a circle of radius R and area πR^2. Integration of Eq. 8.5-15 with y in place of x gives

$$\left(\frac{L_f}{L_{cone}}\right)^2 - \frac{2}{3}\left(\frac{L_f}{L_{cone}}\right)^3 = \frac{1}{L_{cone}^2}\sqrt{\frac{2K}{\varphi}}\frac{MC_{spread}\sigma}{(S_{wf} - S_{wi})}t \qquad 8.5\text{-}23$$

when the position of the front is at a distance L_f from the open face at time t. The fraction f of total imbibition when the front is at L_f is the ratio of the volume of the cone truncated at a length L_f divided by the volume of the complete cone:

$$f = 1 - \left(1 - \frac{L_f}{L_{cone}}\right)^3 \qquad 8.5\text{-}24$$

The time for the front to reach the end of the cone is

$$t_{\text{end}} = \frac{L_{\text{cone}}^2}{3}\sqrt{\frac{\phi}{2K}}\frac{(S_{\text{wf}} - S_{\text{wi}})}{MC_{\text{spread}}\sigma} \qquad 8.5\text{-}25$$

Numerically therefore, imbibition into a cone is very similar to imbibition into a sphere. The characteristic length for a cone is $L_{\text{cone}}/\sqrt{3}$ which also agrees with the prediction of Eq. 8.5-2. Interestingly, and usefully because it simplifies later equations, it is independent of the angle of the cone.

Imbibition into a long toroid

For one half-length of the cylindrical core, the toroid ring is the space around the outside of the complete cone. The toroid has its outer cylindrical face open and the conical face sealed. The remaining circular face at half-length is also sealed, making this like one half of an all-faces-open core. Let the toroid have a length L_{toroid} (which is half of the cylinder length) and a radius R_{max}.

From the curved outer face of the cylinder there is radial imbibition into a space of decreasing area (because the boundary of the cone is sealed). From Fig. 8.5-4a the distance from the half-length of the core to a point on the cone at radius R is given by:

$$x = L_{\text{toroid}} - L_{\text{cone}} + \frac{L_{\text{cone}}}{R_{\max}}R \qquad 8.5\text{-}26$$

To simplify let $a = L_{\text{toroid}} - L_{\text{cone}}$ and $b = L_{\text{cone}}/R_{\max}$. The analysis follows the same pattern as before. For the toroid ring, at some general radius, R, the area, A_R, through which the flow q_{w}^{R} is passing is the area of the cylinder of length x

$$A_{\text{R}} = 2\pi Rx = 2\pi R(a + bR) \qquad 8.5\text{-}27$$

Integration of Eq. 8.5-15 using this expression gives

$$\left[\left[\frac{1}{2}R_{\text{f}}^2 + \frac{1}{3}\frac{bR_{\text{f}}^3}{a}\right]\ln\left[\frac{(a + bR_{\max})}{(a + bR_{\text{f}})}\frac{R_{\text{f}}}{R_{\max}}\right] + \frac{1}{6}\left(\frac{a}{b}\right)^2\left[\ln(a + bR_{\text{f}}) - \frac{bR_{\text{f}}}{a} - \left(\frac{bR_{\text{f}}}{a}\right)^2\right]\right]_{R_{\max}}^{R_{\text{f}}}$$
$$= \frac{1}{2}\sqrt{\frac{2K}{\varphi}}\frac{MC_{\text{spread}}}{(S_{\text{wf}} - S_{\text{wi}})}t_{\text{f}} \qquad 8.5\text{-}28$$

The time, t_f, is when the front has reached R_f. The time when the axis is reached, t_{end} is:

$$t_{\text{end}} = \frac{R_{\max}^2}{3}\left(\left(\frac{L_{\text{toroid}}}{L_{\text{cone}}}-1\right)^2 \ln\left(1-\frac{L_{\text{cone}}}{L_{\text{toroid}}}\right)+\frac{L_{\text{toroid}}}{L_{\text{cone}}}\right)\sqrt{\frac{\varphi}{2K}}\frac{\left(S_{\text{wf}}-S_{\text{wi}}\right)}{MC_{\text{spread}}\sigma} \qquad 8.5\text{-}29$$

The characteristic length is thus $\frac{R_{\max}}{\sqrt{3}}\sqrt{\left(\frac{L_{\text{toroid}}}{L_{\text{cone}}}-1\right)^2 \ln\left(1-\frac{L_{\text{cone}}}{L_{\text{toroid}}}\right)+\frac{L_{\text{toroid}}}{L_{\text{cone}}}}$. This expression differs from the characteristic length given by Eq. 8.5-2.

Imbibition into a short toroid

If the half-length of the core is less than the radius, then the imbibition front coming into the cones from the opposite ends of the core meet before the radial imbibition reaches the core axis (Fig. 8.5-4b). Thus, when the radial imbibition does not reach the core axis, the region of imbibition from the ends correspond to a truncated cone. The radius where the cone is truncated at the mid-point of the cylinder is R_{final}. The analysis is similar to the long toroid but the integrals have different limits. The basic equation for imbibition into the toroid Eq. 8.5-14 is unchanged and gives

$$\left[\left[\frac{1}{2}R_{\text{f}}^2+\frac{1}{3}\frac{bR_{\text{f}}^3}{a}\right]\ln\left[\frac{\left(a+bR_{\max}\right)}{\left(a+bR_{\text{f}}\right)}\frac{R_{\text{f}}}{R_{\max}}\right]+\frac{1}{6}\left[\left(\frac{a}{b}\right)^2\ln\left(a+bR_{\text{f}}\right)-\frac{a}{b}R_{\text{f}}-{R_{\text{f}}}^2\right]\right]_{R_{\max}}^{R_{\text{final}}} =$$

$$\frac{1}{2}\sqrt{\frac{2K}{\varphi}}\frac{MC_{\text{spread}}\sigma}{\left(S_{\text{wf}}-S_{\text{wi}}\right)}t_{\text{end}} \qquad 8.5\text{-}30$$

Evaluation gives

$$t_{\text{end}} = \left(\frac{1}{3}R_{\text{final}}^2\ln\frac{R_{\text{final}}}{R_{\max}}+\frac{1}{3}R_{\max}^2\left(1-\frac{R_{\text{final}}}{R_{\max}}\right)\right)\sqrt{\frac{\varphi}{2K}}\frac{\left(S_{\text{wf}}-S_{\text{wi}}\right)}{MC_{\text{spread}}\sigma} \qquad 8.5\text{-}31$$

Thus, for the short toroid ring, the characteristic length is $\frac{R_{\text{final}}}{\sqrt{3}}\sqrt{\ln\frac{R_{\text{final}}}{R_{\max}}+\frac{R_{\max}^2}{R_{\text{final}}^2}-\frac{R_{\max}}{R_{\text{final}}}}$, which is not the same as the prediction of Eq. 8.5-2.

Cylindrical imbibition

Imbibition into a core with all faces open can be broken down into two parts. From the flat ends there is a conical imbibition region. From the outer cylindrical surface there is imbibition into the remaining toroid. Imbibition into the cylinder is the sum of imbibition into the external surface of the toroid and into the end of the cone. For a long core, it will take the same time, t_{end}, for the front

in the cone to reach the cone apex as it takes for the front in the toroid ring to reach the core axis. For the short core, the times are the same when the front is at R_{final}.

For the long core, t_{end} for the cone given by Eq. 8.5-11 will be the same as t_{end} for the toroid given by Eq. 8.28. Equating these two imbibition times gives

$$t_{\text{end}} = \frac{R_{\max}^2}{3}\left(\left(\frac{L_{\text{toroid}}}{L_{\text{cone}}}-1\right)^2 \ln\left(1-\frac{L_{\text{cone}}}{L_{\text{toroid}}}\right)+\frac{L_{\text{toroid}}}{L_{\text{cone}}}\right)=\frac{L_{\text{cone}}^2}{3} \qquad 8.5\text{-}32$$

By elimination of t_{end} the resulting equation gives the length of the conical section as a function of the length of the cylinder and its radius. Unfortunately Eq. 8.31 is only explicit for $L_{\text{cone}}/R_{\max}$. However, for a given value of $L_{\text{cone}}/L_{\text{toroid}}$, we can calculate $R_{\max}/L_{\text{cone}}$ using Eq. 8.5-32 and, since we know $L_{\text{cone}}/L_{\text{toroid}}$, we can find the aspect ratio of the core $L_{\text{toroid}}/R_{\max}$. Now, knowing R_{max}, the left hand side of Eq. 8.5-28 can be evaluated and t_f can be found for any given value of R_f using

$$\left[\frac{1}{2}R_{\text{f}}^2+\frac{1}{3}\frac{bR_{\text{f}}^3}{a}\right]\ln\left[\frac{\left(a+bR_{\max}\right)}{\left(a+bR_{\text{f}}\right)}\frac{R_{\text{f}}}{R_{\max}}\right]+\frac{1}{6}\left[\left(\frac{a}{b}\right)^2\ln\left(\frac{a+bR_{\text{f}}}{a+bR_{\max}}\right)-\frac{a}{b}\left(R_{\text{f}}-R_{\max}\right)-\left(R_{\text{f}}^2-R_{\max}^2\right)\right]$$
$$=\frac{1}{2}\sqrt{\frac{2K}{\varphi}}\frac{MC_{\text{spread}}\sigma}{\left(S_{\text{wf}}-S_{\text{wi}}\right)}t_{\text{f}} \qquad 8.5\text{-}33$$

At this value of t_f, the front will have advanced a distance L_f into the cone. The time for this is given by Eq. 8.5-24 and is given by

$$L_{\text{cone}}^2\left(\left(\frac{L_{\text{f}}}{L_{\text{cone}}}\right)^2-\frac{2}{3}\left(\frac{L_{\text{f}}}{L_{\text{cone}}}\right)^3\right)=\sqrt{\frac{2K}{\varphi}}\frac{MC_{\text{spread}}\sigma}{\left(S_{\text{wf}}-S_{\text{wi}}\right)}t_{\text{f}} \qquad 8.5\text{-}34$$

Since t_f and L_{cone} are known, Eq. 8.5-34, a cubic, can be solved to find L_f. All of the dimensions are then known and the fraction of the cylinder invaded by the displacing phase can be found from the sum of the volume imbibed by the toroid and the volume imbibed by the cone

$$f=1-\left(\frac{R_{\text{f}}}{R_{\max}}\right)^2\left(1-\frac{L_{\text{cone}}}{L_{\text{toroid}}}\right)-\frac{L_{\text{cone}}}{L_{\text{toroid}}}\left(\frac{2}{3}\left(\frac{R_{\text{f}}}{R_{\max}}\right)^3+\frac{1}{3}\left(1-\left(\frac{L_{\text{f}}}{L_{\text{cone}}}\right)^3\right)\right) \qquad 8.5\text{-}35$$

For the short core the situation is slightly different. As before, the time for the front to reach R_{final}, its final position at the half-length of the core, will be the same as the time for the front from the flat end to reach the mid-point of the core (L_{toroid}). From Eq. 8.5-24 for the cone, this time is

$$t_{\text{end}} = L_{\text{cone}}^2 \left[\left(\frac{L_{\text{toroid}}}{L_{\text{cone}}} \right)^2 - \frac{2}{3} \left(\frac{L_{\text{toroid}}}{L_{\text{cone}}} \right)^3 \right] \sqrt{\frac{\varphi}{2K}} \frac{\left(S_{\text{wf}} - S_{\text{wi}} \right)}{MC_{\text{spread}}\sigma} \qquad 8.5\text{-}36$$

And changing the limits in Eq. 8.5-28, for the toroid

$$\left[\left[\frac{1}{2} R_{\text{f}}^2 + \frac{1}{3} \frac{bR_{\text{f}}^3}{a} \right] \ln \left[\frac{\left(a + bR_{\text{max}} \right)}{\left(a + bR_{\text{f}} \right)} \frac{R_{\text{f}}}{R_{\text{max}}} \right] + \frac{1}{6} \left[\left(\frac{a}{b} \right)^2 \ln\left(a + bR_{\text{f}} \right) - \frac{a}{b} R_{\text{f}} - {R_{\text{f}}}^2 \right] \right]_{R_{\text{max}}}^{R_{\text{final}}}$$

$$= \frac{1}{2} \sqrt{\frac{2K}{\varphi}} \frac{MC_{\text{spread}}\sigma}{\left(S_{\text{wf}} - S_{\text{wi}} \right)} t_{\text{end}} \qquad 8.5\text{-}37$$

Evaluation gives

$$t_{\text{end}} = \left(\frac{1}{3} R_{\text{final}}^2 \ln \frac{R_{\text{final}}}{R_{\text{max}}} + \frac{1}{3} R_{\text{max}}^2 \left(1 - \frac{R_{\text{final}}}{R_{\text{max}}} \right) \right) \sqrt{\frac{\varphi}{2K}} \frac{\left(S_{\text{wf}} - S_{\text{wi}} \right)}{MC_{\text{spread}}\sigma} \qquad 8.5\text{-}38$$

The characteristic length is thus $\frac{R_{\text{final}}}{\sqrt{3}} \sqrt{\ln \frac{R_{\text{final}}}{R_{\text{max}}} + \frac{R_{\text{max}}^2}{R_{\text{final}}^2} - \frac{R_{\text{max}}}{R_{\text{final}}}}$. If the two values of t_{end} from Eq. 8.5-36 and Eq. 8.5-38 are equal, they can be eliminated. Also, simple geometry gives

$$\frac{L_{\text{toroid}}}{L_{\text{cone}}} = 1 - \frac{R_{\text{final}}}{R_{\text{max}}} \qquad 8.5\text{-}39$$

and so

$$t_{\text{end}} = \frac{1}{3} R_{\text{final}}^2 \ln \frac{R_{\text{final}}}{R_{\text{max}}} + \frac{1}{3} R_{\text{max}}^2 \left(1 - \frac{R_{\text{final}}}{R_{\text{max}}} \right) = L_{\text{toroid}}^2 \left(1 - \frac{2}{3} \left(1 - \frac{R_{\text{final}}}{R_{\text{max}}} \right) \right) \qquad 8.5\text{-}40$$

If we make R_{max} = 1 and take a value for R_{final} (less than 1) then Eq. 8.5-40 is explicit for L_{toroid}. We now know the core aspect ratio, L_{toroid} /R_{max}. Once L_{toroid} is known, the length of the apex of

the cone can be found using Eq. 8.5-39. For any intermediate value of front position R_f, we can now use Eq. 8.5-33 to find the appropriate t_f and the cubic Eq. 8.5-34 to find L_f. As before, the fraction of the core filled with invading phase can be found from Eq. 8.5-35

Comparison of the predictions for all-faces-open

For the special case of a cylindrical core of length equal to its diameter, the equations given above simplify to give behaviour similar to that of a sphere (Eq. 8.5-30). However, if the core is longer or shorter than its diameter then behaviour tends to that of a core with one end open when it is short, and to that of a core with both ends closed as the length of the cylinder increases.

Shape of the production curve

Figure 8.5-5 shows production curves for imbibition into cylindrical cores with all-faces-open for a range of aspect ratios. The shapes of the curves are all very similar. Experiments show much the same behaviour.

Figure 8.5-6 shows these examples plotted as the square root of time divided by the characteristic length given by Eq. 8.5-29 and Eq. 8.5-31. As expected these functions are all similar and show the core with the lowest aspect ratio tending towards linear imbibition.

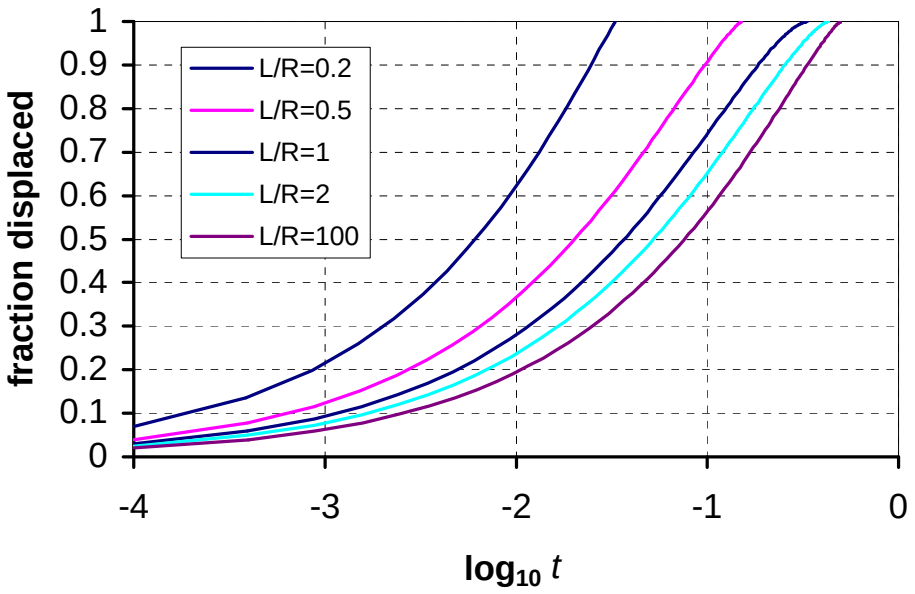

Fig 8.5-5. Examples of imbibition into all-faces-open cores with unit radius. Again, the factor $\sqrt{\frac{2K}{\varphi}}\frac{MC_{\text{spread}}\sigma}{(S_{\text{wf}}-S_{\text{wi}})}$ **has been set at 1. When *L*/*R* is large, imbibition is essentially radial; when *L*/*R* is unity there is spherical imbibition and when *L*/*R* is small, imbibition is linear. *L* is the half-length of the core.**

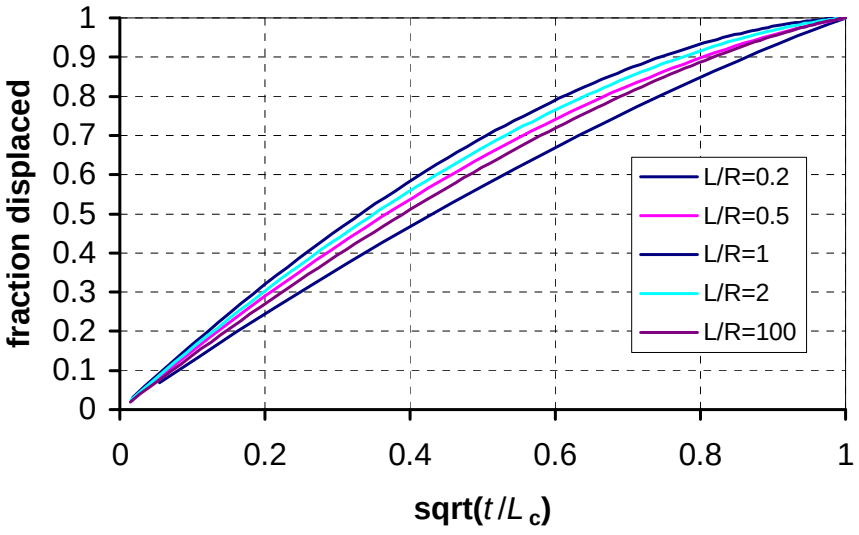

Figure 8.5-6 Examples of all-faces-open imbibition plotted using the square root of time and scaling using the characteristic length. For an aspect ratio of 0.2 (*L*/*R*=0.2), imbibition tends towards the linear case, for *L*/*R*=100, the radial case and for *L*/*R*=1, the spherical case. A core with all faces open and with a *L*/*R* ratio of 0.35 has almost exactly the same normalised production curve as a core with two ends closed (radial imbibition).

Comparison of the characteristic lengths

Eq. 8.5-3 gives Ma's characteristic length for an all-faces-open core as

$$L_c = \frac{L_{core} d}{2\sqrt{d^2 + 2L_{core}^2}} \qquad 8.5\text{-}3$$

For a core with a diameter greater than its length, the characteristic length given by the combination of a cone and toroid ring is

$$L_c = \frac{R_{final}}{\sqrt{3}} \sqrt{\ln \frac{R_{final}}{R_{max}} + \frac{R_{max}^2}{R_{final}^2} - \frac{R_{max}}{R_{final}}} = L_{toroid} \sqrt{1 - \frac{2}{3}\left(1 - \frac{R_{final}}{R_{max}}\right)} \qquad 8.5\text{-}41$$

with

$$\frac{L_{toroid}}{L_{cone}} = 1 - \frac{R_{final}}{R_{max}} \qquad 8.5\text{-}38$$

For a core with a diameter less than its length

$$L_c = \frac{R_{max}}{\sqrt{3}} \sqrt{\left(\frac{L_{toroid}}{L_{cone}} - 1\right)^2 \ln\left(1 - \frac{L_{cone}}{L_{toroid}}\right) + \frac{L_{toroid}}{L_{cone}}} = \frac{L_{cone}}{\sqrt{3}} \qquad 8.5\text{-}42$$

The characteristic lengths from these functions are compared on Fig. 8.5-7. They show close agreement. The percentage difference between the characteristic length given by the Ma relationship and the cone/toroid model is shown on Fig. 8.5-8. The difference is less than 7% and only 2% for cores with a typical aspect ratio of about 2. However, imbibition times depend on the square of the characteristic length, and so in experiments, the differences in time would be approximately doubled. Even so, it is unlikely that the differences would be detectable in standard experiments. Figure 8.5-9 gives the correction factor by which the characteristic length calculated from the Ma equation should be multiplied to make it agree with the cone/toroid model.

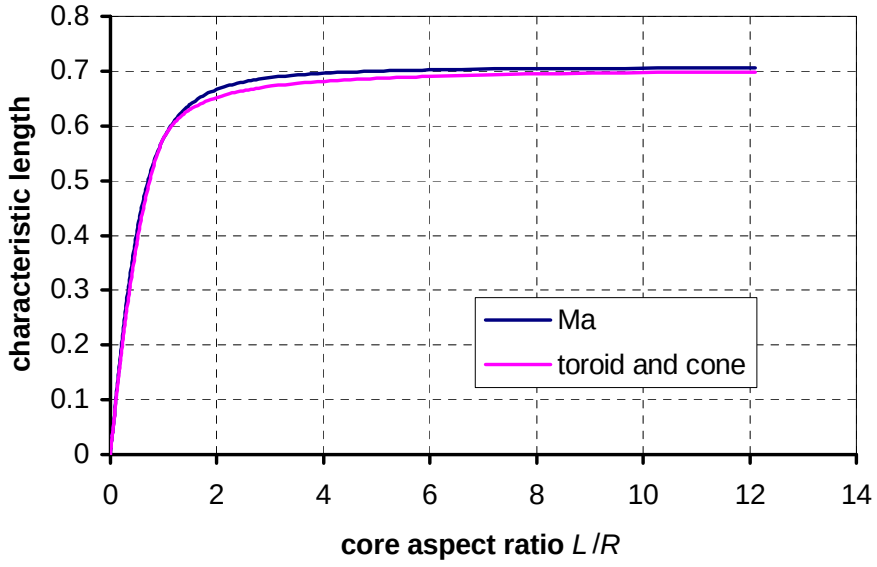

Figure 8.5-7 Comparison of the characteristic length predicted by Ma's equation (Eq. 8.5-3) with that from the current toroid and cone analysis. The two are very similar. The Ma characteristic length is always greater than, or equal to, the characteristic length of the cone/toroid model.

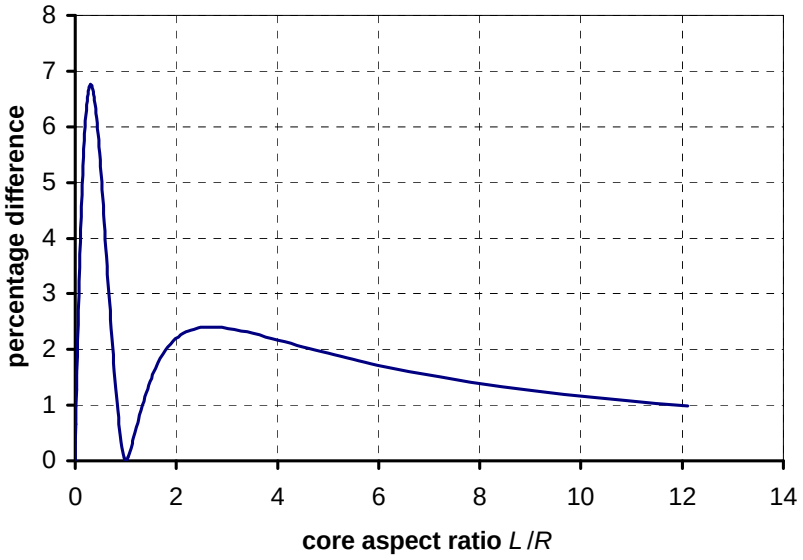

Figure 8.5-8. The percentage increase (see Fig. 8.5-7) in the Ma characteristic length required for agreement with the toroid/cone analysis.

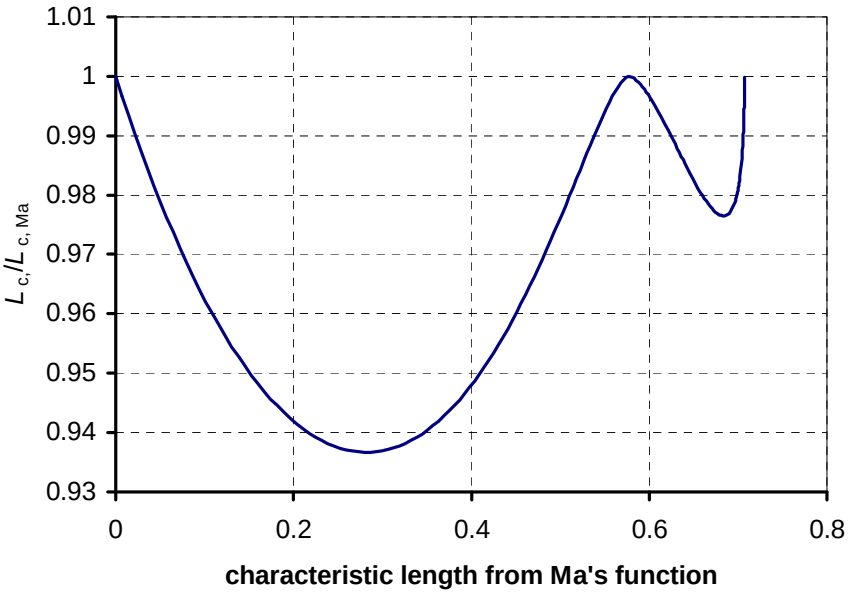

Figure 8.5-9 The correction factor by which the characteristic length calculated from the Ma equation has to be multiplied to bring it into agreement with the cone/toroid model.

Comparison with experiments

It is clear that there are only subtle differences in shape between production curves from cores with different boundary conditions and so only repeated averaged experiments might show the differences. One such set of experiments has been reported by Fischer and Morrow (2005). The

experiments were on cores of the same sandstone with almost identical size and shape. The only parameter that was intentionally varied was the viscosity of the two fluids, one being mineral oil and the other a brine. The viscosity of the brine was made to match the viscosity of the oil by the addition of glycerol. This made dramatic variation of the viscosity (4-170cp) possible with only relatively small changes to interfacial tension. It was found that the results scaled quite well, as expected (Ruth et al. (2004), by the dimensionless time given in Eq. 8.5-1. However, for our purposes the results are sufficient in number and correlate so well that they do show the small changes in the shapes of the production curves predicted by the core/toroid model. Figure 8.5-10 shows the results taken from Fischer and Morrow (2005) for the all-faces open cores. The aspect ratio (L/R) was about 1.7 in all cases.

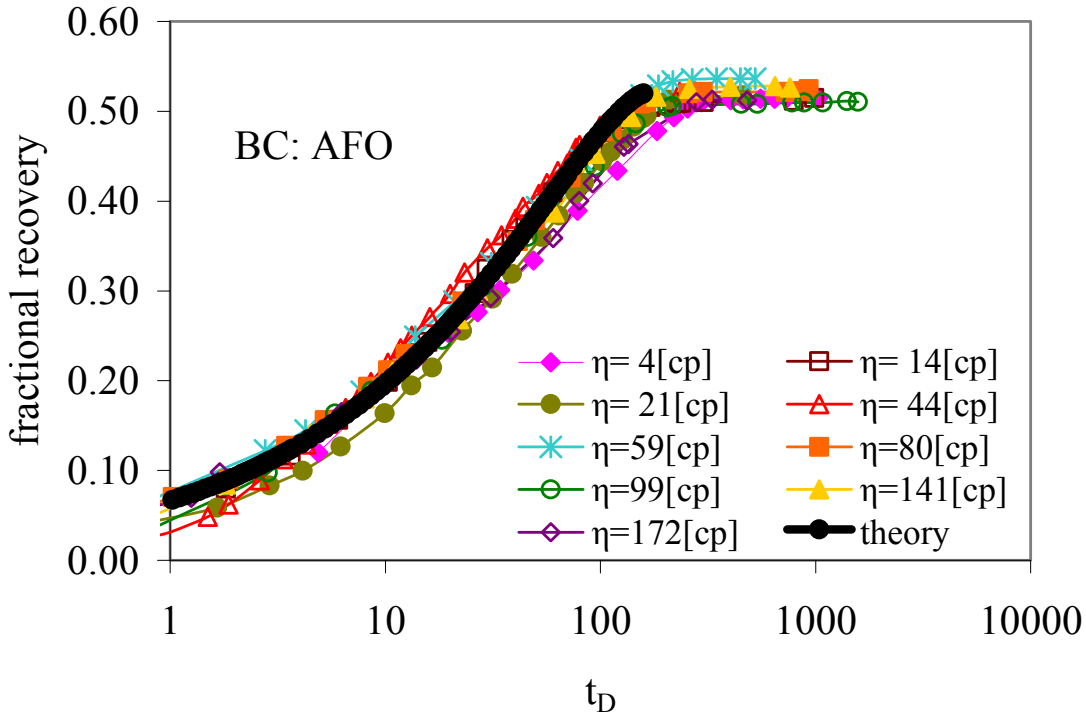

Figure 8.5-10. The experimental data of Fisher and Morrow (2005) for cores with all faces open, matched viscosities, and an aspect ratio of 1.7, are shown compared to the predictions of the cone/toroid theory. The theory assumes piston-like displacement and includes a single properties factor optimised to give the best fit to this data.

Because there is an unknown constant linking the dimensionless time with the cone/toroid theory, the theory line can be moved left and right on the $\log_{10}$ graph to find the position which gives the best fit to the experimental data. In Fig. 8.5-10 the fit is generally as good as the data, and falls within the range of the data points. The same comparison is made for cores with two ends closed (giving radial imbibition) in Fig. 8.5-11. Again the theory does not go outside the spread of the data, although the data is slightly more spread than for the all-faces-open cores. The same

properties constant as in Fig. 8.10 has been used. Finally, the results for one-end-open geometry (giving linear imbibition) are shown in Fig. 8.5-12, again using the same properties constant as in Fig. 8.5-10. The fit is not quite as good but this is only in regard to the position of the theory line; its shape is almost perfect.

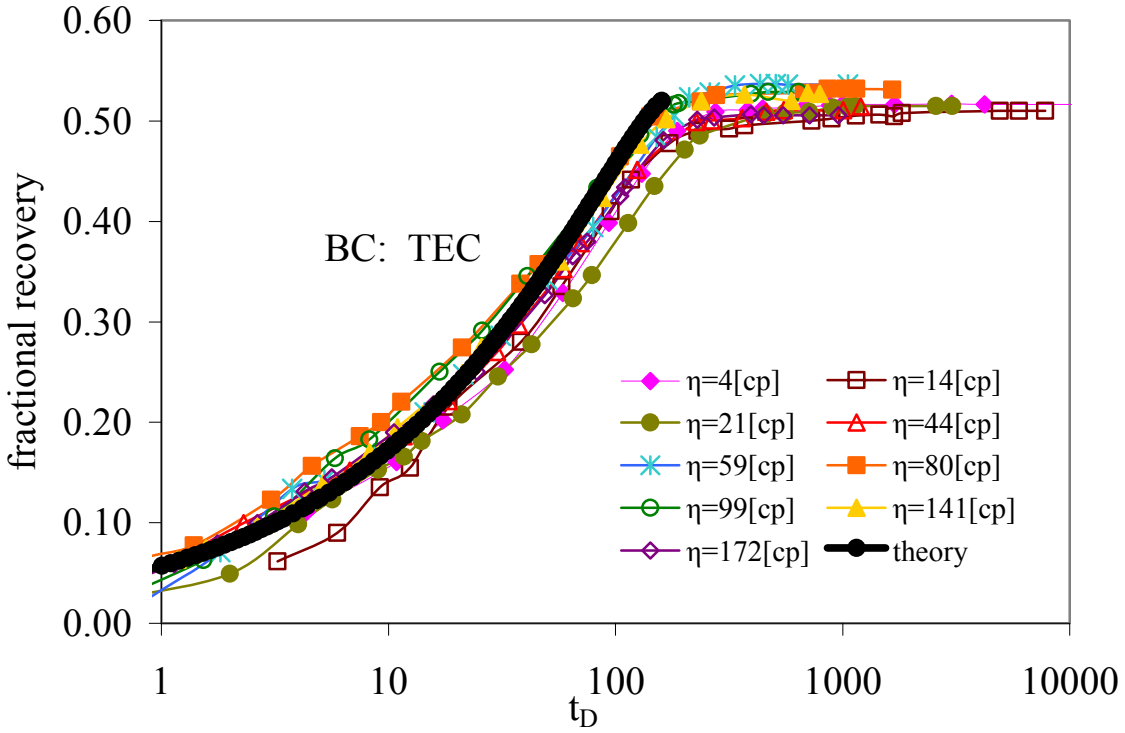

Figure 8.5-11 The experimental data of Fisher and Morrow (2005) for cores with matched viscosities and the boundary condition of two ends closed. The same constant has been used to place the theory curve as in Fig 8.5-10.

So why does the assumption of piston-like displacement work so well? One reason is that analytically, for linear imbibition, there is a self-similar front for much of the displacement and the distance advanced by any fixed saturation is proportional to the square root of time (Tavassoli et al., 2005; Ruth et al., 2007). It is only when the leading edge of the front reaches the end of the core that a saturation versus $\sqrt{time}$ plot will deviate from a straight line. For radial imbibition the front is not exactly self-similar (Standnes, 2006) but is a close approximation to it. Furthermore, the volume involved as the front approaches the centre is proportionally quite small, with the last 25% of the distance corresponding to only 6% of the volume. The second reason is that, in most experiments, there is no initial water saturation and a significant fraction of the brine reaching the front is used to raise the brine permeability from zero, thus giving a front sharpening effect.

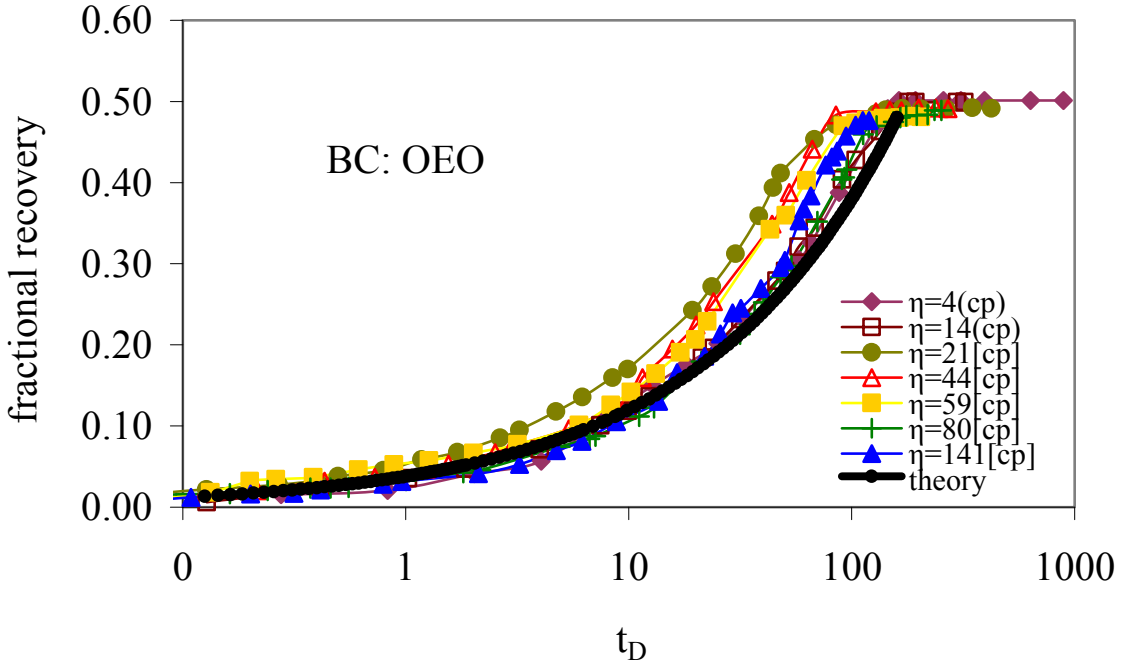

Figure 8.5-12. The experimental data of Fisher and Morrow (2005) for cores with matched viscosities and the boundary condition of one end open. The same constant has been used to place the theory curve as in Figs 8.5-10 and 8.5-11. In this case it places the curve slightly too far to the right. The shape, however, is almost perfect. When plotted against the square root of dimensionless time, all of the experimental points give straight lines except at late times.

Task 9. *Increased oil recovery by spontaneous imbibition.*

9.1 Increased rate and volume of production of oil by countercurrent spontaneous imbibition through use of surfactants

Background

This task related to increasing production, both rate and total recovery, by alteration of the capillary pressure that resists oil production at the rock face. It was thought that the capillary back pressure could be lowered by reducing the oil/water interfacial tension by means of surfactant. Consequently, the effect of imbibition of surfactant solutions on end pressures, frontal advance, and oil recovery were investigated. This is an example of how improved fundamental understanding leads to new approaches in improving oil recovery from fractured reservoirs.

Experiments

Measurements have been made on Berea sandstone, for which imbibition under very strongly water wet conditions is well characterized. The imbibition tests were run with the apparatus set up as shown in Fig. 9.1-1. The absolute permeabilities and porosities and the dimensions of this and the other tested cores are included in Tables 9.1-1, 2, and 3.

The oil was either purified Soltrol 220 mineral oil (an isoparaffin oil) with polar components removed by flow through silica gel and alumina or Cottonwood crude oil. A 10,000 *ppm* NaCl brine (viscosity of 0.00102 *Pa.s*) was used as the wetting phase. Tomadol 9-18, an alcohol ethoxylate, was chosen as the surfactant because of its comapability with brine. Tomadol is a commonly used nonionic surfactant, which gives large but not extreme lowering of interfacial tension.

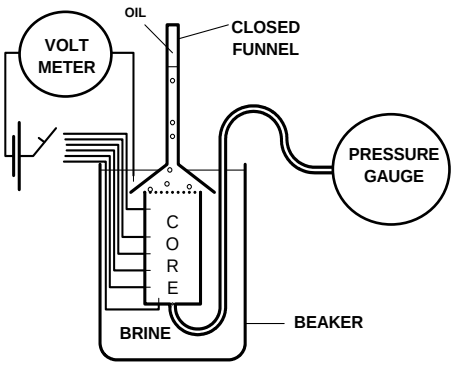

Figure 9.1-1. Schematic diagram of the apparatus.

A side effect of the addition of surfactant was that it caused oil to be produced as an emulsion. During the surfactant imbibition stages of the tests, shaking or other means of removing produced oil from the core end face were never attempted. The collected sample was heated at $80^{o}C$ to break the emulsion. The volume of oil produced was determined by reducing the volume of produced

emulsion by the ratio of the volume of demulsified oil to the volume of emulsion determined at the end of the test.

A range of fundamentally different experiments was performed and an attempt made at quantitative interpretation.

The brine/Soltrol 220 interfacial tension was 47 *mN/m*. Interfacial tensions measured after addition of surfactant to brine for surfactant concentrations ranging from 0 to 3000ppm are plotted in Fig. 9.1-2. Interfacial tensions for the brine containing surfactant and Cottonwood crude oil are also shown in Fig. 1. Surfactant solutions with concentrations of 1,000 and 3,000 *ppm*, giving interfacial tensions of 3.65 and 2.19 *mN/m,* respectively were adopted for the experiments on core plugs (see Fig. 9.1-2).

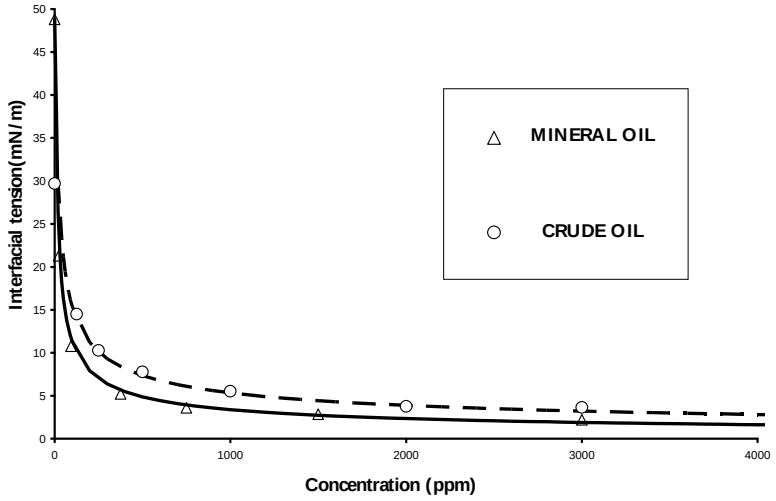

Fig. 9.1-2 Interfacial tension vs concentration of surfactant (TOMADOL 9-18) in brine against refined oil and Cottonwood crude oil. Concentrations of 3,000 and 1000 ppm were used in imbibition tests.

Refined oil/ brine 3000ppm surfactant solution

Continuous refined oil/ 0ppm surfactant brine COUCSI

Core: NS1

The core was initially saturated with refined oil ($S_{wi} = 0$) and then immersed in brine. COUCSI caused the end pressure, $P_{end,}$ to rise quickly to 7.5 *kPa* within 1.5 *minutes* (Fig. 9.1-3*)*. After P_{end} had reached 8.8 *kPa* it remained constant until the front reached the end of the core 16.7 *hours* after immersion. The oil recovery relative to the pore volume Q_o/V_ϕ was 38% OOIP when the imbibition front reached the end of the core (Fig. 9.1-3). The rate of oil recovery then showed marked decay and the end pressure (P_{end}) decreased. P_{end} eventually dropped to 0 *kPa* about 13 *days* after the start of imbibition. The final oil recovery Q_o/V_ϕ was 43% OOIP.

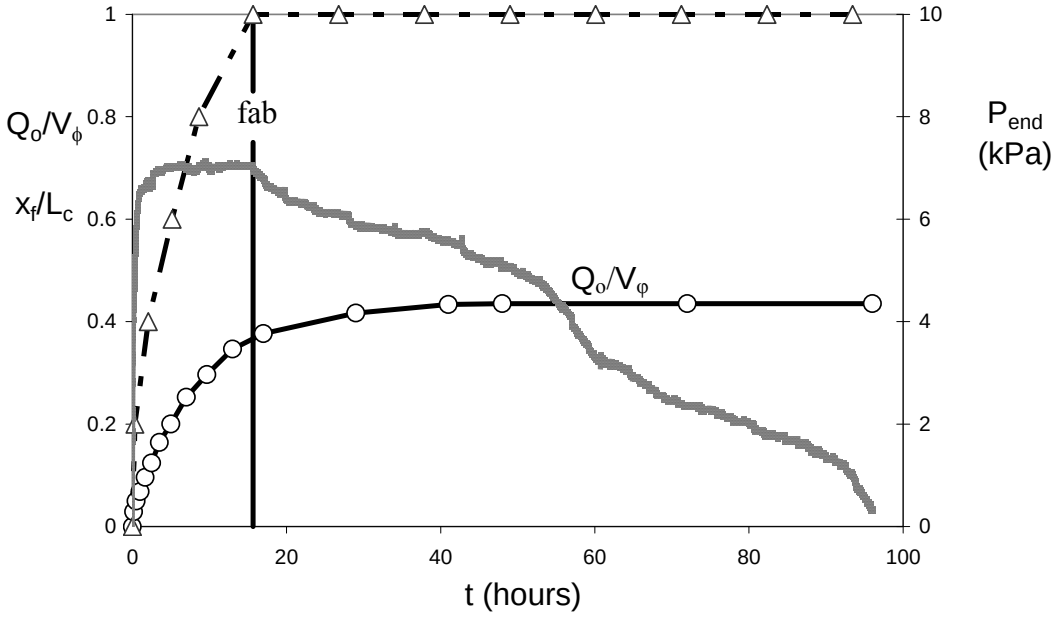

Fig. 9.1-3 Test NS1; COUCSI with brine and refined oil. Distance of advance of the imbibition front, oil recovery and end pressure versus time for oil recovery by spontaneous imbibition.

COUCSI with surfactant added part way through experiment

Refined oil/3000ppm surfactant solution

In these experiments using refined oil/brine, COUCSI was started normally with brine (Stage 1) but, about half way through the imbibition process, the brine was changed to 3000 *ppm* surfactant solution(Stage 2).

Core: IS1 (9.2.2a)

Stage 1: Refined oil/brine COUCSI

First the one end open (OEO) Core IS1 was immersed in brine. As for test NS1, COUCSI caused P_{end} to rise quickly to 6.6 *kPa* in the first 2 *minutes* (Fig. 9.4). When the front had advanced 2.67 cm from the open face (x = 0.4), the oil recoveryR_o was 16.8% OOIP (Fig. 9.4). The results up to this stage were, as expected, very close to those for test NS1.

Stage 2: Imbibition of 3000ppm surfactant solution

a) Frontal flow period in surfactant solution

Core IS1 was then immersed in the surfactant solution. The produced oil soon changed from large to very small drops. The oil was collected in an inverted funnel as an emulsion.

Immersion in surfactant solution resulted in increase in rate of imbibition. The end pressure (P_{end}) dropped from 6.6 *kPa* to 4 *kPa* as the front advanced through the core. The front arrived at the end of the core, 5.1 *hours* after immersion in surfactant solution. At this time the oil recovery, Q_o/V_φ, was 36.2% OOIP. The front reached the end of the core 5.1 hours after immersion in the surfactant solution.

Stage 3: Imbibition of 3000ppm surfactant solution after frontal flow

After the front arrived at the end of the core, the end pressure (P_{end}) continued to drop and after 3 *hours* had decreased down to its lowest value of 3.7 *kPa*. Then the end pressure (P_{end}) rose again to a peak value of 5.48 *kPa* over the next 3.1 *hours*. Over the next 32 *hours*, the end pressure (P_{end}) gradually dropped to 0.25 *kPa*. The final oil recovery was 47.2% OOIP. In addition to faster recovery, the recovery was 3.7% OOIP higher than that for core NS1 (NS1). Immersion in surfactant solution even after establishing an initial bank of imbibed brine still resulted in increased oil recovery.

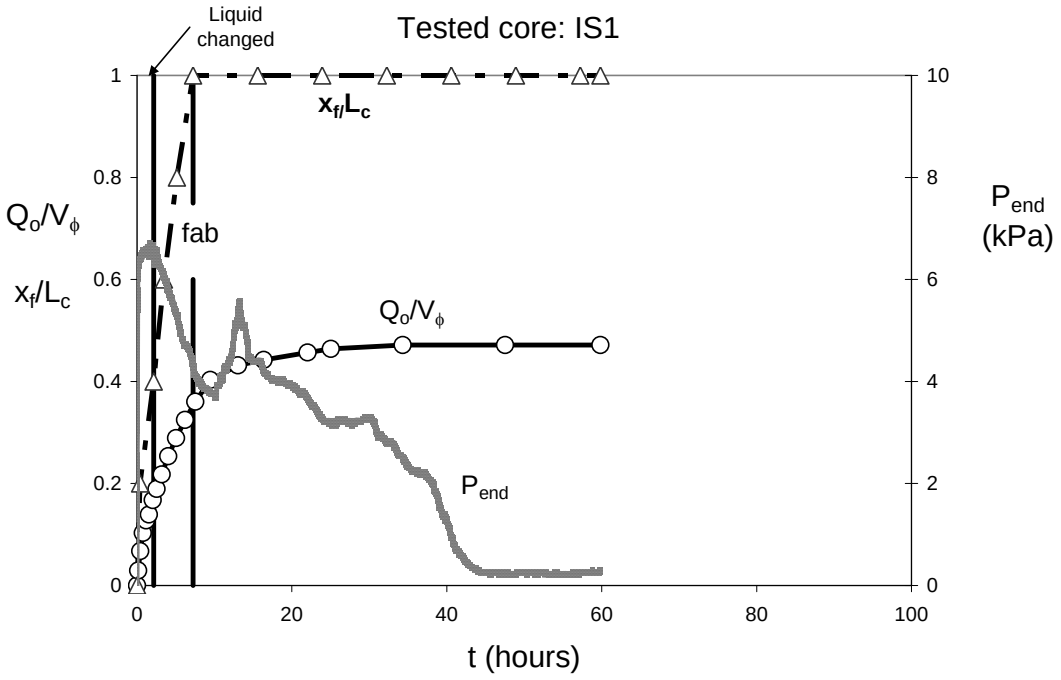

Fig. 9.4 Imbibition of 0ppm surfactant brine slug (to x=0.4) followed by 3000ppm surfactant brine for core IS1.

Core: IS2

Stage 1: Refined oil/surfactant solution COUCSI

After immersion of the core in brine, the front reached advanced 2.67 cm from the open face (x = 0.4) after 2 *hours*. By this time the end pressure, P_{end} had risen to 6.7 *kPa* and 15.2% OOIP had been produced (see Fig. 9.1-5).

Stage 2: Imbibition of 3000ppm surfactant solution

After immersion in surfactant solution, the front advanced from 0.4 of the core length to the end of the core in 6.35 *hours*. P_{end} fell from 6.7 to 4.2 *kPa* within three hours and remained close to this value until the front reached the end of the core. The additional oil recovery during that period was 36.3% OOIP. The main difference between IS1 and IS2 during frontal flow is that the end pressure for IS1 fell continuously through the frontal flow period, whereas IS2 fell to a constant value for x>0.8.

Stage 3: Imbibition of 3000ppm surfactant solution after frontal flow

At the end of frontal flow the pressure drop increased sharply from 4.2 *kPa* to a peak value of 5.22 *kPa* within 2 *hours* and then showed overall decrease with time to a stable value of 0.23 *kPa*. The final oil recovery was 47.4% OOIP.

After completion of COUCSI, 2 cc of brine were removed from the dead end of the core.

The interfacial tension against refined oil was 17.06 *mN/m* indicating that the concentration of surfactant in the produced brine was about 46ppm, which was very much lower than the concentration in the original (3000 *ppm*) surfactant solution. Test IS2 gave 3.9% OOIP additional oil recovery compared to the imbibition without surfactant (Test NS1).

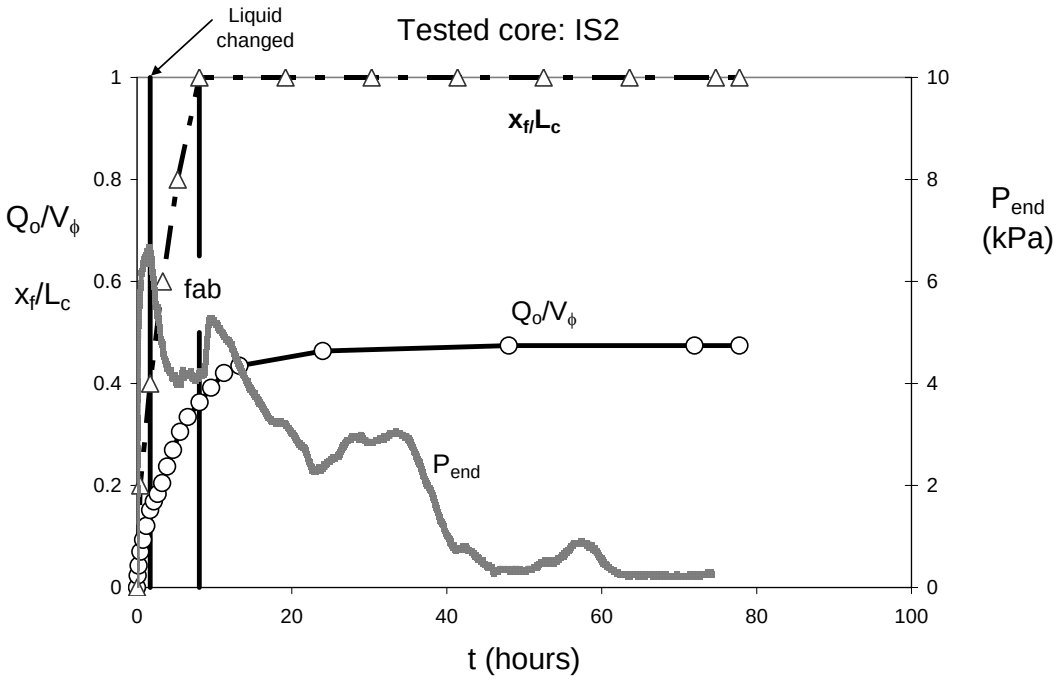

Fig. 9.1-5 Imbibition of brine to x=0.4 followed by 3000ppm surfactant solution for core IS2.

Refined oil/1000ppm surfactant solution

In these experiments using refined oil/brine, COUCSI was started normally with brine (Stage 1) but, about half way through the imbibition process the brine was changed to 1000 *ppm* surfactant solution (Stage 2).

Core: IS3

Stage 1: Refined oil/brine COUCSI

First, the one end open (OEO) Core IS3 was immersed in brine. As for test NS1 (see Fig. 9.1-3), P_{end} quickly rose to 8 *kPa* in the first 2 *hours*. When the front had advanced 2.6 cm from the open face (x= 0.4), the oil recovery Q_o/V_φ was 15,6% OOIP (Fig. 9.1-6). The results up to this stage were similar to those for test NS1.

Stage 2: Imbibition of 1000ppm surfactant solution

Core IS3 was then immersed in the 1000 *ppm* surfactant solution. The produced oil soon changed to an emulsion.

Upon immersion in surfactant solution, the rate of imbibition increased and the end pressure (P_{end}) dropped from 8 *kPa* to 7.4 *kPa* over the next 5 *hours*. Then the end pressure (P_{end}) rose from 7.4 *kPa* to 7.6 *kPa*. The front arrived at the end of the core 8.5 *hours* after immersion in surfactant solution (twice as fast as for Test NS1). At this time the oil recovery, $Q_o/V_{\square}$, was 38.0% OOIP.

Stage 3: Imbibition of 1000ppm surfactant solution after frontal flow

After the front arrived at the end of the core, the end pressure (P_{end}) continued to rise and, after 5 *hours,* had increased up to its highest value of 7.8 *kPa*. Then the end pressure (P_{end}) dropped down to 0.65 *kPa* over the next 64 *hours* and remained constant over the next 15 *hours*. The final oil recovery was 47.0% OOIP. In addition to faster recovery, the recovery was 3.6% OOIP higher than that for core NS1. Details of k_{oe}, k_{rw} and k_{we} are given in Table 9.1-4.

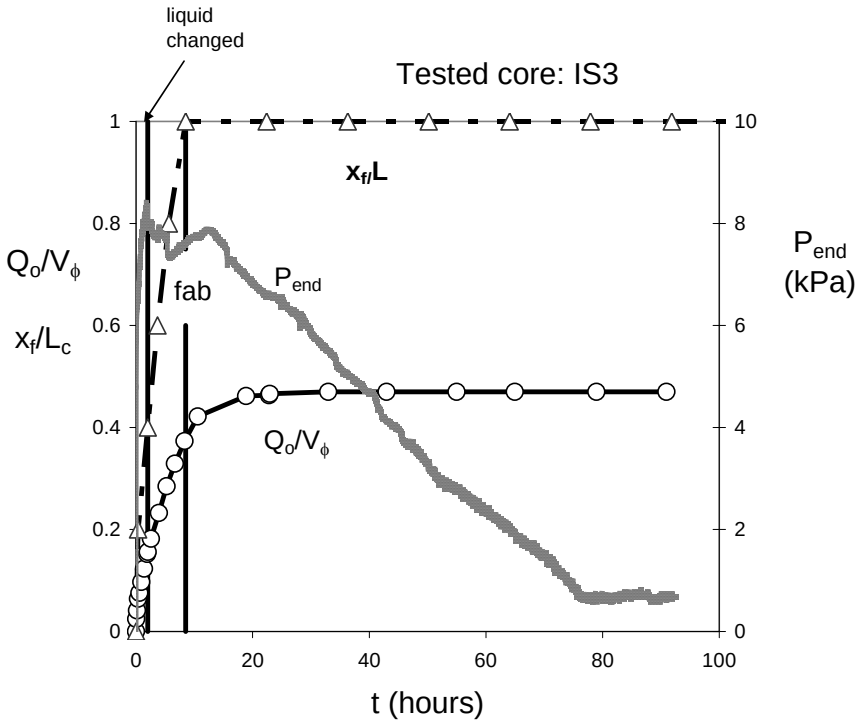

Fig. 9.1-6 Imbibition of brine to x=0.4 followed by COUCSI using 1000 ppm surfactant solution for core IS3.

Core: IS4

Stage 1: Refined oil/brine COUCSI

After immersion of the OEO core in brine, the front had advanced 2.58 cm from the open face x = 0.4 after 1.83 *hours*. By this time P_{end} had risen to 8.2 *kPa* and 11 % OOIP had been produced (Fig. 9.1-7).

Stage 2: Imbibition of 1000ppm surfactant solution

After immersion in surfactant solution, the front advanced from 0.4 of the core length to the end of the core in 6.8 *hours*; the end pressure (P_{end}) dropped from 8.2 *kPa* to 7.3 *kPa*. The additional oil recovery during that period was 25.0% OOIP.

Stage 3: Imbibition of 1000 ppm surfactant solution after frontal flow

At the end of frontal flow the pressure increased from 7.3 *kPa* to a peak value of 7.7 *kPa* in the next 8.3 *hours*. After correction for the volume of oil contained in the produced emulsion, the final oil recovery was 47.0% OOIP.

Details of k_{oe}, k_{rw} and k_{we} are given in Table 9.1-4.

Test IS2 gave 3.9% OOIP additional oil recovery compared to that for oil/brine (Fig. 9.1-3). The increased recovery over oil/brine was produced by imbibition of surfactant solution subsequent to the frontal flow period.

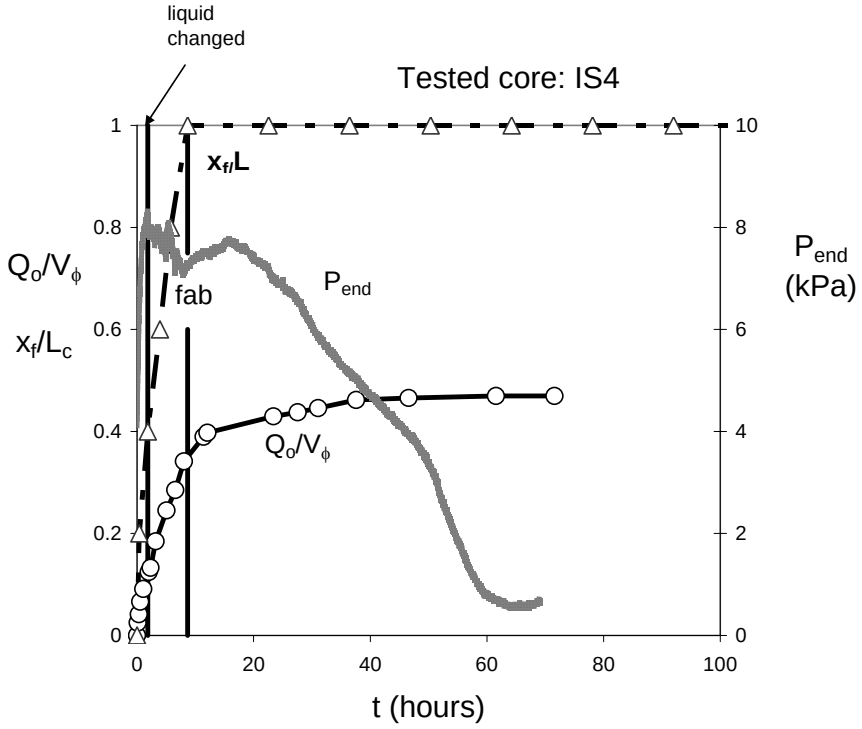

Fig. 9.1-7 Imbibition of brine to x=0.4 followed by imbibition of 1000 ppm surfactant solution for core IS4.

COUCSI with continuous imbibition of surfactant solution

Imbibition of surfactant solutions **without** the initial imbibition of brine were tested for Berea sandstones cores (see Table 9.1-1) that were initially saturated with refined oil.

Refined oil/3000ppm surfactant solution

Core: DS1

Stage 1: Refined oil/3000ppm surfactant solution COUCSI

The core was immersed directly in surfactant solution. P_{end} quickly rose to 1.25 *kPa* in the first 1.5 *minutes* and held close to constant at about 1.4 *kPa* with slight rise to 1.5 *kPa* just before the front reached the end of the core. Even though the capillary driving pressure for surfactant imbibition, as indicated by P_{end}, was reduced by a factor of about 6, the recovery rate was slightly faster than the rate for non-surfactant COUCSI (Test NS1, Fig. 9.1-3). It took 14.8 *hrs* for the front to reach the end of the core (as compared to15.7 *hours* in Test NS1). The oil was collected as an emulsion. When the imbibition front reached the end of the core, the oil recovery had reached 36.5% OOIP (Fig. 9.1-8).

Stage 2: Imbibition of 3000ppm surfactant after frontal flow

After the front reached the end of the core, the end pressure (P_{end}) increased significantly and, 8 *hrs* later, reached a maximum of 4.97 *kPa* and remained close to this value for a further 8 *hrs*. Then P_{end} gradually declined to 1.48 *kPa* over the next 87.5 *hours*

The final oil recovery was 50.8% OOIP. Imbibition of 3000 *ppm* surfactant solution resulted in 7.1% OOIP additional oil recovery compared to imbibition of brine (Fig 9.1-3).

.

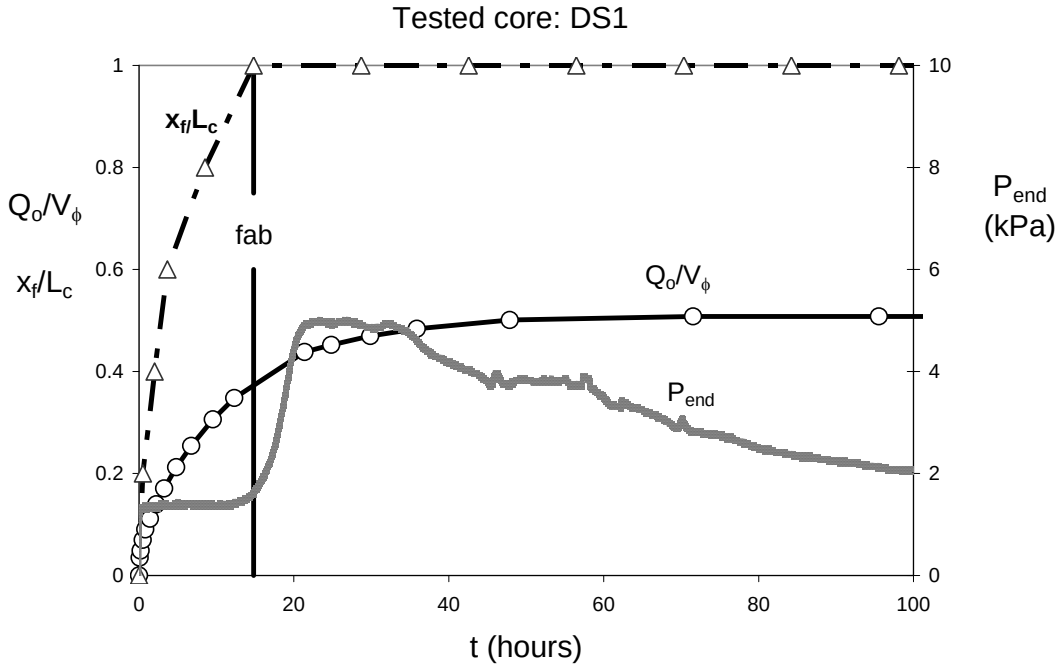

Fig.9.8 Continuous imbibition of 3000ppm surfactant solution, Core DS1.

Core: DS2

Stage 1: Refined oil/3000ppm surfactant solution COUCSI

Except for slightly faster flow, the recovery and end pressure response was similar to that for Test DS1 during frontal flow. The front arrived at the end of the core after 13 *hours*. The oil recovery reached 36.1% OOIP during the frontal flow period (Fig. 9.9). The collected oil, in the form of an emulsion, was more transparent than the emulsion produced in Test DS1. P_{end} remained at about 1.55 *kPa* until the front had almost reached the end of the core.

Stage 2: Imbibition of 3000ppm surfactant solution after frontal flow

The end pressure rose slowly for 5 *hours* after completion of frontal flow and then rapidly, to a maximum of 4.81 *kPa* over the next 7.9 *hours*. Then P_{end} gradually decayed to about 1.7 *kPa* after 45 *hours* and then more slowly with minor fluctuation to 0.9 *kPa* over the next 25 *hours*. The final oil recovery was 48.1% OOIP. Recovery was 5% OOIP higher than given by imbibition of brine (Core NS1). Much of the increase in recovery relative to that for brine occurred after completion of frontal flow.

The produced brine/refined oil interfacial tension obtained using 2 cc of aqueous phase produced after completion of the COUCSI test was 14.25 *mN/m*.

.

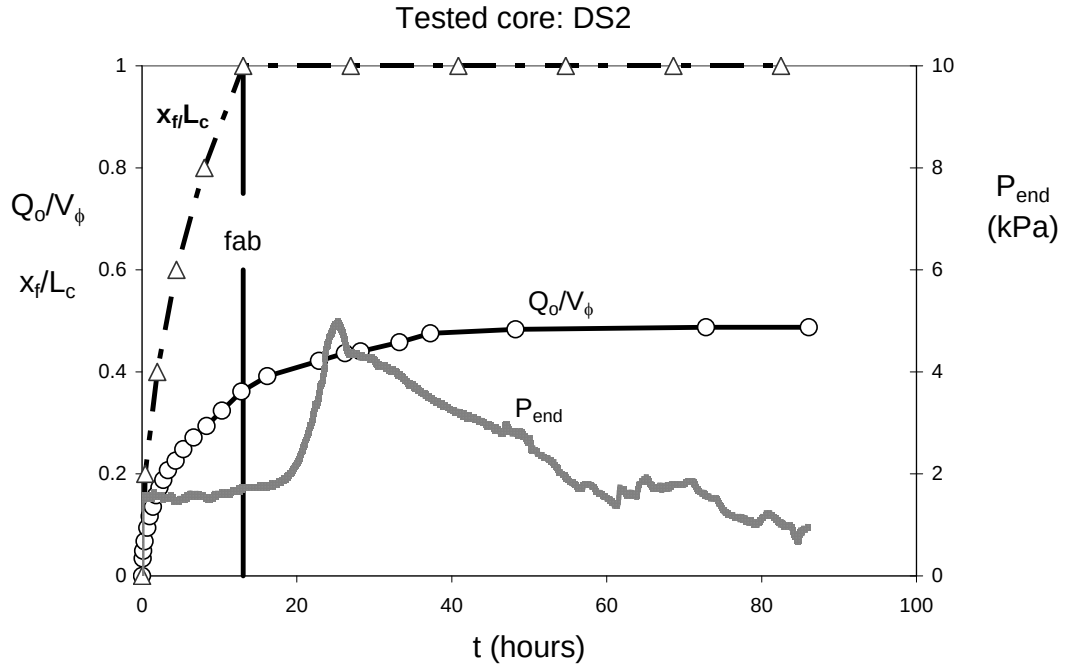

Fig.9.1-9 Continuous imbibition of 3000ppm surfactant solution, Core DS2

Table 9.1-1 Core properties, oil recovery, and end pressures

EXPERIMENT	CORE	d (cm)	L_c (cm)	φ (%)	K (μm^2)	R at fab	R after fab	Pend at fab (kPa)	Max Pend after fab (kPa)
COUCSI (brine)	**NS1**	3.755	6.51	17.3	0.072	0.362	0.435	7	7
Surf. COUCSI	**IS1**	3.788	6.674	17.2	0.071	0.362	0.472	4.3	5.4
follows COUCSI	**IS2**	3.781	6.686	17.2	0.07	0.363	0.474	4.3	5.2
Surf. COUCSI	**DS1**	3.786	6.531	17.2	0.07	0.365	0.508	1.7	5
	DS2	3.785	6.521	17.2	0.071	0.361	0.483	1.7	4.9

Refined oil/1000ppm surfactant solution (direct)
Imbibition of 1000ppm surfactant solution **without** the initial imbibition of brine.

Core: DS3 (9.6.3b)
Stage 1: Refined oil/1000ppm surfactant solution COUCSI
The oil-saturated core was immersed directly in surfactant solution. Oil was produced as very small droplets that were collected as an emulsion. The recovery rate was slightly faster than the rate for COUCSI of brine (Test NS1) before the front reached the end of core. It took 14.25 *hrs* for the front to reach the end of core (as compared to16.7 *hours* in Test NS1). P_{end} quickly rose to 7.9 *kPa* in the first 2.7 *hours,* then slowly decreased to 7.6 *kPa* as the front reached the end of the core. The end pressure (P_{end}) at fab (front at boundary) was 86% of that for Test NS1. Oil recovery after Stage I was 42% OOIP (Fig. 9.11) which is 4% more than in Stage 1 of NS1.

Stage 2: Imbibition of 1000ppm surfactant solution after frontal flow
After the frontal flow period, the end pressure (P_{end}) gradually decreased from 7.6 to 4.3 *kPa*. The final oil recovery was 48.9% OOIP. Imbibition of surfactant solution resulted in 5.5 % OOIP additional oil recovery compared to recovery by imbibition of brine (Test NS1).

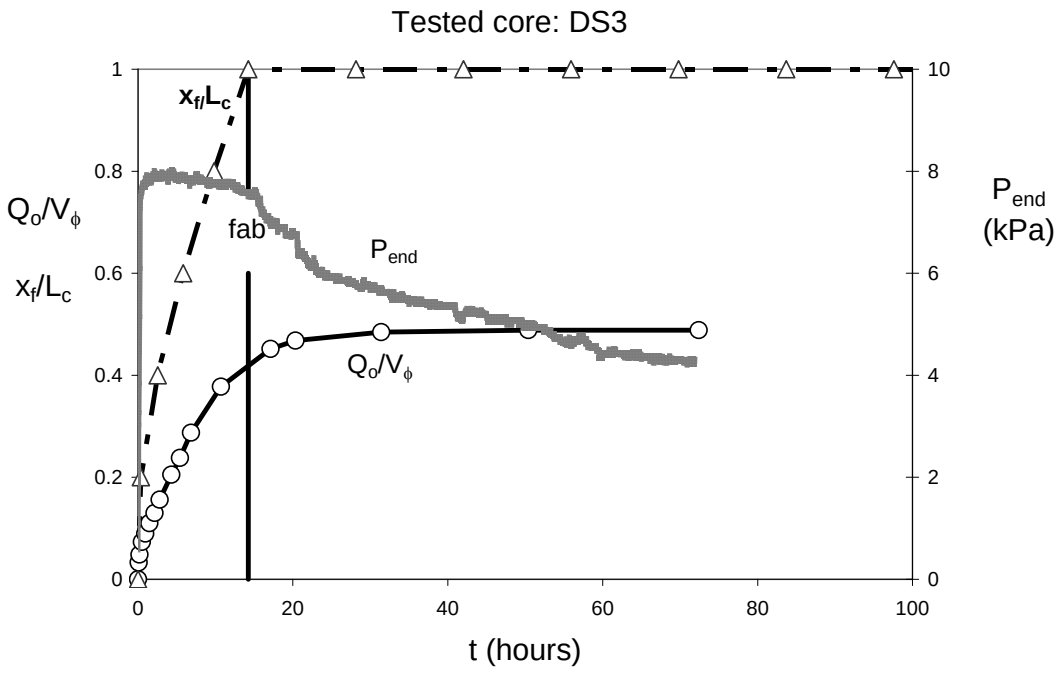

Fig. 9.1-11 Imbibition of 1000 ppm surfactant solution into an initially-oil-saturated core, DS3.

Core: DS4

Stage 1: Refined oil/1000ppm surfactant solution COUCSI

Except for slightly faster flow, the recovery and end pressure response was similar to that for Test DS3 during frontal flow. The front arrived at the end of the core after 12.7 *hours*. The oil recovery reached 44.2% OOIP during the frontal flow period (Fig. 9.12). P_{end} quickly rose to 7.85 *kPa* in the first 3 *hours,* then slowly decreased to 7.6 *kPa* as the front reached the end of the core. The end pressure (P_{end}) at fab was 86% of that for Test NS1. The produced oil in the form of an emulsion. About 6% more oil was produced during Stage 1 than for imbibition of brine in test NS1.

Stage 2: Imbibition of 1000ppm surfactant solution after frontal flow

After the frontal flow period, the end pressure (P_{end}) decreased as did the end pressure for the the imbibition of brine (test NS1). The P_{end} gradually decreased from 7.6 to 3.8 *kPa* (at 99 *hours)*.
The final oil recovery was 50.4% OOIP. Overall, imbibition of surfactant solution resulted in 7 % OOIP additional oil recovery compared to recovery by imbibition of brine (Test NS1).

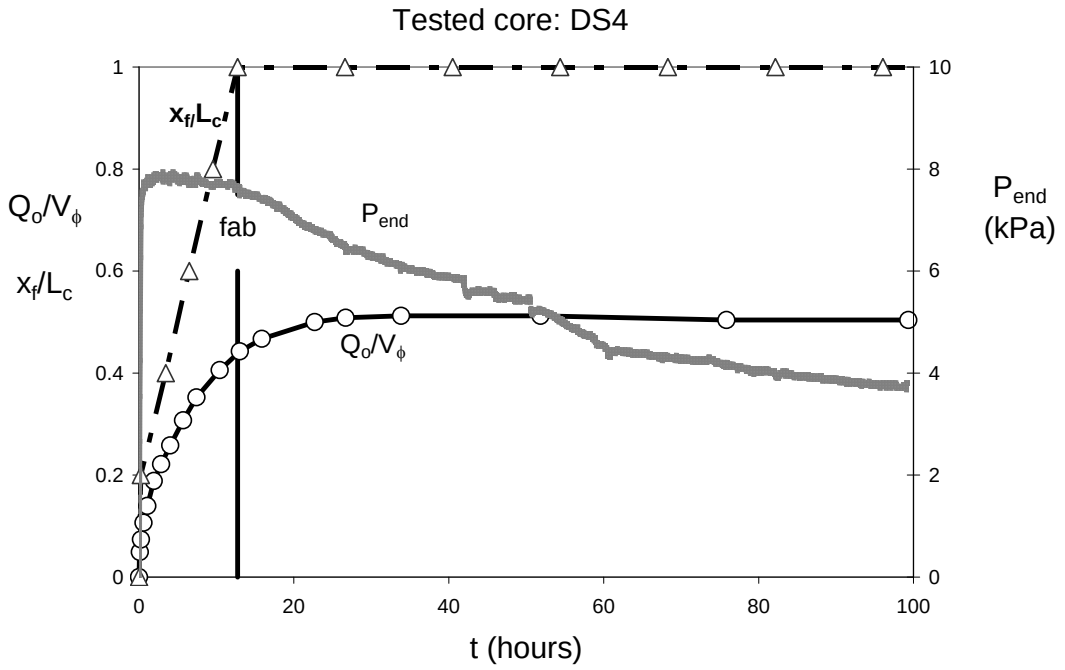

Fig. 9.1-12 Imbibition of surfactant by COUCSI for initially-oil-saturated core DS4.

Table 9.1-2. Core properties, oil recovery, and end pressure

EXPERIMENT	CORE	d (cm)	L_c (cm)	φ (%)	K (μm^2)	R at fab	R after fab	Pend at fab (kPa)	Max Pend after fab (kPa)
COUCSI (brine)	**NS1**	3.797	6.000	17.1	0.065	0.38	0.434	8.9	8.9
Surf. COUCSI follows COUCSI	**IS3**	3.749	6.489	17.0	0.065	0.38	0.470	7.6	7.8
	IS4	3.744	6.454	17.0	0.065	0.36	0.470	7.3	7.7
Surf. COUCSI	**DS3**	3.748	6.455	17.1	0.067	0.420	0.489	7.6	7.6
	DS4	3.746	6.510	17.0	0.071	0.442	0.504	1.7	4.9

Crude oil/ brine COUCSI experiments

Interfacial tensions

The Cottonwood crude oil/brine interfacial tension was 29.7 *mN/m*. The density of Cottonwood crude oil is 0.8874 and the viscosity is 24.1 *Pa.s*. (20^oC). A surfactant concentration of 3,000 *ppm*, giving an interfacial tension of 3.65 *mN/m,* was adopted for the experiments with crude oil.

Measurement of effective capillary pressure at the imbibition front for Cottonwood crude oil/brine by restricted COUCSI

Core: CL1

The core was completely saturated with Cottonwood crude oil and aged at 75°C for 10 days. The interfacial tension between the crude oil and brine was 29.7 *mN/m*. A 1.53 *cm* long segment of Texas Leuders limestone (permeability of 0.002μm^2) was saturated with brine and then butted against the main segment. This technique gave restricted COUCSI and an indication of the maximum capillary pressure generated at the imbibition front (Li et al., 2008).

The composite core was immersed in brine, but the end pressure did not rise for 6 days. It then took 19 days for the end pressure to reach 0.4 *kPa*. The end pressure remained unchanged for more than 17 days. By this time, the brine front had advanced by 20% of the core length (see Fig. 9.1-13).

Main core seg-ment	D (cm)	L (cm)	K (μm^2)	φ (%)	Low K core	D (cm)	L (cm)	K (μm^2)	φ (%)	P_{cf} (kPa)	P_{cf}/σ (μm^{-1})
CL1	3.773	6.361	0.072	17.1	TL16	3.78	1.54	0.002	16.5	0.4	0.11

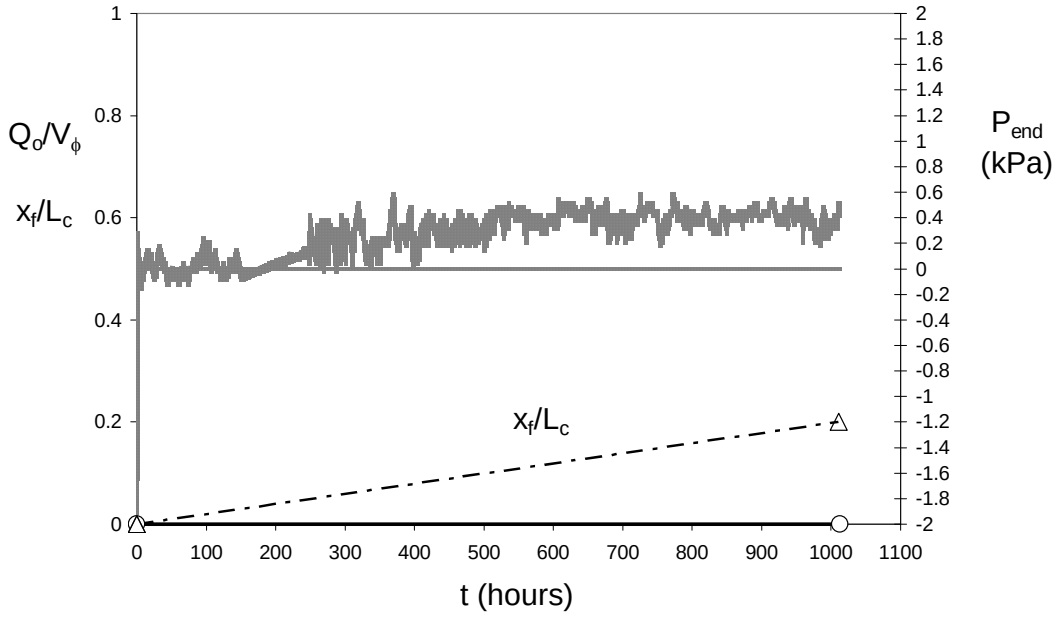

Fig. 9.1-13 Effective capillary pressure at the front for Cottonwood crude oil/brine restricted COUCSI

Crude oil/brine COUCSI (Reference Test)

Core: CL2

Core CL2 was completely saturated with crude oil and then aged at 75°C for 10 days and then immersed in brine. The end pressure rose to 0.246 *kPa* after 3.7 days and remained at this value until the front reached the end of the core, 60 *days* after the start of imbibition). The recovery, R_o was 31.5% OOIP when the front arrived at the end of the core. The rate of oil recovery then decayed and P_{end} decreased slowly to 0.2 *kPa* in 38 *days*. The final recovery was 37% OOIP (Fig. 9.1-14).

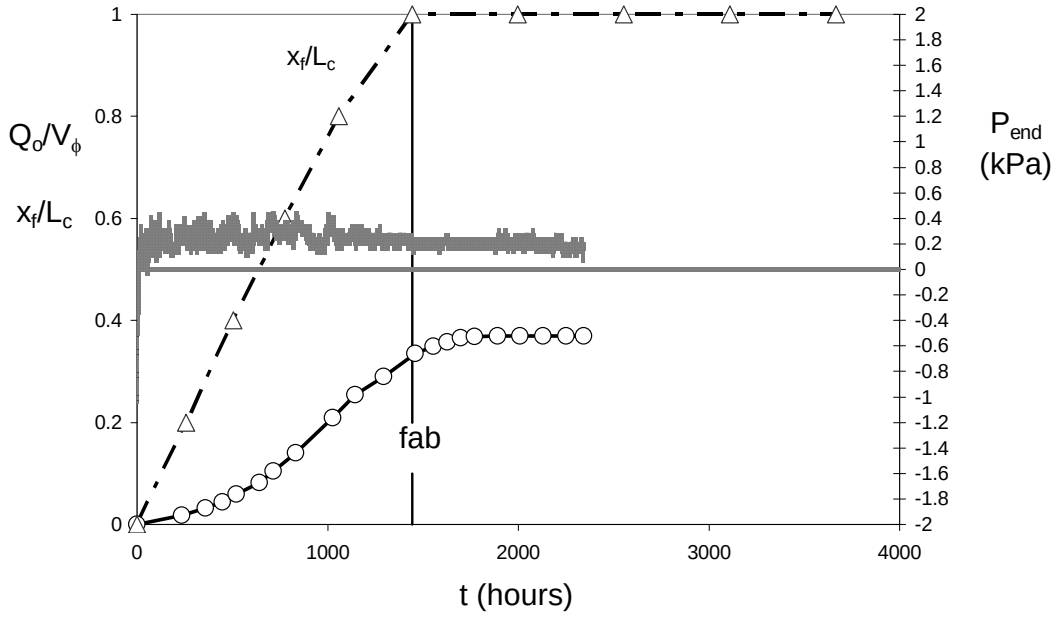

Fig. 9.1-14 Distance of advance of the imbibition front, oil recovery and end pressure versus time for recovery of crude oil by spontaneous imbibition of brine for core CL2.

Crude oil/ 3000ppm surfactant solution COUCSI

There was no initial period of imbibition of brine.

Core: CDS1 (9.3.3)

Stage 1: Crude oil/3000ppm surfactant brine COUCSI

Core CDS1 was completely saturated with crude oil and then aged at 75°C for 10 days. The core was then immersed in 3,000 ppm T9-18 surfactant solution. The end pressure increased but oil production was not observed until after 25 *days*. The pressure continued to rise and was about 0.73 *kPa* and the oil recovery was 0.325 OOIP when the imbibition front reached the end of the core (Fig. 9.1-15). The oil was produced as an emulsion.

Imbibition of 3000ppm surfactant solution after frontal flow

The end pressure (P_{end}) started to fall after the front reached the end of core. P_{end} gradually dropped to 0.4 *kPa* over the next 8 *days* and then remained at about 0.4 *kPa* for 51 *days*. The final oil recovery was 42.4% OOIP. This corresponds to 5.4 % OOIP extra oil recovery compared to the brine/crude oil recovery obtained for Core CL2.

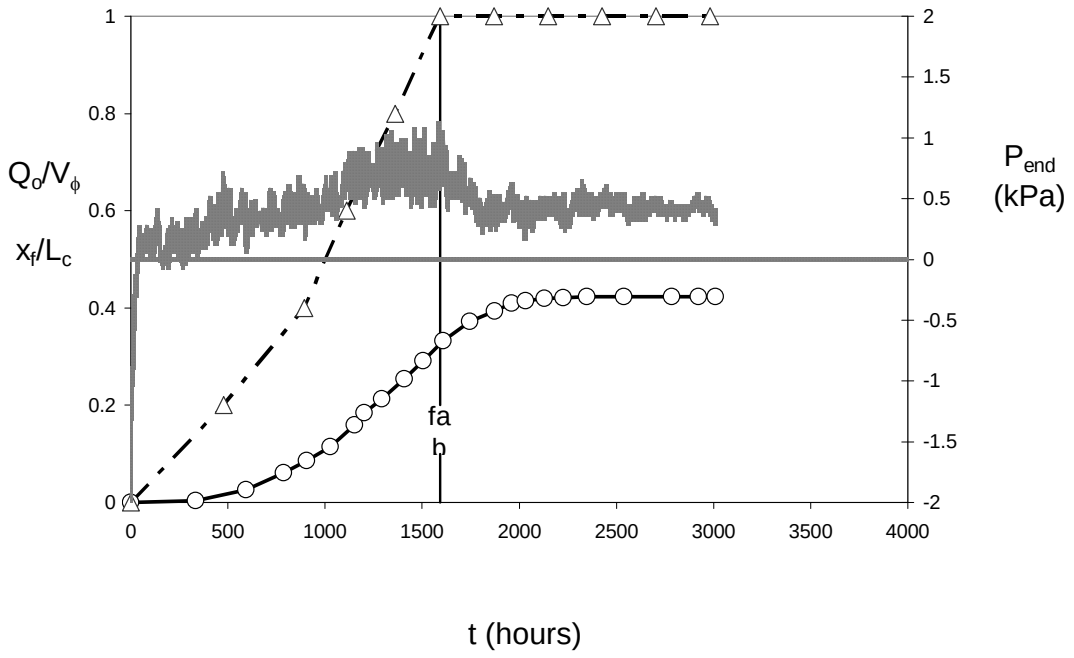

Fig. 9.1-15 Performances of COUCSI of surfactant solution in core CDS1

The measured k_{rw} was 0.0049 as compared to 0.048 for brine in test HC4 (0.991 μm^2) with aged Cottonwood crude oil. The open face of the core was cut away to leave a core of 3.684 cm in length. The measured k_{rw} for the shortened core was 0.005, showing that the increased resistance was not related to blocking at the core face.

Table 9.1-3. Core properties, oil recovery, and end pressure

EXPERIMENT	CORE	d (cm)	L_c (cm)	φ (%)	K (μm^2)	R at fab	R after fab	Pend at fab (kPa)	Max Pend after fab (kPa)
COUCSI (brine)	**CL2**	3.775	6.369	17.2	0.072	0.315	0.370	0.246	0.246
Surf. COUCSI	**CDS1**	3.771	6.352	17.2	0.071	0.325	0.424	0.73	0.73

Table of measured variables

Table 9.1-4 Oil permeability, water permeability, relative permeability and interfacial tension between oil and water solution from the core outlet

EXPERIMENT	CORE	d (cm)	L_c (cm)	φ (%)	K (μm^2)	ppm of surf (ppm)	Koe	Kwe	krw At Sor	IFT for produced water (mN/m)
COUCSI	**00a**	3.755	6.51	17.3	0.072	0		0.528		
	00a	3.755	6.51	17.3	0.072	1000		0.46		
COUCSI	**NS1**	3.797	6.000	17.1	0.065	0				
Surf. COUCSI	**IS1**	3.788	6.674	17.2	0.071	3000				
follows	**IS2**	3.781	6.686	17.2	0.07	3000			0.008	14.25
COUCSI										
Surf. COUCSI	**DS1**	3.786	6.531	17.2	0.07	3000				
	DS2	3.785	6.521	17.2	0.071	3000			0.008	17.06
Surf. COUCSI	**IS3**	3.749	6.489	17.0	0.065	1000	0.743		0.009	
follows	**IS4**	3.744	6.454	17.0	0.065	1000	0.744		0.012	
COUCSI										
Surf. COUCSI	**DS3**	3.748	6.455	17.1	0.067	1000	0.73		0.012	
	DS4	3.746	6.510	17.0	0.071	1000	0.72		0.011	
COUCSI	**CL2**	3.775	6.369	17.2	0.072	0				
Surf. COUCSI	**CDS1**	3.771	6.352	17.2	0.071	3000			0.0049	

Preliminary analysis of the effect of adding surfactant during counter-current spontaneous imbibition experiments.

Introduction

Although the imbibition process, especially with surfactant solution, is very complicated, by making the approximations that (a) there is a frontal displacement and (b) the saturation behind the front is constant, a simple analytical solution is possible. This assumption enables the analysis of some countercurrent spontaneous imbibition experiments in which surfactant was added to the invading brine. The rate of imbibition speeds up considerably after the addition of the surfactant. On the assumption that the surfactant had reduced the capillary back pressure at the open face the magnitude of the capillary back pressure could be estimated. During the conventional imbibition phase, the back pressure is about one quarter to one third of the actual capillary pressure driving imbibition, and is consequently a significant variable. Furthermore, if the pressure at the dead end of the core is measured as well as the rate change in imbibition, the capillary pressure at the imbibition front can be inferred.

Frontal Imbibition. General

In simulation of one-dimensional counter-current imbibition calculations, the front and its small amount of dispersed imbibition can be represented by a self-similar front (Li *et al.,* 2003). The self-similar front is a consequence of the mathematical formulation of counter-current imbibition. Conventionally, it is assumed that there are three primary functions, all of saturation; there is the

capillary pressure, and two relative permeabilities, one for the wetting phase and the other for the non-wetting phase. The consequence is that, for a thin slice of core, if the relative permeability for one phase is fixed, then there is only a single value for the relative permeability of the other phase. Added to this is the fact that, for pure counter-current spontaneous imbibition, the flow of one phase through the slice is exactly equaled by the reverse flow of the other phase, and both these are over the same area.

As a limiting case we could imagine that ALL of the saturation change takes place at the saturation front where the saturation makes a step change from S_{wi} (the initial wetting phase saturation to S_{wf} (the wetting phase saturation at the front). The assumption means that the saturation behind the front is constant at S_{wf}. Behind the front therefore, the relative permeabilities of each of the two phases are also constant. Also, because there is no change in saturation behind the front, the flow of wetting phase (q_{w}) at one instant in time is invariant with distance from the open face. Up to the front, the flow of non-wetting phase (q_{nw}) is also invariant. It must be stressed that this is an approximation, but it may be realistic for some cases of imbibition. Darcy's law gives the two flows:

$$q_{\mathrm{w}} = -\frac{Kk_{\mathrm{rw}}A}{\mu_{\mathrm{w}}}\frac{\partial P_{\mathrm{w}}}{\partial x} \qquad 9.1\text{-}1$$

$$q_{\mathrm{nw}} = -\frac{Kk_{\mathrm{rnw}}A}{\mu_{\mathrm{nw}}}\frac{\partial P_{\mathrm{nw}}}{\partial x} \qquad 9.1\text{-}2$$

where K is the permeability, k_{rw} and k_{rnw} are the relative permeabilities to the respective phases, μ_{w} and μ_{nw} are the respective viscosities, A is the area and x is a distance. The capillary pressure P_{c} is the difference between the pressure in the non-wetting phase (P_{nw}) and the pressure in the wetting phase (P_{w}).

$$P_{\mathrm{c}} = P_{\mathrm{nw}} - P_{\mathrm{w}} \qquad 9.1\text{-}3$$

and flow continuity gives:

$$q_{\mathrm{w}} = -q_{\mathrm{nw}} \qquad 9.1\text{-}4$$

Combining equations 1 to 4 gives:

$$q_{\mathrm{w}} = \frac{Kk_{\mathrm{rw}}k_{\mathrm{rnw}}A}{\mu_{\mathrm{w}}k_{\mathrm{rnw}} + \mu_{\mathrm{nw}}k_{\mathrm{rw}}}\frac{\partial P_{\mathrm{c}}}{\partial x} \qquad 9.1\text{-}5$$

Because the saturation has been assumed to be constant behind the front, a large part of this equation will be constant. Let M be a mobility factor and let

$$M = \frac{k_{rw} k_{rnw}}{\mu_w k_{rnw} + \mu_{nw} k_{rw}} \qquad 9.1\text{-}6$$

For constant saturation the relative permeabilities have to be constant, also the viscosities, consequently the factor *M* will be constant and so, behind the front

$$q_w = KMA \frac{\partial P_c}{\partial x} \qquad 9.1\text{-}7$$

It should be noted that for the assumption that the saturation behind the front is constant to be approximately true, P_c has to be able to vary a lot (so as to be able to drive the flows) for a small change in S_w. i.e. the gradient of the capillary pressure curve with saturation has to be steep.

Because the mobility factor *M* is constant for the flows behind the wetting front Eq. 9.1-7 can be integrated between the open face of the core and the front. For one-dimensional imbibition, the area, *A,* will be a constant

The flow of wetting phase arriving at the front advances the position of the front. A mass balance gives

$$\frac{dx_f}{dt} = \frac{q_w}{\varphi A(S_{wf} - S_{wi})} \qquad 9.1\text{-}8$$

where x_f is the distance of the front from the open face.

For one dimensional counter-current imbibition q_w, *M* and *A* do not vary with position *x* and so the equation 7 can be integrated between the open face and the front to give:

$$q_w(x_f - 0) = KMA(P_{cf} - P_{co}) \qquad 9.1\text{-}9$$

P_{cf} is the capillary pressure difference at the front. P_{co} is the capillary pressure difference at the open face. At the open face the pressure in the wetting phase is zero but the pressure in the non-wetting phase is not zero. It is not zero because non-wetting phase has to be bubbled from the rock into the wetting phase. Substituting for q_w using Eq. 9.1-9 in Eq. 9.1-8 and integrating between the open face and the distance of the front, x_f, gives:

$$x_f^2 = \frac{2KM(P_{cf} - P_{co})}{\varphi(S_{wf} - S_{wi})} t \qquad 9.1\text{-}10$$

Equation 9.1-10 contains a difference in capillary pressures $(P_{cf} - P_{co})$. The capillary pressure at the front (P_{cf}) is mainly produced by the smaller pores and the capillary pressure at the open face (P_{co}) is mainly produced by the larger pores. The difference between them is thus related to the spread of the pore size distribution. However, when surfactant is present at the open face but not at the front then the difference in pressure driving imbibition depends on *both* the difference in effective pore size and in the difference in interfacial tension. Let us consider regimes when where $(P_{cf} - P_{co})$ is constant. We will consider that the pore size at the imbibition front remains constant as does the larger pore size at the open face. Then, either the interfacial tension is the same in both places or it is different and the difference is constant. Both circumstances make $(P_{cf} - P_{co})$ constant. Also, x_f equals $L_{core}R_{scaled}$ where R_{scaled} is an intermediate volume of oil recovered divided by the final volume of oil recovered. This makes x_f proportional to recovery. Consequently, provided that the group $\frac{2KM(P_{cf} - P_{co})}{\phi(S_{wf} - S_{wi})}$ is constant, a plot of (*recovery*)^2 versus time should be a straight line. This is demonstrated in Fig. 9.1-16 which shows the results for imbibition of brine (test NS1) are very close to linear.

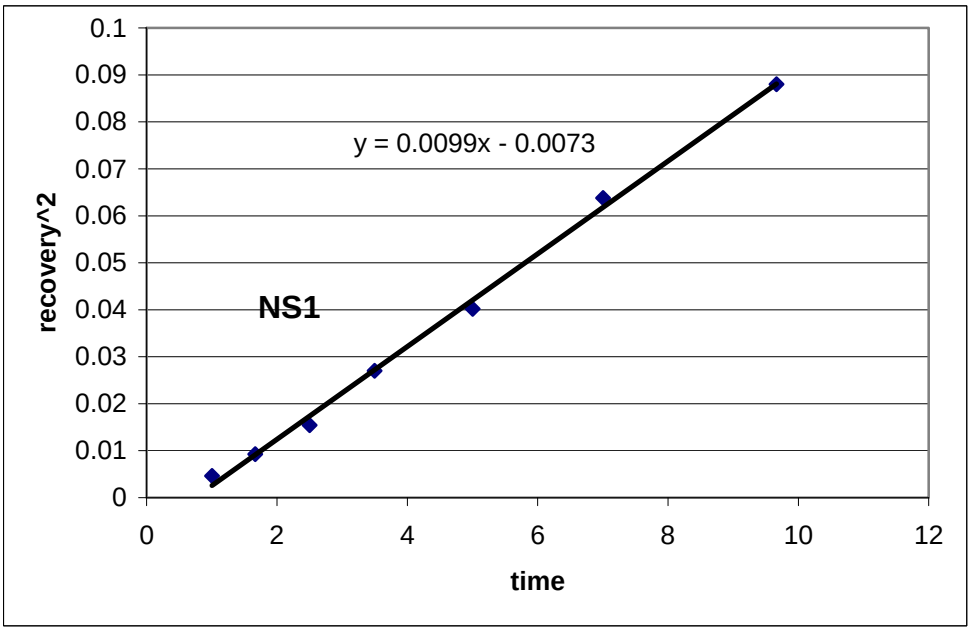

Figure 9.1-16 Results with no surfactant present plotted to show the dependence on (recovery)^2 .

Now consider an experiment in which spontaneous imbibition is started with brine. In Stage 1 of the experiment, normal linear countercurrent imbibition takes place. Next, in Stage 2 the core is immersed in surfactant solution. The only variable that changes between the two Stages is that in Stage 2 the capillary pressure at the open face (P_{co}) is reduced, because of the action of the surfactant, to a fraction, *f*, of its previous value. Consequently, if we plot x_f^2 versus *t* for Stages 1 and 2 of the experiment, both should give straight lines, the equations for which are

$$x_{f,1}^2 = \frac{2KM\left(P_{cf} - P_{co}\right)}{\varphi\left(S_{wf} - S_{wi}\right)}\left(t - t_0\right) \qquad 9.1\text{-}11$$

$$x_{f,2}^2 = \frac{2KM\left(P_{cf} - fP_{co}\right)}{\varphi\left(S_{wf} - S_{wi}\right)}\left(t - t_s\right) \qquad 9.1\text{-}12$$

The reason for using these variables is that if we take the ratio of the gradients of these lines, the times cancel out, as do most of the other parameters to give

$$\frac{G_1}{G_2} = \frac{P_{cf} - P_{co}}{P_{cf} - fP_{co}} \qquad 9.1\text{-}13$$

which gives

$$P_{cf}\left(G_1 - G_2\right) = P_{co}\left(fG_1 - G_2\right) \quad 14$$

and

$$\frac{P_{co}}{P_{cf}} = \frac{G_2 - G_1}{G_2 - fG_1} \qquad 9.1\text{-}15$$

Figure 9.1-17 shows the first set of results using surfactant plotted as the square of the recovery (recovery is proportional to x_f). .

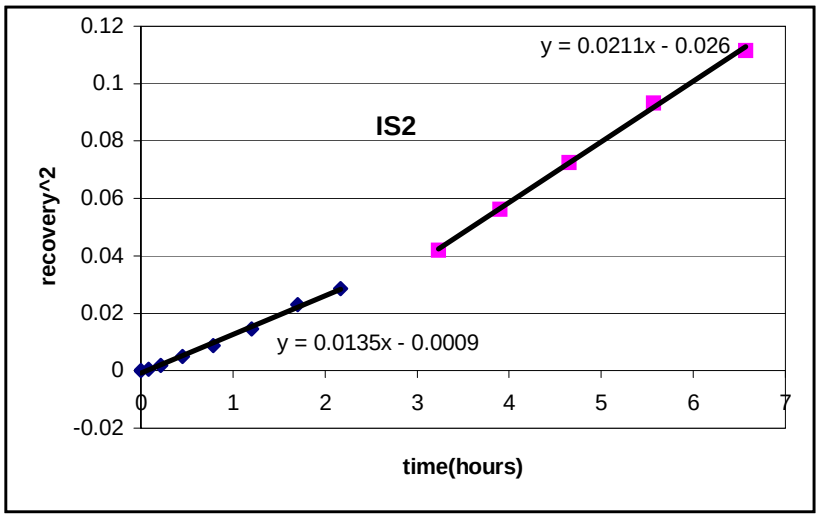

Figure 9.1-17 for IS2 data where the brine was changed to 3000 ppm surfactant solution brine part way through the imbibition process.

The gradients from this graph gives

$$\frac{P_{co}}{P_{cf}} = \frac{G_2 - G_1}{G_2 - fG_1} = \frac{0.0211 - 0.0135}{0.0211 - f\,0.0135} \quad 16$$

The ratio of the back pressure to the front pressure depends on the value assumed for *f*. However, provided *f* is reduced to less than 0.5, then its magnitude makes only a small difference to the pressure ratio, see Fig. 9.1-18

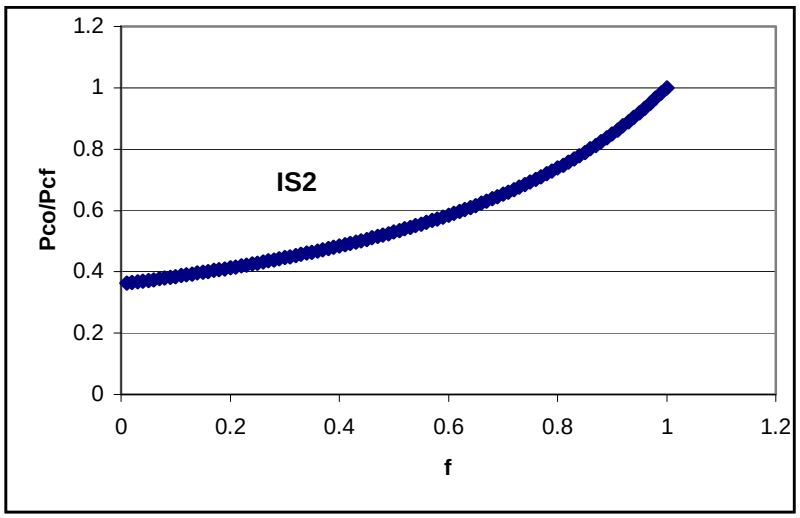

Fig 9.1-18 Dependence on the ratio of the back pressure to the front pressure to the fractional interfacial tension reduction.

So, for the Experiment IS2, the capillary back pressure at the open face is almost one third of the capillary pressure actually driving the displacement if f is zero and about one half if the interfacial tension is reduced to 50% of its initial value by the surfactant. . If we assume that f is given by the ratio of the interfacial tension after the addition of surfactant to the initial interfacial tension then f is about 0.05 and in experiment IS2 the ratio P_{co}/P_{cf} is 0.372 .

For experiment IS1 the change in the rate of production is not as great (Fig 9.1-19).

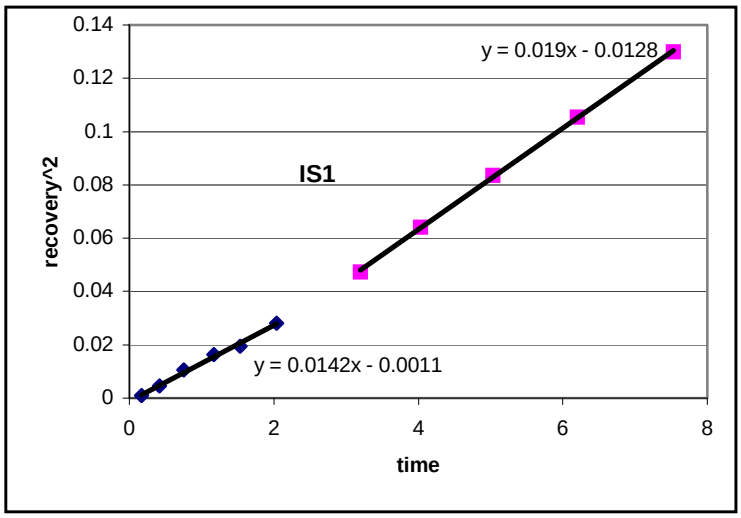

Figure 9.1-19 The results for IS1.

$$\frac{P_{\mathrm{co}}}{P_{\mathrm{cf}}}=\frac{G_2-G_1}{G_2-fG_1}=\frac{0.019-0.0142}{0.019-f\,0.0142}$$

Again, taking a value of 0.05 for f gives $P_{\mathrm{co}}/P_{\mathrm{cf}}$ as 0.262.

For IS2 we also have sensible values (constant, at least) for the dead end pressure before and after the addition of surfactant. In experiment IS1, there was no stable pressure after the switch to surfactant. To use the dead end pressures we need to go back to the basic equation for flow of the non wetting phase.

$$q_{\mathrm{nw}}=-\frac{Kk_{\mathrm{rnw}}A}{\mu_{\mathrm{nw}}}\frac{\partial P_{\mathrm{nw}}}{\partial x} \qquad 9.1\text{-}17$$

If we assume piston-like displacement with a constant saturation behind the front, then the flow of wetting phase is constant everywhere behind the front. As a consequence, so is the flow of non-wetting phase, and Eqn 17 can be integrated to give

$$q_{\mathrm{nw}}\left[x\right]_{front}^{openface}=-\frac{Kk_{\mathrm{rnw}}A}{\mu_{\mathrm{nw}}}\left[P_{\mathrm{nw}}\right]_{front}^{openface} \qquad 9.1\text{-}18$$

which gives, for Stage 1,

$$q_{\mathrm{nw1}}\left[0-x_{\mathrm{f},1}\right]=-\frac{Kk_{\mathrm{rnw}}A}{\mu_{\mathrm{nw}}}\left[P_{\mathrm{BP}}-P_{\mathrm{DE1}}\right] \qquad 9.1\text{-}19$$

The mass balance equation for the advance of the front is given by

$$\frac{\mathrm{d}x_{\mathrm{f}}}{\mathrm{d}t}=\frac{q_{\mathrm{w}}}{\varphi A\left(S_{\mathrm{wf}}-S_{\mathrm{wi}}\right)} \qquad 9.1\text{-}20$$

and, because the flows of wetting and non-wetting phases are equal and opposite, this equation can be used to eliminate the flow from Eqn(19), allowing it to be integrated.

$$-\varphi A\left(S_{\mathrm{wf}}-S_{\mathrm{wi}}\right)\left[0-x_{\mathrm{f},1}\right]\mathrm{d}x_{\mathrm{f},1}=-\frac{Kk_{\mathrm{rnw}}A}{\mu_{\mathrm{nw}}}\left[P_{\mathrm{BP}}-P_{\mathrm{DE1}}\right]\mathrm{d}t \qquad 9.1\text{-}21$$

$$x_{f,1}^2=-\frac{Kk_{\mathrm{rnw}}}{\mu_{\mathrm{nw}}\varphi\left(S_{\mathrm{wf}}-S_{\mathrm{wi}}\right)}\left[P_{\mathrm{BP}}-P_{\mathrm{DE1}}\right]\left(t-t_0\right) \qquad 9.1\text{-}22$$

There is a similar equation for the period (Stage 2) after the surfactant has been added and the back pressure at the open face reduced by the factor f,

$$x_{f,2}^2=-\frac{Kk_{\mathrm{rnw}}}{\mu_{\mathrm{nw}}\varphi\left(S_{\mathrm{wf}}-S_{\mathrm{wi}}\right)}\left[fP_{\mathrm{BP}}-P_{\mathrm{DE2}}\right]\left(t-t_s\right) \qquad 9.1\text{-}23$$

The gradients of these two equations are the same as before, giving’

$$\frac{G_1}{G_2} = \frac{P_{DE1} - P_{BP}}{P_{DE2} - fP_{BP}} \qquad 9.1\text{-}24$$

From above we also have

$$\frac{P_{co}}{P_{cf}} = \frac{G_2 - G_1}{G_2 - fG_1} \qquad 9.1\text{-}15$$

Also, because the pressure in the wetting phase is defined as zero at the open face

$$P_{co} = P_{BP} \qquad 25$$

Combining 24, 15 and 25 gives

$$G_1 P_{DE2} - G_2 P_{DE1} = P_{BP}\left(fG_1 - G_2\right) = P_{cf}\left(G_2 - G_1\right) \qquad 9.1\text{-}26$$

Solving for P_{cf} gives

$$P_{cf} = \frac{G_2 P_{DE1} - G_1 P_{DE2}}{G_2 - G_1} \qquad 9.1\text{-}27$$

which, it should be noted, **is independent of the value assumed for *f*.** The gradients have been determined above and the two dead end pressures are about 7 kPa and about 4.2 making

$$P_{cf} = \frac{G_2 P_{DE1} - G_1 P_{DE2}}{G_2 - G_1} = \frac{0.0211 \times 7 - 0.0135 \times 4.2}{0.0211 - 0.0135} = 11.97 kPa \qquad 9.1\text{-}28$$

This is close to the front pressure measured in separate restricted imbibition experiments using the same rock and fluids. If P_{cf} is 12 *kPa* then P_{co} before the switch to surfactant is about 4.5*kPa.*

9.2 Effect of Sodium Sulfate and Surfactant on Oil Recovery from Dolomite by Spontaneous Imbibition.

Introduction

Methods of improved recovery by enhanced imbibition either through use of surfactants or by manipulation of brine composition or some combination of both are being investigated. Austad and co-investigators (Strand *et al*., 2003) recently reported that the concentration of sodium sulphate had a major impact on oil recovery from chalk when cationic surfactants were used to promote spontaneous imbibition at 40ºC. The effect of surfactant and Na_2SO_4 on enhanced oil recovery through spontaneous imbibition is reported here for crude oil/brine/rock combinations from a dolomite reservoir.

Experimental

Rocks

Rock samples are dolomite, taken from depth ranging from 4378 to 4392ft, from San Andres formation of Fuhrman-Mascho Field of Permian Basin, Texas. The rock properties are listed in Table 9.3-1.

Crude oil
San Andres formation crude oil has viscosity of 9.9 cP at reservoir temperature, 40ºC, with density of 0.8920 g/cm^3 at 20ºC. The crude oil contains 1.0% asphaltenes. The interfacial tension between the crude oil and seawater is 20.3 mN/m at 40ºC.

Brines
Two types of brine, simulated seawater and San Andres formation brine, are used in the tests, with the total dissolved solids (TDS) of 36.779 and 75.788 g/L, respectively (see Table 9.2-2).

Surfactants
One nonionic surfactant, TOMADOL's 91-8—RO-$(CH_2CH_2O)_8H$, R = C_{9-11}, was tested with concentration of 3000 ppm.

Imbibition
In initial tests, dry rock samples were directly saturated with the crude oil to obtain baseline results for an initial water saturation of zero. The oil-saturated cores were then aged in sealed metal cells filled with the parent crude for ten days at 40ºC.

Oil recovery tests started with spontaneous imbibition of seawater at 40ºC. After oil recovery ceased, the samples were switched to surfactant solution. Oil recovery in percentage of the original oil in place was recorded against time.

Results and discussion
Oil recovery from spontaneous imbibition of brine
Results of oil recovery through spontaneous imbibition of seawater are plotted in Figs. 9.2-1a and b, and listed in Table 9.2-3 for the ten cores. There is a trend for lower permeability cores (less than 2 md) to have higher oil recovery (higher than 30% OOIP) than higher permeability ones (greater than 40 md, less than 7% OOIP), except for Core 4384.9d (82.4 md, 18.8% OOIP) and 438.88c (1.6 md, 6.2% OOIP). This is in line with the likely original mixed wettability condition of the reservoir whereby the lower permeability regions, as represented by core plugs, tend to be more water wet than the higher permeability regions.

Effect of T91-8 and Na_2SO_4 on enhanced oil recovery through spontaneous imbibition
At the termination of imbibition of seawater, the cores were transferred to surfactant solution prepared with simulated Fuhrman-Mascho formation brine with different concentrations of Na_2SO_4. The results are also plotted in Figs. 9.2-1a and b, and listed in Table 9.2-3. Overall, the nonionic surfactant T91-8 increases oil recovery from the dolomite rocks. Contrary to the results for imbibition of seawater, the higher permeability cores have higher incremental oil recovery (greater than 14% OOIP) from the surfactant action than the lower permeability ones (less than 10% OOIP), except for Core 4379.4c (47.3 md, which did not respond to surfactant), and 4378.8c (1.6md, 18.6% OOIP for the surfactant action). In contrast to the response reported for chalk, incremental oil recovery did not change systematically with increase of Na_2SO_4 concentration from 0 to 6280 ppm for the tested dolomite.

Table 9.2-1 Rock properties

Cores	D, cm	L, cm	K_g, md	ϕ, %
4378.9d	3.784	4.483	144	0.1384
4380b	2.511	5.880	131	0.1108
4380a	2.514	5.458	125	0.1061
4384.9d	2.518	5.469	82.4	0.1598
4379.4c	2.512	4.803	47.3	0.0810
4378.8c	2.528	4.643	1.6	0.1384
4384.6d	2.518	5.140	1.6	0.1308
4384.7c	2.516	5.236	1.4	0.1455
4384.7d	2.519	5.761	1.3	0.1521
4384.6c	2.523	5.833	0.9	0.1397

Table9.2-2 Synthetic brine composition (g/L)

Composition	**NaCl**	**KCl**	**$CaCl_2$**	**$MgCl_2$**	**Na_2SO_4**	**TDS**
seawater	**28**	**0.935**	**2.379**	**5.365**	**-**	**36.779**
San Andres Res.	**61.773**	**-**	**5.944**	**1.787**	**6.280**	**75.784**

Table 9.2-3 Results for oil recovery for imbibition of brine followed by surfactant solution

Cores	K_g, md	ϕ, %	OR for imb. of water, %OOIP	Na_2SO_4, ppm	Surfactant	ΔOR for imb. of surfactant, %OOIP
4378.9d	144	0.1384	5.9	0	T91-8	14.0
4380b	131	0.1108	5.9	4750	T91-8	16.1
4380a	125	0.1061	6.9	1500	T91-8	14.9
4384.9d	82.4	0.1598	18.8	3150	T91-8	16.1
4379.4c	47.3	0.0810	4.6	6280	T91-8	0
4378.8c	1.6	0.1384	6.2	3150	T91-8	18.6
4384.6d	1.6	0.1308	32.5	4750	T91-8	1.5
4384.7c	1.4	0.1455	37.5	6280	T91-8	5.3
4384.7d	1.3	0.1521	35.6	0	T91-8	9.2
4384.6c	0.9	0.1397	39.1	1500	T91-8	6.2

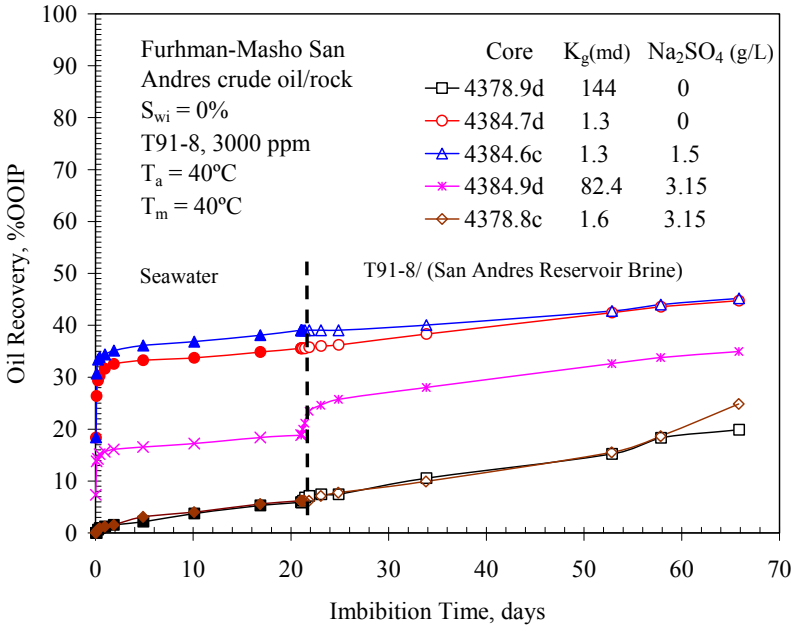

(a)

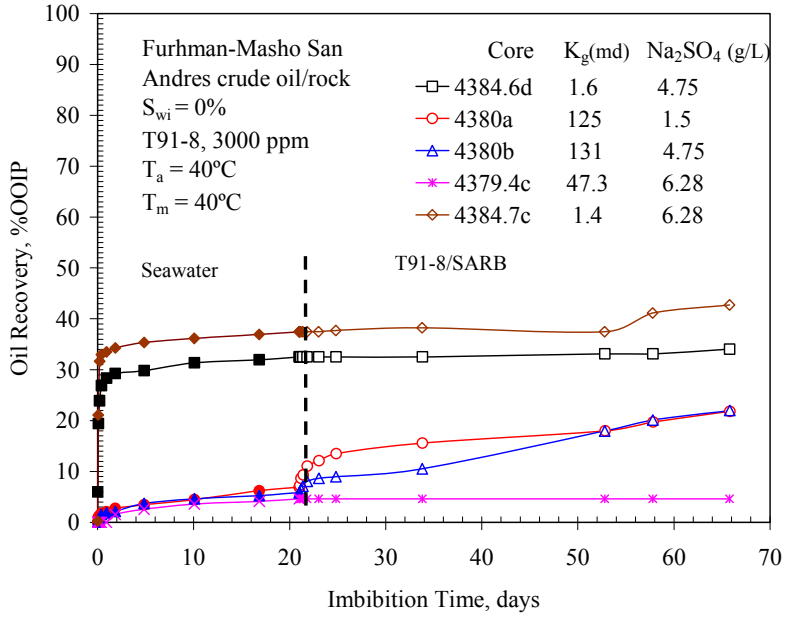

(b)

Fig. 9.2-1. Effect of T91-8 and Na_2SO_4 on enhanced oil recovery through spontaneous imbibition for San Andres dolomites (solid symbols correspond to initial imbibition of sea water)

9.3 Effect of Low Salinity on Oil Recovery from Limestone.

Introduction

Numerous examples of increase in oil recovery by waterflooding with decrease in salinity have been reported previously. Improved oil recovery by spontaneous imbibition with decrease in salinity have also been observed (Tang and Morrow,). Recovery of crude oil by spontaneous imbibition into Edwards GC limestone was tested in the present work. Five cores were selected that had comparable permeability and porosity were selected. (see Table 9.3-1) The basic brine was seawater with the composition listed in Table 9.3-1. Imbibition was also tested for brines of 1/10, 1/20, 1/50, and 1/100 dilution. Even though the initial brine saturations were only about 7%, after aging with an asphaltic crude oil, the Edwards carbonate exhibited strong imbibition of brine at elevated temperature (see Fig. 9.3-1 (a)).

Experiments

The imbibition results for Edwards carbonate show no consistent trend with respect to salinity. Extent and rate of recovery were only slightly higher or lower than the base case given by seawater. The spread in the data is somewhat reduced after compensating for differences in permeability and porosity through correlation of the data. (see Fig 9.3-1). It is concluded that for the crude oil/brine/rock combination that was tested, there is no effect of brine dilution on recovery by spontaneous imbibition. Further work on carbonates was therefore tuned to improved recovery by addition of surfactant to the imbibing phase.

Discussion

Although no generalizations can be drawn with certainty from these results as to the behavior of other carbonate rock/crude oil combinations, they do provide counter examples to the common observation that carbonates tend to be oil wet.

Table 9.3-1 Properties of Edwards Limestone GC Cores used in Tests on Effect of Salinity on Imbibition

Core	D (in)	L (in)	Φ	k_g (mD)
EGC1	1.49	2.72	20.97	32.75
EGC2	1.50	2.67	21.36	34.47
EGC3	1.50	2.64	20.28	27.43
EGC5	1.50	2.62	21.27	34.31
EGC11	1.49	2.72	20.16	30.94

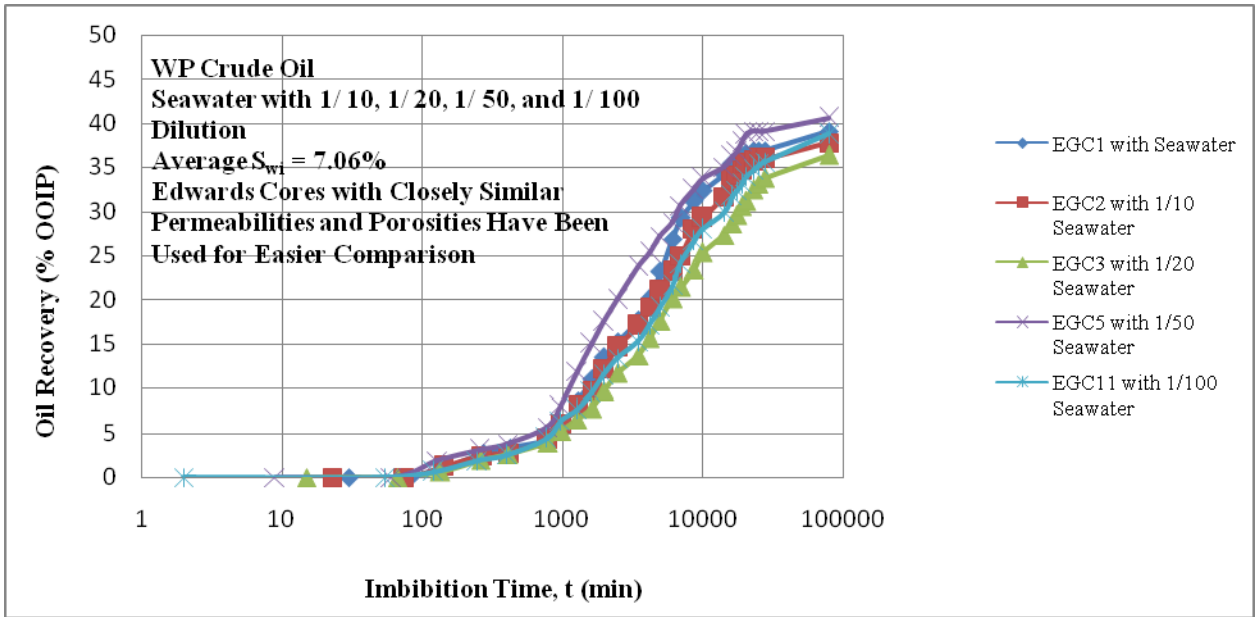

(a)

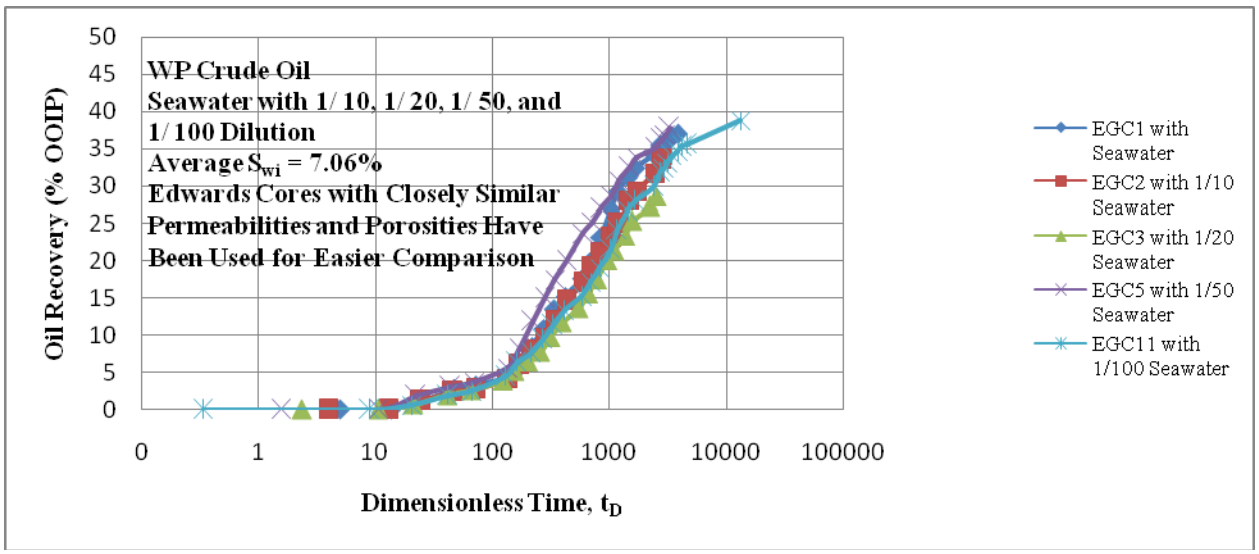

(b)

Fig. 9.3-1 Spontaneous imbibition data of Edwards GC using WP crude oil with initial water saturation and varying the invading aqueous phase brine salinity.

9.4 Second Stage Enhanced Imbibition by Surfactant Solution

Introduction

Two outcrop carbonate rocks, Edwards GC (Garden City) limestone and Whitestone Upper Zone (UZ) limestone were tested for enhanced imbibition with surfactant solutions using a crude oil designated as WP and seawater as the base oleic/ aqueous phases. COUCSI (counter current spontaneous imbibition) was first run using seawater or an aqueous phase of the same ionic strength and composition of seawater with varied viscosity by addition of glycerol. A surfactant concentration of 3000 ppm was used for all of the prepared surfactant solutions. 1 wt. % sodium metaborate was added to the anionic surfactants to increase the pH of the solutions in order to inhibit adsorption of anionic surfactants on positively charged carbonate rock surfaces.

The choice of surfactants were based partly on a previous study (Xie et al., 2005). The surfactants were first tested for precipitation at room temperature and at 75 ^{0}C, the temperature at which all of the experiments were performed. All of the chosen surfactant solutions showed no precipitation at either temperature. At least two surfactants from the nonionic, cationic, anionic, and amphoteric groups were tested using Edwards GC and Whitestone UZ cores. The cores were tested with no initial water as base case comparisons of the action of surfactants for the different types of limestone. Later tests were performed with an initial water saturation using Tomadol 91-8, which showed the highest incremental oil recovery for both Edwards GC and Whitestone UZ limestones.

Materials and Experimental Methods

Materials

Cores

Edwards GC (Garden City) Limestone

The Edwards GC is a limestone also known as West Texas Crème, Cedar Hill Crème, and Valencia Ivory. These core blocks are quarried from the Edwards formation near Garden City, Texas. It is a grainstone which contains well-sorted fossils cemented by sparry calcite (Tie, 2006). Cylindrical shaped cores were cut with diameters of 3.81 cm and approximate lengths of 6.35 cm. After cutting the cores, they were washed, oven dried at 100 ^{0}C for about a day, and then dried in a dessicator at ambient conditions. The nitrogen gas permeabilities of these cores were measured using 300 psi confining pressure. The gas permeabilities varied from 17 to 47 md. The porosities of the cores were obtained from the weight of the dry and fully saturated sample. Porosities varied from 20 to 25%.

Whitestone UZ Limestone

The Whitestone Upper Zone limestone, also known as the Texas Crème limestone, was quarried from the Lower Cretaceous Walnut Formation, Texas. It is also a grainstone containing well-sorted fossils cemented by sparry calcite similar to Edwards GC, but is much more heterogeneous in permeability and porosity even within a single core block (Tie, 2006). These cores were cut and prepared for experiments using the same methods as for the Edwards GC described above. The gas permeabilites varied from about 8 to 45 md and the porosities varied from 21 to 28%.

Aqueous Phases

Synthetic seawater was used as the brine with 35.5875 g/ L of Total Dissolved Solids (TDS) with the composition given by Fischer et al., 2006 shown in Table 9.4-1.

Table 9.4-1 Synthetic seawater composition

Component	(g/ L)
NaCl	28.0000
KCl	0.9350
$MgCl_2$	5.3625
$CaCl_2$	1.1900
NaN_3	0.1000
TDS	35.5875

In some tests, glycerol was used to viscosify the aqueous phase. The ionic strength of the mixtures was held equal to seawater for the brine/glycerol mixtures. Glycerol is a trihydric aliphatic alcohol which is an odorless and colorless liquid with a 92.09 molecular weight. The density of glycerol is 1.261 g/cm3 and the viscosity is 1650 cP at 20 0C. An advantage of glycerol is that it is completely soluble in water, but not in hydrocarbons. The brine and glycerol mixtures were prepared based on weight percent. Five compositions were tested: seawater; seawater with 40% glycerol; 60% glycerol; 80% glycerol; and 90% glycerol. The brine and glycerol mixture properties are listed in Table 9.4-2.

Table 9.4-2 Properties of the aqueous/ oleic phases at 22 ^{0}C and at 75 ^{0}C

Aqueous/ Oleic Phase	ρ (g/ cm^3)	μ at 22 ^{0}C (cP)	μ at 75 ^{0}C (cP)
Seawater	1.023	1.1	0.30
40 wt.% Glycerol	1.120	4.1	1.05
60 wt.% Glycerol	1.173	12.1	1.20
80 wt.% Glycerol	1.226	65.8	9.00
90 wt.% Glycerol	1.244	207.6	11.00
WP Crude Oil	0.931	274.5	

All of the tested surfactants passed a preliminary screening test for precipitation at room temperature or at 75 ^{0}C. The surfactants used for enhanced oil recovery are listed in Table 9.4-3 for Edwards GC limestone and for Whitestone UZ limestone. The last two surfactants, Amphosol CG-50 and Petrostep CB, were only tested for Whitestone UZ limestone.

Table 9.4-3 Properties of the surfactants used for Edwards GC and Whitestone UZ limestone imbibition tests at 22 ^{0}C

Surfactant	μ_o (cp)	μ_{ap} (cp)	ρ_{ap} (g/ cm^3)	σ_{ow} (dyne/ cm)
Tomadol 91-8	274.5	1.2	1.022	2.85
Arquad C-50	274.5	1.2	1.021	0.77
Mirataine CB	274.5	1.1	1.023	3.49
Antarox L-64	274.5	1.1	1.023	5.49
Rhodacal	274.5	1.2	1.023	0.41
Rhodapex CD-128	274.5	1.1	1.022	2.78
Stepanquat 8358	274.5	1.4	1.020	0.20
Amphosol CG-50	274.5	1.1	1.023	3.18
Petrostep CB	274.5	2.9	1.021	0.10

Oleic Phase
An asphaltic crude oil was used for this study. The crude oil was first filtered and then vacuumed for three to four hours to remove light ends. Densities, viscosities of the oils, and the interfacial tensions with respect to the aqueous phases are included in Table 9.4-2.

Spontaneous Imbibition Procedure
The cores were vacuum saturated with the oleic phase to essentially constant weight for the experiments with zero initial water saturation. For the experiments with initial water saturation, the cores were first vacuum saturated with seawater and left for at least ten days to reach ionic equilibrium. Initial water saturation was established by the porous plate method and then the cores were vacuum saturated with the crude oil and aged at 75 ^{0}C for ten days. The initial water saturations for each rock type were all close to constant.

The cores were next placed in imbibition cells and covered with the desired aqueous phase. All of the experiments were performed at 75 ^{0}C. Oil recovery versus time was recorded until the oil recovery had stabilized or until the imbibition rate was extremely slow. Then the surfactant solutions were added to test for increase in oil recovery.

Results
Edwards GC Limestone
Edwards GC Limestone Surfactant Comparison
The Edwards GC results are shown below in the Figures 9.4-1 to 9.4-4 for nonionic, cationic, anionic, and amphoteric surfactants respectively. For each data set, the change from solid to open symbols indicates the change from imbibition of brine to imbibition of surfactant solution.

Table 9.4-4 Properties for Edwards GC cores used in tests with zero initial water saturation

Core	D (in)	L (in)	Φ	k_g (mD)
EGC11B	1.48	2.43	21.75	24.04
EGC12A	1.48	2.44	24.27	46.42
EGC12B	1.48	2.41	21.99	18.06
EGC13A	1.48	2.58	22.76	20.55
EGC13B	1.48	2.40	21.91	32.81
EGC14A	1.48	2.52	22.23	23.53
EGC14B	1.48	2.46	21.05	17.02

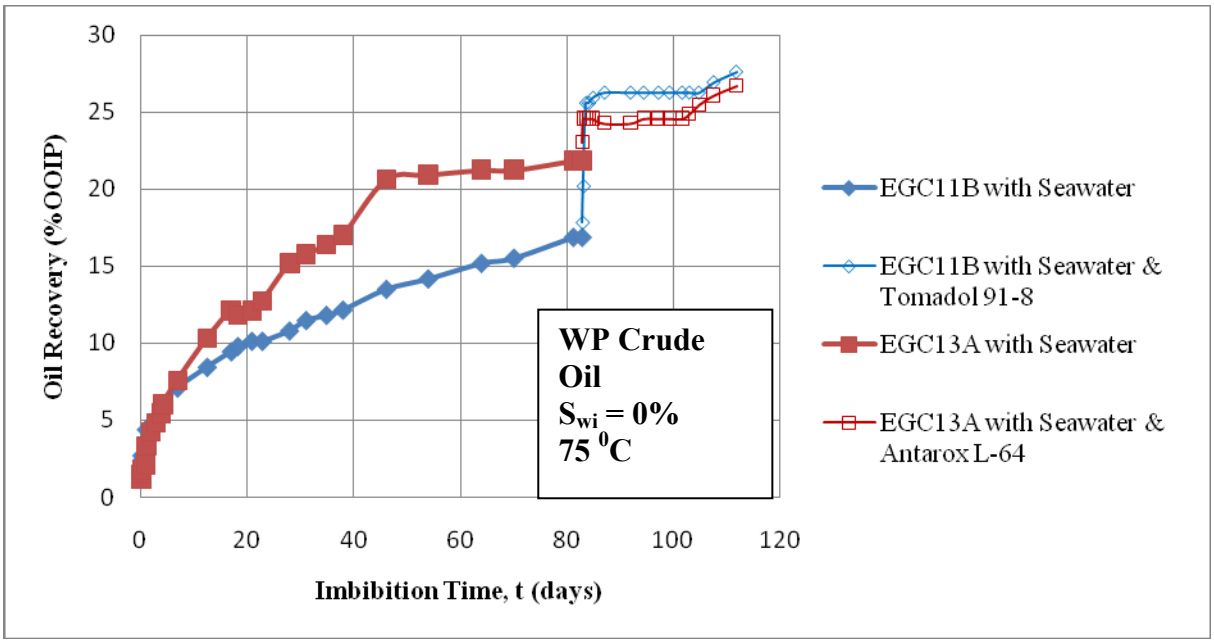

Fig 9.4-1 Recovery of WP crude oil from Edwards GC limestone by spontaneous imbibition of seawater followed by seawater plus nonionic surfactant.

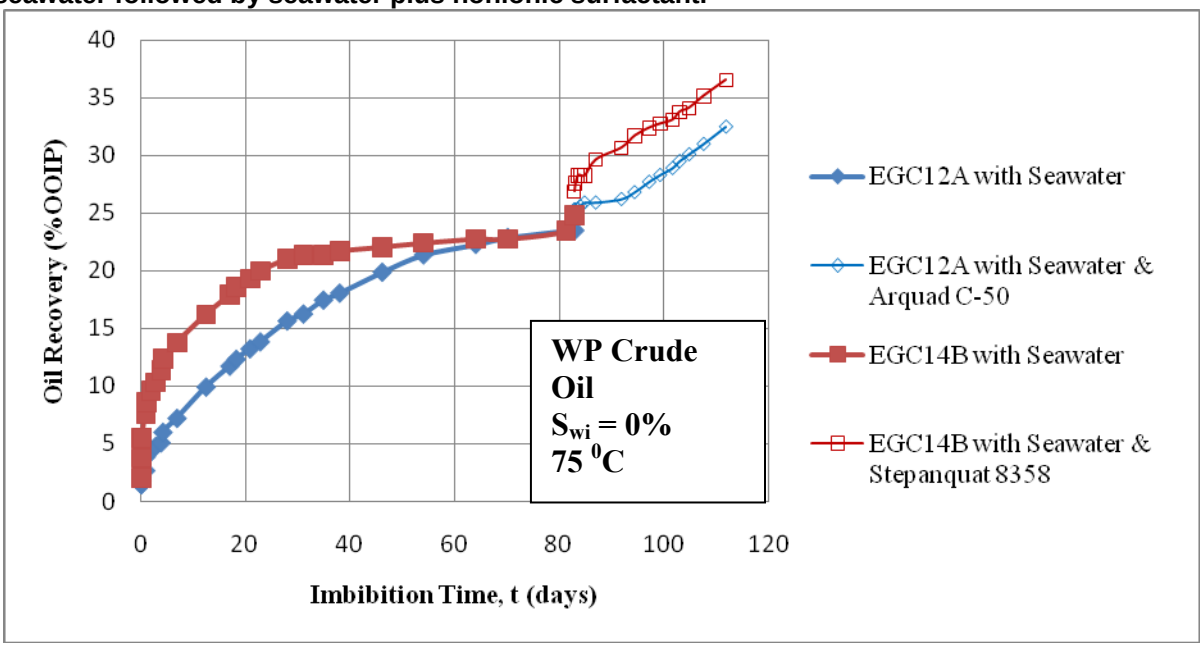

Fig 9.4-2 Recovery of WP crude oil from Edwards GC limestone by spontaneous imbibition of seawater followed by seawater plus cationic surfactant.

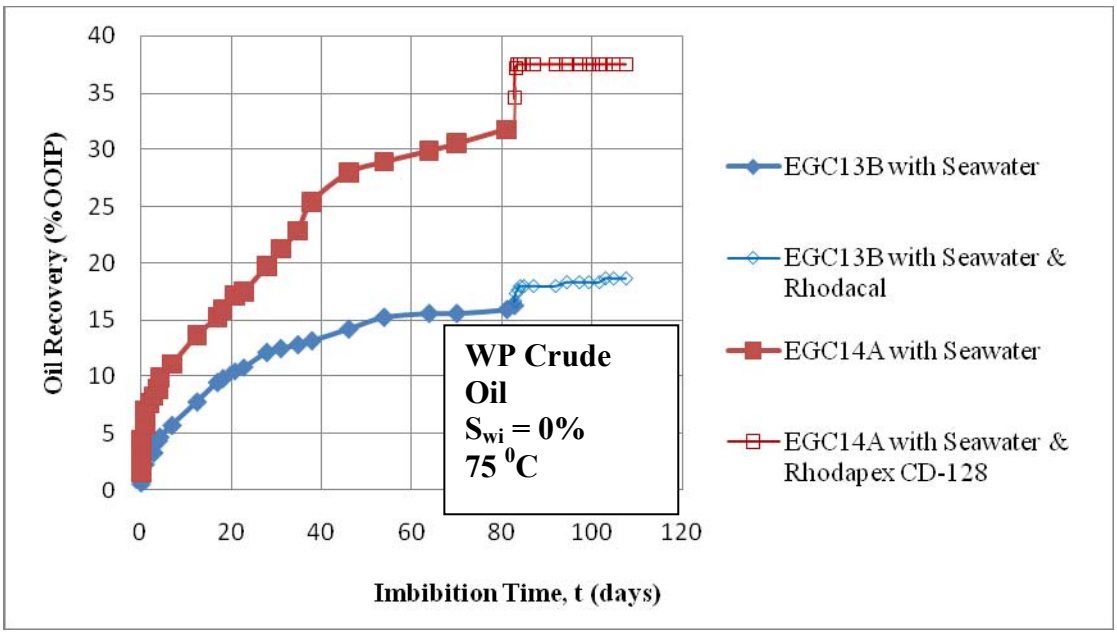

Fig 9.4-3 Recovery of WP crude oil from Edwards GC limestone by spontaneous imbibition of seawater followed by seawater plus anionic surfactant.

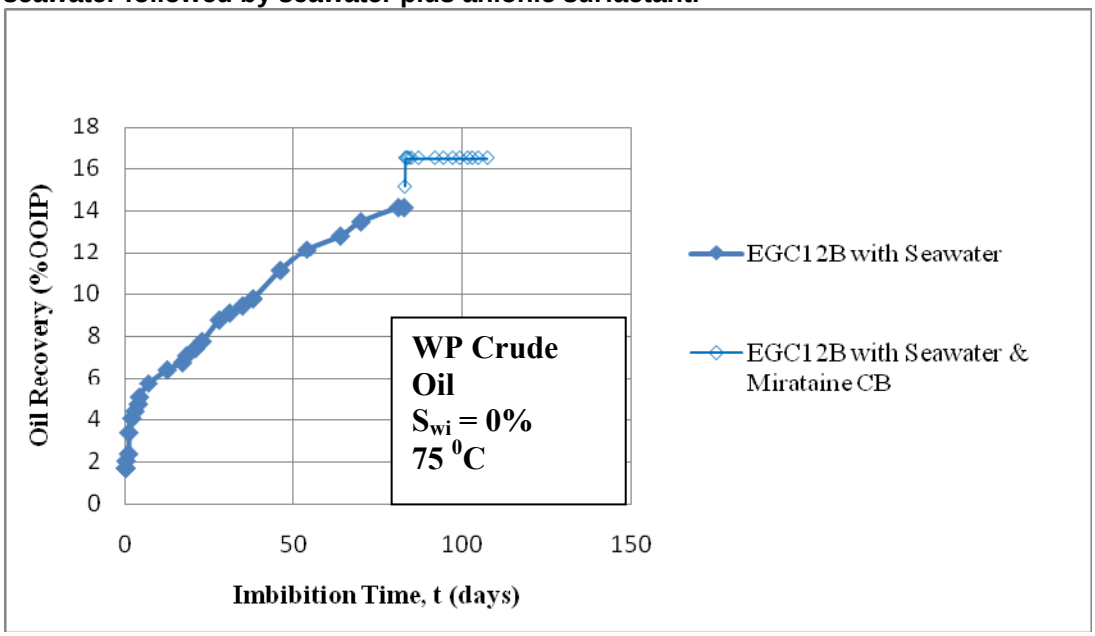

Fig 9.4-4 Recovery of WP crude oil from Edwards GC limestone by spontaneous imbibition of seawater followed by seawater plus amphoteric surfactant.

Edwards GC showed the highest and fastest incremental oil recovery for Tomadol 91-8, a nonionic surfactant. A cationic surfactant, Stepanquat 8358 showed the same increase in oil recovery, but the rate was slower. The lowest recoveries were given by an anionic surfactant, Rhodacal and an amphoteric surfactant, Miratine CB. The two cationic surfactants, Arquad C-50 and Stepanquat 8358 showed gradual increases in oil recovery with time. All the other surfactants exhibited rapid increases in oil recovery once the surfactant solutions were added. Even though the cationic surfactants showed promising results, they are generally not used in practice because of environmental concerns. Uncertaintainties in the comparisons exist because the final oil recoveries

from the initial imbibition of seawater for duplicate core plugs often showed differences, probably because of differences in core properties (see Fig. 9.4-1 to 9.4-4 plots of all Edwards GC imbibition curves before adding the surfactant).

Recovery for Cores Initially Saturated with Crude Oil by Imbibition of Viscosified Brine Followed by Seawater Plus Tomadol 91-8

In the following experiments, recovery of crude oil was compared for imbibition of seawater and a series of viscosified brines. Because of the recovery performance for Tomadol 91-8 exceeded that of all the other surfactants, the imbibition test was extended to a second stage by immersion of the cores in a 3000 ppm solution of Tomadol in seawater. Properties of the tested cores are listed in Table 9.4-5.

Table 9.4-5 Properties for Edwards GC cores used in seawater plus glycerol followed by seawater plus Tomadol 91-8 imbibition.

Core	D (in)	L (in)	Φ	k_g (mD)
EGC01A	1.48	2.51	23.47	26.57
EGC02A	1.48	2.47	23.94	33.68
EGC02B	1.48	2.54	20.48	17.03
EGC03A	1.48	2.51	22.94	23.18
EGC03B	1.48	2.44	23.55	36.17

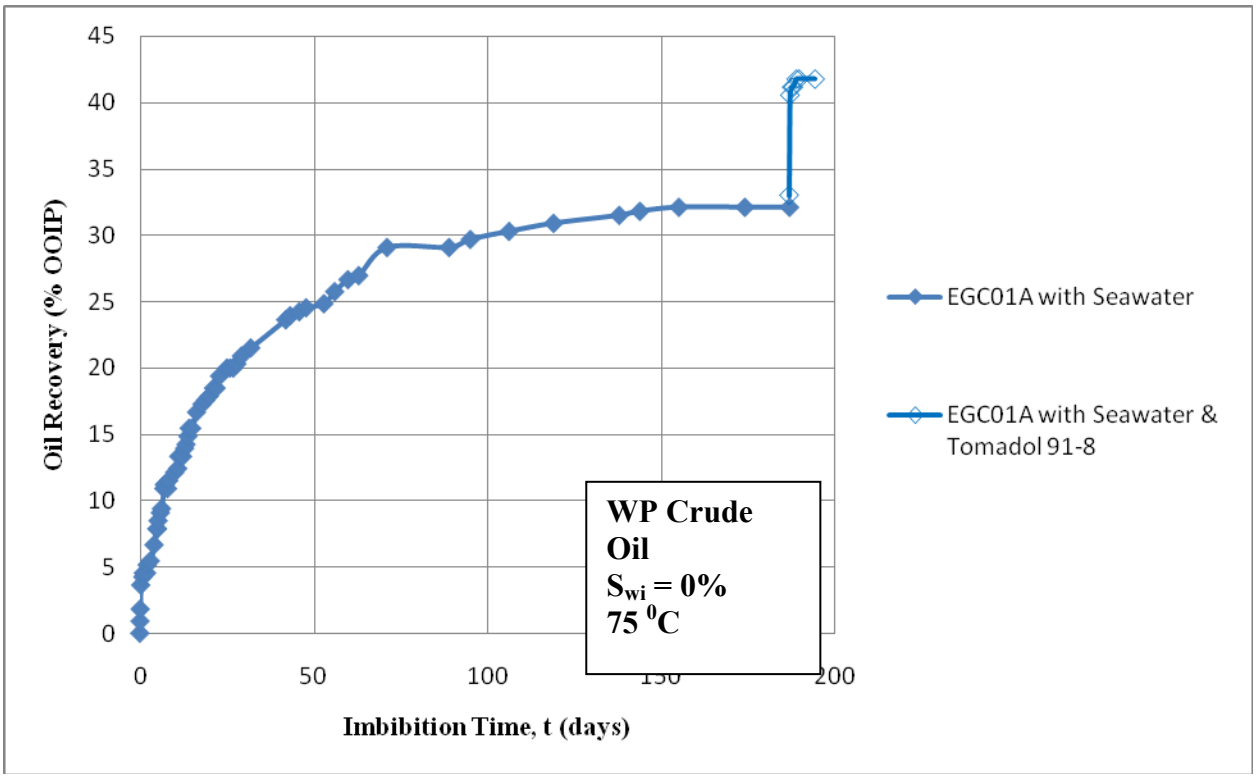

Fig. 9.4-5 Recovery of WP crude oil from Edwards GC limestone by spontaneous imbibition of seawater followed by seawater plus Tomadol 91-8.

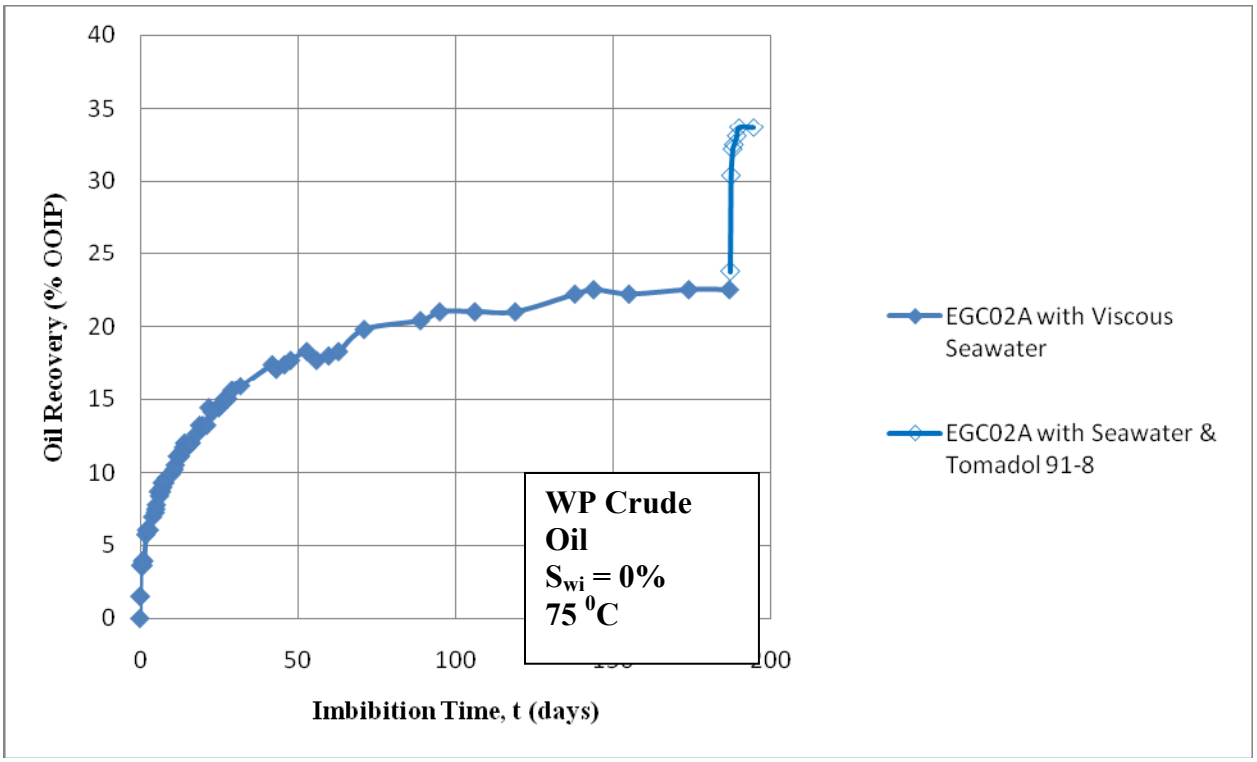

Fig. 9.4-6 Recovery of WP crude oil from Edwards GC limestone by spontaneous imbibition of viscous seawater (40% glycerol) followed by seawater plus Tomadol 91-8.

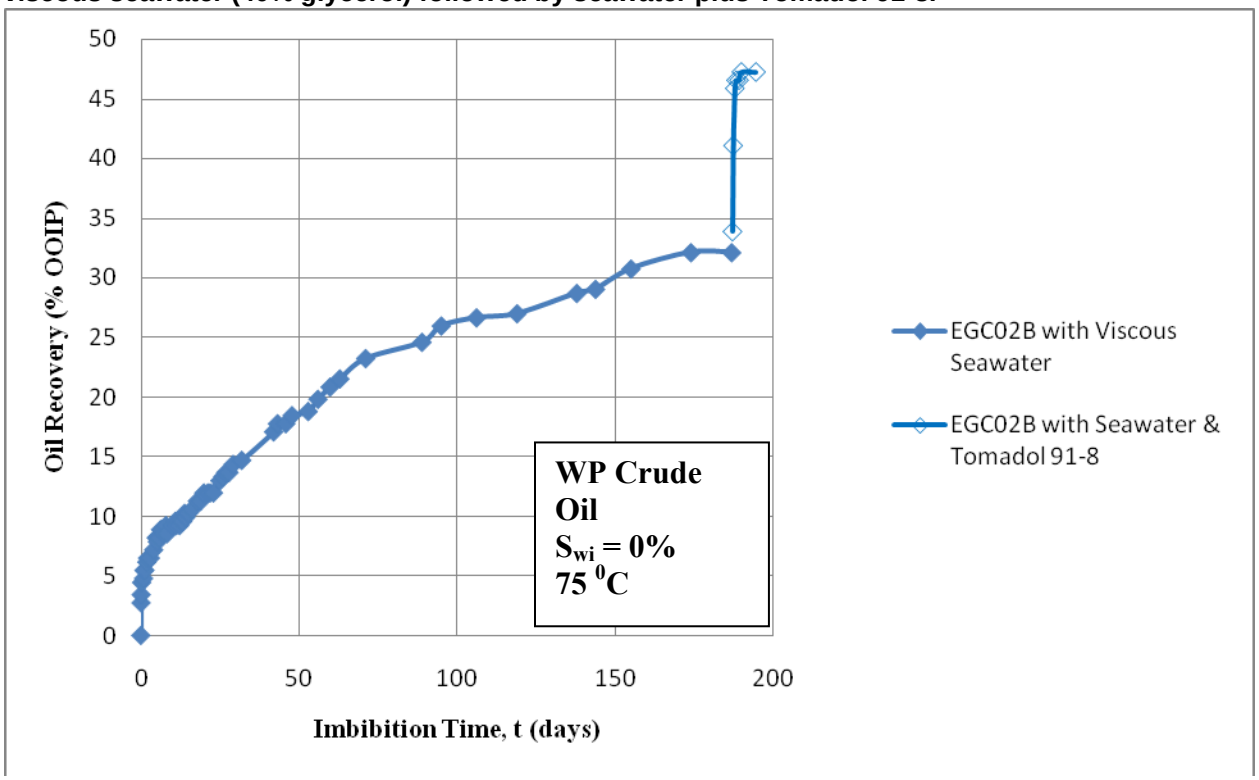

Fig. 9.4-7 Recovery of WP crude oil from Edwards GC limestone by spontaneous imbibition of viscous seawater (60% glycerol) followed by seawater plus Tomadol 91-8.

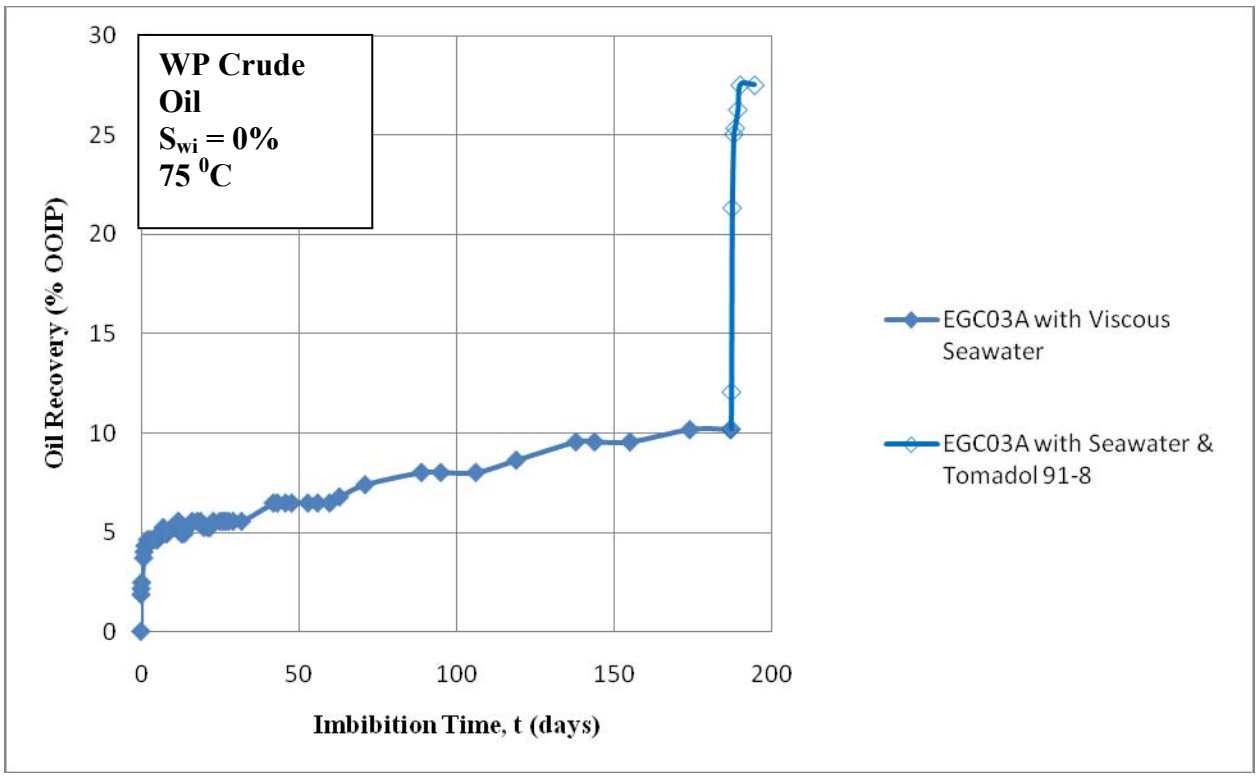

Fig. 9.4-8 Recovery of WP crude oil from Edwards GC limestone by spontaneous imbibition of viscous seawater (80% glycerol) followed by seawater plus Tomadol 91-8.

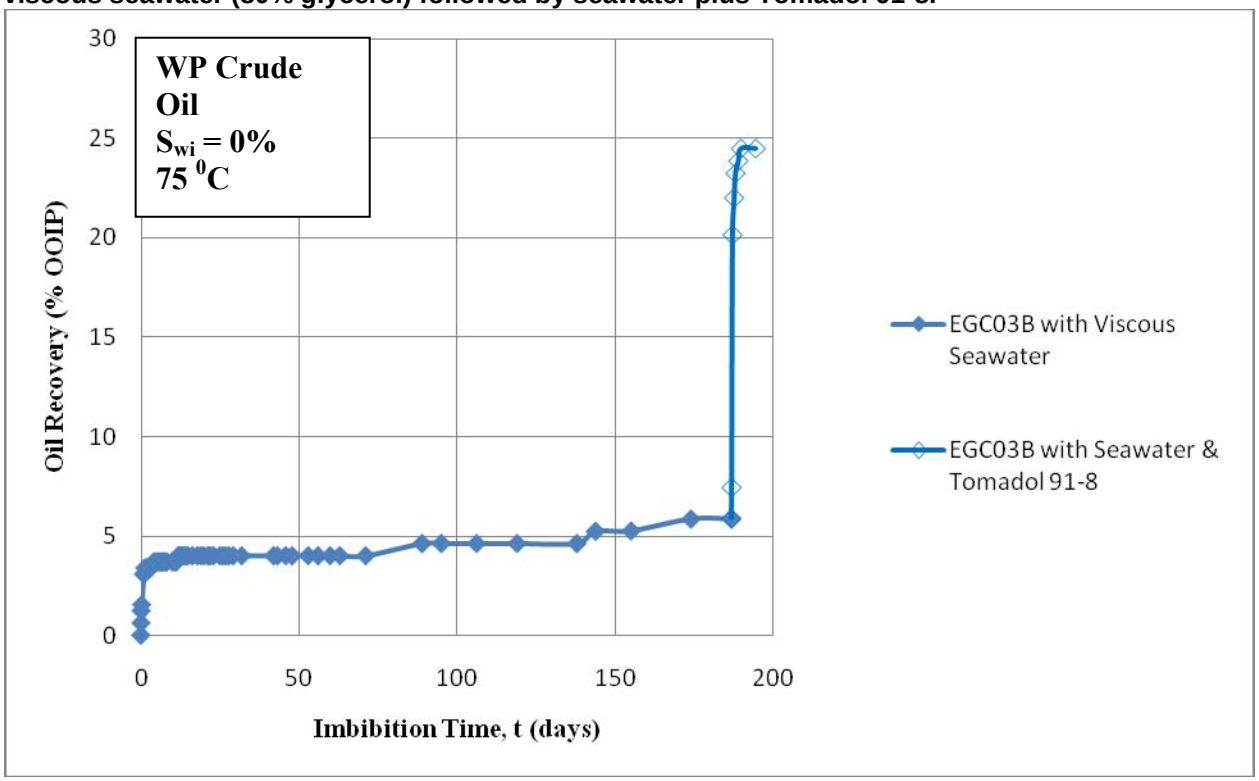

Fig. 9.4-9 Recovery of WP crude oil from Edwards GC limestone by spontaneous imbibition of viscous seawater (90% glycerol) followed by seawater plus Tomadol 91-8.

Results for imbibition of seawater (Fig. 9.4-5) were close to those observed previously for the Edwards GC limestone. Oil recovery for the first stage of imbibition decreased significantly with increase in aqueous phase viscosity. However, after immersion in surfactant solution the total recoveries for the two stages of imbibition were roughly equal. Thus, the recovery for the surfactant stage increased with increase of the aqueous phase viscosity used for the first stage of imbibition.

Recovery of Crude Oil from Cores Containing a Low Initial Seawater Saturation by Imbibition of Viscosified Brine Followed by Seawater Plus Tomadol 91-8

Recovery of crude oil from Edwards limestone was next compared for imbibition of seawater and a series of viscosified brines with the core containing a low initial water saturation. The brine can play a significant role in mediating the wettability change induced by adsorption from the crude oil. After reaching essentially stable oil saturations, the imbibition test was extended to a second stage by immersion of the cores in a 3000 ppm solution of Tomadol in seawater. Properties of the tested cores are listed in Table 9.4-6.

Table 9.4-6 Core properties of Edwards GC used in imbibition tests with initial seawater saturation and seawater with glycerol imbibition followed by seawater plus Tomadol 91-8.

Core	D (in)	L (in)	Φ	k_g (mD)
EGC09A	1.47	2.58	21.47	23.99
EGC09B	1.48	2.44	22.09	25.88
EGC10A	1.48	2.52	20.58	24.29
EGC10B	1.48	2.47	20.16	26.13
EGC11A	1.48	2.58	21.98	28.96

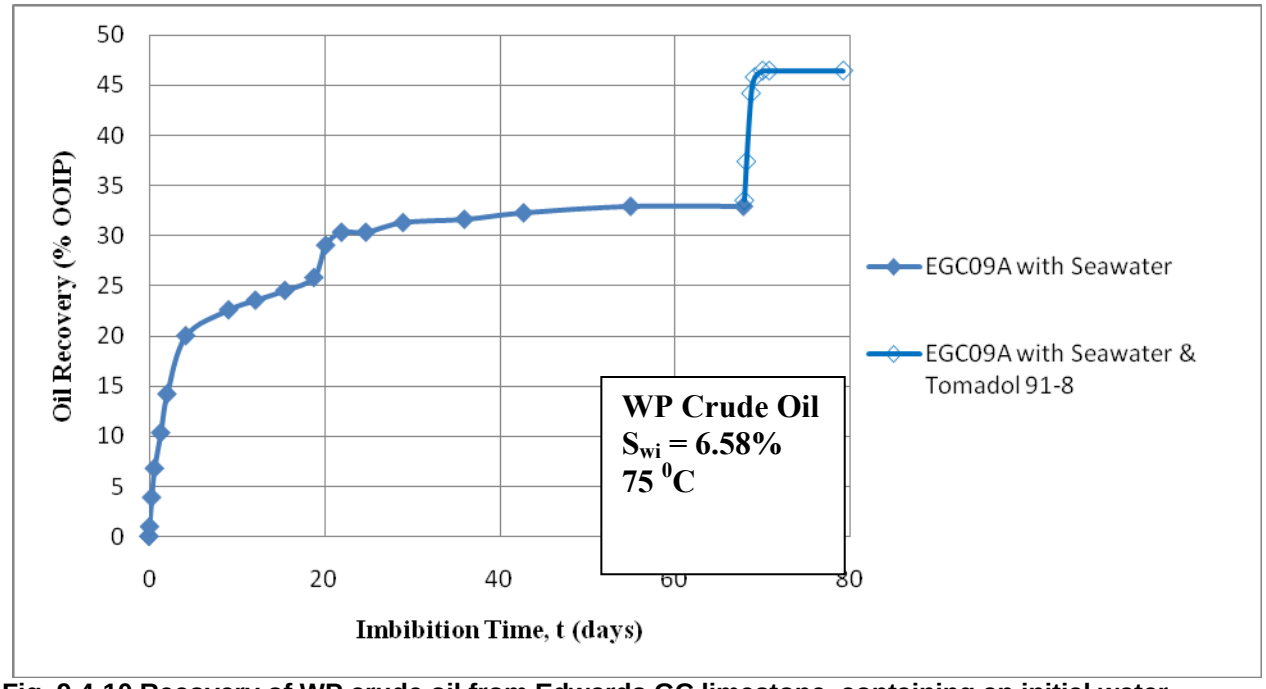

Fig. 9.4-10 Recovery of WP crude oil from Edwards GC limestone, containing an initial water saturation, by spontaneous imbibition of seawater followed by seawater plus Tomadol 91-8.

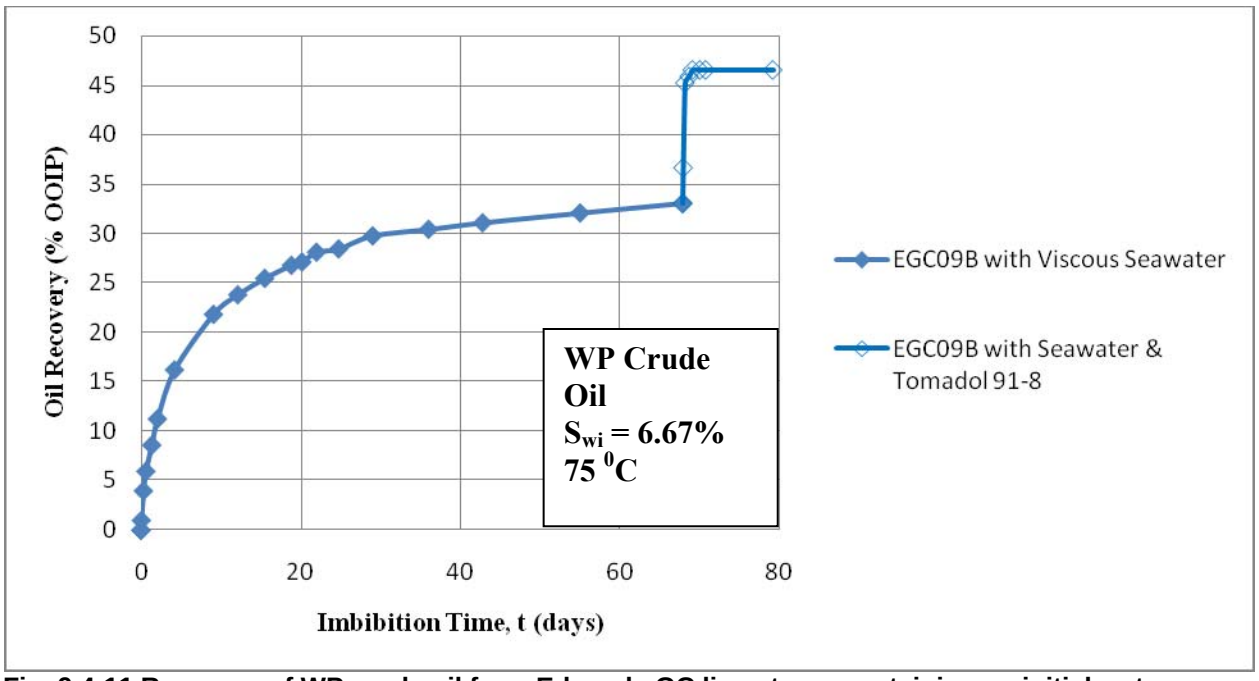

Fig. 9.4-11 Recovery of WP crude oil from Edwards GC limestone, containing an initial water saturation, by spontaneous imbibition of viscous seawater (40% glycerol) followed by seawater plus Tomadol 91-8.

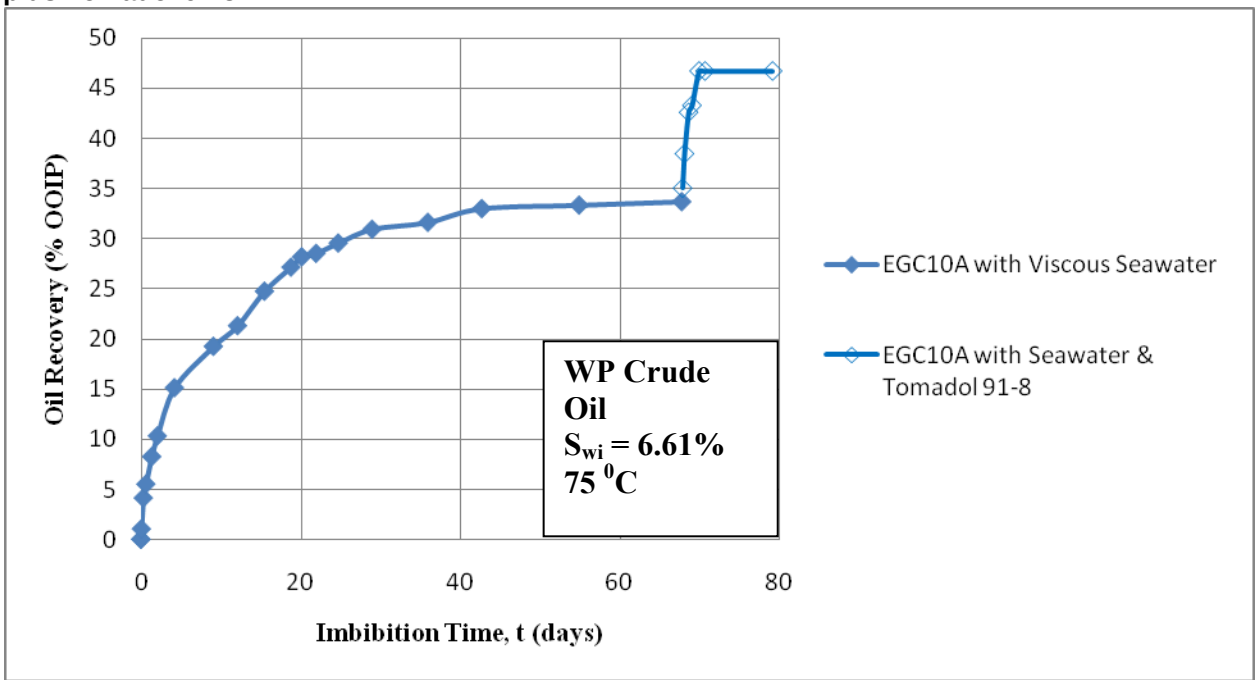

Fig. 9.4-12 Recovery of WP crude oil from Edwards GC limestone, containing an initial water saturation, by spontaneous imbibition of viscous seawater (60% glycerol) followed by seawater plus Tomadol 91-8.

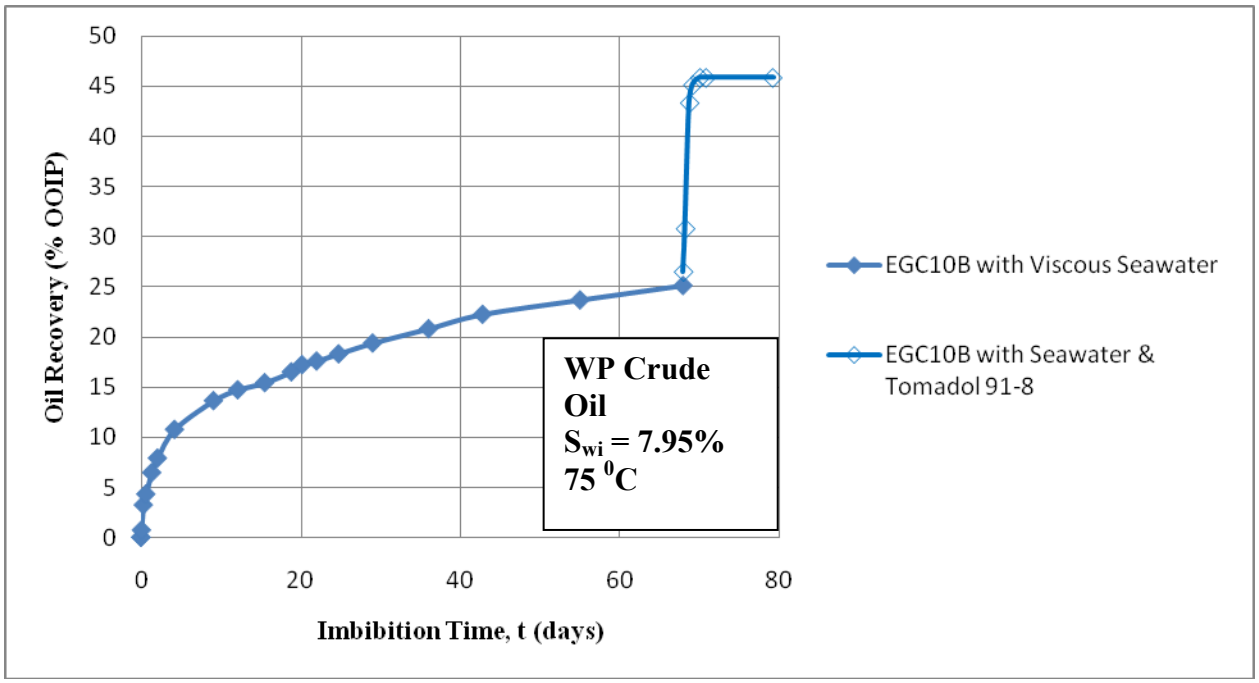

Fig. 9.4-13 Recovery of WP crude oil from Edwards GC limestone, containing an initial water saturation, by spontaneous imbibition of viscous seawater (80% glycerol) followed by seawater plus Tomadol 91-8.

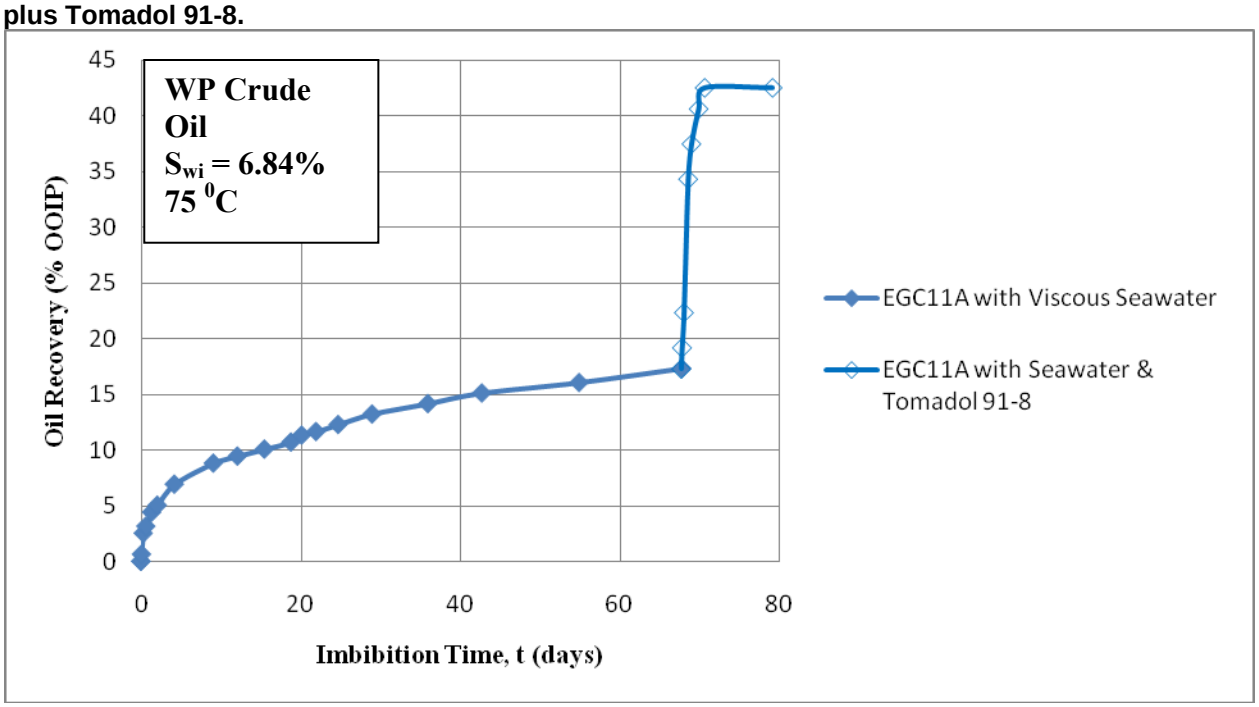

Fig. 9.4-14 Recovery of WP crude oil from Edwards GC limestone, containing an initial water saturation, by spontaneous imbibition of viscous seawater (90% glycerol) followed by seawater plus Tomadol 91-8.

Results for first and second stage incremental recoveries for surfactant solution for cores with and without initial water saturation are summarized in Tables 9.4-7 and 9.4-8. The imbibition recovery rates for the first stage of imbibition were always faster than for experiments with the same viscosity aqueous phase but no initial water saturation. Recoveries for the initial stage of

imbibition decreased with increase in viscosity for the two most viscous aqueous phases, but the effect was much less than observed in the absence of initial water. Incremental and final oil recoveries after the surfactant imbibition were also generally much higher than obtained with no initial water present in the cores.

Table 9.4-7 Summary of first and second (surfactant) stage incremental oil recoveries for without initial water saturation

Aqueous Phase	ΔR_1 (OOIP %)	ΔR_2 (OOIP %)
Seawater	32.08	9.69
Seawater with 40% Glycerol	22.56	11.12
Seawater with 60% Glycerol	32.15	15.05
Seawater with 80% Glycerol	10.21	17.31
Seawater with 90% Glycerol	5.89	18.59

Table 9.4-8 Summary of first and second (surfactant) stage incremental oil recoveries for with initial water saturation

Aqueous Phase	ΔR_1 (OOIP %)	ΔR_2 (OOIP %)
Seawater	32.87	13.54
Seawater with 40% Glycerol	33.01	13.54
Seawater with 60% Glycerol	33.66	13.05
Seawater with 80% Glycerol	25.08	20.77
Seawater with 90% Glycerol	16.05	26.43

Whitestone UZ Limestone

Whitestone UZ Limestone Surfactant Comparison

Properties of the Whitestone UZ cores used in imbibition tests with no initial water saturation are presented in Table 9.4-9. Tests of enhanced imbibition by surfactant solution after imbibition of seawater were made for nonionic, cationic, anionic, and amphoteric surfactants; results are presented respectively in Figures 9.4-15 through 9.4-18.

Table 9.4-9 Whitestone UZ limestone cores used in tests of enhanced imbibition by means of surfactant

Core	D (in)	L (in)	Φ	k_g (mD)
3TC23B	1.48	2.50	25.65	17.93
3TC24B	1.48	2.51	24.60	23.71
T2TC1A	1.47	2.49	26.45	20.19
T2TC1B	1.47	2.53	26.47	22.81
T2TC2A	1.48	2.51	24.31	16.49
T2TC2B	1.48	2.50	27.51	17.65
T2TC6B	1.48	2.53	23.20	9.10
T2TC7A	1.47	2.50	25.90	15.26
T2TC7B	1.48	2.53	22.01	11.77

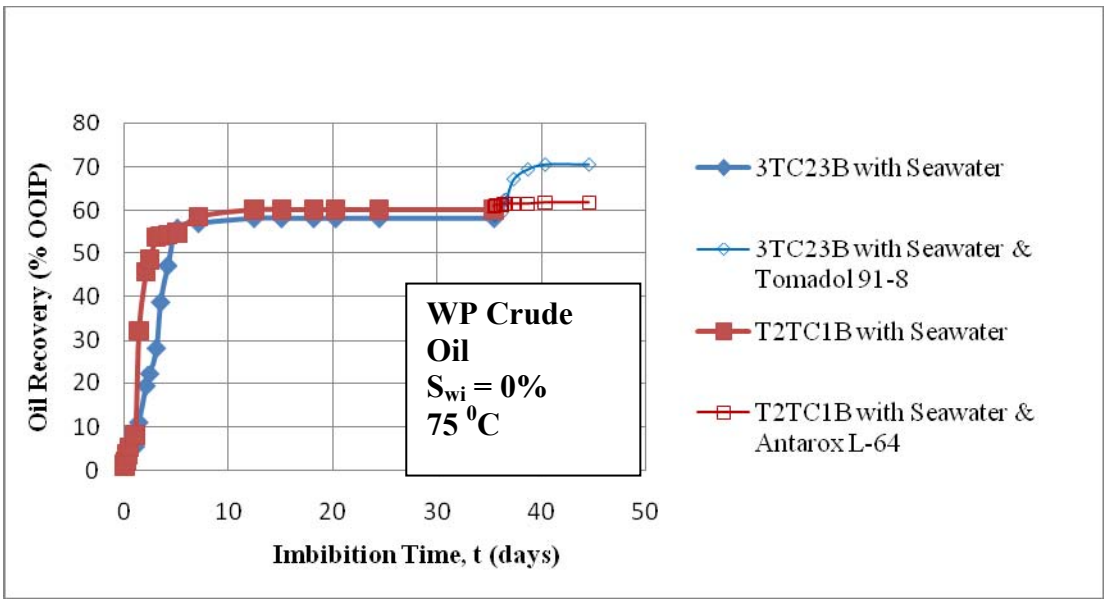

Fig 9.4-15 Recovery of WP crude oil from Whitestone UZ limestone by spontaneous imbibition of seawater followed by seawater plus nonionic surfactant.

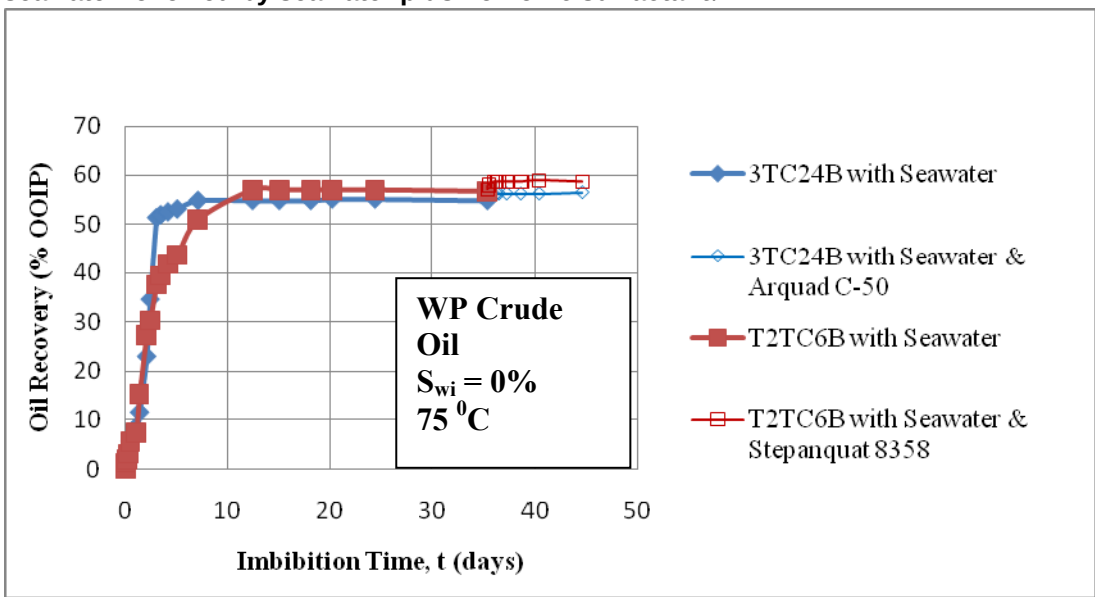

Fig 9.4-16 Recovery of WP crude oil from Whitestone UZ limestone by spontaneous imbibition of seawater followed by seawater plus cationic surfactant.

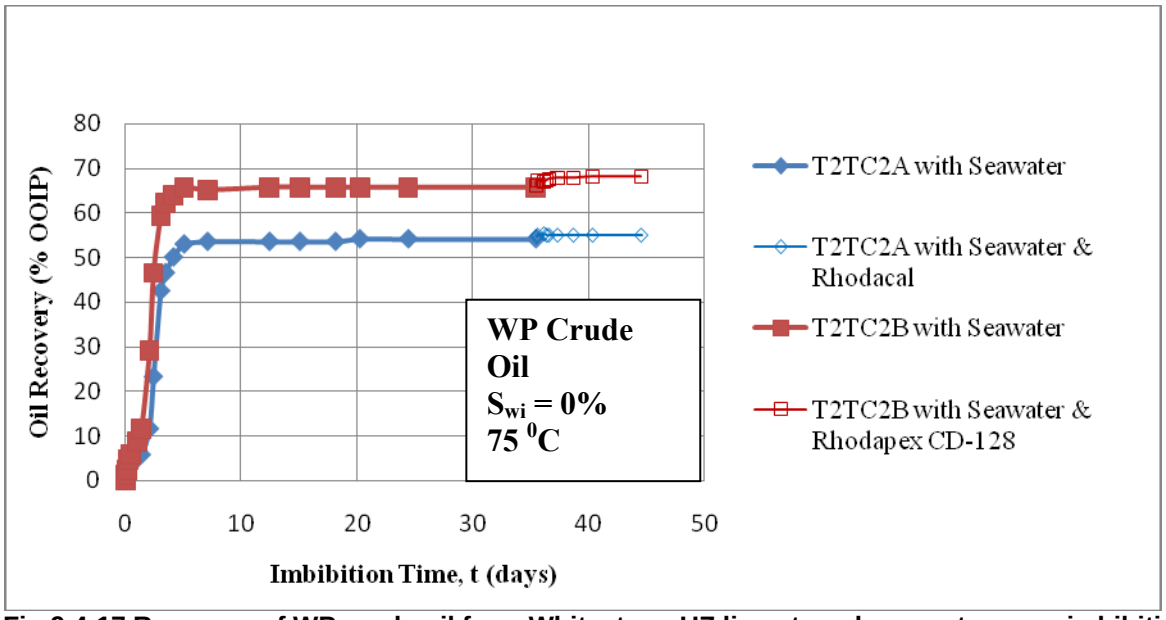

Fig 9.4-17 Recovery of WP crude oil from Whitestone UZ limestone by spontaneous imbibition of seawater followed by seawater plus anionic surfactant.

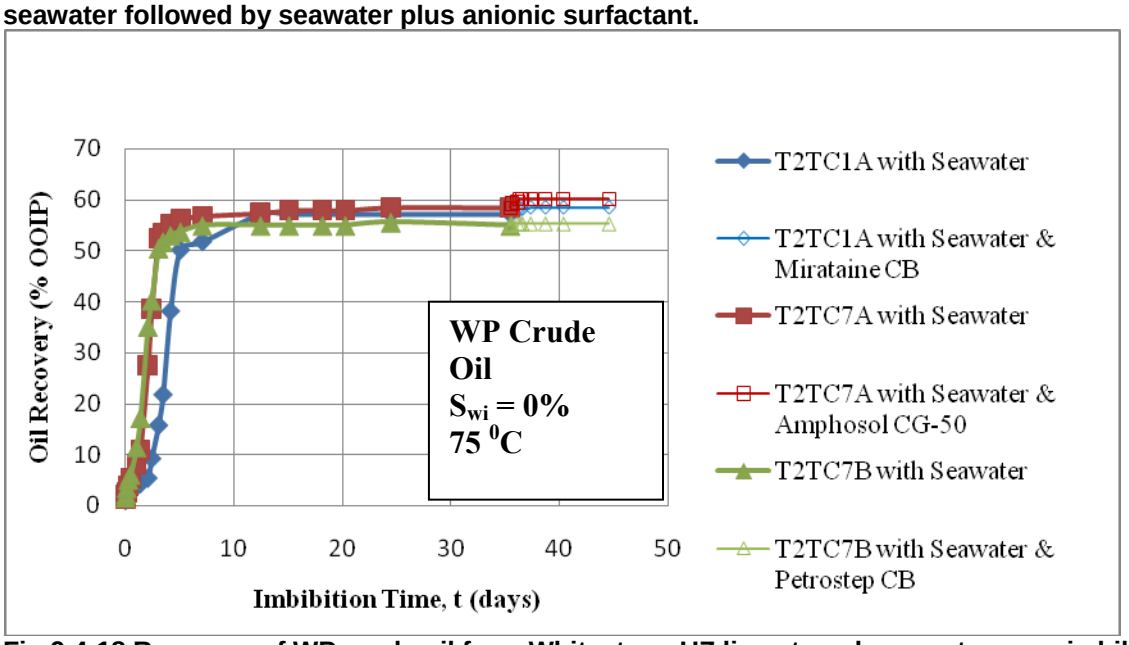

Fig 9.4-18 Recovery of WP crude oil from Whitestone UZ limestone by spontaneous imbibition of seawater followed by seawater plus amphoteric surfactant.

Whitestone UZ gave much higher overall recoveries than Edwards GC limestone for imbibition of seawater. However, after immersion in surfactant solution there was little or no recovery except for Tomadol 91-8, which also performed best with Edwards GC limestone. The Tomadol solution gave 11% OOIP recovery over and above the 59% OOIP recovery given by imbibition of seawater to give a total recovery of about 70% OOIP.

Imbibition of Viscosified Seawater Followed by Seawater Plus Tomadol 91-8

Tomadol 91-8 showed the highest incremental oil recovery for both Edwards GC and Whitestone UZ limstone. It was therefore further tested for enhanced recovery after imbibition of a viscosified

aqueous phase into Whitestone UZ limestone initially saturated with WP crude oil. Core properties are given in Table 9.4-10. Results for aqueous phase viscosities of 1.1 cp, 4.1 cp, 12.1 cp, and 65.8 cp are presented in Figures 9.4-19 to 9.4-22 respectively.

Table 9.4-10 Core properties for Whitestone UZ limestone for imbibition of seawater plus glycerol followewd by seawater plus Tomadol 91-8

Core	D (in)	L (in)	Φ	k_g (mD)
TC16A	1.476	2.487	24.8637	8.0654
TC16B	1.476	2.485	25.1895	9.7949
TC17A	1.475	2.438	24.5784	11.0717
TC18A	1.475	2.456	25.3526	15.7933

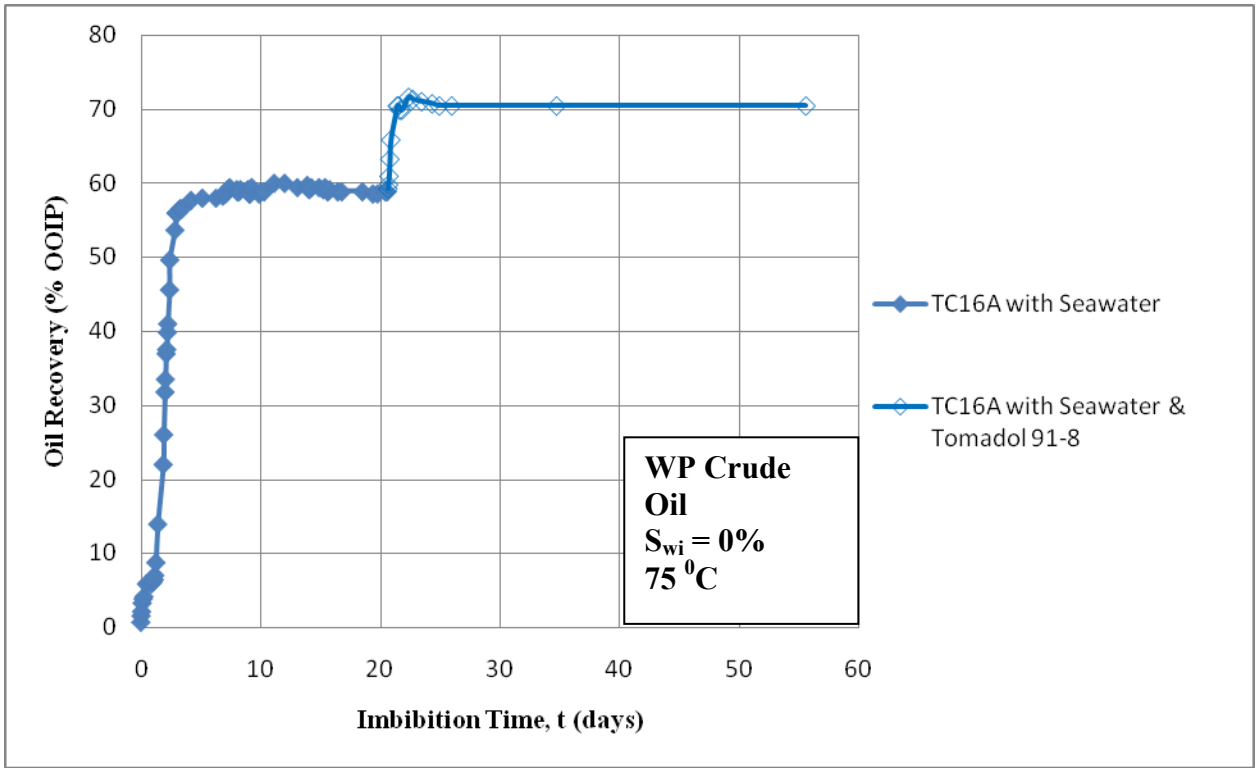

Fig. 9.4-19 Recovery of WP crude oil from Whitestone UZ limestone by spontaneous imbibition of seawater followed by seawater plus Tomadol 91-8.

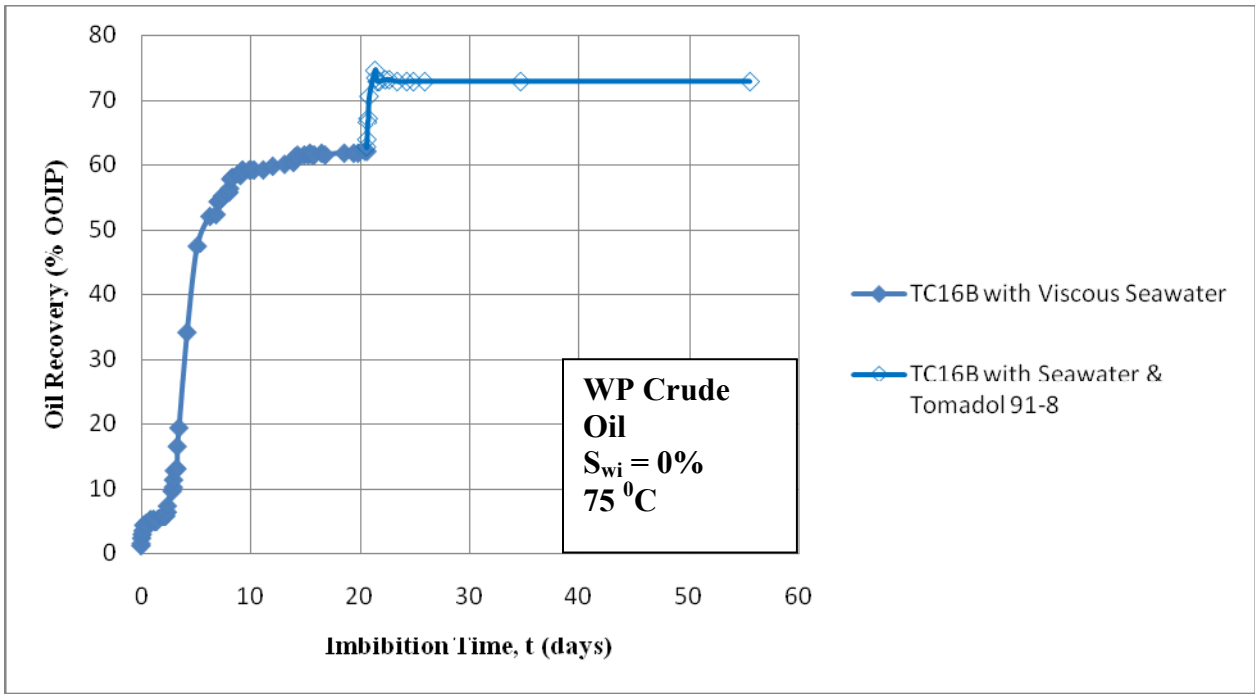

Fig. 9.4-20 Recovery of WP crude oil from Whitestone UZ limestone by spontaneous imbibition of viscous seawater (40% glycerol) followed by seawater plus Tomadol 91-8.

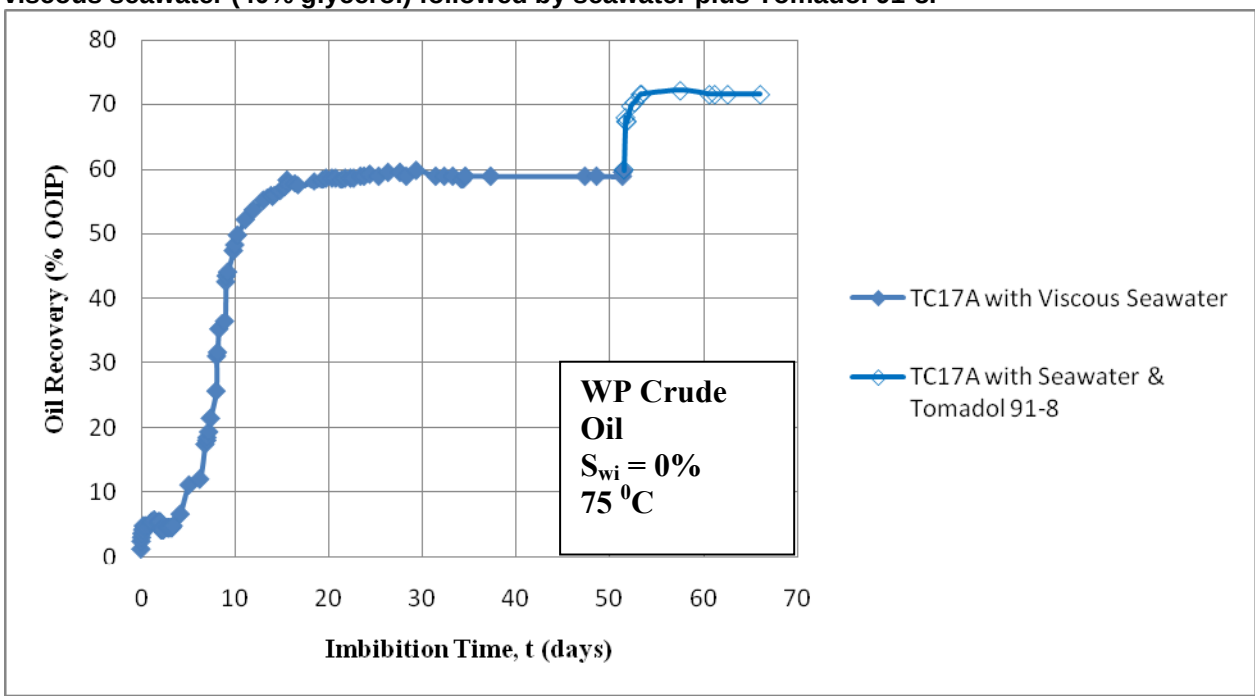

Fig. 9.4-21 Recovery of WP crude oil from Whitestone UZ limestone by spontaneous imbibition of viscous seawater (60% glycerol) followed by seawater plus Tomadol 91-8.

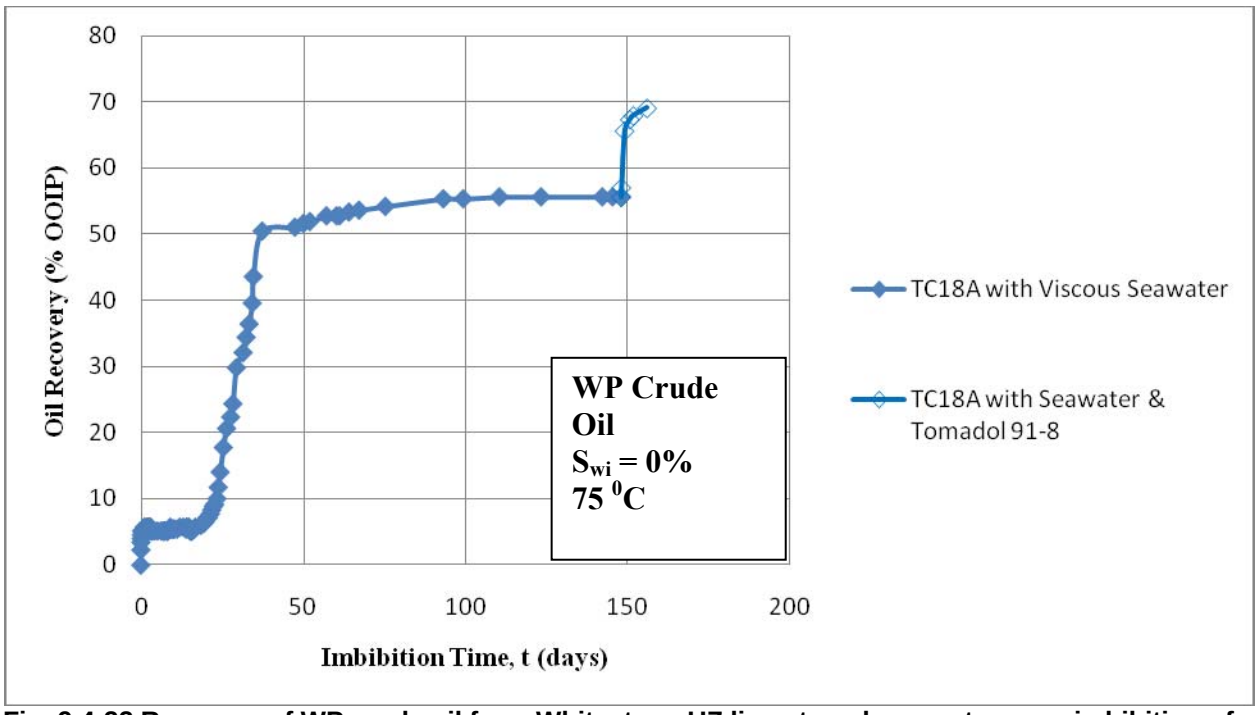

Fig. 9.4-22 Recovery of WP crude oil from Whitestone UZ limestone by spontaneous imbibition of viscous seawater (80% glycerol) followed by seawater plus Tomadol 91-8.

For the first stage of spontaneous imbibition, recovery decreased only slightly with increase in aqueous phase viscosity. Incremental recovery after immersion in surfactant rose systematically from 10.7 to 13.5% OOIP with increase in the imbibing phase viscosity for the first stage of imbibition. However, there was no trend in total recovery which ranged from 69.1 to 72.9% OOIP. The incremental oil recovery and the final oil recovery for seawater and seawater with Tomadol 91-8 were closely reproduced.

Imbibition of Viscosified Seawater into Cores Containing a Low Initial Seawater Saturation Followed by Imbibition of Seawater Plus Tomadol 91-8

Tests for enhanced oil recovery after imbibition of a viscosified aqueous phase into Whitestone UZ limestone initially saturated with WP crude oil were extended to include cores that contained an initial water saturation. Properties of cores used in the tests are given in Table 9.4-11. Results for aqueous phase viscosities of 1.1 cp, 4.1 cp, and 65.8 cp are presented in Figures 9.4-23 to 9.4-25 respectively.

Table 9.4-11 Core properties for Whitestone UZ limestone with initial water saturation and seawater/ seawater with Glycerol/ seawater with Tomadol 91-8

Core	D (in)	L (in)	Φ	k_g (mD)
3TC21B	1.479	2.535	21.8641	37.3353
3TC22A	1.476	2.509	23.6300	40.4629
3TC23A	1.479	2.558	22.6771	44.5989

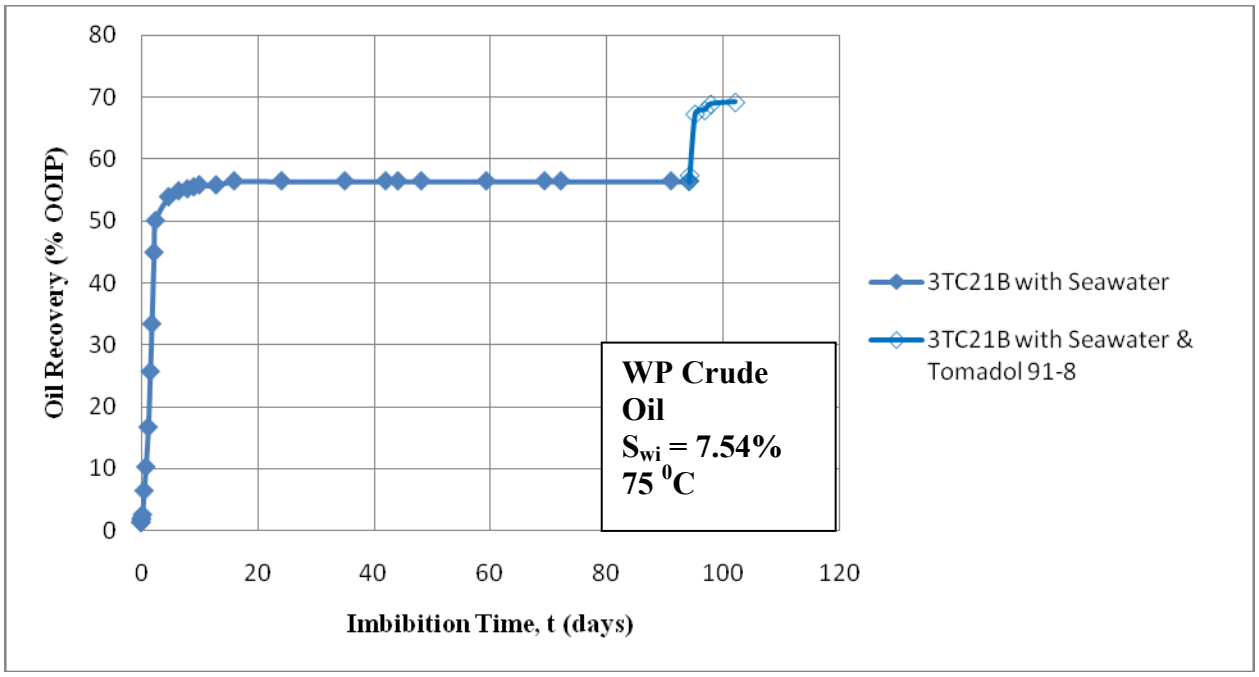

Fig. 9.4-23 Recovery of WP crude oil from Whitestone UZ limestone by spontaneous imbibition of seawater followed by seawater plus Tomadol 91-8.

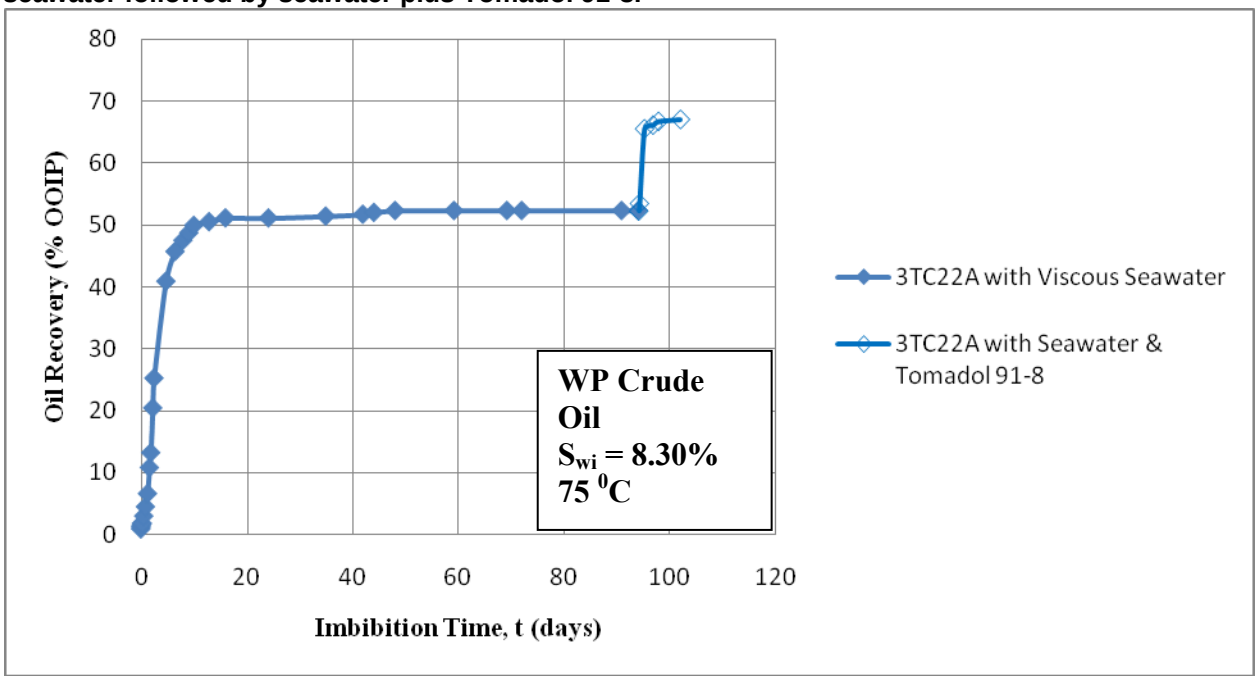

Fig. 9.4-24 Recovery of WP crude oil from Whitestone UZ limestone by spontaneous imbibition of viscous seawater (40% glycerol) followed by seawater plus Tomadol 91-8.

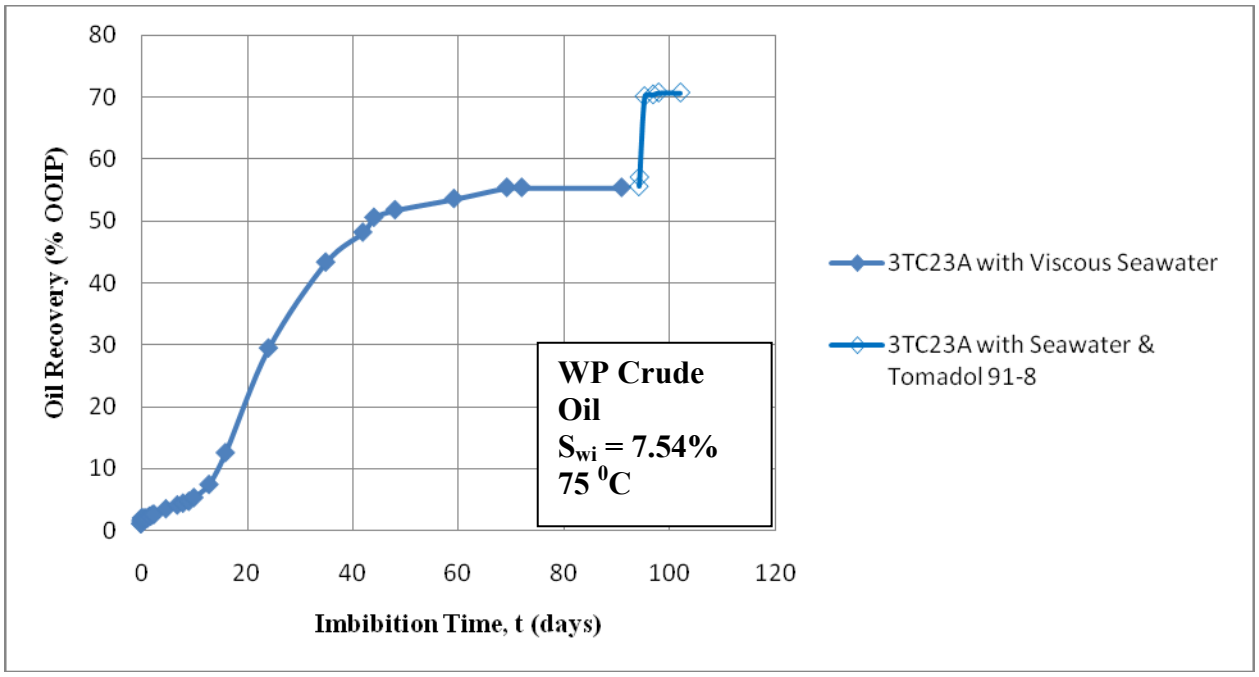

Fig. 9.4-25 Recovery of WP crude oil from Whitestone UZ limestone by spontaneous imbibition of viscous seawater (80% glycerol) followed by seawater plus Tomadol 91-8.

Oil recoveries, expressed as % OOIP (Original Oil In Place) are about 4.4% lower than for comparable tests on cores without initial water saturation. However, incremental recoveries were higher and total recoveries were about the same as for cores without initial brine saturation. Results for first and second stage incremental recoveries for surfactant solution for cores with and without initial water saturation are again summarized in Tables 9.4-12 and 9.4-13.

Table 9.4-12 Summary of first and second (surfactant) stage incremental oil recoveries without initial water saturation

Aqueous Phase	ΔR_1 (OOIP %)	ΔR_2 (OOIP %)
Seawater	59.74	10.68
Seawater with 40% Glycerol	62.09	10.82
Seawater with 60% Glycerol	58.98	12.51
Seawater with 80% Glycerol	55.63	13.48

Table 9.4-13 Summary of first and second (surfactant) stage incremental oil recoveries with initial water saturation

Aqueous Phase	ΔR_1 (OOIP %)	ΔR_2 (OOIP %)
Seawater	56.38	12.81
Seawater with 40% Glycerol	52.33	14.74
Seawater with 80% Glycerol	55.34	15.34

CONCLUSIONS

Task 1.
Consistent relationships have been found between work of displacement from capillary pressure drainage curves and directly measured changes in interfacial areas.

Task 2.
Spontaneous imbibition data for different boundary conditions have been correlated by a simple tube model that compensates for radial versus linear flow and for cores will all faces open.

Task 3.
A period of frontal flow has been identified for linear COUCSI during which the distance advanced by the front is proportional to the square root of time. This result is consistent with a similarity solution for the frontal advance period.

The capillary back pressure associated with production of NWP at the open face of the sample, is essentially constant during the frontal flow period. The production mechanism at the open face is basically a drainage process.

From simulations that assume fixed relative permeabilities and scaled imbibition capillary pressure, the capillary back pressure in the oil/air case is about 2/5 down to 1/3 and in the water/oil case about 1/4 down to 1/9 of the capillary pressure at the imbibition front in Berea sandstone with permeabilities ranging from 0.065 to 1.1 μm^2.

Task 4.
Imbibition results for viscosity ratios of less than 4 were closely correlated by the Ma et al. scaling group with only very small but systematic dependence of dimensionless time on viscosity ratio. However, final oil recovery for unmatched liquid viscosities increased slightly with increase in aqueous phase/oil viscosity ratio up to about 4. Increase in dimensionless time for imbibition with viscosity ratio was observed for viscosity ratios greater than 4 but final oil recoveries were close to constant.

Task 5.
The present study has presented an analytical solution for one-dimensional, linear, counter-current, spontaneous imbibition into a porous sample for the period before the invading phase contacts the end of the sample. The analytical method is valid for arbitrary relative permeability, capillary pressure, and other sample parameters. In order for the solution to be used, the saturation at the open face and the saturation at the front must be specified.

Task 6
6.1
A technique involving centrifuging and solidification of liquid resins enabled the distribution of wetting and nonwetting phases and interfacial areas to be determined from thin sections for sandstone and carbonate.

The total area created by invasion of the nonwetting phase increased linearly with decrease in wetting-phase saturation for both sandstone and carbonate.

6.2
Pressures in the oil phase ahead of the imbibition front (end pressures) for restricted countercurrent spontaneous imbibition have been determined for a range of conditions. These novel measurements include strongly water wet cores with and without initial water saturation, mixed wet cores with different levels of initial water saturation, and cores initially saturated with crude oil.

Strongly water wet cores showed decrease in end pressure with increase in initial water saturation consistent with decrease in the capillary driving force.

In contrast to water wet conditions, mixed wet cores showed increase in driving pressure with increase in initial water saturation. This result is consistent with the effect of aging on the available surface energy for imbibition and with standard imbibition tests on mixed wet rocks having a range of initial water saturations.

Measured pressures stayed close to constant until the imbibition front reached the end of the core sample.

6.3
End pressure data for imbibition into mixed wet and weakly water wet behavior are reported for the first time. Results for duplicate tests were closely reproduced.

End pressures for the investigated MXW state were one seventh of the end pressures for strongly water wet conditions at comparable initial water saturation to the MXW core and one thirteenth of the end pressure for strongly water wet cores initially saturated with mineral oil.

For VSWW states, both with and without an initial water saturation, the invading brine advanced as a front with constant saturation behind the front. The amount of brine imbibed was proportional to the distance of advance. The rate of advance decreased as the square root of time.

6.4
The interfacial area between the wetting and nonwetting phase was always only a small fraction of the nonwetting phase/solid area.

Comparison of created surface area with rock surface area measured by gas adsorption showed that, after primary drainage to 20% wetting-phase saturation, most of the rock surface area is still overlain by bulk wetting phase.

The efficiency of conversion of work of displacement (based on air/brine capillary pressure measurements) to surface free energy for displacement to 20% wetting-phase saturation was only 36% for sandstones and 16% for limestone. These values are very low compared to the value of 85% measured for sphere packs.

Drainage of a spherical cavity provides an explanation of how aspect ratio (pore body to pore throat size) can have a dominant effect on the efficiency of conversion of work of displacement to surface free energy.
The wettability of individual pores will depend on the combined effect of pore geometry, the change in surface energy caused by adsorption from crude oil and the fraction of the pore surface at the microscopic level that remains overlain by water. This explains which spontaneous displacement of oil by brine is often observed even when contact angles through the aqueous phase at smooth mineral surfaces are high. Topographic features which affect wetting behavior at the microscopic level includes, surface roughness, edges, and micro-porous grains and cements.

Task 7

7.1

If the uptake of wetting phase for linear imbibition is proportional to the square root of time, the capillary pressure acting at the imbibition front has to be independent of imbibition rate. For such a system, monitoring the end pressure for one-end-open linear imbibition under conditions of restricted COUCSI where the production of non-wetting phase is prevented provides an estimate of the capillary pressure acting at a slow-moving to essentially static imbibition front.

During restricted COUSCI, after limited invasion of WP, the end pressure in the NWP rises to a maximum value and shows only small decline as the WP redistributes by simultaneous imbibition and drainage without change in the overall brine content.

The capillary pressures at the oil/water displacement front ranged from 6.6 to 21.3 *kPa* for Berea sandstones with permeabilities between 1.067 and 0.06 ($\mu m)^2$. Frontal_capillary pressures for different Berea sandstones did not give a direct correlation with permeability as would be given by porous media with different pore length scales but with similar pore geometry.

7.2

An approximate analytic solution for countercurrent imbibition was obtained by assuming a frontal displacement with constant saturations ahead of and behind the front, and taking the capillary back pressure at the open face to be a constant fraction of the capillary pressure at the front. This gives the production *vs* time functions for different core shapes. Comparison of these functions with experimental data using Berea sandstone and refined oil for both the linear and radial cases shows reasonable agreement. In practice, variability between the cores caused by not having enough surface area and not enough volume seems of greater importance than the precise core scale factor functions. For consistent data the core should have a surface area of 40 cm^2 and an imbibition depth greater than 1 cm.

Task 8

8.1

Spontaneous imbibition for a wide range of oil to water viscosity ratios and three boundary conditions showed systematic dependence on viscosity ratio with strong dependence for values less than 0.25.

A mathematical model based on displacement as a piston-like front with counter-flow of oil related imbibition time to the position of the advancing front.

The model correlates results for different boundary conditions through the conversion of the oil recovery to frontal position.

The model takes into account the experimentally observed effects of viscosity ratio by the definition of a dimensionless function of viscosity ratio, $E(\eta)$. Dimensionless parameters of $E(\eta)$ that were independent of η were obtained by fitting experimental data to the model.

The model relates the dimensionless position of the front to the n-th root of dimensionless time t_D* given by the product of dimensionless time, t_D, (Ma *et al*.) and a dimensionless function of viscosity ratio $E(\eta)$.

The model gives a linear correlation between the normalized frontal position, x_D, and t_D* with a slope (power index) of 0.5 (n= 2) on a log-log scale.

Comparison with experimental data showed that the values of $E(\eta)$ determined from radial imbibition data provided close match with linear imbibition (one-end-open, OEO) and with imbibition into cylindrical cores, modeled as a combination of spherical and radial flow (all-faces-open, AFO).

A very close correlation of all data was obtained when imbibition data were plotted as normalized frontal position versus the n-th root of t_D*. Predictive capability is indicated by the close match with the correlation given by n = 2.

Additional experimental work is required to evaluate the dependency of the dimensionless function $E(\eta)$ on the square root of the viscosity ratio, η, for other rock types.

8.2

A simple analysis of co- and counter-current imbibition for tubes of non-circular cross-section has been carried out. Shape factors were needed to describe the tube areas, hydraulic resistances and capillary pressures. Experiments using model pore systems and measurements of capillary rise were used to confirm the capillary pressures. Co-current imbibition experiments were used to measure the hydraulic resistances. Both these values were then used to quantify counter-current imbibition. When theory was compared to experiment, the agreement was generally good except that the bubble snap-off pressure was not well described by the tube incircle curvature. This was probably because the prediction of snap-off at the incircle curvature is quasi-static, whereas in the real system there was rapid bubble growth.

In general, co-current imbibition was observed to occur at about four times the rate of counter-current imbibition even though more fluid was being imbibed. Furthermore, it takes a significant positive pressure, the capillary back pressure, for air to be driven out in counter-current imbibition and this can make a significant difference to the imbibition rate. At the liquid inlet face there was growth of bubbles and subsequent snap-off giving significant fluctuations of the capillary back pressure. Co-current theory was in good agreement with the experiments; it follows the Washburn equation.

The Mayor and Stowe–Princen theory appears to predict meniscus curvatures well, even when they are moving. This is probably because the arc menisci keep far enough ahead of the main terminal meniscus for the MS-P approximations to hold.

8.3

An interacting capillary model, which is based on pressure equilibration among the capillaries with non-circular crosssections has been used to analyze a series of experiments. The model predicts a behavior that differs from the behavior of the classic 'bundle of independent cylindrical tubes' model. The model also predicts that imbibition will give a self-similar front thus making it akin to the classic analysis of Buckley and Leverett. The equations do not have analytical solutions. The model is part way between network models, which are complex and which only give simulation solutions, and the independent tube model which gives analytic solutions. Analyses for both co- and counter-current imbibition have been made for non-circular tubes when one phase has zero viscosity. Shape factors are needed to describe the tube areas, hydraulic resistances and capillary pressures. Experiments in model cells having precise geometry, using co- and countercurrent imbibition when no bubbles were formed, were used to verify the theory. If air flows from the liquid inlet face, then bubbles are formed and the behavior is complex.

8.4

The snap off pressure of bubbles emerging from a non-axisymmetic uniform tubes has been measured and compared to theoretical predictions. The snap off is caused by capillary instability of an almost-cylindrical meniscus in the tube. It was observed that snap off occurred at about 66% of the curvature of a theoretical cylindrical meniscus in the non-axisymmetric tubes. There was little dependence on the shape of the tube, or whether it was open in one part of the perimeter or not. Similarly, snap off occurred at about 41% of the curvature of a meniscus in the non-axisymmetric tube, again with little dependence on tube shape, indicating a bubble size about 2.5 times the pore size.

8.5

Analytical solutions were developed with the assumption that displacement by imbibition can be modeled as a piston-like front with provision for flow of the non-wetting phase. Cylindrical cores, the most commonly tested sample shape were modeled as two cones and a residual torroidal ring. Shape factors calculated with the model are close to the semi-empirical values proposed by Ma et al. (1977). Theoretical predications give a reasonable fit to experimental data.

Production versus time curves can be predicted with the model.

Task 9

9.1

By approximating the countercurrent imbibition process to a frontal displacement with constant saturations ahead of and behind the front an analytical solution becomes possible. Comparison of the results for Berea sandstone and refined oil before and after adding surfactant to the invading brine shows that the capillary back pressure at the open face is about one quarter to one third of the capillary pressure actually driving imbibition when the cores were immersed directly into a brine/surfactant solution.

9.2

Overall, low concentration of nonionic surfactant gave increased oil recovery from San Andres limestone by spontaneous imbibition for a wide range of permeability. Oil recovery from chalk with a cationic surfactant has been reported to give significant increase in recovery with sulfate concentration. However, sulfate concentration did not give a consistent trend for the crude oil/limestone surfactant combination used in the present work.

9.3

Change in salinity of the invading brine had no effect on the rate and extent of recovery of crude oil from Edwards GC carbonate.

9.4

Recovery of an asphlatic crude oil from Edwards limestone by imbibition of seawater ranged from 14 to 32%. Recovery by spontaneous imbibition was taken for cores containing an initial water saturation.

A nonionic surfactant, Tormadal 91-8, consistently gave the highest extended imbibition performance for a range of circumstances.

Recovery of the same asphaltic crude oil by spontaneous imbibition from Whitestone UZ limestone which is more heterogeneous in terms of permeability variation was much higher than for the Edwards limestone, ranging from 55 to 70%. As for the Edwards limestone, rate of recovery was always higher for cores containing an initial brine saturation. Tomadal 91-8 also gave the highest extended imbibition performance for the Whitestone UZ limestone.

REFERENCES

Akin, S., Schembre, J.M., Bhat, S.K., Kovscek, A.R., "Spontaneous imbibition characteristics of diatomite", *J. Pet. Sci. Eng*., 2000, 25, 149-165.

Al-Gharbi, M.S. & Blunt, M.J., "Dynamic network modeling of two-phase drainage in porous media", *Physical Review E*, 2005, 71, Art No 016308.

Alpak F.O., Lake L.W. and, Embid S.M., "Validation of a modified Carman – Kozeny equation to model two phase relative permeabilities", SPE 56479, presented at Annual Technical Conference and Exhibition, Houston, TX, 3 – 6th Oct 1999.

Aronofsky, J.S., Masse, L., Natanson, S.G., "A model for the mechanism of oil recovery from the porous matrix due to water invasion in fractured reservoirs", *Trans. AIME*, 1958, 213, 17–19.

Aziz, K.,K., Settari, A., "Petroleum Reservoir Simulation", Applied Science Publishers, London, 1979.

Baldwin, B.A., Spinler, E.A., "In-situ saturation development during spontaneous imbibition", Proceedings of the International Society of Core Analysts, 1999, SCA-9922, pp. 1-11.

Barenblatt, G.I., Entov, V.M. and Ryzhik, V.M., "Theory of Fluid Flow Through Natural Rocks", Kluwer Academic Publishers, 1990.

Barenblatt, G.I. and Gil'man, A.A., "Nonequilibrium Counterflow Capillary Impregnation", *Journal of Engineering Physics (A translation of Inzhenero-fizcheskii Zhurnal)*, **52**, pp. 335-339.

Barenblatt, G.I., Patzek, T.W. & Silin, D.B., "The mathematical model of non-equilibrium effects in water-oil displacement", *Soc. Petrol. Engng J.,* 2002, 409-416.

Barrett, E.P., Joyner, L.G., and, Halenda, P.P., "The Determination of Pore Volume and Area Distribution in Porous Substances I. Computations from Nitrogen Isotherms", *J. American Chemical Soc.* 1951, **73,** 373–380.

Behbahani, H.S., Donato, G.D. & Blunt, M.J., "Simulation of counter-current imbibition in water-wet fractured reservoirs", *J. Pet. Sci. Eng*, 2006, 50, 21-39.

Beliaev, A.Y. and Hassanizadeh, S.M., "A Theoretical Model of Hysteresis and Dynamic Effects in the Capillary Relation for Two-Phase Flow in Porous Media", *Transport in Porous Media*, 2001, **43**, 487–510.

Bentsen, R.G. and Anli, J., "Using Parameter Estimation Technique to Convert Centrifuge Data into Capillary Pressure Curve", *SPEJ*, 1977, **17** (1): 57–64; *Trans,* AIME, **263.** SPE-5026-PA.

Bernardiner, M.G., "A capillary structure of the wetting front", *Transport in Porous Media*, 1998, **30**, 251-265.

Blair, P.M., “Calculation of Oil Displacement by Countercurrent Water Imbibition”, *SPEJ*, 1964, (**Sep**), 195-202.

Blunt, M.J.: “Pore Level Modeling of the Effects of Wettability,” *SPEJ* (Dec. 1997) **2**, 494-510.

Blunt, M.J., “Flow in porous media — pore-network models and multiphase flow”, *Current Opinion in Colloid and Interface Science*, 2001, 6, 197-207,

Bourbiaux, B.J. and Kalaydjian, F.J., “Experimental Study of Cocurrent and Countercurrent Flows in Natural Porous Media”, *SPE Res. Eng*., 1990, **5**, 361-368.

Bradford S., Leij F, “Estimating area for multi-fluid soil systems”, *Journal of Contaminant Hydrology*, 27, 1997, 83-105

Brunauer, S., Emmett, P.H., and Teller E., “Adsorption of Gases in Multimolecular Layers”, *J. American Chemical Soc.* 1938, **60:** 309–319.

Buckley, J.S., “Wettability Effect In Crude Oil”, 2008, http://baervan.nmt.edu/petrophysics/mixed-wetting-in-micromodel.wmv

Buckley, S.E. and Leverett, M.C., “Mechanism of displacement in sands”, *Trans. AIME,* 1942, **146**, pp. 107-116.

Buckley, J.S. and Liu, Y., "Some Mechanisms of Crude Oil/Brine/Solid Interactions," *J. Pet. Sci. Eng.* 1998, **20**, 155-160.

Chatzis I, Morrow N R, “Correlation of capillary number relationships for sandstone”, *Soc. Pet. Eng. J.,* 1984, pp. 555-562.

Chatzis, I., Morrow, N.R., and Lim, H.T., “Magnitude and Detailed Structure of Residual Oil Saturation”, *SPEJ*, 1983,**23** (2): 311–326. SPE-10681-PA.

Chen, Z.-X., “Some invariant solutions to two-phase fluid displacement problems including capillary effects”, *SPE Reservoir Engineering,* 1988, **3**, pp. 691-700.

Cheng, J.T., Pyrak-Nolte, L.J., Nolte, D.D, and Giordano, N., “Linking Pressure and Saturation Through Interfacial Areas in Porous Media”, *Geophysical Research Letters,* 2004, **31:** L08502.

Cil, M. & Reis, J.C., “A multi-dimensional, analytical model for counter-current water imbibition into gas-saturated matrix blocks”, *J. Pet. Sci. Eng*, 1996.16, 61-69.

Corey, A.T., “Mechanics of Immiscible Fluids in Porous Media”, Water Resources Publications, Colorado, 1994.

CRC Handbook of Chemistry and Physics, 1976-1977, CRC Press, 57th Edition, Cleveland, OH.

Dixit, A.B., McDougall, S.R., Sorbie, K.S. and Buckley, J.S., "Pore Scale Modeling of Wettability Effects and Their Influence on Oil Recovery", *SPEREE,* 1999, Feb, 2, 25-36.

Dong, M., F.A.L. Dullien, "A new Model for Immiscible Displacement in Porous Media", *Transp. Porous Media,* 27, 1997, 185.

Dong, M., F.A.L. Dullien, J.Zhou, "Characterization of Waterflood Saturation Profile Histories by the Complete Capillary Number", *Transp. Porous Media*, 31, 1998, 213.

Dong, M., Dullien, F.A. L., I. Chatzis, "Imbibition of Oil in Film Form over Water Present in Edges of Capillaries with an Angular Cross Section", *J. Colloid Interface Sci*., 172, 1995, 278.

Dong, M., Dullien, F. A. L., Dai, L. & D. Li, "Immisible displacement in the interacting capillary bundle model, Part1, Development of interacting capillary bundle model", *Transport in Porous Media*, 2005, 59, 1-18.

Dong, M., F.A.L. Dullien, L. Dai, D. Li, "Immiscible Displacement in the Interacting Capillary Bundle Model Part II. Applications of Model and Camparison of Interacting and Non-Interacting Cappilary Bundle Models", *Transp. Porous Media*, 63, 2006, 289.

Dullien, F.A.L., in: V. Kambiz (Eds), Handbook of Porous Media Marcel Dekker, Inc., New York, 2000, p. 53.

Everett, D.H. & Haynes, J.M., "Model studies of capillary condensation: 1. Cylindrical pore model with zero contact angle", *J. Colloid Interface Sci*., 1972, **38**, 128-137.

Fischer, H., 2006. "Oil recovery by spontaneous imbibition for a wide range of viscosity ratios", PhD dissertation, University of Wyoming, May 2006, p146.

Fischer, H. & Morrow, N.R., "Spontaneous imbibition with matched viscosities", SPE 96812, SPE Annual Technical Conference, Dallas, Texas, 2005.

Fischer, H. & Morrow, N.R., "Scaling of oil recovery by spontaneous imbibition for wide variation in aqueous phase viscosity with glycerol as the viscosifying agent", *J. Pet. Sci. Eng*, 2006, 52, 35-53.

Forbes, P., "Centrifuge Data Analysis Techniques: An SCA Survey on the Calculation of Drainage Capillary Pressure Curves from Centrifuge Measurements", Paper SCA 9714 presented at the Intl. Symposium of the SCA, Calgary, 7-10 September, 1997.

Fulcher R. A.,Jr., Ertekin, T., Stahl, C. D., Effect of capillary number and its constituents on two-phase relative permeability curves", *Journal of Petroleum Technology*. February, 1985, pp. 249-260.

Gauglitz, P.A., St. Laurent, C.M. & Radke, C.J., "An experimental investigation of gas-bubble breakup in constricted square capillaries", *J. Petroleum Technology*, Sept 1987, 1137-1146.

Gauglitz, P.A. & Radke, C.J., "The dynamics of liquid film breakup in constricted cylindrical capillaries", *J. Colloid Interface Sci*., 1990, **134**, 14-40.

Gladkikh M., Jain V., Bryant S., Sharma M.M., "Experimental and theoretical basis for a wettability-interfacial area-relative permeability relationship", SPE 84544 Annual Technical Conference and Exhibition, Denver, CO, USA, 5-8th October 2003

Gladkikh, M., and Bryant, S.L., "Influence of wettability on Petrophysical Properties during Imbibition in a Random Dense Packing of Equal Spheres", *JPSE*, 52, 2006, 19 -34.

Gladkikh, M., and Bryant, S., "Prediction of Imbibition from Grain-Scale Interface Movement", *Advances in Water Resources*, 30, 2007, 249 -260.

Goodman, T.R, "Application of Integral Methods to Transient Nonlinear Heat Transfer, *Advances in Heat Transfer*", 1964, **1**, pp.51-122.

Graham, J.W., J.G. Richardson, "Theory and Application of Imbibition Phenomena in Recovery of Oil", *Petroleum Transactions. AIME*, 216, 1959, 377.

Haines, W.B., "Studies in the Physical Properties of Soil v. the Hysteresis Effect in Capillary Properties and the Modes of Moisture Distribution Associated Therewith", *J. Agric. Sci.*, 1930, **20:** 97.

Hamon G. and Pellerin, F.M., "Evidencing Capillary Pressure and Relative Permeability Trends for Reservoir Simulation", SPE 38898 presented at the SPE Annual Technical Conference and Exhibition, San Antonio, Texas, 5–8 October, 1997.

Handy, L.L., "Determination of Effective Capillary Pressures for Porous Media from Imbibition" Data, *Petroleum Transactions of AIME*, (T.P. 8109), 1960,**219**, pp.75-80.

Hassanizadeh, S.M. and Gray, W.G., "Thermodynamic Basis of Capillary Pressure in Porous Media", *Water Resources Research*, 1993, **29,** 10, 3389–3405.

Hatiboglu, C.U. & Babadagli, T., "Oil recovery by counter-current spontaneous imbibition. Effects of matrix shape factor, gravity, IFT, oil viscosity, wettability, and rock type", *J. Pet. Sci. Eng.* doi:10.1016/j.petrol.2007.03.005

Heil, M. & White, J.P., "Airway closure: surface-tension-driven non-axisymmetric instabilities of liquid-lined elastic rings", *J. Fluid Mechanics*, 1962, **462**, 79-109.

Hughes, R.G. & Blunt, M.J., "Pore Scale Modeling of Rate Effects in Imbibition", *Transport in Porous Media*, 2000, **40**, 295–322.

Jain V., Bryant S., Sharma M.M., "Influence of wettability and saturation on liquid-liquid interfacial areas", *Environ. Sci. Technol*., 2003, 37, 584-591.

Joscelyne, S.M. and Tragårdh, G., “Membrane emulsion – a literature review”, *Journal of Membrane Science*, 2000, 169, 107-117.

Kashchiev, D., Firoozabadi, A., “Analytical solutions for 1-D counter-current imbibition in water-wet media”, SPE 75166, Presented at the SPE/DOE Improved Oil Recovery Symposium, Tulsa, OK, USA, 2002.

Kashchiev, D. and Firoozabadi, A., “Analytical solutions for 1D countercurrent imbibition in water-wet media”, *SPEJ*, 2003, **8**, pp.401-408.

Kim H., Rao S.C., Annable M.D., “Determination of effective air-water interfacial area in partially saturated porous media using surfactant adsorption”, *Water Resources Research*, 33 , 2705-2711, Dec 1997

Kobayashi, I., Mukataka, S., Nakajima, M., “Novel asymmetric through-hole array microfabricated on a silicon plate for formulating monodisperse emulsions”, *Langmuir*, 2005, 21, 7629-7632.

Kovscek, A.R. & Radke, C.J., “Gas bubble snap-off under pressure-driven flow in constricted noncircular capillaries”, *Colloids & Surfaces*, 1996, **117**, 55-76.

Kovscek, A.R. & Radke, C.J., “Pressure-driven capillary snap-off if gas bubbles at low wetting-liquid content”, *Colloids & Surfaces A*, 2003, **212**, 99-108.

Kovscek, A.R., Tang, G.-Q. & Radke, C.J., “Verification of Roof snap off as a foam-generation mechanism in porous media at steady state”, *Colloids & Surfaces*, 2007, **302**, 251-160.

Kovscek, A.R., Wong, H., and Radke, C.J., "A Pore-Level Scenario for the Development of Mixed Wettability in Oil Reservoirs," *AIChE J.,* June 1993, **39**, No. 6, 1072-1085.

Kyte, J.R., Rapoport, L.A., “Linear behavior and end effects in water-wet porous media”, *Petroleum Trans. AIME*, 1958, v.213, pp.423-426.

Le Guen, S.S. & Kovscek, A.R., “Nonequilibrium effects during spontaneous imbibition”, *Transp. Porous Media*, 2006, 63, 127-146.

Lenormand, R., R., E. Toubul, C. Zarcone, “Numerical models and experiments on immiscible displacements in porous media”, *J. Fluid Mech*., 189, 1988, 165-187.

Leverett, MC., “Flow of oil-water mixtures through unconsolidated sands. *Trans. AIME,* 1939, 132, 151-169.

Leverett, M.C., “Capillary Behavior in Porous Solids”, *Trans.,* AIME , 1941, **142,** 152–169.

Li, R-Q., Wraith, A.E. & Harris, R., "Gas dispersion phenomena at a narrow slot submerged in a liquid", *Chemical Engineering Science*, 1994, 49, 531-540.

Li, Y & Wardlaw, N.C., "The influence of wettability an critical pore-throat size ratio on snap off", *J. Colloid Interface Sci*., 1986a, **109**, 461-472.
Li, Y & Wardlaw, N.C., "Mechanisms of nonwetting phase trapping during imbibition at slow rates", *J. Colloid Interface Sci*., 1986b, **109**, 473-496.

Li, Y., Laidlaw, W.C., and Wardlaw, N.C., "Sensitivity of drainage and imbibition to pore structure as revealed by computer simulation of displacement process", *Advances in Colloid & Interface Science*, 1986, 26, 1-68.

Li,Y., Morrow,N.R., Ruth,D.W., "Similarlity solution for linear counter-current spontaneous imbibition", *Journal of Petroleum Science and Engineering*, 2003, 39, pp. 309-326.

Li, Y., Ruth, D., Mason, G., Morrow, N.R., "Pressures acting in counter-current spontaneous imbibition", *J. Pet. Sci. Eng*. 2006, 52, 87-99.

Li, Y, Mason, G., Morrow, N.R. & Ruth, D.W., "Capillary pressure at the imbibition front during water/oil counter-current spontaneous imbibition", *Transport in Porous Media*, 2008, in press.

Loimer, T., Machu, G. & Schaflinger, U., "Inviscid bubble formation on porous plates and sieve plates", *Chemical Engineering Science*, 2004, 59, 809-818.

Ma, S., Mason, G. and Morrow, N.R., "Effect of Contact Angle on Drainage and Imbibition in Regular Polygonal Tubes," PS-1191, *Colloids and Surfaces,* **117**, 1996, 273-291

Ma, S., Zhang, X., Morrow, N.R., "Influence of fluid viscosity on mass transfer between rock matrix and fractures", *Journal of Canadian Petroleum Technology*, 1999, v.38, no.7, pp.25-30.

Ma, S., Morrow, N.R., Zhang, X., "Generalized scaling of spontaneous imbibition data for strongly water-wet systems", *Journal of Petroleum Science and Engineering*, 1997.v.18, 165-178.

Ma, S., Zhang, X., and Morrow, N.R.: "Influence of Fluid Viscosity on Mass Transfer Between Rock Matrix and Fractures" *J. Can. Pet. Tech*., July 1999, 38, (7) 25-30.

Masalmeh, S.K., "Studying the Effect of Wettability Heterogeneity on the Capillary Pressure Curves using the Centrifuge Technique", *JPSE*, 33, 1-3, April 2002, 29 -38.

Mason, G., "An Experimental Determination of the Stable Length of a Cylindrical Bubble", *J. Colloid Interface Science*, 1970,**32,** 172-176.

Mason, G., "Mobilisation of Oil Blobs in the Pore Space of a Random Sphere Packing", Chem. Eng. J. 38, 1983, 1455.

Mason, G. and Morrow, N.R.: "Meniscus Curvatures in Capillaries of Uniform Cross Section," *J.C.S. Faraday Trans. I.*, 1984, 80, 2375.

Mason, G. and Morrow, N.R.: "Meniscus Displacement Curvatures of Perfectly Wetting Liquid in Capillary Pore Throats Formed by Spheres," *J. Coll. Inter. Sci.,* Jan. 1986, **109**, 46-56.

Mason, G. and Morrow, N.R., "Meniscus Configurations and Curvatures in Non-Asymmetric Pores of Open and Closed Uniform Cross-Section", *Proc. Royal Soc. London*, (1987), A414, 111-33.

Mason, G. and Morrow N.R., "Capillary Behavior of a Perfectly Wetting Liquid in Irregular Triangular Tubes", *J. Coll. Inter. Sci.*, Jan. 1991, 141, 262-74.

Mason, G. and Morrow, N.R.: "Effect of Contact Angle on Capillary Displacement Curvatures in Pore Throats Formed by Spheres," *J. Coll. Inter. Sci.,* 1994, **168**, 130-41.

Mason, G. and Morrow, N.R., "Counter-Current Spontaneous Imbibition into Model Systems", in press. Studies in Surface Science and Catalysis, Characterization in Porous Solids VII (COPS VII). Copyright 2005 by Elsevier Science B.V.

Mason, G., Morrow, N.R., Walsh, T.J., "Interaction Between Menisci in Adjacent Pores", *Stud. Surf. Sci. Catal.*, 128, 2000, 495-504.

Mason, G., Nguyen, M.D., and Morrow, N.R., "Effect of Contact Angle on the Meniscus between Two Equal Contacting Rods and a Plate," *J. Coll. Inter. Sci*., 1983, 95, 494.

Mattax, C.C., Kyte, J.R., Imbibition oil recovery from fractured, water-drive reservoir. *SPEJ*, June, 1962, 177-184.

Matthews, G.P., Ridgway, C.J. & Spearing, M.C., "Void space modeling of mercury intrusion hysteresis in sandstone, paper coating and other porous-media", *J. Colloid Interface Sci*., 1995, **171**, 8-27.

Mayer, R.P. and Stowe, R.A., "Mercury Porosimetry—Breakthrough Pressure for Penetration between Packed Spheres," *J. Coll. Interface Sci.,* 1965, **20**, 893-911.

Melrose, J.C., "Wettability as Related to Capillary Action in Porous Media", *SPE Journal,* Sept. 1965, 259 – 270.

Melrose, J.C., Dixon, J.R., and Mallinson, J.E., "Comparison of Different Techniques for Obtaining Capillary Pressure Data in the Low-Saturation Region", *SPEFE,* 1994, **9** (3): 185–192. SPE-22690-PA.

Melrose, J.C., "Valid Capillary Pressure Data at Low-Wetting Phase Saturations, SPE 18331, *SPE Reservoir Engineering*, 5, 1, Feb. 1990, 95 – 99.

Melrose, J.C., "Interpretation of Mixed Wettability States in Reservoir Rocks," paper SPE 10971 presented at the 1982 SPE Annual Fall Technical Conference and Exhibition, New Orleans, Sept. 26-29.

McWhorter, D.B. and Sunada, D.K., "Exact solutions for two-phase flow", *Water Resources Research*, 1990, **26**, pp.399-413.

Mitrovic, J., "Upon equilibrium of gas bubble in infinite liquid", *Chemical Engineering Science*, 2000, 55, 2265-2270.

Monick, John A., Alcohols: their chemistry, properties and manufacture. Reinhold Book Corp., New York. 1968.

Morrow, N.R., "Physics and thermodynamics of capillary action in porous media", *I&EC* 1970

Morrow, N.R.: "Irreducible Wetting Phase Saturations in Porous Media," *Chem. Eng. Sci.,* 1971, **25**, 1799-1815.

Morrow, N.R., "The Effects of Surface Roughness on Contact Angle with Special Reference to Petroleum Recovery", *J. Cdn. Pet. Tech.* 1975, **14,** October–December, 42 - 53.

Morrow, N.R., "Wettability and Its Effect on Oil Recovery," SPE Distinguished Author Series *J. Pet. Tech*., Dec. 1990, **42** (12), 1476-84.

Morrow, N. R. and Mason, G., "Recovery of oil by spontaneous imbibition", *Current Opinion in Colloid and Interface Science,* 2001, 6, 321–337.

Morrow, N.R. and McCaffery F.G., Fluid Displacement Studies in Uniformly Wetted Porous Media. *Wetting, Spreading and Adhesion*, ed. J.F. Padday, 289–319. New York City: Academic Press, 1978.

Morrow, N.R., Buckley, J.S., Cather, M.E.. "Rock Matrix and Fracture Analysis of Flow in Western Tight Gas Sands". Final Report to the US Dept. of Energy, 155–169, February 1990.

Morrow, N.R., Chatzis, I., and Taber, J.J., "Entrapment and Mobilization of Residual Oil in Bead Packs:, *SPERE,* 1988, **3** (4): 927–934. SPE-14423-PA.

Morrow, N.R., and Mason, G., "Recovery of oil by spontaneous imbibition", *Curr. Opin. Colloid and Interface Sci*., 2001, **6**, 321-337.

Mysels, K.J., "The maximum bubble pressure method of measuring surface tension, revisited", *Colloids and Surfaces*, 1990, 43, 241-262.

Nakashima, T, Shimizu, M. and Kukizaki, "Particle control of emulsion by membrane emulsification and its applications", *Advanced Drug Delivery Reviews*, 2000, 45, 47-56.

Nicholson, D., J.H. Petropoulos, “Capillary Models for Porous Media: III. Two-phase flow in a three-dimensional network with Gaussian radius distribution”, *J. Physics D: Applied Physics*, 4 (1971) 181.

Nicholson, D., J.H. Petropoulos, “Capillary models for porous media: IV. Flow properties of parallel and serial capillary models with various radius distributions”, *J. Physics D: Applied Physics*, 6, 14, 1973, 1737.

Øren, P.-E., Bakke, S., and Arntzen, O.J., “Extending Predictive Capabilities to Network Models,” *SPEJ,* Dec. 1998, 324-336.

Patzek, T.W., “Verification of a Complete Pore Network Simulator of Drainage and Imbibition”, SPE 71310, *SPE Jounral*, 6, 2, June 2001, 144 – 156.

Patzek, T.W., J.G. Kristensen, “Shape Factor Correlations of Hydraulic Conductance in Noncircular Capillaries I. One-Phase Creeping Flow”, *J. Colloid Interface Sci*. 236, 2001, 295.

Patzek, T.W., D.B. Silin, “Shape Factor Correlations of Hydraulic Conductance in Noncircular Capillaries II. Two-Phase Creeping Flow”, J. Colloid Interface Sci. 236, 2001, 305.

Payne, D., “A Method for the Determination of the Approximate Surface Areas of Particulate Solids”, *Nature,* 1953, **172,** 261.

Pirson, S., 1958. *Oil Reservoir Engineering*, McGraw-Hill New York.

Plateau, J., Statique Experimentale et Theorique des Liquides Soumis aux Seules Forces Moleculaire, Vol.2, Gauthier-Villars, Paris. 1873

Pooladi-Darvish, M. and Firoozabadi, A., “Experiments and Modeling of Water Injection in Water-Wet Fractured Porous Media”, *J. Can. Pet. Tech*., 2000, Mar, **39**, 3:31-42.

Princen, H.M., “Capillary phenomena in assemblies of parallel cylinders, I”, *Journal of Colloid and Interface Science*. 1969a, **30**, 69-75.

Princen, H.M., “Capillary Phenomena in Asseblies of Parallel Cylinders, II. Capillary Rise in Systems with More Than Two Cylinders”, *J. Coll. Inter. Sci*., 30, 3, July 1969b, 359.

Princen, H.M., “Capillary Phenomena in Assemblies of Parallel Cylinders, III. Journal of Colloid and Interface Science”, 1970, **34**, 171-184.

Princen, H.M.: "Capillary pressure behavior in pores with curved triangular cross-section: effect of wettability and pore size distribution," *Colloids and Surfaces* (1992) **65**, 221-230.

Purcell, W.R. “Capillary Pressures—Their Measurement Using Mercury and the Calculation of Permeability Therefrom”, *Trans.,* AIME 1949, **186:** 39–48.

Purcell, W.R., "Interpretation of Capillary Pressure Data", *Trans,* AIME, 1950, 189, 369.

Raimondi, P. and Torcaso, M.A., "Distribution of the Oil Phase Obtained Upon Imbibition of Water", *SPEJ*, 1964, Mar, 49-55.

Rangel-German, E.R. & Kovscek, A.R., "Experimental and analytical study of multidimensional imbibition in fractured porous media", *J. Pet. Sci. Eng.,* 2002, 36, 45-60.

Ransohoff, T.C., Gauglitz, P.A., Radke, C.J., "Snap-off of gas bubbles in smoothly constricted non-circular capillaries", *AIChE Journal*, 1987, **33**, 753-765.

Ransohoff, T.C., C.J. Radke, "Laminar Flow of a Wetting Liquid along the Corners of a Predominantly Gas-Occupied Noncircular Pore", *J. Colloid Interface Sci*. 121, 2, 1988, 178.

Rapoport, L.A., "Scaling laws for use in design and operation of water-oil flow models", *Trans.* AIME, 1955, .204, 143-150.

Rapoport, L.A. and Leas, W.J., "Relative Permeability to Liquid in Liquid-Gas Systems", *Trans.,* AIME, 1951, **192:** 83–98.

Rapoport, L.A., Leas, W.J., "Properties of linear waterfloods", *Trans.* AIME, 1953, 198, pp139-148.

Rapoport, L. A., "Scaling laws for use in design and operation of water-oil flow models, P*etroleum Trans*. AIME, 1955, (T.P. 4121) 204, 143–150.

Rayleigh, Lord, "Scientific Papers", Vol. I, pp. 377-401, Cambridge University Press, London 1899.

Raynor, M., Trägårdh, G., Trägårdh, C. & Dejmek, P., "Using the Surface Evolver to model droplet formation processes in membrane emulsification", *J. Colloid Interface Sci*.., 2004, 279, 175-185.

Reeves, P.C. and Celia, M.A., "A Functional Relationship between Capillary Pressure, Saturation, and Interfacial Area as Revealed by a Pore-Scale Network Model", *Water Resources Research,* 1996, **32** (8), 2345–2358.

Reis, J.C. & Cil, M., "A model for oil expulsion by counter-current water imbibition in rocks: one-dimensional geometry", *J. Pet. Sci. Eng*., 1993, 10, 97-107.

Richtmyer, R.D., Morton, K.W., Difference Methods for Initial-Value Problem, 2nd edn., Interscience*,* Publishers, New York, 1973.

Roof, J.G., "Snap-off of oil droplets in water-wet pores", *Society of Petroleum Engineers Journal*, 1970, 10, 85-95.

Root, L., Berne, B.J., "Effect of pressure on hydrogen bonding in glycerol: a molecular dynamics investigation", *J. Chem. Phys* 1997, 107 (11), pp. 4350-4357.

Rootare, H.M. and Prenzlow, C.F., "Surface Area from Mercury. Porosimeter Measurements", *J Phys. Chem.* 1967, **71:** 2733–2736.

Rossen, W.R., Comment on "Verification of Roof snap-off as a foam-generation mechanism in porous media at steady state", *Colloids and Surfaces A*, 2008, 322, 261-269.

Russ, John C. and Dehoff, Robert T., *"Practical Stereology"*, 2nd edition, Kluwer Academic/Plenum Publishers, New York, NY, 2000.

Ruth, D. and Bartley, J., "A Perfect-Cross-Flow Model for Two Phase Flow in Porous Media." Proc. 2002 International Symposium of the Society of Core Analysts, Monterey, California, 2003, SCA2002-05, pp12.

Ruth, D.W., Li, Y., Mason, G. and Morrow, N.R., "An approximate analytical solution for counter-current spontaneous imbibition", *Transport in Porous Media*, 2007, 66, 373–390.

Ruth, D.W., Mason, G., and Morrow, N.R., "A numerical study of the influence of sample shape on spontaneous imbibition, Proc. Int. Sym. of SCA, Pau, France, 2003, Paper 2003-55.

Ruth, D.W, Mason, G., Morrow, N. and Li, Y., "The effect of fluid viscosities on counter-current spontaneous imbibition", Proc. Int. Sym. of SCA, Abu Dhabai, UAE, 2004, Paper 2004-56.

Ruth, D., Morrow, N.R., Li, Y., Buckley, J.S., "A simulation study of spontaneous imbibition", Proceedings of the International Society of Core Analysts Annual Meeting, Abu Dhabi, UAE, Oct. 2000.

Ruth, D. and Wong, S., "Calculation of Capillary Pressure Curves from Data Obtained by the Centrifuge Method". *The Log Analyst,* 1991, **32** (5): 575–582.

Sabatier, L., "Comparative Study of Drainage Capillary Pressures Using Different Techniques and for Different Fluid System". Paper presented at the Intl. Symposium of the SCA, Stavanger, 1994.

Sallier, B. and Hamon, G., "Micritic Limestone of the Middle-East: Influence of Wettability, Pore Network and Experimental Technique on Drainage Capillary Pressure Curve", Paper presented at the Intl. Symposium of the SCA, Toronto, 21–25 August 2005.

Salathiel, R.A., "Oil Recovery by Surface Film Drainage in Mixed-Wettability Rocks," *J. Pet. Tech.,* Oct. 1973. 1216-24; *Trans.*, AIME, **255**.

Schaefer, C.E, DiCarlo, D.A., and Blunt, M., "Determination of Water-Oil Interfacial Area during 3-Phase Gravity Drainage in Porous Media", *J. Colloid and Interface Science,* 2000a, **221:** 308–312.

Schaefer, C.E., DiCarlo, D.A., and Blunt, M.,. "Experimental Measurement of Air-Water Interfacial Area during Gravity and Secondary Imbibition in Porous Media", *Water Resources Research,* 2000b, **36** (4): 885–890.

Seth, S., "Increase in Surface Energy by Drainage of Sandstone and Carbonate", PhD thesis, U. of Wyoming, Laramie, Wyoming, 2006.

Seth, S. and Morrow, N.R., "Efficiency of conversion of work of drainage to surface energy for a sandstone", SPE 102490, *SPE Reservoir Evaluation & Engineering,* August 2007, 338-347.

Silin, D. and Patzek, T., z"On Barenblatt's Model of Spontaneous Imbibition", *Transport in Porous Media*, 2004, **54**, pp.297-322.

Sisavath, S., X. Jing, R.W, Zimmerman, " Laminar Flow Through Irregularly-Shaped Pores in Sedimentary Rocks ", *Transp. Porous Media*. 45, 1, 2001, 41-62.

Standnes, D.C., "Spontaneous imbibition of water into cylindrical cores with high aspect ratio: Numerical and experimental studies", *J. Pet. Sci. Eng*. 2006, 50, 151-160.

Strand, S., Standnes, D.C., and Austad, T., "Spontaneous Imbibition of Aueous Surfact Solutions into Neutral to Oil-West Carbonate Cores: Effect of Brine Salinity and Composition" *Energy & Fuels*, 2003, 17, 1133-1144.

Sugiura, S., Nakajima, M., Iwamoto, S & Seki, M., "Interfacial tension driven monodispersed droplet formation from microfabricated channel arrays", *Langmuir,* 2001, 17, 5562-5566.

Sugiura, S., Nakajima, M., Kumazawa, N., Iwamoto, S & Seki, M., "Characterization of spontaneous transformation-based droplet formation during microchannel emulsification", *J. Phys. Chem. B*, 2002, 106, 9405-9409.

Swanson, B.F., "Rationalizing the Influence of Crude Wetting on Reservoir Fluid Flow with Electrical Resistivity Behavior," *JPT* , Aug. 1980, 1459-1464.

Tang, G.Q. and Morrow, N.R., "Salinity Temperature, Oil Composition and Oil Recovery by Waterflooding," *SPE Reservoir Engineering,* November 1997, **12**, (4) 269-276.

Tang, G. and Morrow, N.R., "Influence of Brine Composition and Fines Migration on Crude Oil/Brine/Rock Interactions and Oil Recovery" *J. Pet. Sci. Eng*, **24**, Dec. 1999, 99-111.

Tate, T., "On the magnitude of a drop of liquid formed under different circumstances", *The London, Edinburgh, and Dublin Philosophical Magazine*, 1864, 27, p176-180.

Tavassoli, Z, Zimmerman, R.W., & Blunt, M.J., "Analytic analysis for oil recovery during counter-current imbibition in strongly water-wet syatems", *Transp. Porous Media*, 2005. **58**, 173-189

Tie, H., “Oil recovery from Carbonates”, PhD thesis, U. of Wyoming, Laramie, Wyoming, 2006.

Tie, H.G., Tong, Z.X., and Morrow, N.R., “The Effect of Different Crude Oil/Brine/Rock Combinations on Wettability through Spontaneous Imbibition” Proceedings of the International Society of Core Analysts Annual Meeting, Pau, France, Sept., 2003.

Tie, H. and Morrow, N.R., “Low-Flood-Rate Residual Saturations in Carbonate Rocks”. Paper IPTC 10470 presented at the International Petroleum Technology Conference, Doha, Qatar, 21–23 November, 2005.

Tong, Z., Xie, X., Morrow, N.R., “Scaling of viscosity ratio for oil recovery by imbibition from mixed-wet rocks”, *Petrophysics*, 2002, 43, 4, pp. 332-340.

Treiber, L.E., Archer, D.L., and Owens, W.W., "A Laboratory Evaluation of the Wettability of Fifty Oil-Producing Reservoirs," *SPEJ,* Dec. 1972, 531-540.

Tsai, T.M. & Miksis,M.J., “Dynamics of a drop in a constricted capillary tube”, *Journal of Fluid Mechanics*, 1994, 274, 197-217.

Tsakiroglou, C.D. & Payatakes, A.C., “A new simulator of mercury porosimetry for the characterization of porous materials”, *J. Colloid Interface Sci*., 1990, 137, 315-339.

Underwood, Ervine E., *“Quantitative Stereology”*, Addison-Wesley Publishing Company, Reading, MA, 1970.

Unsal, E., Mason, G., Morrow, N.R. and Ruth, D.W., “Spontaneous co- and counter-current imbibition into model pore systems”, presented at the 7th International Symposium on the Charaterization of Porous Solids, Aix-en-Provence, France, 26-28 May 2005.

Unsal, E., Mason, G., Ruth, D.W., Morrow, N.R., “Co- and counter-current imbibition in independent tubes”, *J. Colloid Interface Sci*., 2007a, **306**, 105-117.

Unsal, E., Mason, G., Ruth, D.W., Morrow, N.R., “Co- and counter-current spontaneous imbibition into groups of capillary tubes with lateral connections permitting cross flow”, *J. Colloid Interface Sci.*, 2007b, **315**, 200-209.

van de Ven, T. G. M., 1989. Colloidal Hydrodynamics, Academic Press, San Diego, 1989.

Viksund, B.G., Morrow, N.R., Ma, S., Wang, W., Graue, A.., “Initial Water Saturation and Oil Recovery From Chalk and Sandstone by Spontaneous Imbibition” Proceedings International Symposium of Society of Core Analysts, The Hague, September 1998.

Vladisavljević, G.T. & Schubert, H., “Influence of process parameters on droplet size distribution in SPG membrane emulsification and stability of prepared emulsion drops”, *J. of Membrane Science*, 2003, 225, 15-23.

Wade, L. G., Organic Chemistry; Englewood Cliffs, N.J., Prentice-Hall, 1987.

Wan, J. and Tokunaga, T., "Partitioning of Clay Colloids at Air–Water Interfaces", *J. Coll. Interf. Sci.* 2002, **247:** 54–61.

Wang, R., "Gas recovery from porous media by spontaneous imbibition of liquid", MS Thesis, University of Wyoming, 1999.

Wardlaw, N.C. and Casson, J.P., "Oil Recovery Efficiency and the Rock-Pore Properties of Some Sandstone Reservoirs", *Bull. Cdn. Petr, Geol*. 1979, **27:** 117–138.

Wardlaw, N.C., Li, Y., "Fluid topology, pore size and aspect ratio during imbibition"*, Transport in Porous Media*, 1988, 3, pp. 17-34.

Wardlaw, N.C., Li, Y., and Forbes, D., "Pore-Throat Size Correlation from Capillary Pressure Curves", *Transport in Porous Media,* 1987, **2:** 597–614.

Wardlaw, N.C., Taylor, R.P., "Mercury capillary pressure curves and the interpretation of pore structure and capillary behavior in reservoir rocks", *Bull. Can. PETR. Geol.* 1976, 24, pp. 225-262.

Washburn, E.W., "The Dynamics of Capillary Flow", *Physical Review*, 1921, 17, 273-283.

Walsh, T.J., "Capillary properties of model pores". PhD Thesis, Loughborough University of Technology, 1989.

Wells, J.D. and Amaefule, J.O., "Capillary Pressure and Permeability Relationships in Tight Gas Sands", Paper SPE 13879 presented at the SPE/DOE Low Permeability Gas Reservoirs Symposium, Denver, 19–22 March, 1985.

Wo, S., "User Guide for ImbiSim," University of Wyoming, USA, May, 2002.

Xie, X., and Morrow N.R, "Oil recovery by spontaneous imbibition from weakly water-wet rocks", *Petrophysics*, 2001, 42, 4, pp. 313-322.

Xie, X., Wiess, W., Tong, Z.X., and Morrow, N.R., "Improved Oil Recovery from Carbonate Reservoirs by Chemical Stimulation", *SPEJ*, Sept. 2005, 276 – 285.

Yildiz, H.O., Gokmen, M, & Cesur, Y., "Effect of shape factor, characteristic length, and boundary conditions on spontaneous imbibition", *J. Pet. Sci. Eng*. 2006, 53, 158-170.

Yuan, H.H., "Pore-Scale Heterogeneity from Mercury Porosimetry Data", *SPEFE* , 1991.6, 2, 233–240; *Trans.*, AIME, 291. SPE-14892-PA.

Yortsos, Y. and Fokas, A.S., "An analytical solution for linear waterflood including the effects of capillary pressure", *SPEJ*, 1983, **23**, pp.115-124.

Zhang H., Liu Q., Li, F., Lu, Y., "Variations in Petrophysical Properties after Sandstone Reservoirs Watered Out in Daqing Oil Field", *SPE Advanced Technology Series*, 1995, Vol. **5**, No. 1, 128-139

Zhang, X., Morrow, N.R., MA, S., "Experimental verification of a modified scaling group for spontaneous imbibition", *SPE Reservoir Engineering*, Nov. 1996, pp.280-285.

Zhou, D., Jia, L., Kamath, J. and Kovscek, A.R., "Scaling of Counter-Current Imbibition Process in Low-Permeability Porous Media", *J. Petr. Sci. Eng*., 2002, 33, 61-74.

Zhou, X., Morrow, N.R., Ma, S., "Interrelationship of wettability, initial water saturation, aging time, and oil recovery by spontaneous imbibition and waterflooding", *SPE Journal*, Jun. 2000, v.5. 2.

Zimmerman, R.W., Bodvarsson, G.S. and Kwicklis, E.M., "Absorption of water into porous blocks of various shapes and sizes", *Water Resources Research*, 1990, 26, 2797-2806.

National Energy Technology Laboratory

626 Cochrans Mill Road
P.O. Box 10940
Pittsburgh, PA 15236-0940

3610 Collins Ferry Road
P.O. Box 880
Morgantown, WV 26507-0880

One West Third Street, Suite 1400
Tulsa, OK 74103-3519

1450 Queen Avenue SW
Albany, OR 97321-2198

2175 University Ave. South
Suite 201
Fairbanks, AK 99709

Visit the NETL website at:
www.netl.doe.gov

Customer Service:
1-800-553-7681